

# Spectroscopy in Materials Chemistry

Guest Editors: Tifeng Jiao, Nikša Krstulović, Bing Wu, Xinqing Chen, and Qingrui Zhang



# Spectroscopy in Materials Chemistry

Journal of Spectroscopy

---

## **Spectroscopy in Materials Chemistry**

Guest Editors: Tifeng Jiao, Nikša Krstulović, Bing Wu,  
Xinqing Chen, and Qingrui Zhang



---

Copyright © 2015 Hindawi Publishing Corporation. All rights reserved.

This is a special issue published in "Journal of Spectroscopy." All articles are open access articles distributed under the Creative Commons Attribution License, which permits unrestricted use, distribution, and reproduction in any medium, provided the original work is properly cited.

## Editorial Board

João Abrantes, Portugal	Roberto Flammini, Italy	Yehia Mechref, USA
Khalique Ahmed, USA	Anatoly Frenkel, USA	Gellert Mezei, USA
Faisal M. Alamgir, USA	Nives Galicfh, Croatia	Shinichi Morita, Japan
Wolfgang Anwand, Germany	Javier Garcia-Guinea, Spain	Kouichi Nakagawa, Japan
Gabriele Arnold, Germany	Martin Giera, Netherlands	Austin Nevin, Italy
Naoki Asakawa, Japan	Gianfranco Giubileo, Italy	Masaki Oura, Japan
Luciano Bachmann, Brazil	Andras Gorzsas, Sweden	Giancarlo Pace, Portugal
Mark A. Baker, UK	S. P. Hernandez-Rivera, Puerto Rico	C. Andres Palacio, Belgium
Adam G. Balogh, Germany	Tino Hofmann, USA	Jisheng Pan, Singapore
Malgorzata Baranska, Poland	Shuchen Hsieh, Taiwan	Jose M. Pedrosa, Spain
Lahcen Bih, Morocco	Xinyang Huang, China	Simona C. Pinzaru, Romania
Dhananjay Bodas, India	Hiromi Ikeura-Sekiguchi, Japan	Piotr Przybylski, Poland
Lars H. Böttger, Germany	Fumiyuki Ito, Japan	Maria Ramil, Spain
Damien Boyer, France	Rodolphe Jaffiol, France	K. S. V. Krishna Rao, India
Stefano Caldarelli, France	Christopher K. Jankowski, Canada	Ihtesham ur Rehman, UK
Jose S. Camara, Portugal	ZhiLiang Jiang, China	Tomasz Ruman, Poland
Brian Cannon, USA	Dale Keefe, Canada	Davidson Sajan, India
Elizabeth A. Carter, Australia	Rizwan Hasan Khan, India	Alan C. Samuels, USA
Jairo Castillo-Chara, USA	Jeongkwon Kim, Republic of Korea	Stephane Schilt, Switzerland
Wee Chew, Singapore	Scott J. Kirkby, USA	Feride Severcan, Turkey
Jau-Wern Chiou, Taiwan	Piotr Koczon, Poland	Zhifeng Shao, USA
Daniel O. Cicero, Italy	Nikolaos Kourkoumelis, Greece	Masanori Shinohara, Japan
Malcolm R. Clench, UK	Christoph Krafft, Germany	Maciej Sitarz, Poland
Stephen Cooke, USA	Nika Krstulović, Croatia	Rafal Sitko, Poland
Daniel Cozzolino, Australia	Violeta Lazic, Italy	Massimo Tallarida, Germany
Vincenza Crupi, Italy	Adam F. Lee, UK	Riad Ternane, Tunisia
Arnaud Cuisset, France	Young Jong Lee, USA	Pedro D. Vaz, Portugal
Eugen Culea, Romania	Nicolae Leopold, Romania	Stéphane Viel, France
Eric Da Silva, Canada	Min Soo Lim, USA	Annemarie Wagner, Sweden
Lesley Davenport, USA	Alessandro Longo, Italy	Thomas Walther, UK
Alessandro De Giacomo, Italy	Paola Luches, Italy	Chuji Wang, USA
Marcella Dell'aglio, Italy	Burkhard Luy, Germany	Chih-Che Wu, Taiwan
Renata Diniz, Brazil	Mahmoud A. Mahmoud, USA	Lu Yang, Canada
Ana Dominguez-Vidal, Spain	Petre Makreski, Macedonia	M. Carmen Yebra-Biurrun, Spain
Christophe Dujardin, France	Dmitriy Malinovsky, UK	Guoqiang Yu, USA
Thomas R. Eykyn, UK	Djordje Mandrino, Slovenia	Kassym Zhumadilov, Japan
Michele Fedel, Italy	Artem E. Masunov, USA	Z. D. Zujovic, New Zealand
Davide Ferri, Switzerland	Thomas G. Mayerhofer, Germany	M. Gizdavic-Nikolaidis, New Zealand

## Contents

**Spectroscopy in Materials Chemistry**, Tifeng Jiao, Nikša Krstulović, Bing Wu, Xinqing Chen, and Qingrui Zhang  
Volume 2015, Article ID 943894, 2 pages

**Spin-Glass Behavior, Magnetic, and IR Spectroscopy Analysis of Multimetallic Compound  $\text{Ni}_{0.25}\text{Mn}_{1.25}[\text{Fe}(\text{CN})_6]6.1\text{H}_2\text{O}$** , Qing Lin, Xiaofang Liu, Yun He, Haifu Huang, and Xingcan Shen  
Volume 2015, Article ID 385215, 6 pages

**Raman Spectroscopy for Understanding of Lithium Intercalation into Graphite in Propylene Carbonated-Based Solutions**, Yang-Soo Kim and Soon-Ki Jeong  
Volume 2015, Article ID 323649, 5 pages

**Solar Photocatalytic Degradation of Typical Indoor Air Pollutants Using  $\text{TiO}_2$  Thin Film Codoped with Iron(III) and Nitrogen**, Shuaijie Wang and Xingxing Cheng  
Volume 2015, Article ID 259829, 6 pages

**Effect of Contact Time and Gas Component on Interfacial Tension of  $\text{CO}_2$ /Crude Oil System by Pendant Drop Method**, Xin Wang, Lifeng Liu, Zengmin Lun, Chengyuan Lv, Rui Wang, Haitao Wang, and Dong Zhang  
Volume 2015, Article ID 285891, 7 pages

**Preparation and Application of Titanate Nanotubes on Dye Degradation from Aqueous Media by UV Irradiation**, Rui Liu, Wein-Duo Yang, Hui-Ju Chueng, and Bin-Qiao Ren  
Volume 2015, Article ID 680183, 9 pages

**Synthesis and Catalytic Performances of a Novel Zn-MOF Catalyst Bearing Nickel Chelating Diimine Carboxylate Ligands for Ethylene Oligomerization**, Suyan Liu, Ying Zhang, Quan Huo, Sasa He, and Yang Han  
Volume 2015, Article ID 310162, 7 pages

**Laser Raman Spectroscopy with Different Excitation Sources and Extension to Surface Enhanced Raman Spectroscopy**, Md. Wahadoszamen, Arifur Rahaman, Nabil Md. Rakinul Hoque, Aminul I Talukder, Kazi Monowar Abedin, and A. F. M. Yusuf Haider  
Volume 2015, Article ID 895317, 8 pages

**Improving Hyperspectral Image Classification Method for Fine Land Use Assessment Application Using Semisupervised Machine Learning**, Chunyang Wang, Zengzhang Guo, Shuangting Wang, Liping Wang, and Chao Ma  
Volume 2015, Article ID 969185, 8 pages

**Effects of Chlorinated Polypropylene on the Conformation of Polypropylene in Polypropylene/Chlorinated Polypropylene/Polyaniline Composites**, Jianjun Chen, Yueyue Jia, Zhiye Zhang, Xinlong Wang, and Lin Yang  
Volume 2015, Article ID 317813, 8 pages

**Evaluation of Temper Embrittlement of 30Cr2MoV Rotor Steels Using Electrochemical Impedance Spectroscopy Technique**, Zhang Shenghan, Lv Yaling, and Tan Yu  
Volume 2015, Article ID 957868, 7 pages

**Hydrothermal Synthesis of High Crystalline Silicalite from Rice Husk Ash,**

Chaiwat Kongmanklang and Kunwadee Rangsriwatananon

Volume 2015, Article ID 696513, 5 pages

**Setting Reaction of Dental Resin-Modified Glass Ionomer Restoratives as a Function of Curing Depth**

**and Postirradiation Time**, Young Kyung Kim, Kyo-Han Kim, and Tae-Yub Kwon

Volume 2015, Article ID 462687, 8 pages

**Synthesis and Characterization of an Iron Nitride Constructed by a Novel Template of Metal Organic**

**Framework**, Suyan Liu, Quan Huo, Rongna Chen, Peipei Chen, Yuan Li, and Yang Han

Volume 2015, Article ID 362103, 8 pages

**One-Step Synthesis of High-Quality Water-Soluble CdSe Quantum Dots Capped by N-Acetyl-L-cysteine**

**via Hydrothermal Method and Their Characterization**, Chunjin Wei, Jinyu Li, Fang Gao, Shuxia Guo,

Yongcui Zhou, and Dan Zhao

Volume 2015, Article ID 369145, 7 pages

**Characterization of the Key Material for Elimination of PM2.5 Particles in the Atmosphere**, Bo Qiu,

Qingshan Li, Wei Hong, and Guangzhong Xing

Volume 2015, Article ID 472019, 5 pages

**The Drug Metabolism and Pharmacokinetics Investigation about Baicalin Effect and Baicalein on Mice**

**U14 Cervical Cancer**, Zhanzhao Fu, Ya Di, Liming Gao, Jiandong Wu, Ming Shi, and Fulu Zheng

Volume 2015, Article ID 632062, 7 pages

**Infrared Spectroscopic Characterization of Photoluminescent Polymer Nanocomposites**, Kyle Gipson,

Kathryn Stevens, Phil Brown, and John Ballato

Volume 2015, Article ID 489162, 9 pages

**Characterization of Polysaccharide by HPLC: Extraction and Anticancer Effects**, Liming Gao, Ya Di,

Jiandong Wu, Ming Shi, and Fulu Zheng

Volume 2014, Article ID 751496, 8 pages

**Experimental Study of the Composition and Structure of Granular Media in the Shear Bands Based on**

**the HHC-Granular Model**, Guang-jin Wang, Xiang-yun Kong, and Chun-he Yang

Volume 2014, Article ID 232178, 7 pages

**Insights into the Synergistic Effect of Fungi and Bacteria for Reactive Red Decolorization**,

Dandan Zhou, Xueying Zhang, Yilin Du, Shuangshi Dong, Zhengxue Xu, and Lei Yan

Volume 2014, Article ID 237346, 4 pages

**Characterization of Binary Organogels Based on Some Azobenzene Compounds and Alkyloxybenzoic**

**Acids with Different Chain Lengths**, Yongmei Hu, Qingshan Li, Wei Hong, Tifeng Jiao, Guangzhong Xing,

and Qilong Jiang

Volume 2014, Article ID 970827, 10 pages

**Use of Novel Polyurethane Microspheres in a Curcumin Delivery System**, Yongmei Hu, Qingshan Li,

Wei Hong, Guangzhong Xing, Qilong Jiang, and Wenfeng Lv

Volume 2014, Article ID 926268, 7 pages

**Heat-Activated Persulfate Oxidation of Chlorinated Solvents in Sandy Soil**, Jialu Liu, Xijun Gong, Shijun Song, Fengjun Zhang, and Cong Lu  
Volume 2014, Article ID 578638, 5 pages

**Microstructural and Mössbauer Spectroscopy Studies of  $Mg_{1-x}Zn_xFe_2O_4$  ( $x = 0.5, 0.7$ ) Nanoparticles**, Jinpei Lin, Yun He, Qing Lin, Ruijun Wang, and Henian Chen  
Volume 2014, Article ID 540319, 5 pages

**Performance of a Novel Hydrophobic Mesoporous Material for High Temperature Catalytic Oxidation of Naphthalene**, Guotao Zhao, Zhenxiao Zhao, Junliang Wu, and Daiqi Ye  
Volume 2014, Article ID 136067, 7 pages

**Study on the Gelation of Foamed Gel for Preventing the Spontaneous Combustion of Coal**, Leilin Zhang and Botao Qin  
Volume 2014, Article ID 163742, 7 pages

**Analysis of the Oil Content of Rapeseed Using Artificial Neural Networks Based on Near Infrared Spectral Data**, Dazuo Yang, Hao Li, Chenchen Cao, Fudi Chen, Yibing Zhou, and Zhilong Xiu  
Volume 2014, Article ID 901310, 5 pages

**Infrared Spectroscopic Study on the Modified Mechanism of Aluminum-Impregnated Bone Charcoal**, Hao Li, Yufan Yang, Shuangjun Yang, Anpu Chen, and Dazuo Yang  
Volume 2014, Article ID 671956, 7 pages

**Spectral Separation for Multispectral Image Reproduction Based on Constrained Optimization Method**, Bangyong Sun, Han Liu, and Shisheng Zhou  
Volume 2014, Article ID 345193, 8 pages

**Liquid Chromatography-Tandem Mass Spectrometric Assay for Determination of Stavudine in Human Plasma**, Fengdan Jin  
Volume 2014, Article ID 517089, 5 pages

**Thickness-Controllable Silica Coating of CdTe QDs by Reverse Microemulsion Method for the Application in the Growth of Rice**, Aiwu Wang, Yuhong Zheng, and Feng Peng  
Volume 2014, Article ID 169245, 5 pages

**Size Effects: The Relation to the Percentage of Atoms That Participate in the Deformation of ZrCu Metallic Glass**, L. K. Gao, F. L. Zhao, N. Xu, L. Qi, and R. P. Liu  
Volume 2014, Article ID 627679, 5 pages

**Preparation and Characterization of Binary Organogels via Some Azobenzene Amino Derivatives and Different Fatty Acids: Self-Assembly and Nanostructures**, Haiying Guo, Tifeng Jiao, Xihai Shen, Qingrui Zhang, Adan Li, and Faming Gao  
Volume 2014, Article ID 758765, 7 pages

**Preparation and Characterization of P(AN-VAc-PMMT) Nanocomposites and Nanofibers**, Jun Liu, Yuguo Zhuo, Qingshan Li, Wei Hong, and Guangzhong Xing  
Volume 2014, Article ID 142691, 4 pages

---

**Synthesis of Hydrophobic Mesoporous Material MFS and Its Adsorption Properties of Water Vapor,**

Guotao Zhao, Zhenxiao Zhao, Junliang Wu, and Daiqi Ye

Volume 2014, Article ID 965037, 7 pages

**The Application of Resonance-Enhanced Multiphoton Ionization Technique in Gas Chromatography**

**Mass Spectrometry**, Adan Li, Jianzheng Song, Yang Sun, and Tifeng Jiao

Volume 2014, Article ID 134828, 8 pages

**Remote Sensing of CO<sub>2</sub> Absorption by Saline-Alkali Soils: Potentials and Constraints**, Wenfeng Wang,

Xi Chen, and Zhi Pu

Volume 2014, Article ID 425753, 8 pages

## Editorial

# Spectroscopy in Materials Chemistry

Tifeng Jiao,<sup>1</sup> Nikša Krstulović,<sup>2</sup> Bing Wu,<sup>3</sup> Xinqing Chen,<sup>4</sup> and Qingrui Zhang<sup>5</sup>

<sup>1</sup>School of Environmental and Chemical Engineering, Yanshan University, Qinhuangdao 066004, China

<sup>2</sup>Institute of Physics, Bijenička 46, 10000 Zagreb, Croatia

<sup>3</sup>Bodega Marine Laboratory, University of California, Davis, 2099 Westside Road, Bodega Bay, CA 94923, USA

<sup>4</sup>Department of Chemical and Biomolecular Engineering, Hong Kong University of Science and Technology, Clear Water Bay, Kowloon, Hong Kong

<sup>5</sup>Department of Environmental Engineering, Yanshan University, Qinhuangdao 066004, China

Correspondence should be addressed to Tifeng Jiao; [tfjiao@ysu.edu.cn](mailto:tfjiao@ysu.edu.cn)

Received 26 January 2015; Accepted 26 January 2015

Copyright © 2015 Tifeng Jiao et al. This is an open access article distributed under the Creative Commons Attribution License, which permits unrestricted use, distribution, and reproduction in any medium, provided the original work is properly cited.

Today, as nanotech continues to develop, materials chemistry is one of the key fields covering topics such as porous materials, metal-organic-framework materials, photocatalysts, magnetic materials, nanobiomaterials, and energy materials for fuel cells and batteries. The development of materials chemistry has made important progress through use of spectroscopic methods, such as UV-VIS-IR, OES, optical absorption spectroscopy, LIBS, XRD, vibrational spectroscopy, Raman/SERS/SERRS, photoluminescence, and photospectrometry/plasmonics, which are often supported by SEM, TEM, and AFM analyses to form the foundations of nanoscience and nanotechnology in recent decades. In addition, many scientists investigate also some special reaction mechanisms using spectroscopic tools.

This special issue addresses the research studies on the spectroscopy applications in materials chemistry. For example, W. Wang et al. reported the CO<sub>2</sub> absorption by saline-alkali soils in arid and semiarid ecosystems and developed the preliminary theory and methodology for the quantitative analysis. A. Li et al. investigated gas chromatography resonance-enhanced multiphoton ionization time-of-flight mass spectrometry (GC/REMPI-TOFMS) using a nanosecond laser to analyze the 16 polycyclic aromatic hydrocarbons (PAHs). G. Zhao et al. prepared fluorine-containing hydrophobic mesoporous material (MFS) with high surface area successfully synthesized with hydrothermal synthesis method by using a perfluorinated surfactant template. J. Liu et al. reported the preparation of P(AN-VAc-PMMT)

nanocomposites using in situ emulsion polymerization and further confirmed it by FTIR. H. Guo et al. investigated the gelation behaviors of binary organogels composed of azobenzene amino derivatives and fatty acids with different alkyl chains in various organic solvents. L. K. Gao et al. reported the molecular dynamics simulations for the model diameter gradually decreasing the deformation mode of ZrCu metallic glass from highly localized shear band formation to homogeneous deformation with obvious transition. A. Wang et al. investigated the synthesis and surface modification of CdTe quantum dots (QDs) and the application in the rice growth. F. Jin reported the determination of stavudine in human plasma by LC-MS/MS method applied to the pharmaceutical formulations bioequivalence study. B. Sun et al. investigated the constrained optimization method employed to calculate the colorant values of the multispectral images. H. Li et al. reported the utilization of infrared spectroscopy to examine the bone charcoal and the aluminum-impregnated bone charcoal. D. Yang et al. investigated the analysis for the oil content of 29 rapeseed samples based on near infrared spectral data with different wavelengths by an artificial neural network (ANN) method. L. Zhang and B. Qin reported a new technique named foamed gel developed to prevent coal mine fire efficiently. G. Zhao et al. reported the synthesis of a high surface area, hydrophobic mesoporous material (MFS) by a hydrothermal synthesis method using a perfluorinated surfactant, SURFLON S-386, as the single template. J. Lin et al. reported the preparation of zinc substituted magnesium

ferrite powders by a sol-gel autocombustion method. J. Liu et al. investigated the heat-activated persulfate oxidative treatment of chlorinated organic solvents containing chlorinated ethenes and ethanes in soil with different persulfate dosages and temperatures. Y. Hu et al. reported the preparation of novel polyurethane microspheres containing curcumin (Cur-PUMs) using carboxymethyl cellulose sodium to improve the bioavailability and prolong the retention time of curcumin. In addition, Y. Hu et al. also investigated the gelation behaviors of binary organogels composed of azobenzene amino derivatives and alkylbenzoic acids with different lengths of alkyl chains in various organic solvents.

### Acknowledgments

Finally, the guest editors would like to express sincere appreciation to all the authors for their contributions. Moreover, thanks are extended to all reviewers for their time enhancing the quality of these papers.

*Tifeng Jiao  
Nikša Krstulović  
Bing Wu  
Xinqing Chen  
Qingrui Zhang*

## Research Article

# Spin-Glass Behavior, Magnetic, and IR Spectroscopy Analysis of Multimetallic Compound $\text{Ni}_{0.25}\text{Mn}_{1.25}[\text{Fe}(\text{CN})_6]\cdot6.1\text{H}_2\text{O}$

Qing Lin,<sup>1,2</sup> Xiaofang Liu,<sup>1</sup> Yun He,<sup>1</sup> Haifu Huang,<sup>1,3</sup> and Xingcan Shen<sup>4</sup>

<sup>1</sup>College of Physics and Technology, Guangxi Normal University, Guilin 541004, China

<sup>2</sup>Department of Information Technology, Hainan Medical College, Haikou 571101, China

<sup>3</sup>Department of Physics, Nanjing University, Nanjing 210093, China

<sup>4</sup>School of Chemistry and Chemical Engineering, Guangxi Normal University, 541004 Guilin, China

Correspondence should be addressed to Yun He; [hy@gxnu.edu.cn](mailto:hy@gxnu.edu.cn)

Received 5 June 2014; Accepted 2 July 2014

Academic Editor: Qingrui Zhang

Copyright © 2015 Qing Lin et al. This is an open access article distributed under the Creative Commons Attribution License, which permits unrestricted use, distribution, and reproduction in any medium, provided the original work is properly cited.

Multimetallic Prussian blue compound  $\text{Ni}_{0.25}\text{Mn}_{1.25}[\text{Fe}(\text{CN})_6]\cdot6.1\text{H}_2\text{O}$  has been prepared by coprecipitation. The temperature-dependent magnetic susceptibilities show the magnet transition for the compound at 8.5 K. According to DC variable-temperature magnetic susceptibility paramagnetic Curie temperature  $\theta$  is  $-9.32$  K. The observed value of coercive field ( $H_c$ ) and the remanent magnetization ( $M_r$ ) for the compound are  $0.32$  KOe and  $0.36 \mu_B$ . According to study of zero-field-cooled (ZFC) and field-cooled (FC) magnetization curves and AC magnetization curves, there exists a spin-glass behaviour in the compound, which exhibits freezing temperature  $T_g = 7.76$  K, below magnetic transition  $T_C = 8.5$  K; that glass behavior is termed “reentrant” spin glass.

## 1. Introduction

Recently, molecule-based magnets, which can be synthesized by chemical process and have a main property of supramolecular structure, exhibit magnetic properties due to magnetic exchange interaction between magnetic ions [1–3]. The design and synthesis of molecule-based magnets have become one of the research foci on the physics and chemistry. Ones have attracted extensive attention recently owe to the high  $T_C$  molecular ferromagnets had been discovered and the molecule-based magnets show a kinds of fascinating magnetic phenomenon such as photomagnetic effect, thermal induced magnetic properties, and magnetic-pole reversal which have important potential application [4–6]. Among various types of molecule-based magnetism materials, Prussian blue analogues  $A_p[B(\text{CN})_6]_q \cdot x\text{H}_2\text{O}$  [4] (molecular structure of Prussian blue analogue compound as shown in Figure 1) play an important role due to their special structure and outstanding magnetic properties as molecule-based magnets. The multimetal Prussian blue compound  $\text{Ni}_{0.25}\text{Mn}_{1.25}[\text{Fe}(\text{CN})_6]\cdot6.1\text{H}_2\text{O}$  was synthesized and has been

studied for its magnetic properties through elemental analysis, IR, Mossbauer spectrum, magnetic measurements, and so forth.

## 2. Experimental

**2.1. Materials and Physical Measurements.**  $\text{NiCl}_2\cdot6\text{H}_2\text{O}$ ,  $\text{Mn}(\text{SO}_4)_2\cdot6\text{H}_2\text{O}$ , and  $\text{K}_3\text{Fe}(\text{CN})_6$  are of reagent grade and without further purification. Elemental analyses (C, H, and N) were performed on Perkin-Elmer 2400 II analyser. IR spectrum was recorded on a Perkin-Elmer FT-IR spectrophotometer as KBr pellet in the  $4000\text{--}400\text{ cm}^{-1}$  range. Magnetization measurements were measured by a Quantum Design MPMS-7S superconducting quantum interference device (SQUID) magnetometer in the scope of 2–300 K.

**2.2. Synthesis of  $\text{Ni}_{0.25}\text{Mn}_{1.25}[\text{Fe}(\text{CN})_6]\cdot6.1\text{H}_2\text{O}$ .** Polycrystalline samples of  $\text{Ni}_{0.25}\text{Mn}_{1.25}[\text{Fe}(\text{CN})_6]\cdot6.1\text{H}_2\text{O}$  have been

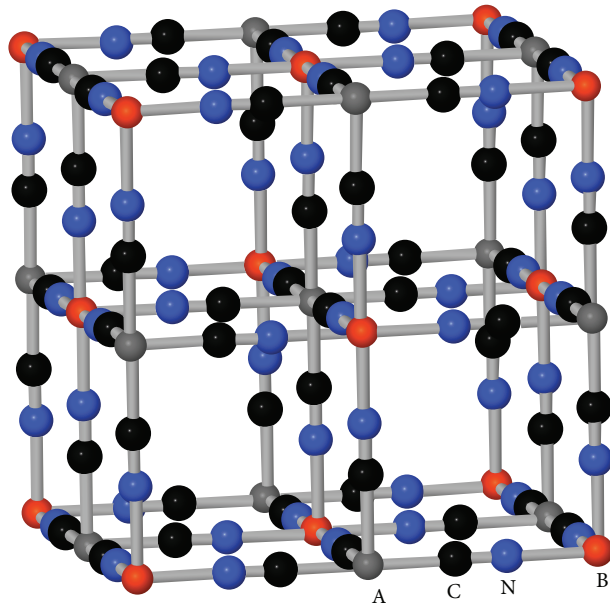


FIGURE 1: Structure of Prussian blue analog  $A_p[B(CN)_6]_q \cdot xH_2O$ .

prepared in coprecipitation method. A mixture of aqueous solutions of  $Co(NO_3)_2$  (25 mL, 0.25 mmol) and  $NiSO_4$  (125 mL, 1.25 mmol) was poured in aqueous solution of  $K_3[Fe(CN)_6]$  (100 mL, 1 mmol). Then the mixture solution was left to stand at room temperature for an appropriate period of time until those reactants were finished. A light brown precipitation was obtained, and precipitation then was filtered, washed many times with demineralized water, and finally dried under IR lamp for about 50 minutes. Elemental analysis to measure C, H, and N mass ratio: found: C, 17.44%; H, 3.09%; N, 21.23%; calculation: C, 17.79%; H, 3.03%; N, 20.74%.

### 3. Results and Discussion

**3.1. IR Spectrum Analysis.** IR spectrum of the compound has been recorded over the 400–4000  $cm^{-1}$  range shown in Figure 2. It shows two obvious bands at 2075.01 and 2151.74  $cm^{-1}$  indicating the existence of two types of cyanide groups in the crystal lattice of compound [7–9]. Compounds with  $CN^-$  functional group are easily identified by their stretching frequencies in 2200–2000  $cm^{-1}$  range, which are consistent with the formation of bridging cyanide groups, and there are two different coordination environments. Moreover, the broad peaks at 3432.90  $cm^{-1}$  and 1615.02  $cm^{-1}$  are assigned to the  $\nu$  (O–H) of the crystal water stretching vibrations.

**3.2. DC Magnetic Susceptibility.** The magnetic susceptibility of the compound was measured from 2 K to 300 K in 250 Oe field. Figure 3 shows the field-cooled magnetization ( $M$ ) versus temperature ( $T$ ) curve and a sharp increase in  $M$  is observed around 21 K. Magnetic transition temperature was estimated from minima of  $dM/dT$  versus  $T$  curve, which

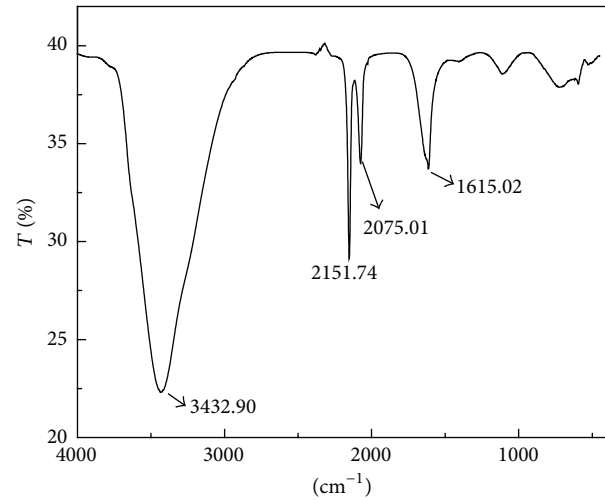


FIGURE 2: FT-IR spectrum of the compound.

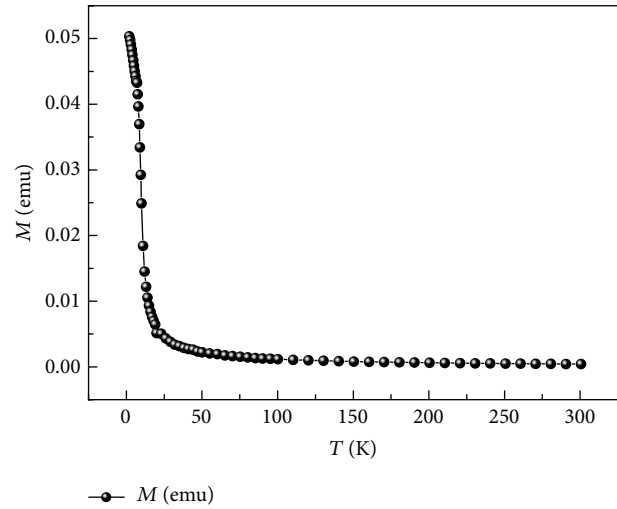
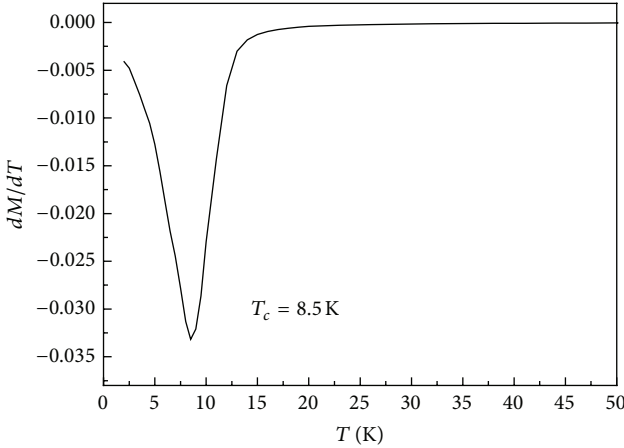
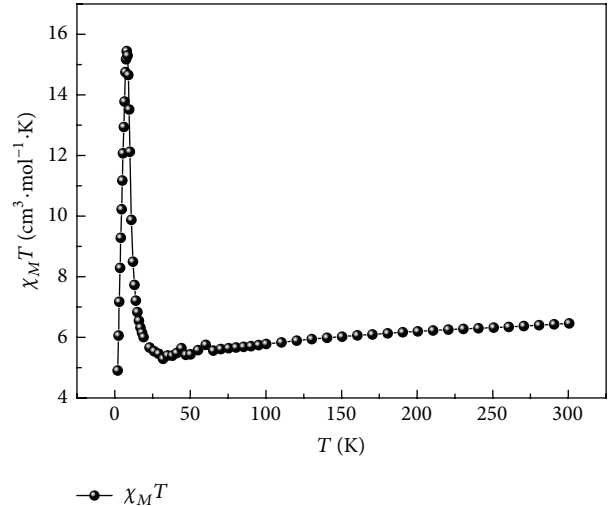
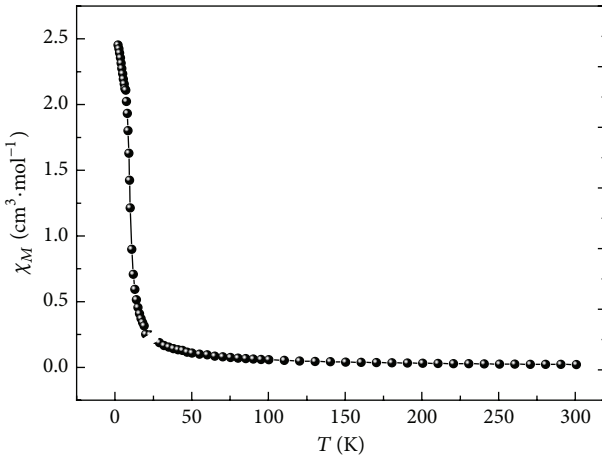
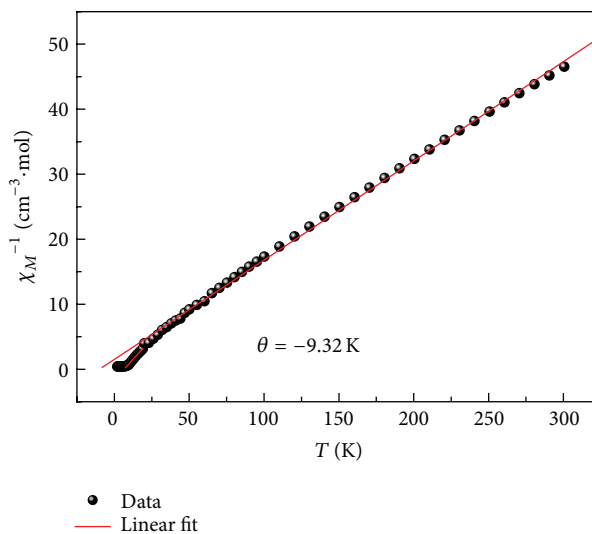


FIGURE 3:  $M$  versus  $T$  for the compound.

corresponds to the steepest increase of magnetization with decreasing temperature (as shown in Figure 4). The phase transition the compound undergoes from a paramagnetic to ferro/ferrimagnetic type is about 8.5 K, which is lower than that for the parent compound  $Ni_{1.5}[Fe(CN)_6] \cdot xH_2O$  ( $T_C = 23.6$  K) [10].

The inverse susceptibility as a function of temperature in the paramagnetic state is shown in Figure 5. The curve rises slowly with decrease of temperature from 300 to 25 K and then rises sharply as temperature continues to decrease. The  $\chi_m$  shows a sharp maximum at 2 K. This kind of behaviour is a characteristic of a ferromagnet. The magnetic order results from the combination of ferromagnetic and neighboring antiferromagnetic interactions. Furthermore, high temperature DC susceptibility ( $\chi_m = M/H$ ) is found to obey the Curie-Weiss law.

Figure 6 shows the temperature dependence of  $\chi_m^{-1}$  in the temperature range of 20–280 K. The Curie constant ( $C$ )

FIGURE 4:  $dM/dT$  versus  $T$  for the compound.FIGURE 7:  $\chi_m T$  versus  $T$  for the compound.FIGURE 5:  $\chi_m$  versus  $T$  for the compound.FIGURE 6:  $\chi_m^{-1}$  versus  $T$  for the compound.

and the Curie-Weiss temperature ( $\theta$ ) are estimated by a linear fitting of  $1/\chi = (T - \theta)/C$  at the linear region [8–10]. Fitting yielded that the Curie constant  $C = 15.20 \text{ cm}^3 \cdot \text{K} \cdot \text{mol}^{-1}$  and paramagnetic Curie temperature  $\theta = -9.32 \text{ K}$ . The values of  $T_C$ ,  $\theta$ , and  $C$  are different from those values for ferrimagnet  $\text{Ni}_{1.5}[\text{Fe}(\text{CN})_6] \cdot x\text{H}_2\text{O}$  [10] and  $\text{Mn}_3[\text{Fe}(\text{CN})_6]_2 \cdot 15\text{H}_2\text{O}$  ( $T_C = 9 \text{ K}$ ) [11].

A curve of  $\chi_m T$  versus  $T$  is shown in Figure 7, and the  $\chi_m T$  value at room temperature is  $5.7 \text{ cm}^3 \cdot \text{K} \cdot \text{mol}^{-1}$ . Upon lowering the temperature,  $\chi_m T$  value sharply increases after 15 K with a further decrease of the temperature. The  $\chi_m T$  shows a sharp maximum value of  $35.3 \text{ cm}^3 \cdot \text{K} \cdot \text{mol}^{-1}$  at 9 K and then finally decreases more rapidly on further cooling. For a ferromagnetic compound,  $\chi_m T$  versus  $T$  curve reaches a minimum before rising around magnetic ordering temperature [12–14].

A curve of  $\mu_{\text{eff}}$  versus  $T$  is shown in Figure 8. The effective moment  $\mu_{\text{eff}}$  first slowly decreases to reach a minimum of  $6.47 \mu_B$  at 23 K and then sharply increases to reach maximum of  $16.83 \mu_B$  at 9 K and final decrease at lower temperature, indicating antiferromagnetic interaction between paramagnetic centers [15–17]. Magnetic transition temperature was estimated from minimum of  $d\mu_{\text{eff}}/dT$  versus  $T$  curve, which corresponds to the steepest increase of magnetization with decreasing temperature (as shown in Figure 6; insert: plot of  $d\mu_{\text{eff}}/dT$  versus  $T$ ). The compound undergoes a paramagnetic to ferro/ferrimagnetic type phase transition at 9.5 K, which could be attributed to an intermolecular antiferromagnetic interaction and/or a zero-field splitting (ZFS) effect. This kind of behaviour is a characteristic of a ferromagnet [18, 19].

**3.3. Zero-Field-Cooled (ZFC) and Field-Cooled (FC) Magnetization.** Figure 9 shows the curves of zero-field-cooled (ZFC) and field-cooled (FC) magnetization of the compound at different field  $H = 20, 100, 250$ , and  $500 \text{ Oe}$ . The values of  $M$  increase and exhibit weak irreversibility in

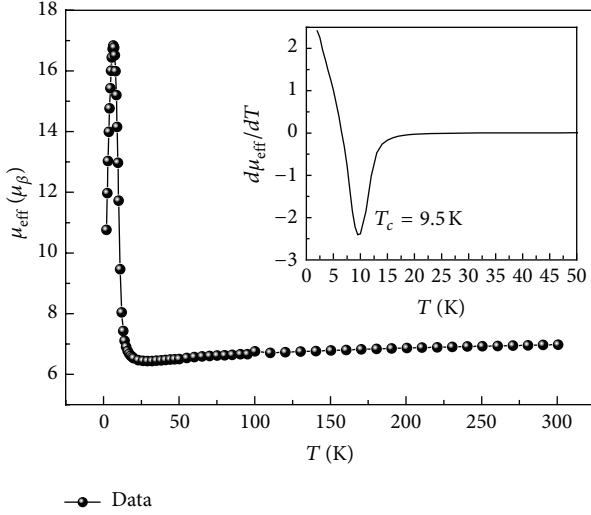


FIGURE 8:  $\mu_{\text{eff}}$  versus  $T$  for the compound (insert: plot of  $d\mu_{\text{eff}}/dT$  versus  $T$ ).

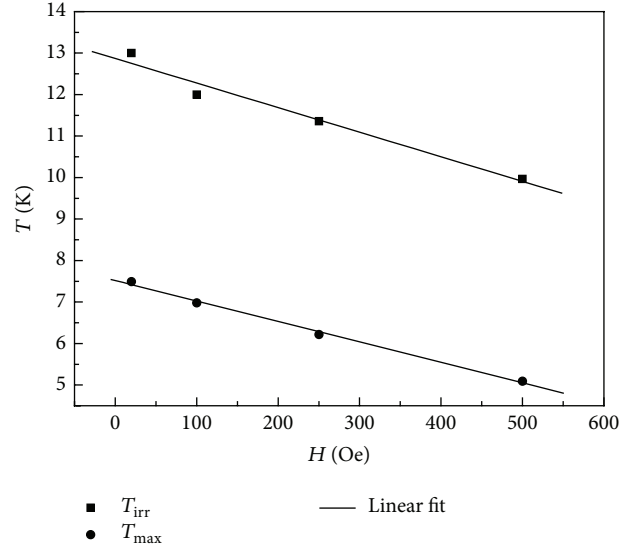


FIGURE 10:  $T_{\text{irr}}$  and  $T_{\text{max}}$  versus  $H$  for the compound.

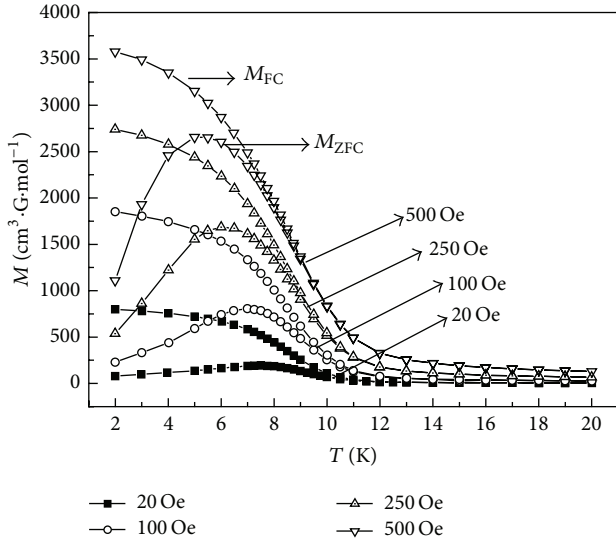


FIGURE 9: ZFC and FC magnetization curves with different field.

the field-cooled (FC) magnetization curves below  $T_C = 12$  K. There is a clear bifurcation phenomenon of the field-cooled ( $M_{\text{FC}}$ ) and zero-field-cooled ( $M_{\text{ZFC}}$ ) magnetization curves.  $T_{\text{irr}}$  is a bifurcation temperature point of which FC and ZFC magnetization curves separate out. In addition, the behavior that  $M_{\text{ZFC}}$  exhibits a maximum below  $T_{\text{irr}}$  is attributed to the cooperative freezing of spin glass (as shown in Figure 10). The irreversible behavior of  $M$  and shift of bifurcation point to lower temperature with increasing  $H$  are characteristic for spin glasses [10, 11]. It may be reasonable that these metal ions  $\text{Fe}^{\text{III}}$ ,  $\text{Ni}^{\text{II}}$ , and  $\text{Mn}^{\text{II}}$  through cyanide-bridged ligand have the coexistence of different valence states or spin states, the presence of inhomogeneity, and inherent structural disorder, which propagate possibly the ferromagnetic and antiferromagnetic exchange interaction via bridging cyanide,

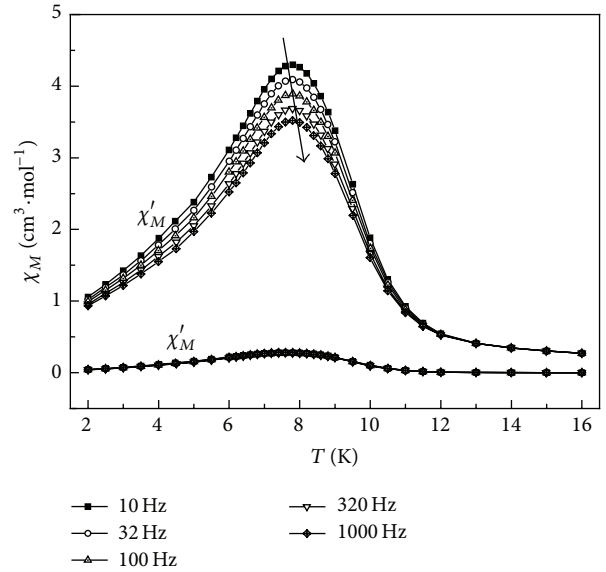
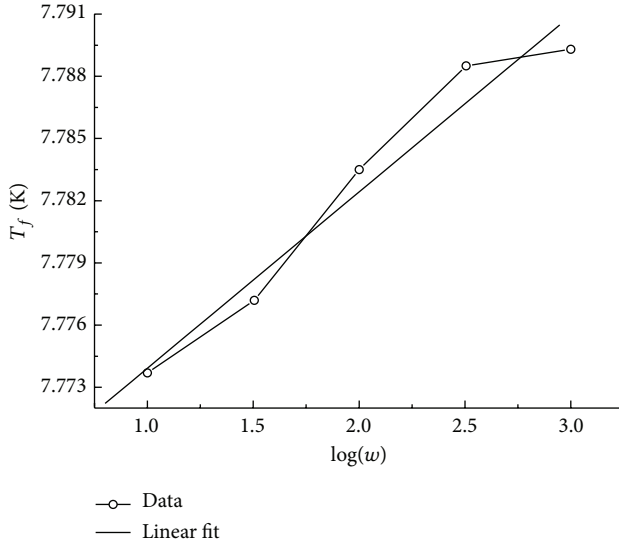


FIGURE 11:  $\chi'(T)$  and  $\chi''(T)$  curves of AC magnetic susceptibility of the compound with different frequencies.

and there exist a structural disorder and a certain content of crystallization water which lead to the weak spin-orbit coupling. The spin-glass property is due to magnetic domain kinetics under different cooling conditions and the presence of available vacant sites in the lattice for the water molecules.

**3.4. AC Magnetic Susceptibility.** It was also confirmed that there exists a spin-glass behavior in the compound through AC magnetic susceptibility. The AC magnetic susceptibility of the compound was measured at 4 Oe AC amplitude with zero-applied DC field when varying the frequencies ( $f$ ) from 10 to 1000 Hz, as shown in Figure 11. The temperature dependence of zero-static field AC magnetic susceptibilities shows

FIGURE 12: The  $\log(w)$  dependence of the  $T_f$ .

that the in-phase component ( $\chi'$ ) has a maximum at about 7.7 K for frequencies of 10, 32, 100, 320, and 997 Hz and that a significant out-of-phase component ( $\chi''$ ) appears, confirming the long-range ferromagnetic ordering. On decreasing temperature, the in-phase signals  $\chi'$  increase abruptly at around 12 K, reach the maximum at about 7.7 K, and then decrease slowly. The out-of-phase signals  $\chi''$  increase steadily to the maximum around 8 K and then decrease slowly, as shown in Figure 11. The fact that the  $\chi'(T)$  clearly shows a frequency dependence is typically assigned to spin glasses [12, 13]. The freezing temperature ( $T_f$ ),  $T_f = 7.7$  K, is defined by the maximum in the  $x_{AC}(T)$  plot at low frequency. It undergoes a paramagnetic to ferromagnetic transition at around 7.7 K. In fact, the temperature value of the maximum of  $\chi$  at a given frequency ( $n$ ) corresponds to the blocking temperature ( $T_N = T_{\max}$ ), whereby it is assumed that the switching of the oscillating AC field matches the relaxation rate of the magnetization.

Proportional relationship between freezing temperature  $T_f$  and logarithm of frequency in spin-glass system can be described by quantifying the frequency dependence through the ratio  $c$ , which can be written as  $c = \Delta T_f / T_f \Delta \log w$ .  $T_f(w)$  versus  $\log(w)$  is shown in Figure 12. The value of freezing temperature of zero frequency is  $T_g = 7.76$  K by extrapolation method and the value of  $c$  obtained for the compound is 0.0011, which fall within the range typical for the conventional spin-glass system ( $10^{-2}$ - $10^{-3}$ ). Surprisingly, both the in-phase and out-of-phase signals ( $\chi'$  and  $\chi''$ ) go through a maximum with strong frequency dependence. Both in the real and in the imaginary components the peaks shift to lower temperatures with decreasing frequencies. However, the intensities of the peaks behave differently. While the intensity of the peaks for the real component increases with decreasing frequencies, in the imaginary component the intensity of the peaks decreases with decreasing frequencies.

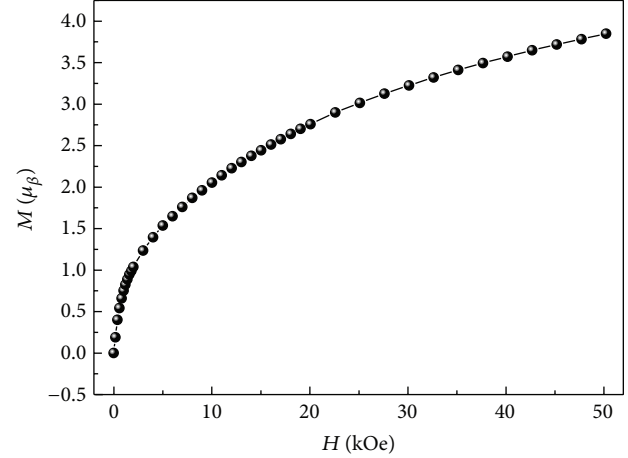


FIGURE 13: Field-dependent magnetization curves.

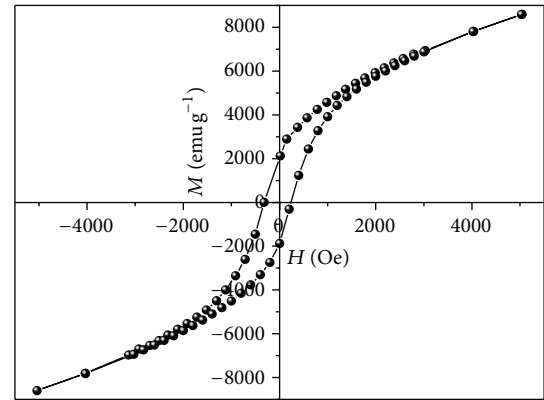


FIGURE 14: The hysteresis loop for the compound.

This behaviour of  $\chi''$  and  $\chi''$  is typical of a spin-glass state [16–19].

**3.5. Field-Dependent Magnetization and Hysteresis Behavior.** In order to further understand the nature of magnetic ordering, the ferromagnetism behavior is characterized by the measurements of field-dependent magnetization, as shown in Figures 11 and 13. The observed  $M_s$  value is  $3.85 \mu_B$  at 50 kOe, but the compound does not reach full saturation and this behavior is likely to be related to the spin-glass behavior as well as the amount of spin and type of coupling in the compounds  $\text{Ni}_{1.5}[\text{Fe}(\text{CN})_6] \cdot x\text{H}_2\text{O}$  [18] and  $\text{Mn}_3[\text{Fe}(\text{CN})_6]_2 \cdot 15\text{H}_2\text{O}$  [10].

Ferromagnetism in the compound  $\text{Ni}_{0.25}\text{Mn}_{1.25}[\text{Fe}(\text{CN})_6] \cdot 6\text{H}_2\text{O}$  is also supported by hysteresis loop curves measured at 4 K as shown in Figure 14. The coercive field ( $H_c$ ) was 0.32 kOe, which was smaller than that of the compound  $\text{Ni}_{1.5}[\text{Fe}(\text{CN})_6] \cdot x\text{H}_2\text{O}$  ( $H_c = 2.5$  KOe, 4.4 K) [12]. The remanent magnetization ( $M_r$ ) with  $0.32 \mu_B$  for the compound. It is also obtained by the hysteresis loop curves.

Therefore, synthesis ideas of molecular alloy magnet can be regarded as a synthesis method to expand a new type of magnetic functional materials, whose magnetic properties

can be tuned and controlled by changing the composition of different transition metal cations [15, 17–19].

## 4. Conclusion

We have reported a detailed investigation of magnetic properties of multimetallic Prussian blue compounds  $\text{Ni}_{0.25}\text{Mn}_{1.25}[\text{Fe}(\text{CN})_6] \cdot 6\text{H}_2\text{O}$ . The temperature-dependent magnetic susceptibilities show the magnetism transition for the compound at 8.5 K. The Curie constant ( $C = 15.20 \text{ cm}^3 \cdot \text{K} \cdot \text{mol}^{-1}$ ) and the Curie-Weiss temperature ( $\theta = -9.32 \text{ K}$ ) are obtained through a linear fitting of  $1/\chi = (T - \theta)/C$  at the linear region [8–10].

The observed values of coercive field ( $H_c$ ) and remanent magnetization ( $M_r$ ) for the compound are 0.32 KOe and  $0.36 \mu_B$ . Moreover, there exists a spin-glass behaviour in the compound according to study of zero-field-cooled (ZFC) and field-cooled (FC) magnetization curves and AC magnetization curves, which exhibits freezing temperature  $T_g = 7.76 \text{ K}$ , below magnetic transition  $T_c = 8.5 \text{ K}$ . Such a glass behavior is termed “reentrant” spin glass. It was also confirmed by the behaviour of  $\chi''$  and  $\chi'''$ , which go through a maximum with strong frequency dependence.

## Conflict of Interests

The authors declare that there is no conflict of interests regarding the publication of this paper.

## Acknowledgments

This work was financially supported by the National Natural Science Foundation of China (nos. 11164002 and 11364004) and Innovation Project of Guangxi Graduate Education under Grant no. 0991092.

## References

- [1] J. M. Manriquez, G. T. Yee, R. S. Mclean, A. J. Epstein, and J. S. Miller, “A room-temperature molecular/organic-based magnet,” *Science*, vol. 252, no. 5011, pp. 1415–1417, 1991.
- [2] S. Ferlay, T. Mallah, R. Ouahès, P. Veillet, and M. Verdaguer, “A room-temperature organometallic magnet based on Prussian blue,” *Nature*, vol. 378, no. 6558, pp. 701–703, 1995.
- [3] O. Sato, T. Iyoda, A. Fujishima, and K. Hashimoto, “Electrochemical tunable magnetic phase transition in a high- $T_c$  chromium cyanide thin film,” *Science*, vol. 271, no. 5245, pp. 49–51, 1996.
- [4] M. Giorgetti, “A review on the structural studies of batteries and host materials by X-ray absorption spectroscopy,” *ISRN Materials Science*, vol. 2013, Article ID 938625, 22 pages, 2013.
- [5] S.-I. Ohkoshi, T. Iyoda, A. Fujishima, and K. Hashimoto, “Magnetic properties of mixed ferro-ferrimagnets composed of Prussian blue analogs,” *Physical Review B Condensed Matter and Materials Physics*, vol. 56, no. 18, pp. 11642–11652, 1997.
- [6] S. Ohkoshi, O. Sato, T. Iyoda, A. Fujishima, and K. Hashimoto, “Tuning of superexchange couplings in a molecule-based ferro-ferrimagnet:  $(\text{Ni}_x^{II} \text{Mn}_{1-x}^{II})_{1.5} [\text{Cr}^{III} (\text{CN})_6]$ ,” *Inorganic Chemistry*, vol. 36, pp. 268–269, 1997.
- [7] S.-I. Ohkoshi, Y. Abe, A. Fujishima, and K. Hashimoto, “Design and preparation of a novel magnet exhibiting two compensation temperatures based on molecular field theory,” *Physical Review Letters*, vol. 82, no. 6, pp. 1285–1288, 1999.
- [8] A. Kumar and S. M. Yusuf, “Magnetic properties of multi-metal Prussian Blue analogue  $\text{Co}_{0.75}\text{Ni}_{0.75}[\text{Fe}(\text{CN})_6] \cdot 6\text{H}_2\text{O}$ ,” *Physica B: Condensed Matter*, vol. 362, no. 1–4, pp. 278–285, 2005.
- [9] A. Kumar, S. M. Yusuf, and L. Keller, “Neutron diffraction study of molecular magnetic compound  $\text{Ni}_{1.125}\text{Co}_{0.375}[\text{Fe}(\text{CN})_6] \cdot 6\text{H}_2\text{O}$ ,” *Physica B*, vol. 385–386, pp. 444–446, 2006.
- [10] O. Kahn, S. J. Miller, and F. Palacio, Eds., *Magnetic Molecular Materials*, vol. 198 of *NATO ASI Series E*, Plenum, New York, NY, USA, 1991.
- [11] S. Juskzyk, C. Johansson, M. Hansson, A. Ratusnas, and G. Makckill, “Ferromagnetism of the  $\text{Me}_3[\text{Fe}(\text{CN})_6] \cdot \text{H}_2\text{O}$  compounds, where  $\text{Me} = \text{Ni}$  and  $\text{Co}$ ,” *Journal of Physics: Condensed Matter*, vol. 6, pp. 5697–5765, 1994.
- [12] J. S. Miller and A. J. Epstein, “Organic and organometallic molecular magnetic materials-designer magnets,” *Angewandte Chemie International Edition in English*, vol. 33, no. 4, pp. 385–415, 1994.
- [13] O. Kahn, *Molecular Magnetism*, Wiley-VCH, New York, NY, USA, 1993.
- [14] W. E. Buschmann and J. S. Miller, “Magnetic ordering and spin-glass behavior in first-row transition metal hexacyanomanaganate(IV) Prussian Blue analogues,” *Inorganic Chemistry*, vol. 39, no. 11, pp. 2411–2421, 2000.
- [15] Y. He, Y.-D. Dai, H.-B. Huang, J. Lin, and Y.-F. Hsia, “Spin-glass state and ferromagnetic order in Cu(II)-Fe(III) cyanides,” *Chinese Physics*, vol. 13, no. 5, pp. 746–749, 2004.
- [16] H. Huang, L. Wei, Y. He, X. Li, and F. Liang, “Ferromagnetic order and spin-glass behavior in multi-metallic compound  $\text{Ni}_{1.125}\text{Co}_{0.375}[\text{Fe}(\text{CN})_6] \cdot 6\text{H}_2\text{O}$ ,” *Current Applied Physics*, vol. 9, no. 5, pp. 1160–1164, 2009.
- [17] S.-I. Ohkoshi, S. Yorozu, O. Sato, T. Iyoda, A. Fujishima, and K. Hashimoto, “Photoinduced magnetic pole inversion in a ferro-ferrimagnet:  $(\text{Fe}_{0.40}^{II} \text{Mn}_{0.60}^{II})_{1.5} \text{Cr}^{III} (\text{CN})_6$ ,” *Applied Physics Letters*, vol. 70, no. 8, pp. 1040–1042, 1997.
- [18] D. Sherrington and S. Kirkpatrick, “Solvable model of a spin-glass,” *Physical Review Letters*, vol. 35, no. 26, pp. 1792–1796, 1975.
- [19] M. Gabay and G. Toulouse, “Coexistence of spin-glass and ferromagnetic orderings,” *Physical Review Letters*, vol. 47, no. 3, pp. 201–204, 1981.

## Research Article

# Raman Spectroscopy for Understanding of Lithium Intercalation into Graphite in Propylene Carbonated-Based Solutions

Yang-Soo Kim<sup>1</sup> and Soon-Ki Jeong<sup>2</sup>

<sup>1</sup> Korea Basic Science Institute, Suncheon Center, Suncheon 540-742, Republic of Korea

<sup>2</sup> Department of Chemical Engineering, Soonchunhyang University, Asan, Chungnam 336-745, Republic of Korea

Correspondence should be addressed to Soon-Ki Jeong; hamin611@sch.ac.kr

Received 22 August 2014; Accepted 2 October 2014

Academic Editor: Tifeng Jiao

Copyright © 2015 Y.-S. Kim and S.-K. Jeong. This is an open access article distributed under the Creative Commons Attribution License, which permits unrestricted use, distribution, and reproduction in any medium, provided the original work is properly cited.

Electrochemical lithium intercalation within graphite was investigated in propylene carbonate (PC) containing different concentrations, 0.4, 0.9, 1.2, 2.2, 2.8, 3.8, and 4.7 mol dm<sup>-3</sup>, of lithium perchlorate, LiClO<sub>4</sub>. Lithium ion was reversibly intercalated into and deintercalated from graphite in 3.8 and 4.7 mol dm<sup>-3</sup> solutions despite the use of pure PC as the solvent. However, ceaseless solvent decomposition and intense exfoliation of the graphene layers occurred in other solutions. The results of the Raman spectroscopic analysis indicated that contact ion pairs are present in 3.8 and 4.7 mol dm<sup>-3</sup> solutions, which suggested that the presence of contact ion pairs is an important factor that determines the solid electrolyte interphase- (SEI-) forming ability in PC-based electrolytes.

## 1. Introduction

In commercially available lithium secondary batteries, lithium ions are electrochemically intercalated into and deintercalated from the graphite negative electrode during charging and discharging, respectively. These electrochemical reactions are basically reversible; however, the reversibility depends greatly on the kind of electrolyte solutions. They are highly reversible in ethylene carbonate- (EC-) based solutions containing lithium salts such as LiClO<sub>4</sub>, LiPF<sub>6</sub>, and LiCF<sub>3</sub>SO<sub>3</sub>. The discovery of EC-based electrolyte systems is a seminal breakthrough that has enabled the electrochemical preparation of lithium-graphite intercalation compounds (Li-GICs) [1, 2]. On the other hand, propylene carbonate (PC)-based solutions are attractive electrolyte systems owing to their superior ionic conductivities when compared to EC-based solutions at low temperatures [3]. However, it is very difficult to get Li-GICs in PC-based electrolytes because of poor compatibility between graphite and PC [4–6].

In a previous study [7], we reported a simple electrochemical preparation of Li-GICs in PC-based solutions, LiN(SO<sub>2</sub>C<sub>2</sub>F<sub>5</sub>)<sub>2</sub> (LiBETI) dissolved in PC. The work showed that lithium intercalation within graphite from the LiBETI-PC solutions is an electrochemical reaction that strongly

depends on the electrolyte concentration. Lithium ions were intercalated within graphite to form a stage 1 Li-GIC in concentrated LiBETI-PC solutions whereas solvent decomposition or the intensive exfoliation of graphene layers occurred continuously in relatively low-concentration solutions; that is, the poor compatibility between graphite and PC could be improved by increasing electrolyte concentration. However, the details for the effects of electrolyte concentration on lithium intercalation and deintercalation reactions are still unclear. In this study, we performed Raman spectroscopic analysis to know the correlations between electrolyte concentration and interfacial reactions between graphite and PC-based solutions.

## 2. Experimental

The electrolyte solutions were prepared by dissolving LiClO<sub>4</sub> in PC. All these reagents were purchased from Kishida Chemical Co. and were used as received. The concentrations of LiClO<sub>4</sub> were 0.4, 0.9, 1.2, 2.2, 2.8, 3.8, and 4.7 mol dm<sup>-3</sup>, which correspond to 20 : 1, 1 : 9, 1 : 7, 1 : 5, 1 : 4, 1 : 3, and 1 : 2, respectively, by the molar ratio of Li<sup>+</sup> to PC. The water content in each solution was less than 30 ppm, which was confirmed using a Karl-Fischer moisture titrator (Kyoto Electronics

Manufacturing Co., MKC-210). The concentration of all electrolyte solutions is expressed as the molarity of lithium salt ( $\text{mol dm}^{-3}$ ).

Natural graphite powder (The Kansai Coke and Chemicals Co., NG-7) was used for the charge/discharge tests. The test electrode was prepared by coating a mixture of the graphite powder (90 wt%) and a polymeric binder (10 wt%) on copper foil, as described elsewhere [8]. The charge and discharge tests were carried out using conventional three-electrode cells at a constant current of  $5.2 \text{ mA g}^{-1}$  in an argon-filled glove-box (Miwa, MDB-1B+MM3-P60S) with a dew point below  $-60^\circ\text{C}$ . Lithium foil was used as the counter and reference electrodes. All potentials are referred to as volts versus  $\text{Li}^+/\text{Li}$ .

Raman spectra of the electrolyte solutions were recorded using a triple monochromator (Jobin-Yvon, T-64000). Excitation was carried out with a 514.5 nm line (50 mW) from an argon ion laser (NEC, GLG2265). The scattered light was collected in a direction of  $90^\circ$  to the incident light.

### 3. Results and Discussion

In a previous study [7], we used LiBETI-PC solutions of different concentrations as electrolytes, as mentioned in the introduction, to investigate the effects of electrolyte concentration on lithium intercalation into graphite. In the present study, however,  $\text{LiClO}_4$ -PC solutions instead of LiBETI-PC solutions were used as electrolytes because a lot more information on ion-solvent or ion-ion interactions which would be expected to have an effect on interfacial reactions between electrode and electrolyte can be obtained from the former solution by Raman spectroscopy. Before the Raman spectroscopic analysis, the charging (lithium intercalation) and discharging (lithium deintercalation) of the graphite electrode was executed in seven  $\text{LiClO}_4$ -PC electrolytes of different concentrations: 0.4, 0.9, 1.2, 2.2, 2.8, 3.8, and  $4.7 \text{ mol dm}^{-3}$ . The graphite electrode showed electrolyte concentration dependence of the electrochemical lithium intercalation reaction in  $\text{LiClO}_4$ -PC solutions similar to that observed in LiBETI-PC solutions. Among the electrolytes, the 3.8 and  $4.7 \text{ mol dm}^{-3}$  solutions were effective for the electrochemical preparation of Li-GICs. No lithium intercalation and deintercalation reactions occurred in the other solutions.

The potential profiles of natural graphite powder during the first charging and discharging cycles in 2.8 and  $3.8 \text{ mol dm}^{-3}$  solutions are shown in Figure 1 (potential profiles obtained in the other solutions are not shown here). It is well known that the electrochemical intercalation of lithium into graphite mainly occurs at potentials below  $0.25 \text{ V}$  [9–11]. There was no charge capacity at the potential profile obtained in  $2.8 \text{ mol dm}^{-3}$  solution. In contrast, the charge capacity corresponding to lithium intercalation was recorded at potentials below  $0.25 \text{ V}$  in  $3.8 \text{ mol dm}^{-3}$  solution. Potential plateaus observed at  $0.170$ ,  $0.080$ , and  $0.045 \text{ V}$  during charging and  $0.135$ ,  $0.180$ , and  $0.255 \text{ V}$  during discharging in Figure 1(b) are direct evidence of lithium intercalation and deintercalation. The potential plateaus can be assigned to reversible stage transformations between Li-GICs of different stage numbers.

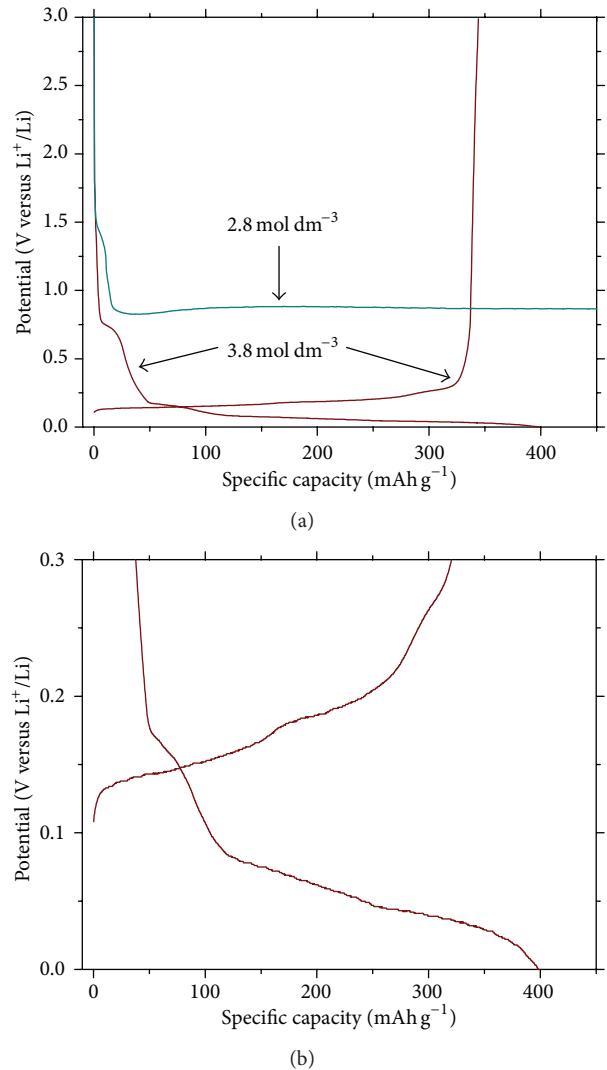


FIGURE 1: (a) Charge and discharge curves in the first cycle of natural graphite powder (NG-7) in  $2.8$  and  $3.8 \text{ mol dm}^{-3}$   $\text{LiClO}_4$  dissolved in PC. (b) Magnified view of panel (a).

The above results demonstrate that the solid electrolyte interphase- (SEI-) forming ability of  $\text{LiClO}_4$ -PC electrolytes is greatly dependent on the concentration of  $\text{LiClO}_4$ . The following two possibilities can be considered as the reason for SEI formation on graphite surface to form Li-GICs in high-concentration solutions. First, it may be due to the structural changes in solvated lithium ions as the concentration increases, because the electrolyte decomposition and exfoliation of graphene layers at around  $0.8 \text{ V}$  in the  $2.8 \text{ mol dm}^{-3}$  solution are originated from the intercalation of solvated lithium ions [12]. The structural changes may lower the potential of solvated lithium ions to be intercalated into graphite, resulting in forming an SEI by the decomposition of electrolyte below  $0.8 \text{ V}$ . Second, a new chemical species may have been produced in high-concentration solutions, resulting in their decomposition to form an SEI.

The ion-solvent interactions between lithium ions and PC molecules were investigated by laser Raman spectroscopy

TABLE 1: Mole fraction of solvated PC molecules and charge-discharge behaviors of graphite in  $\text{LiClO}_4$ -PC solutions.

Concentration (mol dm <sup>-3</sup> )	Charging-discharging	Mole fraction of solvated PC
4.7	Success	0.91
3.8	Success	0.82
2.8	Failure	0.63
2.2	Failure	0.52
1.2	Failure	0.36
0.9	Failure	0.26
0.4	Failure	0.05

to confirm the first possibility. Figure 2 shows the Raman spectra of pure PC and  $\text{LiClO}_4$ -PC solutions of different concentrations in the wavenumber range of 660 to  $800\text{ cm}^{-1}$ . The vibrational spectroscopy of PC in this frequency region provides useful information on the interactions between lithium ions and PC molecules [13–17]. In pure PC, the strong band at  $712\text{ cm}^{-1}$  is assigned to the symmetric ring deformation mode of free PC molecules [13]. The shape of this band became less symmetric and a new band appeared at around  $723\text{ cm}^{-1}$ . The intensity of the new band increased with an increase in the concentration of  $\text{LiClO}_4$  whereas the intensity of the band from free PC decreased. This indicates that the new band is originated from the interaction between PC molecules and lithium ions and is assigned to the symmetric ring deformation mode of solvated PC [13–15]. The band from free PC almost disappeared in 3.8 and 4.7 mol dm<sup>-3</sup> solutions, indicating that most of PC molecules solvate lithium ions in the solutions. The mole fraction of the solvated PC molecules in each solution was obtained from the integrated intensities of the free or solvated PC bands (Table 1). Curve fitting was performed to separate each band. The 82 and 91% of PC molecules were solvated to lithium ions in 3.8 and 4.7 mol dm<sup>-3</sup> solutions, respectively, where an effective SEI was formed on graphite.

Figure 2 and Table 1 clearly show that there are structural changes in solvated lithium ions as the concentration changes. The solvation number of lithium ions in  $\text{LiClO}_4$ -PC solution is expected to decrease with an increase in the concentration of the lithium salt. Such a difference in the solvation number may result in suppressing the intercalation of solvated lithium ions and their decomposition occurring at around 0.8 V in the 2.8 mol dm<sup>-3</sup> solution or the solvated lithium ions may be intercalated at lower potentials than 0.8 V, resulting in forming an SEI by the decomposition of electrolyte below 0.8 V. If this assumption is correct, an SEI may be generated when the electrode potential is forced to step to a lower potential than 0.8 V in a short time. This is because the intercalation of solvated lithium ions is suppressed by the formation of an SEI although the two reactions are competing at the low potential. However, such an effective SEI was not formed, as shown in Figure 3.

Figure 3 shows chronoamperograms obtained after potential step from 2.9 to 0.3 V in 2.8 and 3.8 mol dm<sup>-3</sup>

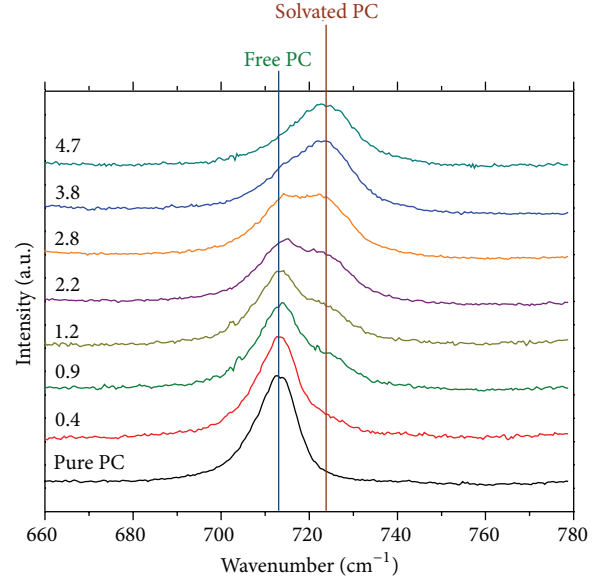


FIGURE 2: Raman spectra of pure PC and  $\text{LiClO}_4$ -PC solutions of different concentrations. The concentration of all solutions is expressed as the molality of  $\text{LiClO}_4$  (mol dm<sup>-3</sup>) inside figure.

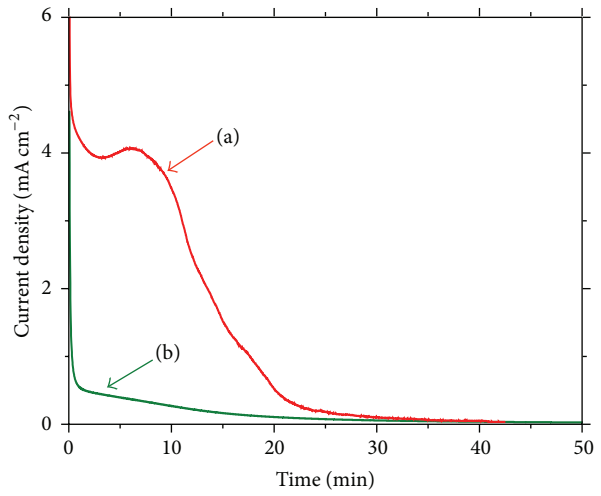


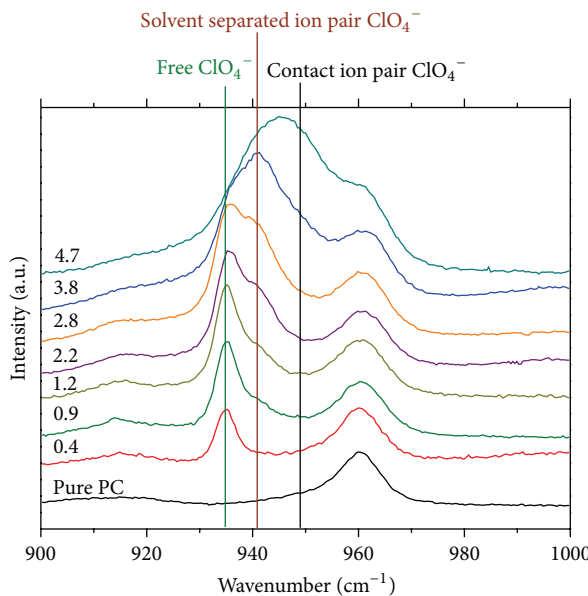
FIGURE 3: Current-time curves of the natural graphite powder (NG-7) observed in response to the potential step from 2.9 to 0.3 V in (a) 2.8 and (b) 3.8 mol dm<sup>-3</sup>  $\text{LiClO}_4$  dissolved in PC.

solutions. In 2.8 mol dm<sup>-3</sup> solution, more than 10 times more charge was consumed compared to that consumed in 3.8 mol dm<sup>-3</sup> solution, and exfoliation of graphene layers was also observed. This indicates that no SEI is formed on graphite by the decomposition of 2.8 mol dm<sup>-3</sup> solution. The above results demonstrate that a chemical species with the ability to generate an effective SEI is present in 3.8 mol dm<sup>-3</sup> solution, but not present in 2.8 mol dm<sup>-3</sup> solution. This, as mentioned earlier, supports the second possibility.

We noted that ion pairs are formed only in concentrated solutions and investigated them by laser Raman spectroscopy. Figure 4 shows the Raman spectra of pure PC and  $\text{LiClO}_4$ -PC solutions of different concentrations in the wavenumber

TABLE 2: Mole fraction of  $\text{ClO}_4^-$  anions and charge-discharge behaviors of graphite in  $\text{LiClO}_4\text{-PC}$  solutions.

Concentration ( $\text{mol dm}^{-3}$ )	Charging-discharging	Mole fraction		
		Free	Solvent-separated	Contact
4.7	Success	0.02	0.58	0.40
3.8	Success	0.08	0.72	0.20
2.8	Failure	0.22	0.78	0.00
2.2	Failure	0.38	0.62	0.00
1.2	Failure	0.48	0.52	0.00
0.9	Failure	0.55	0.45	0.00
0.4	Failure	1.00	0.00	0.00

FIGURE 4: Raman spectra of pure PC and  $\text{LiClO}_4\text{-PC}$  solutions of different concentrations. The concentration of all solutions is expressed as the molality of  $\text{LiClO}_4$  ( $\text{mol dm}^{-3}$ ) inside figure.

range of 900 to 1000  $\text{cm}^{-1}$ . The vibrational spectroscopy of  $\text{ClO}_4^-$  anions in this frequency region provides useful information on ion pairs. James et al. studied ion-ion-solvent interactions in  $\text{LiClO}_4$ -acetone solutions with Raman spectroscopy [18]. They reported that there are four kinds of the symmetrical stretching vibration of  $\text{ClO}_4^-$  anions in solutions originating from (i) free anions,  $\text{ClO}_4^-$  ( $934 \text{ cm}^{-1}$ ), (ii) solvent-separated ion pairs,  $\text{Li}^+ \text{-solvent-ClO}_4^-$  ( $939 \text{ cm}^{-1}$ ), (iii) contact ion pairs,  $[\text{Li}^+\text{ClO}_4^-]$  ( $948 \text{ cm}^{-1}$ ), and (iv) multiple ion aggregates,  $\{\text{Li}^+\text{ClO}_4^-\}_n$  ( $n \geq 2$ ) ( $958 \text{ cm}^{-1}$ ). On the basis of this report, curve fitting was performed to separate each band. From the fitting results, the mole fraction of each species was obtained in a manner similar to the method used to obtain Table 1, and the results are shown in Table 2. Among the four kinds of  $\text{ClO}_4^-$  anions, three species were observed, except multiple ion aggregates, from  $\text{LiClO}_4\text{-PC}$  solutions. It should be noted that an effective SEI formation and reversible lithium intercalation and deintercalation reactions took place

in 3.8 and 4.7  $\text{mol dm}^{-3}$  solutions, in which contact ion pairs are present. In the other solutions, only free anions and solvent-separated ion pairs are present. These results suggest that the presence of contact ion pairs in the electrolyte enhances the SEI-forming ability. On the other hand, ion paring in  $\text{LiClO}_4\text{-PC}$  solutions reduces the conductivity of the electrolyte. The maximum ionic conductivity is observed at 1.3  $\text{mol dm}^{-3}$   $\text{LiClO}_4\text{-PC}$  solution [13]. At a higher concentration the conductivity decreases because of the higher viscosity originating from the formation of ion pairs in the solution. The conductivity appears to have little effect on SEI formation reactions. The detailed interpretation of the direct correlations between the conductivity and the SEI formation reactions is beyond the scope of the present work.

## 4. Conclusions

This study was conducted to better understand SEI formation reactions occurring at the interface between the graphite electrodes and PC-based electrolyte in lithium secondary batteries. Lithium ions were electrochemically intercalated into graphite in  $\text{LiClO}_4$  dissolved in PC by increasing the concentration of  $\text{LiClO}_4$ . An effective SEI was formed on graphite in concentrated solutions without the aid of any SEI-forming agents. The results of this study suggest that the presence of contact ion pairs is an important factor that determines the SEI-forming ability in PC-based electrolytes. We are yet to understand the causative reasons for the SEI formation by contact ion pairs and intend to focus our future reports on gaining an understanding of the factors contributing to the electrolyte-concentration dependence of SEI formation in PC-based electrolytes.

## Conflict of Interests

The authors declare that there is no conflict of interests regarding the publication of this paper.

## Acknowledgments

This study was financially supported by the Small & Medium Business Administration (no. S2136830). This work was supported by the Soonchunhyang University Research Fund.

## References

- [1] R. Fong, U. von Sacken, and J. R. Dahn, "Studies of lithium intercalation into carbons using nonaqueous electrochemical cells," *Journal of the Electrochemical Society*, vol. 137, no. 7, pp. 2009–2013, 1990.
- [2] Y. Ein-Eli, B. Markovsky, D. Aurbach, Y. Carmeli, H. Yamin, and S. Luski, "The dependence of the performance of Li-C intercalation anodes for Li-ion secondary batteries on the electrolyte solution composition," *Electrochimica Acta*, vol. 39, no. 17, pp. 2559–2569, 1994.
- [3] J. T. Dudley, D. P. Wilkinson, G. Thomas et al., "Conductivity of electrolytes for rechargeable lithium batteries," *Journal of Power Sources*, vol. 35, no. 1, pp. 59–82, 1991.
- [4] A. N. Dey and B. P. Sullivan, "The electrochemical decomposition of propylene carbonate on graphite," *Journal of the Electrochemical Society*, vol. 117, no. 2, pp. 222–224, 1970.
- [5] J. O. Besenhard and H. P. Fritz, "Cathodic reduction of graphite in organic solutions of alkali and  $\text{NR}_4^+$  salts," *Journal of Electroanalytical Chemistry*, vol. 53, no. 2, pp. 329–333, 1974.
- [6] G. Eichinger, "Cathodic decomposition reactions of propylene carbonate," *Journal of Electroanalytical Chemistry and Interfacial Electrochemistry*, vol. 74, no. 2, pp. 183–193, 1976.
- [7] S.-K. Jeong, M. Inaba, Y. Iriyama, T. Abe, and Z. Ogumi, "Interfacial reactions between graphite electrodes and propylene carbonate-based solutions: electrolyte-concentration dependence of electrochemical lithium intercalation reaction," *Journal of Power Sources*, vol. 175, no. 1, pp. 540–546, 2008.
- [8] S.-K. Jeong, M. Inaba, R. Mogi, Y. Iriyama, T. Abe, and Z. Ogumi, "Surface film formation on a graphite negative electrode in lithium-ion batteries: atomic force microscopy study on the effects of film-forming additives in propylene carbonate solutions," *Langmuir*, vol. 17, no. 26, pp. 8281–8286, 2001.
- [9] T. Ohzuku, Y. Iwakoshi, and K. Sawai, "Formation of lithium-graphite intercalation compounds in nonaqueous electrolytes and their application as a negative electrode for a lithium ion (shuttlecock) cell," *Journal of the Electrochemical Society*, vol. 140, no. 9, pp. 2490–2497, 1993.
- [10] J. R. Dahn, "Phase diagram of  $\text{Li}_x\text{C}_6$ ," *Physical Review B*, vol. 44, no. 17, pp. 9170–9177, 1991.
- [11] A. Funabiki, M. Inaba, T. Abe, and Z. Ogumi, "Influence of defects on the phase-boundary movement in a stage transformation of lithium-graphite intercalation compounds," *Carbon*, vol. 37, no. 10, pp. 1591–1598, 1999.
- [12] M. Inaba, Z. Siroma, Y. Kawatake, A. Funabiki, and Z. Ogumi, "Electrochemical scanning tunneling microscopy analysis of the surface reactions on graphite basal plane in ethylene carbonate-based solvents and propylene carbonate," *Journal of Power Sources*, vol. 68, no. 2, pp. 221–226, 1997.
- [13] D. Battisti, G. A. Nazri, B. Klassen, and R. Aroca, "Vibrational studies of lithium perchlorate in propylene carbonate solutions," *The Journal of Physical Chemistry*, vol. 97, no. 22, pp. 5826–5830, 1993.
- [14] K. Kondo, M. Sano, A. Hiwara et al., "Conductivity and solvation of  $\text{Li}^+$  ions of  $\text{LiPF}_6$  in propylene carbonate solutions," *The Journal of Physical Chemistry B*, vol. 104, no. 20, pp. 5040–5044, 2000.
- [15] Z. Wang, W. Gao, X. Huang, Y. Mo, and L. Chen, "Spectroscopic studies on interactions and microstructures in propylene carbonate—LiTFSI electrolytes," *Journal of Raman Spectroscopy*, vol. 32, no. 11, pp. 900–905, 2001.
- [16] W. Huang and R. Frech, "In situ Raman studies of graphite surface structures during lithium electrochemical intercalation," *Journal of the Electrochemical Society*, vol. 145, no. 3, pp. 765–770, 1998.
- [17] L. J. Hardwick, H. Buqa, M. Holzapfel, W. Scheifele, F. Krumeich, and P. Novák, "Behaviour of highly crystalline graphitic materials in lithium-ion cells with propylene carbonate containing electrolytes: an in situ Raman and SEM study," *Electrochimica Acta*, vol. 52, no. 15, pp. 4884–4891, 2007.
- [18] D. W. James and R. E. Mayers, "Ion-ion-solvent interactions in solution. I. Solutions of  $\text{LiClO}_4$  in acetone," *Australian Journal of Chemistry*, vol. 35, no. 9, pp. 1775–1784, 1982.

## Research Article

# Solar Photocatalytic Degradation of Typical Indoor Air Pollutants Using TiO<sub>2</sub> Thin Film Codoped with Iron(III) and Nitrogen

Shuaijie Wang and Xingxing Cheng

*School of Environmental and Chemical Engineering, Yanshan University, Qinhuangdao 066004, China*

Correspondence should be addressed to Shuaijie Wang; wangshuaijie@ysu.edu.cn

Received 23 June 2014; Revised 23 August 2014; Accepted 25 August 2014

Academic Editor: Xinqing Chen

Copyright © 2015 S. Wang and X. Cheng. This is an open access article distributed under the Creative Commons Attribution License, which permits unrestricted use, distribution, and reproduction in any medium, provided the original work is properly cited.

A type of iron and nitrogen codoped titania thin film was prepared by sol-gel method to degrade three typical indoor air pollutants: formaldehyde (HCHO), ammonia (NH<sub>3</sub>), and benzene (C<sub>6</sub>H<sub>6</sub>) under solar light. X-ray diffraction (XRD), UV-Vis spectroscopy, and energy dispersive spectra (EDS) were employed to characterize the photocatalysts. The results showed that the Fe/N codoped TiO<sub>2</sub> had a stronger absorption in the visible region than pure, Fe-doped, and N-doped TiO<sub>2</sub> and exhibited excellent photocatalytic ability for the degradation of indoor HCHO, NH<sub>3</sub>, and C<sub>6</sub>H<sub>6</sub>. When the three pollutants existed in indoor air at the same time, the removal percentages of HCHO, NH<sub>3</sub>, or C<sub>6</sub>H<sub>6</sub> after 6 h photocatalytic reaction under solar light reached 48.8%, 50.6%, and 32.0%. The degradation reaction of the three pollutants followed the pseudo-first-order kinetics with the reaction rate constants in the order of 0.110 h<sup>-1</sup> for ammonia, 0.109 h<sup>-1</sup> for formaldehyde, and 0.060 h<sup>-1</sup> for benzene. The reaction rate constant decreased with the increase of initial reactant concentration, which reflected that there was oxidation competition between the substrate and its intermediate during the photocatalytic process.

## 1. Introduction

Indoor air quality within buildings has been paid great attention, since many metropolitans generally spend more than 80% of time in indoor environment [1]. Indoor air pollutants mainly include carbonyl compounds, volatile organic compounds, ammonia, particulate matter, and so forth. Among them, formaldehyde, ammonia, and benzene are the most representative, which come from the furnishings and decorating materials, causing nausea, chest tightness, wheezing, skin rashes, allergic reaction, and chronic poisoning [2].

Photocatalysis is an emerging and promising technology for the indoor air purification [3], and titania has been identified as the most effective and useful photocatalyst because of its outstanding physical and chemical properties [4–8]. However, with a wide band gap energy of 3.0–3.2 eV, titania cannot be activated to generate photoexcited electrons and holes to promote redox reaction unless it is irradiated by ultraviolet. But the ultraviolet light energy only accounts for

4–6% of solar energy reaching the ground, so the solar energy cannot be utilized efficiently in the photocatalytic process, which hinders the application of TiO<sub>2</sub> as a photocatalyst with response to solar light [6, 9].

In the enhancement of the photoresponse of TiO<sub>2</sub> from ultraviolet to the visible range without decreasing photocatalytic activity, the modification to titania by doping with metal or nonmetal has been considered as one of the most promising methods [10–15]. Choi et al. conducted a systematic study of metal ions doping into TiO<sub>2</sub> for 21 metal ions [16]. Among various transition metal ions, Fe<sup>3+</sup> was considered to be a successful doping element due to its half-filled electronic configuration [17]. Nitrogen and carbon doping have received attention due to low costs and the demonstration of band-gap narrowing, with significant improvement in visible light absorption capability [18]. Recent research results showed that the modification to titania by codoping may be a more effective method to improve the photocatalytic activity

under visible light [19, 20]. Zhao et al. prepared the B-Ni codoped photocatalyst using the modified sol-gel method. They pointed out that incorporation of B into  $\text{TiO}_2$  could extend the spectral response to the visible region and that Ni doping could increase greatly the photocatalytic activity [21].

In this paper, a new solar photocatalyst,  $\text{TiO}_2$  thin film codoped with iron(III) and nitrogen, was developed with flat glass as carrier to degrade three typical indoor air pollutants, formaldehyde, ammonia, and benzene, under solar light. The research finding provides a feasible way for enhancement of indoor air quality.

## 2. Experimental Procedure

**2.1. Photocatalyst Preparation.** Pure and doped  $\text{TiO}_2$  thin films were prepared by sol-gel technique. The schematic diagram of preparing procedures of gels was described in Figure 1.

Then the plate glass was inserted vertically into the gel. After keeping for 30 seconds, it was pulled out of the gel with the speed of 12 cm/min. Thus, the gel film was formed on the glass surface. Then the glass coated with the gel was dried for 30 min at 100°C. At last, the glass was calcined for 4 h at 450°C (20°C/min).

**2.2. Photocatalyst Characterization.** The crystal structures of pure and doped  $\text{TiO}_2$  were determined by a D-max-2500/PC X-ray diffractometer (XRD) equipped with Cu-K $\alpha$  radiation. The ultraviolet-visible (UV-Vis) absorption spectra of pure and doped  $\text{TiO}_2$  thin films were recorded on a Shimadzu (Japan) UV-2550 spectrophotometer. The energy dispersive spectra of the Fe/N codoped  $\text{TiO}_2$  thin film were recorded on JEM-2010 transmission electron microscopy (EDS).

**2.3. Photodegradation of Gaseous Indoor Pollutants.** Photocatalytic experiments with the prepared photocatalysts were carried out in a self-designed, cuboid, airtight, glass reactor (60 × 60 × 20 cm) with two holes, which were connected to sampling tubes of KC-6D air sampler. An electric fan was installed on the bracket of the airtight reactor in order to circulate the mixture of gaseous pollutants and air. Eight pieces of coated glass were placed vertically and evenly in the reactor. A predetermined amount of pollutant was injected in vessel under dark. The sunlight illumination was started following a dark period of 2 h which was sufficient to attain adsorption equilibrium with the pollutants. The residual concentration of pollutant was periodically measured every 60 min.

## 3. Results and Discussion

### 3.1. Results of Characterization

**3.1.1. XRD Spectra.** Figure 2 shows the XRD patterns of undoped  $\text{TiO}_2$ , Fe-doped  $\text{TiO}_2$  with the doping proportion (mole ratio) is 1.00%, N-doped  $\text{TiO}_2$  with the doping proportion (mole ratio) is 25.0%, and Fe/N codoped  $\text{TiO}_2$  with the doping proportions (mole ratio) of iron and nitrogen is

1.00 and 25.0%, respectively. The results showed that all the samples had anatase structure mainly with the formation of characteristic diffraction peaks at  $2\theta = 25.28^\circ, 37.80^\circ, 48.05^\circ, 53.89^\circ, 55.06^\circ$ , and  $62.69^\circ$ , corresponding to (101), (04), (200), (105), (211), and (204) crystal surface. Compared to undoped  $\text{TiO}_2$ , the patterns of doped  $\text{TiO}_2$ , especially Fe/N codoped  $\text{TiO}_2$ , became weak and broadening, which indicated that the crystallite sizes decreased. From the obtained XRD peaks the crystallite size of the catalysts was determined by applying Scherrer's formula. The formula is given as follows:

$$D = \frac{0.89\lambda}{(\beta \cdot \cos \theta)}, \quad (1)$$

where  $D$  is crystallite size (nm),  $\lambda$  is X-ray wavelength (1.5406 Å),  $\beta$  is width of the obtained peak at half maximum, and  $\theta$  is contour peak angle (radian). According to the Scherrer's formula, the crystallite sizes of the photocatalysts can be ranked in an order of Fe/N codoped  $\text{TiO}_2$  (6.28 nm) <Fe-doped  $\text{TiO}_2$  (7.35 nm)<N-doped  $\text{TiO}_2$  (10.72 nm) <pure  $\text{TiO}_2$  (12.02 nm).

**3.1.2. UV-Vis Spectra.** Figure 3 shows the ultraviolet-visible (UV-Vis) absorption spectra of the undoped  $\text{TiO}_2$  thin film, Fe-doped  $\text{TiO}_2$  thin film (the doping mole ratio is 1.00%), N-doped  $\text{TiO}_2$  thin film (the doping mole ratio is 25.0%), and Fe/N codoped  $\text{TiO}_2$  thin film (the doping mole ratios of iron and nitrogen are 1.00% and 25%, resp.). According to Figure 3, all the doped  $\text{TiO}_2$  have stronger absorption than the undoped  $\text{TiO}_2$  in the visible region. Among the photocatalysts, Fe/N codoped  $\text{TiO}_2$  thin film has the strongest absorption in the visible region.

**3.1.3. EDS Spectra.** Figure 4 shows the energy dispersive spectra of the Fe/N codoped  $\text{TiO}_2$  with the doping mole ratio of iron and nitrogen are 1.00 and 25.0%, respectively. The result showed that the iron and nitrogen were doped in the  $\text{TiO}_2$  photocatalyst successfully. The mole ratio of Fe and Ti was very close to 1%, and the mole ratio of N and Ti was very close to 25%.

### 3.2. Photocatalytic Experiment

**3.2.1. The Optimal Doping Amount of Iron and Nitrogen.** The solar photocatalytic activity of doped  $\text{TiO}_2$  thin films was determined by testing the degradation ratio of formaldehyde after 6 h photocatalytic reaction. Figure 5 shows the effect of Fe(III) doping amount on the photocatalytic activity of Fe-doped  $\text{TiO}_2$  thin films, and Figure 6 shows the effect of N doping amount on the photocatalytic activity of N-doped  $\text{TiO}_2$  thin films. From Figures 5 and 6, we could see that the solar photocatalytic performance of doped  $\text{TiO}_2$  thin films exceeded that of pure  $\text{TiO}_2$  thin film, indicating that both of Fe and N dopant could increase the solar photocatalytic activity. Among the Fe-doped  $\text{TiO}_2$  thin films, the film with the doping mole ratios of iron was 1.00% and owned the best solar photocatalytic activity. And the solar photocatalytic activity of N-doped  $\text{TiO}_2$  thin film with the doping mole ratio of nitrogen was 25.0% and was the best among the N-doped

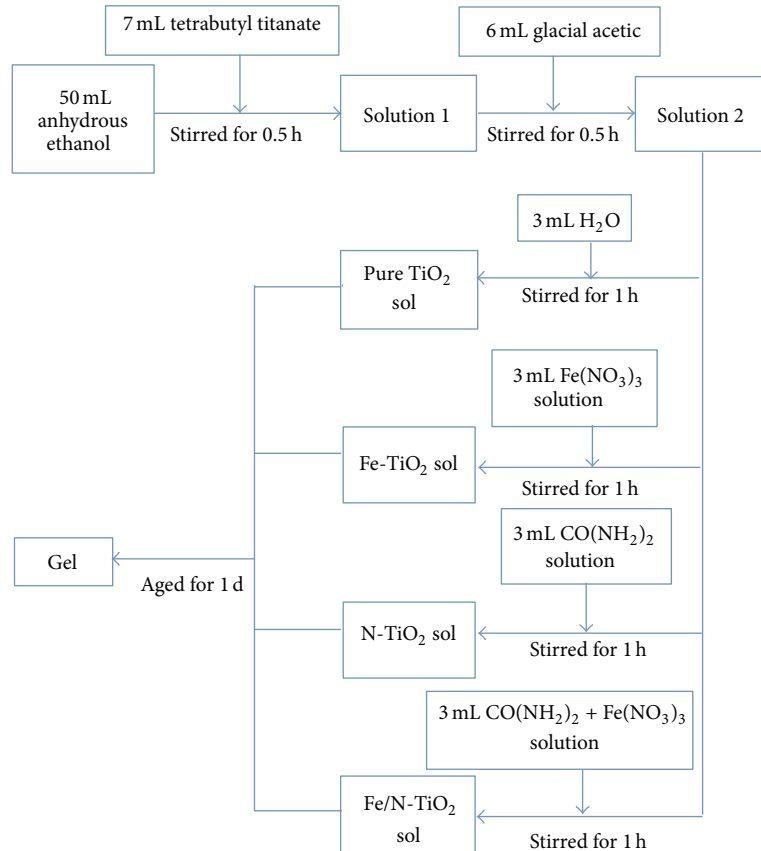
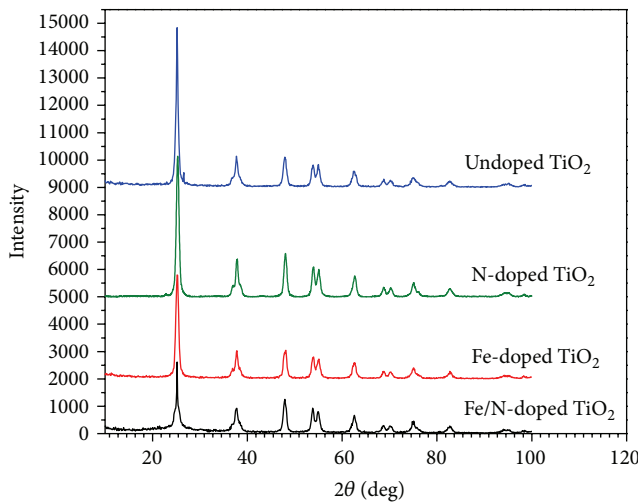


FIGURE 1: The schematic diagram of preparing procedures of gels.

FIGURE 2: XRD spectra of  $\text{TiO}_2$  catalysts.

$\text{TiO}_2$  thin films. So the Fe/N codoped  $\text{TiO}_2$  thin film was prepared with the doping mole ratio of iron and nitrogen that was 1.00 and 25.0%, respectively.

**3.2.2. Degradation of Formaldehyde, Ammonia, and Benzene.** Formaldehyde, ammonia, and TVOC exist in the indoor air at

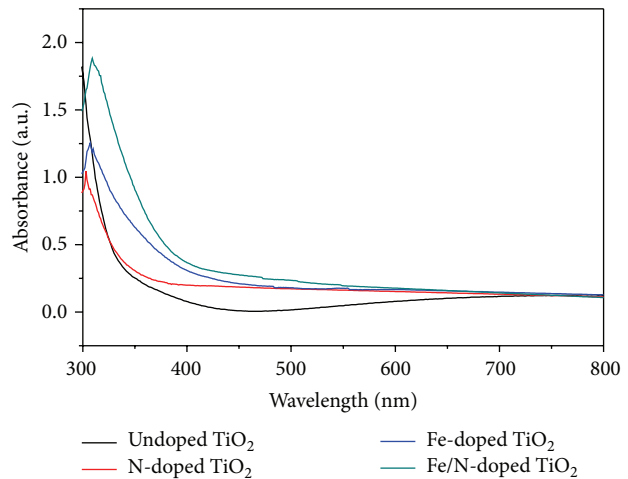


FIGURE 3: UV-Vis absorption spectra.

the same time usually. So, we not only studied the photocatalytic degradation of formaldehyde, ammonia, and benzene when they exist in indoor air separately but also studied the photocatalytic degradation of the mixed formaldehyde, ammonia, and benzene in the indoor air. Figure 7 shows the degradation ratios of separate formaldehyde, ammonia,

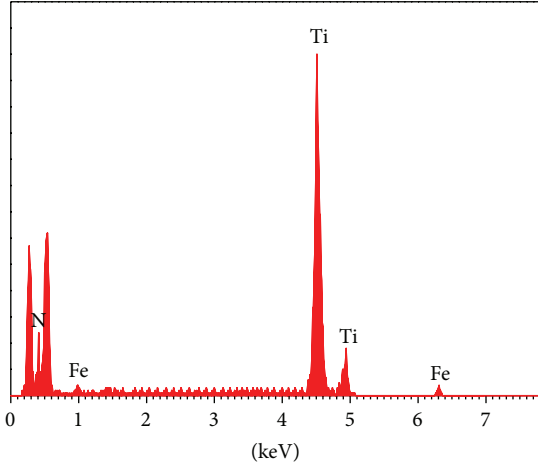


FIGURE 4: EDS spectra.

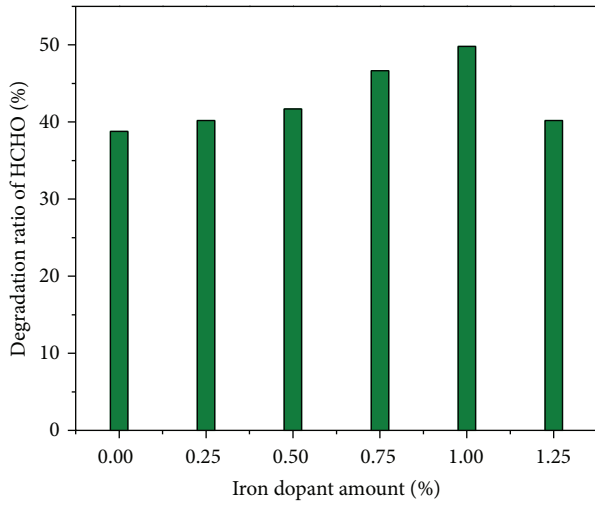
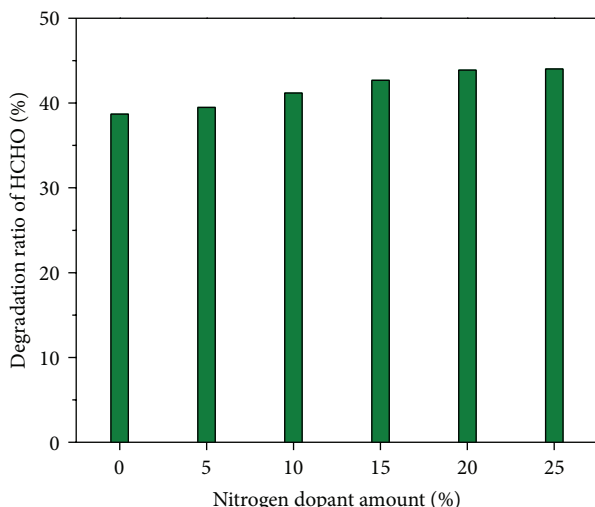
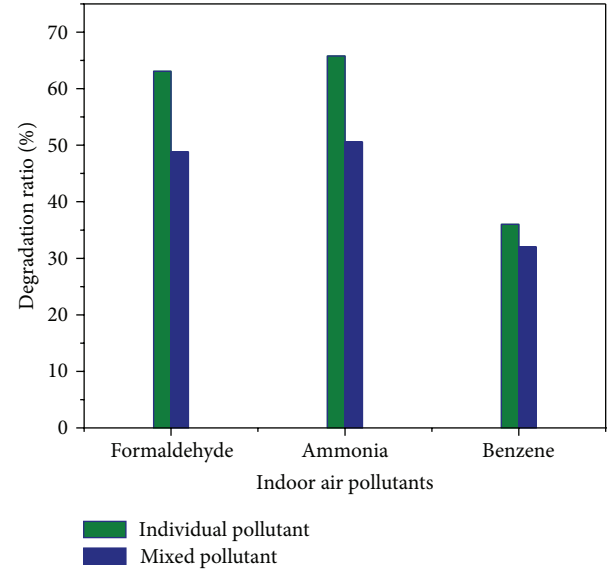
FIGURE 5: Effect of iron doping amount on photocatalytic activity of Fe-doped  $\text{TiO}_2$ .FIGURE 6: Effect of nitrogen doping amount on photocatalytic activity of N-doped  $\text{TiO}_2$ .

FIGURE 7: Degradation ratios of formaldehyde, ammonia, and benzene.

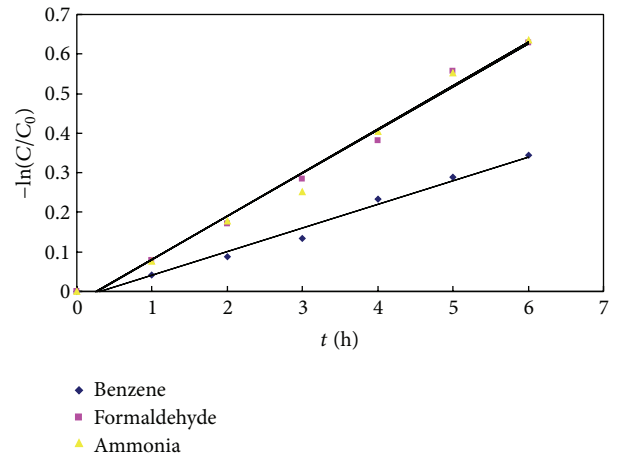


FIGURE 8: Kinetics of degradation reaction of the mixed pollutants.

and benzene and the mixture of three pollutants after 6 h of photocatalytic reaction under solar light.

As shown in Figure 7, appropriate amount of  $\text{Fe}^{3+}$  and N codoped into the  $\text{TiO}_2$  thin film was helpful to further improve photocatalytic activity. The removal percentage of separate HCHO in the presence of the Fe/N codoped  $\text{TiO}_2$  thin film was 63.1%, which was much greater than that in the presence of Fe-doped  $\text{TiO}_2$  thin film (49.8%) and N-doped  $\text{TiO}_2$  thin film (44.0%). The cooperation of  $\text{Fe}^{3+}$  and nitrogen could induce the formation of new energy levels close to the conduction band and valence band, respectively, leading to the much narrowing band gap. Besides,  $\text{Fe}^{3+}$  could trap the photogenerated electrons, while nitrogen could trap the photogenerated holes; thus, the codoping of  $\text{Fe}^{3+}$  and nitrogen could further restrain the recombination of the photogenerated electron and hole and enhance photocatalytic activity [22].

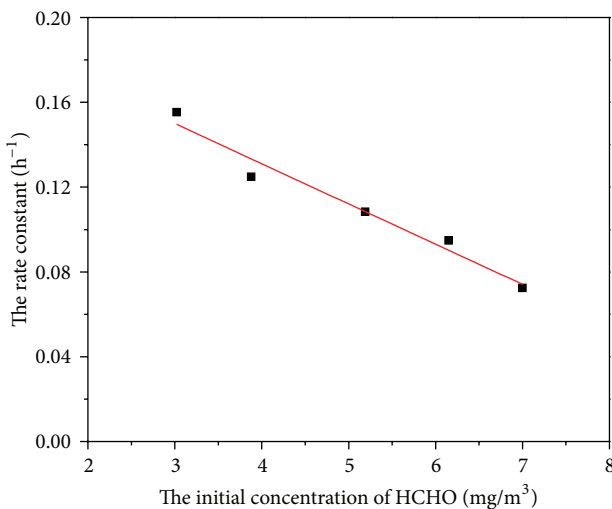


FIGURE 9: The relationship of reaction rate constant and initial concentration of HCHO.

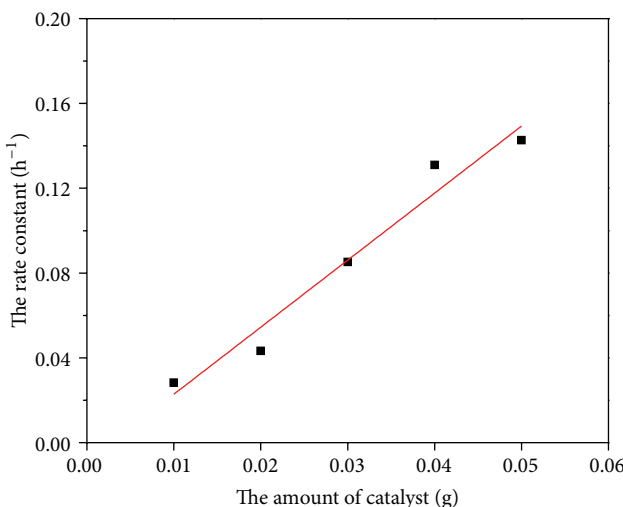


FIGURE 10: The relationship of reaction rate constant and the amount of catalyst.

Whether the three pollutants, formaldehyde, ammonia, and benzene, existed separately or mixed, they could be removed effectively using the Fe/N codoped TiO<sub>2</sub> thin film. But the removal percentage of formaldehyde, ammonia, and benzene in gas mixture (48.8%, 50.6%, and 32.0%) after 6 h photocatalytic reaction under solar light was lower than those of formaldehyde, ammonia, and benzene existing in air separately (63.1%, 65.8%, and 36.0%). This is due to gas molecules occupying fully the active sites of the photocatalyst, different molecules compete with each other, and the intermediate product of different pollutant accumulating on the photocatalyst surface prevents the effective contact of gas molecules and photocatalyst.

**3.2.3. Kinetics of Photocatalytic Reaction.** Formaldehyde, ammonia, and benzene exist in the indoor air at the same time

usually, so the kinetics of photocatalytic reaction was studied with the experimental data of mixed pollutants over the Fe/N codoped TiO<sub>2</sub> thin film. Langmuir-Hinshelwood (L-H) equation has been widely used to describe the process of photocatalytic reaction. At low reactant concentration, which is a reasonable assumption for most indoor air pollution problems, the L-H model is simplified to a pseudo-first-order expression

$$\ln\left(\frac{C}{C_0}\right) = -kt, \quad (2)$$

where the reactant residue ( $C/C_0$ ) is a ratio of the instantaneous concentration of gaseous pollutant ( $C$ ) to the initial concentration ( $C_0$ ),  $k$  is the reaction rate constant, and  $t$  is the irradiation time. The experimental data were fitted by plotting  $-\ln(C/C_0)$  against irradiation time. The fitting result was shown in Figure 8.

As shown in Figure 8, almost good linear relationships with the correlation coefficient  $R^2 > 0.98$  were observed, indicating that the degradation reaction of formaldehyde, ammonia, and benzene followed the pseudo-first-order kinetics. The reaction rate constants of three pollutants were in the following order: ammonia (0.110 h<sup>-1</sup>), formaldehyde (0.109 h<sup>-1</sup>), and benzene (0.060 h<sup>-1</sup>). This shows that the photocatalytic reaction is controlled by surface chemical reaction and reaction rate is controlled by reactant concentration.

**3.2.4. Effect of Initial Reactant Concentration and Amount of Catalyst on the Reaction Rate.** Since the photocatalytic reaction rate is controlled by reactant concentration, the photocatalytic degradation experiments with different initial concentration of HCHO (3.02 mg/m<sup>3</sup>, 3.88 mg/m<sup>3</sup>, 5.19 mg/m<sup>3</sup>, 6.15 mg/m<sup>3</sup>, and 7.00 mg/m<sup>3</sup>) as degradation objects were conducted in order to understand controlling mechanism, and the results were shown in Figure 9. From Figure 9, we could see that there was good linear relationship between the rate constant and initial reactant concentration. The relation equation was  $k = 0.207 - 0.0189C_0$ ,  $R^2 = 0.956$ . The rate constant decreased with the increase of initial reactant concentration. This reflected that there was oxidation competition between substrate concentration and its intermediate.

In addition, the amount of the photocatalyst is also the important influencing factor of photocatalytic reaction. Figure 10 shows the effect of the amount of Fe/N codoped TiO<sub>2</sub> (0.01 g, 0.02 g, 0.03 g, 0.04 g, and 0.05 g) on the photocatalytic degradation rate of formaldehyde. The results showed that the photocatalytic reaction rate constant increased with the increase of the amount of photocatalyst. The relation equation was  $k = 3.16m - 0.0088$  with the correlation coefficient  $R^2 = 0.964$ , and  $m$  was the amount of catalyst.

## 4. Conclusions

The Fe/N codoped TiO<sub>2</sub> thin film was prepared by means of sol-gel method. The Fe/N codoped TiO<sub>2</sub> exhibited much higher photocatalytic activities than the pure one and those doped with Fe(III) or nitrogen alone under solar light. Indoor

HCHO, NH<sub>3</sub>, and C<sub>6</sub>H<sub>6</sub> could be removed effectively using the Fe/N codoped TiO<sub>2</sub> thin film under solar light. The removal percentages of three indoor pollutants with solar light irradiation for 6 h reached 63.1%, 65.8%, and 36.0% for separate formaldehyde, ammonia, and benzene and 48.8%, 50.6%, and 32.0% for mixed formaldehyde, ammonia, and benzene. The photocatalytic degradation reaction kinetic of mixed pollutants followed the pseudo-first-order kinetic model, the photocatalytic reaction was controlled by the surface chemical reaction, and the reaction rate was controlled by concentration of reactants. Overall, using the Fe/N codoped TiO<sub>2</sub> thin film to purify indoor air under solar light is very promising.

## Conflict of Interests

The authors declared that there is no conflict of interests regarding the publication of this paper.

## References

- [1] S. Hellweg, E. Demou, R. Bruzzi et al., "Integrating human indoor air pollutant exposure within life cycle impact assessment," *Environmental Science & Technology*, vol. 43, no. 6, pp. 1670–1679, 2009.
- [2] P. N. Breysse, G. B. Diette, E. C. Matsui et al., "Indoor air pollution and asthma in children," *Proceedings of the American Thoracic Society*, vol. 7, no. 2, pp. 102–106, 2010.
- [3] Y. You, S. Zhang, L. Wan, and D. Xu, "Preparation of continuous TiO<sub>2</sub> fibers by sol-gel method and its photocatalytic degradation on formaldehyde," *Applied Surface Science*, vol. 258, no. 8, pp. 3469–3474, 2012.
- [4] J. Zita, J. Krysa, and U. Cernigoj, "Photocatalytic properties of different TiO<sub>2</sub> thin films of various porosity and titania loading," *Catalysis Today*, vol. 161, no. 1, pp. 29–34, 2011.
- [5] Y.-B. Luo, X.-L. Wang, D.-Y. Xu, and Y.-Z. Wang, "Preparation and characterization of poly(lactic acid)-grafted TiO<sub>2</sub> nanoparticles with improved dispersions," *Applied Surface Science*, vol. 255, no. 15, pp. 6795–6801, 2009.
- [6] A. Zaleska, E. Grabowska, J. W. Sobczak, M. Gazda, and J. Hupka, "Photocatalytic activity of boron-modified TiO<sub>2</sub> under visible light: the effect of boron content, calcination temperature and TiO<sub>2</sub> matrix," *Applied Catalysis B: Environmental*, vol. 89, no. 3-4, pp. 469–475, 2009.
- [7] U. G. Akpan and B. H. Hameed, "Parameters affecting the photocatalytic degradation of dyes using TiO<sub>2</sub>-based photocatalysts: a review," *Journal of Hazardous Materials*, vol. 170, no. 2-3, pp. 520–529, 2009.
- [8] D. Papoulis, S. Komarneni, D. Panagiotaras et al., "Halloysite-TiO<sub>2</sub> nanocomposites: synthesis, characterization and photocatalytic activity," *Applied Catalysis B: Environmental*, vol. 132-133, pp. 416–422, 2013.
- [9] D. Mitoraj and H. Kisch, "The nature of nitrogen-modified titanium dioxide photocatalysts active in visible light," *Angewandte Chemie—International Edition*, vol. 47, no. 51, pp. 9975–9978, 2008.
- [10] Z. Yuan, J. L. Zhang, B. Li, and J. Li, "Effect of metal ion dopants on photochemical properties of anatase TiO<sub>2</sub> films synthesized by a modified sol-gel method," *Thin Solid Films*, vol. 515, no. 18, pp. 7091–7095, 2007.
- [11] C. Cai, J. Zhang, F. Pan, W. Zhang, H. Zhu, and T. Wang, "Influence of metal (Au, Ag) micro-grid on the photocatalytic activity of TiO<sub>2</sub> film," *Catalysis Letters*, vol. 123, no. 1-2, pp. 51–55, 2008.
- [12] X. Yang, F. Ma, K. Li et al., "Mixed phase titania nanocomposite codoped with metallic silver and vanadium oxide: new efficient photocatalyst for dye degradation," *Journal of Hazardous Materials*, vol. 175, no. 1-3, pp. 429–438, 2010.
- [13] M. Yoshinaga, K. Yamamoto, N. Sato, K. Aoki, T. Morikawa, and A. Muramatsu, "Remarkably enhanced photocatalytic activity by nickel nanoparticle deposition on sulfur-doped titanium dioxide thin film," *Applied Catalysis B: Environmental*, vol. 87, no. 3-4, pp. 239–244, 2009.
- [14] O. Lorret, D. Francová, G. Waldner, and N. Stelzer, "W-doped titania nanoparticles for UV and visible-light photocatalytic reactions," *Applied Catalysis B: Environmental*, vol. 91, no. 1-2, pp. 39–46, 2009.
- [15] E. Wang, W. Yang, and Y. Cao, "Unique surface chemical species on indium doped TiO<sub>2</sub> and their effect on the visible light photocatalytic activity," *Journal of Physical Chemistry C*, vol. 113, no. 49, pp. 20912–20917, 2009.
- [16] W. Choi, A. Termin, and M. R. Hoffmann, "The role of metal ion dopants in quantum-sized TiO<sub>2</sub>: correlation between photoreactivity and charge carrier recombination dynamics," *Journal of Physical Chemistry C*, vol. 98, pp. 13669–13679, 1994.
- [17] J. Choi, H. Park, and M. R. Hoffmann, "Effects of single metal-ion doping on the visible-light photoreactivity of TiO<sub>2</sub>," *Journal of Physical Chemistry C*, vol. 114, no. 2, pp. 783–792, 2010.
- [18] T. C. Jagadale, S. P. Takale, R. S. Sonawane et al., "N-doped TiO<sub>2</sub> nanoparticle based visible light photocatalyst by modified peroxide sol-gel method," *The Journal of Physical Chemistry C*, vol. 112, no. 37, pp. 14595–14602, 2008.
- [19] Y. Xie, Q. N. Zhao, X. J. Zhao, and Y. Li, "Low temperature preparation and characterization of N-doped and N-S-codoped TiO<sub>2</sub> by sol-gel route," *Catalysis Letters*, vol. 118, no. 3-4, pp. 231–237, 2007.
- [20] Y. Wu, J. Zhang, L. Xiao, and F. Chen, "Preparation and characterization of TiO<sub>2</sub> photocatalysts by Fe<sup>3+</sup> doping together with Au deposition for the degradation of organic pollutants," *Applied Catalysis B: Environmental*, vol. 88, no. 3-4, pp. 525–532, 2009.
- [21] W. Zhao, W. Ma, C. Chen, J. Zhao, and Z. Shuai, "Efficient degradation of toxic organic pollutants with Ni<sub>2</sub>O<sub>3</sub>/TiO<sub>2-x</sub>B<sub>x</sub> under visible irradiation," *Journal of the American Chemical Society*, vol. 126, no. 15, pp. 4782–4783, 2004.
- [22] S. Z. Hu, F. Y. Li, Z. P. Fan, and C. C. Chang, "Enhanced photocatalytic activity and stability of nano-scaled TiO<sub>2</sub> co-doped with N and Fe," *Applied Surface Science*, vol. 32, no. 3, pp. 182–188, 2011.

## Research Article

# Effect of Contact Time and Gas Component on Interfacial Tension of CO<sub>2</sub>/Crude Oil System by Pendant Drop Method

Xin Wang,<sup>1</sup> Lifeng Liu,<sup>2</sup> Zengmin Lun,<sup>1</sup> Chengyuan Lv,<sup>1</sup> Rui Wang,<sup>1</sup> Haitao Wang,<sup>1</sup> and Dong Zhang<sup>1</sup>

<sup>1</sup>EOR Technology Division, Petroleum Exploration & Production Research Institute, Sinopec, Beijing 100083, China

<sup>2</sup>Research Institute of Petroleum Exploration & Development, PetroChina, Beijing 100083, China

Correspondence should be addressed to Rui Wang; wrzhds@126.com

Received 6 August 2014; Accepted 20 September 2014

Academic Editor: Qingrui Zhang

Copyright © 2015 Xin Wang et al. This is an open access article distributed under the Creative Commons Attribution License, which permits unrestricted use, distribution, and reproduction in any medium, provided the original work is properly cited.

Pendant drop method has been used to measure the equilibrium interfacial tension and dynamic interfacial tension of CO<sub>2</sub>/crude oil system under the simulated-formation condition, in which the temperature is 355.65 K and pressure ranges from 0 MPa to 30 MPa. The test results indicated that the equilibrium interfacial tension of CO<sub>2</sub>/crude oil systems decreased with the increase of the systematic pressure. The dynamic interfacial tension of CO<sub>2</sub>/original oil, CO<sub>2</sub>/remaining oil, and CO<sub>2</sub>/produced oil systems is large at the initial contact and decreases gradually after that, and then finally it reaches dynamic balance. In addition, the higher the pressure is, the larger the magnitude of changing of CO<sub>2</sub>/crude oil interfacial tension with time will reduce. Moreover, by PVT phase experiment, gas-oil ratio, gas composition, and well fluid composition have been got, and different contents of light components in three oil samples under reservoir conditions have also been calculated. The relationship between equilibrium interfacial tensions and pressures of three different components of crude oil and CO<sub>2</sub> system was studied, and the higher C<sub>1</sub> is, the lower C<sub>2</sub>–C<sub>10</sub> will be, and the equilibrium interfacial tension will get higher. Therefore, the effect of light weight fractions on interfacial tension under formation conditions was studied.

## 1. Introduction

The EOR technology of gas injection is theoretically better than water injection in the enhancement of oil recovery. Gas injection has developed rapidly in recent years overseas, and it has become the most important EOR method besides thermal recovery [1–3]. There are a variety of gases that can be injected, and CO<sub>2</sub>, for its wide sources and good flooding effect, has been widely put into practical application in oil fields [4–7]. When CO<sub>2</sub> is in a supercritical state, at the temperature above the critical temperature of 31.26°C and the pressure higher than the critical pressure of 7.2 MPa, its property will change. The density of CO<sub>2</sub> is close to liquid, and the viscosity of it is close to gas at this condition; moreover, the diffusion coefficient of the CO<sub>2</sub> is 100 times higher than liquid. Therefore, CO<sub>2</sub> has a great ability to dissolve in liquid [8–15]. This is helpful in improving the overall mass transfer rate when supercritical solubility increases and the reservoir

structure is conducive to increase inner diffusion and external diffusion, in order to increase the opportunity of the contact of CO<sub>2</sub> with oil and make them easier to mix. Therefore, CO<sub>2</sub> miscible flooding can meet the requirements for injected solvent in many oil fields [16–22].

The data of gas and crude oil interfacial tension under conditions of formation has very important theoretical and practical value, and the key of miscible flooding technology is to determine the minimum miscibility pressure of injection agent and crude oil [23–27]. The phenomenon that the interfacial tension changes with pressure significantly affects the reservoir fluid transfer behavior [28–31]. Miscible flooding technology is considered as one of the most cost-effective methods of EOR [32–35].

Pendant drop has been used to measure the relationship between the equilibrium interfacial tension and the pressure of CO<sub>2</sub>/crude oil system under the condition of the stratum temperature. Changes of interfacial tension with time

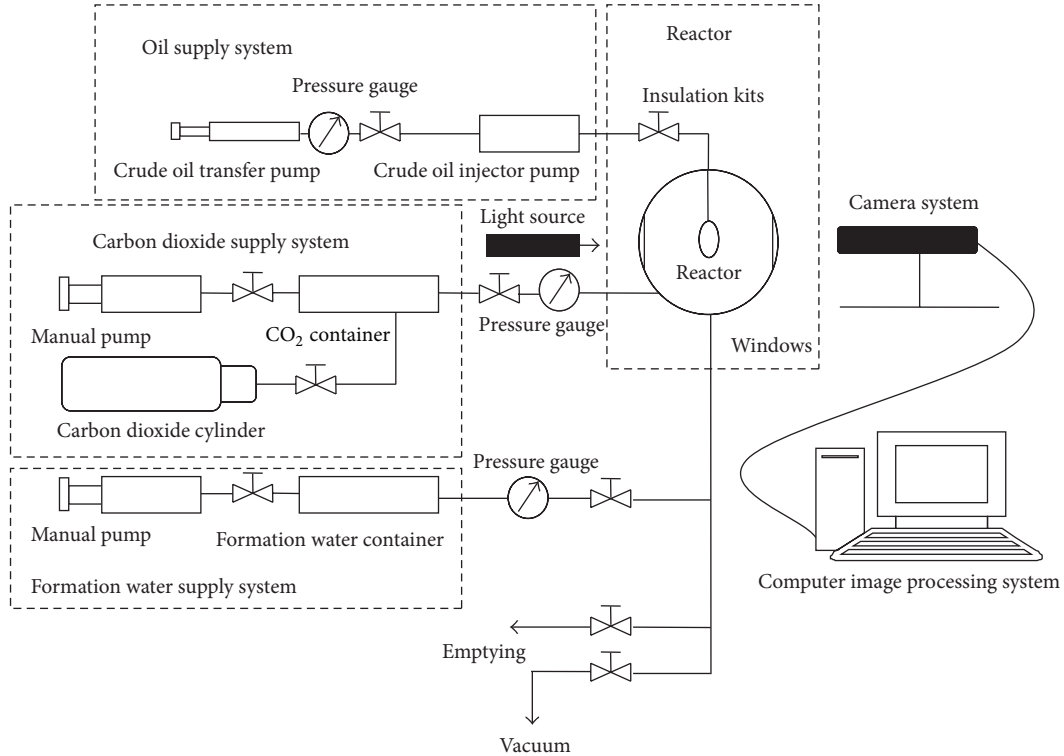


FIGURE 1: The schematic for the determination of interfacial tension by pendent drop method.

and pressure were measured by this method. By PVT phase experiment, the gas-oil ratio, gas composition, and well fluid composition have been measured. And the effect of light weight fractions on the interfacial tension under formation conditions was also calculated.

## 2. Experiment

**2.1. Experimental Apparatus.** High temperature and pressure interfacial tension meter has been used in the experiments, made by a French production company ST. The core of the device is a reactor with a window, which has an operating temperature of 0~200°C and a maximum working pressure of 70 MPa. Diameter of the needle used in the experiment is 0.81 mm, which is used for hanging droplets and using PVT analyzer for routine analysis.

Pendant drop method technology is the most accurate method to measure the interfacial tension under high temperature and high pressure conditions. First, the pump is used to form droplets on stainless steel needle department, and then the droplets shape photos are shot by amplifying camera system; after that the computer image processing systems are used to get the outer contour of the oil droplets. Ultimately calculated the interfacial tension, by using corrected image magnification, the density of light phase and heavy phase. The apparatus is shown in Figure 1.

**2.2. Experimental Samples.** Crude oil was provided by Zhonggyuan oilfield, and formation temperature was 355.65 K. Experiment with CO<sub>2</sub> gas was produced by Beijing Hua

Yuan Co. with a purity of 99.995% and petroleum ether was produced by Sinopharm Chemical Reagent Company.

## 3. Experimental Phenomena and Results Analysis

### 3.1. CO<sub>2</sub>/Oil Equilibrium Interfacial Tension

#### 3.1.1. Experimental Phenomena

(1) *The Dissolution and Extraction Effect.* The experimental temperature is 82.5°C, and the pressure ranged from 0 MPa to 30 MPa. During the experiment, there is a medium exchange as the oil drop from the tip of the needle interacts with the CO<sub>2</sub> from the reactor on the condition that the experiment pressure is higher than the bubble point pressure [16–18]. CO<sub>2</sub> has been dissolved into the oil droplets constantly, and the light group of oil droplets also spread to CO<sub>2</sub> [19–22]. At the beginning of the contact of oil and CO<sub>2</sub>, the reaction is much stronger, and the light component of crude oil has been dissolved by supercritical CO<sub>2</sub> constantly [23–25], as shown in Figure 2. After some dissolution and extraction, the heavy component of crude oil will be left behind, and the crude oil and CO<sub>2</sub> will eventually reach equilibrium state as shown in Figure 3. The interfacial tension of this time can be seen as the equilibrium interfacial tension.

(2) *The Effect of Pressure on the Dissolution and Extraction.* It can be seen from the picture that, with the increase of the pressure, the extraction of crude oil increases, and the



FIGURE 2: The initial phase.



FIGURE 3: The equilibrium phase.

interface between  $\text{CO}_2$  and crude oil becomes unstable. A small amount of light components can be extracted out at the pressure of 16 MPa, but the extraction effect becomes more significant when the pressure reaches 30 MPa, as shown in Figure 4, taken at the initial state. At this time, the oil droplets gravity is equal to the  $\text{CO}_2$ /oil interfacial tension, so that the oil droplets could suspend on the needle without dripping.

**3.1.2. The Experimental Curve.** The relationship between interfacial tension and pressure is shown in Figure 5. The equilibrium interfacial tension between crude oil and  $\text{CO}_2$  decreases with the increase of pressure. The minimum miscibility pressure of the system calculated by extrapolation method is 18.97 MPa. When the pressure is lower than 18.97 MPa, the interfacial tension decreased rapidly; but while the pressure reaches 18.97 MPa, the reduction of interfacial tension will get slower.

**3.2. The Dynamic Interfacial Tension between Crude Oil and  $\text{CO}_2$ .** The experiment showed that the interaction between  $\text{CO}_2$  and crude oil is strong at the early stage, but with the extraction of light weight fractions of crude oil by  $\text{CO}_2$  and the dissolution of  $\text{CO}_2$  into the oil, the interfacial tension between them changes. In order to study the effect of this process on the interfacial tension, the contact time's effect on the interfacial tension between crude oil and  $\text{CO}_2$  should also be tested.

TABLE 1: The equilibrium interfacial tension of three  $\text{CO}_2$ /crude oil systems.

Oil sample	Equilibrium interfacial tension/MPa
Original oil	18.9744
Remaining oil	19.4748
Produced oil	20.5144

Figures 6, 7, and 8 show how the three oil samples' interfacial tension changes with time. The oil samples include original oil, remaining oil, and produced oil. It can be seen from the figure that the interfacial tension of  $\text{CO}_2$  and oil is large at the initial contact; but as the contact time is getting longer, the interfacial tension decreases gradually and eventually reaches dynamic balance.

Figures 9 and 10 compared the curves of  $\text{CO}_2$ /crude oil interfacial tension change with time in two different pressures. It can be seen from the figure that the higher the pressure is, the larger the magnitude of  $\text{CO}_2$ /crude oil interfacial tension changing with time will reduce. The value of equilibrium interfacial tension under 12 MPa is more than 90% of the initial interfacial tension, but it turns to 80% at the pressure of 21 MPa. Obviously, the interaction between  $\text{CO}_2$  and oil is stronger, and the change of interfacial tension is bigger at a higher pressure. This phenomenon is due to the fact that more lightweight components are extracted out and the dynamic mass transfer is getting active at high pressure. The actual reservoir  $\text{CO}_2$  flooding belongs to multicontact miscible flooding, it's a process that after the contact of  $\text{CO}_2$  and oil, and many times extraction and dissolution, the oil and  $\text{CO}_2$  eventually get miscible. This leads to the interfacial tension between crude oil and  $\text{CO}_2$  which becomes an inevitable result of dynamic change.

**3.3. Effects of Gas Composition on  $\text{CO}_2$ /Oil Interfacial Tension.** Using PVT phase experiment, gas-oil ratio, gas composition, and well fluid composition have been got as shown in Figures 11, 12, and 13. And calculate different contents of light weight fractions in the three oil samples under reservoir condition. Contents of  $C_1$ ,  $C_2-C_{10}$ , and  $C_{11+}$  of three oil samples are shown in Figure 14.

As can be seen from Figure 13, the higher the  $C_1$  is, the lower its corresponding  $C_2-C_{10}$  will be, and the  $C_{11+}$  content of the three oil samples is relatively at a low level.

Using extrapolation method, calculate the equilibrium interfacial tension of  $\text{CO}_2$ /original oil system,  $\text{CO}_2$ /remaining oil system, and  $\text{CO}_2$ /produced oil system. The equilibrium interfacial tension of three different systems is shown in Table 1.

It can be seen from Figure 13 and Table 1 that the content of  $C_1-C_{10}$  component is continually increasing. The higher  $C_1$  is, the lower  $C_2-C_{10}$  will be, and the equilibrium interfacial tension is getting higher. On the contrary, the lower  $C_1$  is, the higher  $C_2-C_{10}$  will be, and the equilibrium interfacial tension becomes lower. In other words,  $C_1$  is negative for  $\text{CO}_2$  and oil miscibility, and  $C_2-C_{10}$  promotes the miscibility of  $\text{CO}_2$  and oil system. Therefore, factors that affect the  $\text{CO}_2$  and crude oil system interfacial tension are pressure, gas composition,

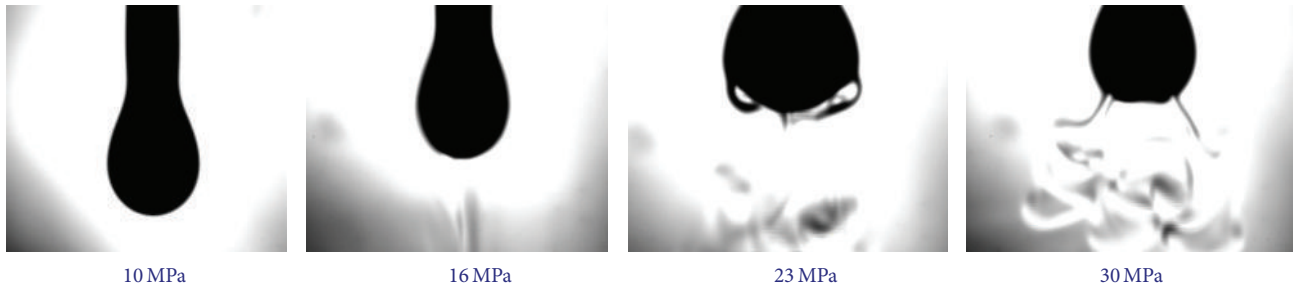


FIGURE 4: Images of the pendant oil drop in  $\text{CO}_2$ /crude oil system under different pressure.

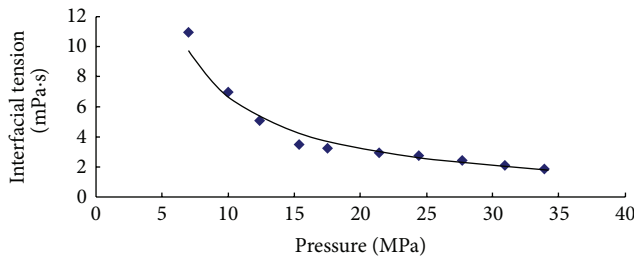


FIGURE 5: Interfacial tension of  $\text{CO}_2$ /crude oil system under different pressure.

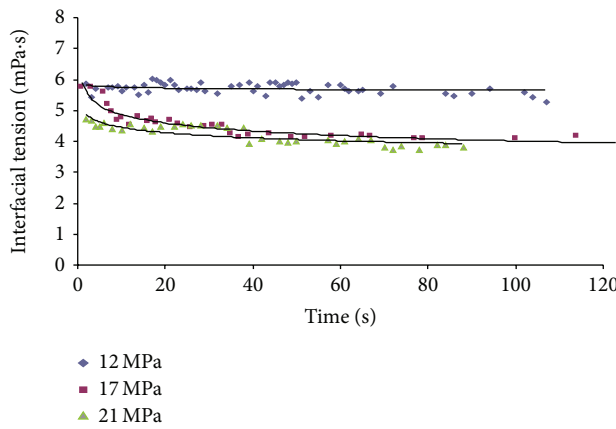


FIGURE 6: The relationship between interfacial tension and time of  $\text{CO}_2$ /original oil system.

and time. In hydrocarbons and  $\text{CO}_2$  compound flooding process, the selection of  $\text{C}_2\text{-C}_{10}$  and  $\text{CO}_2$  as a composite system will achieve better results in flooding.

Recent studies mostly focused on the research and application of equilibrium interfacial tension, and the study of dynamic interfacial tension is rare. But the actual reservoir  $\text{CO}_2$  flooding belongs to multicontact miscible flooding, and this leads to the interfacial tension between crude oil and  $\text{CO}_2$  becoming an inevitable result of dynamic change. So the dynamic interfacial tension can better simulate the situation under reservoir conditions and is more valuable. Historical studies do not mention hydrocarbons and  $\text{CO}_2$  compound flooding, but the data from the experimental measurements are conducive to the development of hydrocarbons and

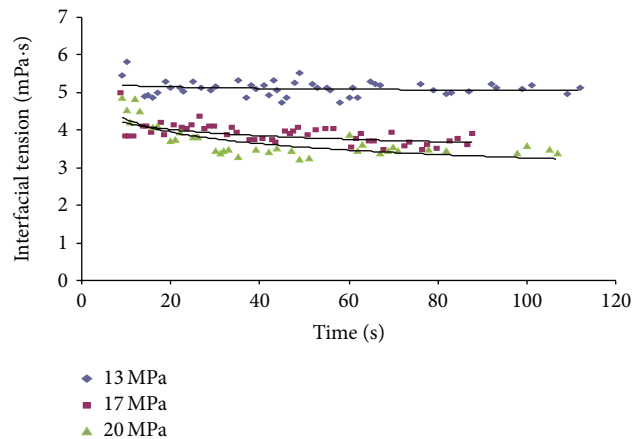


FIGURE 7: The relationship between interfacial tension and time of  $\text{CO}_2$ /remaining oil system.

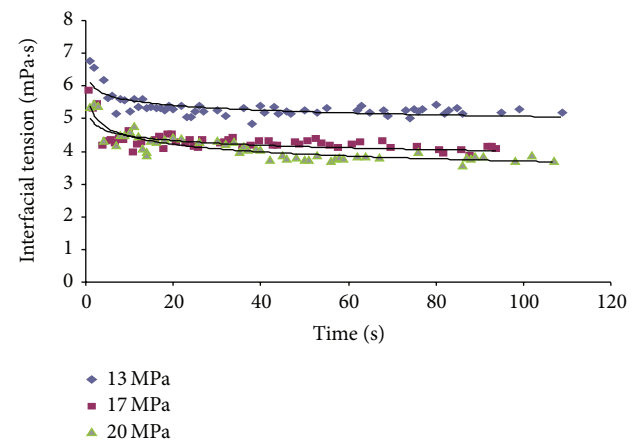


FIGURE 8: The relationship between interfacial tension and time of  $\text{CO}_2$ /produced oil system.

$\text{CO}_2$  compound flooding technology. The findings not only provide experimental evidence for indoor hydrocarbons and  $\text{CO}_2$  compound flooding but also make it not just stick to a single  $\text{CO}_2$  flooding. The experimental results provide a broad prospect for  $\text{CO}_2$  flooding and opened up new areas for hydrocarbons and  $\text{CO}_2$  compound flooding technology.

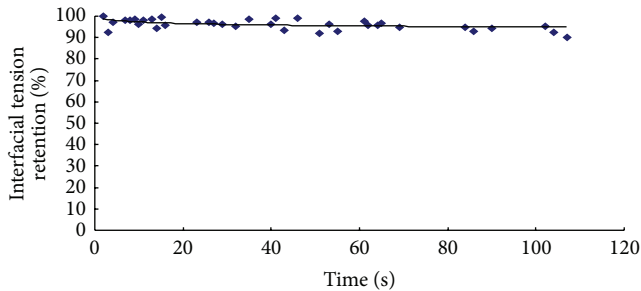


FIGURE 9: The curve of  $\text{CO}_2$ /crude oil system interfacial tension change with time under 12 MPa.

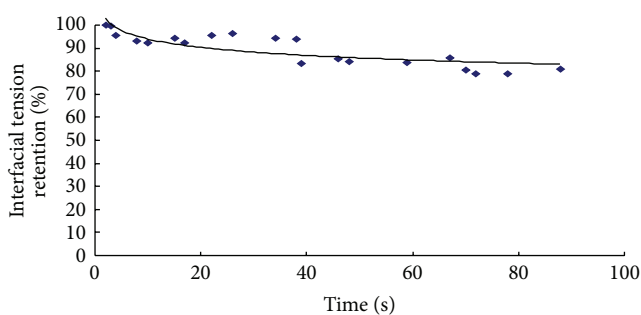


FIGURE 10: The curve of  $\text{CO}_2$ /crude oil system interfacial tension change with time under 21 MPa.

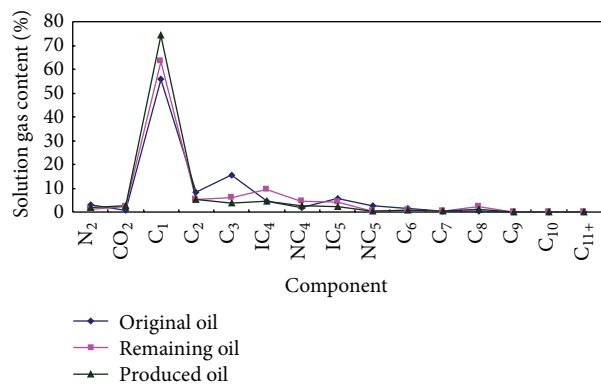


FIGURE 11: Gas phase composition of crude oil.

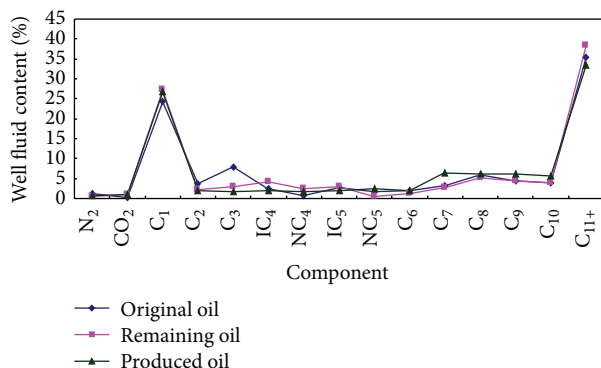


FIGURE 12: Well fluid composition of crude oil.

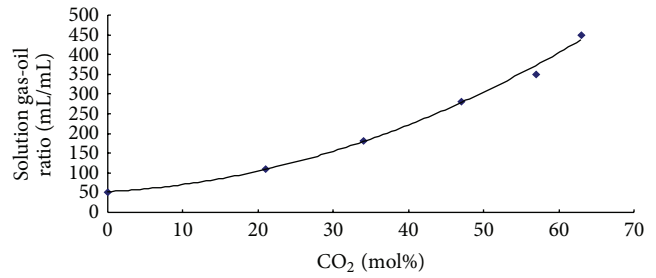


FIGURE 13: Gas-oil ratio of crude oil.

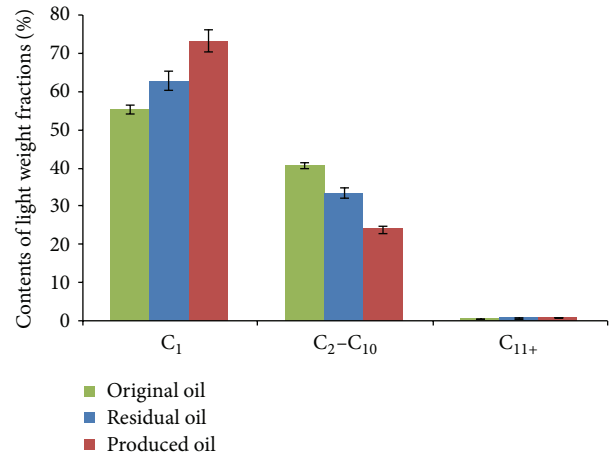


FIGURE 14: Content of different light weight fractions of original oil, remaining oil, and produced oil.

#### 4. Conclusions

(1) Using the pendant drop method, the interaction between  $\text{CO}_2$  and crude oil can be seen through the reactor under simulated-formation conditions of temperature and pressure. There is a strong mutual diffusion at the beginning of the contact of  $\text{CO}_2$  and crude oil, and as the pressure goes higher, the dissolution and extraction become easier.

(2) Data of  $\text{CO}_2$  and crude oil interfacial tension under conditions of the temperature of 355.65 K and the pressure ranging from 0 MPa to 30 MPa were measured by experiment. Experimental results show that  $\text{CO}_2$ /crude oil equilibrium interfacial tension decreases with the increasing of pressure.

(3) The interfacial tension of  $\text{CO}_2$  and oil is large at the initial contact, and as time is getting longer, the interfacial tension decreases gradually and eventually reaches dynamic balance. Moreover, the higher the pressure is, the more the magnitude of changing of  $\text{CO}_2$ /crude oil interfacial tension with time will reduce.

(4) The higher the content of  $\text{C}_1$  in crude oil is, the lower the content of  $\text{C}_2\text{-C}_{10}$  will be, and the equilibrium interfacial tension will get higher. On the contrary, the lower the content of  $\text{C}_1$  is, the higher the content of  $\text{C}_2\text{-C}_{10}$  will be, and the equilibrium interfacial tension will become lower. In other words,  $\text{C}_1$  is negative for the miscibility of  $\text{CO}_2$  and oil, and  $\text{C}_2\text{-C}_{10}$  can promote the miscibility of  $\text{CO}_2$  and crude oil system.

## Conflict of Interests

The authors declare that there is no conflict of interests regarding the publication of this paper.

## References

- [1] L. Mengtao, S. Wenwen, L. Xiangui, and S. Genhua, "Laboratory study on miscible oil displacement mechanism of supercritical carbon dioxide," *Acta Petrolei Sinica*, vol. 27, no. 3, pp. 80–83, 2006.
- [2] T. W. Teklu, N. Alharthy, H. Kazemi, X. Yin, and R. M. Graves, "Vanishing interfacial tension algorithm for MMP determination in unconventional reservoirs," in *Proceedings of the SPE Western North American and Rocky Mountain Joint Meeting (SPE-169517-MS)*, 2014.
- [3] M. Stukan and W. Abdallah, "Interfacial tension (IFT) and surface alteration interplay," in *Abu Dhabi International Petroleum Exhibition and Conference—Sustainable Energy Growth: People, Responsibility, and Innovation (ADIPEC '12)*, Proceedings of the SPIE, pp. 1155–1164, Abu Dhabi, UAE, November 2012.
- [4] D. Makimura, M. Kunieda, Y. Liang, T. Matsuoka, S. Takahashi, and H. Okabe, "Application of molecular simulations to CO<sub>2</sub>-enhanced oil recovery: phase equilibria and interfacial phenomena," *SPE Journal Paper*, vol. 18, no. 2, pp. 319–330, 2013.
- [5] V. Mirchi, S. Saraji, L. Goual, and M. Piri, "Dynamic interfacial tensions and contact angles of surfactant-in-brine/oil/shale systems: implications to enhanced oil recovery in shale oil reservoirs," in *Proceedings of the SPE Improved Oil Recovery Symposium (169171-MS SPE Conference Paper)*, 2014.
- [6] S. Shehbaz and B. T. Hoffman, "CO<sub>2</sub> flooding the elm coulee field," in *Proceedings of the SPE Rocky Mountain Petroleum Technology Conference*, Society of Petroleum Engineers, Denver, Colorado, April 2009.
- [7] J. Phirani and K. K. Mohanty, "Kinetic simulation of CO<sub>2</sub> flooding of methane hydrates," in *Proceedings of the SPE Annual Technical Conference and Exhibition*, 2010.
- [8] R. M. Brush, H. J. Davitt, O. B. Aimar, J. Arguello, and J. M. Whiteside, "Immiscible CO<sub>2</sub> flooding for increased oil recovery and reduced emissions," in *Proceedings of the Improved Oil Recovery Symposium*, Tulsa, Okla, USA, April 2000.
- [9] D. S. Sequeira, S. C. Ayirala, and D. N. Rao, "Reservoir condition measurements of compositional effects on gas-oil interfacial tension and miscibility," in *SPE Symposium on Improved Oil Recovery*, Tulsa, Okla, USA, 2008.
- [10] Y.-X. Zuo, J.-Z. Chu, S.-L. Ke, and T.-M. Guo, "A study on the minimum miscibility pressure for miscible flooding systems," *Journal of Petroleum Science and Engineering*, vol. 8, no. 4, pp. 315–328, 1993.
- [11] B.-G. Liu, P. Zhu, Z.-Q. Yong, and L.-H. Lu, "Pilot test on miscible CO<sub>2</sub> flooding in Jiangsu oil field," *Acta Petrolei Sinica*, vol. 23, no. 4, pp. 56–61, 2002.
- [12] Y. Daoyong and G. Yongan, "A new experimental technique for studying gas mass transfer in the crude oil by analysis of the measured dynamic and equilibrium interfacial tensions," in *Proceedings of the SPE Annual Technical Conference and Exhibition*, Society of Petroleum Engineers, San Antonio, Tex, USA, September 2006.
- [13] T. W. Teklu, N. Alharthy, H. Kazemi, X. Yin, and R. M. Graves, "Vanishing interfacial tension algorithm for MMP determination in unconventional reservoirs," in *SPE Western North American and Rocky Mountain Joint Meeting*, Denver, Colo, USA, 2014.
- [14] B. Peng, H. Luo, G. Chen, and C. Sun, "Determination of the minimum miscibility pressure of CO<sub>2</sub> and crude oil system by vanishing interfacial tension method," *Acta Petrolei Sinica*, vol. 28, no. 3, pp. 93–95, 2007.
- [15] C. Y. Sun, W. Q. Wang, G. J. Chen, and C. F. Ma, "Interfacial tension experiment of oil and water, oil and gas for CO<sub>2</sub> injected reservoir fluid system," *Journal of China University of Petroleum*, vol. 30, no. 5, pp. 109–112, 2006.
- [16] Y. Daoyong and Y. Gu, "Visualization of interfacial interactions of crude Oil-CO<sub>2</sub> systems under reservoir conditions," in *Proceedings of the SPE/DOE Symposium on Improved Oil Recovery*, Society of Petroleum Engineers, Tulsa, Okla, USA, April 2004.
- [17] A. M. Elsharkawy, F. H. Poettmann, and R. L. Christiansen, "Measuring CO<sub>2</sub> minimum miscibility pressures: slim-tube or rising-bubble method?" *Energy and Fuels*, vol. 10, no. 2, pp. 443–449, 1996.
- [18] D. B. Bennion and S. Bachu, "correlations for the interfacial tension between supercritical phase CO<sub>2</sub> and equilibrium brines at in situ conditions," in *Proceedings of the Annual Technical Conference and Exhibition*, Denver, Colo, USA, September 2008.
- [19] K. Jessen and F. M. Orr, "On interfacial-tension measurements to estimate minimum miscibility pressures," *SPE Reservoir Evaluation & Engineering*, vol. 11, no. 5, pp. 933–939, 2008.
- [20] M. Dong, S. Huang, S. B. Dyer, and F. M. Mourits, "A comparison of CO<sub>2</sub> minimum miscibility pressure determinations for Weyburn crude oil," *Journal of Petroleum Science and Engineering*, vol. 31, no. 1, pp. 13–22, 2001.
- [21] D. N. Rao, "A new technique of vanishing interfacial tension for miscibility determination," *Fluid Phase Equilibria*, vol. 139, no. 1-2, pp. 311–324, 1997.
- [22] D. Yang and Y. Gu, "A new experimental technique for studying gas mass transfer in the crude oil by analysis of the measured dynamic and equilibrium interfacial tensions," in *Proceedings of the SPE Annual Technical Conference and Exhibition (ATCE '06)*, Paper SPE 95844, pp. 2081–2094, Dallas, Tex, USA, September 2006.
- [23] S. Siregar, P. Mardisewojo, D. Kristanto, and R. Tjahyadi, "Dynamic interaction between CO<sub>2</sub> gas and crude oil in porous medium," in *Proceedings of the Asia Pacific Improved Oil Recovery Conference*, Kuala Lumpur, Malaysia, October 1999.
- [24] U. W. R. Siagian and R. B. Grigg, "The extraction of hydrocarbons from crude oil by high pressure CO<sub>2</sub>," in *SPE/DOE Improved Oil Recovery Symposium*, Tulsa, Okla, USA, 1998.
- [25] A. Y. Zekri, S. A. Shedad, and R. A. Almehaideb, "An experimental investigation of interactions between supercritical CO<sub>2</sub>, asphaltenic crude oil, and reservoir brine in carbonate cores," in *Proceedings of the International Symposium on Oilfield Chemistry*, Society of Petroleum Engineers, Houston, Tex, USA, 2007.
- [26] D. N. Rao and J. I. Lee, "Determination of gas-oil miscibility conditions by interfacial tension measurements," *Journal of Colloid and Interface Science*, vol. 262, no. 2, pp. 474–482, 2003.
- [27] R. A. DeRuiter, L. J. Nash, and M. S. Singletary, "Solubility and displacement behavior of a viscous crude with CO<sub>2</sub> and hydrocarbon gases," *SPE Reservoir Engineering*, vol. 9, no. 2, pp. 101–106, 1994.
- [28] D. Yang, P. Tontiwachwuthikul, and Y. Gu, "Interfacial tension phenomenon and mass transfer process in the reservoir brine-CO<sub>2</sub> system at high pressures and elevated temperatures," in

- Proceedings of the International Green Energy Conference (IGEC-I), Waterloo, Canada, 2005.*
- [29] Q.-Y. Ren, G.-J. Chen, W. Yan, and T.-M. Guo, "Interfacial tension of  $(CO_2 + CH_4) +$  water from 298 K to 373 K and pressures up to 30 MPa," *Journal of Chemical and Engineering Data*, vol. 45, no. 4, pp. 610–612, 2000.
  - [30] C.-Y. Sun, G.-J. Chen, and L.-Y. Yang, "Interfacial tension of methane + water with surfactant near the hydrate formation conditions," *Journal of Chemical and Engineering Data*, vol. 49, no. 4, pp. 1023–1025, 2004.
  - [31] R. Ghez, *Diffusion Phenomena: Cases and Studies*, Kluwer Academic & Plenum, New York, NY, USA, 2001.
  - [32] C. A. Gratttoni and R. A. Dawe, "Gas and oil production from waterflood residual oil: effects of wettability and oil spreading characteristics," *Journal of Petroleum Science and Engineering*, vol. 39, no. 3-4, pp. 297–308, 2003.
  - [33] D. Yang and Y. Gu, "Visualization of interfacial interactions of crude oil- $CO_2$  systems under reservoir conditions," in *SPE/DOE Symposium on Improved Oil Recovery*, Tulsa, Okla, USA, 2004.
  - [34] J. Zappe, A. Wesch, and K. H. Ebert, "Measurement of the mass transfer into single drops in the system of water/supercritical carbon dioxide," *Journal of Colloid and Interface Science*, vol. 231, no. 1, pp. 1–7, 2000.
  - [35] D. Yang and Y. Gu, "Interfacial interactions between crude oil and  $CO_2$  under reservoir conditions," *Petroleum Science and Technology*, vol. 23, no. 9-10, pp. 1099–1112, 2005.

## Research Article

# Preparation and Application of Titanate Nanotubes on Dye Degradation from Aqueous Media by UV Irradiation

Rui Liu,<sup>1</sup> Wein-Duo Yang,<sup>2</sup> Hui-Ju Chueng,<sup>2</sup> and Bin-Qiao Ren<sup>3</sup>

<sup>1</sup>Institute of Petroleum and Commodity, Harbin University of Commerce, 138 Tongda Street, Harbin 150076, China

<sup>2</sup>Department of Chemical and Materials Engineering, National Kaohsiung University of Applied Sciences, 415 Chien-Kung Road, Kaohsiung 807, Taiwan

<sup>3</sup>Institute of Advanced Technology of Heilongjiang Academy of Sciences, 135 Nanma Road, Harbin 150020, China

Correspondence should be addressed to Rui Liu; 57776806@qq.com and Wein-Duo Yang; ywd@cc.kuas.edu.tw

Received 30 June 2014; Accepted 15 July 2014

Academic Editor: Tifeng Jiao

Copyright © 2015 Rui Liu et al. This is an open access article distributed under the Creative Commons Attribution License, which permits unrestricted use, distribution, and reproduction in any medium, provided the original work is properly cited.

Titanate nanotubes were synthesized by a hydrothermal method using commercial  $\text{TiO}_2$  powder and then used as a photocatalyst. The titanate nanotubes were synthesized by varying the hydrothermal temperature from 110°C to 180°C. The morphological changes and phase transformation of the  $\text{TiO}_2$  nanotubes were analyzed by X-ray diffraction (XRD), scanning electron microscopy (SEM), and transmission electron microscopy (TEM). The particles' scattering behavior was investigated by Raman studies, and the surface area of the nanotubes was determined by a Brunauer, Emmett, and Teller (BET) analysis. Comparative studies show that the surface area of nanotubes increases with increasing temperature up to 130°C. The catalytic behavior of the synthesized nanotubes was also studied. The as-prepared titanate nanotubes were applied to methylene blue (MB, an organic dye) degradation in aqueous media by UV irradiation. Approximately 99% of the dye was removed from the aqueous media using 2 g/L titanate nanotube when the initial dye concentration was 9 mg/L. The total irradiation time was 2 h.

## 1. Introduction

Nanoparticles and their applications are of great interest in modern science due to their unique properties, which differ from those of the corresponding bulk materials, and their diverse applications [1–4]. Gold, silver, ruthenium, platinum, and bimetallics or nanoalloys of those elements have been synthesized in various ways and used in biochemistry in particular for biomedical applications [5–10]. Among these materials, Titania ( $\text{TiO}_2$ ) is believed to be the most promising due to its nontoxicity, long-term stability, and low cost. Its applications are strongly dependent on the crystallographic structure, morphology, and size of the particles. Due to its desirable band gap (3.2 eV),  $\text{TiO}_2$  nanoparticles are also used in solar cells. It is also worth mentioning that Titania nanotubes and nanowires are used as photocatalysts due to their strong oxidizing power, biological and chemical inertness, and long-term stability against light-based and chemical corrosion [11, 12]. Presently, groups of researchers are attempting

to use this nanoparticle to remove toxic contaminants from aqueous media and air for the remediation of environmental contamination [13–15].

Various synthetic routes have been explored for the synthesis of size-controlled  $\text{TiO}_2$  nanoparticles. The simple hydrolysis of titanium salts results in  $\text{TiO}_2$  nanoparticles [16–19]. However, this technique produces a mixture of anatase and rutile polymorphs, which inhibits the formation of well-shaped anatase nanocrystals [20, 21], which have the highest photocatalytic activity towards the degradation of most organic contaminants in aqueous media [20]. Several groups have reported the preparation of titanate nanotubes (TNTs) using different hydrothermal reaction temperatures and durations [22, 23]. This method does not require a template, and the obtained nanotubes have a small diameter (~10 nm) with high crystallinity. Many groups have tried to analyze the characteristics of TNTs, which can then be used to evaluate the synthetic mechanism as well as sheet-folding mechanism [24, 25]. TNTs derived from the hydrothermal

method possess ion-exchange properties and are characterized by a high surface area and pore volume. They may also offer a special environment for the adsorption of large cations, such as basic dyes. Moreover, the hydrothermal method is also a simple, cost-effective, and ecofriendly technology and can prepare TNTs in high yields. Therefore, examining the potential applications of TNTs synthesized from this method, which is ecofriendly and cost-effective, is important.

Water pollution due to organic dyes is of great concern for human health as well as the environment because colored water is aesthetically unpleasant. The production of different by-products due to the degradation of some organic dyes poses a severe health risk due to their carcinogenicity. The literature contains physical, chemical, and biological methods that have been applied to remove the color from dye-contaminated wastewater [26–30], and physical adsorption has been identified as a potentially efficient and economical way to remove dyes from waste streams and control the biochemical oxygen demand [31]. Although activated carbon is believed to be an efficient adsorbent for organic hazardous removal from aqueous media, it is expensive. Hence, a number of groups have tried to remove toxic organic dyes from aqueous media using titanate nanotubes by activating its photocatalytic activity using UV irradiation.  $\text{TiO}_2/\text{UV}$  photocatalysis is among the most promising advanced oxidation technologies due to the effectiveness of  $\text{TiO}_2$  in generating hydroxyl radicals along with its environmentally benign properties and relatively low cost [32–34].

In this paper, we have focused on the synthesis of titanate nanotubes using a hydrothermal method with different reaction temperatures and times. The performances of the titanate nanotubes synthesized under different reaction temperatures were analyzed analytically by XRD, Raman, TEM, BET, and FTIR. Finally, the removal of an organic dye, methylene blue (MB), was from an aqueous environment attempted using the synthesized titanate nanotubes and UV irradiation.

## 2. Materials and Methods

**2.1. Reagents.** All the chemicals used were of analytical grade and were used as received.  $\text{HNO}_3$ ,  $\text{NaOH}$ ,  $\text{TiO}_2$  (P25) powder, and methylene blue (MB) were purchased from Acros Organics (New Jersey, USA). A 100 ppm stock MB solution was prepared in double-distilled water and diluted as required.

**2.2. Instrumentation.** All the glass apparatus used were soaked in concentrated  $\text{HNO}_3$  for 12 h and then washed with large volumes of double-distilled water followed by tap water. Next, the apparatus were dried in a hot-air oven for 2 h at 90°C. A high-precision electronic balance was used for weighing, and a high-precision digital electronic pH meter was used to measure the pH of the medium. FTIR spectrometry was conducted using a Bio-Rad Digilab FIS-165 spectrophotometer. A Lambda Dimension-P2 Raman spectrometer was used to measure the Raman shift. Powder XRD patterns were recorded using a PANalytical X'Pert PRO X-ray diffractometer with  $\text{CuK}\alpha$  ( $\lambda = 1.5406 \text{ \AA}$ ) radiation. A

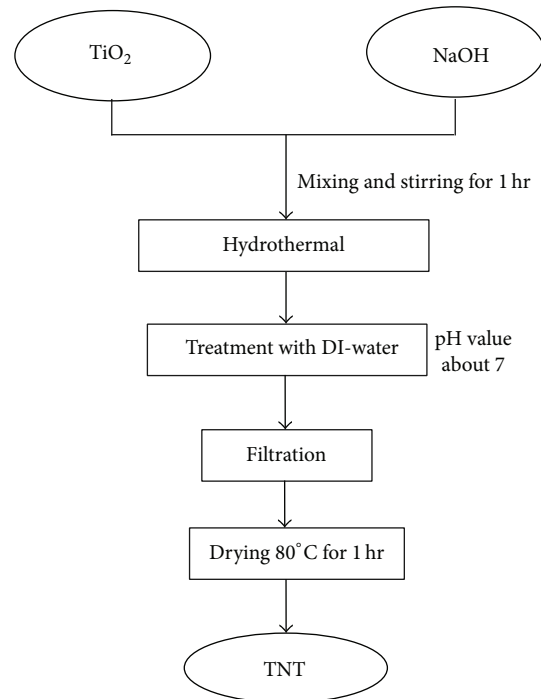


FIGURE 1: Preparation of titanate nanotubes by the hydrothermal method.

Micromeritics ASAP 2101 instrument was used for BET analysis. TEM measurements were performed using a Philips M-200 transmission electron microscope operating at 200 kV. All absorbance measurements were carried out using a UV-Vis spectrophotometer (HITACHI, U-2800) equipped with a 1 cm quartz cell. Gilson micropipette and microtips were used to add samples.

**2.3. Preparation of Titanate Nanotubes.** Hydrothermally titanate nanotubes were synthesized and the total synthesis process is shown in Figure 1. Set of experiments were conducted by the mixing of commercially available (0.8 g) (P25)  $\text{TiO}_2$  powder in 50 mL aqueous  $\text{NaOH}$  (10 M) solution. The mixtures were allowed to continuous stirring for 1 h with a magnetic stirrer. After the aging time finished, the reactions mixtures were hydrothermally treated at different temperatures in a stainless Teflon-lined autoclave. The autoclave was put into an oven and was heated to 110–180°C for a prescribed period of 24 h and cooled to room temperature naturally in air. Next, the final reaction products were washed thoroughly with large volumes of double-distilled water to achieve the neutral pH of the medium and that is ~7. Finally, obtained white cotton-battting-like solid was filtrated and dried at 80°C for 1 h and then characterized and used for photodegradation of organic dye, methylene blue from aqueous media.

**2.4. Photocatalytic Degradation of Aqueous Methylene Blue (MB).** To investigate the photocatalytic activity of the synthesized titanate nanotubes, the degradation of a toxic organic dye, methylene blue ( $\text{C}_{16}\text{H}_{18}\text{ClN}_3\text{S}$ ) (Figure 2), in aqueous

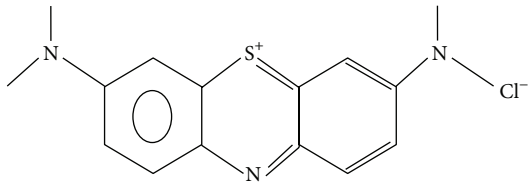
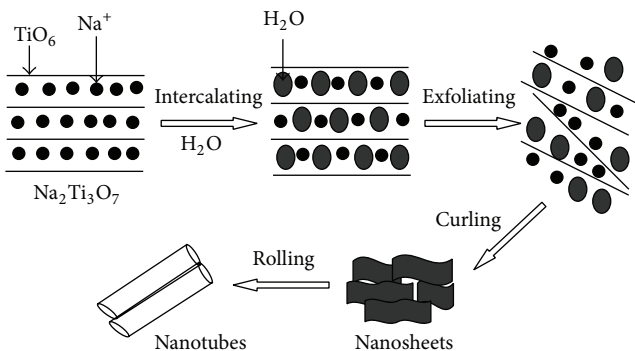


FIGURE 2: Structure of MB.

FIGURE 3: Exfoliating-rolling model of nanotube formation from the layered  $\text{Na}_2\text{Ti}_3\text{O}_7$  particles by a soft chemical process.

media was attempted using UV irradiation. First, 0.2 g of as-prepared titanate nanotubes was dispersed in 100 mL of synthetic MB solution when the initial dye concentration was 9 mg/L (titanate nanotubes dose, 2 g/L). The mixture of dye and catalyst was then placed in a photocatalytic reactor and subjected to UV irradiation. A 6-W, 254 nm UV lamp was used as the light source. The aqueous system of the suspended catalyst was oxygenated to ensure the presence of sufficient oxygen in the system. The experiment was conducted at room temperature ( $\sim 25 \pm 2^\circ\text{C}$ ). The total UV irradiation time was 2 h. Next, the titanate nanotube suspension was centrifuged at 3200 rpm for 10 min to separate the solid and liquid phases. Collecting the supernatant liquid, after centrifugation, the remaining dye concentration in the solution was measured by UV-Vis spectrophotometry at 669 nm.

### 3. Results and Discussion

**3.1. Formation Mechanism of Titanate Nanotubes.**  $\text{Na}^+$  resides between the edge-shared  $\text{TiO}_6$  and  $\text{Na}_2\text{Ti}_3\text{O}_7$  octahedral layers, as is well known. The strong static interaction force between the  $\text{Na}^+$  and  $\text{TiO}_6$  units holds the layers together tightly and makes it impossible to roll these layers into nanotubes. Under the hydrothermal conditions,  $\text{Na}^+$  is gradually released with intercalated  $\text{H}_2\text{O}$  molecules into the interlayer space of the  $\text{TiO}_6$  sheets. Because  $\text{H}_2\text{O}$  molecules are larger than  $\text{Na}^+$  ions, the interlayer distance increases during the release of  $\text{Na}^+$ , weakening the static interaction force between neighboring  $\text{TiO}_6$  and octahedral sheets. As a result, the  $\text{Na}_2\text{Ti}_3\text{O}_7$  layer was gradually exfoliated to form numerous sheet-shaped products [32, 33]. The nanotube formation mechanism is shown in Figure 3 [35].

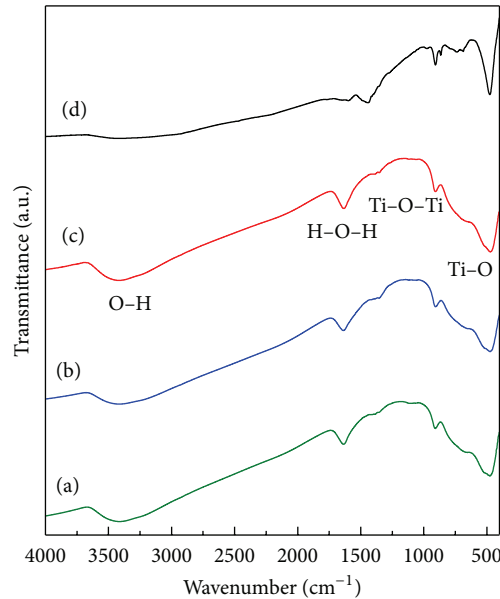


FIGURE 4: FTIR spectra of the samples prepared at different reaction temperatures: (a) 110°C, (b) 130°C, (c) 150°C, and (d) 180°C.

**3.2. Characterization of Titanate Nanotubes.** The synthesized titanate nanotubes were characterized by different methods. Figure 4 shows the FTIR spectra of the as-prepared nanotubes (using KBr pellets) synthesized at different hydrothermal temperatures and compares these values to those from a previous work [36]. The broad peaks at 3200~3400  $\text{cm}^{-1}$  are ascribed to the stretching vibration of the hydroxyl groups (O-H) from the residual water in the precursors. The peak of 1630  $\text{cm}^{-1}$  is attributed to the bending vibration of the hydroxyl groups (H-O-H) present in the titanate nanotubes. The other broad bands at 700~1200  $\text{cm}^{-1}$  and 300~900  $\text{cm}^{-1}$  are assigned to the Ti-O and Ti-O-Ti skeletal frequency regions, respectively. As the hydrothermal temperature increased to 180°C, the peaks of the stretching (O-H) and bending (H-O-H) vibrations of the hydroxyl groups disappeared completely. This disappearance is due to the very low content of organic compounds and water at high reaction temperatures.

The X-ray diffraction patterns (XRD) of titanate nanotubes synthesized at different hydrothermal temperatures are shown in Figure 5. The intense peak at approximately 9.1° is thought to be due to the layered structure of the  $\text{NaHTi}_3\text{O}_7$  nanotube wall, while the smaller broad peaks at approximately 24°, 28°, and 48° suggest the presence of sodium (Na) in the synthesized nanotubes, for example,  $\text{Ti}_6\text{O}_{13}$ ,  $\text{Ti}_6\text{O}_{12}$ , and  $\text{Ti}_9\text{O}_{18}$ . However, as the hydrothermal temperature increases to 180°C, curve (d) of Figure 5 suggests the presence of  $\text{Na}_2\text{Ti}_6\text{O}_{13}$ , the hydrothermally synthesized product [36–39]. This finding indicates that the titanate nanotube structure is changing from tube to rod. The nanorods are formed by the parallel arrangement of the nanotubes, which is a result of the adsorption of the nanotube surface of the water molecules and the evaporation of the inner layer

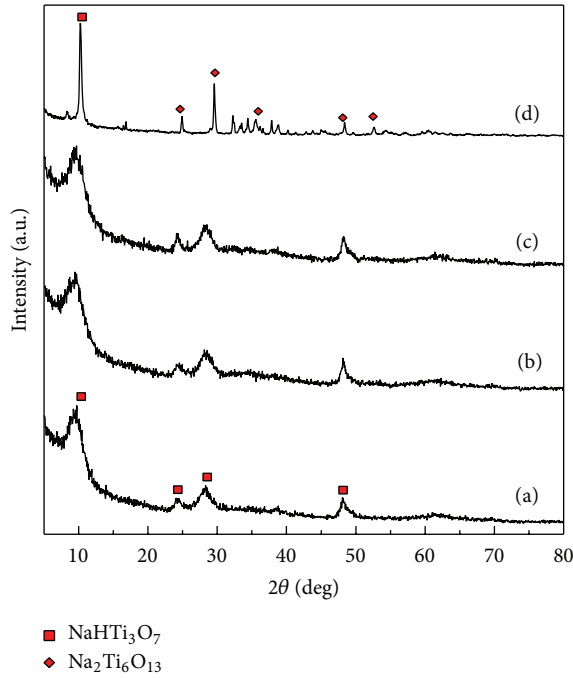


FIGURE 5: XRD patterns of the samples prepared at different reaction temperatures: (a) 110°C, (b) 130°C, (c) 150°C, and (d) 180°C.

of moisture to release the high stress inside the nanotube structure.

Figure 6 shows the TEM images of titanate nanotubes hydrothermally synthesized at different temperatures. When the hydrothermal treatment temperature was 110°C, the tubular structure was absent, and sheet-like structures were observed. Titanate nanotube clusters can be clearly seen when the hydrothermal treatment temperature was increased to 130°C. As the hydrothermal temperature increased to 180°C, the titanate nanotubes adopted a rod-like structure. It is inferred that the tubular structure is clearer and tube pore diameter larger at high hydrothermal temperatures. Overall, no damage of the titanate nanotubes was observed during the hydrothermal process with increasing temperature. The nanotubes were 200~300 nm in length and approximately 10 nm in diameter. Some of the long tubes synthesized at high temperature broke into shorter tubes. The tubular structure was retained, but the tubes were deposited onto one another [37, 40].

The surface morphology of the synthesized nanotubes was monitored by SEM (JEOL, TFSEM-6330), and the micrographs are shown in Figure 7. Figure 7 implies that the nanotube formation depends on temperature. The formation of nanotubes is due to the warping or splitting of the surface of  $\text{Na}_2\text{Ti}_3\text{O}_7$  octahedral layers. A number of cumulative steps followed the formation of nanotubes. Figure 8 depicts the  $\text{H}_2\text{Ti}_3\text{O}_7$  nanotube and nanowire formation processes. Initially, lamellar structures were grown on the brim of  $\text{TiO}_2$  particles. These lamellar structures grow along the [001] direction with the (010) plane as the top/bottom surface (a). Second, the lamellar structures split into nanosheets between

TABLE 1: BET analysis of as-prepared titanate nanotubes at different temperature and after 24 h.

Sample at different temperature	$S_{\text{BET}}$ ( $\text{m}^2/\text{g}$ )	Pore volume ( $\text{cm}^3/\text{g}$ )	Size (nm)
P25	60.0	0.06	3.8
110°C	126.7	0.20	3.2
130°C	186.8	0.23	3.2
150°C	183.6	0.39	4.8
180°C	9.9	0.05	11.6

TABLE 2: BET analysis of the prepared titanate nanotubes at different time at constant temperature of 130°C.

Sample at different time	$S_{\text{BET}}$ ( $\text{m}^2/\text{g}$ )	Pore volume ( $\text{cm}^3/\text{g}$ )	Size (nm)
P25	60.0	0.06	3.8
12 h	161.0	0.30	3.7
24 h	186.8	0.31	3.3
48 h	170.3	0.28	3.3

the (100) planes. The height of these nanosheet structures (in the *b* direction) is the thickness of the original lamellar structure (b). In the third step, the nanosheets wrapped into nanotubes with diameters dependent on the height of the nanosheets (c). Additionally, thick layers or wires may be formed after prolonged reaction at elevated temperature (d). Afterwards, splitting may occur between the (100) and (010) planes of these thick layers or wires (e). Finally, further splitting leads to the formation of thin nanowires (d) [41].

The nanotubes synthesized at various temperatures for various durations were subjected to BET analysis to determine the surface area of the synthesized titanate particles after degassing with nitrogen. The obtained result is given in Table 1. The specific surface area of the nanotubes increased with temperature, which in turn proves that the nanotubes are relatively small. This result can be interpreted as the titanate nanotubes steadily turning into tubular nanocomposites. At temperatures above 130°C, the surface area slowly decreases, which indicates that the nanotubes became larger (Table 1). The maximum surface area of the nanotubes,  $186.8 \text{ m}^2/\text{g}$ , was produced at 130°C after 24 h of synthesis. A time-resolved study of the surface area of the synthesized nanotubes was also conducted by varying the synthesis duration from 0 to 48 h, keeping the temperature constant at 130°C. It is observed that the surface area of the nanotubes increases with reaction time at this constant temperature. The time dependence of the nanotube surface area can be attributed to a continuous conversion of nanosheets into nanotubes during the reaction time. However, the obtained result suggests that the maximum surface area,  $186.8 \text{ m}^2/\text{g}$ , is found after 24 h of synthesis (Table 2). In contrast, this value was  $60 \text{ m}^2/\text{g}$  for P25 under room-temperature conditions.

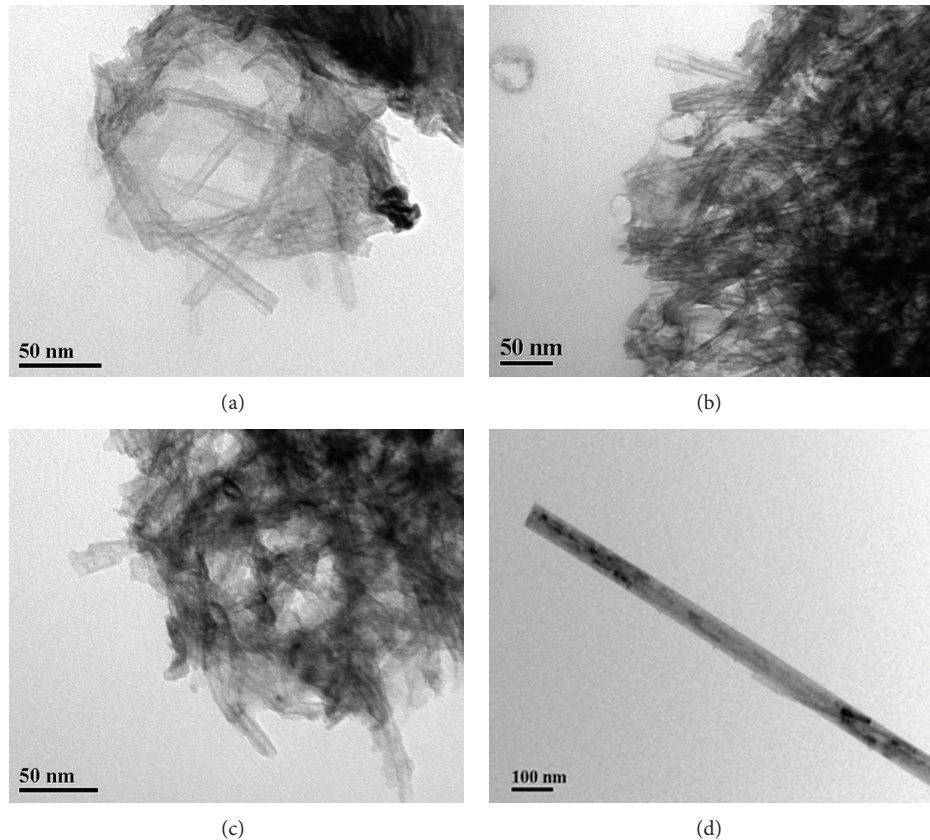


FIGURE 6: TEM images of the samples prepared at different reaction temperatures: (a) 110°C, (b) 130°C, (c) 150°C, and (d) 180°C.

The Raman spectrum of the as-prepared nanotubes is shown in curve (a) in Figure 9. For hydrothermal temperatures below 150°C, the modes at 662 cm<sup>-1</sup> and 700 cm<sup>-1</sup> are ascribed to the vibrations of Ti–O–Na and Ti–O–H, respectively, given that the 662 cm<sup>-1</sup> mode disappears from the as-prepared sample after washing with deionized (DI) water, which proves the exchange of Na<sup>+</sup> by H<sup>+</sup>. The 910 cm<sup>-1</sup> mode can be ascribed to the vibrations of Ti–O, which indicates that the structure is NaHTi<sub>3</sub>O<sub>7</sub>. At 180°C, the characteristic peaks of NaHTi<sub>3</sub>O<sub>7</sub> disappeared, while the Raman modes at 197 cm<sup>-1</sup>, 224 cm<sup>-1</sup>, 278 cm<sup>-1</sup>, 306 cm<sup>-1</sup>, 414 cm<sup>-1</sup>, 475 cm<sup>-1</sup>, 680 cm<sup>-1</sup>, and 874 cm<sup>-1</sup> were strongly consistent with the previously reported results, which once again supports the presence of titanate nanotubes in the products synthesized by the hydrothermal process [36, 39].

### 3.3. Photocatalytic Degradation of MB

**3.3.1. Calibration Curve.** UV-Visible spectra were recorded with various dye concentrations and are shown in Figure 10. The study was first conducted without the addition of the titanate nanotube photocatalyst or UV irradiation. A linear calibration curve of MB ( $\lambda_{\text{max}} = 669 \text{ nm}$ ) was drawn in the concentration range of 0–18 mg/L. The linear equation obtained is Absorbance ( $y$ ) =  $0.1719 \times (\text{mg/L}) + 0.191$ . The specific correlation coefficient was ( $R^2$ ) = 0.9999. The

obtained linear calibration equation was used through this study to determine the remaining dye concentration in the degraded dye solution after UV irradiation.

**3.3.2. Photodegradation of Dye.** First, 2 g/L of the titanate nanotubes prepared at different temperatures was mixed with 100 mL of the synthetic MB solution. Next, the mixture was photoirradiated with UV light for 2 h. The reaction mixture was stirred with a magnetic stirrer. The experiment was conducted at room temperature with an initial MB concentration of 9 mg/L. The pH of the medium was ~7. Kinetically, within 20 min of photoirradiation, ~99% of the dye had degraded. Hence, a 20 min photoirradiation time was identified as the equilibrium time for the dye photodegradation. No further acceleration of dye degradation was observed over an additional 100 min of irradiation time. The dye degradation efficiency was almost the same for each as-prepared titanate nanotube sample except that prepared at 180°C (Figure 11). The higher specific surface area (186.8 m<sup>2</sup>/g) allows more of the organic pollutant to be adsorbed onto the photocatalyst surface, while the high pore volume results in a faster diffusion of various reaction products during the photocatalytic reaction. All these factors contributed to enhancing the photocatalytic activity [42]. However, unlike the conventional adsorption of other aquatic contaminants on the adsorbent, which depends on both the particle size and the surface area

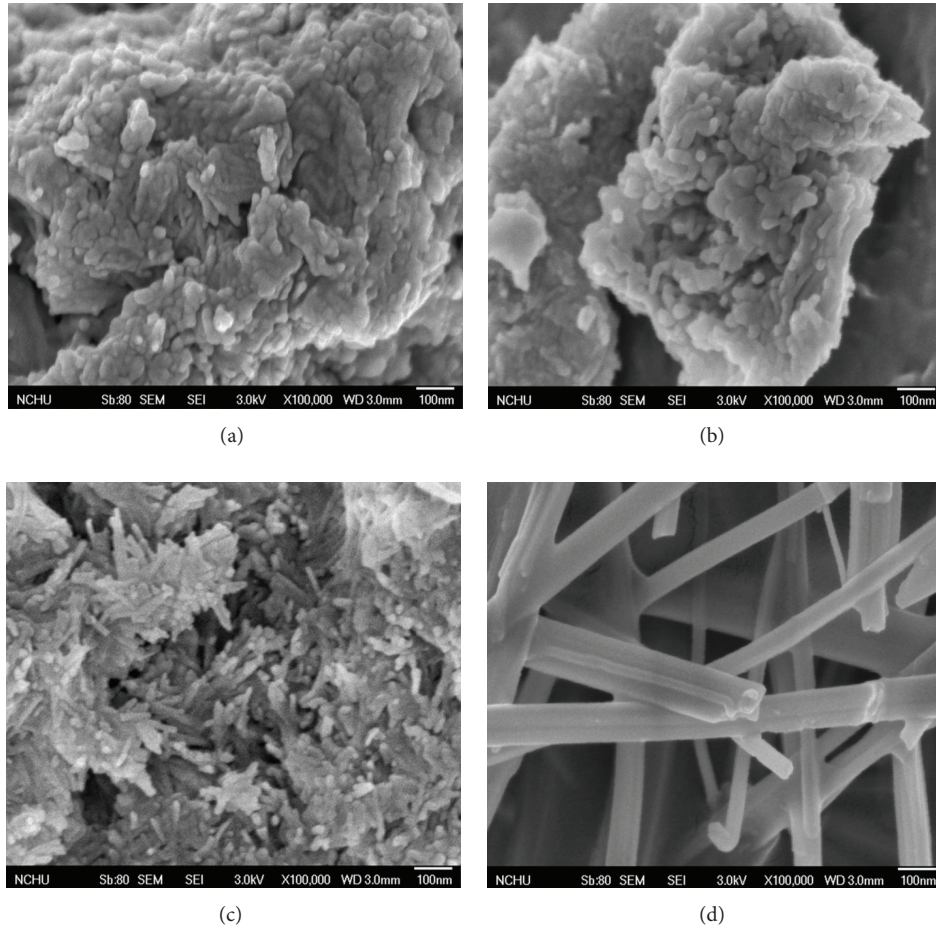


FIGURE 7: SEM images of the samples prepared at different reaction temperatures: (a) 110°C, (b) 130°C, (c) 150°C, and (d) 180°C.

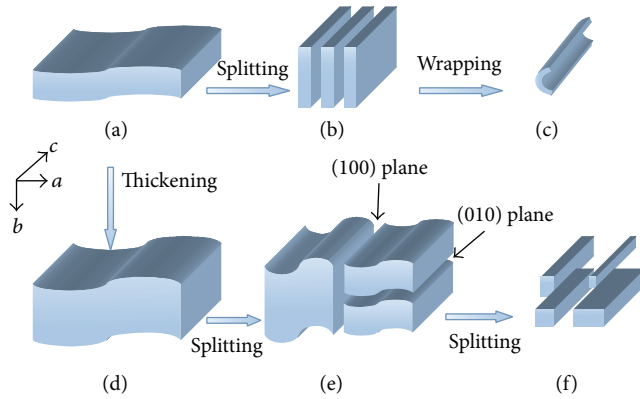


FIGURE 8: Nanotube/nanorod formation mechanism.

of the particle [43], the photodegradation of aquatic organic contaminants (here, dye) may also depend on the photon absorption and electronic transition between the organic dye (in the presence of oxygen) and titanate nanotubes, which in turn may enhance the MB degradation in the aquatic environment in the present study.

**3.3.3. Photodegradation Mechanism.** It is well known that anatase, titanate, and Degussa P-25 are not excited by visible light but can be used to degrade most colored contaminants because of their photosensitization effect [44]. Titanate nanotubes have a large BET surface area of approximately  $186.8 \text{ m}^2/\text{g}$  and therefore show a high adsorption capacity, which is beneficial for collecting organic contaminant molecules such as MB. Under UV irradiation, the MB molecules were adsorbed onto the nanotube surfaces, and the produced electrons were transferred to titanate nanotubes and then injected into the conduction band of the anatase nanoparticles connected with these nanotubes through the nanotube channels [45]. This injective process could also be directly performed by radical MB molecules [46]. The injected electrons were captured by the surface-adsorbed  $\text{O}_2^-$  and  $\text{HO}^\cdot$  radical ions, among others. Finally, the MB molecules could be quickly mineralized by the radical ions. Due to the anatase nanoparticles' high absorption capacity and high concentration of excited electrons, the MB molecules adsorbed onto the surface of anatase will be easily photodegraded; thus, the photocatalytic activity of the nanocomposite is substantially improved. The

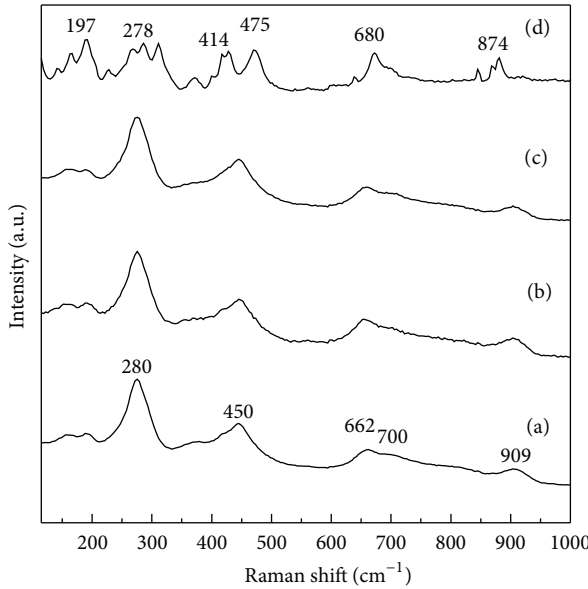
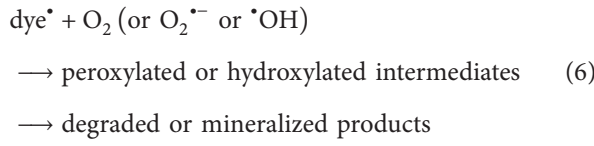
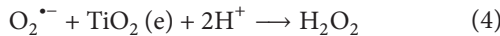
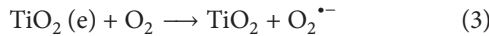
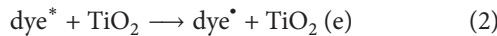


FIGURE 9: Raman spectra of the samples prepared at different reaction temperatures: (a) 110°C, (b) 130°C, (c) 150°C, and (d) 180°C.

probable photodegradation mechanism of dye under UV light using titanate nanotubes is shown as follows [47]:



According to the above formulae, radicals and hydroxyl groups play a key role in the degradation process, and a greater amount of radicals or hydroxyl groups corresponds to better photocatalytic activity. In the present case, the catalyst, which obeyed a similar mechanism of dye photodegradation, contained hydroxyl groups, which means that the synthesized samples have good potential for photocatalytic applications. The maximum absorption boundaries of the samples mean that the samples can absorb more photons under UV light or sunlight [36].

#### 4. Conclusions

A hydrothermal method was explored for the synthesis of titanate nanotubes. The nanotubes were characterized by SEM, TEM, and FTIR studies. The particles' scattering behavior was investigated by Raman studies. The surface area

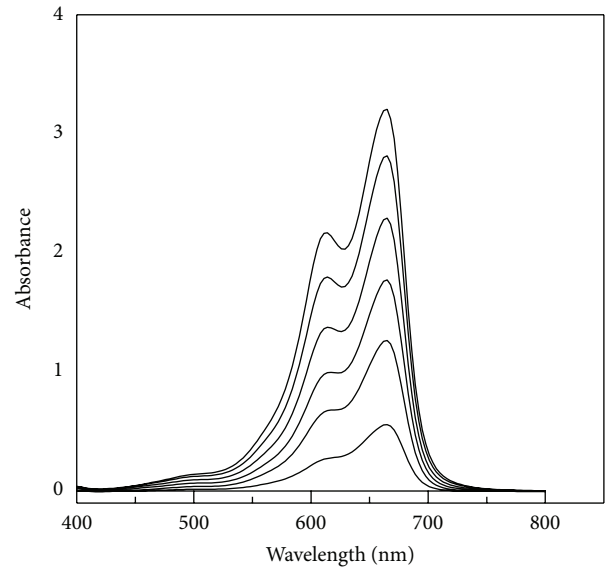


FIGURE 10: UV-Visible spectra of the dye at different concentrations at room temperature: 0, 3, 6, 9, 12, 15, and 18 mg/L.

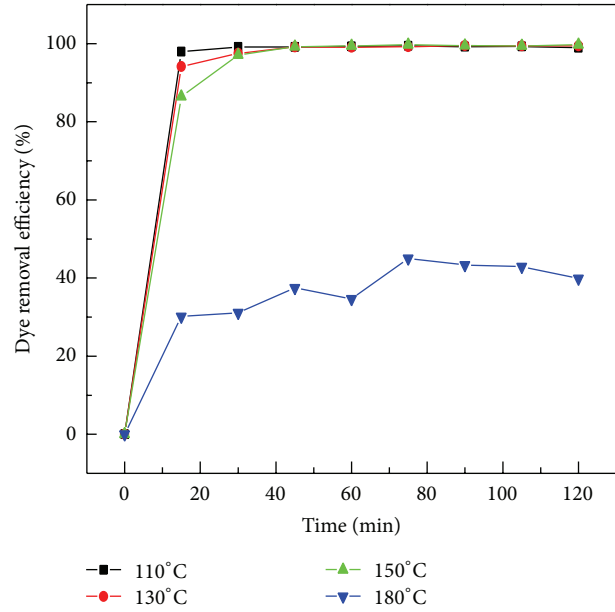


FIGURE 11: Dye degradation (%) by the as-prepared nanotubes.

of the nanotubes was determined by BET analysis. It was observed that the surface area of the synthesized nanotubes is governed by the hydrothermal temperature and reaction time. At 130°C and 24 h of reaction time, the surface area of the titanate nanotubes was 186.8 m<sup>2</sup>/g. The photocatalytic activity of the synthesized nanotubes for dye degradation was investigated using a dye-contaminated aqueous solution. The equilibrium time for dye degradation was 20 min. At equilibrium, ~99% of the MB was degraded from the aqueous media by UV irradiation when the initial dye concentration was 9 mg/L. The maximum absorption boundaries of the dye-contaminated samples mean that the samples can absorb

more photons under UV light or sunlight. Hence, the synthesized titanate nanotubes are a suitable photocatalyst for the degradation of MB, an organic dye, from aqueous media.

## Conflict of Interests

The authors declare that there is no conflict of interests regarding the publication of this paper.

## Acknowledgment

The authors would like to express their gratitude to Ph.D. program of Harbin University of Commerce for supporting this research under Grant 14LG13.

## References

- [1] B. O'Regan and M. Grätzel, "A low-cost, high-efficiency solar cell based on dye-sensitized colloidal  $\text{TiO}_2$  films," *Nature*, vol. 353, pp. 737–740, 1991.
- [2] A. Fujishima, T. N. Rao, and D. A. Tryk, "Titanium dioxide photocatalysis," *Journal of Photochemistry and Photobiology C: Photochemistry Reviews*, vol. 1, no. 1, pp. 1–21, 2000.
- [3] S. A. Al-Thabaiti, R. Hahn, N. Liu et al., "NH<sub>3</sub> treatment of  $\text{TiO}_2$  nanotubes: from N-doping to semimetallic conductivity," *Chemical Communications*, vol. 50, no. 59, pp. 7960–7963, 2014.
- [4] T. Rajh, Z. Saponjic, J. Liu et al., "Charge transfer across the nanocrystalline-DNA interface: probing DNA recognition," *Nano Letters*, vol. 4, no. 6, pp. 1017–1023, 2004.
- [5] H. Tokuhisa and P. T. Hammond, "Solid-state photovoltaic thin films using  $\text{TiO}_2$ , organic dyes, and layer-by-layer polyelectrolyte nanocomposites," *Advanced Functional Materials*, vol. 13, no. 11, pp. 831–839, 2003.
- [6] A. Pal and S. K. Maji, "Arsine-induced formation of silver nanoparticles in micellar medium. Application to spectrophotometric determination of arsenic," *Chemia Analityczna*, vol. 50, no. 6, pp. 1077–1086, 2005.
- [7] A. Pal and S. K. Maji, "Spectrophotometric determination of arsenic via nanogold formation in micellar medium," *Indian Journal of Chemistry A: Inorganic, Physical, Theoretical and Analytical Chemistry*, vol. 45, no. 5, pp. 1178–1182, 2006.
- [8] I. Srnová-Šloufová, F. Lednický, A. Gemperle, and J. Gemperlová, "Core-shell (Ag)Au bimetallic nanoparticles: analysis of transmission electron microscopy images," *Langmuir*, vol. 16, no. 25, pp. 9928–9935, 2000.
- [9] F. Bensebaa, N. Patrito, Y. le Page, P. L'Ecuyer, and D. Wang, "Tunable platinum-ruthenium nanoparticle properties using microwave synthesis," *Journal of Materials Chemistry*, vol. 14, no. 22, pp. 3378–3384, 2004.
- [10] J. Yang, J. Yang Lee, and H.-P. Too, "Phase-transfer identification of core-shell structures in bimetallic nanoparticles," *Plasmonics*, vol. 1, no. 1, pp. 67–78, 2006.
- [11] M. A. Fox and M. T. Dulay, "Heterogeneous photocatalysis," *Chemical Reviews*, vol. 93, no. 1, pp. 341–357, 1993.
- [12] Q. Kang, J. Cao, Y. Zhang, L. Liu, H. Xu, and J. Ye, "Reduced  $\text{TiO}_2$  nanotube arrays for photoelectrochemical water splitting," *Journal of Materials Chemistry A*, vol. 1, no. 18, pp. 5766–5774, 2013.
- [13] T. N. Obee and R. T. Brown, " $\text{TiO}_2$  photocatalysis for indoor air applications: effects of humidity and trace contaminant levels on the oxidation rates of Formaldehyde, Toluene, and 1,3-Butadiene," *Environmental Science and Technology*, vol. 29, pp. 1223–1231, 1995.
- [14] C. Ooka, H. Yoshida, K. Suzuki, and T. Hattori, "Highly hydrophobic  $\text{TiO}_2$  pillared clay for photocatalytic degradation of organic compounds in water," *Microporous and Mesoporous Materials*, vol. 67, no. 2–3, pp. 143–150, 2004.
- [15] M. Qamar, M. Saquib, and M. Muneer, "Photocatalytic degradation of two selected dye derivatives, chromotrope 2B and amido black 10B, in aqueous suspensions of titanium dioxide," *Dyes and Pigments*, vol. 65, no. 1, pp. 1–9, 2005.
- [16] W. Wang, B. Gu, L. Liang, W. A. Hamilton, and D. J. Wesolowski, "Synthesis of rutile ( $\alpha\text{-TiO}_2$ ) nanocrystals with controlled size and shape by low-temperature hydrolysis: effects of solvent composition," *Journal of Physical Chemistry B*, vol. 108, no. 39, pp. 14789–14792, 2004.
- [17] M. Visca and E. J. Matijević, "Preparation of uniform colloidal dispersions by chemical reactions in aerosols. I. Spherical particles of titanium dioxide," *Journal of Colloid and Interface Science*, vol. 68, no. 2, pp. 308–319, 1979.
- [18] H. K. Park, Y. T. Moon, D. K. Kim, and C. H. Kim, "Formation of monodisperse spherical  $\text{TiO}_2$  powders by thermal hydrolysis of  $\text{Ti}(\text{SO}_4)_2$ ," *Journal of the American Ceramic Society*, vol. 79, no. 10, pp. 2727–2732, 1996.
- [19] E. A. Barringer and H. K. Bowen, "High-purity, monodisperse  $\text{TiO}_2$  powders by hydrolysis of titanium tetraethoxide. 1. Synthesis and physical properties," *Langmuir*, vol. 1, no. 4, pp. 414–420, 1985.
- [20] Q.-H. Zhang, L. Gao, and J.-K. Guo, "Preparation and characterization of nanosized  $\text{TiO}_2$  powders from aqueous  $\text{TiCl}_4$  solution," *Nanostructured Materials*, vol. 11, pp. 1293–1300, 1999.
- [21] F. Cavani, E. Foresti, F. Parrinello, and F. Trifirò, "Role of the chemistry of solutions of titanium ions in determining the structure of V/Ti/O catalysts," *Applied Catalysis*, vol. 38, no. 2, pp. 311–325, 1988.
- [22] T. Kasuga, M. Hiramatsu, A. Hoson, T. Sekino, and K. Niihara, "Formation of titanium oxide nanotube," *Langmuir*, vol. 14, no. 12, pp. 3160–3163, 1998.
- [23] T. Kasuga, M. Hiramatsu, A. Hoson, T. Sekino, and K. Niihara, "Titania nanotubes prepared by chemical processing," *Advanced Materials*, vol. 11, no. 15, pp. 1307–1311, 1999.
- [24] Y. Q. Wang, G. Q. Hu, X. F. Duan, H. L. Sun, and Q. K. Xue, "Microstructure and formation mechanism of titanium dioxide nanotubes," *Chemical Physics Letters*, vol. 365, no. 5–6, pp. 427–431, 2002.
- [25] X. Sun and Y. Li, "Synthesis and characterization of ion-exchangeable titanate nanotubes," *Chemistry—A European Journal*, vol. 9, no. 10, pp. 2229–2238, 2003.
- [26] N. D. Lourenço, J. M. Novais, and H. M. Pinheiro, "Effect of some operational parameters on textile dye biodegradation in a sequential batch reactor," *Journal of Biotechnology*, vol. 89, no. 2–3, pp. 163–174, 2001.
- [27] Z. Sun, Y. Chen, Q. Ke, Y. Yang, and J. Yuan, "Photocatalytic degradation of a cationic azo dye by  $\text{TiO}_2$ /bentonite nanocomposite," *Journal of Photochemistry and Photobiology A: Chemistry*, vol. 149, pp. 169–174, 2002.
- [28] C.-C. Wang, L.-C. Juang, T.-C. Hsu, C.-K. Lee, J.-F. Lee, and F.-C. Huang, "Adsorption of basic dyes onto montmorillonite," *Journal of Colloid and Interface Science*, vol. 273, no. 1, pp. 80–86, 2004.

- [29] A. Andrzejewska, A. Krysztafkiewicz, and T. Jasionowski, "Treatment of textile dye wastewater using modified silica," *Dyes and Pigments*, vol. 75, no. 1, pp. 116–124, 2007.
- [30] A. Andrzejewska, A. Krysztafkiewicz, and T. Jasionowski, "Adsorption of organic dyes on the aminosilane modified TiO<sub>2</sub> surface," *Dyes and Pigments*, vol. 62, no. 2, pp. 121–130, 2004.
- [31] G. Crini, "Non-conventional low-cost adsorbents for dye removal: a review," *Bioresource Technology*, vol. 97, no. 9, pp. 1061–1085, 2006.
- [32] J. Yu, H. Yu, B. Cheng, X. Zhao, and Q. Zhang, "Preparation and photocatalytic activity of mesoporous anatase TiO<sub>2</sub> nanofibers by a hydrothermal method," *Journal of Photochemistry and Photobiology A: Chemistry*, vol. 18, no. 2, pp. 121–127, 2006.
- [33] Y. Xiao, L. Dang, L. An, S. Bai, and Z. Lei, "Photocatalytic degradation of rhodamine B and phenol by TiO<sub>2</sub> loaded on mesoporous graphitic carbon," *Chinese Journal of Catalysis*, vol. 29, no. 1, pp. 31–36, 2008.
- [34] H. Choia, E. Stathatosb, and D. D. Dionysioua, "Photocatalytic TiO<sub>2</sub> films and membranes for the development of efficient wastewater treatment and reuse systems," *Desalination*, vol. 202, no. 1–3, pp. 199–206, 2007.
- [35] M. Wei, Y. Konishi, H. Zhou, H. Sugihara, and H. Arakawa, "Formation of nanotubes TiO<sub>2</sub> from layered titanate particles by a soft chemical process," *Solid State Communications*, vol. 133, no. 8, pp. 493–497, 2005.
- [36] G.-S. Guo, C.-N. He, Z.-H. Wang, F.-B. Gu, and D.-M. Han, "Synthesis of titania and titanate nanomaterials and their application in environmental analytical chemistry," *Talanta*, vol. 72, no. 5, pp. 1687–1692, 2007.
- [37] L.-H. Huang, C. Sun, and Y.-L. Liu, "Pt/N-codoped TiO<sub>2</sub> nanotubes and its photocatalytic activity under visible light," *Applied Surface Science*, vol. 253, no. 17, pp. 7029–7035, 2007.
- [38] V. P. Godbole, Y.-S. Kim, M. A. Dar, G.-S. Kim, and H.-S. Shin, "Synthesis of titanate nanotubes and its processing by different methods," *Electrochimica Acta*, vol. 52, no. 4, pp. 1781–1787, 2006.
- [39] K. R. Zhu, Y. Yuan, M. S. Zhang, J. M. Hong, Y. Deng, and Z. Yin, "Structural transformation from NaHTi<sub>3</sub>O<sub>7</sub> nanotube to Na<sub>2</sub>Ti<sub>6</sub>O<sub>13</sub> nanorod," *Solid State Communications*, vol. 144, no. 10–11, pp. 450–453, 2007.
- [40] H. Tokudome and M. Miyauchi, "N-doped TiO<sub>2</sub> nanotube with visible light activity," *Chemistry Letters*, vol. 33, no. 9, pp. 1108–1109, 2004.
- [41] D. Wu, J. Liu, X. Zhao, A. Li, Y. Chen, and N. Ming, "Sequence of events for the formation of titanate nanotubes, nanofibers, nanowires, and nanobelts," *Chemistry of Materials*, vol. 18, no. 2, pp. 547–553, 2006.
- [42] J. Yu, H. Yu, B. Cheng, and C. Trapalis, "Effects of calcination temperature on the microstructures and photocatalytic activity of titanate nanotubes," *Journal of Molecular Catalysis A: Chemical*, vol. 249, no. 1–2, pp. 135–142, 2006.
- [43] S. K. Maji, A. Pal, and T. Pal, "Arsenic removal from aqueous solutions by adsorption on laterite soil," *Journal of Environmental Science and Health, Part A: Toxic/Hazardous Substances and Environmental*, vol. 42, no. 4, pp. 453–462, 2007.
- [44] D. Chatterjee and S. Dasgupta, "Visible light induced photocatalytic degradation of organic pollutants," *Journal of Photochemistry and Photobiology C: Photochemistry Reviews*, vol. 6, pp. 186–205, 2005.
- [45] T. Tachikawa, S. Tojo, M. Fujitsuka, T. Sekino, and T. Majima, "Photoinduced charge separation in titania nanotubes," *The Journal of Physical Chemistry B*, vol. 110, no. 29, pp. 14055–14059, 2006.
- [46] K. Vinodgopal, D. E. Wynkoop, and P. V. Kamat, "Environmental photochemistry on semiconductor surfaces: photosensitized degradation of a textile azo dye, Acid Orange 7, on TiO<sub>2</sub> particles using visible light," *Environmental Science and Technology*, vol. 30, no. 5, pp. 1660–1666, 1996.
- [47] J. Li, W. Ma, C. Chen, J. Zhao, H. Zhu, and X. Gao, "Photodegradation of dye pollutants on one-dimensional TiO<sub>2</sub> nanoparticles under UV and visible irradiation," *Journal of Molecular Catalysis A: Chemical*, vol. 261, no. 1, pp. 131–138, 2007.

## Research Article

# Synthesis and Catalytic Performances of a Novel Zn-MOF Catalyst Bearing Nickel Chelating Diimine Carboxylate Ligands for Ethylene Oligomerization

Suyan Liu,<sup>1</sup> Ying Zhang,<sup>1</sup> Quan Huo,<sup>2</sup> Sasa He,<sup>1</sup> and Yang Han<sup>1</sup>

<sup>1</sup>The State Key Laboratory of Heavy Oil Processing, Department of Materials Science and Engineering, China University of Petroleum (Beijing), Changping District, Beijing 102249, China

<sup>2</sup>Hebei Key Laboratory of Applied Chemistry, College of Environmental and Chemical Engineering, Yanshan University, Qinhuangdao, Hebei 066004, China

Correspondence should be addressed to Ying Zhang; [y.zhang@cup.edu.cn](mailto:y.zhang@cup.edu.cn) and Quan Huo; [quanhuo@ysu.edu.cn](mailto:quanhuo@ysu.edu.cn)

Received 31 July 2014; Accepted 20 August 2014

Academic Editor: Xinqing Chen

Copyright © 2015 Suyan Liu et al. This is an open access article distributed under the Creative Commons Attribution License, which permits unrestricted use, distribution, and reproduction in any medium, provided the original work is properly cited.

A novel Zn-MOF[ $Zn_3(OH)_2L_2$ ] was synthesized from dicarboxylate ligands with diimine groups (1,4-bis(4-CO<sub>2</sub>HC<sub>6</sub>H<sub>4</sub>)-2,3-dimethyl-1,4-diazabutadiene). The physicochemical properties of the material were characterized by a series of technologies including XRD, SEM, and ICP. In order to adapt to the ethylene oligomerization process, a catalyst [ $Zn_3(OH)_2(L_1^{Ni})_2$ ] (denoted as Cat.A) possessing active Ni<sup>2+</sup> centers was prepared by a postsynthetic treatment method using dichloride nickel as a nickel source in this work. For comparison,  $\alpha$ -diimine ligands with/without dicarboxylic acid groups reacted with dichloride nickel to obtain homogenous Cat.B and Cat.C, respectively. The effects of reaction parameters, including  $n(Al)/n(Ni)$ , temperature, and pressure on the oligomerization activities and oligomers distribution were investigated. The results demonstrated that all of catalysts used with diethylaluminum chloride were active for the ethylene oligomerization. Among them, Cat.A and Cat.B showed higher catalytic activities and higher selectivities to low-carbon  $\alpha$ -olefins at atmospheric pressure. The Cat.A exhibited the optimal catalytic activity [ $6.7 \times 10^5$  g/(mol-Ni·h·atm)] for C4 (91.8%) under the conditions of Al/Ni = 1500,  $P$  = 1.0 atm,  $T$  = 20°C. In addition, Cat.A and Cat.B presented large amount of ethylene polymer, while Cat.C had a higher catalytic activity of ethylene oligomerization at high pressure.

## 1. Introduction

Low-carbon linear  $\alpha$ -olefins are extensively used as comonomer of linear low-density polyethylene, plasticizers, and synthetic lubricants [1, 2]. Among technologies of producing low-carbon linear  $\alpha$ -olefins, ethylene oligomerization is a major industrial process. Today, the well-known industrial processes of ethylene oligomerization include Shell Higher Olefin Process (SHOP) employing homogeneous nickel catalysts bearing [P,O] ligands and Philips ethylene selective trimerization or tetramerization processes using homogeneous chromium catalysts [3, 4]. Although a lot of research efforts focus on homogenous oligomerization catalysts, the process has a serious drawback of separation of oligomerization products from catalysts and solvent

mixtures. The added separation process will lead to the significant increase of operation costs and environmental pollution. With respect to the green chemistry principles, heterogeneous catalysis is an environmentally friendly alternative to the traditional homogenous process. Heterogeneous catalysts using porous solids (MCM-36, MCM-22, [5] MCM-41 [6]) as supporting materials exhibit good catalysis performances for the ethylene oligomerization. Unfortunately, characteristic results show that anchored active species are not evenly located within pore channels. As a result, a rapid enrichment of polymeric waxes occurs in the part; thus the selectivity to low-carbon linear  $\alpha$ -olefins has been seriously affected. This phenomenon is commonly encountered in ethylene oligomerization processes using porous solids as the supports of catalysts. Therefore, the development

of new supporting strategy on porous materials is desirable.

In the past decade, metal-organic frameworks (MOFs) have attracted a great deal of attention [7]. Due to their outstanding features of tunable pore sizes, high specific surface areas, and the possibility to functionalize, they have been widely used in the processes of hydrogen storage [8, 9], gas separation [10], catalysis [11], sensing [12, 13], and drug delivery [14, 15]. In particular, an important feature of MOFs as catalysts is their self-assembled metal active sites, which are uniformly distributed over porous frameworks. Recently, MOFs for ethylene oligomerization have come into notice by several research groups. Kyogoku and coworkers [16] have prepared metal-organic framework (MOF) compounds containing Ni-bipyridyl complex. The material used with diethyl aluminum chloride had high potential as a catalyst for the oligomerization of ethylene with high selectivity for linear butenes. Canivet and coworkers [17] have anchored a molecular nickel complex into a mesoporous metal-organic framework (Ni@Fe)MIL-101 using the one-pot postfunctionalization method. It is generating a very active and reusable catalyst for the liquid-phase ethylene dimerization to selectively form 1-butene. Mlinar and coworkers [18] have reported two  $\text{Ni}^{2+}$ -containing metal-organic frameworks with high concentrations of coordinatively unsaturated  $\text{Ni}^{2+}$  sites, which exhibit activity comparable to  $\text{Ni}^{2+}$ -exchanged aluminosilicates but maintain high selectivity for linear oligomers. However, examples of metal-organic framework bearing metal-binding organic ligands as ethylene oligomerization catalysts compared with the before-assembled metalloorganic ligands, particularly in liquid-phase oligomerization reactions, are rare.

Here we are interested in assembling dicarboxylate ligands with diimine groups into MOF framework followed by nickel complexation with  $\alpha$ -diimine groups to realize the self-support of nickel active sites. The difference of catalytic performances of these self-supported nickel active sites in the ethylene oligomerization between nickel sites coordinated with corresponding unassembled ligands is of interest. For this purpose,  $\alpha$ -diimine ligand with dicarboxylic acid ( $L_1$ , Scheme 1) is synthesized according to literature [19]. Such ligand as a linker is connected by  $\text{Zn}^{II}$  ions nodes to construct MOF framework. The catalyst active  $\text{Ni}^{2+}$  centers are generated by postsynthetic treatment of MOF with dichloride nickel to form  $[\text{Zn}_3(\text{OH})_2(L_1^{\text{Ni}})_2]$  (Cat.A). For comparison,  $\alpha$ -diimine ligands with dicarboxylic acid groups ( $L_1$ ) and without dicarboxylic acid groups ( $L_2$ ) react with dichloride nickel to obtain homogenous Cat.B and Cat.C [20]. All the three catalysts are employed in the ethylene oligomerization and their catalytic performance is investigated under various reaction conditions.

## 2. Experimental

### 2.1. Material Preparations

**2.1.1. Preparation of  $\text{NiL}_1\text{Cl}_2$  (Cat.B) and  $\text{NiL}_2\text{Cl}_2$  (Cat.C) Catalysts.**  $\text{NiL}_2\text{Cl}_2$  catalyst was synthesized according to the

method described in the literature [20]. Similarly, the mixture composed of aminobenzoic acid and 2,3-butanedione was stirred at room temperature by Schiff-Alkali condensation reaction to obtain ligand  $L_1$  [19]. The dichloride nickel catalysts Cat.B were obtained by stirring the ligand  $L_1$  (0.84 g, 2.6 mmol),  $\text{NiCl}_2$  (DME) (0.57 g, 2.6 mmol) with THF (30 mL) at room temperature for 48 h. Then, the powder was washed by ether for three times and dried to obtain the  $\text{NiL}_1\text{Cl}_2$  catalyst.

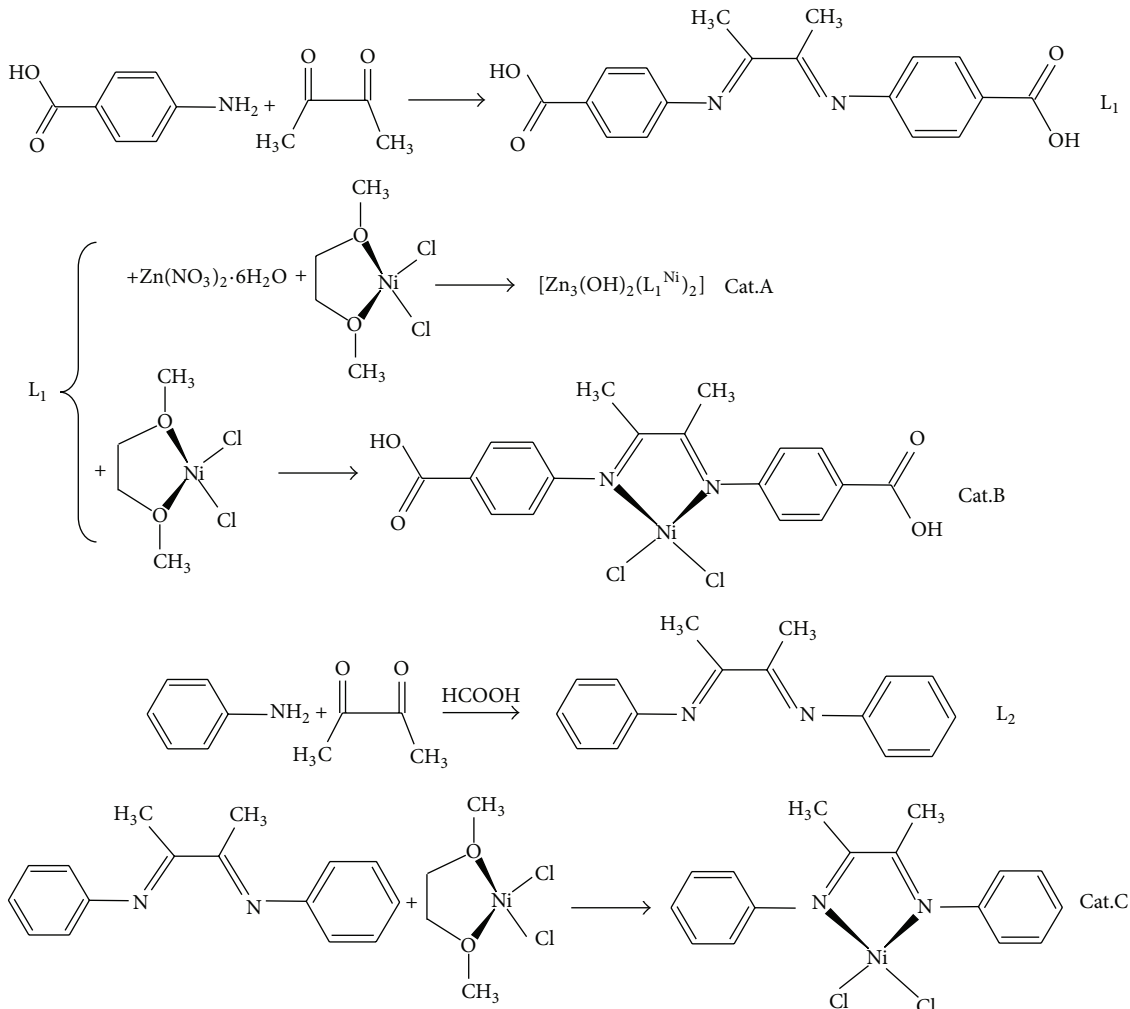
**2.1.2. Preparation of  $[\text{Zn}_3(\text{OH})_2(L_1^{\text{Ni}})_2]$  (Cat.A) Catalyst.**  $[\text{Zn}_3(\text{OH})_2(L_1^{\text{Ni}})_2$ ] catalyst was synthesized according to the method described in the literature and divided into two processes [21]. First, ligand  $L_1$  (0.97 g, 0.3 mol) was added to ethanol solution and stirred at room temperature for 4 hours, then  $\text{Zn}(\text{NO}_3)_2 \cdot 6\text{H}_2\text{O}$  was added to the mixture, dripping 1.5 mL triethylamine and stirred for 8 h, and the power (Zn-MOF) was collected by repeated centrifugation and thorough washing with distilled water and dried in vacuum at 60°C for 5 h. Then, the mixture composed of Zn-MOF (0.84 g, 2.6 mmol),  $\text{NiCl}_2$  (DME) (0.54 g, 2.5 mmol), and THF (30 mL) was stirred for 48 h to obtain powder. The powder was washed by ether for three times and dried. The obtained product is  $[\text{Zn}_3(\text{OH})_2(L_1^{\text{Ni}})_2]$  catalyst.

**2.2. Characterization.** The crystallinity and phase purity of the product were measured by means of XRD patterns, which were recorded in a Shimadzu X-6000 diffractometer in the 2 theta range of 1.3–30° at a scan speed of 4°/min using Cu KR radiation to determine the crystallinity. The photographs of samples were taken by scanning electron microscopy (SEM) analyses, which were performed using FEI-QUANTA 200F equipment. The chemical compositions of the samples were measured by inductively coupled plasma (ICP) technique on a Perkin-Elmer Optima 3300DV spectrometer.

### 2.3. Ethylene Oligomerization

**2.3.1. Procedure for Atmospheric Pressure Ethylene Oligomerization and Polymerization.** The as-prepared nickel catalyst was added to a fully dried Schlenk flask under nitrogen. The flask was backfilled three times with  $\text{N}_2$  and twice with 1 atm ethylene, and then charged with toluene and  $\text{AlEt}_2\text{Cl}$  solution in turn. Under prescribed temperature, the reaction solution was vigorously stirred under 1 atm ethylene for the desired period. The polymerization reaction was quenched by addition of 10%  $\text{HCl}/\text{EtOH}$  solution. About 1.0 mL of organic solution was taken for GC analysis. The remained mixture was poured into 100 mL of ethanol to precipitate the polymer. The polymer was isolated via a filtration and dried at 60°C to constant weight in a vacuum oven. The activity of oligomer (Ao) or polymer (Ap) was calculated according to the following equation:

$$\text{Ao (Ap)} = \frac{\text{Yield (g) / catalyst (mol)}}{\text{Time (h) } \times \text{Pressure (atm)}}, \quad (1)$$



SCHEME 1: Prepared processes of the three catalysts.

wherein the yield of oligomers was calculated by referencing with the mass of the solvent on the basis of the prerequisite that the mass of each fraction is approximately proportional to its integrated areas in the GC trace, and the yield of polymer was directly obtained by weighing polymer product with an electronic balance.

**2.3.2. Procedure for High-Pressure Ethylene Oligomerization and Polymerization.** High-pressure ethylene polymerization was performed in a stainless steel autoclave (500 mL capacity) equipped through a solenoid valve for continuous feeding of ethylene at constant pressure. 100 mL toluene containing the catalyst precursor was transferred to the fully dried reactor under ethylene atmosphere. Then the required amount of cocatalyst ( $\text{AlEt}_2\text{Cl}$ ) was injected into the reactor using a syringe. As the temperature was reached 20°C, the reactor was pressurized to prescribed pressure. After stirring for one hour, the reaction was quenched and worked up using the similar method described above for ordinary pressure reaction.

### 3. Results and Discussion

The NMR, element analysis, and IR characterization results of catalyst  $\text{NiL}_2\text{Cl}_2$  and  $\text{NiL}_1\text{Cl}_2$  are in well agreement with the literature [19], confirming the successful synthesis of homogenous diimine Cat.B and Cat.C. In the following part, the new material  $[\text{Zn}_3(\text{OH})_2(\text{L}_1)_2]$  (Zn-MOF) will be characterized in detail.

#### 3.1. Characterization of the $[\text{Zn}_3(\text{OH})_2(\text{L}_1)_2]$

**3.1.1. XRD.** XRD pattern of a synthesized Zn-MOF is displayed in Figure 1. The result showed that the XRD pattern of the synthesized sample was similar to that of a simulated pattern obtained from the single-crystal structure in the literature [21]. The crystallographic planes (110) and (220) of the sample have been denoted on the XRD patterns. However, there was a slight shift to lower angle region in the peak positions and the weakening of the peak intensities at higher angle region compared with those of the simulated one. The difference can possibly be caused by the unique

TABLE 1: Effects of  $n(\text{Al})/n(\text{Ni})$  on the activity and distribution of oligomer<sup>a</sup>.

Entry	Cat.	$n(\text{Al})/n(\text{Ni})$	Oligomer distribution <sup>b</sup>				$\alpha$ -Olefin <sup>b</sup> /%	Ao <sup>c</sup>	Ap <sup>c</sup>
			C4/ $\Sigma$ C	C6/ $\Sigma$ C	C8/ $\Sigma$ C	$\geq \text{C}10/\Sigma$ C			
1	A	200	29.8	15.4	24.3	30.5	30.7	0.9	trace
2	A	500	42.5	30.9	20.2	6.4	37.0	1.6	0.018
3	A	1000	87.4	2.9	5.2	4.5	85.8	8.9	trace
4	A	1500	91.8	2.9	3.3	2.0	92.2	6.7	trace
5	B	200	34.4	27.5	28.4	9.7	69.1	2.5	trace
6	B	500	49.2	19.4	18.2	13.2	50.2	7.1	trace
7	B	1000	58.9	14.4	10.5	16.2	20.9	12.0	trace
8	B	1500	72.4	14.1	4.5	9.0	15.0	8.2	trace
9	C	200	29.9	16.6	15.2	38.3	24.9	4.7	—
10	C	500	35.9	22.1	18.9	23.1	19.8	5.7	—
11	C	1000	37.7	18.5	22.5	21.3	23.7	6.9	—
12	C	1500	49.6	25.6	22.8	2.0	24.4	3.2	—

Note: <sup>a</sup>reaction conditions:  $\theta = 1 \text{ h}$ ,  $c = 1 \times 10^{-4} \text{ mol/L}$ ,  $p = 1.0 \text{ atm}$ ,  $T = 20^\circ\text{C}$ ; <sup>b</sup> $\alpha$ -olefin content determined by GC; <sup>c</sup>Ao represents the activity for oligomers, Ap is the activity for polymer, both activities have the same unit of  $\times 10^5 \text{ g}/(\text{mol}\cdot\text{Ni}\cdot\text{h}\cdot\text{atm})$ .

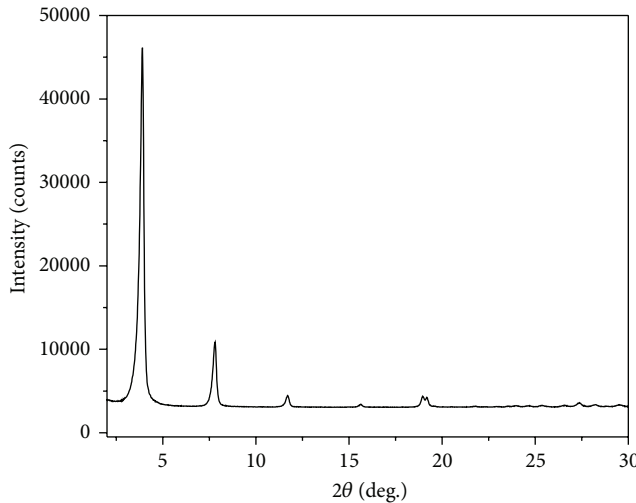


FIGURE 1: XRD pattern of Zn-MOF.

diimine ligands. As a result, it can also be concluded that the synthesized sample and the simulated one possess the similar porous structure.

**3.1.2. SEM.** As shown in Figure 2, the SEM images of  $[\text{Zn}_3(\text{OH})_2(\text{L}_1)_2]$  present a regular flat stick crystal with average size of about  $20 \mu\text{m}$  in the length direction and  $3 \mu\text{m}$  in the width direction. Moreover, a small amount of irregular particles appears (Figure 2(a)), which could be unreacted ligands.

**3.1.3. ICP.** The elemental contents of samples were analyzed by the inductively coupled plasma (ICP) method. The analysis results showed that the content of elements C, H, and N over the Zn-MOF was 31.41, 3.08, and 4.12%. Furthermore, the total Ni content of porous coordination polymer  $[\text{Zn}_3(\text{OH})_2(\text{L}^{\text{Ni}})_2]_n$  was 11.39%. Obviously, the content is

apparently higher than those of traditional heterogeneous catalysts reported by some researchers before [22]. The results also suggested that the catalyst  $[\text{Zn}_3(\text{OH})_2(\text{L}^{\text{Ni}})_2]_n$  (Cat.A) had much more metal active sites for oligomerization catalysis compared to the other heterogeneous oligomerization catalysts. Much more metal active sites are helpful to improve the catalytic performance of ethylene oligomerization catalysts.

### 3.2. Ethylene Oligomerization and Polymerization with $\text{Et}_2\text{AlCl}$ as Cocatalyst

**3.2.1. Effects of  $n(\text{Al})/n(\text{Ni})$  Values.** In the present work, the catalytic activities of three catalysts (Cat.A, Cat.B, and Cat.C) were investigated. The catalytic test results were listed in Table 1.

As can be seen in Table 1, the optimal catalytic activities of all three catalysts were obtained when the  $n(\text{Al})/n(\text{Ni})$  value was 1000 : 1, respectively. As suggested in the literature [23], the surface of active species being overlaid with an excess amount of  $\text{Et}_2\text{AlCl}$  can lead to the deactivation of active catalytic sites. It indicated that the proper  $n(\text{Al})/n(\text{Ni})$  value was the key factor for the catalytic performance of the catalyst. However, for the product distributions, it was surprising to observe that the content of C4 oligomers increases significantly with the increase of the  $n(\text{Al})/n(\text{Ni})$  values. In particular, for Cat.A, the content of C4 oligomers was obviously increased from 29.8% to 91.8%. One reason for these results is that the chain transfer rate increased with the increase of  $n(\text{Al})/n(\text{Ni})$  values. Meanwhile, it also led to the decrease in the molecular weight of polyethylenes. In addition, the contents of C4 oligomers obtained over different catalysts were different; they followed the order: Cat.C (49.6%) < Cat.B (72.4%) < Cat.A (91.8%). This is because nickel active sites locate in different electronic and special environments in three catalysts. The electron withdrawing inductive effect of carboxyl substituent groups attaching to the diimine ligands in Cat.A and Cat.B has positive effects

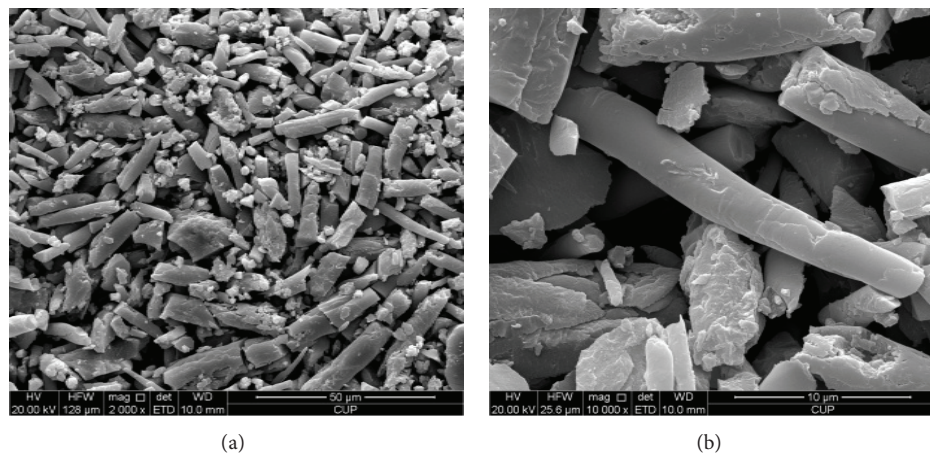


FIGURE 2: SEM images of Zn-MOF.

TABLE 2: Effects of temperature on the distribution of oligomer.

Entry	Cat.	$T/^\circ\text{C}$	Oligomer distribution				$\alpha$ -Olefin/%	Ao	Ap
			C4/ $\Sigma$ C	C6/ $\Sigma$ C	C8/ $\Sigma$ C	$\geq$ C10/ $\Sigma$ C			
1	A	0	29.8	30.9	34.8	4.5	37.0	0.9	trace
2	A	20	87.4	2.9	5.2	4.5	85.8	8.9	trace
3	A	40	39.9	26.1	26.8	7.2	55.3	1.1	0.02
4	A	60	20.1	37.0	39.1	3.8	30.3	0.76	trace
5	B	0	21.8	23.9	27.1	27.2	27.2	1.6	trace
6	B	20	58.9	14.4	10.5	16.2	50.2	12.0	trace
7	B	40	50.9	26.3	22.4	0.4	30.5	5.7	trace
8	B	60	38.9	26.7	28.9	5.5	27.7	1.2	—
9	C	0	59.4	6.1	9.5	25	28.1	10.9	—
10	C	20	37.7	18.5	22.5	21.3	23.7	4.7	—
11	C	40	35.9	14.3	11.6	38.2	43.9	2.9	—
12	C	60	26.9	21.1	17.1	34.9	15.1	1.6	—

Reaction conditions:  $\theta = 1 \text{ h}$ ,  $c = 1 \times 10^{-4} \text{ mol/L}$ ,  $n(\text{Al})/n(\text{Ni}) = 1000$ ,  $p = 1.0 \text{ atm}$ .

for C4 formation. Apparently, Cat.A with self-supported nickel active sites possessed the best catalytic activity for C4 oligomer.

**3.2.2. Effects of Reaction Temperature.** As shown in Table 2, the result phenomena for the oligomerization activities of the catalysts with temperatures changing from 0 to  $60^\circ\text{C}$  were the same as those for the influences of  $n(\text{Al})/n(\text{Ni})$  values on the catalytic activities. The optimal activity of the catalyst was obtained at 20, 20, and  $0^\circ\text{C}$  for Cat.A, Cat.B, and Cat.C, respectively. And the reaction temperature was continued to increase and it resulted in the decreasing of catalytic activity. The reason might be caused by deactivation of some active centers and the lower concentration of ethylene in the reaction solution [24].

In addition, with the increasing of the reaction temperature, both catalytic reaction rate and the reversible  $\beta$ -H elimination rate increase, which also led to the lower selectivity for C4 [25]. In our experiments, the major products are C4

and the minor products are C6 and C8 by using Cat.A and Cat.B, while the Cat.C also produced a large amount of C10. This phenomenon might be attributed to the carboxyl group, which led to stereo-hindrance effects.

**3.2.3. Effects of Ethylene Pressure.** The effects of pressure on the activities and distributions of oligomer and polymer are listed in Table 3. It can be seen that when the reaction pressure changed from 10 to 20 atm, for Cat.B and Cat.C, the catalytic activity of oligomerization increased. It attributed to the higher monomer concentration around active nickel centers at a proper higher pressure. However, further increasing reaction pressure resulted in lower catalytic activities. The reason was considered the saturation of ethylene and obstruction contacted with active species by polymer. Interestingly, the oligomerization activity of the Cat.A only varied between 9.15 and  $11 \times 10^5 \text{ g}/(\text{mol-Ni}\cdot\text{h}\cdot\text{atm})$ . Its activity was less affected by pressures compared with those of other catalysts. The reason can be concluded that the heterogeneous catalyst Cat.A was

TABLE 3: Effects of pressure on the distribution of oligomer.

Entry	Cat.	<i>p</i> /atm	Oligomer distribution				$\alpha$ -Olefin/%	Ao	Ap
			C4/ $\Sigma$ C	C6/ $\Sigma$ C	C8/ $\Sigma$ C	$\geq$ C10/ $\Sigma$ C			
1	A	10	71.9	2.3	3.6	22.2	50.6	11.0	0.023
2	A	15	86.3	0.8	3.6	9.3	61.4	9.15	9.4
3	A	20	86.4	5.6	5.3	2.7	71.7	10.8	0.24
4	A	25	87.6	6.0	4.6	1.8	72.3	9.25	0.025
5	B	10	58.9	2.2	1.9	37.0	50.2	13.0	0.65
6	B	15	66.5	23.5	4.6	5.4	48.8	19.5	22.5
7	B	20	93.0	3.2	2.4	1.4	60.4	24.0	34.0
8	B	25	94.9	1.1	2.4	1.6	93.4	10.0	5.0
9	C	10	39.7	25.9	24.1	10.3	31.7	16.0	0.19
10	C	15	44.0	18.4	13.1	24.5	36.3	69.0	0.24
11	C	20	49.0	20.2	11.2	19.6	51.4	108	0.38
12	C	25	48.2	12.6	10.2	29.0	71.4	16.3	0.225

Reaction conditions:  $\theta = 1$  h,  $n(\text{Al})/n(\text{Ni}) = 1000$ ,  $T = 20^\circ\text{C}$ ,  $c = 1 \times 10^{-4}$  mol/L.

insoluble in the toluene. Moreover, Ni active sites were able to be effectively immobilized and to be evenly distributed on the metal-organic framework of the catalyst.

Comparing the catalytic activities over Cat.B and Cat.C, it is able to be found that the Cat.B with carboxyl groups in diimine ligands was inferior to the Cat.C without carboxyl groups in diimine ligands. However, the content of C4 compounds for the Cat.B had a distinct advantage over that for the Cat.C. The phenomena were due to the fact that the electron withdrawing effects of the carboxyl groups in Cat.B decreased the electron cloud density of nickel centers and thus increased its infinity with ethylene molecules. Compared with the results at 1 atm, the higher pressure showed that the activity of polymer remarkably increased, especially for Cat.A and Cat.B. It can be explained that the propagation rate was faster than hydrogen elimination rate at higher pressure [26].

## 4. Conclusions

An original Zn-MOF[ $\text{Zn}_3(\text{OH})_2\text{L}_2$ ] was synthesized by the self-assembly of diimine ligands (1,4-bis(4-CO<sub>2</sub>HC<sub>6</sub>H<sub>4</sub>)-2,3-dimethyl-1,4-diazabutadiene). In addition, the novel ethylene oligomerization catalyst [ $\text{Zn}_3(\text{OH})_2(\text{L}_1^{\text{Ni}})_2$ ] was successfully prepared by a postsynthetic treatment method. The ICP characterization results demonstrated that this material possessed a higher Ni content than traditional heterogeneous catalysts. All catalysts showed the catalytic performance of ethylene oligomerization under various reaction conditions. Among the catalysts, the heterogeneous Cat.A exhibited the optimal selectivity for the low-carbon olefin C4. It was attributed to carboxyl electronic effects and space-confined channel effects. It is noteworthy that the Cat.B with dicarboxylic acid groups had the best activity obtained at 20°C. The activity was higher than that of the Cat.C without dicarboxylic acid groups (obtained at 0°C). Obviously, the system temperature had a distinct influence on the catalytic performances. Compared with Cat.C, the dicarboxylic acid groups of Cat.A and Cat.B played important roles in promoting ethylene polymers at high pressure. Furthermore, the system pressure

also presented a significant effect on the activities of the catalysts.

## Conflict of Interests

The authors declare that there is no conflict of interests regarding the publication of this paper.

## Acknowledgments

The authors acknowledge the support of this work by the National Natural Science Foundation of China (Grant no. 51072230, U1162118, 21106123) and the Scientific Research Foundation of the Education Ministry for Returned Chinese Scholars and the Scientific Research Foundation of China University of Petroleum, Beijing (01JB0149).

## References

- [1] B. Cornils and W. A. Herrmann, *Applied Homogeneous Catalysis with Organometallic Compounds*, vol. 1, Wiley-VCH, Weinheim, Germany, 1996.
- [2] H. A. Wittcoff, B. G. Reuben, and J. S. Plotkin, *Industrial Organic Chemicals in Perspective*, Wiley Interscience, New York, NY, USA, 1980.
- [3] W. Keim, F. H. Kowaldt, R. Goddard, and C. Krüger, "Novel coordination of (Benzoylmethylene) triphenylphosphorane in a nickel oligomerization catalyst," in *Angewandte Chemie International Edition*, vol. 17, pp. 466–467, 6 edition, 1987.
- [4] W. Keim, A. Behr, B. Limbacker, and C. Kruger, "Novel nickel-oligomerization catalysts with arsenic-oxygen chelate ligands," *Angewandte Chemie International Edition*, vol. 22, no. 6, p. 503, 1983.
- [5] M. Lallemand, O. A. Rusu, E. Dumitriu, A. Finiels, F. Fajula, and V. Hulea, "NiMCM-36 and NiMCM-22 catalysts for the ethylene oligomerization: effect of zeolite texture and nickel cations/acid sites ratio," *Applied Catalysis A: General*, vol. 338, no. 1-2, pp. 37–43, 2008.

- [6] V. Hulea and F. Fajula, "Ni-exchanged AlMCM-41—an efficient bifunctional catalyst for ethylene oligomerization," *Journal of Catalysis*, vol. 225, no. 1, pp. 213–222, 2004.
- [7] R. J. Kuppler, D. J. Timmons, Q.-R. Fang et al., "Potential applications of metal-organic frameworks," *Coordination Chemistry Reviews*, vol. 253, no. 23-24, pp. 3042–3066, 2009.
- [8] M. Dincă and J. R. Long, "Hydrogen storage in microporous metal-organic frameworks with exposed metal sites," *Angewandte Chemie*, vol. 47, no. 36, pp. 6766–6779, 2008.
- [9] B. Chen, X. B. Zhao, A. Putkham et al., "Surface interactions and quantum kinetic molecular sieving for H<sub>2</sub> and D<sub>2</sub> adsorption on a mixed metal-organic framework material," *Journal of the American Chemical Society*, vol. 130, no. 20, pp. 6411–6423, 2008.
- [10] J.-R. Li, R. J. Kuppler, and H.-C. Zhou, "Selective gas adsorption and separation in metal-organic frameworks," *Chemical Society Reviews*, vol. 38, no. 5, pp. 1477–1504, 2009.
- [11] L. Q. Ma, C. Abney, and W. B. Lin, "Enantioselective catalysis with homochiral metal-organic frameworks," *Chemical Society Reviews*, vol. 38, no. 5, pp. 1248–1256, 2009.
- [12] M. D. Allendorf, C. A. Bauer, R. K. Bhakta, and R. J. T. Houk, "Luminescent metal-organic frameworks," *Chemical Society Reviews*, vol. 38, no. 5, pp. 1330–1352, 2009.
- [13] B. Chen, L. Wang, Y. Xiao et al., "A luminescent metal-organic framework with Lewis basic pyridyl sites for the sensing of metal ions," *Angewandte Chemie*, vol. 48, no. 3, pp. 500–503, 2009.
- [14] P. Horcajada, C. Serre, G. Maurin et al., "Flexible porous metal-organic frameworks for a controlled drug delivery," *Journal of the American Chemical Society*, vol. 130, no. 21, pp. 6774–6780, 2008.
- [15] K. M. L. Taylor-Pashow, J. D. Rocca, Z. Xie, S. Tran, and W. Lin, "Postsynthetic modifications of iron-carboxylate nanoscale metal-organic frameworks for imaging and drug delivery," *Journal of the American Chemical Society*, vol. 131, no. 40, pp. 14261–14263, 2009.
- [16] K. Kyogoku, C. Yamada, Y. Suzuki et al., "Syntheses of metal-organic framework compounds containing Ni-bipyridyl complex for oligomerization of ethylene," *Journal of the Japan Petroleum Institute*, vol. 53, no. 5, pp. 308–312, 2010.
- [17] J. Canivet, S. Aguado, Y. Schuurman, and D. Farrusseng, "MOF-supported selective ethylene dimerization single-site catalysts through one-pot postsynthetic modification," *Journal of the American Chemical Society*, vol. 135, no. 11, pp. 4195–4198, 2013.
- [18] A. N. Mlinar, B. K. Keitz, D. Gygi, E. D. Bloch, J. R. Long, and A. T. Bell, "Selective propene oligomerization with nickel(II)-based metal organic frameworks," *ACS Catalysis*, vol. 4, no. 3, pp. 717–721, 2014.
- [19] B. P. Buffin and A. Kundu, "Synthesis, characterization, and crystal structure of platinum(II) and palladium(II) chlorides with an acidic  $\alpha$ -diimine ligand," *Inorganic Chemistry Communications*, vol. 6, no. 6, pp. 680–684, 2003.
- [20] M. Helldörfer, J. Backhaus, W. Milius, and H. G. Alt, " $(\alpha$ -diimine)nickel(II) complexes containing chloro substituted ligands as catalyst precursors for the oligomerization and polymerization of ethylene," *Journal of Molecular Catalysis A: Chemical*, vol. 193, no. 1-2, pp. 59–70, 2003.
- [21] R. Kitaura, G. Onoyama, H. Sakamoto, R. Matsuda, S.-I. Noro, and S. Kitagawa, "Immobilization of a metallo Schiff base into a microporous coordination polymer," *Angewandte Chemie*, vol. 43, no. 20, pp. 2684–2687, 2004.
- [22] M. Lallemand, A. Finiels, F. Fajula, and V. Hulea, "Catalytic oligomerization of ethylene over Ni-containing dealuminated Y zeolites," *Applied Catalysis A: General*, vol. 301, no. 2, pp. 196–201, 2006.
- [23] S. Zhang, S. Y. Jie, Q. S. Shi, and W.-H. Sun, "Chromium(III) complexes bearing 2-imino-1,10-phenanthrolines: synthesis, molecular structures and ethylene oligomerization and polymerization," *Journal of Molecular Catalysis A: Chemical*, vol. 276, no. 1-2, pp. 174–183, 2007.
- [24] S. Y. Jie, D. H. Zhang, T. Z. Zhang et al., "Bridged bis-pyridinylimino dinickel(II) complexes: syntheses, characterization, ethylene oligomerization and polymerization," *Journal of Organometallic Chemistry*, vol. 690, no. 7, pp. 1739–1749, 2005.
- [25] R. Gao, M. Zhang, T. Liang, F. Wang, and W.-H. Sun, "Nickel(II) complexes chelated by 2-arylimino-6-benzoxazolylpyridine: syntheses, characterization, and ethylene oligomerization," *Organometallics*, vol. 27, no. 21, pp. 5641–5648, 2008.
- [26] W. J. Zhang, W.-H. Sun, S. Zhang et al., "Synthesis, characterization, and ethylene oligomerization and polymerization of [2,6-bis(2-benzimidazolyl)pyridyl]chromium chlorides," *Organometallics*, vol. 25, no. 8, pp. 1961–1969, 2006.

## Research Article

# Laser Raman Spectroscopy with Different Excitation Sources and Extension to Surface Enhanced Raman Spectroscopy

**Md. Wahadoszamen, Arifur Rahaman, Nabil Md. Rakinul Hoque, Aminul I Talukder, Kazi Monowar Abedin, and A. F. M. Yusuf Haider**

*Department of Physics, University of Dhaka, Dhaka 1000, Bangladesh*

Correspondence should be addressed to Md. Wahadoszamen; wahado@univdhaka.edu and Arifur Rahaman; phdu.arif@yahoo.com

Received 23 August 2014; Accepted 6 October 2014

Academic Editor: Nikša Krstulović

Copyright © 2015 Md. Wahadoszamen et al. This is an open access article distributed under the Creative Commons Attribution License, which permits unrestricted use, distribution, and reproduction in any medium, provided the original work is properly cited.

A dispersive Raman spectrometer was used with three different excitation sources (Argon-ion, He-Ne, and Diode lasers operating at 514.5 nm, 633 nm, and 782 nm, resp.). The system was employed to a variety of Raman active compounds. Many of the compounds exhibit very strong fluorescence while being excited with a laser emitting at UV-VIS region, hereby imposing severe limitation to the detection efficiency of the particular Raman system. The Raman system with variable excitation laser sources provided us with a desired flexibility toward the suppression of unwanted fluorescence signal. With this Raman system, we could detect and specify the different vibrational modes of various hazardous organic compounds and some typical dyes (both fluorescent and nonfluorescent). We then compared those results with the ones reported in literature and found the deviation within the range of  $\pm 2 \text{ cm}^{-1}$ , which indicates reasonable accuracy and usability of the Raman system. Then, the surface enhancement technique of Raman spectrum was employed to the present system. To this end, we used chemically prepared colloidal suspension of silver nanoparticles as substrate and Rhodamine 6G as probe. We could observe significant enhancement of Raman signal from Rhodamine 6G using the colloidal solution of silver nanoparticles the average magnitude of which is estimated to be  $10^3$ .

## 1. Introduction

Raman Spectroscopy is based on the Raman Effect, which is the inelastic scattering of photons by molecules or molecular aggregates [1]. In typical Laser Raman Spectroscopy (LRS), light from a laser in the UV-Vis-IR range of a known frequency and polarization is allowed to be scattered from a Raman active sample. The scattered light is then analyzed for frequency and polarization [2]. If the emitted photon has the same wavelength as the absorbing photon; the phenomenon is known as Rayleigh scattering [3]. A small fraction of the incident photons, about  $1 \text{ in } 10^7$ , undergoes interaction with the targeted sample and thereby experiences inelastic scattering [4]. In such a case, the incident laser light interacts with molecular vibrations, phonons, or other possible excitation sources present in the system and thereby resulting in a shift in the energy of the scattered laser photons either up or down. If the frequency of the scattered photon is lowered, then the phenomenon is called Stokes scattering. If the energy of the

photon is shifted upward it is called anti-Stokes scattering. The shift in energy provides vital information about the inherent vibrational modes of the molecule or a molecular aggregate under investigation. Although, Raman scattered light is frequency-shifted with respect to the excitation frequency, the magnitude of the shift in energy is independent of the excitation frequency [5]. The resulting “Raman shift” is therefore an intrinsic property of a molecule, which makes the Raman Spectroscopy a powerful experimental tool for analytical studies. In fact, Raman spectroscopy is commonly designed to monitor intrinsic vibrational spectral fingerprints of a molecule and/or molecular composite. Therefore, Raman spectroscopy can primarily be used to diagnose the presence of a molecule and/or molecular composite in an ensemble [6]. It is also capable of giving detailed information about molecular structure and quantitative analysis [7].

Raman signal arises mainly from a magnetic dipole active vibrational transition of a molecule and thus intrinsically very weak in nature. Therefore, it is sometimes very difficult

to detect the Raman signal of the compounds that are highly fluorescent, as the very weak Raman signals of such compounds are often severely masked by the intense fluorescence signal. As a matter of fact, sensitivity remained a vital issue for Raman spectroscopy which resulted in Raman spectroscopy not being widely used earlier. Therefore, huge flurry of research on Raman spectroscopy and its intensity optimization are found over recent few decades [8]. The simple approach to avoid the fluorescence emission can be to select the suitable laser excitation wavelength. The choice of a near infrared (NIR) excitation wavelength can avoid strong fluorescence, since, in the NIR excitation, the photon does not have enough energy to induce molecular fluorescence. The combination of metal surface (nano) technology and Raman spectroscopy has given rise to "Surface Enhanced Raman Spectroscopy" (SERS) [9, 10]. SERS has so far eased many difficulties associated with the intensity optimization of intrinsically weak Raman signal(s). SERS is a surface sensitive technique that results in the enhancement of Raman scattering by adsorbing molecules on rough metal surfaces or on the surface of the colloidal nano-clusters of suitable dimension. The enhancement factor can be as much as  $10^4$ - $10^5$ , which allows the technique to be sensitive enough to detect single molecule [11]. In this paper, we used a homebuilt Laser Raman system with three different excitation sources and applied the Raman system to a variety of Raman active compounds (hazardous organic compounds and some typical dyes). Many of the selected compounds have very strong intrinsic fluorescence. Therefore, the construction of Raman system with variable and suitable excitation laser sources was primarily aimed to provide a desired flexibility toward the suppression of unwanted fluorescence while detecting the Raman signal. Then, an effort is made to evaluate the potential of Raman spectroscopy to achieve SERS activity. To this end, we used chemically prepared colloidal suspension of silver nanoparticles (AgN) as substrate and Rhodamine 6G (R6G) as probe.

## 2. Experimental

We previously constructed a dispersive laser Raman system with He-Ne or diode laser as excitation sources and used it to acquire and measure the Raman spectra of a variety of molecules, pharmaceuticals, and edible oils [13–15]. In this experiment, we modified the Raman system to operate with three types of excitation lasers, Argon-Ion laser, He-Ne laser, and Diode laser operating at 514.5 nm, 633 nm, and 782 nm, respectively. Out of the three excitation sources, we have used mostly the Argon-Ion laser and Diode laser for our experiments. The schematic layout of the modified Laser Raman system operated with Argon-Ion laser is shown in the Figure 1.

Argon-Ion laser is a broadband laser which emits simultaneously at a number of different wavelengths (e.g., 454.6 nm, 488.0 nm, 496.5 nm, and 514.5 nm) at the head [16]. Among the different wavelengths, we used the strongest and well-distinguished 514.5 nm one as the excitation wavelength for the Raman system. The extraction of the 514.5 nm wavelength was done as follows: the broadband output of the Argon-Ion laser was dispersed by a prism, then the 514.5 nm emission

was separated upon passing the well separated light through a narrow homemade pinhole of suitable dimension (diameter around 5 mm).

The beam was then focused on the cylindrical glass vial containing sample and the Raman-scattered radiations were collected at an oblique geometry at (45–90) $^{\circ}$  by a large-aperture convex lens (f/0.98) which was ultimately focused to the entrance window of the optical fiber. A suitable holographic notch filter was used just in the front of the entrance of the optical fiber, which in turn allows the desired Raman signals to pass through it and thus attenuating the unwanted Rayleigh scattering. The entire system was used in a dark room to avoid densitization of the sensitive detection system by ambient light. Furthermore, a light tight housing (with beam dump in the path way of the laser beam) was used to cover the sample, lenses, filter, mirror, and entrance slit of the spectrograph in order to prevent light reaching from computer monitor and other glowing/radiant objects. The outlet of the optical fiber was connected to the entrance slit of the spectrograph. Inside the spectrograph, the frequency-shifted signal was dispersed by the triple grating turret to resolve spectrally the available Raman signatures. The spectrometer used is an Acton SpectraPro-2758 system with a Czerny-Turner configuration having a focal length of 750 mm. It has three ruled gratings (150 lines/mm blazed at 500 nm, 300 lines/mm blazed at 500 nm, and 300 lines/mm blazed at 1  $\mu$ m), which can be selected at will electronically. The output port of the spectrometer is equipped with an ultrasensitive CCD camera (Princeton Instruments PIXIS100B), which records the spectrum. The camera has a 1340  $\times$  100 pixels imaging array and was cooled to  $-65^{\circ}\text{C}$  by a Peltier cooler in order to reduce thermal noise. Both the CCD camera and the spectrometer were controlled by computer using the software Winspec/32. Throughout the experiment, the instrumental parameters were as follows unless stated otherwise in the figure caption: focused mode (Readout mode: Full Frame, Digitization rate: 100 kHz, slow type), 100% laser, entrance slit width 30 microns, 1340  $\times$  100 CCD array ( $-65^{\circ}\text{C}$  detector temperature), grating selection of 300 lines/mm grooves blazed at 500 nm for Argon-Ion/He-Ne laser excitation, and 300 lines/mm grooves blazed at 1  $\mu$ m for the diode laser excitation. The collection time for spectral acquisition with good signal-to-noise ratio depended on Raman scattering intensity; however, we used 60 seconds acquisition time quite frequently. The Raman Spectrometer reported herein possesses multitude of advantages compared to some commercially available portable Raman spectrometers. Some merits, among the others, of our Raman spectrometer can be summed as follows. (1) It provides one with the ultimate flexibility towards choosing the excitation wavelength. The spectrometer is designed on top of a large optical table with three laser excitation sources in such way that, within the spectrometer configuration, one can easily change (based on the necessity) the source of the excitation during the course of experiments. (2) The sample irradiation and the Raman signal collection optics of this spectrometer are assembled on top of a fairly spacious mechanically movable lab-jack, thereby enabling one to change the irradiation as well as the collection geometry at will for the quest of better

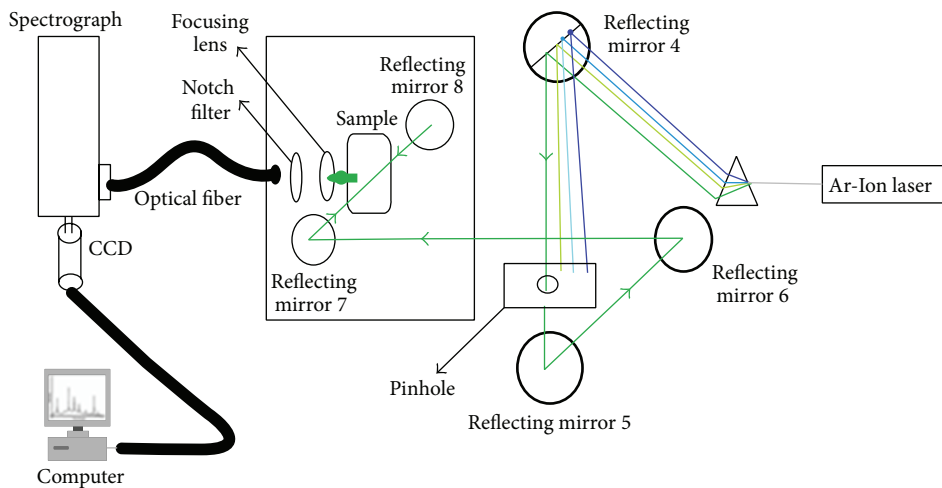


FIGURE 1: Schematic diagram of the modified Raman System using Argon-Ion laser (514.5 nm emission).

Raman signal. This novel design facilitated for us to inspect characteristics lines as close as  $200\text{ cm}^{-1}$  from the laser line with a resolution less than  $2\text{ cm}^{-1}$  ample for analyzing Raman fingerprints for many compounds. (3) The Raman signal is collected through an optical fiber and thus, once the sample collection geometry is changed to some extent for optimizing the Raman signal, one can easily change the position of the head of the optical fiber to make it compatible with the new geometry. (4) The detection system of this spectrometer is equipped with highly sensitive spectrograph, Acton SpectraPro-2758. The frequency selector of this spectrograph has high-aperture optics and feature coma-corrected Czerny-Turner configuration with computer-optimized optics to reduce astigmatism. The spectrograph is suitably interfaced with an ultrasensitive CCD camera (PIXIS 100B). The used CCD camera is Peltier cooled and thereby enabling one to detect weak Raman signal with sufficient resolution.

All the samples, except AgN, used in this study were commercially available and used without further purification. AgN is prepared by chemical synthesis by following the same procedures reported in [17]. A multitude of chemical reduction methods have been used to synthesize AgN from silver salts. For all the methods, some experimental conditions are rigorously controlled so as to obtain chemically stable AgN colloid of specific size. The method of AgN synthesis designed for this experiment is based on the controlled reduction of silver nitrate ( $\text{AgNO}_3$ ) by sodium borohydride ( $\text{NaBH}_4$ ). For this purpose, commercially available  $\text{AgNO}_3$  (99.8%) and  $\text{NaBH}_4$  (99%) were purchased from Sigma Aldrich (Germany). Nano pure water was used as the dissolving media for both  $\text{AgNO}_3$  and  $\text{NaBH}_4$ .

A 10 mL volume of 1.0 mM  $\text{AgNO}_3$  was added drop wise (roughly 1 drop per second) to 30 mL of 2.0 mM  $\text{NaBH}_4$  solution that had been chilled in an ice bath. The reaction mixture was stirred vigorously in a controlled manner on a magnetic stir plate. The solution turned a brighter yellow when all of the silver nitrate had been added. The entire addition took about three minutes, after which the stirring

was stopped and the stir bar removed. The AgN colloid prepared through this protocol would have size less than 50 nm [17].

### 3. Results and Discussion

For the course of experiment, we have selected some hazardous organic compounds (such as benzene, aniline, chlorobenzene, and pyridine) and some typical dyes (such as R6G, Ketone Red and Prussian blue) having well characterized Raman fingerprints. Since some of the selected organic compounds (such as Ketone red, pyridine, Prussian blue, etc.) have strong absorption around UV-to-visible region, the 514.5 nm excitation of the Argon ion laser for the Raman measurements of these compounds resulted in strong fluorescence. Therefore, we could not measure the Raman signal for those samples using Argon-Ion laser. To avoid the inherent fluorescence problem, we used the Diode laser which emits 782 wavelengths, at which wavelength the selected compounds do not have appreciable absorption and thereby do not exhibit measurable fluorescence.

Figures 2(a, c) and 2(b, d) display the spectra of pyridine/Prussian blue measured with Argon-Ion laser excitation at 514.5 nm and Diode laser excitation at 782 nm, respectively. It is apparent from Figures 2(a) and 2(c) that the Argon-Ion laser excitation at 514.5 nm gives broad, diffused, and intense fluorescence signal of both the compounds. On the other hand, Diode laser excitation at 782 nm yielded reasonably structured Raman fingerprints of the two compounds with almost negligible fluorescence background. Therefore, from Figure 2, one can easily assess that, albeit producing comparatively weak Raman signals, excitation at 782 nm from Diode laser in our modified Raman system offers a suitable way of diminishing strong fluorescence signal of a compound and thus enabling to measure the corresponding Raman signals.

In addition, some of the selected compounds (such as benzene, nitrobenzene, and chlorobenzene) exhibit almost no fluorescence. For such nonfluorescent compounds, we

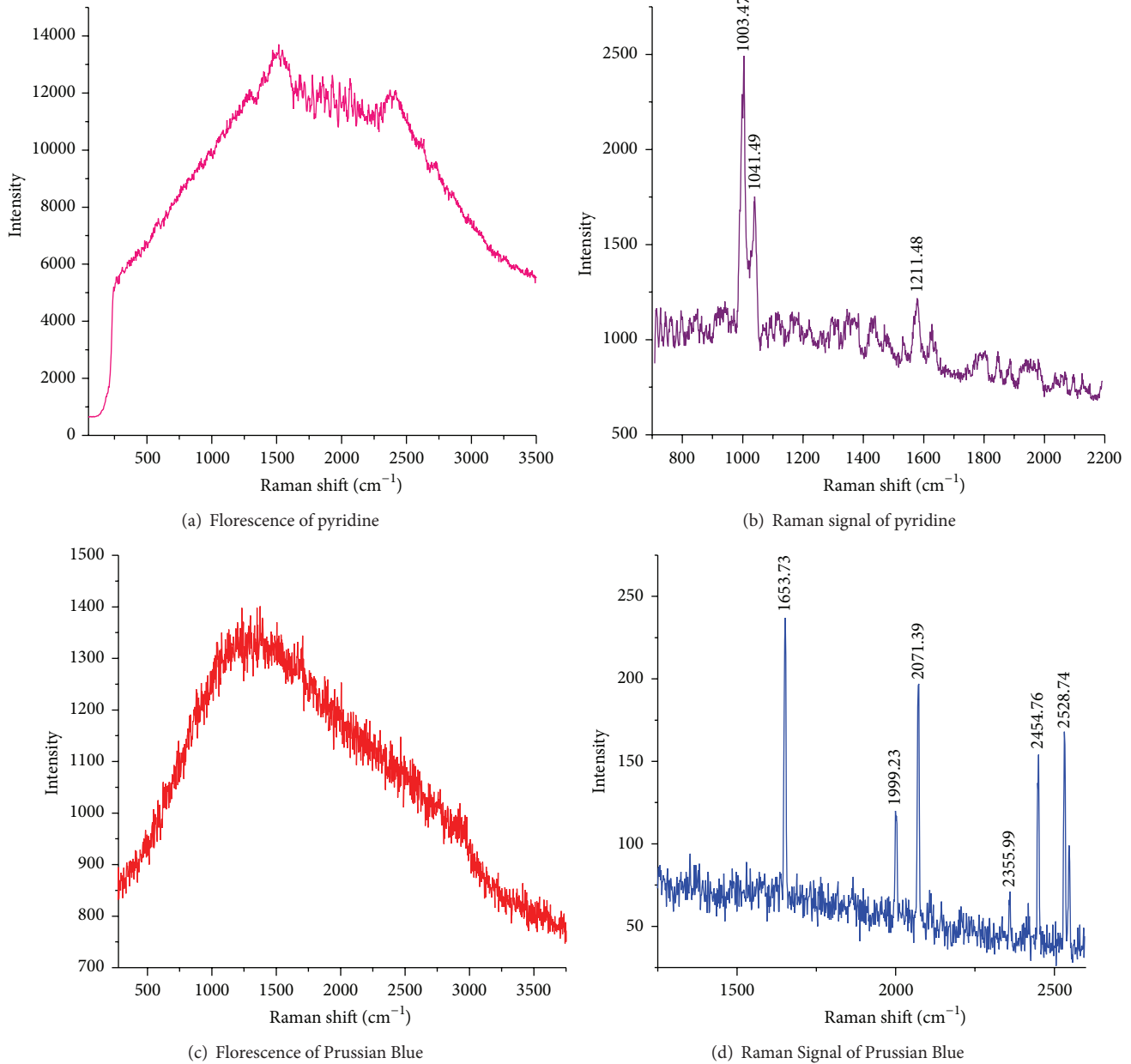


FIGURE 2: (a, b) Fluorescence/Raman signal of pyridine measured by Ar-Ion/Diode laser. (c, d) Fluorescence/Raman signal of Prussian blue measured by Argon-Ion/Diode laser.

observed notably larger Raman signal intensity with Argon-Ion laser than the Diode laser, which is reasonable as the Raman intensity varies as the inverse of the fourth power of the excitation wavelength. To show the intensity variation, the Raman signals of benzene and nitrobenzene were taken using the Argon-Ion laser and also the Diode laser excitation with the same experimental condition (Figure 3).

One can easily observe from the two figures that, for the two nonfluorescent compounds with the same experimental condition, the Argon-Ion laser can yield significantly stronger Raman intensity than the Diode laser. This result in fact points the better usability of the Argon-Ion laser towards

measuring Raman signals of the non-fluorescent molecules compared to the Diode laser. Similarly, we obtained much stronger Raman signal using the Argon-Ion laser than the diode laser from other nonfluorescent organic compounds such as chlorobenzene and aniline (spectra not shown). We then compiled the Raman shifts of different vibrational modes of aniline, chlorobenzene, nitrobenzene, and benzene (Table 1) and made a comparison with the values available in literature.

From Table 1, one can see that the values of Raman shifts, obtained through the Raman scattering, due to different vibrational modes of different samples lie very close (within

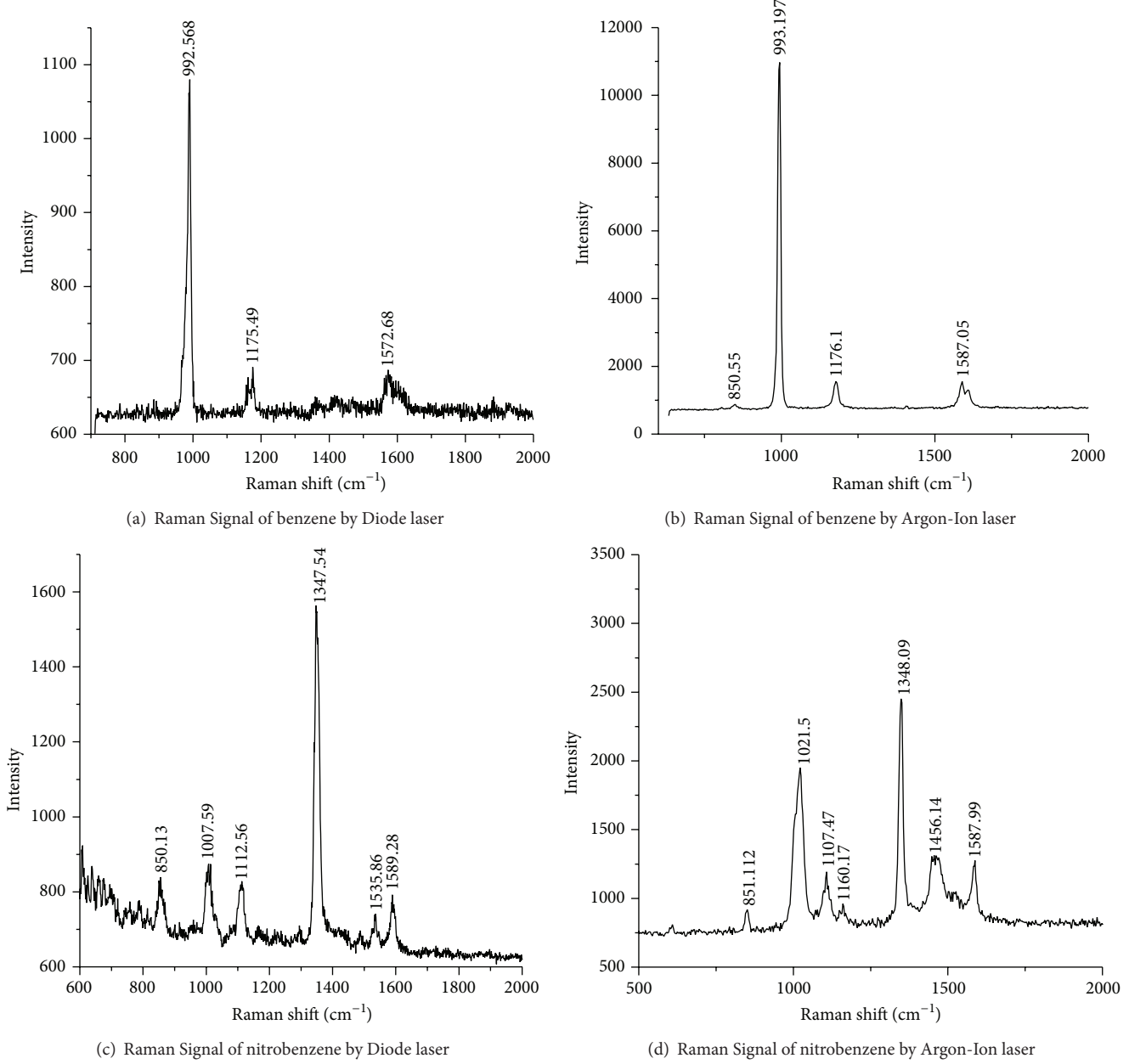


FIGURE 3: (a, b) and (c, d) depict the Raman spectra of Benzene/Nitrobenzene taken with Diode laser/Argon-Ion laser, respectively.

TABLE 1: Raman shift of benzene, aniline, chlorobenzene, and nitrobenzene with their corresponding vibrational bands and Literature values.

Aniline (cm <sup>-1</sup> )	Chlorobenzene (cm <sup>-1</sup> )		Nitrobenzene (cm <sup>-1</sup> )		Benzene (cm <sup>-1</sup> )		Band		
Measured value	Literature value	Measured value	Literature value	Measured value	Literature value	Measured value	Literature value		
531.8	531							$\omega$ (C-C)	
618.7	619.5	610.4	609	614.7		608	609.17	$\omega$ (C-C)	
996.8	996	1002.7	1001		1021.5		992	993.19	$\omega$ (C-C)
								$\delta$ (C-H)	
1150.5	1150	1156.2	1156	1160.2	1159	1178	1176.5	$\delta$ (C-H)	
1604.4	1603	1581.9	1580	1587.9	1590	1588	1587.1	$\omega$ (C-C)	
3057.2	3056	3068	3068	3081.1	3080	3061	3061.1	$v$ (C-H)	

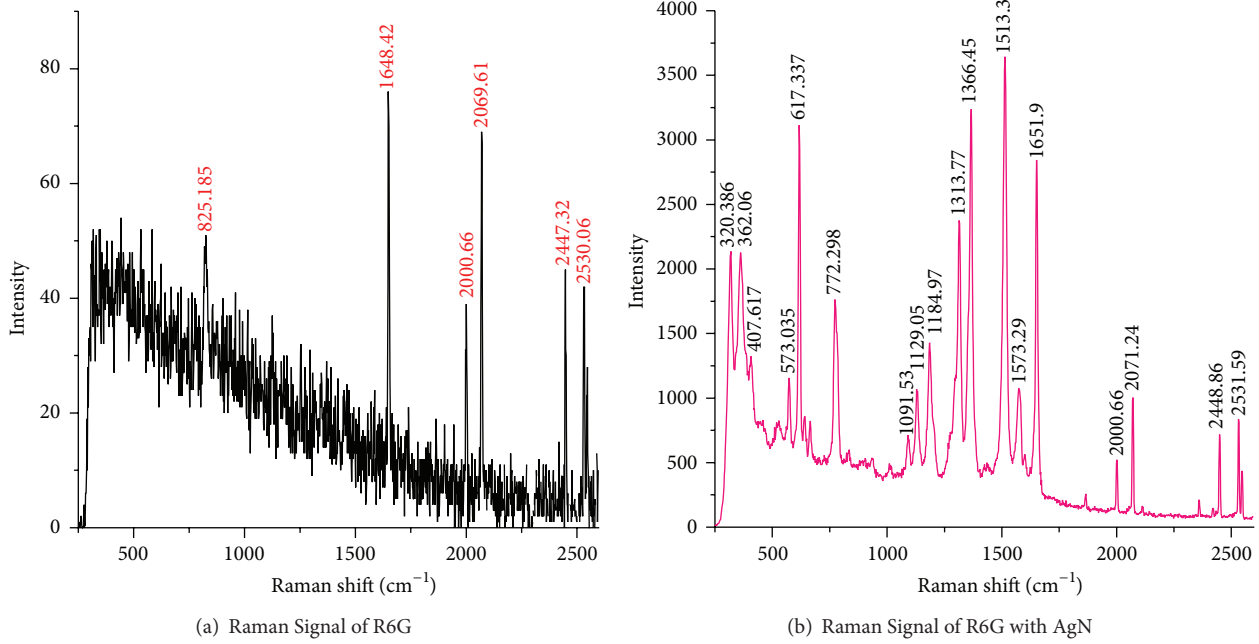


FIGURE 4: (a) Raman Signal of R6G without AgN and (b) Raman Signal of R6G with AgN with acquisition time 60 s.

TABLE 2: Comparison between literature values and experimental values of different vibrational modes of Rhodamine 6G.

Sample	Vibrational modes and functional groups	Literature values (cm <sup>-1</sup> ) [12]	Experimental values (cm <sup>-1</sup> )
Rhodamine 6G	C-H op bend	785	772.3
	C-H ip bend		1186.9
	Arom C-C str	1303	1313.3
	Arom C-C str	1357	1366.66
	Arom C-C str	1508	1513.3
	Arom C-C str	1647	1651.9

$\pm 2 \text{ cm}^{-1}$ ) to the values reported in literature for those bands [18, 19]. This in fact demonstrates the reasonable accuracy and reliability of the present Raman system.

Then, we have extended our work to obtain SERS upon adsorbing the probe R6G onto the AgN prepared by chemical synthesis. Figure 4(a) shows the Raman signal of the R6G at the acquisition time 60 s using diode laser and Figure 4(b) shows the Raman signal of R6G with chemically prepared AgN with the same acquisition time and same laser. Note that R6G is strongly fluorescent with Argon-Ion laser excitation and thus we have used the Diode laser excitation for measuring its Raman spectrum.

From Table 2, one can see that the values of Raman shifts due to different vibrational modes of R6G, obtained through the SERS protocol, lie close to the values reported in literature [12]. This in fact demonstrates further the reasonable accuracy and reliability of the present Raman system.

In Figure 5, we overlaid the two Raman spectra in the same layout to see at a glance the resulting enhancement of the signals. One can easily notice that the Raman band intensities of R6G throughout the selected spectral region

experience huge enhancement when measured upon incubation with the AgN collide. We have estimated the magnitude of enhancement for different Raman bands. The average enhancement of the Raman intensity was found to  $10^3$ .

In addition to the overall intensity enhancement, some more Raman features are also readily apparent especially around  $0\text{--}1500 \text{ cm}^{-1}$ , indicating that the Raman modes of R6G residing around this region suffer larger extent of enhancement. This observation can be interpreted by considering the fact that the Raman spectrum under SERS conditions can be affected by the Plasmon resonances (producing the enhancement) which are typically wavelength dependent [20]. As a consequence, different parts of the spectrum can be amplified by different amounts, depending on the dispersion of the underlying resonance producing the enhancement.

#### 4. Conclusion

In this paper, we report the use of a dispersive Laser Raman system operable with three different excitation sources (Argon-ion, He-Ne, and Diode lasers) and applied the system

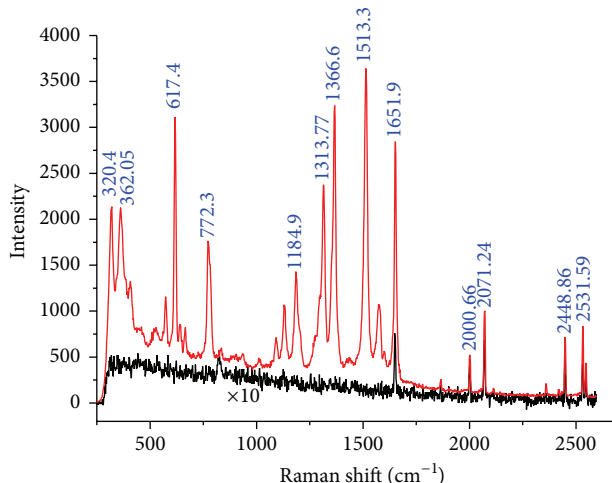


FIGURE 5: Raman signal of R6G with (red curve) and without (black curve) AgN.

to a variety of Raman active (hazardous organic compounds and dyes) molecules, some of which are strongly fluorescent. Then, an effort was made to evaluate the potential of Raman spectroscopy to achieve SERS activity. The chemical analysis of liquid samples containing organic components either as the main constituent or as a contaminant was of our prime interest. Raman spectra of some well-known and basic solvents were probed and verified with literature values. The spectra of the samples under investigation could be well acquired with a spectral range  $200\text{--}4000\text{ cm}^{-1}$  and the shifting of prominent bands were less than  $\pm 2\text{ cm}^{-1}$  which proves the accuracy of our system. We used frequently the Argon-Ion laser (514.5 nm) and Diode laser (782 nm) for the Raman excitation.

Following are the three important parts, what we obtained from our Laser Raman system. (i) We found that the accuracy of our Raman system lies within the range  $\pm 2\text{ cm}^{-1}$ . (ii) During our experiment, we used mostly two different excitation sources: Diode laser with wavelength at 782 nm and Argon-Ion laser with excitation wavelength at 514.5 nm. We observed that Argon-Ion laser is more efficient for nonfluorescent compounds. Besides, we found that Diode laser serves as very suitable source of excitation towards elimination of inherent fluorescence of some compounds under Raman study. (iii) The most exciting and important part of our experiment was to obtain SERS using the chemically synthesized AgN, in which case the average enhancement of the Raman intensity was found to be  $10^3$ .

It is to be mentioned here that, due to the huge dumping of industrial byproducts, most of the rivers in our country are receiving a large volume of hazardous materials and composites every day. The continuous dumping of mostly untreated industrial affluent is imposing a severe threat not only to the surrounding inhabitants dependent directly or indirectly to the river water but also the underneath living bodies and aquatic microorganism and thus throwing a big challenge to the overall biodiversity in the surrounding areas. Among the other possible pollutants, hazardous organic

and inorganic composites give direct effects to the water pollution, as many of them may have good dissolving strength to water. Therefore, the proper profiling of the pollutant constituents appears to be a fundamental prerequisite for the better treatment of the polluted water for the use of river bank inhabitants and to underneath aquatic microorganisms. Therefore, our effort of trace detection through SERS would mark a definite progress in the development of SERS based detection systems for different hazardous organic pollutants in our country.

## Conflict of Interests

The authors declare that there is no conflict of interests regarding the publication of this paper.

## Acknowledgment

The experimental work was done by using the facilities of the Nonlinear Optics and Laser Spectroscopy Laboratory of the Center for Advanced Research in Sciences (CARS) of the University of Dhaka.

## References

- [1] B. Schrader, Ed., *Infrared and Raman Spectroscopy: Methods and Applications*, John Wiley & Sons, Chichester, UK, 1995.
- [2] J. M. Chalmers and P. R. Griffiths, *Handbook of Vibrational Spectroscopy*, John Wiley & Sons, Chichester, UK, 2002.
- [3] J. R. Ferraro, K. Nakamoto, and C. W. Brown, *Introductory Raman Spectroscopy*, Academic Press, New York, NY, USA, 2003.
- [4] A. Campion and P. Kambhampati, "Surface-enhanced Raman scattering," *Chemical Society Reviews*, vol. 27, no. 4, pp. 241–250, 1998.
- [5] M. Jain and L. R. Lindvold, "Blue light stimulation and linearly modulated optically stimulated luminescence," *Ancient TL*, vol. 25, no. 2, pp. 69–80, 2007.
- [6] R. A. Meyers, "Interpretation of infrared spectra," in *Encyclopedia of Analytical Chemistry*, John Wiley & Sons, Chichester, UK, 2000.
- [7] X. Wang, T. He, H. Wen, C. Xu, J. Zuo, and F. C. Liu, "Surface-enhanced Raman scattering from citrate, azobenzene, pyridine and cyanine dyes adsorbed on  $\text{Ag}_2\text{O}$  colloids," *Spectrochimica Acta Part A: Molecular and Biomolecular Spectroscopy*, vol. 53, no. 9, pp. 1411–1417, 1997.
- [8] A. Sabur, M. Havel, and Y. Gogotsi, "SERS intensity optimization by controlling the size and shape of faceted gold nanoparticles," *Journal of Raman Spectroscopy*, vol. 39, no. 1, pp. 61–67, 2008.
- [9] R. M. Stöckle, Y. D. Suh, V. Deckert, and R. Zenobi, "Nanoscale chemical analysis by tip-enhanced Raman spectroscopy," *Chemical Physics Letters*, vol. 318, no. 1–3, pp. 131–136, 2000.
- [10] B. Pettinger, B. Ren, G. Picardi, R. Schuster, and G. Ertl, "Nanoscale probing of adsorbed species by tip-enhanced Raman spectroscopy," *Physical Review Letters*, vol. 92, Article ID 096101, 2004.
- [11] E. C. Le Ru and P. G. Etchegoin, "Single-molecule surface-enhanced raman spectroscopy," *Annual Review of Physical Chemistry*, vol. 63, pp. 65–87, 2012.

- [12] A. M. Michaels, M. Nirmal, and L. E. Brus, "Surface enhanced Raman spectroscopy of individual rhodamine 6G molecules on large Ag nanocrystals," *Journal of the American Chemical Society*, vol. 121, no. 43, pp. 9932–9939, 1999.
- [13] K. M. Abedin, S. F. U. Farhad, M. R. Islam, M. A. I. Talukder, and A. F. M. Y. Haider, "Construction and operation of a dispersive laser Raman spectrograph using interference filter," *Journal of Bangladesh Academy of Sciences*, vol. 32, no. 1, pp. 114–122, 2008.
- [14] K. M. Abedin, M. A. Habib, M. Wahadoszamen, A. I. Talukder, and A. F. M. Y. Haider, "Construction of laser raman system using diode laser and its performance," *Journal of Bangladesh Academy of Sciences*, vol. 33, no. 1, pp. 55–62, 2009.
- [15] S. Farid Uddin Farhad, K. M. Abedin, M. Rafiqul Islam, A. I. Talukder, and A. F. M. Y. Haider, "Determination of ratio of unsaturated to total fatty acids in edible oils by laser Raman spectroscopy," *Journal of Applied Sciences*, vol. 9, no. 8, pp. 1538–1543, 2009.
- [16] *Encyclopedia of Laser Physics and Technology*, vol. 2, John Wiley & Sons, Chichester, UK, 2008.
- [17] S. D. Solomon, M. Bahadory, A. V. Jeyarajasingam, S. A. Rutkowsky, C. Boritz, and L. Mulfinger, "Synthesis and study of silver nanoparticles," *Journal of Chemical Education*, vol. 84, no. 2, pp. 322–325, 2007.
- [18] G. Varsanyi, *Vibrational Spectra of Benzene Derivatives*, Akadémiai Kiado, Budapest, Hungary; Academic Press, New York, NY, USA, 1969.
- [19] P. Kolek, K. Pirowska, Ł. Chacaga, and J. Najbar, "LIF excitation spectra of jet-cooled 3,5-dicyanoaniline," *Physical Chemistry Chemical Physics*, vol. 5, no. 19, pp. 4096–4107, 2003.
- [20] J. M. Pitarke, V. M. Silkin, E. V. Chulkov, and P. M. Echenique, "Theory of surface plasmons and surface-plasmon polaritons," *Reports on Progress in Physics*, vol. 70, no. 1, pp. 1–87, 2007.

## Research Article

# Improving Hyperspectral Image Classification Method for Fine Land Use Assessment Application Using Semisupervised Machine Learning

Chunyang Wang,<sup>1</sup> Zengzhang Guo,<sup>1</sup> Shuangting Wang,<sup>1</sup> Liping Wang,<sup>2</sup> and Chao Ma<sup>1</sup>

<sup>1</sup>School of Surveying and Land Information Engineering, Henan Polytechnic University, Jiaozuo 454000, China

<sup>2</sup>Sansom Institute for Health Research and School of Pharmacy and Medical Science, University of South Australia, Adelaide, SA 5001, Australia

Correspondence should be addressed to Zengzhang Guo; gzc@hpu.edu.cn and Liping Wang; wlp2005518@gmail.com

Received 25 August 2014; Accepted 13 September 2014

Academic Editor: Tifeng Jiao

Copyright © 2015 Chunyang Wang et al. This is an open access article distributed under the Creative Commons Attribution License, which permits unrestricted use, distribution, and reproduction in any medium, provided the original work is properly cited.

Study on land use/cover can reflect changing rules of population, economy, agricultural structure adjustment, policy, and traffic and provide better service for the regional economic development and urban evolution. The study on fine land use/cover assessment using hyperspectral image classification is a focal growing area in many fields. Semisupervised learning method which takes a large number of unlabeled samples and minority labeled samples, improving classification and predicting the accuracy effectively, has been a new research direction. In this paper, we proposed improving fine land use/cover assessment based on semisupervised hyperspectral classification method. The test analysis of study area showed that the advantages of semisupervised classification method could improve the high precision overall classification and objective assessment of land use/cover results.

## 1. Introduction

Remote sensing can quickly obtain surface information, achieve understanding, and study surface characteristics of the spatial distribution through transferring, processing, and analyzing the data. The advantage of high spectral resolution remote sensing is that it can obtain many continuous band spectral images therefore, it achieves a fine description of ground targets and reaches the purpose of identifying features, especially suitable for plant fine classification compared with the conventional remote sensing methods [1–5].

The land use information has great significance to land resource survey, planning, and dynamic monitoring. The analysis of land use/cover assessment using hyperspectral image remote sensing has attracted more and more attention in recent years [6–9]. Currently, supervised classification and unsupervised classification are the two traditional classification methods for land use/cover. The supervised classification is based on class probability density function for samples in spatial feature. Generally, it takes higher classification

accuracy and needs a lot of correct training samples. Pal reported the usage of the extreme learning machine (ELM) algorithm for land use of hyperspectral image and achieved good effect [10]. Bao et al. proposed that SVM and random feature selection (RFS) are applied to explore the potential of a synergetic use of the two concepts in order to produce highly accurate [11]. Stankevich et al. proposed a new supervised hyperspectral imagery classification using the imagery spectral bands as fuzzy data source attributes and cumulative mutual information resulting fuzzy classification as decision tree inducing criterion [12].

Unsupervised classification is a clustering method and can detect unknown classes on images. The advantage of unsupervised classification is simple and efficient. However, it cannot guarantee the real relationship between the clustering features classes and surface features classes [13, 14].

Accessing training data for land cover classification using hyperspectral data is time consuming and expensive especially for hard-to-reach areas. Semisupervised learning research for land use/cover classification using a small amount of

labeled samples based hyperspectral image becomes a new research hotspot. Rajan et al. proposed that an active learning is well suited for learning or adapting classifiers when there is substantial change in the spectral signatures between labeled and unlabeled data [15]. Jun and Ghosh proposed a semisupervised learning algorithm called Gaussian process expectation-maximization (GP-EM) for classification of land cover based on hyperspectral data analysis [16]. Munoz-Mari et al. proposed a semiautomatic procedure to generate land cover maps from remote sensing images [17]. Jun and Ghosh proposed a semisupervised spatially adaptive mixture model (SESSAMM) to identify land covers from hyperspectral images in the presence of previously unknown land-cover classes and spatial variation of spectral responses [18].

So far, these research results have promoted the development of the land use/cover assessment, but there were some problems with these study methods. On the one hand, the misjudgment probability of this strategy is relatively big. On the other hand, these methods still cannot improve classification accuracy significantly especially because the types classified are many.

A new fine land use/cover assessment method was proposed using hyperspectral image classification based on combining Rényi entropy and multinomial logistic regression semisupervised learning model. Finally, the paper has land use/cover assessment experiment by the real hyperspectral remote sensing image data. It shows that it can improve the accuracy of classification and improve fine land use/cover assessment.

## 2. Modelling of Fine Land Use/Cover Assessment

**2.1. Differences between the Spectral Characteristics.** The fine land use/cover classification is able to use the hyperspectral image data because the features of spectral characteristics are the basis of recognition of feature attributes for remote sensing image. The description model of hyperspectral image data is shown in Figure 1. The spectral curves of different tree species are shown in Figure 2.

Furthermore, the green artificial paints and hyperspectral remote sensing can identify vegetation that cannot be distinguished by the human eyes. Liu et al. proposed that the outside laboratory spectrometer using ultraviolet, visible, near-infrared spectrometer can be used to measure all kinds of vegetation reflectance spectra such as Indus, Camphor, *Broussonetia papyrifera*, and Vine vegetable and compared with some reflection curve of green paint. The results show that the spectral curves feature can distinguish between vegetation and green paint [19]. The differences between green paint spectrum and vegetation spectrum are shown in Figure 3.

**2.2. The Method of Semisupervised Classification.** The core idea of this method of semisupervised classification is that, firstly, selected small amount of sample data are performed by multinomial logistic regression algorithm. The fitted regression coefficient can describe the direct relationship between selected sample pixel and its category effectively.

Then, hyperspectral image is classified by using the fitted regression coefficient. Secondly, the entropy of the experimental area is calculated through Rényi entropy calculation method that was proposed by Rényi in 1961 [20], and then some unlabeled samples of maximum Rényi entropy are selected from the calculation data to be added to the sample data. The classification of multinomial logistic regression is not iterated repeatedly for many times until the classification accuracy tends to be stable.

**2.2.1. Problem Description.** For hyperspectral classification problems, assuming that the hyperspectral remote sensing image is  $X = (x_1, \dots, x_n) \in R^{d \times n}$ ,  $d$  represents the number of bands, each pixel represents a vector, there are  $d$  observations,  $C \equiv \{1, \dots, C\}$ ,  $C$  represents category set,  $T = \{x_1, \dots, x_k\}$  shows that training set contains sample labels,  $T \subseteq X$ ,  $U$  represents unlabeled sample set,  $X = T \cup U$ , and  $Y = (y_1, \dots, y_k) \in C$  represents classification categories of sample training datasets.

**2.2.2. The Principle of Multinomial Logistic Regression Algorithm.** The multinomial logistic regression algorithm can predict the fitted coefficient quickly and accurately [21, 22]; the vector of parameter coefficient  $\beta = (\beta_1, \dots, \beta_n)$  is gotten by using multinomial logistic regression algorithm for labeled training sample set. Equation (1) represents the probability formula that probability of the event occurring that multinomial logistic model is expressed as outcome variables:

$$P(y_i = j | x_i) = \frac{\exp(x_i h(x_i))}{1 + \sum_{m=1}^C \exp(x_i h(x_i))}. \quad (1)$$

When  $j$  is equal to  $1, \dots, K$ , the  $h(x_i)$  can be represented as

$$h(x_i) = \beta_0 + \beta_1 x_{i1} + \beta_2 x_{i2} + \dots + \beta_p x_{ip} + \varepsilon. \quad (2)$$

The coefficient of  $\beta$  is estimated through the estimation criteria of Bayesian maximum a posteriori and the log-likelihood algorithm [23, 24]; the solving method is given as follows:

$$w = L(\beta) = \sum_{i=1}^k \left[ \sum_{j=1}^C x_i h(x_i) - \log \left( \sum_{i=1}^n \exp(h(x_i)) \right) \right]. \quad (3)$$

Equation (3) calculates fitted coefficient of multinomial logistic classification; the estimating type CLA( $x_{k+1}$ ) brought by a new pixel  $x_{k+1}$  is calculated as follows:

$$\text{CLA}(x_{k+1}) = \arg \max_w \sum_{i=1}^C w. \quad (4)$$

Each predicted category ( $\text{CLA}_1, \dots, \text{CLA}_n$ ) for hyperspectral remote sensing image is calculated through (4); it represents a classification process is completed.

The important issue studied is how to add new samples to the training sample in the process of semisupervised classification. This process is conducted automatically by predicting

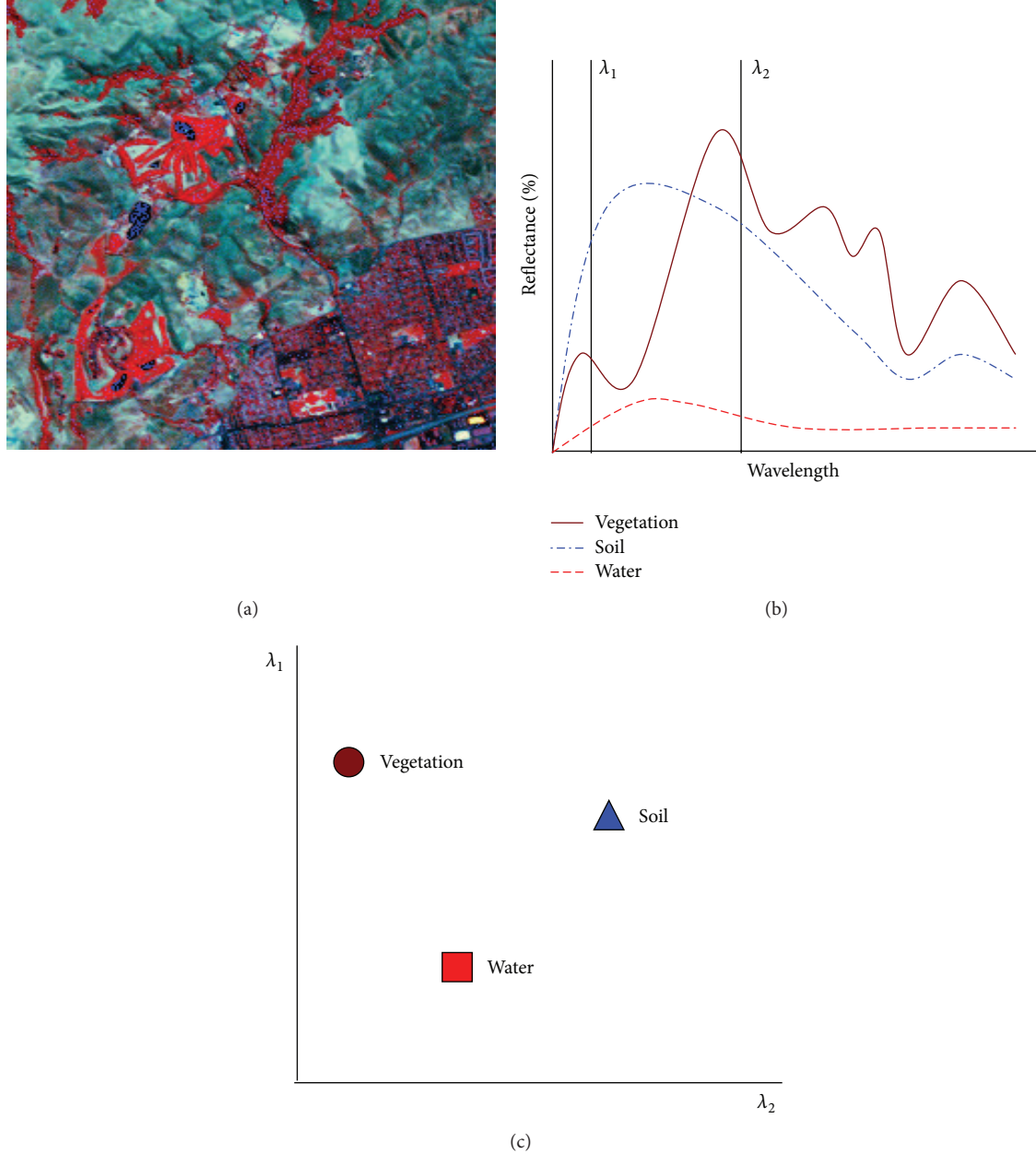


FIGURE 1: The description model of hyperspectral image data. (a) The model of original hyperspectral image. (b) The spectral model of original image. (c) The ground feature model of original image.

through the current classifier. The samples gotten through predicting by multinomial logistic regression classifier, which have the biggest probability, were added. Although sample category is exact, the amount of information contained is least. The positive effect on the next classification process is the smallest and it cannot improve classification accuracy if these samples are added to the training set. On the contrary, it will increase the computational burden of the classification algorithm in the process of selecting training samples. So the research for selecting unlabeled sample added to the training sample is very important.

**2.2.3. Selected Unlabeled Samples Using Rényi Entropy Algorithm.** Rényi proposed Rényi entropy in 1961; the definition form is shown in

$$R_\alpha(X) = \frac{1}{1-\alpha} \ln \left( \sum_{i=1}^n p(x_i)^\alpha \right), \quad \alpha \geq 0, \quad \alpha \neq 1. \quad (5)$$

Rényi entropy can reflect the uniformity of the attribute value distribution, and it is a scale for measuring the degree of uncertainty for information and the amount of information.

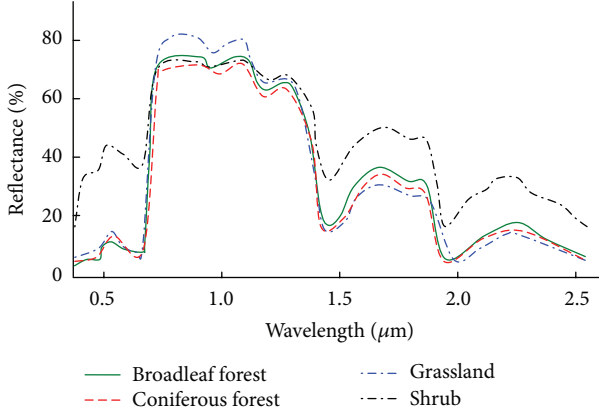


FIGURE 2: The spectral curves of different tree species.

This paper uses Rényi entropy with two times to describe the amount of information. It is shown in

$$R_2(X) = -\ln \left( \sum_{i=1}^n p(x_i)^2 \right), \quad \alpha = 2, \quad (6)$$

where  $p(x_i)$  takes the predicted probability value of each pixel because the object of study is hyperspectral image data. Equation (6) is normalized to prevent infinite value appeared in the process of calculation and obtained as

$$R_2(X) = -p(x_i) \ln \left( \sum_{i=1}^n p(x_i)^2 \right). \quad (7)$$

Hyperspectral image data set contains a large amount of implicit information, through the comprehensive analysis of the statistical information in the data set. Some regularity knowledge is used to obtain data connection. The classification result of sample that has the bigger entropy is uncertain for the current classifier and is the most informative sample. The new training set which is retrained with the unlabeled samples of maximum Rényi entropy is used for the new classification process. The overall accuracy of hyperspectral image classification is greatly improved.  $X = (x_1, \dots, x_n) \in R^{d \times n}$  represents the hyperspectral image data; the maximum Rényi entropy value is calculated by

$$S(U) = \max_k \{R_2(X)\}. \quad (8)$$

$S(U)$  represents the final choice of unlabeled set in the above formula,  $R_2(X)$  represents Rényi entropy calculated for each pixel on image in the process of the last classification, and then values of Rényi entropy are sorted. The  $k$  samples extracted from them are added to the existing training sample set.  $k$  is the number of labels in the supplementary training set.

The process of the algorithm is shown as follows.

**Input.** The original hyperspectral image  $X = (x_1, \dots, x_n) \in R^{d \times n}$ , the selected training sample set  $T = \{x_1, \dots, x_k\}$ ,  $T \subseteq X$ , the corresponding classification categories of training set

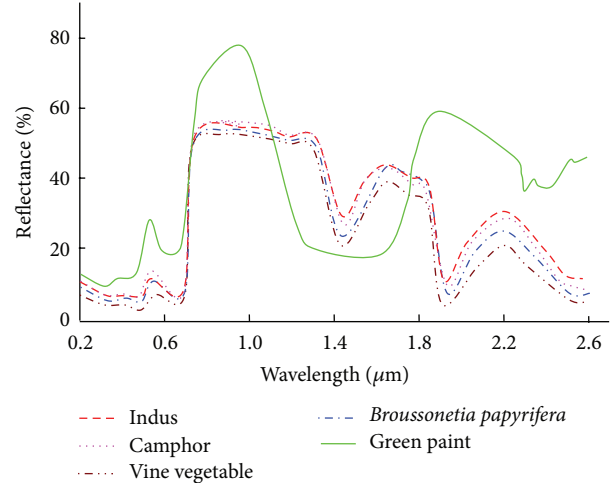


FIGURE 3: The differences between green paint spectrum and vegetation spectrum.

$Y = (y_1, \dots, y_k) \in C$ , unlabeled sample set  $U$ , and  $X = T \cup U$ .  $U_m^{\text{new}}$  represents the number of selected new unlabeled samples every time.  $m$  represents the number of semisupervised training, and  $X_{\overline{T \cup U}_m^{\text{new}}}$  represents the remaining unlabeled tag on image.

**Output.** The classification result of the hyperspectral image data is shown.

**2.2.4. The Process of Algorithm.** The process is described as below.

**Step 1.** Initialize setting and loading original image  $X = (x_1, \dots, x_n) \in R^{d \times n}$  and structure the matrix of the image.

**Step 2.** Load the training set  $T = \{x_1, \dots, x_k\}$  and the categories corresponding to training set  $y = (y_1, \dots, y_k)$ .

**Step 3.** Compute regression coefficient.

**Step 4.** Use regression coefficient to structure the model using the predicting classification.

**Step 5.** Select unclassified pixels  $X_{\overline{T \cup U}_m^{\text{new}}}$  in image  $X$  and predict the classification result ( $\text{CLA}_1, \dots, \text{CLA}_n$ ).

**Step 6.** Calculate the Rényi entropy value of each pixel in  $X_{\overline{T \cup U}_m^{\text{new}}}$ .

**Step 7.** The new  $k$  pixels of unlabeled sample set  $U_m^{\text{new}}$  of maximum Rényi entropy were extracted and used to update training set  $T$ .  $T_{\text{new}} = X_{T \cup U}_m^{\text{new}} + X_{\text{new}}$ ,  $p = (1 \dots m)$ .

**Step 8.** Return to Step 3 and iterate  $m$  times of the semisupervised learning process.

**Step 9.** Output the classification result of the hyperspectral image, and the process of algorithm is over.

TABLE 1: Parameters of the original test images.

Image	Platform	Size (pixel)	Spatial resolution (m)	Band composition	Position
T-1	EO-1	256 × 529	30	242 bands, covering 400–2500 nm	Inner Mongolia Autonomous Region, China

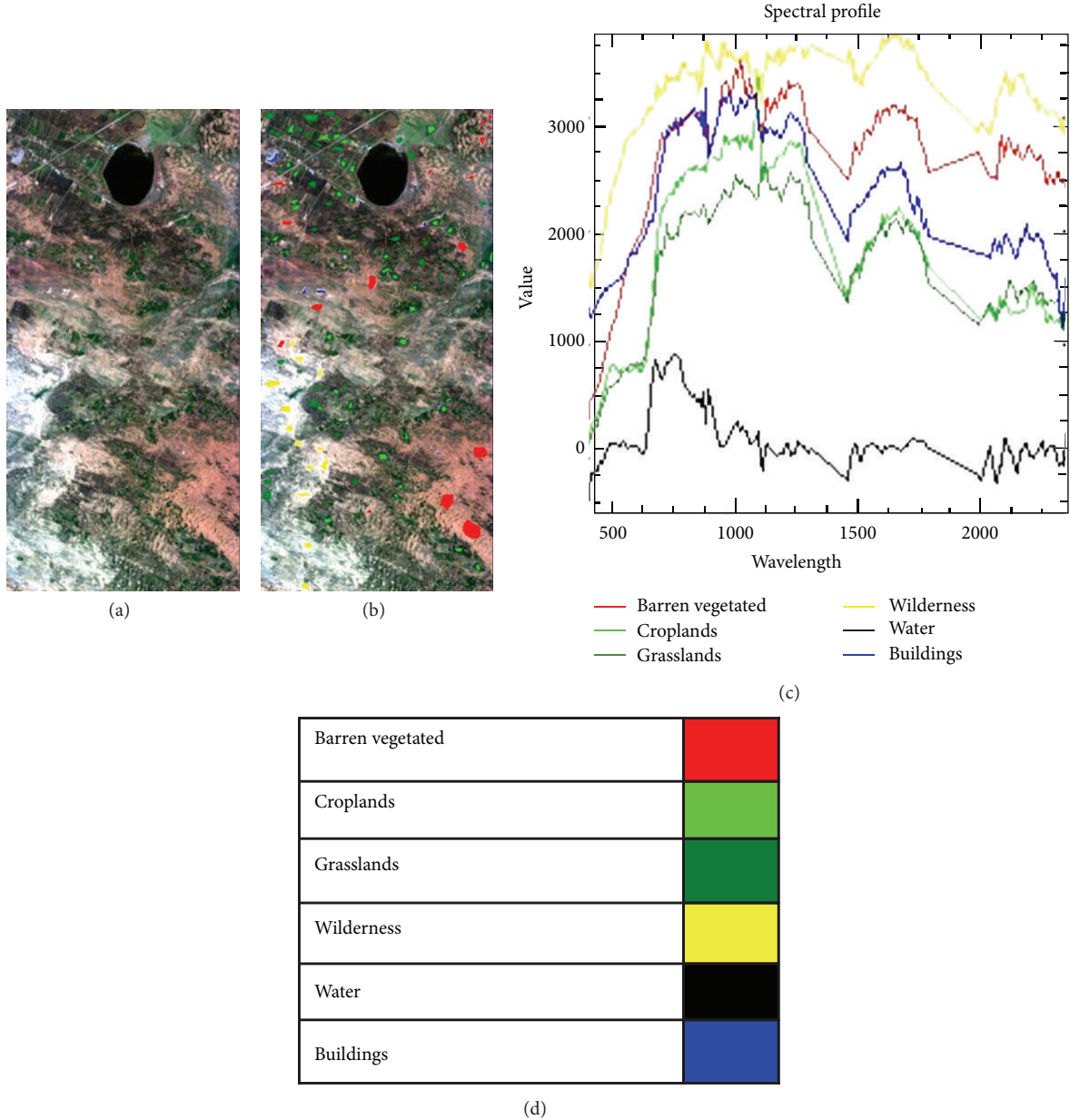


FIGURE 4: The T-1 original image of the study area. (a) The original Hyperion hyperspectral image (bands 29, 20, and 11). (b) The training sites overlay of original image. (c) The spectral curves of 6 kinds of major categories feature representing the land cover types of study area. (d) The thematic maps definition of 6 classes.

### 3. The Study Area and Validation Images

The typical test images and the parameters of which are presented in Table 1. The T-1 data is a subset of an EO-1 Hyperion scene after the atmospheric correction and geometric correction, in Inner Mongolia Autonomous Region, China, on August 21, 2010. The data in 242 bands of 10 nm width with center wavelengths from 400 to 2500 nm have

a spatial resolution of 30 m. In the present study, 124 bands were selected for analysis from the study area data, which is removing the effects of water vapor absorption and low SNR bands. The major land cover categories of the region were barren or sparsely vegetated, grasslands, croplands, wilderness, buildings, and water. The image parameters of experimental zone are listed in Table 1; then Figure 4(a) is the true color image of the experimental area image which selects

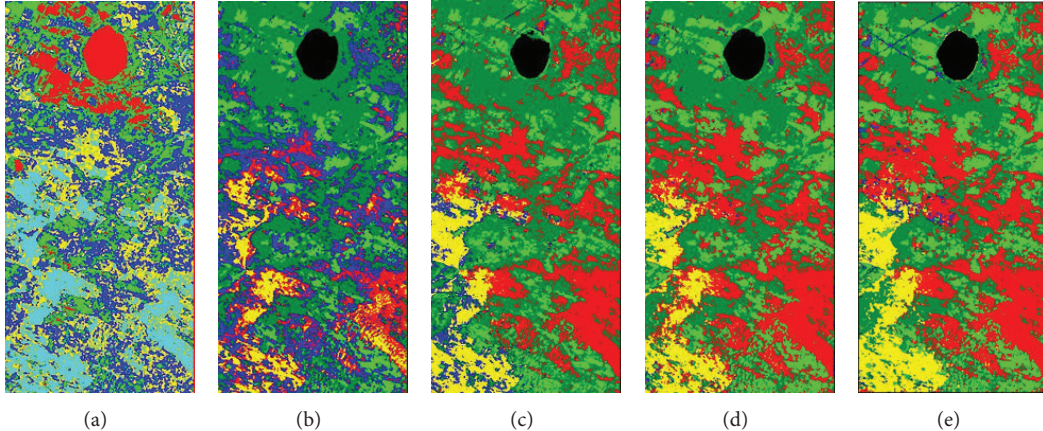


FIGURE 5: The classification results of study area using various classifier methods. (a) The classified image using  $K$ -means classifier method. (b) The classified image using minimum distance classifier method. (c) The classified image using artificial neural network classifier method. (d) The classified image using support vector machine classifier method. (e) The classified image using the semisupervised classifier of the proposed method in this paper.

three bands 29 (640 nm), 20 (548 nm), and 11 (457 nm) to be merged; Figure 4(b) is the training samples of each category feature. Figure 4(c) is the spectral curve of six kinds of major categories feature. The last one Figure 4(d) is the thematic maps definition of six classes.

#### 4. Experiment of Land Use/Cover Assessment

**4.1. Data Preprocessing.** The first step is radiometric correction in data preprocessing. The radiometric correction is the key step of quantitative analysis in data preprocessing and is the premise of the research work of quantitative analysis, reflectance retrieval, and information extraction.

The second step is dimension reduction method for hyperspectral image. Hyperspectral images have the ability to distinguish surface features nuances in high spectral resolution at the same time; also the dimension disaster is brought. This phenomenon has seriously affected the accuracy of classification and efficiency of classification for hyperspectral image. The purpose of dimension reduction techniques is based on image feature extraction to use low-dimensional data to effectively express the characteristics of high-dimensional data. It not only preserves the image information but also reduce the volume of data effectively. The common dimension reduction algorithm is principal component analysis [25].

**4.2. Comparison for Different Classification Methods.** The important step of the land use/cover research is to establish a scientific classification method for study area. To illustrate the effectiveness of the proposed semisupervised classification method, the several representative machines learning classification methods including supervised method and unsupervised method are selected to compare with the method proposed. The Hyperion data set is used to analyze the performance of the proposed method in comparison with other

TABLE 2: Overall accuracy and Kappa coefficient based on comparison of the varying classification methods.

Classification methods	Iteration time (s)	Overall accuracy (%)	Kappa coefficient
$K$ -means classifier	18	52.58%	0.41
Minimum distance classifier	12	80.56%	0.75
Neural network classifier	151	92.78%	0.90
Support vector machine classifier	30	95.23%	0.93
Semisupervised classifier	60	97.31%	0.96

methods. The classification results of a variety of classification methods are shown in Figure 5. The classification results of unsupervised classifier of the  $k$ -means method are shown in Figure 5(a). The classification results of supervised classifier of the minimum distance method are shown in Figure 5(b). The classification results of supervised classifier artificial neural network method are shown in Figure 5(c). The classification results of supervised classifier of support vector machine method are shown in Figure 5(d), and the final Figure 5(e) is the classification results of the semisupervised classifier of the proposed method in this paper. Table 2 is a comparison of various classification method running time, overall accuracy, and Kappa coefficient evaluation indexes.

The results of experiment are shown in Figure 5 and Table 2. Based on the classification results of various classification methods, it can be concluded that the results are analogous with experiment. The overall classification of the  $k$ -means method is lowest although the running time is shortest. The serious leak misclassification is shown in Figure 5 and the only five classes were distinguished from unsupervised classifier.

The overall classification accuracy of supervised classifier of minimum distance method is better than the unsupervised

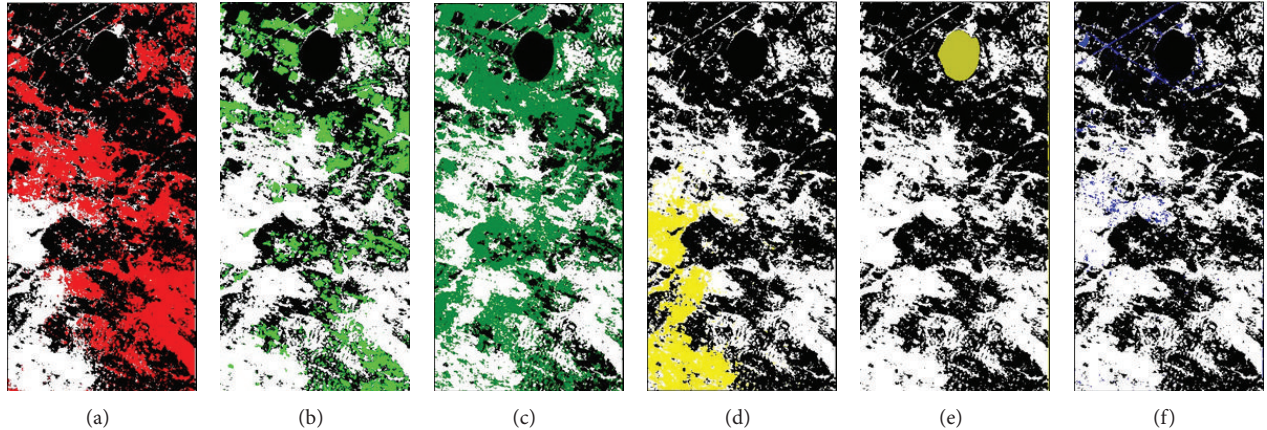


FIGURE 6: The thematic maps of a variety of categories of surface features in study area. (a) The thematic maps of barren vegetated. (b) The thematic maps of croplands. (c) The thematic maps of grasslands. (d) The thematic maps of wilderness. (e) The thematic maps of water. (f) The thematic maps of buildings.

*k*-means classifier method. However, poor quality can be clearly seen from Figure 5(b) that the buildings feature is more serious misclassification error.

The overall classification accuracy of artificial neural network classifier method in experiment is more than unsupervised method because the feature category is simpler and the image size is smaller in experiment. The method disadvantages include longer running time, inefficiency, and misclassification error. Figure 5(c) shows that the buildings feature and wilderness cannot be distinguished by the method. The road feature has almost disappeared in the classification results.

The support vector machine classifier is relatively high quality method including the running speed, the relatively high overall classification accuracy, and the best effect of classification for a large contiguous area. However, this method reveals the low ability for analyzing the small surface features showing the error of leakage. For instance, the SVM method will eliminate the small building and road feature in Figure 5(d).

The semisupervised classification method shows again good performance in experiment from Figure 5 and Table 2. The proposed semisupervised classifier can effectively improve the accuracy of classification and obtain better classification results, especially small features such as road and building features.

From the above results in experiment, the new semisupervised method can obtain better classification results for hyperspectral image data and can effectively improve the accuracy of classification, which is received to be 97.31%, respectively. The experiment also showed that the new semisupervised method includes especially large-size images and complex images.

**4.3. Making the Thematic Maps.** The thematic maps not only are objective assessment of classification result, but also can check the situation of land use/cover in different periods.

The thematic maps of a variety of categories of surface features are shown in Figure 6.

From Figure 6, it is shown that the barren vegetated features are the maximum areas in experimental zone. The buildings features occupy the minimum areas. The overall distributions of grasslands are of high concentration. The croplands are more concentrated around water bodies and are more effectively irrigated by water.

## 5. Conclusions and Future Work

In this study, a semisupervised method of classification for hyperspectral remote sensing images is applied to improve fine land use/cover assessment. Firstly, this paper sets forth the basic theories of fine land use/cover assessment, which are differences between the spectral characteristics. Secondly, the method of semisupervised classification is described in detail. Thirdly, the paper elaborates the study area and the parameters of validation images. Finally, the fine land use/cover test of study area is conducted using the semisupervised hyperspectral image classification. The experimental results show that the method has a high precision overall classification. The thematic maps of classification results are objective assessment of land use/cover. Study on land use/cover can reflect changing rules of population, economy, agricultural structure adjustment, policy, and traffic and provide better service for the regional economic development and urban evolution.

However, the proposed semisupervised method still has inadequacies, such as long-running time, and needs further more computing power and hardware. Future research priority will focus on optimizing method, saving the running time, and promoting working efficiency.

## Conflict of Interests

The authors declare that there is no conflict of interests regarding the publication of this paper.

## Acknowledgments

This research is jointly supported by the Joint Project of National Natural Science Foundation of China and Shenhua Coal Industry Group Co., Ltd. (U1261206) and by NSFC of China under Grant 41401403 and also in part by Henan Province University Technological Innovation Team and Personnel Support Program in 2013 (13IRTSTHN029). The authors would like to thank Dr. Jianghui Dong at Flinders University (Australia) for greatly helping to improve the quality of this paper.

## References

- [1] A. F. H. Goetz, "Three decades of hyperspectral remote sensing of the Earth: a personal view," *Remote Sensing of Environment*, vol. 113, supplement 1, pp. S5–S16, 2009.
- [2] F. Wufa, Y. Guopeng, and C. Wei, *Hyperspectral Image Analysis and Application*, Science Press, Beijing, China, 2013.
- [3] P. K. Mallupattu and J. R. S. Reddy, "Analysis of land use/land cover changes using remote sensing data and GIS at an Urban Area, Tirupati, India," *The Scientific World Journal*, vol. 2013, Article ID 268623, 6 pages, 2013.
- [4] G. Camps-Valls, D. Tuia, L. Bruzzone, and J. A. Benediktsson, "Advances in hyperspectral image classification: earth monitoring with statistical learning methods," *IEEE Signal Processing Magazine*, vol. 31, no. 1, pp. 45–54, 2014.
- [5] B. B. Damodaran and R. R. Nidamanuri, "Assessment of the impact of dimensionality reduction methods on information classes and classifiers for hyperspectral image classification by multiple classifier system," *Advances in Space Research*, vol. 53, no. 12, pp. 1720–1734, 2014.
- [6] Z. Wang and L. Liu, "Assessment of coarse-resolution land cover products using CASI hyperspectral data in an arid zone in Northwestern China," *Remote Sensing*, vol. 6, no. 4, pp. 2864–2883, 2014.
- [7] Y. Zhang, Y. Du, F. Ling, S. Fang, and X. Li, "Example-based super-resolution land cover mapping using support vector regression," *IEEE Journal of Selected Topics in Applied Earth Observations and Remote Sensing*, vol. 7, no. 4, pp. 1271–1283, 2014.
- [8] S. Padma and S. Sanjeevi, "Jeffries Matusita based mixed-measure for improved spectral matching in hyperspectral image analysis," *International Journal of Applied Earth Observation and Geoinformation*, vol. 32, pp. 138–151, 2014.
- [9] B. T. Zabe, O. O. Olugbara, and T. Marwala, "Experimental comparison of support vector machines with random forests for hyperspectral image land cover classification," *Journal of Earth System Science*, vol. 123, no. 4, pp. 779–790, 2014.
- [10] M. Pal, "Extreme-learning-machine-based land cover classification," *International Journal of Remote Sensing*, vol. 30, no. 14, pp. 3835–3841, 2009.
- [11] J. Bao, M. Chi, and J. A. Benediktsson, "Spectral derivative features for classification of hyperspectral remote sensing images: experimental evaluation," *IEEE Journal of Selected Topics in Applied Earth Observations and Remote Sensing*, vol. 6, no. 2, pp. 594–601, 2013.
- [12] S. Stankevich, V. Levashenko, and E. Zaitseva, "Fuzzy decision tree model adaptation to multi- and hyperspectral imagery supervised classification," in *Proceedings of the 9th International Conference on Digital Technologies (DT '13)*, pp. 198–202, Žilina, Slovakia, May 2013.
- [13] N. Alajlan, Y. Bazi, F. Melgani, and R. R. Yager, "Fusion of supervised and unsupervised learning for improved classification of hyperspectral images," *Information Sciences*, vol. 217, pp. 39–55, 2012.
- [14] K. Ashwini, S. Siddhesh, M. Rakesh, and P. Bhavesh, "A novel approach for object detection in VHR images," *International Journal of Signal Processing, Image Processing and Pattern Recognition*, vol. 6, no. 4, pp. 355–366, 2013.
- [15] S. Rajan, J. Ghosh, and M. M. Crawford, "An active learning approach to hyperspectral data classification," *IEEE Transactions on Geoscience and Remote Sensing*, vol. 46, no. 4, pp. 1231–1242, 2008.
- [16] G. Jun and J. Ghosh, "Spatially adaptive semi-supervised learning with Gaussian processes for hyperspectral data analysis," *Statistical Analysis and Data Mining*, vol. 4, no. 4, pp. 358–371, 2011.
- [17] J. Munoz-Mari, D. Tuia, and G. Camps-Valls, "Semisupervised classification of remote sensing images with active queries," *IEEE Transactions on Geoscience and Remote Sensing*, vol. 50, no. 10, pp. 3751–3763, 2012.
- [18] G. Jun and J. Ghosh, "Semisupervised learning of hyperspectral data with unknown land-cover classes," *IEEE Transactions on Geoscience and Remote Sensing*, vol. 51, no. 1, pp. 273–282, 2013.
- [19] Z. M. Liu, B. R. Hu, W. J. Wu, and Y. Zhang, "Spectral imaging of green coating camouflage under hyperspectral detection," *Guangzi Xuebao/Acta Photonica Sinica*, vol. 38, no. 4, pp. 885–890, 2009.
- [20] A. Rényi, "On measures of entropy and information," in *Proceedings of the 4th Berkeley Symposium on Mathematical Statistics and Probability*, vol. 1, pp. 547–561, University of California Press, Berkeley, Calif, USA, 1961.
- [21] B. Krishnapuram, L. Carin, M. A. T. Figueiredo, and A. J. Hartemink, "Sparse multinomial logistic regression: fast algorithms and generalization bounds," *IEEE Transactions on Pattern Analysis and Machine Intelligence*, vol. 27, no. 6, pp. 957–968, 2005.
- [22] J. Bioucas-Dias and M. Figueiredo, "Logistic regression via variable splitting and augmented lagrangian tools," Tech. Rep., Instituto Superior Técnico, Lisboa, Portugal, 2009.
- [23] Y. B. Zhang, J. W. Zhao, J. M. Li, and Y. Sun, "Decision feedback blind equalization algorithm based on RENYI entropy for underwater acoustic channels," *Journal of Electronics and Information Technology*, vol. 31, no. 4, pp. 911–915, 2009.
- [24] D. Dou, L. Li, and Y. Zhao, "Fault diagnosis of rolling bearings using EEMD- Renyi entropy and PCA-PNN," *Journal of Southeast University (Natural Science Edition)*, vol. 41, supplement 1, pp. 107–111, 2011.
- [25] L. T. Jolliffe, *Principal Component Analysis*, Springer, New York, NY, USA, 2nd edition, 2002.

## Research Article

# Effects of Chlorinated Polypropylene on the Conformation of Polypropylene in Polypropylene/Chlorinated Polypropylene/Polyaniline Composites

Jianjun Chen, Yueyue Jia, Zhiye Zhang, Xinlong Wang, and Lin Yang

College of Chemical Engineering of Sichuan University, Chengdu, Sichuan 610065, China

Correspondence should be addressed to Xinlong Wang; wangxl@scu.edu.cn

Received 19 August 2014; Revised 13 October 2014; Accepted 20 October 2014

Academic Editor: Nikša Krstulović

Copyright © 2015 Jianjun Chen et al. This is an open access article distributed under the Creative Commons Attribution License, which permits unrestricted use, distribution, and reproduction in any medium, provided the original work is properly cited.

We investigated the changes in the conformation and crystalline structure of polypropylene (PP) using a combination of Fourier transform infrared spectroscopy (FTIR), wide-angle X-ray diffraction (WAXD), and differential scanning calorimetry (DSC) based on PP/chlorinated PP (CPP)/polyaniline (PANI) composites. The DSC heating thermograms and WAXD patterns of the PP/CPP/PANI composites showed that the  $\beta$ -crystal was affected greatly by the CPP content. Characterization of the specific regularity in the infrared band variation showed that the conformational orders of the helical sequences in PP exhibited major changes that depended on the CPP content. Initially, the intensity ratio of  $A_{840}/A_{810}$  increased with the CPP concentration and reached its maximum level when the CPP content was <13.22% before decreasing as the CPP content increased further. The effect of increased temperature on the conformation of PP was studied by *in situ* FTIR. Initially, the intensity ratio of  $A_{999}/A_{973}$  decreased slowly with increasing the temperature up to 105°C before decreasing sharply with further increases in temperature and then decreasing slowly again when the temperature was higher than 128°C.

## 1. Introduction

Conductive polymers are expected to yield attractive combinations of properties and are getting more and more attention for researchers from all over the world. Among conductive polymers, polyaniline has the best potential to become economically competitive, for its cheap materials, simple synthetic method, and stability in environment [1]. Although polyaniline has many merits, it is very difficult to be processed in usual methods used in conventional polymers due to its strong intermolecular and intramolecular interactions [2]. For these reasons, wide scale industrial application of polyaniline has been strongly impeded over several years. Many new protonating agents such as sulfonic acids, phosphoric acid esters [2, 3], and phosphoric acid [4] have been introduced in recent years in order to improve the processability of polyaniline. To be worthy and mentioned, it was Cao et al. [5] that firstly introduced sulfonic acid as a protonating agent, and this made polyaniline possible to be processed in solvent. Another method to improve

the processability of polyaniline was that polyaniline was blended with thermoplastic polymers due to polyaniline poor mechanical properties [4, 6–8]. A unique specialty of this method lies in the combination of electric properties of polyaniline and mechanical properties of thermoplastic polymers.

In a series of previous studies, we have prepared PP/CPP/PANI composites by melt processing, and investigated the influence of the concentration of CPP on the electric property of PP/CPP/PANI composites and the influence of CPP on the formation of the intermolecular and innermolecular hydrogen bond in the PP/CPP/PANI composites which is carefully proved by FTIR. We found that the hydrogen bond between CPP and PANI plays a prominent role in the decision of composites' electric property [9, 10]. Does there exist a kind of interaction between CPP and PP in the PP/CPP/PANI composites? Hence, how to detect and identify the interaction between CPP and PP in the PP/CPP/PANI composites becomes one of the most important work.

Since Natta et al. [11] first synthesized high molecular weight isotactic polypropylene (iPP) in 1955, the IR spectroscopy has been used to elucidate the structure of this crystalline polymer. In the infrared spectra of isotactic polypropylene, some absorption bands are connected with the intramolecular vibration coupling within a single chain, and this kind of band is defined as a regularity band or helix band [12, 13]. Therefore, FTIR spectroscopy can provide much meaningful structural information and it is an effective method of denoting the changes of helical conformation of PP [14, 15]. During the past decades, it has been well established that specific regularity bands are related to the different critical length “*n*” of isotactic sequences [16–18]. For example, the minimum *n* values for appearance of bands at 973, 998, 841, and 1220 cm<sup>-1</sup> are 5, 10, 12, and 14 monomer units in helical sequences, respectively. Zhu et al. [17] adopted in situ FTIR and arranged the various regularity bands in terms of the order degree from high to low: 940, 1220, 1167, 1303, 1330, 841, 998, 900, 808, 1100, and 973 cm<sup>-1</sup>. Hence, the information of effects of CPP on the conformation of PP can be obtained by calculating the absorbance ratios of different regularity bands in FTIR spectra. It has been reported that, for iPP samples when the fully isotactic sequences are very short, iPP crystallizes in the  $\gamma$  form, whereas very long regular isotactic sequences generally crystallize only in the  $\alpha$  form [19–23]. Therefore, the crystal structure is greatly affected by the helical conformation regularity.

In this investigation, DSC, WAXD and FTIR are adopted to detect and identify the interaction between CPP and PP in the PP/CPP/PANI composites. The variation of conformation and crystalline structure of PP has been discussed. Conductive polymers are expected to yield attractive combinations of properties, and they are gaining increasing attention from researchers throughout the world. In particular, polyaniline (PANI) is considered to have the highest potential to become an economically competitive conductive polymer due to the cheap materials required for its production, simple synthetic method, and environmental stability [1]. Although PANI has many merits, it is very difficult to process with the standard methods used for conventional polymers because of its strong intermolecular and intramolecular interactions [2]. Thus, large-scale industrial applications of PANI have been hindered for several years. However, many new protonating agents such as sulfonic acid, phosphoric acid esters [2, 3], and phosphoric acid [4] have been employed in recent years to improve the processability of PANI. It should be mentioned that Cao et al. [5] were the first to introduce sulfonic acid as a protonating agent, thereby allowing PANI to be processed in a solvent. Another method for improving the processability of PANI is blending with thermoplastic polymers, which due to the poor mechanical properties of PANI [4, 6–8]. A unique feature of this method is the combination of the electric properties of PANI and mechanical properties of thermoplastic polymers.

In a series of previous studies, we prepared polypropylene (PP)/chlorinated PP (CPP)/PANI composites by melt processing and investigated the effects of the CPP concentration on the electric properties of PP/CPP/PANI composites, as well as the influence of CPP on the formation of

intermolecular and intramolecular hydrogen bonds in the PP/CPP/PANI composites, which were carefully examined by Fourier transform infrared spectroscopy (FTIR). We found that the hydrogen bonds between CPP and PANI have a major role in determining the electric properties of composites [9, 10]. However, there may also be important interactions between CPP and PP in PP/CPP/PANI composites. Thus, detecting and identifying the interactions between CPP and PP in PP/CPP/PANI composites has become a major focus of our research.

In this study, we used differential scanning calorimetry (DSC), wide-angle X-ray diffraction (WAXD), and FTIR to detect and identify the interactions between CPP and PP in PP/CPP/PANI composites. We discuss the variations in the conformations and crystalline structure of PP.

## 2. Experimental

**2.1. Materials.** PANI protonated with HCl was supplied by Chengdu Organic Chemicals Co., Ltd. (China) and its electrical conductivity was ca 1 S cm<sup>-1</sup>. PANI was synthesized using the air oxidation method (China patent: CN1626564A). The granularity of PANI-HCl was about 30  $\mu$ M.

PP (PPH-XD-045, melt flow index = 3.5 g 10 min<sup>-1</sup>) was supplied by PetroChina Co., Ltd. (China).

Dodecylbenzenesulfonic acid (DBSA) was supplied by Kewei Chemicals Co., Ltd. (China) and its content was about 96% (wt).

CPP was supplied by Sichuan Weiye Chemicals Co., Ltd. (China) and its chlorine content was about 31% (wt).

**2.2. Preparation of Composites.** PANI protonated with HCl was neutralized with 20% (wt) sodium hydroxide (NaOH) aqueous solution for 48 h (the NaOH aqueous solution was in great excess compared with the amount of PANI-HCl) where the pH of the blend (i.e., PANI-HCl and NaOH aqueous solution) was ca 11, which was followed by filtration and washing with deionized water until the pH of percolate was 6–8. The polyemeraldine base (PANI<sub>emer</sub>) obtained was dried under vacuum. The purified and dried PANI<sub>emer</sub> was blended with DBSA, where the molar ratio of DBSA relative to PANI<sub>emer</sub> was 0.5. The blend was stirred for 48 h at ambient temperature, thereby obtaining PANI protonated with DBSA (PANI-DBSA).

The PP/CPP/PANI composites were prepared on a two-roll mill. The compositions of the blends are shown in Table 1.

**2.3. FTIR Measurement.** The specimens used to obtain FTIR measurements were molded into very thin films. Compression molding was performed in the following conditions: preheating at 180°C for 5 min at low pressure and compression for 10 min at 15 MPa at the same temperature, followed by cooling in the mold to ambient temperature with a cooling rate of 30°C min<sup>-1</sup> at 15 MPa. FTIR analysis was conducted using a Nicolet 170X FTIR spectrometer (Nicolet Co., USA) at a resolution of 2 cm<sup>-1</sup>. For in situ FTIR, the spectra were obtained at elevated temperatures using a miniature heat controller. The spectrum was collected every 30 s and a heating rate of 5°C min<sup>-1</sup> was employed. The temperature was

TABLE 1: Formation of PP/PANI composition (in wt %).

Sample code	PP	PANI <sub>emer</sub>	DBSA	CPP	Theoretical degree of protonation
PP/PANI 1	87.23	4.10	7.79	0.88	0.5
PP/PANI 2	83.70	4.10	7.79	4.41	0.5
PP/PANI 3	79.30	4.10	7.79	8.81	0.5
PP/PANI 4	74.89	4.10	7.79	13.22	0.5
PP/PANI 5	70.49	4.10	7.79	17.62	0.5

monitored using a copper-constantan thermocouple, which was placed directly on the sample. During detection, the specimen was protected by nitrogen.

**2.4. DSC.** The calorimetric measurements of all samples were obtained using a NETZSCH DSC 204 at a scan rate of  $10^{\circ}\text{C min}^{-1}$  under a flowing nitrogen atmosphere, and the sample weight was ca 10 mg.

**2.5. Wide-Angle X-Ray Diffraction.** WAXD investigations were performed using a DX-2500 SSC diffractometer (China) in the reflection mode. Cu K $\alpha$  radiation was used at 40 kV and 25 mA. The scan step was  $0.06^{\circ}$  (in  $2\theta$ ) with a period of 2 s per step. The  $\beta$ -crystal content was deduced from the X-ray data according to standard procedures [24] using the relationship:

$$k = \frac{H_{\beta(300)}}{H_{\beta(300)} + H_{\alpha(110)} + H_{\alpha(040)} + H_{\alpha(130)}}, \quad (1)$$

where  $H_{\alpha(hkl)}$  and  $H_{\beta(hkl)}$  represent the heights of the  $(hkl)$  peak for the  $\alpha$  and  $\beta$  phases, respectively.

### 3. Results and Discussion

**3.1. Effect of CPP on the Crystal Structure of PP.** Figure 1 shows the DSC heating thermograms for PP/CPP/PANI blends, which were recorded at a heating rate of  $10^{\circ}\text{C min}^{-1}$ . In order to clearly demonstrate the differences in the DSC curves, only two curves are shown in Figure 1. The two samples produced melting endotherms with characteristic doublet peaks. The peak at the lower temperature is represented as a shoulder of the peak at the higher temperature. The multiple peaks in the DSC curves are attributable to the melting of the two polymorphic forms of PP [25]. In general, the  $\beta$  form melted at a lower temperature and the  $\alpha$  form melted at a higher temperature. Figure 1 also shows clearly that the  $\beta$  peak of PP/PANI 4 is more prominent than that of PP/PANI 2. This demonstrates that the  $\beta$ -crystal is affected greatly by the CPP content.

Figure 2 shows the WAXD patterns for the PP/CPP/PANI composites. PP is crystallizable and it has three crystalline phase types:  $\alpha$ -crystal,  $\beta$ -crystal, and  $\gamma$ -crystal. In Figure 2, the presence of  $\alpha$ -crystal is indicated by the crystalline peaks at ca  $14^{\circ}$ ,  $17^{\circ}$ ,  $18.5^{\circ}$ ,  $21^{\circ}$ , and  $21.8^{\circ}$ , while the crystalline peak at ca  $16^{\circ}$  is attributed to  $\beta$ -crystal [25]. According to the standard procedures [24], the  $\beta$ -PP contents are 12.7% and 27.7% for PP/PANI 1 and PP/PANI 4, respectively, thereby indicating

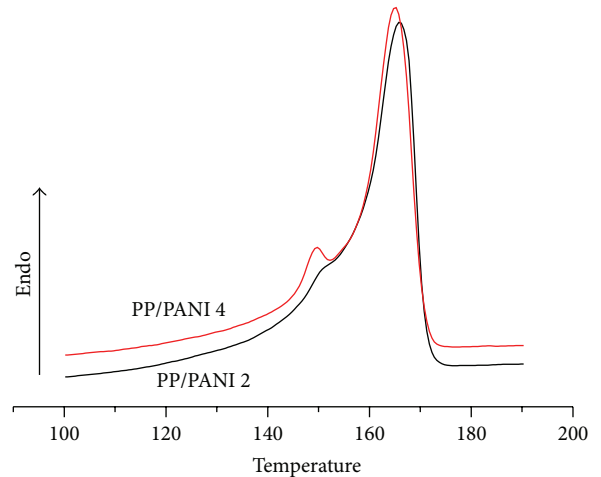


FIGURE 1: DSC heating thermograms of PP/CPP/PANI blends.

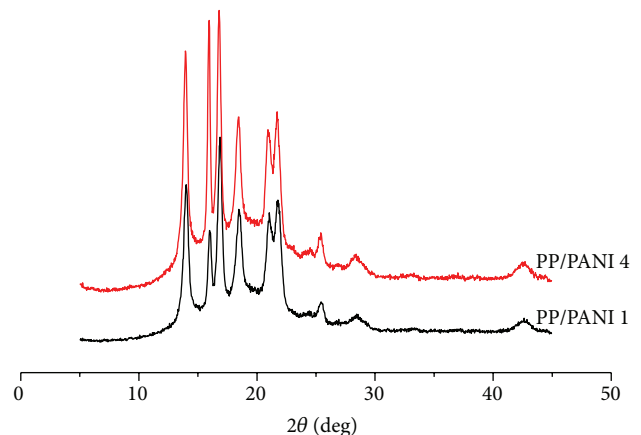


FIGURE 2: WAXD patterns of PP/PANI 1 and PP/PANI 4.

that the CPP content has a major impact on the  $\beta$ -crystal type. These results are consistent with those obtained by DSC.

**3.2. Effect of the CPP Content on the Conformation Structure of PP.** In general, the regularity bands of PP are related to the different helical lengths " $n$ " of the isotactic sequences [15–17]. The intensity of the regularity bands can reflect the quantity of different helical lengths " $n$ " in isotactic sequences. Therefore, the conformational ordering of different samples can be determined based on the absorbance ratios of the various regularity bands.

Figure 3 shows the FTIR spectra of the PP/CPP/PANI composites with different CPP contents, which demonstrate that the intensities of different regularity bands ( $810$ ,  $840$ ,  $973$ , and  $999\text{ cm}^{-1}$ ) changed slightly as the CPP concentration increased. The variations in these regularity bands indicate that the conformation of PP is affected by the CPP concentration. These regularity bands can be divided into two groups ( $810/40\text{ cm}^{-1}$  and  $973/999\text{ cm}^{-1}$ ), which we will discuss in detail later.

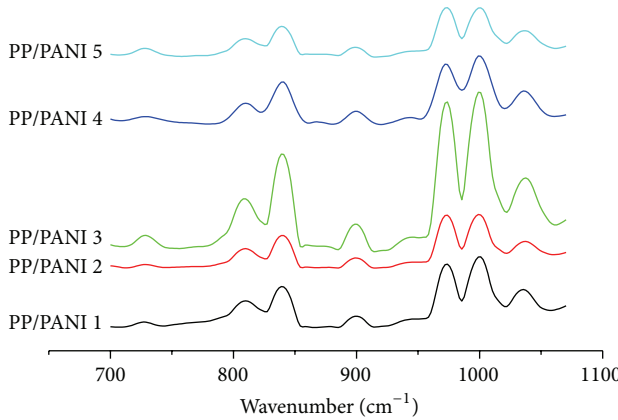


FIGURE 3: FTIR spectra of the PP/CPP/PANI composites.

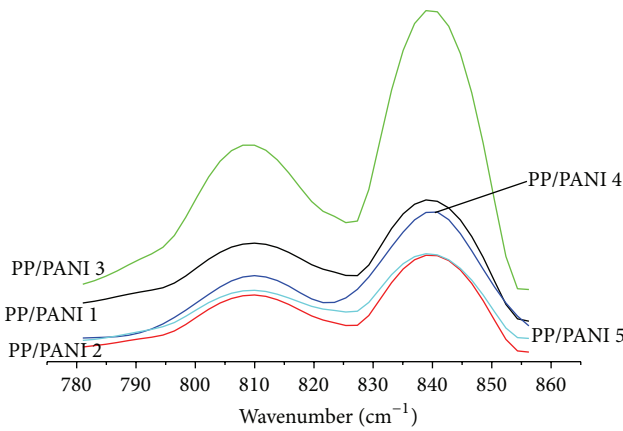


FIGURE 4: FTIR spectra of the PP/CPP/PANI composites with different CPP concentrations ( $780\text{--}856\text{ cm}^{-1}$ ).

**3.2.1. The Region ( $780\text{--}856\text{ cm}^{-1}$ ) of the FTIR Spectra.** Figure 4 shows the FTIR spectra in the  $780\text{--}856\text{ cm}^{-1}$  region for the PP/CPP/PANI composites with different CPP contents. Obviously, there are two Gaussian bands in this region, where the first band is at around  $810\text{ cm}^{-1}$  and the second band is at around  $840\text{ cm}^{-1}$  for all of the PP/CPP/PANI composites. In general, the intensity of the two bands was closely related to the size of the two critical lengths “ $n$ ” for isotactic sequences of PP. Each FTIR band has its own intensity coefficient and each sample has its own thickness; thus, the intensities of the regular helical conformation bands should be processed in order to determine the effect of the CPP content. In the present study, the variation in the intensity ratio was used to indicate the effect of the CPP content on the two critical lengths “ $n$ ” for isotactic sequences of PP.

The FTIR results for this region are shown in Table 2, where  $\text{XS}_{810} = A_{810}/(A_{810} + A_{840})$  and  $\text{XS}_{840} = A_{840}/(A_{810} + A_{840})$ . The relationship between the  $A_{840}/A_{810}$  ratio and the CPP content is shown in Figure 5.

Table 2 and Figure 5 show that the appearances of bands at  $840/810\text{ cm}^{-1}$  for the two critical lengths “ $n$ ” of isotactic sequences were affected by the CPP content. The  $A_{840}/A_{810}$

TABLE 2: Curve-fitting results for spectra of the region ( $780\text{--}856\text{ cm}^{-1}$ ).

Sample code	First band			Second band		
	$\nu 1\text{ cm}^{-1}$	$A_{810}$	$\text{XS}_{810}$	$\nu 2\text{ cm}^{-1}$	$A_{840}$	$\text{XS}_{840}$
PP/PANI 1	809.9	1.137	0.546	840.1	0.944	0.454
PP/PANI 2	809.8	0.669	0.453	839.9	0.807	0.547
PP/PANI 3	809.3	1.753	0.421	839.9	2.410	0.579
PP/PANI 4	809.8	0.697	0.362	839.7	1.229	0.638
PP/PANI 5	810.1	0.671	0.458	839.8	0.794	0.542

$\nu$ : wavenumber;  $A$ : intensity; XS: percent of  $A$ .

ratio determined the ratio of the two critical lengths “ $n$ ” of isotactic sequences. The critical length “ $n$ ” of isotactic sequences was larger for the second band than for the first band. Apparently, the order degree was higher when the ratio was larger. As shown in Figure 5, the  $A_{840}/A_{810}$  ratio increased initially with the CPP content and it reached a maximum when the CPP content was 13.22%, after which it decreased as the CPP content increased further. Thus, the critical length “ $n$ ” of the isotactic sequences with a band at  $840\text{ cm}^{-1}$  corresponded to that with a band at  $810\text{ cm}^{-1}$ , which increased with the CPP content up to 13.22% before decreasing as the CPP content increased further. These results indicate that the conformational structures or the order degrees of the helical sequences of PP were affected significantly by the CPP content. This may be attributable to interactions between CPP and the PP matrix.

**3.2.2. The Region ( $950\text{--}1020\text{ cm}^{-1}$ ) of the FTIR Spectra.** Figure 6 shows the FTIR spectra in the  $950\text{--}1020\text{ cm}^{-1}$  region for the PP/CPP/PANI composites with different CPP contents, which demonstrates that there are two Gaussian bands in this region, where the first band is at around  $973\text{ cm}^{-1}$  and the second band is at around  $999\text{ cm}^{-1}$ . The critical length “ $n$ ” values of the isotactic sequences for the appearance of bands at  $973$  and  $999\text{ cm}^{-1}$  were 2–4 and 5–10 monomer units in the helical sequences, respectively [13]. The intensities of the two bands are shown in Table 3.

In Table 3,  $\text{XS}_{973} = A_{973}/(A_{973} + A_{999})$  and  $\text{XS}_{999} = A_{999}/(A_{973} + A_{999})$ . The  $A_{999}/A_{973}$  ratio determines the ratio of the two critical lengths “ $n$ ” of isotactic sequences. The relationship between the  $A_{999}/A_{973}$  ratio and CPP content is shown in Figure 7.

Table 3 and Figure 7 show the effects of the CPP content on the  $A_{999}/A_{973}$  ratio. Figure 7 demonstrates that the  $A_{999}/A_{973}$  ratio changed slightly with different CPP contents, which shows that the critical length “ $n$ ” of isotactic sequences for the appearance of a band at  $999\text{ cm}^{-1}$ , which corresponded to that for the appearance of a band at  $973\text{ cm}^{-1}$ , was affected slightly by the CPP content.

**3.3. Effect of Temperature on the Conformation Structure of PP in the PP/CPP/PANI Composite.** The crystallization of PP composites is usually affected significantly by the process temperature. Thus, to investigate the influence of temperature

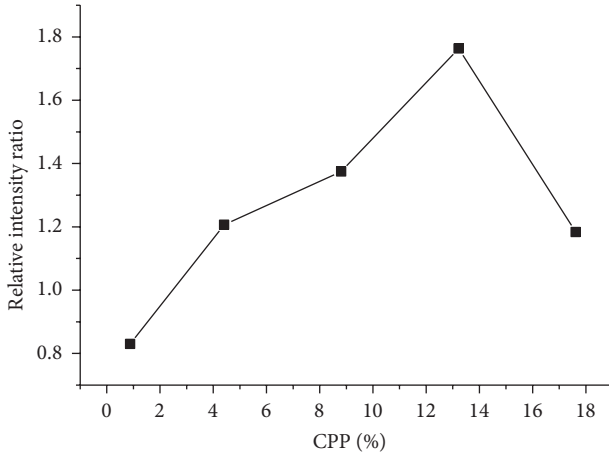


FIGURE 5: The relation between the ratio of  $A_{840}/A_{810}$  and CPP content.

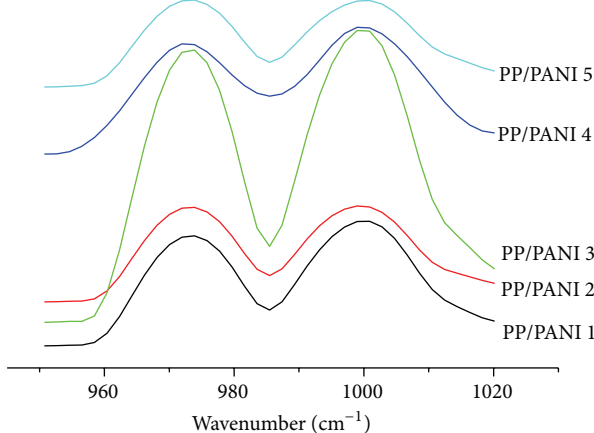


FIGURE 6: FTIR spectra of the PP/CPP/PANI composites with different CPP concentrations ( $950\text{--}1020\text{ cm}^{-1}$ ).

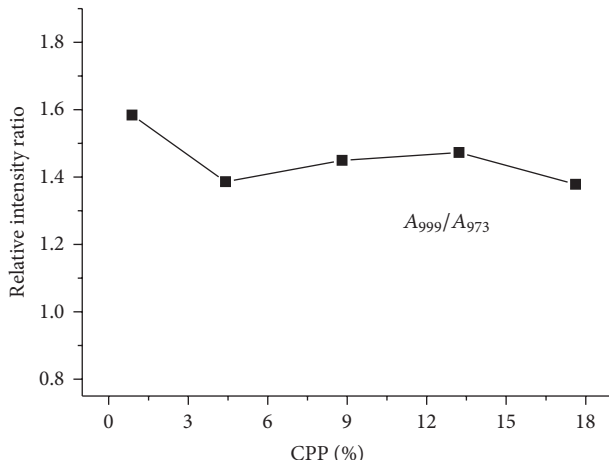


FIGURE 7: The relation between the ratio ( $A_{999}/A_{973}$ ) and CPP content.

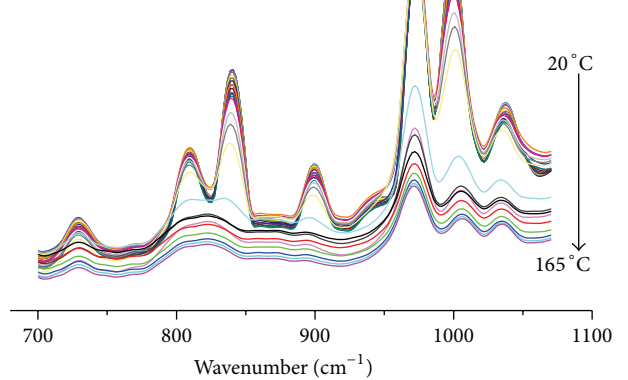


FIGURE 8: FTIR spectra of PP/PANI 4 at different temperatures.

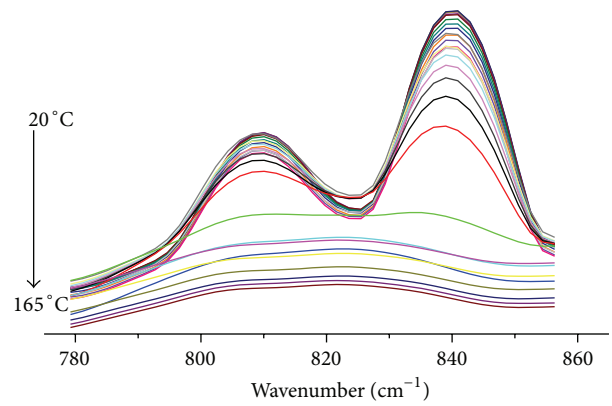


FIGURE 9: FTIR spectra of PP/PANI 4 at different temperatures ( $780\text{--}856\text{ cm}^{-1}$ ).

on the conformation of PP, the PP/PANI 4 sample was analyzed by in situ FTIR.

Figure 8 shows the FTIR spectra of PP/PANI 4 at different temperatures. There are several regularity bands in spectra that changed slightly with the increasing temperature in the composite such as  $810$ ,  $840$ ,  $973$ , and  $999\text{ cm}^{-1}$ , which indicates that the conformation structure of PP is influenced by temperature. Two regions included four regularity bands ( $810$ ,  $840$ ,  $973$ , and  $999\text{ cm}^{-1}$ ) will be discussed in detail later. Figure 8 shows the FTIR spectra of PP/PANI 4 at different temperatures. Several regularity bands in the spectra changed slightly as the temperature increased, such as  $810$ ,  $840$ ,  $973$ , and  $999\text{ cm}^{-1}$ , which indicates that the conformation of PP is affected by the temperature. Two regions included four regularity bands ( $810$ ,  $840$ ,  $973$ , and  $999\text{ cm}^{-1}$ ), which will be discussed in detail later.

**3.3.1. The Region ( $780\text{--}856\text{ cm}^{-1}$ ) of the FTIR Spectra of PP/PANI 4.** Figure 9 shows the FTIR spectra in the  $780\text{--}856\text{ cm}^{-1}$  region for PP/PANI 4 at different temperatures, which demonstrates that there are two Gaussian bands at around  $810\text{ cm}^{-1}$  and  $840\text{ cm}^{-1}$ . Since the intensity of the

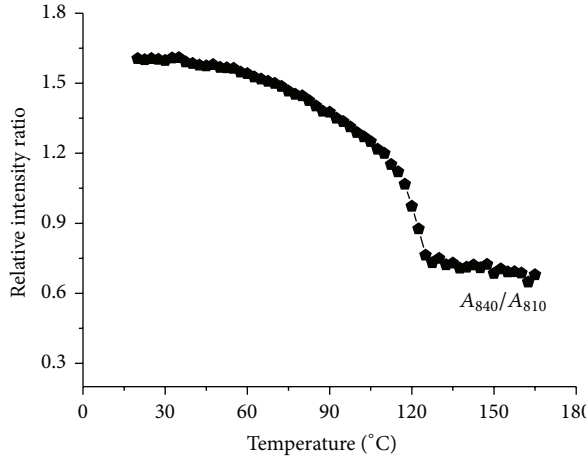


FIGURE 10: Intensity ratio ( $A_{840}/A_{810}$ ) of regularity bands versus temperatures.

TABLE 3: Curve-fitting results for spectra of the region (950–1020 cm<sup>-1</sup>).

Sample code	First band			Second band		
	$\nu_1$ cm <sup>-1</sup>	$A_{973}$	XS <sub>973</sub>	$\nu_2$ cm <sup>-1</sup>	$A_{999}$	XS <sub>999</sub>
PP/PANI 1	973.1	1.288	0.392	998.1	1.993	0.608
PP/PANI 2	972.8	1.101	0.424	999.2	1.494	0.576
PP/PANI 3	972.7	3.177	0.412	998.9	4.537	0.588
PP/PANI 4	972.7	1.442	0.408	999.0	2.089	0.592
PP/PANI 5	972.5	1.028	0.426	999.3	1.385	0.574

two bands is related closely to the size of the two critical lengths “ $n$ ” of isotactic sequences of PP, the relative ratio of the intensity of the two bands can be used to represent the helical conformation of PP.

Figure 10 shows the relationship between the intensity ratio of the regularity bands at 810 and 840 cm<sup>-1</sup> and temperature, which demonstrates that the  $A_{840}/A_{810}$  ratio decreased slowly initially as the temperature increased to 105°C, but it decreased sharply as the temperature increased further before decreasing slowly again when the temperature exceeded 125°C. Furthermore, the size of the critical lengths “ $n$ ” of isotactic sequences related to the appearance of a band at 840 cm<sup>-1</sup>, which corresponded to that for the appearance of a band at 810 cm<sup>-1</sup>, decreases slowly initially as the temperature increased up to 105°C, but it decreased sharply as the temperature increased further before decreasing slowly again when the temperature exceeded 125°C. These results indicate that the ordered regularity of PP decreased as the temperature increased. This may be attributable to differences in the behavior of the amorphous or partly ordered zones of PP at different temperatures.

**3.3.2. The Region (940–1020 cm<sup>-1</sup>) of the FTIR spectra of PP/PANI 4.** Figure 11 shows the FTIR spectra of the 940–1020 cm<sup>-1</sup> region for PP/PANI 4 at different temperatures, which demonstrates that there are two Gaussian bands at around 973 cm<sup>-1</sup> and 999 cm<sup>-1</sup>. Similar to the bands at

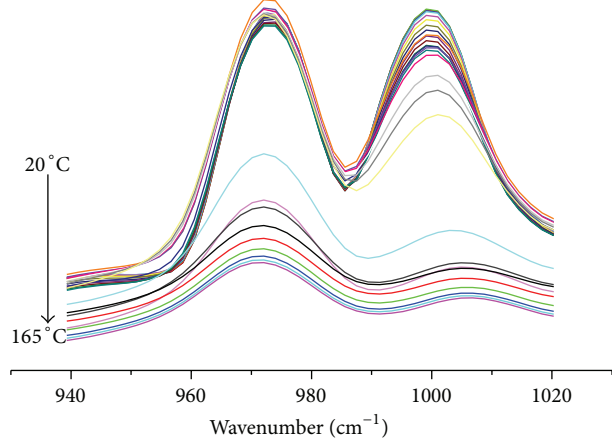


FIGURE 11: FTIR spectra of PP/PANI 4 at different temperatures (940–1020 cm<sup>-1</sup>).

810 cm<sup>-1</sup> and 840 cm<sup>-1</sup>, the  $A_{999}/A_{973}$  intensity ratio can be used to represent the order degree of the PP composites.

Figure 12 shows the  $A_{999}/A_{973}$  intensity ratio versus temperature, which demonstrates that the  $A_{999}/A_{973}$  ratio generally decreased as the temperature increased. The  $A_{999}/A_{973}$  ratio decreased slowly initially as the temperature increased up to 105°C, but it decreased sharply as the temperature increased further before decreasing slowly again as the temperature exceeded 128°C. The relationship between the conformational ordering of the helical sequences of PP and temperature was determined from the relationship between the  $A_{999}/A_{973}$  ratio and temperature. The order degree decreased slowly initially as the temperature increased up to 105°C, but it decreased sharply as the temperature increased further before decreasing slowly again subsequently. This may be attributable to differences in the behavior of the different ordered zones as the temperature increased. These results were consistent with the relationship between the  $A_{840}/A_{810}$  intensity ratio and temperature.

#### 4. Conclusions

The analysis of the DSC heating thermograms and WAXD patterns of the PP/CPP/PANI composites showed that the  $\beta$ -crystal was affected greatly by the CPP content. Furthermore, the crystal structure was affected by the regularity of the helical conformation. FTIR was used to investigate the effects of the CPP content and temperature on the conformation of PP in the PP/CPP/PANI composites, which showed that four regularity bands (810, 840, 973, and 999 cm<sup>-1</sup>) were related to different critical lengths “ $n$ ” of the isotactic sequences of PP. The results obtained in this study suggest the following conclusions.

- (i) The  $A_{840}/A_{810}$  intensity ratio increased initially with the CPP concentration and reached its maximum when the CPP content was lower than 13.22% before decreasing as the CPP content increased further. Thus, the  $A_{999}/A_{973}$  ratio was affected slightly by the CPP content.

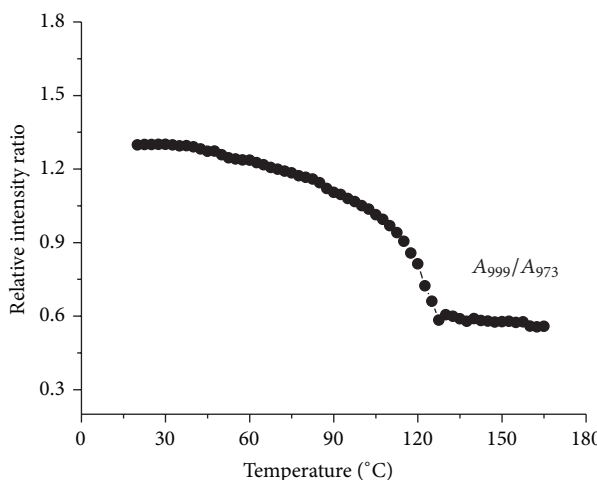


FIGURE 12: The relation between intensity ratio ( $A_{999}/A_{973}$ ) and temperature.

(ii) The  $A_{840}/A_{810}$  intensity ratio decreased slowly initially as the temperature increased up to 105°C, but it decreased sharply as the temperature increased further before decreasing slowly again when the temperature exceeded 125°C, where the  $A_{999}/A_{973}$  intensity ratio was similar to  $A_{840}/A_{810}$ .

## Conflict of Interests

The authors declare that there is no conflict of interests regarding the publication of this paper.

## References

- [1] A. G. MacDiarmid, "Polyaniline and polypyrrole: where are we headed?" *Synthetic Metals*, vol. 84, no. 1-3, pp. 27–34, 1997.
- [2] W. Łuzny, T. Kaniowski, and A. Proń, "Structural and transport properties of thermally processable conducting polymer: polyaniline protonated with diphenyl phosphate," *Polymer*, vol. 39, no. 2, pp. 475–483, 1998.
- [3] A. Pron, W. Luzny, and J. Laska, "Thermally processable polyaniline protonated with diphenyl phosphate—preparation and structural aspects," *Synthetic Metals*, vol. 80, no. 2, pp. 191–193, 1996.
- [4] R. Fryczkowski, C. Ślusarczyk, and J. Fabia, "Structure and conducting properties of thermoplastic composites of polypropylene and polyaniline protonated in solid state," *Synthetic Metals*, vol. 156, no. 2-4, pp. 310–317, 2006.
- [5] Y. Cao, P. Smith, and A. J. Heeger, "Counter-ion induced processibility of conducting polyaniline and of conducting polyblends of polyaniline in bulk polymers," *Synthetic Metals*, vol. 48, no. 1, pp. 91–97, 1992.
- [6] J. Laska, K. Zak, and A. Pron, "Conducting blends of polyaniline with conventional polymers," *Synthetic Metals*, vol. 84, no. 1-3, pp. 117–118, 1997.
- [7] J. Laska, A. Pron, M. Zagorska, S. Lapkowski, and S. Lefrant, "Thermally processable conducting polyaniline," *Synthetic Metals*, vol. 69, no. 1-3, pp. 113–115, 1995.
- [8] P. Passiniemi, J. Laakso, H. Osterholm, and M. Pohl, "TEM and WAXS characterization of polyaniline/PP fibers," *Synthetic Metals*, vol. 84, no. 1-3, pp. 775–776, 1997.
- [9] L. Yang, J. Y. Chen, and H. L. Li, "Investigation on the microstructure and the electric property of poly(propylene)/chlorinated poly(propylene)/poly(aniline) composites," *Journal of Applied Polymer Science*, vol. 111, no. 2, pp. 988–997, 2009.
- [10] L. Yang, J. Y. Chen, and H. L. Li, "Effects of chlorinated polypropylene on the hydrogen-bond and electric property of polypropylene/chlorinated polypropylene/polyaniline composites: FTIR analysis," *Polymer Engineering & Science*, vol. 49, no. 3, pp. 462–470, 2009.
- [11] G. Natta, P. Plno, P. Corradini et al., "Crystalline high polymers of  $\alpha$ -olefin," *Journal of the American Chemical Society*, vol. 77, no. 6, pp. 1708–1710, 1955.
- [12] G. Zerbi, F. Ciampelli, and V. Zamboni, "Classification of crystallinity bands in the infrared spectra of polymers," *Journal of Polymer Science Part C*, vol. 7, no. 1, pp. 141–151, 1964.
- [13] M. Kobayashi, K. Akita, and H. Tadokoro, "Infrared spectra and regular sequence lengths in isotactic polymer chains," *Die Makromolekulare Chemie*, vol. 118, no. 1, pp. 324–342, 1968.
- [14] Y. V. Kissin and L. A. Rishina, "Regularity bands in the i.r. spectra of C3H6C3D6 copolymers," *European Polymer Journal*, vol. 12, no. 10, pp. 757–759, 1976.
- [15] Z. Su, H. Wang, J. Dong et al., "Conformation transition and crystalline phase variation of long chain branched isotactic polypropylenes (LCB-iPP)," *Polymer*, vol. 48, no. 3, pp. 870–876, 2007.
- [16] L. A. Hanna, P. J. Hendra, W. Maddams, H. A. Willis, V. Zichy, and M. E. A. Cudby, "Vibrational spectroscopic study of structural changes in isotactic polypropylene below the melting point," *Polymer*, vol. 29, no. 10, pp. 1843–1847, 1988.
- [17] X. Zhu, D. Yan, H. Yao, and P. Zhu, "In situ FTIR spectroscopic study of the regularity bands and partial-order melts of isotactic poly(propylene)," *Macromolecular Rapid Communications*, vol. 21, no. 7, pp. 354–357, 2000.
- [18] X. Zhu, Y. Fang, and D. Yan, "A possible explanation to the structure change of isotactic polypropylene occurring at about 135°C," *Polymer*, vol. 42, no. 21, pp. 8595–8598, 2001.
- [19] R. G. Alamo, M. H. Kim, M. J. Galante, J. R. Isasi, and L. Mandelkern, "Structural and kinetic factors governing the formation of the  $\gamma$  polymorph of isotactic polypropylene," *Macromolecules*, vol. 32, no. 12, pp. 4050–4064, 1999.
- [20] R. G. Alamo, D. L. VanderHart, M. R. Nyden, and L. Mandelkern, "Morphological partitioning of ethylene defects in random propylene-ethylene copolymers," *Macromolecules*, vol. 33, no. 16, pp. 6094–6105, 2000.
- [21] D. L. VanderHart, R. G. Alamo, M. R. Nyden, M. H. Kim, and L. Mandelkern, "Observation of resonances associated with stereo and regio defects in the crystalline regions of isotactic polypropylene: toward a determination of morphological partitioning," *Macromolecules*, vol. 33, no. 16, pp. 6078–6093, 2000.
- [22] R. Thomann, C. Wang, J. Kressler, and R. Muelhaupt, "On the  $\gamma$ -phase of isotactic polypropylene," *Macromolecules*, vol. 29, no. 26, pp. 8425–8434, 1996.
- [23] R. Thomann, H. Semke, R.-D. Maier et al., "Influence of stereoirregularities on the formation of the  $\gamma$ -phase in isotactic polypropene," *Polymer*, vol. 42, no. 10, pp. 4597–4603, 2001.

- [24] M. Blomenhofer, S. Ganzleben, D. Hanft et al., ““Designer” nucleating agents for polypropylene,” *Macromolecules*, vol. 38, no. 9, pp. 3688–3695, 2005.
- [25] M. Obadal, R. Čermák, and K. Stoklasa, “Tailoring of three-phase crystalline systems in isotactic poly(propylene),” *Macromolecular Rapid Communications*, vol. 26, no. 15, pp. 1253–1257, 2005.

## Research Article

# Evaluation of Temper Embrittlement of 30Cr2MoV Rotor Steels Using Electrochemical Impedance Spectroscopy Technique

Zhang Shenghan, Lv Yaling, and Tan Yu

North China Electric Power University, Baoding 071000, China

Correspondence should be addressed to Zhang Shenghan; [zhang\\_shenghan@yeah.net](mailto:zhang_shenghan@yeah.net)

Received 6 August 2014; Accepted 21 August 2014

Academic Editor: Tifeng Jiao

Copyright © 2015 Zhang Shenghan et al. This is an open access article distributed under the Creative Commons Attribution License, which permits unrestricted use, distribution, and reproduction in any medium, provided the original work is properly cited.

Temper embrittlement tends to occur in the turbine rotor after long running, which refers to the decrease in notch toughness of alloy steels in a certain temperature range (e.g., 400°C to 600°C). The severity of temper embrittlement must be monitored timely to avoid further damage, and the fracture appearance transition temperature ( $FATT_{50}$ ) is commonly used as an indicator parameter to characterize the temper embrittlement. Compared with conventional destructive methods (e.g., small punch test), nondestructive approaches have drawn significant attention in predicting the material degradation in turbine rotor steels without impairing the integrity of the components. In this paper, laboratory experiments were carried out based on a nondestructive method, electrochemical impedance spectroscopy (EIS), with groups of lab-charged specimens for predicting the temper embrittlement ( $FATT_{50}$ ) of turbine rotor steel. The results show that there was a linear relationship of interfacial impedance of the specimens and their  $FATT_{50}$  values. The predictive error based on the experiment study is within the range of  $\pm 15^{\circ}\text{C}$ , indicating the predicting model is precise, effective, and reasonable.

## 1. Introduction

Thermal power stations are the most common electricity sources all over the world due to their low running costs and reliability. However, any failures in the main components (e.g., steam turbine rotor) of aged thermal power plants operating in many areas may cause significant costs, long downtime, and even the loss of life. The precisely predicting of the aging process or the remaining service life of turbine rotor is of great importance for safe operation and life extension [1].

Temper embrittlement in low alloy steels (e.g., Cr-Mo-V) of steamed turbine rotors is one of the typical material degradations (e.g., creep, fatigue, embrittlement, and corrosion) [2, 3] and is commonly characterized by fracture appearance transition temperature ( $FATT_{50}$ ), at which the fracture surface of the material is 50% brittle or cleavage and 50% ductile [1]. The turbine rotor steel operated at a high temperature for long time may lose its flexibility and

ductility as the segregation of metalloid impurities such as phosphorus (P), tin (Sn), and antimony (Sb), at the grain boundaries which reduces the cohesion at grain boundaries [4–6]. Among the impurity elements, phosphorus (P) is considered as the main impurity causing temper embrittlement [5, 7, 8]. If the increase of  $FATT_{50}$  value is not detected in time, the rotor steel can be easily damaged or even broken and causes severe safety accidents [4]. Therefore, it is essential to make the accurate predictions and assessments on the temper embrittlement parameters of the turbine rotor material.

To date, different destructive and nondestructive methods have been developed to detect the  $FATT_{50}$  value of turbine rotors, such as small punch test [1, 9–12], electromagnetic method [13], ultrasonic [14–16], auger electron spectroscopy [17, 18], electrochemical method [5, 19, 20], and chemical corrosion [19]. Destructive methods can provide accurate results of mechanical properties (e.g., yield stress, tensile strength,  $FATT_{50}$ , fracture toughness, and creep

properties) from the actual components [11, 12], but their application is highly-limited due to the damage to the turbine rotor.

As a relatively high-precision nondestructive detecting method, electrochemical approach has drawn significant attention in predicting the material degradation in turbine rotor steels without impairing the integrity of the components. Mao and Zhao investigated the electrochemical behaviors of type 321 austenitic stainless steel in sulfuric acid solution and found that the electrochemical polarization curves can be used to estimate the aging embrittlement degradation [21]. Komazaki et al. developed a methodology for thermal aging embrittlement and the results on electrochemical polarization measurements in 1N KOH solution revealed that the peak current density " $I_p$ " value was found to be increasing linearly with the degree of embrittlement as evaluated by impact absorbed energy at 0°C [22, 23]. Anodic and single loop electrochemical potentiokinetic reactivation (SL-EPR) polarization curves of the embrittled specimens have been evaluated; difference in current density (IP2-E-Ipass-E) between active second peak and passive one in an anodic polarization curve of temper-embrittled specimens increases linearly with increase in FATT in the range of mode transfer over transgranular cleavage to intergranular of Charpy impact fracture [24]. Zhang et al. developed a genetic programming (GP) for FATT<sub>50</sub> prediction and single loop electrochemical polarization reactivation (EPR) test has been conducted [5]. The multiple correlation coefficient between predicted and measured FATT<sub>50</sub> was 0.990, indicating the model obtained by GP can be used in predicting temper embrittlement of new rotor materials with a precision of about ±20°C [5]. Bayesian neural network was proposed to model the temper embrittlement of steam turbine rotor in service, and the FATT<sub>50</sub> was predicted as a function of ratio of the two peak current densities ( $I_p/I_{pr}$ ) tested by electrochemical potentiodynamic reaction method [25].

EIS, as an effective electrochemical method, originally was used to study the electrical response characteristic frequency of linear circuit network and has been used by more and more researchers to study the electrode process which could provide more information of interface structure than other methods [26–28].

In this paper, EIS method was employed to study the thermal embrittlement of turbine rotor and a multiple linear regression analysis on interfacial impedance and other relevant parameters was carried out to build a predict model of FATT<sub>50</sub>. The predicted and measured values of FATT<sub>50</sub> were compared and the error was within an acceptable range, indicating an effective and reasonable model was obtained.

## 2. Experimental Method

**2.1. Principle.** The test specimens in this paper were lab-charged phosphorus-doped 30Cr2MoV rotor steel and the chemical composition was shown in Table 1.

To simulate the temper embrittlement during the long-term service of turbine rotor, step cooling treatment was

used to promote the segregation of phosphorus to the grain boundary. Their FATT<sub>50</sub> values were measured by a stress test according to relevant national standard. The result would be used to verify the subsequent test. Impedance of the specimens was measured in a three-electrode system and analyzed by the equivalent circuit method. A predictive model was built based on the analysis results.

**2.2. Experiment.** FATT<sub>50</sub> values of specimens were measured by stress test and the result is shown in Table 2.

To measure the impedance of the specimens, a three-electrode system was employed. As shown in Figure 1, the specimen was cut into cube with side length of 12 mm and was welded on a piece of copper wire. The specimen cube acts as the working electrode in the experiment. In order for the reaction area of the working electrode to remain fixed, five sides of the cube, including some parts of the copper wire, were sealed with epoxy resin; the remaining side was covered with anticorrosion tape with a hole (diameter = 5 mm) after being grinded with sandpaper step by step to 2000#.

Platinum electrode was selected as auxiliary electrode and saturated calomel electrode was used as reference electrode. Electrolyte was made of 0.01 M Na<sub>2</sub>MoO<sub>4</sub> with phosphoric deployed to the pH value of 5.5. The three-electrode system was placed in a water bath filled with circulating hot water of 25°C to maintain a constant temperature.

The three-electrode system was connected to the corresponding position of electrochemical workstation (model of PARTAT 2273). A computer equipped with software of that workstation was used to record measurements.

All specimens were anodic polarized; the result showed that those corrosion potentials are basically the same. In order to measure the EIS, AC potential with amplitude of 5 mV was applied to working electrode at the corrosion potential as input signal. Sixty frequencies were logarithmic sweeply selected from 100 kHz to 100 mHz. Impedance under that condition could be measured by comparing the measured output current with the input potential.

## 3. Results and Discussion

Figure 2 shows the Nyquist plot of measured impedance of specimen. The impedance was represented by a complex. The abscissa of plot in Figure 2 is the real part of the impedance, and the ordinate is the imaginary part. The results showed that the Nyquist plot of all specimens is similar. In the high frequency region, the plots were arcs in the first quadrant, but the centers of arcs were in the fourth quadrant. Some studies claimed that high frequency region was dynamics control district and the diameter of the arc represents the size of charge transfer resistance of the electrode reaction. The higher the diameter of arc, the more difficult the charge transfer in electrode reaction, and the slower the reaction. In the low frequency region, the plots were straight lines of different lengths. This region was considered mass transfer controlled district. If the line in this region was very long, the electrode reaction could be considered as led by mass transfer.

TABLE I: Chemical composition of 30Cr2MoV rotor steel (wt%).

Sample	P	C	Si	Mn	S	Cr	Ni	Mo	Cu	V	As	Sn	Sb
41	0.045	0.28	0.36	0.66	0.013	1.62	0.06	0.62	0.08	0.29	0.013	0.004	0.0013
42	0.107	0.3	0.37	0.69	0.014	1.65	0.05	0.73	0.07	0.29	0.013	0.004	0.0015
43	0.063	0.28	0.36	0.69	0.014	1.68	0.05	0.68	0.1	0.29	0.015	0.006	0.0019
44	0.204	0.3	0.37	0.69	0.015	1.66	0.05	0.75	0.1	0.29	0.015	0.007	0.002
A2	0.065	0.28	0.43	0.68	0.012	1.79	0.28	0.7	0.08	0.3	0.013	0.004	0.0012
A3	0.019	0.24	0.4	0.62	0.001	1.6	0.25	0.69	0.12	0.27	0.007	0.008	0.0015

TABLE 2: The FATT<sub>50</sub> values of different rotor samples.

Sample	Original state	Heat-treated state	Difference
41	67.5	95.6	28.1
42	198.7	211.7	13
43	103.6	142.2	38.6
44	235	275.4	40.4
A2	82	127.1	45.1
A3	-70.9	-54.1	16.8

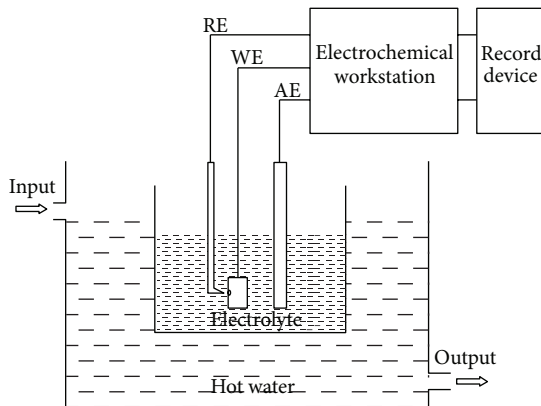


FIGURE 1: A three-electrode system for measuring the impedance of the specimens.

An equivalent circuit based on impedance plots was shown in Figure 3.

$R_L$  is the solution impedance between working electrode and auxiliary electrode. CPE is constant-phase-element which could be expressed by parameters  $Y_0$  and  $n$ .  $R_{ct}$  is the charge transfer impedance of the electrode reaction.  $W$  is mass transfer impedance and can be expressed by parameter  $Y'_0$ . The impedance of the equivalent circuit could be calculated by (1) as follows:

$$\begin{aligned} Z &= Z_{R_L} + \frac{1}{Y_{CPE} + Y_{(CPE(R_{ct}W))}} \\ &= R_L + \frac{1}{Y_0(j\omega)^{-n} + (1/(R_{ct} + (1/Y'_0\sqrt{j\omega})))}. \end{aligned} \quad (1)$$

The impedance value calculated by the formula matched well the experimental results. Figure 4 showed the calculated and measured curves, and the fitting error of each equivalent circuit component parameter was less than 5%.

By analyzing the component parameter values of equivalent circuit, it could be found that the solution impedance of specimens was essentially unchanged, but the interface impedance varied greatly. Figure 5 shows the linear relationship of interfacial impedance of specimen and its FATT<sub>50</sub> at a frequency of 100 kHz. The abscissa of Figure 5 was interfacial impedance value in ohms; ordinate was FATT<sub>50</sub> value in degree Celsius. Their fitting formula was in the upper left corner. The  $y$  in formula represented FATT<sub>50</sub> and  $x$  interfacial impedance. The  $R$  in formula is the correlation coefficient, and it was calculated as 0.836 by  $R^2 = 0.6983$ .  $R_{min}$ , the correlation coefficient threshold, could be looked up from corresponding table as 0.567 [29]. Since  $R$  was greater than  $R_{min}$ , it could be believed that there was a close linear relationship between the interfacial impedance and FATT<sub>50</sub>, and the FATT<sub>50</sub> could be described by linear equations.

In addition to the interfacial impedance, FATT<sub>50</sub> also has linear correlation relationship with other parameters [29] which were shown in Table 3.

By multivariate linear regression analysis using excel software, the regression equation could be expressed by (2), where  $Z$  was interfacial impedance. One has

$$\begin{aligned} \text{FATT}_{50} &= -2002 + 1264 * Z + 178 * P + 4106 * C \\ &\quad + 1318 * Mn - 9214 * S - 0.6 * \psi. \end{aligned} \quad (2)$$

Significant test using Excel software showed that the equation was credible and there was significant linear relationship between FATT<sub>50</sub> and other variables.

Table 3 shows that the residuals of predicted value were  $\pm 15^\circ\text{C}$ , the error was small, and the model was reasonable and effective.

#### 4. Conclusions

In this work, the EIS of turbine rotor at the corrosion potential in 0.01 M Na<sub>2</sub>MoO<sub>4</sub> was studied through laboratory experiments, and the following conclusions are obtained. The electrode reaction of rotor in electrolyte could be represented by an equivalent circuit. The total impedance of the circuit

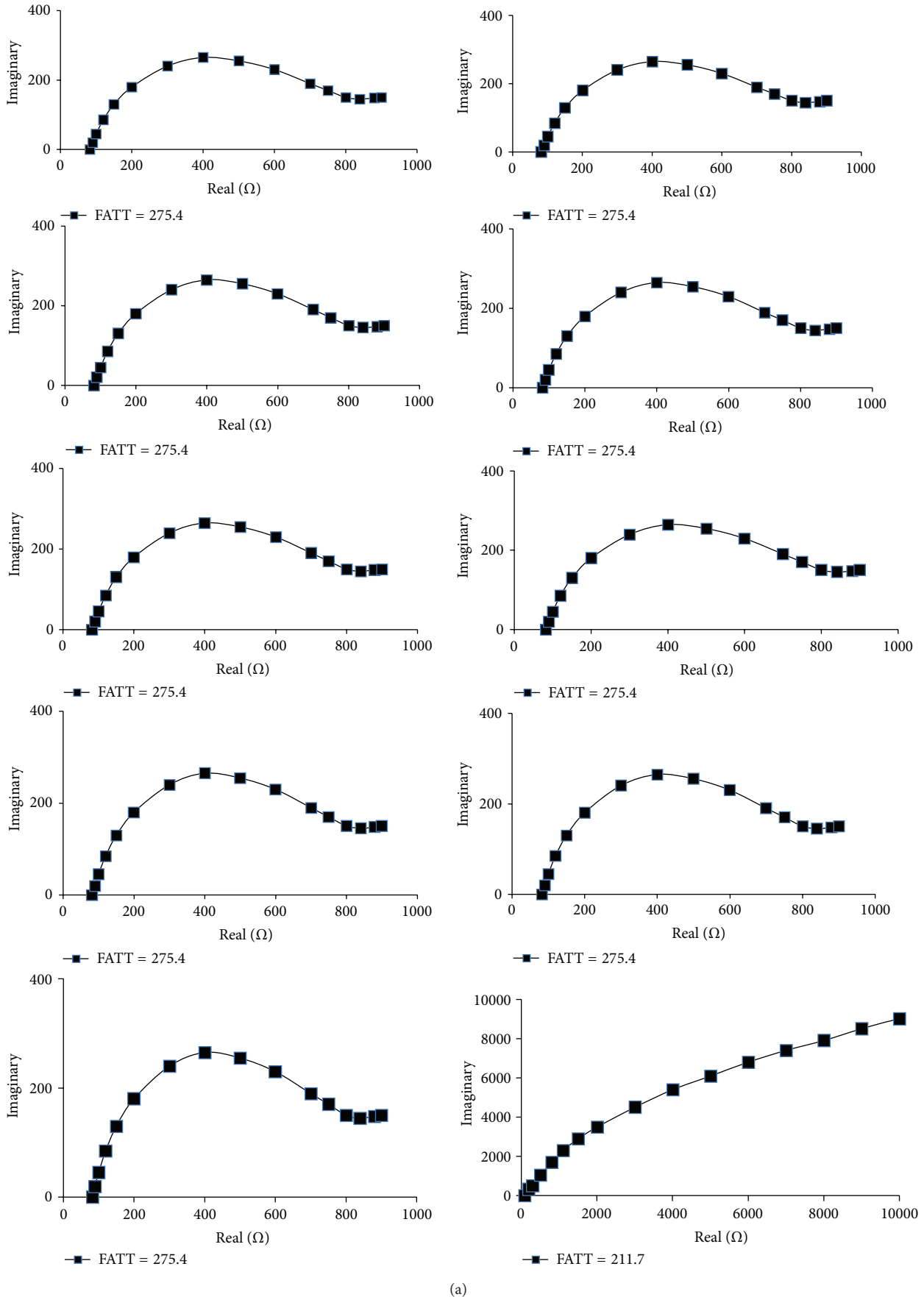


FIGURE 2: Continued.

(a)

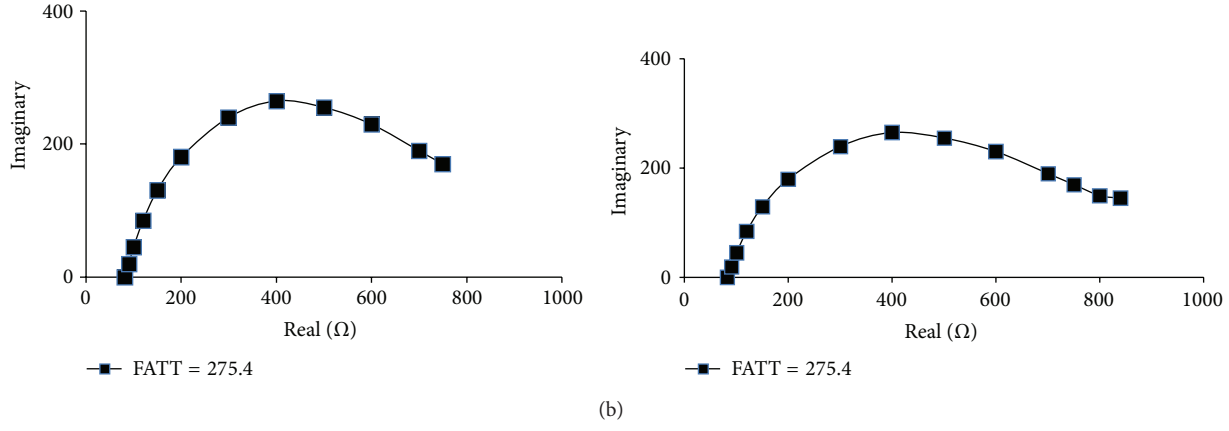


FIGURE 2: Nyquist diagrams of the impedance of different samples.

TABLE 3:  $\text{FATT}_{50}$ -related parameters.

Sample	Measured $\text{FATT}_{50}$	Impedance $Z$ ( $\Omega$ )	P (%)	C (%)	Mn (%)	S (%)	Reduction $\psi$ (%)	Predicted value	Difference
A31	-70.9	0.07	0.019	0.24	0.62	0.001	72.2	-73.432	-2.532
A32	-54.1	0.09	0.019	0.24	0.62	0.001	71.33	-48.674	5.426
411	67.5	0.1	0.045	0.28	0.66	0.013	64.47	70.87	3.37
A21	82	0.09	0.065	0.28	0.68	0.012	60.3	94.862	12.862
412	95.6	0.12	0.045	0.28	0.66	0.013	62.33	94.866	-0.734
431	103.6	0.11	0.063	0.28	0.69	0.014	56.57	112.3	8.7
A22	127.1	0.11	0.065	0.28	0.68	0.012	52.57	115.504	-11.596
432	142.2	0.13	0.063	0.28	0.69	0.014	55.33	136.836	-5.364
421	198.7	0.11	0.107	0.3	0.69	0.014	52.8	199.99	1.29
422	211.7	0.12	0.107	0.3	0.69	0.014	54.17	213.452	1.752
441	235	0.13	0.204	0.3	0.69	0.015	46.65	229.632	-5.368
442	275.4	0.18	0.204	0.3	0.69	0.015	30.5	283.142	7.742

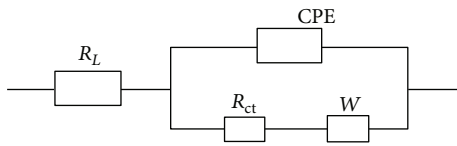


FIGURE 3: Constructed equivalent circuit in accordance with Figure 1.

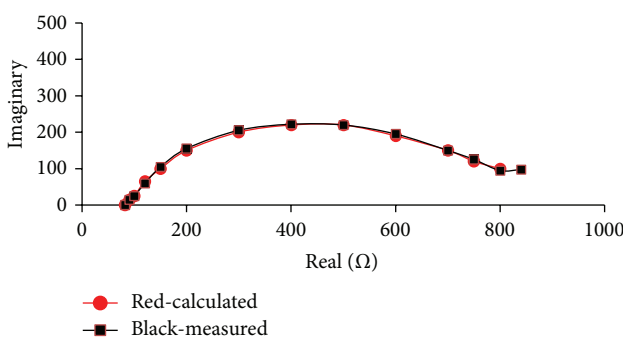
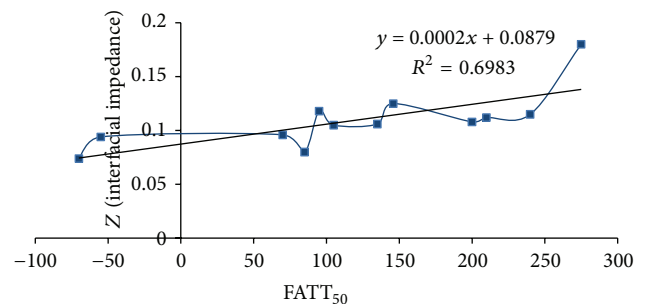


FIGURE 4: Comparison of the calculated and measured curve.

FIGURE 5: Relationship of interface impedance and  $\text{FATT}_{50}$  values.

includes two parts: solution impedance between working electrode and auxiliary electrode and interfacial impedance between the rotor and electrolyte. At higher frequency, there is a linear relationship between the interfacial impedance and its  $\text{FATT}_{50}$ . The larger the interfacial impedance value, the lower the  $\text{FATT}_{50}$ . An effective predictive model could be built by a series of parameters, and the error is small enough indicating the model is reasonable and effective.

## Conflict of Interests

The authors declare that there is no conflict of interests regarding the publication of this paper.

## Acknowledgment

This paper is supported by the “Fundamental Research Funds for the Central Universities of China” (Grant no. 13MS85).

## References

- [1] J. S. Ha and E. Fleury, “Small punch tests to estimate the mechanical properties of steels for steam power plant: II. Fracture toughness,” *International Journal of Pressure Vessels and Piping*, vol. 75, no. 9, pp. 707–713, 1998.
- [2] Y. Kadoya, T. Goto, M. Takei, N. Haruki, T. Ikuno, and Y. Nishimura, “Nondestructive evaluation of temper embrittlement in Cr-Mo-V rotor steel,” *Transactions of the Japan Society of Mechanical Engineers Part A*, vol. 57, no. 537, pp. 1085–1090, 1991.
- [3] H. Uemura and M. Kohno, “Temper embrittlement characteristic of Cr-Mo-V steel steam turbine rotors in long term service,” *Journal of the Iron and Steel Institute of Japan*, vol. 93, no. 4, pp. 324–329, 2007.
- [4] Y.-M. Chen, Y. Long, Z.-G. Han, and Y.-H. Wang, “Predict the temper embrittlement extent of turbine rotor steel by using chemical corrosion method,” in *Proceedings of the Asia-Pacific Power and Energy Engineering Conference (APPEEC '09)*, Wuhan, China, March 2009.
- [5] S.-H. Zhang, Y.-Z. Fan, Y.-M. Chen, and S.-L. Zhou, “A new nondestructive test technique for predicting the temper embrittlement of turbine rotor steel with genetic programming,” in *Proceedings of the IEEE International Conference on Industrial Technology (ICIT '05)*, pp. 768–771, Hong Kong, December 2005.
- [6] A. Fujita, M. Shinohara, H. Yokota, K. Kaku, K. Soeda, and Y. Kuroda, “Effect of chemical composition and manufacturing procedure on toughness of CrMoV HP rotor forgings,” *Journal of the Iron and Steel Institute of Japan*, vol. 84, no. 3, pp. 236–241, 1998.
- [7] J. Kameda and R. Ranjan, “Nondestructive evaluation of steels using acoustic and magnetic barkhausen signals-I. Effect of carbide precipitation and hardness,” *Acta Metallurgica*, vol. 35, no. 7, pp. 1515–1526, 1987.
- [8] J. Kameda and R. Ranjan, “Nondestructive evaluation of steels using acoustic and magnetic barkhausen signals-II. Effect of intergranular impurity segregation,” *Acta Metallurgica*, vol. 35, no. 7, pp. 1527–1531, 1987.
- [9] A. Shekhter, S. Kim, D. G. Carr, A. B. L. Croker, and S. P. Ringer, “Assessment of temper embrittlement in an ex-service 1Cr-1Mo-0.25V power generating rotor by Charpy V-Notch testing, KIC fracture toughness and small punch test,” *International Journal of Pressure Vessels and Piping*, vol. 79, no. 8–10, pp. 611–615, 2002.
- [10] S.-I. Komazaki, T. Shoji, and K. Takamura, “Evaluation of thermal aging embrittlement in directionally solidified Ni-base superalloy by small punch test,” *Journal of Engineering Materials and Technology, Transactions of the ASME*, vol. 127, no. 4, pp. 476–482, 2005.
- [11] K. Turba, R. C. Hurst, and P. Hähner, “Anisotropic mechanical properties of the MA956 ODS steel characterized by the small punch testing technique,” *Journal of Nuclear Materials*, vol. 428, no. 1–3, pp. 76–81, 2012.
- [12] X. Mao, T. Shoji, and H. Takahashi, “Characterization of fracture behavior in small punch test by combined recrystallization-etch method and rigid plastic analysis,” *Journal of Testing and Evaluation*, vol. 15, no. 1, pp. 30–37, 1987.
- [13] G. Dobmann, “NDE for material characterisation of ageing due to thermal embrittlement, fatigue and neutron degradation,” *International Journal of Materials and Product Technology*, vol. 26, no. 1–2, pp. 122–139, 2006.
- [14] H. Jeong, S.-H. Nahm, K.-Y. Jhang, and Y.-H. Nam, “Evaluation of fracture toughness degradation of CrMoV rotor steels based on ultrasonic nonlinearity measurements,” *KSME International Journal*, vol. 16, no. 2, pp. 147–154, 2002.
- [15] H. Jeong, S.-H. Nahm, K.-Y. Jhang, and Y.-H. Nam, “A non-destructive method for estimation of the fracture toughness of CrMoV rotor steels based on ultrasonic nonlinearity,” *Ultrasonics*, vol. 41, no. 7, pp. 543–549, 2003.
- [16] C.-H. Hsu, H.-Y. Teng, and S.-C. Chiu, “Ultrasonic evaluation of temper-embrittlement for martensitic stainless steel,” *Materials Transactions*, vol. 44, no. 11, pp. 2363–2368, 2003.
- [17] R. Ding, A. Islam, S. Wu, and J. Knott, “Effect of phosphorus segregation on fracture properties of two quenched and tempered structural steels,” *Materials Science and Technology*, vol. 21, no. 4, pp. 467–475, 2005.
- [18] S. H. Song, J. Wu, L. Q. Weng, and T. H. Xi, “Phosphorus grain boundary segregation under an intermediate applied tensile stress in a Cr-Mo low alloy steel,” *Materials Science and Engineering A*, vol. 520, no. 1–2, pp. 97–100, 2009.
- [19] Y. Z. Fan, Y. M. Chen, and S. H. Zhang, “Development of nondestructive inspecting of temper embrittlement of turbine rotor steel,” *Turbine Technology*, Article ID 100125884, 2004.
- [20] Y. Kadoya, T. Goto, M. Takei, N. Haruki, K. Ikuno, and Y. Nishimura, “Nondestructive evaluation of temper embrittlement in Cr-Mo-V rotor steel,” *The American Society of Mechanical Engineers, Power Division (Publication) PWR*, vol. 13, pp. 229–234, 1991.
- [21] X. Mao and W. Zhao, “Electrochemical polarization method to detect aging embrittlement of 321 stainless steel,” *Corrosion*, vol. 49, no. 4, pp. 335–342, 1993.
- [22] S.-I. Komazaki, S. Kishi, T. Shoji, H. Chiba, and K. Suzuki, “Thermal aging embrittlement of tungsten-alloyed 9%Cr ferritic steels and electrochemical evaluation,” *Materials Science Research International*, vol. 9, no. 1, pp. 42–49, 2003.
- [23] S.-I. Komazaki, S. Kishi, T. Shoji, H. Chiba, and K. Suzuki, “Thermal aging embrittlement of W alloyed 9%Cr ferritic steels and its evaluation by electrochemical technique,” *Journal of the Society of Materials Science*, vol. 49, no. 8, pp. 919–926, 2000.
- [24] T. Shibuya and T. Misawa, “Electrochemical evaluation of the degree of temper-embrittlement with mode transfer in impact fracture surface of 2.25Cr-1Mo low alloy steels,” *Corrosion Engineering*, vol. 48, no. 3, pp. 146–154, 1999.
- [25] S.-H. Zhang, Y.-Z. Fan, and Y.-M. Chen, “Predicting the temper embrittlement of steam turbine rotor steels with Bayesian neural network,” in *Proceedings of the IEEE International Conference on Industrial Technology (ICIT '05)*, pp. 991–994, Hong Kong, December 2005.
- [26] K. Darowicki, S. Krakowiak, and P. Ślepiski, “Evaluation of pitting corrosion by means of dynamic electrochemical impedance spectroscopy,” *Electrochimica Acta*, vol. 49, no. 17–18, pp. 2909–2918, 2004.

- [27] C. Boissy, C. Alemany-Dumont, and B. Normand, "EIS evaluation of steady-state characteristic of 316L stainless steel passive film grown in acidic solution," *Electrochemistry Communications*, vol. 26, no. 1, pp. 10–12, 2013.
- [28] S. Krakowiak, K. Darowicki, and P. Slepški, "Impedance investigation of passive 304 stainless steel in the pit pre-initiation state," *Electrochimica Acta*, vol. 50, no. 13, pp. 2699–2704, 2005.
- [29] J. T. Zhang, *Nondestructive Method for the Evaluation of the Embrittlement of the Turbine Rotor Steels*, North China Electric Power University, Baoding, China, 2004.

## Research Article

# Hydrothermal Synthesis of High Crystalline Silicalite from Rice Husk Ash

Chaiwat Kongmanklang<sup>1</sup> and Kunwadee Rangsriwatananon<sup>2</sup>

<sup>1</sup>The Center for Scientific and Technological Equipment, Nakhon Ratchasima 30000, Thailand

<sup>2</sup>School of Chemistry, Institute of Science, Suranaree University of Technology, Nakhon Ratchasima 30000, Thailand

Correspondence should be addressed to Kunwadee Rangsriwatananon; [kunwadee@sut.ac.th](mailto:kunwadee@sut.ac.th)

Received 8 August 2014; Accepted 27 October 2014

Academic Editor: Nikša Krstulović

Copyright © 2015 C. Kongmanklang and K. Rangsriwatananon. This is an open access article distributed under the Creative Commons Attribution License, which permits unrestricted use, distribution, and reproduction in any medium, provided the original work is properly cited.

The objective of this research work was to evaluate the hydrothermal synthesis of silicalite with high crystallinity within a small particle size. The current study focused on investigating the effects of silica sources such as rice husk ash (RHA) and silica gel (SG), crystallization time, and ratios of NaOH/SiO<sub>2</sub>, H<sub>2</sub>O/NaOH, and SiO<sub>2</sub>/TPABr. The crystallinity, particle size, and morphology were characterized by FT-IR, XRD, particle size analyser, and SEM. The conclusion of the main findings indicated that the XRD patterns of these samples clearly showed a pure phase of MFI structure corresponding to FT-IR spectra with vibration mode at 550 and 1223 cm<sup>-1</sup>. The highest crystallinity was obtained at reaction time only 6 hours with the mole ratios of NaOH/SiO<sub>2</sub>, H<sub>2</sub>O/NaOH and SiO<sub>2</sub>/TPABr as 0.24, 155, and 30, respectively. When SG was used as a silica source, it was found that the particle size was smaller than that from RHA. The morphologies of all silicalite samples were coffin and cubic-like shape.

## 1. Introduction

Silicalite or high silica ZSM-5 is MFI structure. It contains two intersecting channel systems composed of 10-membered ring straight and sinusoidal channels with a unique pore structure dimension of 0.54–0.56 nm. According to a variety of its useful properties such as strong hydrophobicity, excellent shape selectivity, good catalytic activity, and high thermal stability, hence, it has been widely used in industrial applications for adsorption [1], catalysis [2], and gas and liquid separation [3, 4].

Typically, silicalites are synthesized by the hydrothermal method from the gel compositions of silica, alkaline, and organic cation as a template. Several types of silica source were applied in the synthesis of silicalite such as fume silica in a molar composition of SiO<sub>2</sub>:0.2 TPABr:0.5 NaOH:30 H<sub>2</sub>O at 180°C for 7 days [5], water glass in a reaction mixture of (1–5) Na<sub>2</sub>O:(50–60) SiO<sub>2</sub>:(1–2) TPABr:(600–770) H<sub>2</sub>O at 200°C for 72 hours [6], and TEOS as a silica source in a molar composition of SiO<sub>2</sub>:0.12 TPAOH:0.008 NaOH:60 H<sub>2</sub>O at 95°C for 7 days [7]. However, TEOS, fumed silica and

colloidal silica are much more expensive compared to rice husk ash which is a potential silica source containing amorphous silica about 20% (w/w) [8] considered as a byproduct in form of an industrial waste abundance in agricultural countries. Moreover, another benefit of silica from rice husk is that it is highly reactive silica which can be simply extracted to be highly purifying silica (about 98%) by digesting with dilute acid and burning at 700°C for 4 hours [9].

As a result, the major aim of the present work focused on synthesizing high crystalline silicalite using rice husk ash considering the effect of silica sources, reaction times, and gel compositions by hydrothermal method.

## 2. Materials and Methods

**2.1. Materials.** Silica from the rice husk from a local rice mill in the target area, that is, in Nakhon Ratchasima Province, Thailand, was used as the starting materials in the initial mixture for the silicalite synthesis together with pellets of sodium hydroxide (Merck), tetrapropyl ammonium bromide, TPABr (Sigma-Aldrich), and distilled water. Simultaneously

hydrochloric acid 37% (Carlo-Erba) was used to prepare 1 M HCl.

**2.2. Methods.** The preparation of the rice husk ash (RHA) extracted from rice husk and silica gel (SG) was in the following steps.

Firstly, the rice husk was thoroughly washed with deionized water and dried at 110°C overnight. Next, the dried rice husk was digested with dilute acid, by boiling with 1 M HCl for 3 hours, then repeatedly washed with water until it is neutral, and dried at 110°C overnight. After that the acid digested rice husk was burned at 700°C for 4 hours until it became clearly noticeable white ash. Finally, the white ash was ground till it became fine powder and later was sieved through a mesh with no. 100.

Likewise, silica gel was prepared by dissolving RHA with 1 M NaOH through boiling it by covering its container to form sodium silicate solution. Then, the solution was filtered to remove carbon and silica residue. After the solution was cool, it was titrated with 1 M HCl until pH 4, and then it was left overnight to allow its aging in order to form gel. Later, the gel was crushed and repeatedly washed with distilled water until it was free from chloride ions and it was left overnight to dry at 120°C. Finally, the product was ground and sieved with the similar process as RHA.

**2.3. Synthesis Procedure.** The procedure of silicalite synthesis was carried out from the system SiO<sub>2</sub>-NaOH-TPABr-H<sub>2</sub>O with the mole ratios of NaOH/SiO<sub>2</sub>, H<sub>2</sub>O/NaOH, and SiO<sub>2</sub>/TPABr within the ranges of 0.24–0.48, 155–618, and 30–60, respectively. To begin, after the required amount of NaOH, TPABr, silica, and water was mixed together, it needed to be stirred continuously 5 minutes. Then, the following step was the hydrothermal treatment in a stainless steel bomb lined with PTFE under autogenous pressure at 187°C under various reaction times. Next, after reaching the desirable time, the reaction was stopped through being quenched with distilled water. After that, it was allowed to cool. Later, it was carefully filtered and thoroughly and repeatedly washed with distilled water. Lastly, it was dried overnight at 120°C. The synthesized silicalite samples under different conditions were denoted as SL1, SL2, SL3, SL4, SL5, SL6, and SL7 (see Table 2).

**2.4. Characterization.** Fourier transform infrared (FT-IR) spectroscopy was carried out by Perkin Elmer Spectrum GX. The spectra were recorded within the range of 2000–400 cm<sup>-1</sup> with 32 scans at a resolution of 4.0 cm<sup>-1</sup> and using KBr pellet technique. X-ray powder diffraction (XRD) was collected on Siemens D5005 diffractometer using Cu K $\alpha$  radiation. The percentage of the relative crystallinity was calculated from the ratios of the area of the highest intense reflection peak at 101, 200, 501, 151, and 133 as a reference and as the area of those peaks from the other samples. The chemical compositions of RHA and SG were determined by X-ray fluorescence spectrometer (Oxford DE200). The BET specific surface area and particle size analyzer were carried out by a Micrometric ASAP 2000 and Malvern instruments, respectively. The morphologies of the samples were detected

TABLE 1: The chemical compositions and BET surface areas of silica sources.

Silica source	RHA	SG
	Chemical composition, %wt.	
SiO <sub>2</sub>	98.78	99.29
Al <sub>2</sub> O <sub>3</sub>	0.52	0.52
MgO	0.12	ND.
CaO	0.36	ND.
Others	0.22	ND.
BET surface area, m <sup>2</sup> /g	246.91	790.33

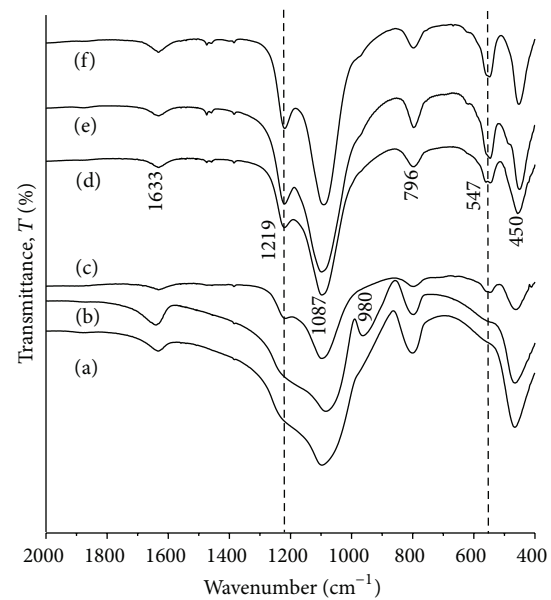


FIGURE 1: FT-IR spectra of silica source. RHA (a), SG (b), and silicalite samples: SL1 (c), SL3 (d), SL6 (e), and SL7 (f) with different gel compositions (see Table 2).

by SEM after gold coating with the operation of a JEOL instrument at 20 KV.

### 3. Results and Discussion

The chemical compositions and BET surface areas of silica sources are shown in Table 1. The purity of white RHA product is 98.78% with a little impurity of natural metal oxides. While the metal oxide and unburned carbon were removed during the procedure to prepare, SG could be clearly observed. Interestingly, the BET surface area was greatly increased from 246.91 to 790.33 m<sup>2</sup>/g.

**3.1. Fourier Transform Infrared Spectroscopy.** The FT-IR spectra of all the samples are shown in Figure 1. All the synthesized silicalite samples (see Figure 1(c-f)) reflect the vibration band at 450, 796, and 1087 cm<sup>-1</sup> corresponding to the typical Si-O-Si bending, Si-O-Si symmetric stretching (outer SiO<sub>4</sub> tetrahedron), and Si-O-Si asymmetric stretching (inner SiO<sub>4</sub> tetrahedron) within silica framework, respectively [10].

TABLE 2: Mole ratios of gel compositions for silicalite synthesis.

Synthesized silicalite (SL)	Silica source	SiO <sub>2</sub>	NaOH/SiO <sub>2</sub>	H <sub>2</sub> O/NaOH	SiO <sub>2</sub> /TPABr	Reaction time (hours)	Relative crystallinity (%)
SL1	RHA	1	0.24	309	60	24	43
SL2	RHA	1	0.24	309	30	24	90
SL3	RHA	1	0.24	618	30	12	67
SL4	RHA	1	0.24	155	30	12	95
SL5	RHA	1	0.48	155	30	12	69
SL6	RHA	1	0.24	155	30	6	98
SL7	SG	1	0.24	155	30	6	100

The clearly observed vibration modes at 547 and 1219 cm<sup>-1</sup> are attributed to double ring tetrahedral vibration and asymmetric stretching of Si tetrahedral in the zeolite framework, correspondingly resulting in MFI-structured zeolite [11, 12], and it was not observed in amorphous silica. The bending vibration of adsorbed water appears at 1633 cm<sup>-1</sup>. When comparing the spectra of RHA and SG (see Figure 1(a-b)), the additional band of Si-OH at 980 cm<sup>-1</sup> is noticeable for SG.

**3.2. X-Ray Diffraction.** Figure 2 shows the XRD patterns of all silicalite samples also demonstrate a pure phase of MFI structure. RHA and SG show amorphous phase with a broad hump at the 2θ of around 20–22° (see Figure 2(a-b)). The typical characteristic patterns of silicalite zeolite indicate its indexable peaks as (101), (200), (501), (151), and (133) reflections [13, 14]. The crystallinity of silicalite is strongly influenced by the starting gel compositions as shown in Table 2. When RHA was used as a silica source with higher ratio of SiO<sub>2</sub>/TPABr (SL1-SL2), a crystallinity percentage sharply decreased from 90% to 43% due to a lower amount of template. Obviously, the mole ratio of SiO<sub>2</sub>/TPABr is 30 optimal for silicalite synthesis. Similarly, with a higher mole ratio of H<sub>2</sub>O/NaOH (SL2-SL4), the crystallinity percentage greatly dropped from 95% to 42%.

With a higher mole ratio of NaOH/SiO<sub>2</sub>, the amount of TPA decreases due to a reaction with NaOH solution producing tripropylamine and propane [15]. As a result, the percentage of crystallinity decreases. The optimal condition of the silicalite synthesis with RHA as a silica source indicated that the mole ratios of NaOH/SiO<sub>2</sub>, H<sub>2</sub>O/NaOH, and SiO<sub>2</sub>/TPABr became 0.24, 155, and 30, respectively, under only 6 hours of reaction time. When RHA was manipulated to improve some properties to become SG (see Table 1), this SG was then further applied as a silica source for silicalite synthesis under the same condition as RHA at the optimal condition. The highest crystallinity is the result. Moreover, a very small amount of template, TPABr, was used in the synthesis of silicalite in this work when compared to those as reported elsewhere [5, 7, 10, 14].

**3.3. Scanning Electron Microscope.** The scanning electron micrographs of silicalite (SL1–SL7) are shown in Figure 3. The SEM images reveal that all silicalite products emerge in

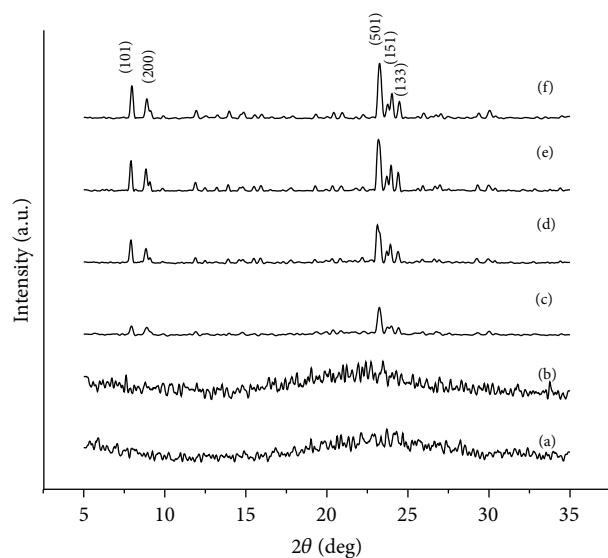


FIGURE 2: X-ray diffraction patterns of silica source. RHA (a), SG (b), and silicalite samples: SL1 (c), SL3 (d), SL6 (e), and SL7 (f) with different gel compositions (see Table 2).

forms of two morphologies of coffin and cubic-like shape. In addition, it indicates amorphous nanoparticle on the crystal face of all silicalite samples when RHA is used as a silica source (SL1–SL6). On the opposite, if SG is used as a silica source (SL7), a clean surface clearly occurs. Figure 4 demonstrates the particle size distribution of two silicalite samples synthesized from RHA and SG under the condition of SL6 and SL7, accordingly. An average particle size of silicalite synthesized from RHA (~10 μm in length) is larger than that from SG (~5 μm). It can be evidently explained that a larger specific surface area of SG could depolymerize silica with NaOH more rapidly than that of RHA resulting in inducing faster nucleation. Additionally, with SG as a silica source, a more narrow size distribution was observed.

#### 4. Conclusions

It is obvious that silica source and synthesis gel composition strongly influences crystallinity, particle size, and morphology of silicalite. An improvement of some properties of rice

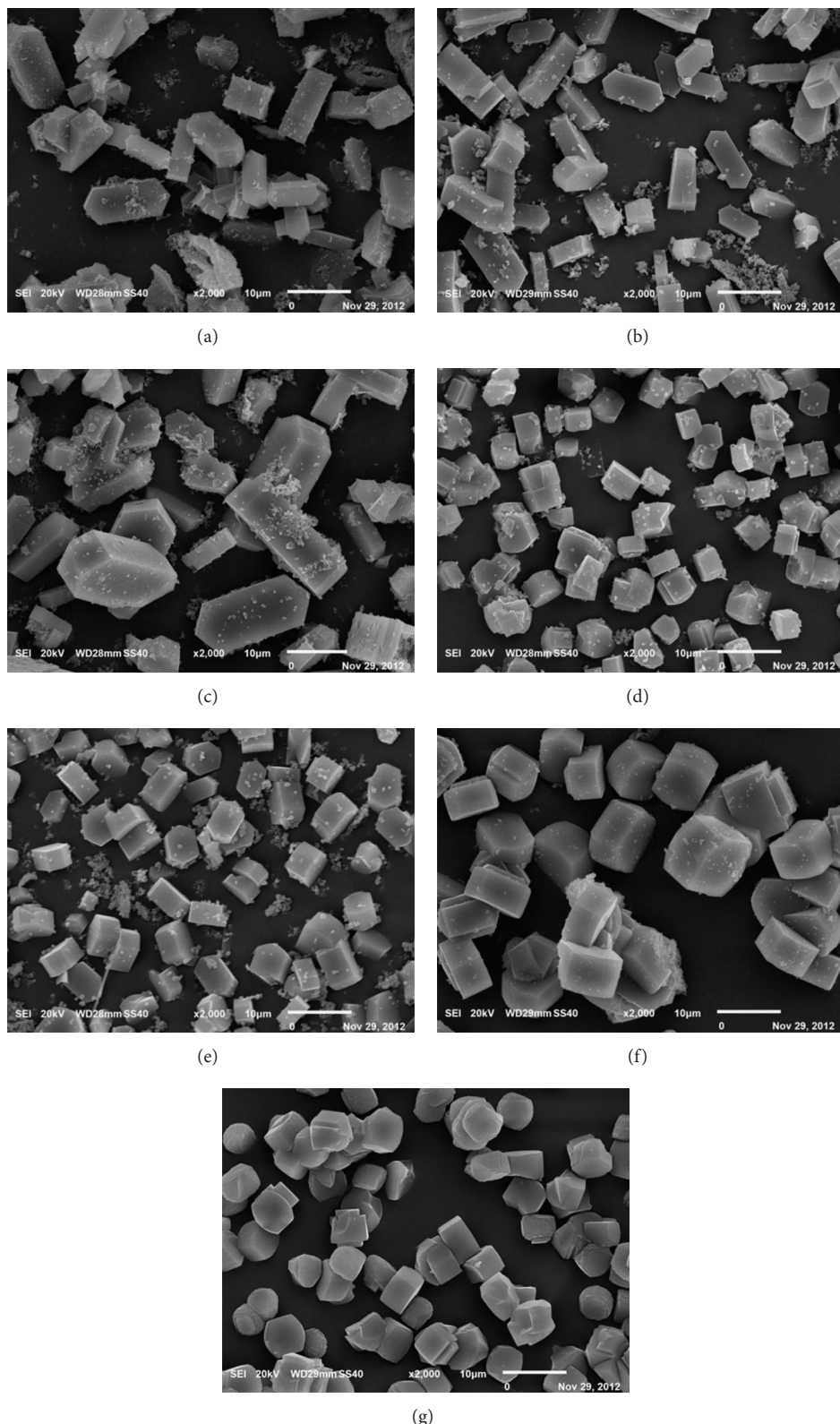


FIGURE 3: Scanning electron micrographs of as-synthesized silicalite prepared from RHA and SG under the synthesis conditions in Table 2: SL1 (a), SL2 (b), SL3 (c), SL4 (d), SL5 (e), SL6 (f), and SL7 (g).

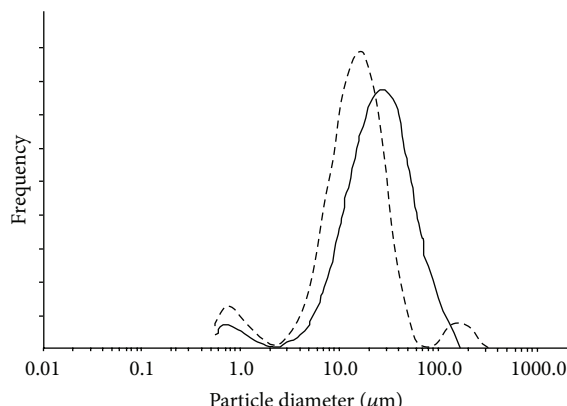


FIGURE 4: Particle size distribution of silicalite synthesized from RHA (SL6) in solid line and SG (SL7) in dashed line.

husk ash such as an increment of a specific surface area and a reduction of impurity can be successfully done by gel formation with a suggested procedure as an outcome of this study. The highest crystallinity, a narrow size distribution, and a smaller particle size of synthesized silicalite are efficiently achieved from silica gel as a silica source by hydrothermal method.

## Conflict of Interests

The authors declare that there is no conflict of interests regarding the publication of this paper.

## Acknowledgments

The authors would like to highly acknowledge the SUT Research and Development Support Fund (contract no. 3/2556) for financial support and The SUT Center for Scientific and Technological Equipment for facility support in carrying out this research.

## References

- [1] M. G. Ahunbay, O. Karvan, and A. Erdem-Senatalar, "MTBE adsorption and diffusion in silicalite-1," *Microporous and Mesoporous Materials*, vol. 115, no. 1-2, pp. 93–97, 2008.
- [2] R. Yang, F. Meng, X. Wang, and Y. Wang, "Influence of Na<sup>+</sup> on the synthesis of silicalite-1 catalysts for use in the vapor phase Beckmann rearrangement of cyclohexanone oxime," *Frontiers of Chemical Science and Engineering*, vol. 5, no. 4, pp. 401–408, 2011.
- [3] W. Xiao, J. Yang, J. Lu, and J. Wang, "A novel method to synthesize high performance silicalite-1 membrane," *Separation and Purification Technology*, vol. 67, no. 1, pp. 58–63, 2009.
- [4] M. Nomura, T. Bin, and S. Nakao, "Selective ethanol extraction from fermentation broth using a silicalite membrane," *Separation and Purification Technology*, vol. 27, no. 1, pp. 59–66, 2002.
- [5] C. Shao, X. Li, S. Qiu, F.-S. Xiao, and O. Terasaki, "Size-controlled synthesis of silicalite-1 single crystals in the presence of benzene-1,2-diol," *Microporous and Mesoporous Materials*, vol. 39, no. 1-2, pp. 117–123, 2000.
- [6] D. Vakili, M. A. Attarnejad, S. K. Massoodian, and M. M. Akbarnejad, "Synthesis of hydrophobic silicalite adsorbent from domestic resources: the effect of alkalinity on the crystal size and morphology," *Iranian Journal of Chemistry and Chemical Engineering*, vol. 24, no. 4, pp. 9–14, 2005.
- [7] M. Rieder, M. Klementová, L. Brabec, and M. Kočířík, "Morphology and structure of silicalite-1 crystals. Evidence of twinning by X-ray and electron diffraction," *Studies in Surface Science and Catalysis*, vol. 158, pp. 741–748, 2005.
- [8] S. R. Kamath and A. Proctor, "Silica gel from rice hull ash: preparation and characterization," *Cereal Chemistry*, vol. 75, no. 4, pp. 484–487, 1998.
- [9] N. Yalcin and V. Sevinc, "Studies on silica obtained from rice husk," *Ceramics International*, vol. 27, no. 2, pp. 219–224, 2001.
- [10] W. Panpa and S. Jinawath, "Synthesis of ZSM-5 zeolite and silicalite from rice husk ash," *Applied Catalysis B: Environmental*, vol. 90, no. 3-4, pp. 389–394, 2009.
- [11] T. Armaroli, L. J. Simon, M. Digne et al., "Effects of crystal size and Si/Al ratio on the surface properties of H-ZSM-5 zeolites," *Applied Catalysis A: General*, vol. 306, pp. 78–84, 2006.
- [12] L. Shirazi, E. Jamshidi, and M. R. Ghasemi, "The effect of Si/Al ratio of ZSM-5 zeolite on its morphology, acidity and crystal size," *Crystal Research and Technology*, vol. 43, no. 12, pp. 1300–1306, 2008.
- [13] J. Qi, T. Zhao, X. Xu, F. Li, and G. Sun, "Hydrothermal synthesis of size-controlled silicalite-1 crystals," *Journal of Porous Materials*, vol. 18, no. 4, pp. 509–515, 2011.
- [14] M. K. Naskar, D. Kundu, and M. Chatterjee, "A facile hydrothermal conversion of rice husk ash to ZSM-5 zeolite powders," *Journal of the American Ceramic Society*, vol. 95, no. 3, pp. 925–930, 2012.
- [15] C. S. Cundy and P. A. Cox, "The hydrothermal synthesis of zeolites: history and development from the earliest days to the present time," *Chemical Reviews*, vol. 103, no. 3, pp. 663–701, 2003.

## Research Article

# Setting Reaction of Dental Resin-Modified Glass Ionomer Restoratives as a Function of Curing Depth and Postirradiation Time

Young Kyung Kim,<sup>1</sup> Kyo-Han Kim,<sup>2</sup> and Tae-Yub Kwon<sup>2</sup>

<sup>1</sup>Department of Conservative Dentistry, School of Dentistry, Kyungpook National University, Daegu 700-412, Republic of Korea

<sup>2</sup>Department of Dental Biomaterials, School of Dentistry, Kyungpook National University, Daegu 700-412, Republic of Korea

Correspondence should be addressed to Tae-Yub Kwon; [tykwon@knu.ac.kr](mailto:tykwon@knu.ac.kr)

Received 20 August 2014; Accepted 1 October 2014

Academic Editor: Qingrui Zhang

Copyright © 2015 Young Kyung Kim et al. This is an open access article distributed under the Creative Commons Attribution License, which permits unrestricted use, distribution, and reproduction in any medium, provided the original work is properly cited.

Specular reflectance Fourier transform infrared (SR-FTIR) spectroscopy was used to study the setting reaction of dental resin-modified glass ionomer (RMGI) restoratives as a function of curing depth and postirradiation time. Two light-cure and one tricure RMGI materials were selected and used according to the manufacturers' instructions. Samples were prepared by filling the mixed materials into custom-made molds and then light-irradiating using a dental curing light. The degree of conversion and the extent of acid-base reaction of the materials at different depths (0, 1, 2, and 4 mm) and postirradiation times (10 min, 1 day, and 7 days) were determined using SR-FTIR spectroscopy in conjunction with the Kramers-Kronig (K-K) transformation. The setting reaction was also investigated using microhardness measurements. The results showed that the depth of cure increased over time by the continuous acid-base reaction rather than photopolymerization or chemical polymerization. Microhardness tests seemed less suitable for studying the setting reaction as a function of postirradiation time, probably due to softening from the humidity. Analysis using specular reflectance in conjunction with the K-K algorithm was an easy and effective method for monitoring the setting reaction of dental RMGI materials.

## 1. Introduction

Dental glass ionomers (GIs) are water-based materials that set by an acid-base reaction between a polyalkenoic acid and fluoroaluminosilicate glass [1, 2]. Resin-modified glass ionomers (RMGIs) were developed to overcome the major drawback of conventional GIs, sensitivity to water during the initial setting, by incorporating resin monomers into an aqueous solution of polyacrylic acid [3]. The primary resin incorporated in RMGIs is a hydrophilic monomer such as 2-hydroxyethyl methacrylate (HEMA) [4]; a small amount of dimethacrylate monomer may be additionally incorporated to form crosslinked poly-HEMA during polymerization [5]. The setting reaction of RMGIs includes radical polymerization (by either light-cure or self-cure) to form a polymer network along with a fundamental acid-base reaction to form a GI polysalt matrix [6, 7].

Light-cure RMGI restoratives may not adequately set when placed in bulk because of the reduced penetration of light into the deeper regions of the restoration, which may not be sufficient to initiate photopolymerization [8]. Tricure RMGI restoratives were developed in order to ensure that these deeper regions of the restoration are properly cured [7–9]. The manufacturers claim that these products undergo chemical polymerization in addition to an acid-base reaction and photopolymerization ("tricure"), which consequently increases the depth of cure [4].

One of the most common methods for evaluating the setting behavior of light-cure or tricure RMGI restoratives as a function of curing depth is measuring the hardness [4, 10]. Although microhardness tests are convenient, they fail to differentiate the relative contribution between radical polymerization and acid-base reaction because the two types

of reactions proceed simultaneously. A previous Fourier transform infrared (FTIR) spectroscopy study demonstrated that the visible light-curing process, for either light- or tri-cure RMGIs, greatly reduces the salt formation (acid-base reaction) rate during the early setting stages, which is likely due to rapid polymer network formation [7]. Another FTIR study showed that the acid-base reaction is greatly delayed in RMGIs compared to conventional GIs [11]. A differential scanning calorimetry (DSC) study showed that early light-activation of RMGIs may limit the acid-base reaction and result in a varied material structure [12]. However, there is still limited experimental and clinical information available concerning the setting reaction of RMGI restorative materials as a function of curing depth and postirradiation time.

In this *in vitro* study, we investigated the monomer-to-polymer conversion and the acid-base reaction of three commercial RMGI restoratives at different depths and postirradiation times using an optical microscope connected to an FTIR spectrophotometer. We also compared the FTIR analysis results with the measured microhardness of the materials. It was assumed that each measured microhardness value reflects the surface hardening by the contribution of both the polymerization reaction and acid-base reaction at a specified depth and postirradiation time.

## 2. Materials and Methods

**2.1. Sample Preparation.** Two light-cure (Fuji II LC capsule, FL; Fuji Filling LC, FF) and one tri-cure (Vitremer, VT) RMGI restoratives were selected for this study. Their codes, manufacturers, types, compositions, batch numbers, and manufacturers' instructions for use are summarized in Table 1.

To prepare samples, two types of silicone molds were fabricated: one with cylindrical cavities, 5 mm diameter and 1 mm depth (mold "A" for measurements at a depth of 0 mm, i.e., samples "A"), and the others with rectangular cavities, 5 mm width and 7 mm length (mold "B" for measurements at a depth of 1, 2, and 4 mm, i.e., samples "B"), as shown in Figure 1. The materials were mixed according to the manufacturers' instructions: FL using an amalgamator (ALMIC-J, Yoshida Dental Mfg. Co., Ltd., Tokyo, Japan) and FF and VT by hand (Table 1). In mold A, the mixed material was transferred into the cavities placed on a polyester strip, covered with another polyester strip, and gently pressed to expel the excess material (Figure 1(a)). Mold B was placed on a polyester strip over a glass slide that had been covered with a black adhesive paper tape (black glass slide). The mixed material was filled into the cavities and then covered with another polyester strip and black glass slide. This assembly was pressed together by means of a clamp to displace excess material. The third polyester strip was placed onto the exposed RMGI material (Figure 1(b)). The filled RMGI material was then irradiated for 40 s by placing the end of the light guide of a dental light-curing unit (Elipar TriLight, 3 M ESPE, Seefeld, Germany; standard mode) onto the top of the polyester strip so that the light could transmit

through the polyester strip over the material ( $n = 6$ ) [10]. The  $750 \text{ mW/cm}^2$  output intensity was constantly measured during the experiment by a built-in radiometer.

**2.2. FTIR Spectroscopy.** The samples were removed from the molds and analyzed with FTIR spectroscopy 10 min, 1 day, and 7 days after light-irradiation [10]. The samples were stored in a dark container at  $37^\circ\text{C}$  with 100% relative humidity except during measurements. Before testing, all samples were blot-dried using a rubber air blower, and all soft material was scraped from the bottom of samples B. FTIR analysis was performed at 0 mm (at the center of the top surface of sample A) and 1, 2, and 4 mm below the surface (along the central axes of samples B) of the cured materials using an FTIR spectrometer (IRPrestige-21, Shimadzu Corp., Kyoto, Japan) connected to an optical microscope (AIM-8800, Shimadzu Corp.). The specular reflectance spectrum was acquired by scanning the samples 50 times over a  $2000\text{--}1100 \text{ cm}^{-1}$  range with a resolution of  $4 \text{ cm}^{-1}$  and then mathematically converted into an absorption spectrum via Kramers-Kronig (K-K) relations using IRSolution software version 1.21 (Shimadzu Corp.) [13, 14].

From each spectrum, the degree of conversion (DC) and the extent of acid-base reaction (EAB) of the material at each specified depth (0, 1, 2, or 4 mm) and each observation time (10 min, 1 day, and 7 days after light-irradiation) were calculated. The peak absorbance height of methacrylate C=C bonds (C=C str at  $\sim 1637 \text{ cm}^{-1}$ ) was used as the analytical frequency, while the peak absorbance height of methacrylate ester bonds (C=O str at  $\sim 1724 \text{ cm}^{-1}$ ) was used as a reference frequency [7]. The DC was then calculated by comparing the C=C/C=O peak absorbance height in the cured material with that in the uncured material, according to the following equation [15]:  $\text{DC} (\%) = (1 - C/U) \times 100$ , where C and U are the normalized absorption peak heights of methacrylate C=C bonds for the cured and uncured materials, respectively. To determine the efficiency of the acid-base reaction of the material, the complex ester peak at  $\sim 1724 \text{ cm}^{-1}$  was deconvoluted into three subpeaks at  $\sim 1732$ ,  $\sim 1724$ , and  $1708 \text{ cm}^{-1}$  from each spectrum [7]. The peak absorbance height ratio of the carboxylate salts formed (C=O str of COOM,  $\sim 1562 \text{ cm}^{-1}$ ) to the remaining unionized carboxyl groups (C=O str of COOH,  $\sim 1732 \text{ cm}^{-1}$ ) was calculated. The EAB was determined using the following equation [7]:  $\text{EAB} = C'/U'$ , where C' and U' are the C=O str of COOM/C=O str of COOH absorption peak height ratios for the cured and uncured materials, respectively.

**2.3. Microhardness Measurements.** The RMGI samples for microhardness measurements were prepared in the same way as for FTIR spectroscopy measurements. Using a Vickers hardness tester (HMV-2, Shimadzu Corp.), three indentations were made at each depth (each indentation separated by approximately 0.5 mm) on each sample using a 10-s dwell time and a 100-g load. The Vickers hardness (VH) at each depth for each sample was recorded as the average of the three readings ( $n = 6$ ) [8].

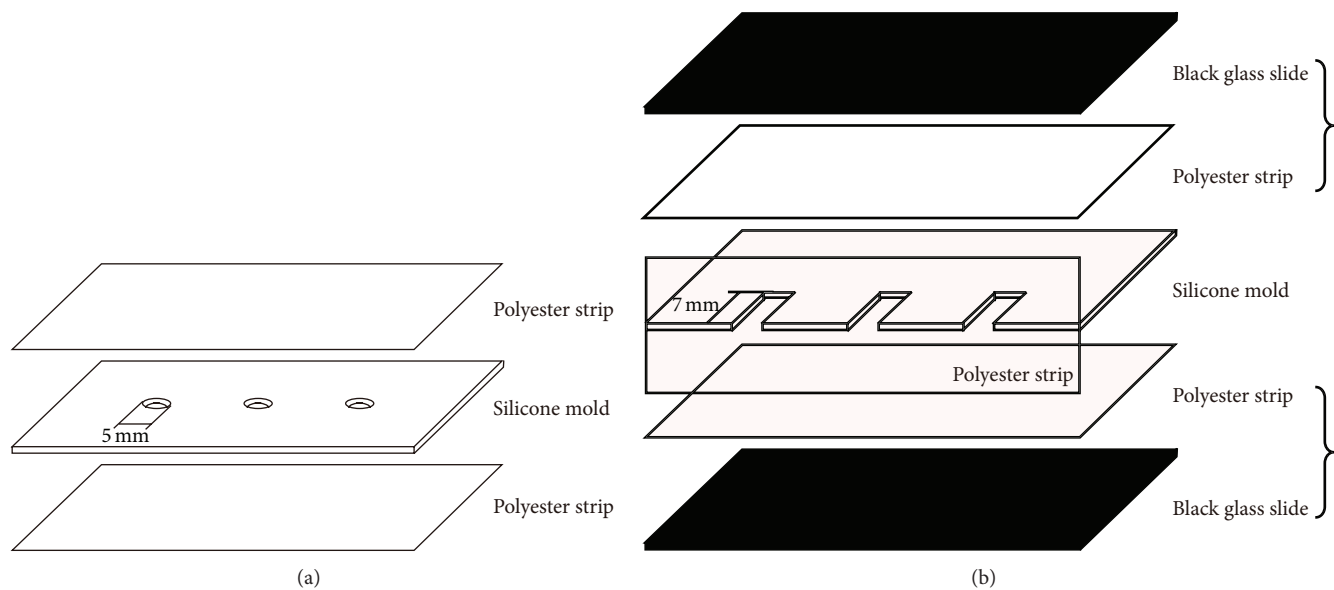


FIGURE 1: Two kinds of custom-made silicone molds simulating cavities prepared in a tooth: (a) for preparation of samples A (measurements at a depth of 0 mm) and (b) for preparation of samples B (measurement at a depth of 1, 2, and 4 mm).

TABLE 1: Code, brand, manufacturer, type, composition, batch number, and manufacturers' instructions of the materials used.

Code (material)	Manufacturer	Type	Composition (manufacturer supplied)	Batch number (shade)	Manufacturers' instructions <sup>a</sup>
FL (Fuji II LC capsule)	GC Corp., Tokyo, Japan	Light-cure	Powder: aluminosilicate glass Liquid: water, polyacrylic acid, HEMA, UDMA, and camphorquinone	1009041 (A3)	After activation, set the capsule into a mixer, and mix for 10 s. Light-cure for 20 s.
FF (Fuji Filling LC)	GC Corp.	Light-cure	Paste A: aluminosilicate glass, HEMA, and UDMA Paste B: water, polyacrylic acid, UDMA, and silicon dioxide	1006091 (A3)	After dispensing, mix thoroughly with lapping strokes for 10 s. Light-cure for 20 s.
VT (Vitremer)	3M ESPE, St. Paul, MN, USA	Tricure	Powder: fluoroaluminosilicate glass, microencapsulated potassium persulfate, and ascorbic acid Liquid: copolymer of acrylic and itaconic acids, water, HEMA, and diphenyliodonium hexafluorophosphate	N136183/N173275 (A3)	Place an equal number of level powder scoops and liquid drops. Mix the powder into the liquid. Light-cure for 40 s.

Monomer abbreviations: HEMA: 2-hydroxyethyl methacrylate; UDMA: urethane dimethacrylate.

<sup>a</sup>In the present study, all materials were light-irradiated for 40 s.

**2.4. Statistical Analysis.** All of the data were compared statistically using one-way analysis of variance (ANOVA) and Duncan's multiple range tests at the 0.05 significance level [10, 16]. The statistical analysis was performed using SPSS 17.0 for Windows (SPSS Inc., Chicago, IL, USA).

### 3. Results and Discussion

Using reflection measurements, IR spectra can be nondestructively obtained from a wide range of sample types. The specular reflectance technique often allows analysis with little

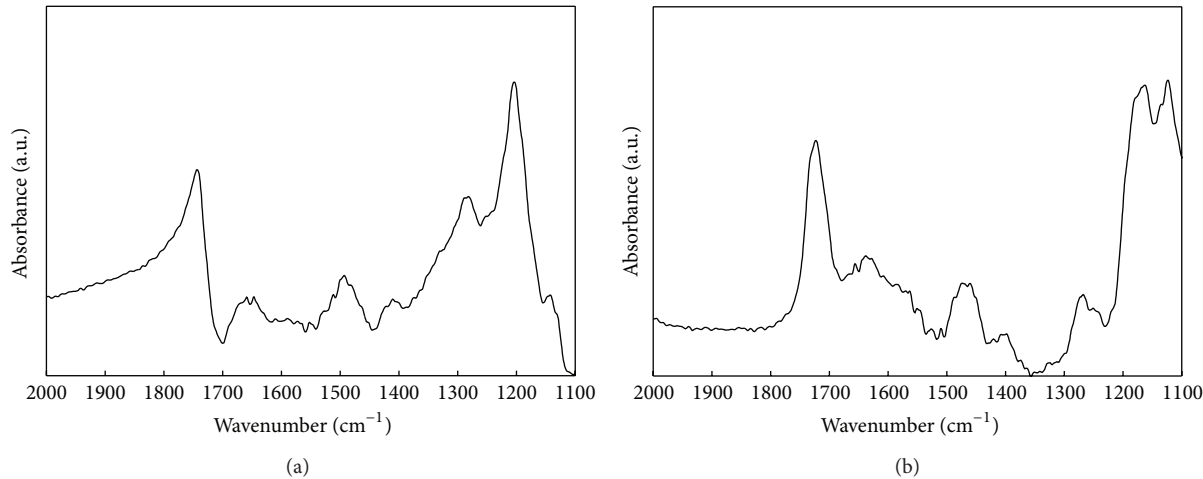


FIGURE 2: (a) Specular reflectance IR spectrum of an RMGI sample (before conversion). (b) Kramer-Kronig transformation of the reflection spectrum (after conversion).

sample preparation and keeps the sample intact for other measurements. However, wavelength-dependent changes in refractive index can yield anomalous bands in reflectance spectra and, as a result, make identification and functional group analysis difficult. Thus, this distorted spectrum should be converted into a normal absorption spectrum using a mathematical algorithm called the K-K transformation [13, 14]. In this study, the Maclaurin method, which provides better calculation accuracy than the double FFT method, was employed for the K-K conversion.

To obtain the specular reflectance spectra, flat, smooth, and shiny surfaces of the RMGI samples were prepared with a polyester strip and glass slide. Figure 2 shows the specular reflectance IR spectra before and after the K-K transformation [14]. To determine the EAB, the peak absorbance height of the unionized carboxyl groups was used for the calculation after the complex ester peak was deconvoluted from each spectrum (Figure 3) [7].

A command setting behavior in RMGIs is made by incorporating photopolymerizable monomers and suitable photoinitiation systems [4]. The light-curable versions of GIs include a photocurable component, which may be an unsaturated organic side chain grafted onto the poly(acrylic acid) backbone, and/or a separate organic precursor such as HEMA or mixtures of HEMA with other acrylic monomers [17]. Thus, HEMA is an important constituent of these hybrid materials. However, Anstice and Nicholson [17] demonstrated that the incorporation of even a small amount of organic compounds (including HEMA) into the liquid interferes with the normal acid-base reaction of an RMGI. Some dental RMGI products include approximately 15–20% HEMA in the liquid compartment, and when mixed with powder, there will be approximately 5% HEMA in the set material [8, 9, 18]. Thus, the initial setting of an RMGI occurs as a result of the photopolymerization of HEMA when the material is light-irradiated after mixing. The DC results of the two light-cure and one tricure RMGI materials at different depths and postirradiation times are summarized in Table 2.

At the initial stage of the measurement, within 10 min after light-irradiation, the values of each material were statistically similar up to a depth of 2 mm compared to those at the top layer (0 mm) ( $P > 0.05$ ). Mount et al. [9] recommended the use of incremental placement of RMGI restoratives to allow for a full irradiation-initiated cure. In the two light-cure RMGIs (FL and FF), significantly lower 10 min DC values at a depth of 4 mm than those at the top layer indicate poor photopolymerization at the deep layer regions, probably due to substantial light attenuation [19].

In the tricure RMGI VT, the additional chemical polymerization mechanism was expected to contribute to the curing depth over time. Kakaboura et al. [7] suggested that chemical polymerization of VT can take place in a deeper cavity region where there is light attenuation and its slow rate can allow proper development of the acid-base reaction. In addition, VT employs a potassium persulfate/ascorbic acid redox initiation system (Table 1), which was developed by Antonucci et al. as a new initiator system for the ambient polymerization of dental monomers [20]. In this study, however, significant chemical polymerization reaction over time (up to 7 days) was not observed in the tricure material VT (Table 2). This finding suggests that photopolymerization was still predominant over chemical polymerization for VT [9]. However, it should be noted that differentiating the relative contribution of the two polymerization mechanisms (photo and chemical) to the setting of VT was not possible because the dark-curing condition (without the light-irradiation) was not included in the present study.

For all the materials tested, each DC value at the initial measurement was not significantly altered over time (up to 7 days) ( $P > 0.05$ ) (Table 2). Although the clinical set (by acid-base reaction) of conventional GIs appears to be completed within a few minutes, a continuing maturation phase occurs over several months through posthardening reactions. For dental resin composites, in contrast, the significant polymerization reaction finishes within 24 h after mix or after light-activation [15]. Moreover, previous studies suggested

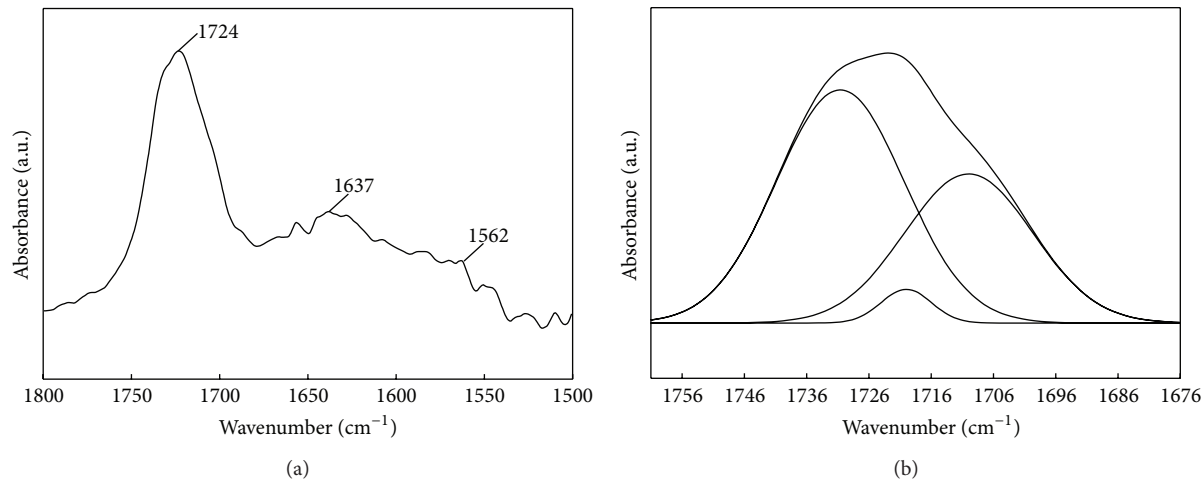


FIGURE 3: (a) FTIR spectrum of an RMGI sample in the range of 1800–1500 cm<sup>-1</sup>: the peak at ~1724 cm<sup>-1</sup> indicates the ester bond (C=O str), the peak at ~1637 cm<sup>-1</sup> indicates the methacrylate C=C bond (C=C str), and the peak at ~1562 cm<sup>-1</sup> indicates the carboxylate salt formed (C=O str of COOM). (b) Deconvolution of the complex ester peak into three subpeaks: unionized carboxyl groups at ~1732 cm<sup>-1</sup>, ~1724 cm<sup>-1</sup> and ester groups dependent on substitution at ~1708 cm<sup>-1</sup>.

TABLE 2: Degree of conversion (DC) (%) of materials at different depths and postirradiation times (mean and SD in parentheses).

Material	Depth	10 min	1 day	7 days
FL	0 mm	46.0 (6.1) a	47.2 (4.8) a	47.8 (6.0) a
	1 mm	44.5 (5.6) a	46.1 (3.0) a	45.2 (5.8) a
	2 mm	42.3 (4.1) ab	41.9 (5.1) ab	44.8 (4.4) a
	4 mm	34.6 (3.8) c	36.7 (3.9) bc	37.3 (4.2) bc
FF	0 mm	56.5 (4.0) a	58.6 (4.1) a	58.5 (5.7) a
	1 mm	53.4 (6.7) a	52.7 (3.9) a	54.9 (2.6) a
	2 mm	52.9 (6.8) a	54.8 (4.4) a	52.6 (4.4) a
	4 mm	37.5 (3.7) b	39.0 (3.4) b	41.2 (4.6) b
VT	0 mm	38.0 (4.3) a	42.5 (6.8) a	40.1 (5.0) a
	1 mm	37.8 (3.7) a	39.9 (6.7) a	41.6 (2.8) a
	2 mm	35.6 (5.9) ab	37.4 (3.2) a	38.5 (3.6) a
	4 mm	29.6 (5.1) bc	28.2 (4.5) c	26.5 (4.3) c

Within the same material, means with same lowercase letters indicate no statistically significant difference between the groups ( $P > 0.05$ ).

that 90% of the conversion obtained after 24 h is developed within the first 10 min in light-activated dual-cure resin composites [15, 21]. The DC results in this study (Table 2) also show that the initial setting of RMGI restoratives by photopolymerization has a similar tendency to that of dental resin composites. In RMGIs, further polymerization after the initial set may be inhibited by the formation of the polysalt matrix [4].

The acid-base reaction of RMGI materials can contribute to the curing depth over time, independent of light-activation. Table 3 presents the EBA of the materials as a function of curing depth and postirradiation time. At the initial stage of the measurement, the values of each material were statistically similar up to a depth of 4 mm compared to those at the top layer ( $P > 0.05$ ), indicating that the acid-base reaction of the materials was depth independent. For FL and VT, the values consistently and significantly increased over time, regardless of the depth ( $P < 0.05$ ). FF showed

significantly higher values at 1 and 7 days than at 10 min at all the depths ( $P < 0.05$ ). This finding shows that the acid-base reaction occurred up to 1 day (for FF) or 7 days (for FL and VT) after light-irradiation and that the reaction also seemed to be more efficient over time than chemical polymerization even for the tricure RMGI VT (Tables 2 and 3). The initial setting of the materials by photopolymerization may decrease the rates of diffusive processes of a gel matrix [11]. Moreover, the reduction in content of water, which is an essential component of the acid-base reaction, may retard the acid-base reaction [9, 11]. Kakaboura et al. [7] and Berzins et al. [12] demonstrated that the acid-base and photopolymerization reactions may compete with and inhibit one another during early RMGI development. However, in accordance with Wan et al. [11], the acid-base reaction of the three RMGI materials was delayed instead of being completely inhibited. Thus, the storage of the RMGI samples in humid condition seems to have allowed a relatively long-term acid-base reaction. It has

TABLE 3: Extent of acid-base reaction (EAB) of materials at different depths and postirradiation times (mean and SD in parentheses).

Material	Depth	10 min	1 day	7 days
FL	0 mm	2.0 (0.2) a	3.8 (0.5) b	5.7 (0.4) c
	1 mm	2.4 (0.3) a	4.1 (0.7) b	5.8 (0.8) c
	2 mm	2.6 (0.5) a	3.8 (0.6) b	5.5 (0.4) c
	4 mm	2.6 (0.4) a	3.7 (0.3) b	5.6 (0.5) c
FF	0 mm	6.8 (0.6) a	11.2 (1.1) b	12.5 (1.6) b
	1 mm	6.3 (0.9) a	17.1 (1.3) c	17.9 (2.4) c
	2 mm	7.4 (1.1) a	16.9 (1.9) c	18.0 (2.3) c
	4 mm	7.7 (1.4) a	23.1 (3.8) d	22.2 (3.5) d
VT	0 mm	1.3 (0.2) a	2.6 (0.4) b	4.1 (0.5) ce
	1 mm	1.0 (0.1) a	2.9 (0.4) b	4.5 (0.4) e
	2 mm	1.1 (0.2) a	3.7 (0.5) c	4.6 (0.7) e
	4 mm	1.3 (0.2) a	5.5 (0.9) d	6.4 (0.8) f

Within the same material, means with same lowercase letters indicate no statistically significant difference between the groups ( $P > 0.05$ ).

TABLE 4: Vickers hardness (VH) of materials at different depths and postirradiation times (mean and SD in parentheses).

Material	Depth	10 min	1 day	7 days
FL	0 mm	34.7 (3.3) a	29.6 (4.0) a	31.8 (4.4) a
	1 mm	32.5 (4.5) a	30.4 (3.2) a	29.6 (3.4) a
	2 mm	30.4 (3.6) a	31.1 (5.4) a	33.4 (2.9) a
	4 mm	22.0 (1.8) b	31.5 (3.1) a	34.8 (3.3) a
FF	0 mm	35.9 (4.2) a	29.7 (3.3) b	27.1 (3.6) b
	1 mm	37.5 (6.5) a	26.5 (4.8) b	26.9 (3.8) b
	2 mm	35.6 (2.7) a	25.8 (4.3) b	26.3 (2.6) b
	4 mm	31.0 (3.8) b	28.9 (3.5) b	29.7 (4.5) b
VT	0 mm	16.0 (3.3) a	16.2 (1.6) a	20.4 (3.7) b
	1 mm	17.9 (2.7) ab	17.9 (3.0) ab	19.8 (1.6) b
	2 mm	15.2 (2.1) a	16.4 (2.7) a	20.6 (2.6) b
	4 mm	5.3 (1.3) c	14.7 (3.2) a	15.8 (1.9) a

Within the same material, means with same lowercase letters indicate no statistically significant difference between the groups ( $P > 0.05$ ).

been suggested that the initial increase in strength of GIs is mainly caused by the formation of metal carboxylates, after which the silicate network reconstruction plays a more significant role [22–24]. This second reaction through the growth of a silicate phase [22] was not investigated in the current SR-FTIR spectroscopy study, but it obviously requires further investigation to elucidate the setting mechanism of GIs with time.

The VH values of the RMGI materials are presented in Table 4. In general, the initial values (at 10 min) showed a similar trend to the DC values (Table 2), indicating that the materials were initially hardened by photopolymerization. In VT, the VH values gradually increased over time. In FF, in contrast, there were significant reductions in the value at 1 day, except at a depth of 4 mm, compared to the initial values ( $P < 0.05$ ). Previous studies using a shear punch strength test [9] or a Knoop hardness test [8] suggested that although the maturation process or slow chemical polymerization can occur over time in poorly or non-irradiated regions of RMGIs, these reactions may not be sufficient to compensate for photopolymerization. However, those tests did not

directly investigate the DC or EBA values of the materials; instead, they only estimated the setting reaction from the mechanical properties of the hardened materials. Crosslinking of polymer chains may contribute to strengthening of conventional GIs, but water uptake may eventually decrease the physical properties of the materials [25]. Similarly, RMGI materials absorb water over time mainly due to the inclusion of the hydrophilic monomer HEMA, and the water sorption contributes to softening of the materials [8, 10]. In this study, such a softening effect appeared prominent in FF (Table 4), implying that the material is more hydrophilic than the other two materials (Table 1). However, this observation should be further studied. Although microhardness measurement is a simple approach, it cannot be the final indicator for evaluating the setting of RMGI materials as a function of time. Moreover, the microhardness value is greatly influenced by material composition, and thus cross-comparison between the different RMGI brands is limited [15].

This *in vitro* study shows that SR-FTIR spectroscopy was more effective than microhardness tests for investigating the complex setting reactions of dental materials such as

RMGIs. The spectroscopy results clearly show that the initial setting of dental RMGIs is made by photopolymerization and then the acid-base reaction progresses over time. Although the photopolymerization and acid-base reactions may be completed during the early setting stage [7, 12], the acid-base reaction progresses over time even at the well-light-irradiated superficial layers of the materials (Table 3) [11]. Thus, the incremental buildup of the restoration and increased exposure time are still recommended when the light source is distant from the cavity floor in order to maximize the physical and mechanical properties of the filled materials [9]. However, further experimental and clinical research is needed to elucidate the mechanisms of the long-term setting reaction of RMGI restoratives in the oral cavity.

## 4. Conclusions

- (1) Sensitive SR-FTIR spectroscopy was an effective analytical method for investigating the setting reactions of dental RMGIs.
- (2) The light-cure RMGI restoratives exhibited increased depth of cure over time by the acid-base reaction rather than photopolymerization. The improvement in depth of cure for the tricure material was also attributed to the acid-base reaction rather than chemical polymerization.
- (3) Microhardness tests seemed less suitable for evaluating the setting of RMGI materials as a function of postirradiation time, probably due to the softening from the humidity.

## Conflict of Interests

The authors declare that there is no conflict of interests regarding the publication of this paper.

## Acknowledgments

This research was supported by Basic Science Research Program through the National Research Foundation of Korea (NRF) funded by the Ministry of Education (2013R1A1A2012382).

## References

- [1] M. J. Tyas and M. F. Burrow, "Adhesive restorative materials: a review," *Australian Dental Journal*, vol. 49, no. 3, pp. 112–154, 2004.
- [2] J. W. McLean, J. W. Nicholson, and A. D. Wilson, "Proposed nomenclature for glass-ionomer dental cements and related materials," *Quintessence International*, vol. 25, no. 9, pp. 587–589, 1994.
- [3] S. Saito, S. Tosaki, and K. Hirota, "Characteristics of glass-ionomer cements," in *Advances in Glass-Ionomer Cements*, C. L. Davidson and I. A. Mjör, Eds., pp. 15–50, Quintessence, Carol Stream, Ill, USA, 1999.
- [4] H. F. Albers, *Tooth-Colored Restoratives: Principles and Techniques*, BC Decker, Hamilton, Canada, 9th edition, 2001.
- [5] D. C. Smith, "Development of glass-ionomer cement systems," *Biomaterials*, vol. 19, no. 6, pp. 467–478, 1998.
- [6] A. D. Wilson, "Resin-modified glass-ionomer cements," *The International Journal of Prosthodontics*, vol. 3, no. 5, pp. 425–429, 1990.
- [7] A. Kakaboura, G. Eliades, and G. Palaghias, "An FTIR study on the setting mechanism of resin-modified glass ionomer restoratives," *Dental Materials*, vol. 12, no. 3, pp. 173–178, 1996.
- [8] H. W. Roberts, D. W. Berzins, and D. G. Charlton, "Hardness of three resin-modified glass-ionomer restorative materials as a function of depth and time," *Journal of Esthetic and Restorative Dentistry*, vol. 21, no. 4, pp. 262–272, 2009.
- [9] G. J. Mount, C. Patel, and O. F. Makinson, "Resin modified glass-ionomers: strength, cure depth and translucency," *Australian Dental Journal*, vol. 47, no. 4, pp. 339–343, 2002.
- [10] E. J. Swift Jr., M. A. Pawlus, M. A. Vargas, and D. Fortin, "Depth of cure of resin-modified glass ionomers," *Dental Materials*, vol. 11, no. 3, pp. 196–199, 1995.
- [11] A. C. Wan, A. U. Yap, and G. W. Hastings, "Acid-base complex reactions in resin-modified and conventional glass ionomer cements," *Journal of Biomedical Materials Research*, vol. 48, no. 5, pp. 700–704, 1999.
- [12] D. W. Berzins, S. Abey, M. C. Costache, C. A. Wilkie, and H. W. Roberts, "Resin-modified glass-ionomer setting reaction competition," *Journal of Dental Research*, vol. 89, no. 1, pp. 82–86, 2010.
- [13] P. Grosse and V. Offermann, "Analysis of reflectance data using the Kramers-Kronig Relations," *Applied Physics A Solids and Surfaces*, vol. 52, no. 2, pp. 138–144, 1991.
- [14] M. A. Calin, R. M. Ion, and N. Herascu, "Kramers-Kronig analysis of 5,10,1,20-tetra-p-sulfonato-phenyl-porphyrin (TSPP) as photosensitizer for photodynamic therapy," *Journal of Optoelectronics and Advanced Materials*, vol. 7, no. 6, pp. 3155–3160, 2005.
- [15] Y. L. Yan, Y. K. Kim, K.-H. Kim, and T.-Y. Kwon, "Changes in degree of conversion and microhardness of dental resin cements," *Operative Dentistry*, vol. 35, no. 2, pp. 203–210, 2010.
- [16] H.-B. Ahn, S.-J. Ahn, S.-J. Lee, T.-W. Kim, and D.-S. Nahm, "Analysis of surface roughness and surface free energy characteristics of various orthodontic materials," *The American Journal of Orthodontics and Dentofacial Orthopedics*, vol. 136, no. 5, pp. 668–674, 2009.
- [17] H. M. Anstice and J. W. Nicholson, "Studies in the setting of polyelectrolyte materials—part II: the effect of organic compounds on a glass poly(alkenoate) cement," *Journal of Materials Science: Materials in Medicine*, vol. 5, no. 5, pp. 299–302, 1994.
- [18] S. K. Sidhu and T. F. Watson, "Resin-modified glass ionomer materials. A status report for the American Journal of Dentistry," *The American Journal of Dentistry*, vol. 8, no. 1, pp. 59–67, 1995.
- [19] M.-J. Kim, K.-H. Kim, Y.-K. Kim, and T.-Y. Kwon, "Degree of conversion of two dual-cured resin cements light-irradiated through zirconia ceramic disks," *Journal of Advanced Prosthodontics*, vol. 5, no. 4, pp. 464–470, 2013.
- [20] J. M. Antonucci, C. L. Grams, and D. J. Termini, "New initiator systems for dental resins based on ascorbic acid," *Journal of Dental Research*, vol. 58, no. 9, pp. 1887–1899, 1979.
- [21] F. A. Rueggeberg and W. F. Caughman, "The influence of light exposure on polymerization of dual-cure resin cements," *Operative Dentistry*, vol. 18, no. 2, pp. 48–55, 1993.
- [22] E. A. Wasson and J. W. Nicholson, "New aspects of the setting of glass-ionomer cements," *Journal of Dental Research*, vol. 72, no. 2, pp. 481–483, 1993.

- [23] S. Matsuya, T. Maeda, and M. Ohta, "IR and NMR analyses of hardening and maturation of glass-ionomer cement," *Journal of Dental Research*, vol. 75, no. 12, pp. 1920–1927, 1996.
- [24] S. Shahid, R. W. Billington, and G. J. Pearson, "The role of glass composition in the behaviour of glass acetic acid and glass lactic acid cements," *Journal of Materials Science: Materials in Medicine*, vol. 19, no. 2, pp. 541–545, 2008.
- [25] M.-A. Cattani-Lorente, C. Godin, and J.-M. Meyer, "Mechanical behavior of glass ionomer cements affected by long-term storage in water," *Dental Materials*, vol. 10, no. 1, pp. 37–44, 1994.

## Research Article

# Synthesis and Characterization of an Iron Nitride Constructed by a Novel Template of Metal Organic Framework

Suyan Liu,<sup>1,2</sup> Quan Huo,<sup>1</sup> Rongna Chen,<sup>1</sup> Peipei Chen,<sup>1</sup> Yuan Li,<sup>1</sup> and Yang Han<sup>2</sup>

<sup>1</sup>Hebei Key Laboratory of Applied Chemistry, College of Environmental and Chemical Engineering, Yanshan University, Qinhuangdao, Hebei 066004, China

<sup>2</sup>The State Key Laboratory of Heavy Oil Processing, Department of Materials Science and Engineering, China University of Petroleum, Beijing, Changping District, Beijing 102249, China

Correspondence should be addressed to Quan Huo; quanhuo@ysu.edu.cn

Received 31 July 2014; Accepted 27 November 2014

Academic Editor: Bing Wu

Copyright © 2015 Suyan Liu et al. This is an open access article distributed under the Creative Commons Attribution License, which permits unrestricted use, distribution, and reproduction in any medium, provided the original work is properly cited.

An iron nitride with high surface area was synthesized from an iron-based metal organic framework (Fe-MOF) in this work. During the synthesis process, the Fe-MOF of MIL-53 served as a hard template, a template to impart a certain degree of morphology for iron oxide products and to form porosities for iron nitride products. Moreover, it played the roles of iron sources for the synthesis of the final iron oxides and the iron nitrides. The physicochemical properties of the materials were characterized by a series of technologies including XRD, SEM, and N<sub>2</sub>-adsorption/desorption. The results showed that the iron nitride synthesized from MIL-53 was  $\alpha$ -Fe<sub>2-3</sub>N. And, the  $\alpha$ -Fe<sub>2-3</sub>N showed the morphology with loosely aggregated particles which favored the formation of rich interparticle porosities. As a result, the surface area of the  $\alpha$ -Fe<sub>2-3</sub>N was larger than those of samples using  $\alpha$ -Fe<sub>2</sub>O<sub>3</sub> as precursors and its value was 41 m<sup>2</sup>/g. In addition, the results agreed that both raw material properties (such as crystallinity and surface areas) and nitriding approaches had significant effects on the surface areas of iron nitrides. Also the results were proved by the iron oxide synthesized with different methods. This new synthetic strategy could be a general approach for the preparation of late transition metal nitrides with peculiar properties.

## 1. Introduction

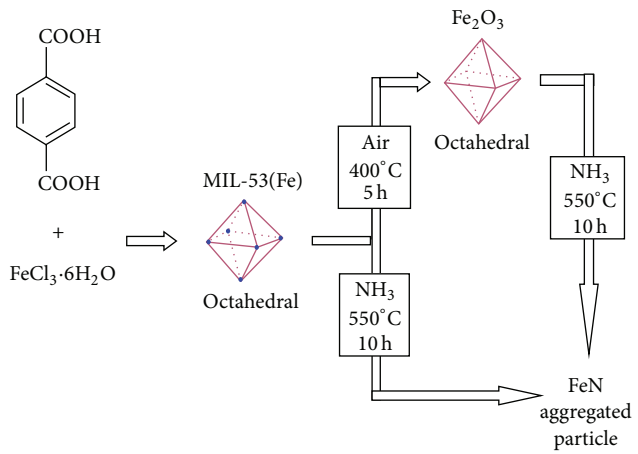
Transition metal nitride catalysts have attracted great attentions because they exhibit noble metal-like characteristics in many reactions, such as fuel cells, optical coatings, electrical contacts, and catalysts [1]. The key to producing successful catalysts lies in the ability to synthesize materials of high surface areas [2]. Synthetic strategies of transition metal nitrides with high surface areas have been intensively studied, including temperature-programmed reaction of solid-state metal compounds with gaseous nitrogen sources [3–6], pyrolysis of metal precursors [7], and solution reactions [8] as well as developed reactive hard template [9] and soft urea pathway [10]. Recently, Yang and DiSalvo [11] reported a simple process prepared mesoporous transition metal nitrides (NbN, VN, Ta<sub>3</sub>N<sub>5</sub>, and TiN) by the ammonolysis of bulk ternary oxides that contain cadmium. Depending upon

the starting composition and the ammonolysis temperature, the TMNs had pore sizes from 10 to 40 nm, domain sizes of 5–40 nm, and the surface areas 15–60 m<sup>2</sup>/g. However, most of the nitrides are early transition metal nitrides focusing on nitrides of molybdenum and tungsten, and only a few papers have reported the synthesis of late transition metal nitrides particles such as iron nitrides, due to their relatively low thermal stability [8, 12–15]. For example, Koltypin et al. [12] reported the sonochemical synthesis of iron nitride nanoparticles by two methods, that is, sonication of Fe(CO)<sub>5</sub> in a decane solution under a gaseous NH<sub>3</sub>/H<sub>2</sub> mixture and nitridation of sonochemically prepared amorphous iron under a mixed NH<sub>3</sub>/H<sub>2</sub> stream. Later on, iron particles of various grain sizes [13], amorphous iron prepared through reducing ferrous sulfate by potassium borohydride [14], and Fe<sub>2</sub>O<sub>3</sub> [15] were also used as precursor to produce iron nitride by a temperature-programmed reaction in NH<sub>3</sub>.

Recently, Choi and Gillan [8] reported the use of solvothermally moderated metal azide decomposition as a route to nanocrystalline mid to late transition metal nitrides. This method utilizes exothermic solid-state metathesis reaction precursor pairs, namely, metal halides ( $\text{NiBr}_2$ ,  $\text{FeCl}_3$ , and  $\text{MnCl}_2$ ) and sodium azide, but conducts the metathesis reaction and azide decomposition in superheated toluene. The reaction temperatures are relatively low ( $<300^\circ\text{C}$ ) and yield thermally metastable nanocrystalline hexagonal  $\text{Ni}_3\text{N}$  and  $\text{Fe}_2\text{N}$  and tetragonal  $\text{MnN}$ . Moszyński et al. [16] reported that three iron samples of various mean sizes of crystallites were nitrided in gas mixtures with  $\text{NH}_3/\text{H}_2$  ratio increasing stepwise up to the pure ammonia. The higher the mean size of crystallites was, the lower nitriding potential was required to initiate the phase transition  $\alpha\text{-Fe} \rightarrow \gamma\text{-Fe}_4\text{N}$  observed during the nitriding process. Unfortunately, the surface areas of these iron nitrides are usually lower than  $40 \text{ m}^2/\text{g}$ . In order to produce promising iron nitride catalysts, new ways to synthesize iron nitrides with higher surface areas are thus in great demand.

Metal organic frameworks (MOFs) as a kind of emerging nanoporous material, built from connectors and organic linkers, have attracted many attentions due to their intriguing architectures and topologies, tunable pore sizes, and wide potential applications such as gas storage and separation and drug delivery [17]. The various pore sizes, high thermal stability, and synthetically flexible environment of MOFs make them feasible as templates for preparing nanoporous carbon materials [18], nanoscale  $\text{NaAlH}_4$  [19], transition metal nanoparticles [20], silver cluster [21], and so forth. Recently, Kim et al. [22] reported a versatile method to prepare metal nanoparticles supported on nanoporous carbon (M/NC3) via carbonization and carbothermal reduction (CCR) of metal-coordinated IRMOF-3 materials by postsynthetic modification (PSM) with metal precursors (i.e., Ru, W, V, and Ti). Use of IRMOF materials as templates/carbon sources led to desirable pore characteristics in the resulting materials, including high surface area ( $900\text{--}2000 \text{ m}^2/\text{g}$ ) coupled with an increased mesoporosity ( $0.14\text{--}0.34 V_{\text{micro}}/V_{\text{pore}}$ ). However, examples of metal organic framework as hard template to synthesis of iron nitride are rare. Transition metal ions are usually used as connectors; thus, MOFs provide the possibility to be a porous reactive hard template candidate. As a typical example of Fe-MOFs, the common MIL-53(Fe) is chosen, which is built from infinite chains of corner sharing  $\text{Fe}^{\text{III}}_4(\text{OH})_2$  octahedra interconnected by dicarboxylate groups of benzene dicarboxylate units [23]. In this way, a 3D microporous framework with 1D diamond shaped channels with free internal diameter of about 0.85 nm is formed.

Herein, we report the synthesis of iron nitride from iron-based metal organic framework exemplified by octahedral MIL-53(Fe) not only as a reactive hard template but also as a provider of Fe source. The difference in BET surface area of iron nitride between MOFs and  $\text{Fe}_2\text{O}_3$  is of interest. For this purpose,  $\text{Fe}_2\text{O}_3$  is synthesized by the sol-gel method and MOFs as template ways [24] according to the literature, respectively. All of the  $\text{Fe}_2\text{O}_3$  and MIL-53 were employed to prepare iron nitride and their BET surface areas were



SCHEME 1: Selective preparation routes of iron oxide and iron nitride using MOFs as a reactive template.

analyzed. The proposed preparation strategy is shown in Scheme 1.

## 2. Experimental

**2.1. Synthesis of MIL-53(Fe).** All the reagents are of analytic grade from Beijing Chemical Reagent Company and used as received. The MIL-53(Fe) was synthesized according to our prior report [25]; the mixture of  $\text{FeCl}_3 \cdot 6\text{H}_2\text{O}$ , terephthalic acid, N,N'-dimethyl formamide (DMF), and hydrofluoric acid (HF) with molar ratios of 1:1:280:2 was heated in Teflon-lined autoclaves. In order to investigate the effect of the crystallinity on the BET surface area, the mixtures were heated at  $150^\circ\text{C}$  for 1 day and 3 days. A yellow powder MIL-53(Fe), loaded with DMF inside its pores, was obtained by filtration method. To remove the occluded DMF, the sample was heated at  $150^\circ\text{C}$  in air atmosphere overnight and then cooled down to room temperature. To further extract the residual traces of DMF, the sample was stirred with a large volume of deionized water (1.0 g of MIL-53 in 500 mL of water) for 4~6 hours and was filtered, and then it was dried at room temperature in air atmosphere.

**2.2. Synthesis of Iron Oxide.** The conventional  $\alpha\text{-Fe}_2\text{O}_3$  nanoparticle was prepared by heating the mixture of 1.0 mol/L  $\text{Fe}(\text{NO}_3)_3$  solution and 2.0 mol/L citric acid solution with the molar ratio of 1:1 at  $90^\circ\text{C}$ , dropwise adding the glycol of a dispersant into the mixture until it became viscous, and then the mixture was dried at  $120^\circ\text{C}$  for 12 h in a crucible to form a gel. Finally, the gel was calcined at  $550^\circ\text{C}$  for 2 h to obtain  $\text{Fe}_2\text{O}_3$  powder, with the obtained sample designated as FO-0.

The as-synthesized iron precursors (MIL-53(Fe)) were positioned at the end of the quartz tube. The quartz tube was then mounted in the middle of the tube furnace. A flow of air was introduced into the quartz tube at a rate of 30 mL/min and was heated to  $400^\circ\text{C}$  for 5 h at a rate of  $10^\circ\text{C}/\text{min}$ . Then, the system was allowed to cool naturally to room temperature. The two  $\alpha\text{-Fe}_2\text{O}_3$  samples were then

collected designated as FO-1 and FO-2, corresponding to the reaction time of 1 day and 3 days, respectively.

**2.3. Synthesis of Iron Nitride.** The as-synthesized iron precursors (MIL-53(Fe), FO-0 and FO-2) were placed in a quartz tube and treated in a flow of nitrogen (30 mL/min) at 150°C to remove air in the system. Then, the precursors were heated in NH<sub>3</sub> flow (60 mL/min) at a rate of 10°C min<sup>-1</sup> to 500°C for 10 h. After that, the sample was cooled naturally to room temperature, then flowing 1% O<sub>2</sub>/N<sub>2</sub> for passivation treatment to sample surface. The products were denoted as FN-1, FN-2, FN-3, and FN-4, corresponding to MIL-53(Fe)'s with the different reaction time of 1 day and 3 days and the different iron precursors of FO-0 and FO-2, respectively.

**2.4. Characterization Techniques.** X-ray diffraction (XRD) measurements were performed using a Rigaku D/MAX-2500 X-ray diffractometer with CuK $\alpha$  radiation. Samples were analyzed over a range of 5–80° $2\theta$  using a step scan mode with a step rate of 4°/min. Scanning Electron Microscopy (SEM) measurements were performed using a FEI Quanta 200F microscope. Nitrogen adsorption experiments of samples were performed on an ASAP 2020 micropore analyzer. The MIL-53(Fe) samples were evacuated at 150°C for 12 h prior to exposing them to nitrogen gas, while the other samples were evacuated at 300°C for 12 h. Their surface areas were calculated using the BET equation and the volumes were determined using the BJH method.

### 3. Results and Discussion

**3.1. XRD Patterns.** To probe the effect of MOFs crystallinity on the preparation strategies, we had synthesized MIL-53(Fe) with different crystallization time. As shown in Figure 1, the XRD patterns of MIL-53(Fe), synthesized with different crystallization time, were similar with our prior report [24]. Relative crystallinity was calculated based on the integrated areas of the MIL-53(Fe) characteristic XRD diffraction peaks at  $2\theta = 9.26^\circ, 11.1^\circ, 16.38^\circ, 17.2^\circ, 18.6^\circ$ , and  $22.3^\circ$  using Origin software after baseline correction. By calculation, the MIL-53(Fe), with shortened crystallization time, was provided with the relative crystallinity of 82%.

The samples of MIL-53(Fe) with different crystallization time were calcined to obtain Fe<sub>2</sub>O<sub>3</sub> powders; their XRD patterns are displayed in Figure 2. As shown in Figure 2, the XRD patterns of FO-1 and FO-2 were similar with that of FO-0 and all the diffraction peaks were able to be assigned to  $\alpha$ -Fe<sub>2</sub>O<sub>3</sub> with a rhombohedral phase (JCPDS card number 33-0064). Also, the results suggested that the hematite could be prepared from the iron-based metal organic framework (Fe-MOF) serving as reactive hard templates. Compared with the relative crystallinity of FO-1 and FO-2, fewer differences than those of MIL-53 used as hard templates existed. The result indicated that MIL-53 possessed little effects on the material crystallinity.

After nitriding, the FN-3 and FN-4 samples from the  $\alpha$ -Fe<sub>2</sub>O<sub>3</sub> precursors showed polycrystalline mixtures consisting mainly of  $\alpha$ -Fe<sub>2</sub>N and  $\gamma'$ -Fe<sub>4</sub>N (Figures 3(c) and 3(d)).

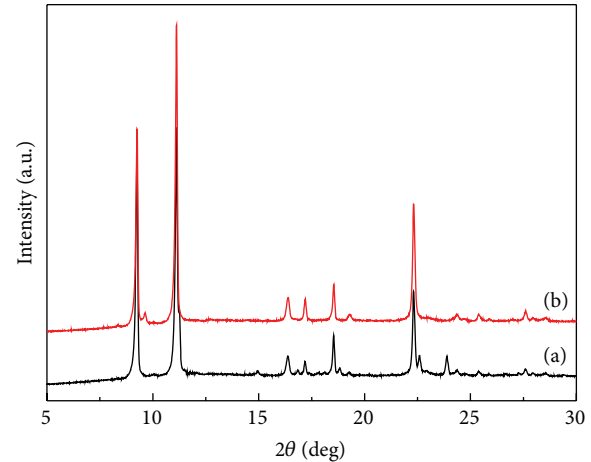


FIGURE 1: XRD patterns of MIL-53 (Fe) samples with different crystallization time. (a) 1 day, (b) 3 days.

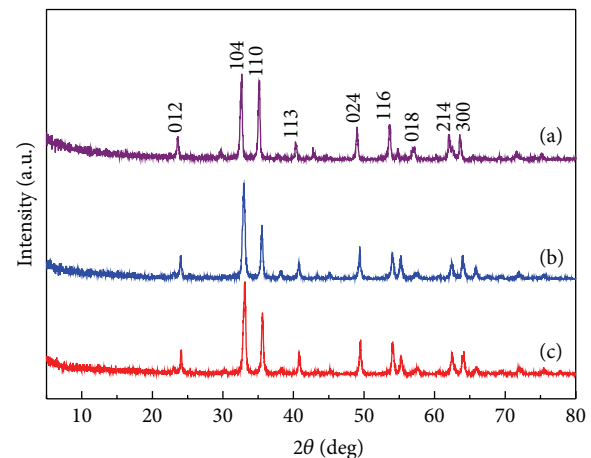


FIGURE 2: XRD patterns of the iron oxide samples. (a) FO-0, (b) FO-1, and (c) FO-2.

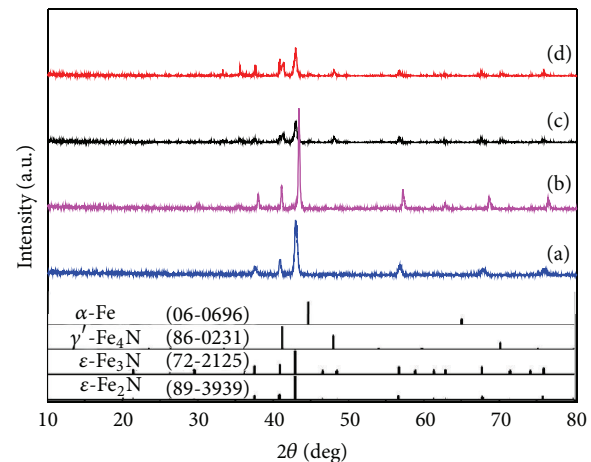


FIGURE 3: XRD patterns of the iron nitride samples. (a) FN-1, (b) FN-2, (c) FN-3, and (d) FN-4.

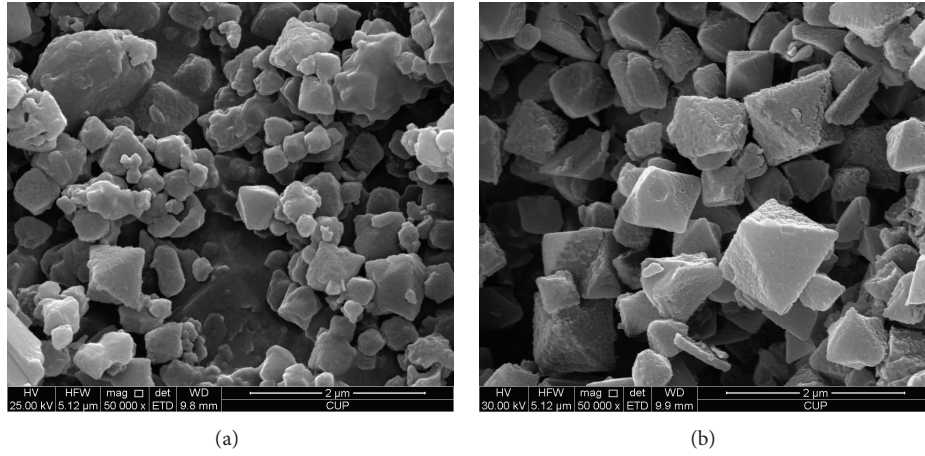


FIGURE 4: SEM images of MIL-53 (Fe) samples. (a) 1 day, (b) 3 days.

However, the FN-1 and FN-2 samples all produced  $\alpha$ -Fe<sub>2,3</sub>N; almost no peaks related to  $\gamma'$ -Fe<sub>4</sub>N were observed. Usually, iron first undergoes initial nitriding to Fe<sub>4</sub>N, and a further nitridation occurs to form Fe<sub>2,3</sub>N (or Fe<sub>3</sub>N<sub>1+x</sub>) and Fe<sub>2</sub>N. Here, given the same nitriding conditions, MIL-53(Fe) underwent further nitridation to form  $\alpha$ -Fe<sub>2,3</sub>N. It was mainly attributed to MIL-53(Fe)'s 3D open microporous system facilitating the contact of NH<sub>3</sub>. Compared with FN-1 and FN-2, the better the crystallinity of MIL-53(Fe) was, the better the crystallinity of the resulting  $\alpha$ -Fe<sub>2,3</sub>N was. The results presented that well-crystallized MIL-53(Fe) was necessary for the formation of iron nitride with high crystallinity.

**3.2. SEM Images.** SEM images given in Figure 4 showed that the MIL-53(Fe) sample possessed an octahedral morphology; its content and uniformity varied depending on the material crystallinity. The low-crystallinity samples prepared by shortening the crystallization time exhibited some irregular blocks, which were unformed crystals and unreacted raw materials. Further increasing crystallization time may promote irregular particles evolving into clear-cut submicron-sized MIL-53 octahedral crystals.

The morphologies of the oxidized products are shown in Figure 5. The conventional FO-0 (Figure 5(a)) showed compact monodisperse nanospheres with the diameter of approximately 50 nm. However, the other samples from MIL-53(Fe) (Figure 5(b)) presented loosely aggregated particles. Among them, FO-1 prepared from MIL-53(Fe) with low crystallinity exhibited irregular particles with the diameters of about 150 nm. Interestingly, the FO-2 sample (Figure 5(c)) from well-crystallized MIL-53(Fe) exhibited octahedral crystals with the size of about 700 nm, faithfully retaining the octahedral morphology of MIL-53(Fe). It demonstrated that the high crystallinity of MIL-53(Fe) was necessary for the formation of  $\alpha$ -Fe<sub>2</sub>O<sub>3</sub> with a regular octahedral morphology. Although a variety of  $\alpha$ -Fe<sub>2</sub>O<sub>3</sub> morphologies were reported in some literatures, the octahedral morphology herein, as far as we know, is the first example. Also, the iron oxide with the octahedral morphology was creatively employed to prepare iron nitride.

In this work, the morphologies of iron nitrides prepared by different strategies are given in Figure 6. The samples from MIL-53(Fe) (Figures 6(a) and 6(b)) showed loosely aggregated particles with rich interparticle porosities. The iron nitride FN-3 corresponding  $\alpha$ -Fe<sub>2</sub>O<sub>3</sub> had compactly aggregated particles. Interestingly, the FN-4 samples from MIL-53 oxide produced peculiar coralloid iron nitrides (Figure 6(d)). It could be because the nitriding temperature led to the disrupting of the MIL-53(Fe) framework; the octahedral morphology disappeared in iron nitride images.

**3.3. N<sub>2</sub> Adsorption Isotherms.** The textural properties and the isotherms of samples were characterized by the N<sub>2</sub> adsorption isotherms. N<sub>2</sub> adsorption results (Figure 7 and Table 1) showed that the shortened crystallization MIL-53 sample had a BET surface area of 611 m<sup>2</sup>·g<sup>-1</sup>. The surface area was lower than 1031 m<sup>2</sup>·g<sup>-1</sup> for the completing crystallized sample. Similarly, Langmuir surface areas, pore volumes, and pore diameter reduced due to some raw materials blocking the pore. Also, the results (see Figure 8 and Table 1) exhibited that the FO-1 and FO-2 samples from MIL-53 had larger BET surface area and total pore volume than those of the conventional FO-0 sample using sol-gel method. Such higher surface areas for both were believed to benefit from the calcination of the MOFs template. Compared to the FO-1 sample, the FO-2 sample had a relatively higher BET surface of 170 m<sup>2</sup>·g<sup>-1</sup>. It illustrated that FO-2 sample was retaining not only the octahedral morphology of MIL-53(Fe) but also the microporous framework. The result was consistent with the SEM image result. As a result, it may be concluded that the crystallinity and BET surface of MOFs template had significant effects on the pore properties of iron oxide.

In addition, in accordance with these observed morphologies, nitrogen adsorption experiment results (see Figure 9 and Table 1) determined that the BET specific area of the sample FN-0~4 was 21, 41, 12, and 17 m<sup>2</sup>·g<sup>-1</sup>, respectively. The surface areas of the FN-1 and FN-2 samples prepared from MIL-53(Fe) were larger than those of FN-3 and FN-4 using  $\alpha$ -Fe<sub>2</sub>O<sub>3</sub> as the precursor. Although

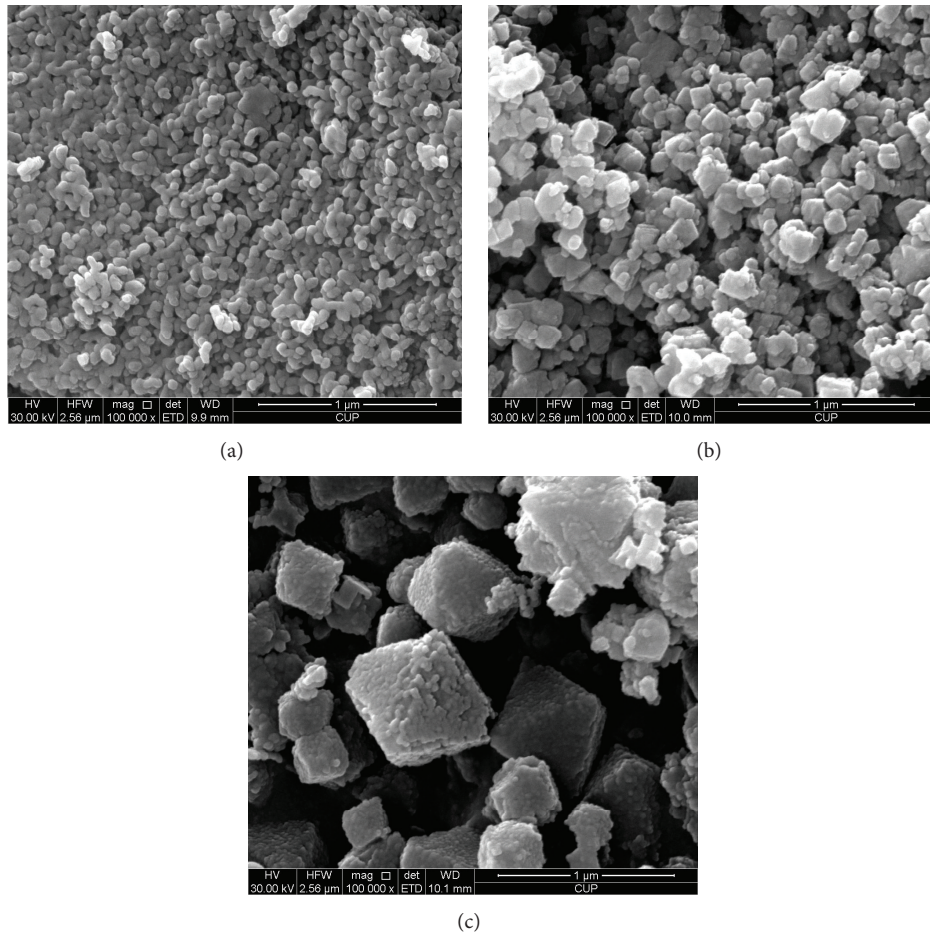


FIGURE 5: SEM images of the iron oxide samples. (a) FO-0, (b) FO-1, and (c) FO-2.

TABLE 1: Textural properties of samples.

Samples	$S_{\text{BET}}/(\text{m}^2 \cdot \text{g}^{-1})$	$S_{\text{Langmuir}}/(\text{m}^2 \cdot \text{g}^{-1})$	Pore volume/(\text{cm}^3 \cdot \text{g}^{-1})	Pore size/nm
MIL-53-a	611	854	0.39	1.85
MIL-53-b	1031	1286	0.47	2.58
FO-0	68	79	0.19	1.12
FO-1	106	118	0.20	1.7
FO-2	170	183	0.28	2.18
FN-1	21	27	0.07	2.13
FN-2	41	46	0.12	3.85
FN-3	12	18	0.02	1.5
FN-4	17	20	0.05	1.93

the nitridation reaction finally disrupted the MIL-53(Fe) framework through the decomposition of dicarboxylate units, the initial microporous crystalline framework was beneficial for the formation of interparticle porosities. Accordingly, MIL-53(Fe) was considered as a hard template to impart a certain degree of porosity to the iron nitride product. Apparently, the increasing of BET surface area for iron nitrides from MIL-53 raw material was mainly ascribed to the prior nitriding pathway.

#### 4. Conclusions

In this work, the iron nitride was creatively prepared through thermal ammonia nitridation of the iron-based metal organic framework (Fe-MOF) serving as the reactive hard template and the iron source. The results demonstrated that the iron nitride directly prepared from the MIL-53(Fe) was provided with the optimal surface area in all the preparation strategies. The high surface area was attributed to the formation of

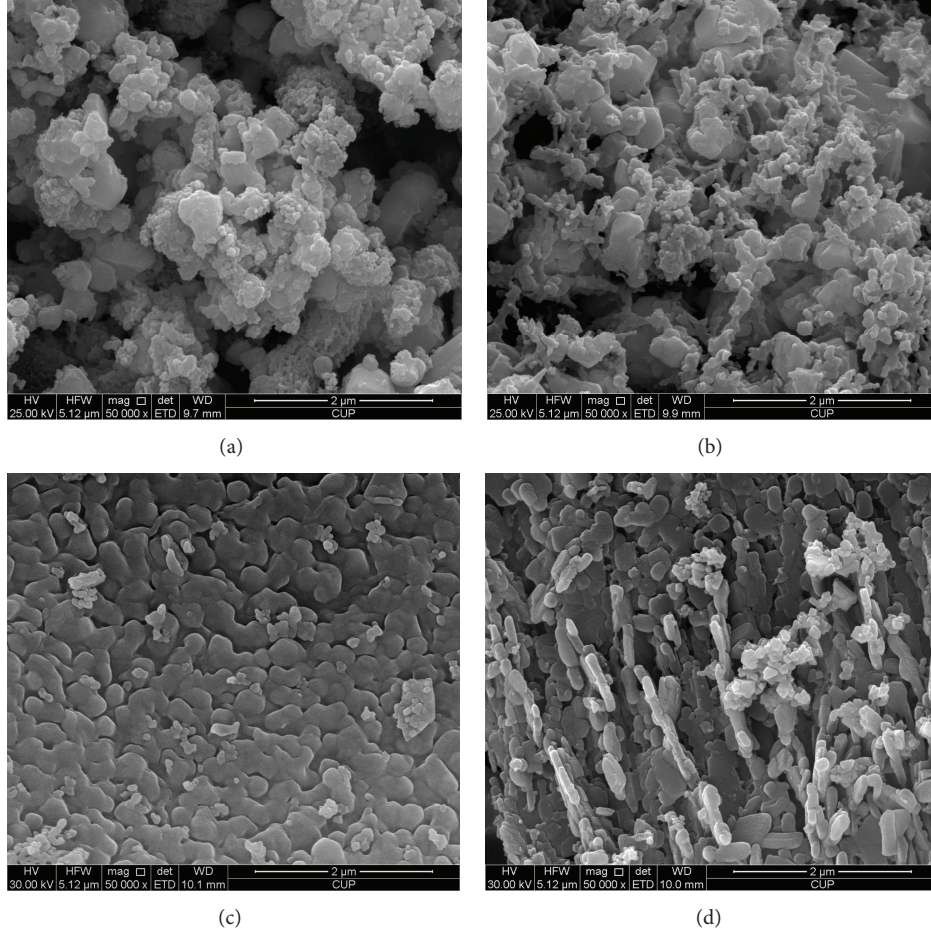


FIGURE 6: SEM images of iron nitride samples. (a) FN-1, (b) FN-2, (c) FN-3, and (d) FN-4.

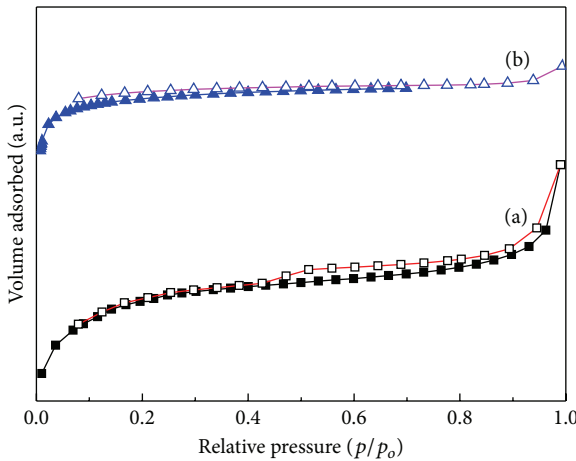


FIGURE 7: N<sub>2</sub> adsorption isotherms of MIL-53 (Fe) samples with different crystallization time. (a) 1 day, (b) 3 days.

interparticle porosity benefited from the initial microporous crystalline framework of the MIL-53(Fe). Accordingly, the MIL-53(Fe) was considered as the hard template to impart a certain degree of porosity to the iron nitride. Thus, the

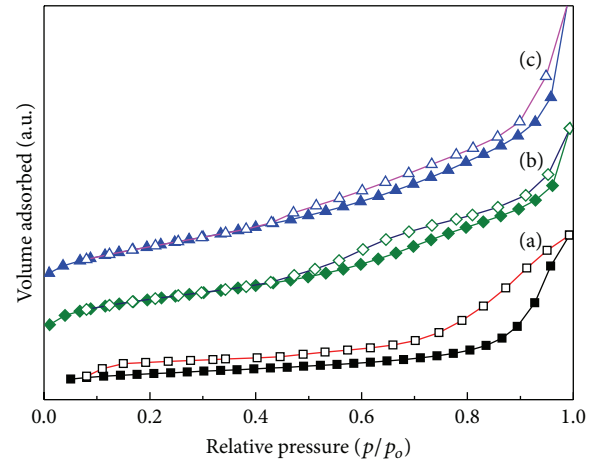


FIGURE 8: N<sub>2</sub> adsorption isotherms of the iron oxide samples. (a) FO-0, (b) FO-1, and (c) FO-2.

increasing of BET surface area for iron nitrides from MIL-53 raw material was mainly ascribed to the prior nitriding pathway. In addition, this new synthetic strategy is able to become a general approach for the preparation of late transition metal nitrides with peculiar properties.

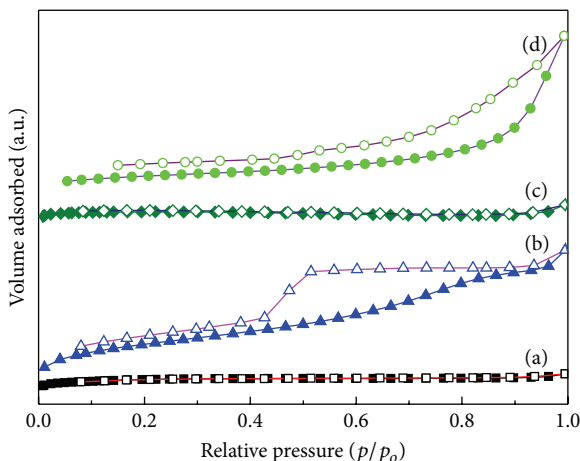


FIGURE 9:  $\text{N}_2$  adsorption isotherms of the iron nitride samples. (a) FN-1, (b) FN-2, (c) FN-3, and (d) FN-4.

## Conflict of Interests

The authors declare that there is no conflict of interests regarding the publication of this paper.

## Acknowledgment

The authors acknowledge the support of this work by the National Natural Science Foundation of China (Grant nos. 21106123 and 21303157).

## References

- [1] S. T. Oyama, *The Chemistry of Transition Metal Carbides and Nitrides*, Blackie Academic Professional, Glasgow, UK, 1996.
- [2] R. W. Chorley and P. W. Lednor, "Synthetic routes to high surface area non-oxide materials," *Advanced Materials*, vol. 3, no. 10, pp. 474–485, 1991.
- [3] L. Volpe and M. Boudart, "Compounds of molybdenum and tungsten with high specific surface area: I. Nitrides," *Journal of Solid State Chemistry*, vol. 59, no. 3, pp. 332–347, 1985.
- [4] C. H. Jagers, J. N. Michaels, and A. M. Stacy, "Preparation of high-surface-area transition-metal nitrides: molybdenum nitrides,  $\text{Mo}_2\text{N}$  and  $\text{MoN}$ ," *Chemistry of Materials*, vol. 2, no. 2, pp. 150–157, 1990.
- [5] J. B. Claridge, A. P. E. York, A. J. Brungs, and M. L. H. Green, "Study of the temperature-programmed reaction synthesis of early transition metal carbide and nitride catalyst materials from oxide precursors," *Chemistry of Materials*, vol. 12, no. 1, pp. 132–142, 2000.
- [6] X. Z. Chen, J. L. Dye, H. A. Eick, S. H. Elder, and K.-L. Tsai, "Synthesis of transition-metal nitrides from nanoscale metal particles prepared by homogeneous reduction of metal halides with an alkali," *Chemistry of Materials*, vol. 9, no. 5, pp. 1172–1176, 1997.
- [7] M. A. Sriram, P. N. Kumta, and E. I. Ko, "Interaction of solvent and the nature of adducts on the chemical synthesis of molybdenum nitride powders," *Chemistry of Materials*, vol. 7, no. 5, pp. 859–864, 1995.
- [8] J. Choi and E. G. Gillan, "Solvothermal metal azide decomposition routes to nanocrystalline metastable nickel, iron, and manganese nitrides," *Inorganic Chemistry*, vol. 48, no. 10, pp. 4470–4477, 2009.
- [9] A. Fischer, J. O. Müller, M. Antonietti, and A. Thomas, "Synthesis of ternary metal nitride nanoparticles using mesoporous carbon nitride as reactive template," *ACS Nano*, vol. 2, no. 12, pp. 2489–2496, 2008.
- [10] C. Giordano, C. Erpen, W. Yao, B. Milke, and M. Antonietti, "Metal nitride and metal carbide nanoparticles by a soft urea pathway," *Chemistry of Materials*, vol. 21, no. 21, pp. 5136–5144, 2009.
- [11] M. Yang and F. J. DiSalvo, "Template-free synthesis of mesoporous transition metal nitride materials from ternary cadmium transition metal oxides," *Chemistry of Materials*, vol. 24, no. 22, pp. 4406–4409, 2012.
- [12] Y. Koltypin, X. Cao, R. Prozorov, J. Balogh, D. Kaptas, and A. Gedanken, "Sonochemical synthesis of iron nitride nanoparticles," *Journal of Materials Chemistry*, vol. 7, no. 12, pp. 2453–2456, 1997.
- [13] K. Nishimaki, S. Ohmae, T. A. Yamamoto, and M. Katsura, "Formation of iron-nitrides by the reaction of iron nanoparticles with a stream of ammonia," *Nanostructured Materials*, vol. 12, no. 1, pp. 527–530, 1999.
- [14] Y. Han, H. Wang, M. Zhang, M. Su, W. Li, and K. Tao, "Low-temperature approach to synthesize iron nitride from amorphous iron," *Inorganic Chemistry*, vol. 47, no. 4, pp. 1261–1263, 2008.
- [15] M. Zheng, X. Chen, R. Cheng et al., "Catalytic decomposition of hydrazine on iron nitride catalysts," *Catalysis Communications*, vol. 7, no. 3, pp. 187–191, 2006.
- [16] D. Moszyński, K. Kiełbasa, and W. Arabczyk, "Influence of crystallites' size on iron nitriding and reduction of iron nitrides in nanocrystalline Fe-N system," *Materials Chemistry and Physics*, vol. 141, no. 2–3, pp. 674–679, 2013.
- [17] M. O'Keeffe, "Design of MOFs and intellectual content in reticular chemistry: a personal view," *Chemical Society Reviews*, vol. 38, no. 5, pp. 1215–1217, 2009.
- [18] B. Liu, H. Shioyama, T. Akita, and Q. Xu, "Metal-organic framework as a template for porous carbon synthesis," *Journal of the American Chemical Society*, vol. 130, no. 16, pp. 5390–5391, 2008.
- [19] R. K. Bhakta, J. L. Herberg, B. Jacobs et al., "Metal—organic frameworks as templates for nanoscale  $\text{NaAlH}_4$ ," *Journal of the American Chemical Society*, vol. 131, no. 37, pp. 13198–13199, 2009.
- [20] F. Schröder, D. Esken, M. Cokoja et al., "Ruthenium nanoparticles inside porous  $[\text{Zn}_4\text{O}(\text{bdc})_3]$  by hydrogenolysis of adsorbed  $[\text{Ru}(\text{cod})(\text{cot})]$ : a solid-state reference system for surfactant-stabilized ruthenium colloids," *Journal of the American Chemical Society*, vol. 130, no. 19, pp. 6119–6130, 2008.
- [21] S. Hermes, F. Schröder, S. Amirjalayer, R. Schmid, and R. A. Fischer, "Loading of porous metal-organic open frameworks with organometallic CVD precursors: inclusion compounds of the type  $[\text{L}_n\text{M}]_a@\text{MOF-5}$ ," *Journal of Materials Chemistry*, vol. 16, no. 25, pp. 2464–2472, 2006.
- [22] J. Kim, G. T. Neumann, N. D. McNamara, and J. C. Hicks, "Exceptional control of catalytic hierarchical carbon supported transition metal nanoparticles using metal-organic framework templates," *Journal of Materials Chemistry A*, vol. 2, no. 34, pp. 14014–14027, 2014.

- [23] P. L. Llewellyn, P. Horcajada, G. Maurin et al., "Complex adsorption of short linear alkanes in the flexible metal-organic-framework MIL-53(Fe)," *Journal of the American Chemical Society*, vol. 131, no. 36, pp. 13002–13008, 2009.
- [24] W. Cho, S. Park, and M. Oh, "Coordination polymer nanorods of Fe-MIL-88B and their utilization for selective preparation of hematite and magnetite nanorods," *Chemical Communications*, vol. 47, no. 14, pp. 4138–4140, 2011.
- [25] S. Y. Liu, Y. Zhang, Y. Meng, F. Gao, S. J. Jiao, and Y. C. Ke, "Fast syntheses of MOFs using nanosized zeolite crystal seeds in situ generated from microsized zeolites," *Crystal Growth & Design*, vol. 13, no. 7, pp. 2697–2702, 2013.

## Research Article

# One-Step Synthesis of High-Quality Water-Soluble CdSe Quantum Dots Capped by *N*-Acetyl-L-cysteine via Hydrothermal Method and Their Characterization

Chunjin Wei, Jinyu Li, Fang Gao, Shuxia Guo, Yongcui Zhou, and Dan Zhao

College of Pharmacy, South-Central University for Nationalities, Hubei, Wuhan 430074, China

Correspondence should be addressed to Dan Zhao; wqzhdpai@163.com

Received 11 August 2014; Revised 24 October 2014; Accepted 27 October 2014

Academic Editor: Qingrui Zhang

Copyright © 2015 Chunjin Wei et al. This is an open access article distributed under the Creative Commons Attribution License, which permits unrestricted use, distribution, and reproduction in any medium, provided the original work is properly cited.

Novel water-soluble CdSe quantum dots (QDs) have been prepared with *N*-acetyl-L-cysteine as new stabilizer through a one-step hydrothermal route. The influence of experimental conditions, including reaction time, molar ratio of reactants, and pH value, on the luminescent properties of the obtained CdSe QDs has been systematically investigated. The characterization of as-prepared QDs was carried out through different methods. In particular, we realized qualitative and semiquantitative studies on CdSe QDs through X-ray photoelectron spectroscopy and electron diffraction spectroscopy. The results show that the as-prepared CdSe QDs exhibit a high quantum yield (up to 26.7%), high stability, and monodispersity and might be widely used in biochemical detection and biochemical research.

## 1. Introduction

Quantum dots (QDs) are nanomaterials usually composed of II-VI or III-V elements [1]. The unique optical properties caused by their small diameters (1–10 nm) lead to their promising applications in biochemistry detections [2], biological labeling [3], cell imaging *in vivo* [4], solar battery [5], and electronic equipment [6].

Among QDs made up of II-VI group elements, CdSe QDs have attracted broad interests due to their fluorescence emission in visible light range [7]. Though selenium and telluride are both VI group elements, the spectra properties of the prepared CdSe QDs are much worse than those of CdTe QDs, because those CdSe QDs with sulphhydryl compounds (such as thioglycolate and cysteine) as stabilizers possess low quantum yields (QYs) and wide emission full width at half maximum (FWHM) (>100 nm) [8]. Since synthesis method and the used stabilizer would greatly affect the optical properties of prepared QDs, the studies on the choice of stabilizer during the synthesis process of water-soluble QDs have been widely reported [8], including thiomalic acid, thioglycolate, *N*-(2-mercaptopropionyl)glycine, glutathione, and L-cysteine. The reports on *N*-acetyl-L-cysteine (NAC) as

the stabilizer during the synthesis, however, have not been seen in literature. NAC is known as an antioxidant and impurity removal reagent and can be used to protect cells from oxidation and QDs induced cytotoxicity [9, 10]. Additionally, it possesses good water-solubility, is nonvolatile and inodorous, have excellent biocompatibility, and is friendly to the environment and its users. The commonly employed methods for direct synthesis of QDs in aqueous solution are reflux method [11–13] and microwave radiation method [14–16]. These methods, however, have obvious weaknesses: the reflux method requires long reaction time and the prepared QDs have low QYs and wide FWHM, while the microwave radiation method requires complex synthesis equipment, which greatly limits their practical applications. The hydrothermal route [17] is a newly developed hydrothermal route for direct synthesis of water-soluble QDs in an airtight reaction vessel (autoclave) under high pressure and temperature. The high temperature (usually supercritical temperature or close to critical temperature) speeds up the growth of QDs, decreases the surface defects, and thus reduces the probability of fluorescence quenching induced by irradiative decay and improves the fluorescence efficiency of prepared QDs [9]. Compared with core/shell CdSe/CdS QDs

prepared by two-step method, the hydrothermal method allows rapid synthesis of QDs through one-step process with stabilizer simultaneously as the sulfur source. The simple synthesis process is thus an ideal method to improve the optical property of prepared QDs.

In this paper, we report the synthesis of high-quality water-soluble CdSe QDs through one-step hydrothermal method and discuss the impacts of important experiment parameters (reaction time, pH, feed ratio, etc.) on the optical properties of prepared QDs. The synthesized CdSe QDs have been characterized through fluorescence spectroscopy, UV absorption spectroscopy, high resolution transmission electron microscopy (HRTEM), X-ray powder diffraction (XRD), X-ray photoelectron spectroscopy (XPS), and electron diffraction spectroscopy (EDS), and their morphology, crystal structure, optical properties, and element composition have been studied with these means. The prepared CdSe QDs meet the requirements for the fluorescence materials in biological labeling and will surely have promising applications in biochemical detection and biomedical researches.

## 2. Experimental Procedures

**2.1. Chemicals.** Selenium (reagent powder) was purchased from Shanghai Mei Xing Chemical Co., Ltd. CdCl<sub>2</sub>, rhodamine 6G, and sodium borohydride (NaBH<sub>4</sub>) were obtained from Sinopharm Chemical Reagent. NAC was purchased from Sigma. All chemicals used were of analytical grade or of the highest purity available. All solutions were prepared using Milli-Q water (Millipore) as the solvent.

**2.2. Preparation of CdSe QDs.** Sodium borohydride (0.0250 g) and selenium powder (0.0100 g) were dissolved in 3 mL ultrapure water in a 5 mL one-necked flask to produce sodium hydroselenide (NaHSe, 0.0422 mol/L). A small outlet connected to the flask was kept open to discharge the pressure from the resulting hydrogen. After approximately 30 min, the black selenium powder disappeared, and the small outlet was then completely shut. Fresh NaHSe solution was then kept in freezer for further use.

CdCl<sub>2</sub> (6.4 mmol/L) and a certain amount of NAC were dissolved in 50 mL of deionized water and stirred vigorously for 20 minutes. The precursor solution was adjusted to desired value (8.5 to 11) by stepwise addition of 1.0 mol/L of NaOH. Subsequently, the fresh NaHSe solution (0.0422 mol/L) was added to a N<sub>2</sub>-saturated mixture of CdCl<sub>2</sub> and NAC with a certain percentage and stirred vigorously for 5 minutes. The Cd<sup>2+</sup> concentration was 6.4 mmol/L in a total volume of 50 mL. The molar ratios of NAC/Cd<sup>2+</sup> used in our experiment are 1.2:1, 2.0:1, 2.4:1, 3.0:1, and 3.6:1, in sequence. The molar ratios of Se<sup>2+</sup>/Cd<sup>2+</sup> used in our experiment are 0.025:1, 0.05:1, 0.10:1, 0.15:1, and 0.20:1, in sequence. Finally, the resulting mixture was put into a 50 mL Teflon-lined stainless steel autoclave. It was loaded in an oven at 200°C for a specified time (50 to 70 min) and then cooled to the room temperature by a hydrocooling process.

To remove NAC-Cd complexes at the end of the synthesis, cold 2-propanol was added to the reaction mixture

to precipitate NAC-capped CdSe QDs. The as-prepared products were dried overnight under vacuum at 40°C for further experiments.

**2.3. Characterization.** UV-visible absorption spectra were acquired with a Lambda-35 UV/visible spectrophotometer (PerkinElmer Company) to determine the absorption of QDs. Fluorescence spectra were recorded on a LS55 spectrophotofluorometer (PerkinElmer Company). All optical measurements were performed at room temperature under ambient conditions. The HRTEM sample was prepared by dropping an aqueous CdSe QDs solution onto an Agar carbon-coated copper grid (400 meshes) with the excess solvent evaporated. The HRTEM image was obtained via JEM-2100 (HR) transmission electron microscope (Japan Electron Optics Laboratory CO., Ltd.). XRD spectrum was recorded on a Shimadzu XRD-2000 X-ray diffractometer. EDS spectrum was captured with an FEI Quanta 200 scanning electron microscope equipped with an energy dispersive X-ray spectrometer. XPS measurements were acquired with a Leybold Heraeus SKL 12 X-ray photoelectron spectrometer. The QY of CdSe QDs was measured according to the literature [18]. Rhodamine 6G in ethanol was chosen as the reference standard (QY = 95%).

## 3. Results and Discussion

**3.1. Influence of Reaction Time.** Since the optical properties of the prepared CdSe QDs are greatly influenced by a series of experimental parameters, such as reaction time, feeding ratio of the reaction reagents, and the pH value, the optimizing experiments were carried out in order to acquire the high-quality QDs.

The reaction temperature is a very important factor that influences optical properties of the prepared QDs. The low temperature (<170°C) would decrease the reaction rate, prolong the reaction time, and consequently lead to the low QYs of the prepared QDs. The high reaction temperature, on the other hand, will produce white precipitates in the autoclave together with pungent odor, which may be the result of the decomposition of NAC under such high temperature, losing its ability as stabilizer. Therefore, the optimum reaction time is in the range of 170 to 210°C.

With other reaction parameters fixed ([Cd] = 6.4 mmol/L, n(Cd):n(Se):n(NAC) = 1.0:0.05:3.0, pH = 9, and reaction temperature at 200°C), experiments were carried out to examine the impact of reaction time (50–70 min) upon the quality of prepared CdSe QDs. As shown in Figure 1, different from the obvious redshifts of the emission peak of NAC-capped CdTe QDs with the prolonged reaction time [17], the emission peaks of CdSe QDs show no obvious shift (540–555 nm) with the increase of reaction time, and their FWHM of fluorescence spectra (26–31 nm) as well as absorption peaks of UV spectra (516–532 nm) also generally stay stable. The QYs of the prepared QDs, however, are greatly influenced by the reaction time. The CdSe QDs prepared at 65 min possess the highest QY. The mechanism of this phenomenon is that at the initial stage of the reaction, NAC

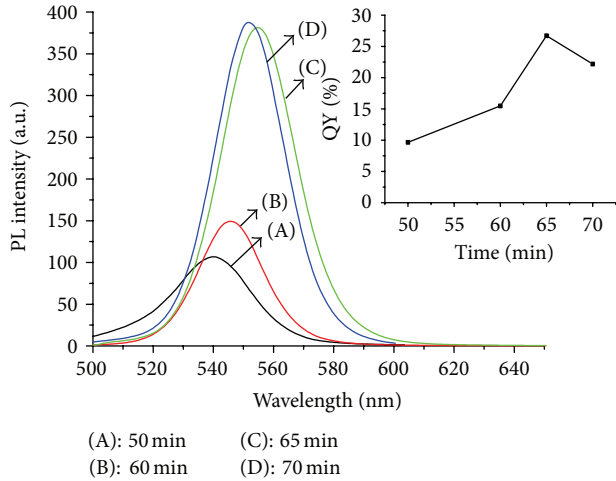


FIGURE 1: Corrected PL spectra of NAC-capped CdSe QDs prepared at various reaction times; the inset shows the QYs of these prepared QDs.

combines with the surface of CdSe QDs as the ligand, while with the reaction continuing, NAC decomposes under high temperature, releases  $S^{2-}$  into the solution, and forms CdS with the Cd ions on the surface of CdSe QDs. The formed CdS through alloying reaction can decrease the surface defects of the QDs and thus improves their QYs. When the reaction time is over 65 min, the overdecomposition of NAC would deprive its ability as stabilizer and thus fails to synthesize water-soluble QDs [9].

**3.2. Influence of Molar Ratio of Se to Cd.** The molar ratio of Se to Cd during the synthesis would greatly influence the element composition of the prepared QDs and thus impact the QYs of the prepared CdSe QDs. With other experiment parameters fixed ( $[Cd] = 6.4 \text{ mmol/L}$ ,  $n(Cd) : n(NAC) = 1.0 : 3.0$ ,  $pH = 9$ , reaction temperature at  $200^\circ\text{C}$ , and reaction time at 65 min), the molar ratios of Se to Cd were gradually increased from 0.025 to 0.20. As shown in Figure 2, the change of molar ratio of Se to Cd does not produce obvious influence upon the emission peak of prepared CdSe QDs, with their emission peak mainly at approximately 554 nm, but it shows great impact on the QYs of prepared QDs. The QYs of QDs reach the maximum when  $n(\text{Se})/n(\text{Cd})$  is at 0.05. The high molar ratio of Se to Cd would increase Se content in the prepared CdSe QDs, and the easy oxidation of Se on the surface of QDs would produce many nonradioactive combination sites, leading to the degradation of QY.

**3.3. Influence of pH of Precursor Solution.** Since QDs are prone to aggregate under acid environment, the impacts of alkaline condition ( $\text{pH} = 8.5\text{--}11$ ) of the precursor solution on the prepared CdSe QDs were the focus of our research. As shown in Figure 3, with other synthesis parameters fixed ( $[Cd] = 6.4 \text{ mmol/L}$ ,  $n(Cd) : n(\text{Se}) : n(NAC) = 1.0 : 0.05 : 3.0$ , reaction time at 65 min, and reaction temperature at  $200^\circ\text{C}$ ), the result shows that the pH also sets no obvious impact

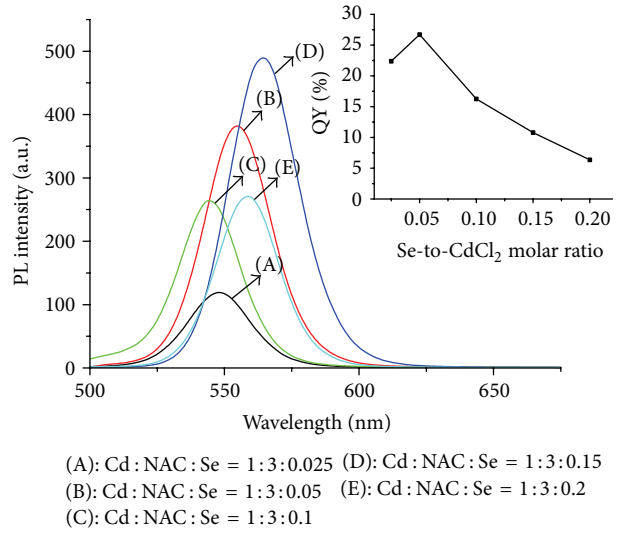
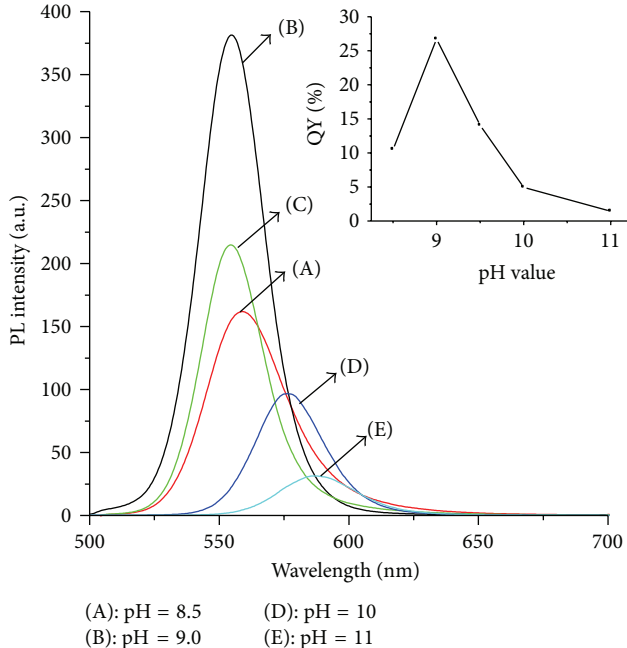


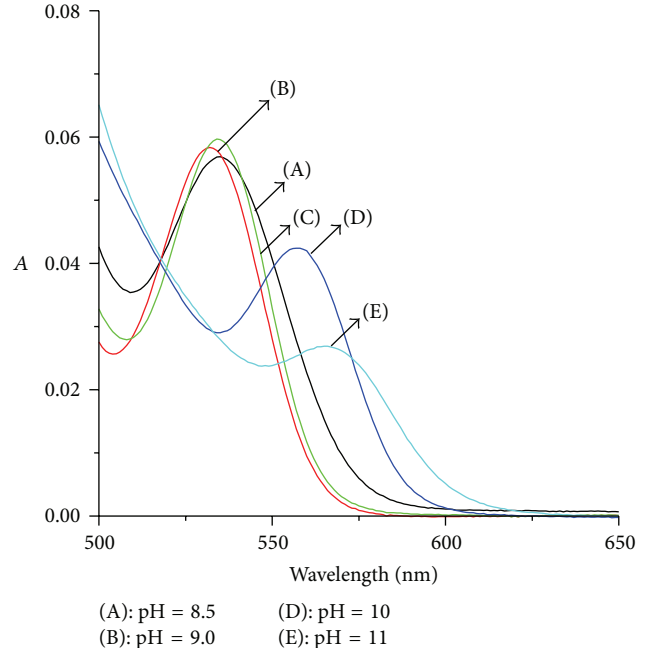
FIGURE 2: Corrected PL spectra of NAC-capped CdSe QDs grown at different  $n(\text{Se})/n(\text{Cd})$  values; the inset shows the QYs of these prepared QDs.

on the emission peak of fluorescence spectra (555 nm) and absorption peak of UV spectra (533 nm) when pH value is in the range of 8.5 to 9.5. However, when pH reaches the range of 9.5 to 11.0, the emission peak red-shifts to 589 nm and the UV absorption peak red-shifts to 566 nm, showing that the alkaline environment is beneficial to the reaction speed of the synthesis and further increases the particle diameter of the prepared QDs. The QY reaches the maximum when the pH is at 9.0.

**3.4. Influence of Molar Ratio of NAC to Cd.** With other experiment parameters fixed ( $[Cd] = 6.4 \text{ mmol/L}$ ,  $n(Cd) : n(\text{Se}) = 1 : 0.05$ ,  $pH = 9$ , reaction time at 65 min, and reaction temperature at  $200^\circ\text{C}$ ), the impacts of varied amount of the stabilizer NAC upon the prepared CdSe QDs have been studied. As shown in Figure 4, when the molar ratio of Cd to NAC reaches 1 : 3, the QY of prepared QDs is the highest, and the higher or lower molar ratio would both lead to decreased quantum yield. Since the effect of stabilizer is to inactivate the surface defects of QDs to decrease the nonradioactive recombination, the concentration of the stabilizer is of great significance for the optical properties of prepared QDs. The improper concentration of the stabilizer would greatly lead to debased fluorescence efficiency. The experiments showed that low molar ratio of NAC to Cd (1.2 : 1) led to weak fluorescence intensity, which may be the result of small amount of NAC capped on the surface of QDs caused by shortage of combination sites [8]. When the molar ratio of NAC to Cd rose to 3 : 1, the fluorescence intensity of prepared CdSe QDs is greatly improved with the emission peak red-shifting from 523 nm to 555 nm and the absorption peak red-shifting from 500 nm to 523 nm. This is because the high ratio of NAC would greatly lessen the surface defects on the surface of QDs [9, 10]. The  $S^{2-}$  ions released from the decomposition of NAC under high temperature dope

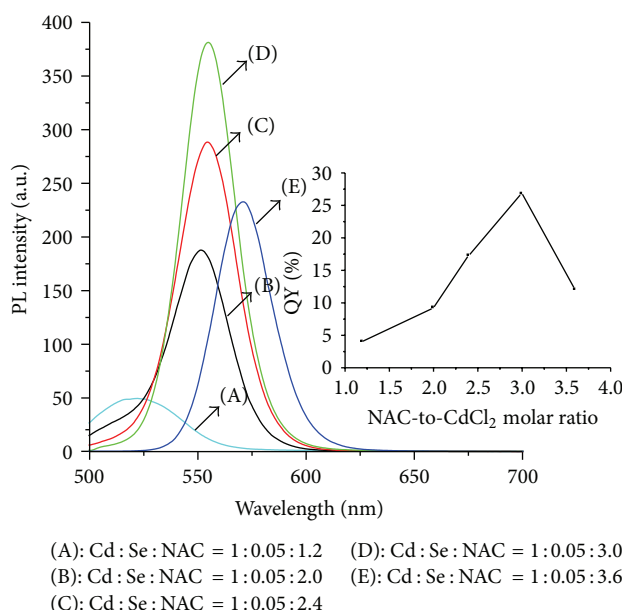


(a)

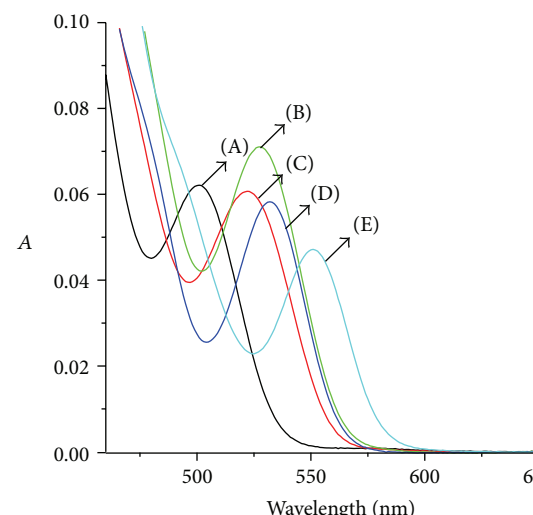


(b)

FIGURE 3: (a) Corrected PL spectra and (b) UV-visible absorption spectra of NAC-capped CdSe QDs grown at different pH values; the inset shows the QYs of these prepared QDs.



(a)



(b)

FIGURE 4: (a) Corrected PL spectra and (b) UV-visible absorption spectra of NAC-capped CdSe QDs grown at different  $n(\text{NAC})/1(\text{Cd})$  values; the inset shows the QYs of these prepared QDs.

with Cd and form CdS onto the surface of QDs, effectively inactivating the surface defects of QDs [9]. Moreover, the formation of CdS can increase the particle diameter of the QDs and decrease the band gap energy, leading to the red shift of the absorption peak. However, when the molar ratio

is too high, the formation of more stable dithio complexes between NAC and Cd can lessen the concentration of free Cd ions, increase the molar ratio of Se in the prepared CdSe QDs, and lead to more surface defects and thus low QYs [17].

Through a series of optimal experiments, the optimum synthesis parameters for NAC-capped CdSe QDs have been acquired:  $[Cd] = 6.4 \text{ mmol/L}$ ,  $n(Cd) : n(Se) : n(NAC) = 1 : 0.05 : 3.0$ , reaction temperature at  $200^\circ\text{C}$ , reaction time at 65 min, and pH = 9.0. The QY of prepared CdSe QDs under such optimum condition is 26.7%. The properties of QDs have been examined via HRTEM, XRD, XPS, and EDS, and the mechanism of S ions doping on the surface of CdSe QDs has been further proven *via* these characterization methods.

**3.5. Characterization via XRD and HRTEM.** The morphology of the as-prepared NAC-capped CdSe QDs was studied by HRTEM. Figure 5 depicts the HRTEM image for as-prepared nanoparticles; the HRTEM image of single QD and electron diffraction pattern (SAED) are shown as insets, demonstrating the relatively narrow size distribution and spherical morphologies of the prepared QDs. The presence of lattice planes in the high resolution image confirms that the nanocrystals have better crystallinity which is further supported by the SAED pattern. In addition, it is noticed that the as-prepared nanoparticles possess good dispersivity. The HRTEM images of the prepared nanoparticles show the average particles sizes of 5.4 nm. The diameter of the prepared particles is in consistency with the already reported core/shell structure model for CdSe/CdS sample (5 nm) [19] and larger than that of the CdSe nanoparticles (3.5 nm) [20], which implies a core/shell structure.

The powder XRD patterns of NAC-capped CdSe QDs are shown in Figure 6. In the XRD pattern of prepared QDs, three characteristic diffraction peaks at  $2\theta = 26.44, 43.56$ , and  $50.38$  degrees standing for the (111), (220), and (311) planes of cubic zinc blende CdSe/CdS could be recognized clearly. In comparison with the XRD pattern of the CdSe QDs [21], the three diffraction peaks only shifted slightly toward larger angles of the values for CdS [22], which demonstrated the formation of the CdS shell on the surface of the CdSe QD. This shows that NAC not only can combine onto the surface of QDs through the combination of its hydrosulfide group with Cd of QDs, but also can release  $S^{2-}$  under high temperature to form doped CdS on the surface of CdSe QDs [9, 10].

**3.6. Characterization via XPS.** XPS is a quantitative, surface analytical tool sensitive to the atomic composition of the outermost 100 Å of a sample surface. As shown in Figure 7, the Cd (3d) peak at a binding energy of 404.03 eV, Se (3d) at 53.2 eV, and S (3d) at 162.0 eV are the characteristic peaks of CdSe QDs, showing the existence of Cd, Se, and S elements.

**3.7. Characterization via EDS.** The EDS technique has been employed to probe a semiquantitative picture of the composition of the NAC-capped CdSe QDs. As shown in Figure 8, the atom percentages of Cd, Se, and S reach 45.98%, 3.96%, and 50.06%, respectively. The S element in QDs derives from the ligand NAC on the surface of QDs, and the high percentage of S is partly the result of the doped CdS on the surface of QDs, which also provides evidence for doping of S on QDs surface.

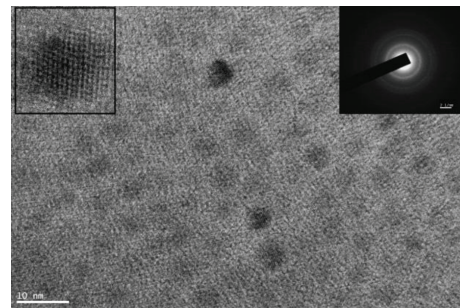


FIGURE 5: HRTEM image of NAC-capped CdSe QDs reacted for 65 min. The inset shows the HRTEM image of a single CdSe quantum dot (left) and electron diffraction (SAED) pattern (right).

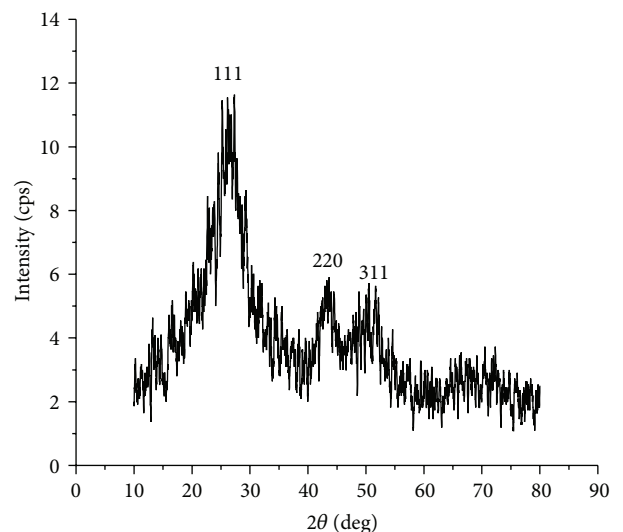


FIGURE 6: XRD pattern of NAC-capped CdSe QDs reacted for 65 min.

**3.8. The Impact of pH of QDs Solution on Their Fluorescence Intensity.** The pH value of the QDs solution would greatly influence its fluorescence intensity and thus its practical applications in biochemistry fields. As shown in Figure 9, the as-prepared QDs show excellent stability when the pH value of the solution is in the range of 4 to 9, better than MSA capped CdSe QDs [13]. The too low or too high pH value would lead to weakened fluorescence intensity. This is because the protonation of NAC under acid condition would cause the detachment of NAC from the surface of QDs, leading to the decrease of fluorescence intensity; when pH value of the solution surpasses 9, the fluorescence weakens because of the formation of the precipitant  $Cd(OH)_2$  [13]. Since the prepared NAC-capped CdSe QDs possess good stability under common biochemical conditions, they will surely be suitable for the applications in the biochemical detections.

#### 4. Conclusion

The high-quality NAC-capped CdSe QDs have been prepared *via* one-step hydrothermal method with NAC as the

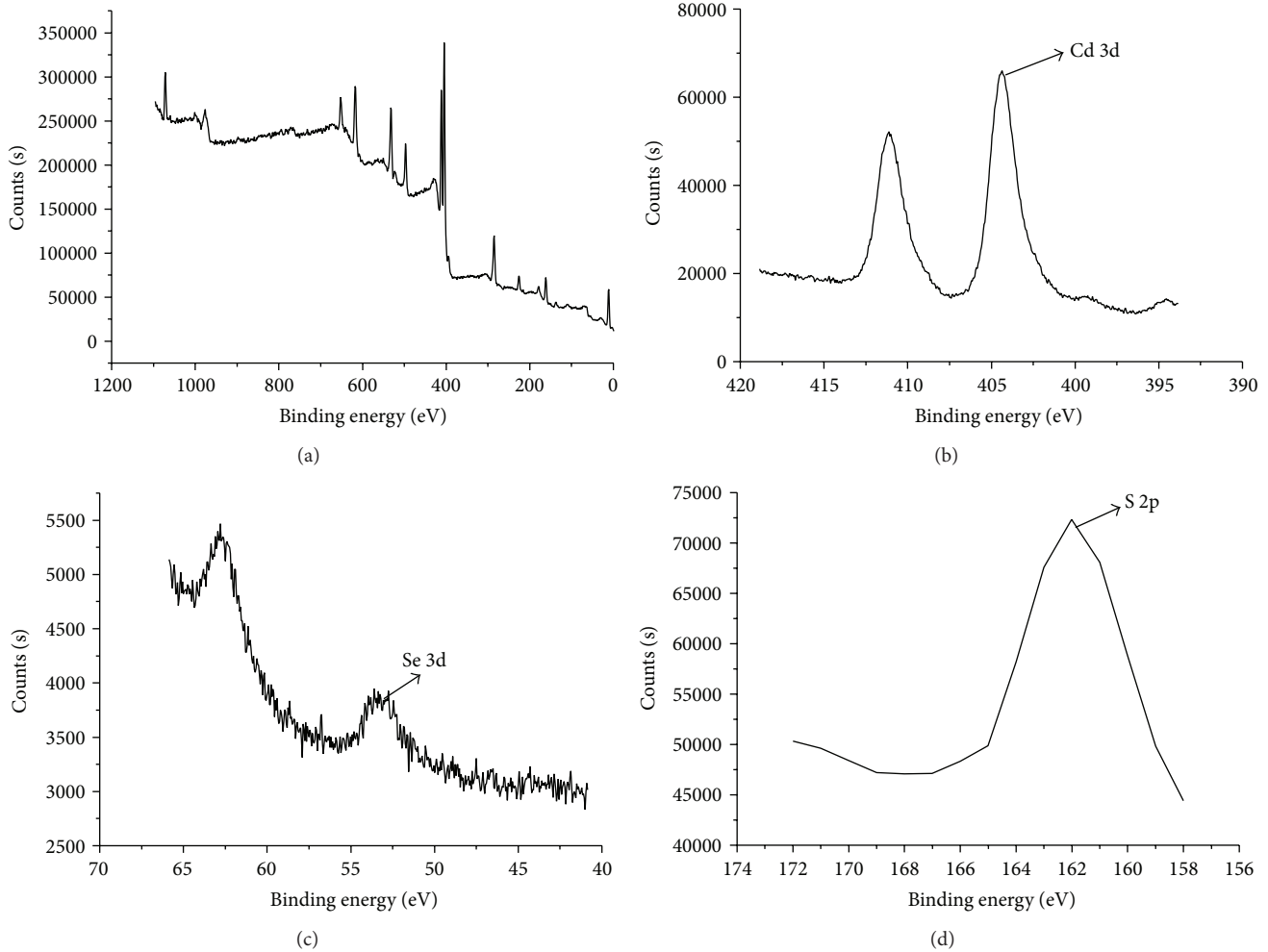


FIGURE 7: XPS spectra recorded from CdSe QDs: (a) overall picture, (b) Cd(3d), (c) Se(3d), and (d) S(2p).

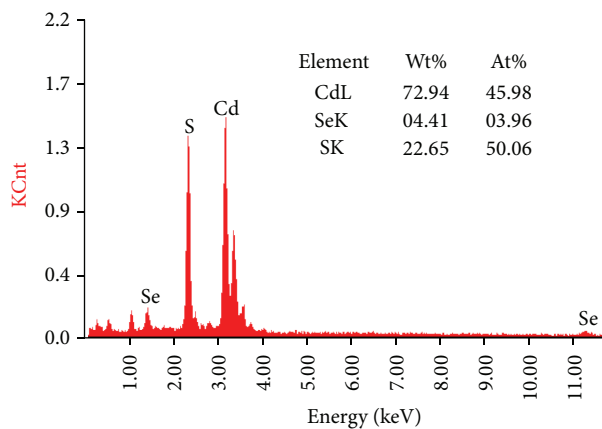


FIGURE 8: EDS spectrum of NAC-capped CdSe QDs at the molar ratio of Cd : Se = 1 : 0.05.

stabilizer. The optimum synthesis parameters have been found, and the prepared CdSe QDs have been characterized in morphology and crystal structure *via* HRTEM and XRD.

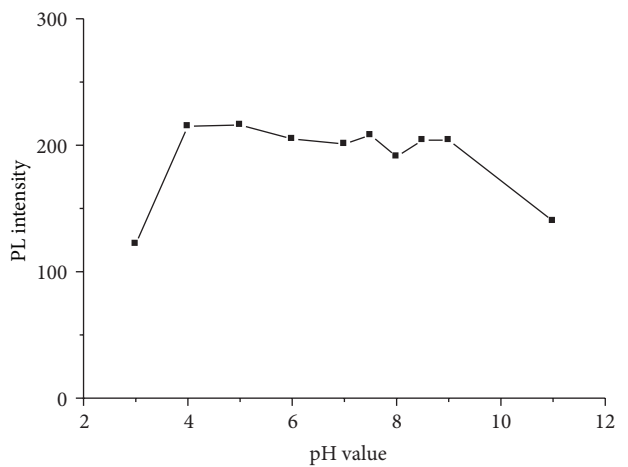


FIGURE 9: PL intensity of NAC-capped CdSe QDs at various pH values.

It is found that the particle size of CdSe QDs is smaller than that of CdSe/CdS, and their crystal structure is not

standard CdSe cubic crystal system but close to CdS cubic crystal system. The XPS image shows the existence of Cd, Se, and S elements, and S atomic percentage calculated by EDs is relatively high. All these evidences prove the doping of S on the surface of CdSe QDs. The prepared NAC-capped CdSe QDs are stable with good monodispersity and high QY, ensuring their promising application in biochemistry detections and biomedical researches.

## Conflict of Interests

The authors declare that there is no conflict of interests regarding the publication of this paper.

## Acknowledgments

This research was supported by the National Science Foundation of China (21105130) and Innovation Training Project for College Students (GXX14210).

## References

- [1] F. H. Huang, C. Cheng, and C. Sun, "Synthesis and characterization of water-soluble citrate-capped CdSe quantum dots," *Chemical Research*, vol. 24, p. 1, 2013.
- [2] Z. L. Xu, K. Y. Yi, Z. N. Ma, M. Wang, and X. F. Liu, "Synthesis of CdSe quantum dots and their applications for labeling of latent fingerprints," *Synthetic Materials Aging and Application*, vol. 42, p. 15, 2013.
- [3] Q. Wang, F. Ye, T. Fang et al., "Bovine serum albumin-directed synthesis of biocompatible CdSe quantum dots and bacteria labeling," *Journal of Colloid and Interface Science*, vol. 355, no. 1, pp. 9–14, 2011.
- [4] A. C. A. Silva, S. L. V. D. Deus, M. J. B. Silva, and N. O. Dantas, "Highly stable luminescence of CdSe magic-sized quantum dots in HeLa cells," *Sensors and Actuators B: Chemical*, vol. 191, pp. 108–114, 2014.
- [5] X. D. Guo, B. B. Ma, L. D. Wang, R. Gao, H. P. Dong, and Y. Qiu, "Electron injection and photovoltaic properties in CdSe/ZnS quantum dot sensitized solar cells," *Acta Physico-Chimica Sinica*, vol. 29, pp. 1240–1246, 2013.
- [6] L. Z. Du and Y. A. Lei, "Synthesis of high-quality Cl-doped CdSe nanobelts and their application in nanodevices," *Materials Letters*, vol. 106, pp. 100–103, 2013.
- [7] D.-W. Deng, J.-S. Yu, and Y. Pan, "Water-soluble CdSe and CdSe/CdS nanocrystals: a greener synthetic route," *Journal of Colloid and Interface Science*, vol. 299, no. 1, pp. 225–232, 2006.
- [8] K. Wang, H. Q. Pan, S. Y. Liu, X. M. Xu, and L. Y. Zhou, "Preparation and characterization of high quality CdSe quantum dots in aqueous solution," *Chemical Journal of Chinese Universities*, vol. 33, no. 12, pp. 2604–2608, 2012.
- [9] Z. K. Zhao, Z. K. He, and M. M. F. Chanand, "Synthesis and characterization of high-quality water-soluble near-infrared-emitting CdTe/CdS quantum dots capped by N-acetyl-L-cysteine via hydrothermal method," *The Journal of Physical Chemistry C*, vol. 113, p. 1293, 2009.
- [10] Q. Wang, X. Zhou, T. Fang, P. Liu, X. Li, and X. Min, "One-step growth of high-quality CdTe quantum dots via hydrothermal method and cytotoxicity evaluation," *Powder Technology*, vol. 247, pp. 81–86, 2013.
- [11] X. L. Rong, Q. Zhao, and G. H. Tao, "Aqueous synthesis of CdSe and CdSe/CdS quantum dots with controllable introduction of Se and S sources," *Chinese Chemical Letters*, vol. 23, no. 8, pp. 961–964, 2012.
- [12] Y. Li, L. Liu, X. Fang, J. Bao, M. Han, and Z. Dai, "Electro-chemiluminescence biosensor based on CdSe quantum dots for the detection of thrombin," *Electrochimica Acta*, vol. 65, pp. 1–6, 2012.
- [13] S. T. Chen, X. L. Zhang, Q. H. Zhang et al., "CdSe quantum dots decorated by mercaptosuccinic acid as fluorescence probe for Cu<sup>2+</sup>," *Journal of Luminescence*, vol. 131, no. 5, pp. 947–951, 2011.
- [14] T. Xuan, X. Wang, G. Zhu, H. Li, L. Pan, and Z. Sun, "One-step microwave-assisted synthesis of water soluble CdSe quantum dots for white light-emitting diodes with excellent color rendering," *Journal of Alloys and Compounds*, vol. 558, pp. 105–108, 2013.
- [15] D. W. Ayele, H. M. Chen, W. N. Su et al., "Controlled synthesis of CdSe quantum dots by a microwave-enhanced process: a green approach for mass production," *Chemistry*, vol. 17, no. 20, pp. 5737–5744, 2011.
- [16] M. M. Moghaddam, M. Baghbanzadeh, A. Keilbach, and C. O. Kappe, "Microwave-assisted synthesis of CdSe quantum dots: Can the electromagnetic field influence the formation and quality of the resulting nanocrystals?" *Nanoscale*, vol. 4, no. 23, pp. 7435–7442, 2012.
- [17] J. T. Li, T. M. Yang, W. H. Chan, M. M. F. Choi, and D. Zhao, "Synthesis of high-quality N-acetyl-L-cysteine-capped CdTe quantum dots by hydrothermal route and the characterization through MALDI-TOF mass spectrometry," *The Journal of Physical Chemistry C*, vol. 117, p. 19175, 2013.
- [18] R. Xie, U. Kolb, J. Li, T. Basché, and A. Mews, "Synthesis and characterization of highly luminescent CdSe-core CdS/Zn<sub>0.5</sub>Cd<sub>0.5</sub>S/ZnS multishell nanocrystals," *Journal of the American Chemical Society*, vol. 127, no. 20, pp. 7480–7488, 2005.
- [19] A. R. B. Suganthi, A. G. Joshi, and P. Sagayaraj, "A novel two-phase thermal approach for synthesizing CdSe/CdS core/shell nanostructure," *Journal of Nanoparticle Research*, vol. 14, no. 2, article 691, 2012.
- [20] K. B. Subila, G. Kishore Kumar, S. M. Shivaprasad, and K. George Thomas, "Luminescence properties of CdSe quantum dots: Role of crystal structure and surface composition," *Journal of Physical Chemistry Letters*, vol. 4, no. 16, pp. 2774–2779, 2013.
- [21] R. M. Hodlur and M. K. Rabinal, "A new selenium precursor for the aqueous synthesis of luminescent CdSe quantum dots," *Chemical Engineering Journal*, vol. 244, pp. 82–88, 2014.
- [22] A. Samadi-maybodi, F. Abbasi, and R. Akhoondi, "Aqueous synthesis and characterization of CdS quantum dots capped with some amino acids and investigations of their photocatalytic activities," *Colloids and Surfaces A: Physicochemical and Engineering Aspects*, vol. 447, pp. 111–119, 2014.

## Research Article

# Characterization of the Key Material for Elimination of PM<sub>2.5</sub> Particles in the Atmosphere

Bo Qiu, Qingshan Li, Wei Hong, and Guangzhong Xing

State Key Laboratory of Metastable Materials Science and Technology, Yanshan University, Qinhuangdao 066004, China

Correspondence should be addressed to Bo Qiu; 1755839034@qq.com

Received 6 July 2014; Revised 12 September 2014; Accepted 14 October 2014

Academic Editor: Xinqing Chen

Copyright © 2015 Bo Qiu et al. This is an open access article distributed under the Creative Commons Attribution License, which permits unrestricted use, distribution, and reproduction in any medium, provided the original work is properly cited.

In recent years, with the gradual deterioration of air quality and with the more and more frequency of haze weather phenomenon, it intrudes into the human body and brings great harm to human health when people are unprepared. The basic theory that anion could purify air and eliminate positive ion explains that anion balata modified bitumen could reduce PM<sub>2.5</sub>, and the number of anion pavement release relates to the air purification. At the same time, building materials plaza and pavement materials with many functions were designed which can release negative ions, eliminate PM<sub>2.5</sub> particles, and decompose harmful components of fuel vehicle exhaust.

## 1. Introduction

There are 30 areas, cities, and provinces, which were shrouded in the four-haze process in January 2013. However, there were only five days without haze in Beijing [1]. The report shows that only less than 1% of cities have achieved air quality standards recommended by the World Health Organization (WHO). At the same time, seven of the world's ten most polluted cities are in China. The gradual deterioration of air quality and more and more frequency of haze weather phenomenon would cause respiratory diseases, cardiovascular system, blood system diseases, reproductive system diseases, and so forth, when people are not prepared, for example, sore throat, emphysema, asthma, rhinitis, bronchitis, and other symptoms. It will lead to lung cancer, myocardial ischemia, and reperfusion injury in the long term in this environment. The main components of the haze are sulfur dioxide, nitrogen oxides, and particulate. The first two belong to the gaseous pollutants; particulate matter is finally a heavier fog and haze pollution culprit. There are toxic particulate matter sources in cities. First, it is the automobile exhaust. Second, it is exhaust gas burning coal for the winter heating in the north, and industrial production emissions, such as metallurgy, furnace or boiler, electrical, mechanical manufacturing industry, and a large number of automotive paint and building materials

production furnace combustion emissions. Finally, dust was caused by the construction sites and road traffic.

The negative ions in the air are called air vitamin, environmental health guardian, which can purify the air. It is beneficial to human health [2, 3]. The negative ion in the air is a single molecular and light ion clusters. The negative ion mainly includes hydroxide ion, oxygen anion, and carbonate ion, but the proportion of oxygen anion is large and relatively stable. In nature, the source of negative ions is mainly to stimulate the universe, sun rays, and radioactive elements in rock and soil release radiation as well as the lightning excitation, storm, waterfall, the wave friction, and other factors. In addition, the decomposition of rain water and forest and plant photosynthesis made more oxygen-enrich air.

However, artificial negative ion mainly uses high voltage electrostatic field, high frequency electric field, ultraviolet radiation, and radiation to hit water in order to make the air ionization and produce negative ion. In recent years, people found that some inorganic oxide composite powder induced negative ion in the air; some rare earth compound salt also has led to the air ionization function. The negative ions in the air have a positive effect on the growth of the body and preventing disease.

(1) Anion can improve the lung organ function and respiratory villi cleaning efficiency. (2) Aoion can reduce blood

pressure and enhance myocardial function. (3) Anion can reduce strong oxidation. Negative oxygen ions can destroy bacteria's cell membrane or the activity of cells bioplasm active enzyme, so as to achieve the purpose of antibacterial sterilization. (4) Aoion can encourage people's spirit. It could increase body alertness and enhance people's imagination, which could improve work efficiency at the same time. (5) Aoion can strengthen the immune system function. The results of the study show that nocturnal sleep in pyjamas with negative ion emission function will reduce to some extent the rectal temperature of the human body, improve the quality of sleep, and improve human immunity [4–6]. Thus, negative ion and human health are closely related, especially in the increasing pollution today.

At present, PM10 is one of the important general pollution indices in the assessment of atmospheric environment quality. When the environment aerodynamic diameter is less than  $2.5\text{ }\mu\text{m}$ , it is called PM2.5 [7, 8]. At present, people gradually realize that the particle size under the  $10\text{ }\mu\text{m}$  endangers the environment and human health; in particular, PM2.5 pollution is the most serious one. In this paper, Gu Haiyan is adopted for nanometer ion additive to prepare road asphalt material. Gu Haiyan not only looks gorgeous but also has nano-single crystalline, nanosphere, nanofiber, and nanosheet layer. Of course, the important function is to release anions. Gu Haiyan can radiate infrared light with a wavelength  $8\text{--}15\text{ }\mu\text{m}$  at ambient temperature  $20^\circ\text{C}$ , and the normal emission rate is 0.88. Since far infrared ray is very close to vibration frequency of human body cellular elements, as long as "Life waves" permeate into the body, it will cause resonance between atoms and molecules in human cells, through the resonance absorption and the heat after the friction between molecules and it will form thermal reaction, thereby promoting the rise of subcutaneous deep temperature, expanding blood capillary, and accelerating the blood circulation. It is beneficial for clearing vascular accumulation and the harmful substances of the body, removing obstruction to hinder metabolism, and reviving the organization. And then it will promote the generation of enzyme in order to activate cells, prevent aging, and strengthen the immune system. Therefore Gu Haiyan is a kind of precious stone and natural nanomineral materials.

## 2. Main Materials and Methods

**2.1. Main Materials.** Recycled rubber powder,  $20\text{--}100\text{ }\mu\text{m}$  in diameter, was obtained from Fang da huang yu Co., Ltd, Donguan. Anion additive: the anion additive of rubber modified asphalt is Gu Haiyan produced in Baotou city of Mongolia of China in this paper which is a kind of sedimentary rocks and belongs to Yellow River basin.

**2.2. Characterization of Scanning Electron Microscope (SEM).** Figure 1 is SEM images of Gu Haiyan.

Because of the specific geographical environment, coles contacting between particles, mainly point-line contacting with medium. In the process of formation rock, a series of diagenetic reactions between sedimentary components with

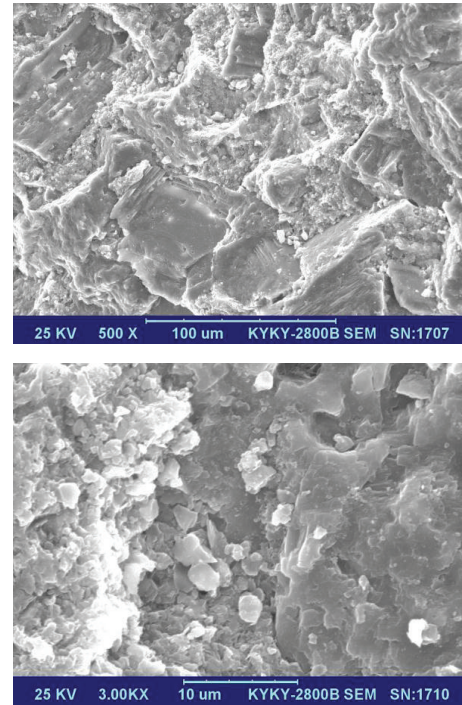


FIGURE 1: SEM images of Gu Haiyan.

pore takes place. Such structure for Gu Haiyan surface has good interfacial energy; when contacting with other polymers, it can increase the stability.

**2.3. Fourier Transform Infrared Spectroscopy (FTIR).** Figure 2 shows the FTIR spectra of the Gu Haiyan. The main characteristic peaks are  $1035\text{ cm}^{-1}\text{--}1108\text{ cm}^{-1}$ ,  $1441\text{ cm}^{-1}$ ,  $1841\text{ cm}^{-1}$ ,  $2530\text{ cm}^{-1}$ , and  $2905\text{ cm}^{-1}$ . The  $1035\text{ cm}^{-1}\text{--}1108\text{ cm}^{-1}$  belong to strong peak of S perssad.  $1441\text{ cm}^{-1}$  is crystal water peak,  $1841\text{ cm}^{-1}$  is absorb water peak, and  $2530\text{ cm}^{-1}$  is S-H perssad, which is weaker than O-H absorption band. The frequency of S-H perssad is not low when it forms hydrogen.  $2905\text{ cm}^{-1}$  is C-H perssad of the methylene.

**2.4. Analysis of XRD.** Figure 3 depicts the XRD pattern of Gu Haiyan. From the XRD diffractogram of Gu Haiyan five peaks at  $2\theta$  value of  $26.73^\circ$ ,  $31.03^\circ$ ,  $41.14^\circ$ ,  $50.6^\circ$ , and  $51.06^\circ$  have been observed. These can be assigned to  $31.03^\circ$  (104) plane of  $\text{CaMg}(\text{CO}_2)_3$ ,  $41.14^\circ$  (113) plane of carbon, and  $50.6^\circ$  (018) and  $51.06^\circ$  (116) planes of  $\text{CaZn}(\text{CO}_2)_3$ . However,  $26.73^\circ$  is of containing S perssad, because Gu Haiyan is mixture, so we cannot be sure of its plane.

The result of Gu Haiyan is consistent with XRD and FTIR. Due to existing O-H and S-H, under the action of outside world, it is easy to be knocked off electronic and generate negative oxygen ion with water vapor in the air. X-ray peak sharp is different; it was affected by temperature which is also different; through the action of high temperature and pressure, it can release negative ion. In addition, because the particle diameter of the anion additive is at the nanolevel, it is easy to release anion in the physical admixing process, and

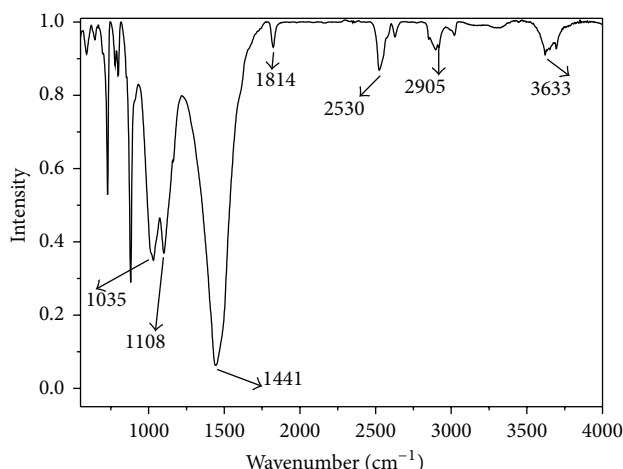


FIGURE 2: FTIR of Gu Haiyan.

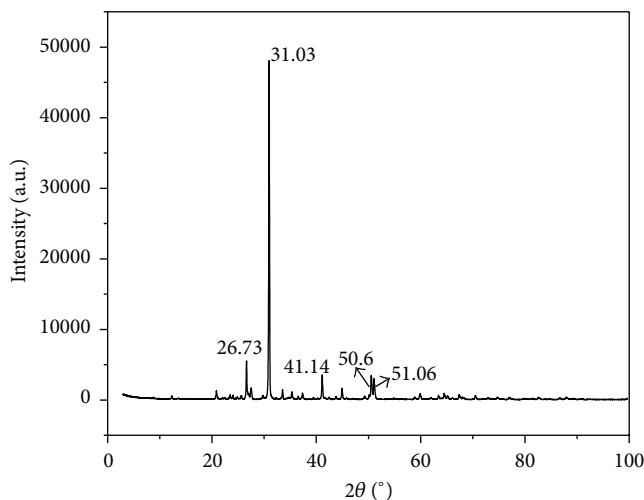


FIGURE 3: XRD of Gu Haiyan.

the miscible system is uniform and stable and thus suitable for productions.

**2.5. Rubber Modified Asphalt Mixture Preparation.** The latest micro/nanocontrollable preparation technology is to control the maximum particle below 5 microns. We developed the technology with the international advanced level which can control the particle size using the efficient equipment developed independently and a unique process, and the technology can adjust particle in the range of 0.2–5 microns. So we successfully developed anion additive using this technology. Figure 4 is negative ion Gu Haiyan additive preparation process.

**2.6. Composite Material Preparation.** Melt a small amount of asphalt after adding recipes and additives, and then stir and warm it using a Magnetic stirrer [9–11]; then make it sheared with high shearing dispersing emulsifier at a temperature of 170°C~190°C and speed of 4000 r/minute~6000 r/minute.

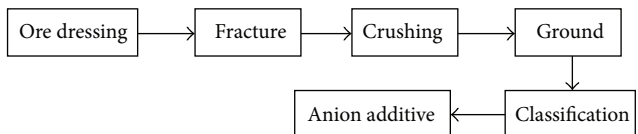


FIGURE 4: Negative ion additive preparation process.

After adding negative ions additives, cutting, cooling, and placing it for 30 minutes, then, it is the rubber modified asphalt of anion. It can be seen in the NMIR and IR that adding anion additive into rubber modified asphalt is a physical miscible process. There is only molecular interaction between the addictive and asphalt, and there is no chemical change which generates a new substance or group. Anion additives are made by opal and tourmaline material and others which can release negative ions [12].

**2.7. Sample Performance Testing and Equipment.** Testing of the asphalt, including designing the proportions of the mixture, evaluating its properties, and evaluating its road capability, was carried out in accordance with “Standard Test Methods of Bitumen and Bituminous Mixtures for Highway Engineering” (JTJ052-2000) and “Technical Specifications for Construction of Highway Asphalt Pavements” (JTGF40-2004). We then evaluated the anion release performance [13–15]. Air ion detectors (DLY-6A232) were performed by Lianteng Electronic Co., Ltd., Zhangzhou, Fujian. X-ray diffraction (D-max-Bsystem) measurements were performed by Japan’s Neo-Confucianism. FTIR (E55+FRA 106) measurements were performed by Germany Bruker Company.

### 3. The Principle of the Relationship between Weakened PM2.5 and Negative Ions Bituminous Materials

The research confirms many experts in the field of UN Air environmental, ecological level negative ions (small particle size anions) can capture dust pellets which will be agglomerated and precipitated and then remove effectively the dust of 2.5 and less 2.5 microns (PM2.5) and even one-micron particles in air which can reduce PM2.5 health hazards on human. The reason why ecological level negative ions purify the air is that ions are combined with airborne bacteria, dust, and smoke and gathered into a ball landing in order to eliminate PM2.5 hazards. Coincidentally, negative ions in the air are making Brownian motion without rules. However, Brownian motion itself is an effective way to eliminate the small dust. After anion binding particulates, it promotes Brownian motion and eliminates dust. Experiment shows that the smaller the diameter of particulates is, the more easily it is precipitated by anion. Water molecules in the air are moving without rules and imping on surface of composite material; under the action of external force, the outermost electrons of additives jump out of original track and combine with water vapor in the air or carbon dioxide, product negative oxygen ions. Figure 5 is a negative ion generation process. There are three main forms of negative ions purification of air. The first

TABLE 1: The results of asphalt pavement anion test.

Sample name		Anion concentration max (a/cm <sup>3</sup> )	Anion concentration average (a/cm <sup>3</sup> )	Temperature °C	Relative humidity %
Rubber modified asphalt anion	Sample 1	-1190	-1076	20	50
	Sample 2	-1150	-968		
Common asphalt	Sample 3	-150	-110		
	Sample 4	-180	-120		

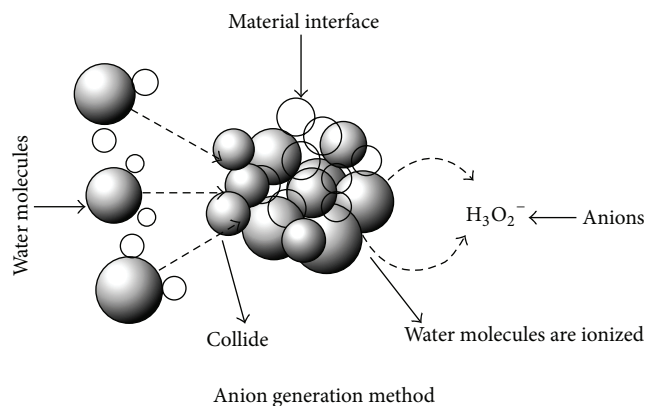


FIGURE 5: A negative ion generation method.

method is that negative ions are adsorbed on the material surface, under the gravity, sinking gradually. The second is that negative ion is adsorbed in the material porosity and influenced by gravity, sinking gradually, so as to eliminate particles and purify air. The third is that neutralization reaction happens when negative ion is mixed with positively charged particles in the air; it can also have effect on elimination of particles. Figure 6 is anion purification principle.

#### 4. Result and Discussion

Anion tire and road materials are designed in order to do the further research mechanism of anion adsorption and settling particles and friction with pavement. Energy saving and reduction mechanism are explored, in order to guide the engineering design and application of materials of anion. Through the research of rubber creep, heat resistance, friction, and aging experiments, they provide basic data for the design of roads.

In the release of negative ions, healthy environment-friendly natural asphalt composite materials, there are 3 polymer species, such as SBS resin, polyacrylamide, recycled rubber, and polyacrylate copolymer; the additives are surfactants that can release negative ions; asphalt is petroleum asphalt, coal tar pitch; natural asphalt is cloth asphalt, Xinjiang Bitumen; fillers are inorganic compounds mixed with two or more kinds of fly ash, mineral ore, and construction waste powder; The natural anion asphalt composites technology is the same as the conventional asphalt mixing technology. Anion test

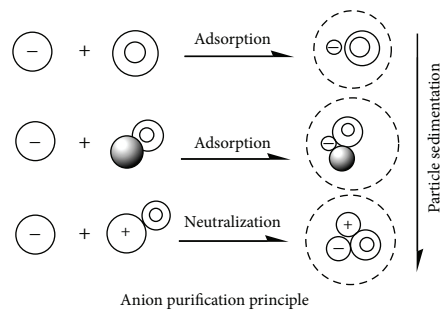


FIGURE 6: The anion purification principle.

of negative ion and general rubber modified asphalt road is shown in Table 1.

The test results prove that the rubber modified asphalt has good release negative ions, which can improve road dust and has a high value for weakening PM2.5.

#### 5. Conclusion

Anion rubber modified asphalt material can release higher concentrations of air ions than ordinary materials and effectively purify the air. The purifying principle is that anions can capture dust pellets which will be agglomerated and precipitated and then remove effectively the dust of 2.5 and less 2.5 microns (PM2.5) and even one-micron particles in air which can reduce PM2.5 health hazards on human. But the work of purifying efficiency which is corresponding with the number of anions still needs to be further studied.

#### Conflict of Interests

The authors declare that there is no conflict of interests regarding the publication of this paper.

#### References

- [1] J. Xu, G. A. Ding, and P. Yan, "It is from the analysis of component characteristics and sources of PM2.5 in Beijing area," *Journal of Applied Meteorology*, vol. 3, pp. 41–43, 2007.
- [2] B. F. Yu, Z. B. Hu, M. Liu, H. L. Yang, Q. X. Kong, and Y. H. Liu, "Review of research on air-conditioning systems and indoor air quality control for human health," *International Journal of Refrigeration*, vol. 32, no. 1, pp. 3–20, 2009.
- [3] W. X. Wang and J. J. Li, "Anion and its textiles influence on human," *Henan Textile Science and Technology*, pp. 2–4, 2002.

- [4] C. G. Sang and H. J. Zhong, "The research about anion fabric on natural fiber fabrics," *Textile Science Research*, vol. 17, pp. 4–7, 2007.
- [5] Z. Xu, Y. Wu, F. Shen, Q. Chen, M. Tan, and M. Yao, "Bioaerosol science, technology, and engineering: past, present, and future," *Aerosol Science and Technology*, vol. 45, no. 11, pp. 1337–1349, 2011.
- [6] S.-G. Lee, J. Hyun, S. Hwa Lee, and J. Hwang, "One-pass antibacterial efficacy of bipolar air ions against aerosolized *Staphylococcus epidermidis* in a duct flow," *Journal of Aerosol Science*, vol. 69, pp. 71–81, 2014.
- [7] J. Wang, Z. M. Hu, and Y. Chen, "Contamination characteristics and possible sources of PM10 and PM2.5 in different functional areas of Shanghai, China," *Atmospheric Environment*, vol. 68, pp. 221–229, 2013.
- [8] D. Mira-Salama, C. Grüning, N. R. Jensen et al., "Source attribution of urban smog episodes caused by coal combustion," *Atmospheric Research*, vol. 88, no. 3-4, pp. 294–304, 2008.
- [9] C. S. Huang and X. Huang, "Purification of anion material," *Clean and Air-Conditioning Technology*, vol. 2, pp. 45–47, 2006.
- [10] J. L. Dong, Q. S. Li, and S. Ma, "A research of anion rubber modified asphalt," *Heilongjiang Science and Technology Information*, vol. 26, p. 85, 2011.
- [11] S. L. Daniels, "'On the ionization of air for removal of noxious effluvia' (air ionization of indoor environments for control of volatile and particulate contaminants with nonthermal plasmas generated by dielectric-barrier discharge)," *IEEE Transactions on Plasma Science*, vol. 30, no. 4 I, pp. 1471–1481, 2002.
- [12] W. Hong, Q. S. Li, and G. Q. Quan, "Pavement performance and application of anion rubber-modified asphalt," *Chinese Science Bulletin*, vol. 57, no. 18, pp. 2323–2328, 2012.
- [13] *Highway Asphalt Pavement Construction Technical Standard*, JTGF04-2004, China Communications Press, Beijing, China, 2004 (Chinese).
- [14] *The Test Criterion for Highway Project Pitch and Pitch Compounds*, JTJ052-2000, China Communications Press, Beijing, China, 2000, (Chinese).
- [15] D. Wang, *Guide for Design and Construction of Asphalt Rubber and Mixture*, China Communications Press, Beijing, China, 2008 (Chinese).

## Research Article

# The Drug Metabolism and Pharmacokinetics Investigation about Baicalin Effect and Baicalein on Mice U14 Cervical Cancer

Zhanzhao Fu,<sup>1</sup> Ya Di,<sup>1</sup> Liming Gao,<sup>1</sup> Jiandong Wu,<sup>1</sup> Ming Shi,<sup>2</sup> and Fulu Zheng<sup>1</sup>

<sup>1</sup>Renmin Hospital of Qinhuangdao, No. 22 Wenhua Road, Qinhuangdao 066004, China

<sup>2</sup>Department of Biological Engineering, College of Environment & Chemical Engineering, Yanshan University, No. 438 Hebei Street, Qinhuangdao 066004, China

Correspondence should be addressed to Zhanzhao Fu; fuzhanzhaoyihao@163.com

Received 26 May 2014; Accepted 29 June 2014

Academic Editor: Tifeng Jiao

Copyright © 2015 Zhanzhao Fu et al. This is an open access article distributed under the Creative Commons Attribution License, which permits unrestricted use, distribution, and reproduction in any medium, provided the original work is properly cited.

The experiment studies the effect of baicalin and baicalein on mice U14 cervical cancer and its pharmacokinetics in mice. By using different mouse models of cancer treatment program administered and uptake kinetics experiments, tissue distribution experiment, excretion, and metabolism in experimental experiments, we found that baicalin and baicalein can improve immunity and the ability of antioxidation and inhibit the growth of tumor. The absorption of intestinal drug takes place in intestinal tract. Tissue distribution was ideal. Because of the ideal drug distribution, the liver and kidney were protected. Drug was mainly excreted through the feces and bile excretion.

## 1. Introduction

Cervical cancer is one of the most worldwide serious malignant tumors that threat the lives of women. It ranks second in malignant tumor in the world [1]. In recent years, scientists explore the prevention, treatment, chance to reduce cervical cancer incidence, and mortality. Working though many years, scientists investigate some effective drugs, but it still needs a large number of experimental data as a powerful support.

*Scutellaria baicalensis* is the roots of *Scutellaria baicalensis Georgi* with the functions of clearing heat, detoxification, hemostasis, and tocolysis. Modern pharmacy studies prove that *Scutellaria baicalensis* root contains many kinds of flavonoids, including baicalin, baicalein, wogonoside, and wogonin which are the main effective components [2]. Baicalin and baicalein perform some pharmacological activities such as antioxidant, antiradiation, antibacterial, antiviral, antitumor [2, 3]. Some researches show that after glycoside bond of baicalin and wogonoside hydrolyzed, they will produce glucuronic acid and aglycones which can be absorbed in the stomach and intestine [4]. As a prodrug of baicalein, baicalin can be hydrolyzed by the intestinal flora enzymatic into the baicalein, which can be absorbed by the colonic epithelial cells. The absorbed baicalein was immediately

reduced to baicalin, with blood circulation to the body organs and tissues; it produces some drug effect. Lots of experiments show that, due to the intestinal circulation, baicalin and baicalein perform a double-peaks phenomenon. At present, *Scutellaria baicalensis* preparations on the market mainly contain baicalin as the main component; the bioavailability is not ideal [5]. So, there is a need to explore the law of absorption of baicalin and baicalein and improve the efficacy of drugs.

In this experiment, baicalin and baicalein were discussed to explore the effects on U14 cervical cancer and its pharmacokinetics in U14 cervical cancer in mice. High performance liquid chromatography was used to detect relevant indicators [6] and provide data support for development and improvement of skullcap root.

## 2. Experiments

**2.1. Materials.** U14 cervical cancer cells taken from mice from the Chinese Academy of Medical Sciences Library of tumor cells in the level passage mice were intraperitoneally passing. Forty female Kunming mice were purchase at the Experimental Animal Center of Military Medical Sciences, Certificate of Conformity: 0023329. The body weight of

each mouse was  $22 \pm 5$  g, aging 3–6 weeks. Purchase at the Experimental Animal Center of Military Medical Sciences, Certificate of Conformity, was 0023329. Baicalin and baicalein were purchased from Chinese Herbal Medicine Company in Qinhuangdao City, Hebei Province; cyclophosphamide (CTX) was purchased from Shanxi Tai Sheng Pharmaceutical Co., Ltd., temporary NS formulated with saline to the required concentration (25 mg/kg) (25 mg/kg); other chemical reagents were analytical grade.

**2.2. U14 Cells of Mice Abdominal Cavity Passing and the Establishment of U14 Cervical Cancer in Mice Model.** Two female mice were selected and disinfected and then the mice were injected into cervical cancer U14 cells [7, 8]. After 5 days, mice abdomen was markedly swollen, diet and activity decreased significantly, and mice ascites was collected. The ascites were centrifuged for 5 min, the supernatant was removed, the added amount of NaCl solution was washed once, adding NaCl solution, adjustment cell concentration of  $2 \times 10^6$ /mL. Subcutaneously injected U14 cells 0.2 mL into per mouse at the left fore alar [6, 7].

**2.3. Research Methods of Antitumor Effect.** The 40 tumor-bearing mice were randomly divided into four groups of 10 [9, 10]. According to the following scheme to drug treatment.

The first group: baicalin (40 mg/kg), lavage, 10 a tumor-burdened mouse, each 0.2 mL.

The second group: radix scutellariae (40 mg/kg), lavage, 10 a tumor-burdened mouse, each 0.2 mL.

The third group: cyclophosphamide (25 mg/kg), injected, 10 a tumor-burdened mouse, each 0.1 mL.

The forth group: physiological saline, lavage, 10 a tumor-burdened mouse, each 0.2 mL.

All mice were administered 1 times/d, continuous administration for 15 d, monitoring changes of tumor volume and weight. The 16th day, eyeball blood, then dissected mouse to collect tumor, thymus, spleen, and liver, weighed and make a record.

The calculation of inhibition rate [11] is as follows:

the tumor inhibition rate = (tumor weight of the control group – tumor weight of the control group)/ tumor weight of the control group  $\times 100\%$ .

Thymus index [11] is as follows:

thymus index = thymus weight (mg)/body weight of mice (g)  $\times 10$ .

The calculation of spleen index is as follows:

spleen index = thymus weight (mg)/body weight of mice (g)  $\times 10$ .

**2.4. Absorption Kinetics Experiments.** Take 18 tumor-bearing mice. A single oral administrate baicalin (20 mg/kg) + baicalein (20 mg/kg). Eyeball blood was added twice after

administration for 7 min, 15 min, 30 min, 1 h, 2 h, 4 h, 8 h, 16 h, and 24 h. The whole blood was added to the pretreated centrifuge centrifuged for 10 min [12]. Plasma 0.2 mL and methanol 1.5 mL were added into tube, 15 min centrifugation, and the supernatant was removed; add 20  $\mu$ L 0.1% phosphoric acid, after mixing, 0.45  $\mu$ m syringe filter with a filter to be analyzed. Remove heart, liver, spleen, lung, kidney, brain tissue, and 0.5 g tissue and add 0.5 mL saline, homogenized. The homogenate was set in centrifuged tube, 0.4 mL of methanol was added, vortex 10 min, and centrifuged for 15 min; the supernatant was added 20  $\mu$ L 0.1% phosphoric acid, using 0.45  $\mu$ m syringe filter to filter the solution.

**2.5. Excretion Experiment.** The experiment was divided into treatment group and control group,  $n = 10$  tumor-bearing mice, which were placed in a metabolic cage rearing. Mice were fasted for 12 h, but water was allowed. 12 h later, a single oral administrate baicalin (20 mg/kg) + baicalein (20 mg/kg). After the control group was administered 0–4 h, 4–8 h, 8–12 h, and 12–24 h, all urine and feces were collected [13]. According to the above processing method, handle the sample processing. Take four tumor-bearing mice, a single oral administrated baicalin (20 mg/kg) + baicalein (20 mg/kg), taking bile. According to the above processing method handle the sample processing.

**2.6. Metabolic Experiments.** A single oral administration in 4 mice, took bile 4 h later, methanol was added to a final volume of 1 mL, using 0.45 um syringe filter to filter, injection analysis.

#### 2.7. Determination of HPLC

Column [12, 14]: Agilent Eclipse XDB-C18 (250 mm  $\times$  4.6 mm, 5  $\mu$ m);

mobile phase: methanol (A) –0.1% phosphoric acid solution (B), 40% A (0 min), 80% A (40 min), 40% A (60 min), detection wavelength of 277 nm, a flow rate of 1.0 mL/min;

analysis voltage: 100 mV;

protection voltage: 500 mV;

column temperature: 30°C;

injection volume: 20.0  $\mu$ L;

number of theoretical plates of not less than 10,000;

preparation of the reference solution: precision weight baicalin, baicalein reference 5 mg and 5 mg, in the same 50 mL volumetric flask; add methanol amount of ultrasound to dissolve, diluted to the mark with methanol.

**2.8. Statistical Data Processing Method.** Experimental data are presented as mean  $\pm$  standard deviation ( $\pm S$ ), each set of data was collected using the *t* test.

TABLE 1: The effect of baicalin and baicalein inhibition rate of U14 cervical cancer in mice.

Groups	The average tumor weight (g)	Inhibition rate (%)
Negative	2.29 ± 0.42	—
Positive	1.47 ± 0.11	35.81
Baicalin	1.06 ± 0.03	53.71
Scutellarein	1.40 ± 0.28	38.86

### 3. Results

**3.1. Established Mouse Model of Cancer U14.** 5d tumors in mice after planting, armpit lump visible success rate of 100% was observed before and after the state of motion modeling in mice and found that mice before modeling activities between eating large; After modeling, reduced activity, food intake, less water than before modeling, created by the above phenomenon known U14 cancer mouse model is successful.

**3.2. Baicalin and Baicalein Chinese Anticancer Effects in Mice U14.** Compared with the positive control group, baicalin and baicalein tumor inhibition rates were higher than the positive control group, but the difference was not statistically significant. And the size of the relationship between the inhibition rate was baicalin > baicalein; the results are shown in Table 1.

**Comparing Thymus Index.** Compared with the positive control group, baicalin and baicalein group were significantly higher than the positive control group ( $P < 0.01$ ); compared with the negative control group, baicalin group was significantly higher than the negative control group ( $P < 0.01$ ).

**Comparing Spleen Index.** Compared with the positive control group, baicalein and baicalin group were significantly higher than the positive control group ( $P < 0.01$ ); compared with the negative control group, baicalein group was higher than the negative control group ( $P < 0.05$ ).

Due to cyclophosphamide lack of targeting, it not only can effectively suppress tumors but also reduces the immune organism. Thymus and spleen are the two organisms immune organ, on behalf of the immunity organisms [15]. So thymus index and spleen index positive control group were lower than the experimental group and control group. Negative control group of mice completely inhibits tumor immunity on its own, so the thymus and spleen compared with normal mice developed; the results are shown in Table 2.

**3.3. Blood Standard Curve Test.** Baicalin was accurately weighed, baicalein reference was 31.89 mg and 10.62 mg, in the same 50 mL volumetric flask; add amount of methanol ultrasound to dissolve. The reference concentration of baicalin was diluted from 637.80 ug/mL times to 31.890 ug/mL; scutellarein concentration was diluted from 212.4 ug/mL fold to 10.62 ug/mL [6, 16, 17].

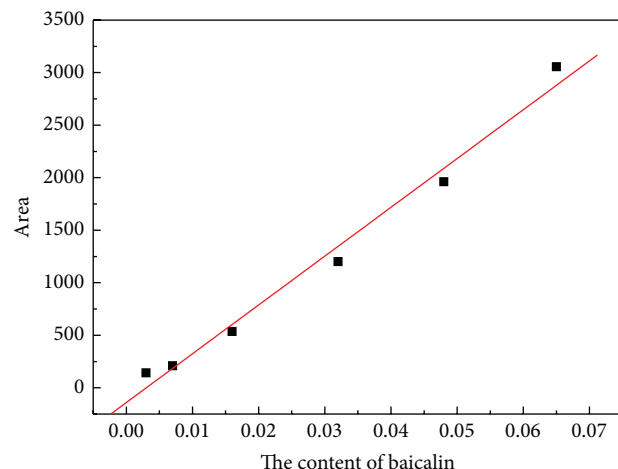


FIGURE 1: Baicalin standard curve.

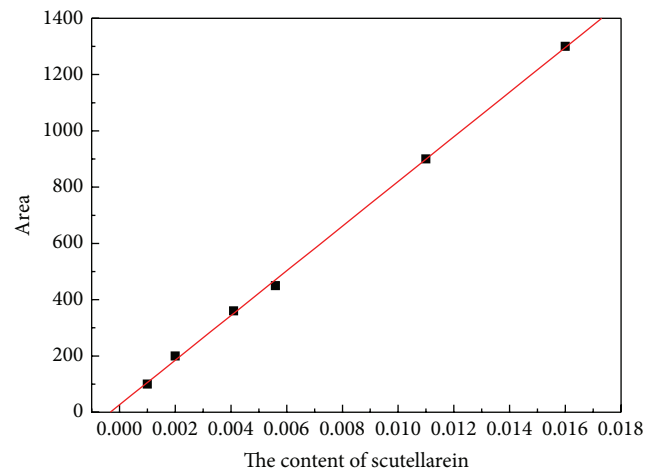


FIGURE 2: Scutellarein standard curve.

Experiments baicalin ( $x_1$ , ug/mL) and the peak area ( $y_1$ ) in the relation:  $y_1 = m_1 x_1 + b_1$ , where  $m_1 = 46869.17$  and  $b_1 = -108.19$ , are shown in Figure 1.

Baicalein content ( $x_2$ , ug/mL) and the peak area ( $y_2$ ) in the relationship:  $y_2 = m_2 x_2 + b_2$ , where  $m_2 = 84244.97$  and  $b_2 = 4.57$ , are shown in Figure 2.

**3.4. Organizations Like the Standard Curve.** In the experiment, baicalin was accurately weighed and baicalein reference was 5 mg and 5 mg, in the same 50 mL volumetric flask; add amount of methanol ultrasound to dissolve. A concentration of 100 ug/mL standard solution using the method of dilution magnification was diluted to 3.125 ug/mL 5 injections gradient [9, 14, 18], the standard curve (Figures 3 and 4).

Experiments baicalin ( $x_3$ , ug/mL) and the peak area ( $y_3$ ) are in relation to  $y_3 = m_3 x_3 + b_3$ , where  $m_3 = 5.99$  and  $b_3 = -0.59$ .

TABLE 2: The effect of baicalin and baicalein on U14 cervical thymus index and spleen index.

Groups	Body weight (g)	The average weight of the thymus (mg)	The average spleen weight (mg)	Thymus index	Spleen index
Negative	34.51 ± 0.99	82.05 ± 20.94	425.03 ± 46.76	23.78	123.16
Positive	30.12 ± 0.94	44.31 ± 18.99	249.52 ± 80.58	14.71 <sup>^</sup>	82.84
Baicalin	28.03 ± 0.85	121.21 ± 16.18	357.63 ± 17.89	43.24** <sup>^</sup> <sup>^</sup>	127.59**
Scutellarein	34.46 ± 2.34	95.03 ± 13.89	492.04 ± 65.81	27.58**	142.79** <sup>^</sup>

The positive control group: \* $P < 0.05$ , \*\* $P < 0.01$ , with the negative control group: <sup>^</sup> $P < 0.05$ , <sup>^</sup><sup>^</sup> $P < 0.05$ .

TABLE 3: Blood concentrations of baicalin—schedule.

Sampling time point	Concentration of baicalin (ng/mL)
7'	937.47
15'	739.35
30'	914.28
1 h	892.17
2 h	906.81
4 h	915.87
8 h	748.83
16 h	924.27
24 h	945.99

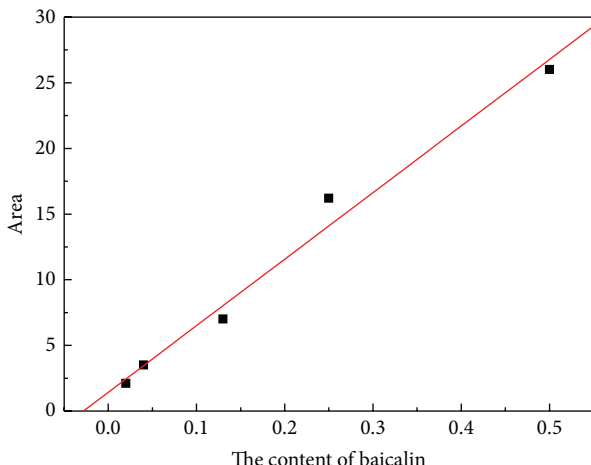


FIGURE 3: Baicalin standard curve.

Scutellarein content ( $x_4$ , ug/mL) and the peak area ( $y_4$ ) are in relation to  $y_4 = m_4 x_4 + b_4$ , where  $m_4 = 49.22$  and  $b_4 = -22.81$ .

**3.5. Absorption Kinetics Experiments.** Blood samples at all time points only detected baicalin absorption peak (peak 1) (Note: Peak 1 baicalin), not scutellarein absorption peaks, as shown in Figure 2. And the baicalin concentration of plasma appears first plateau after administration for 0.5 h~4 h and 16 h~24 h being a second plateau. This is because scutellarein ester-soluble glycosides are better; only baicalin turns into scutellarein; it can be absorbed by the intestinal epithelial cells. Baicalin is absorbed into the blood quickly and converts into scutellarein, so no scutellarein was detected in blood

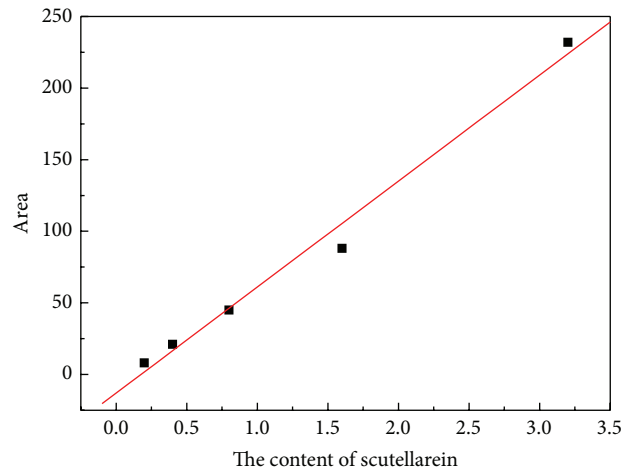


FIGURE 4: Scutellarein standard curve.

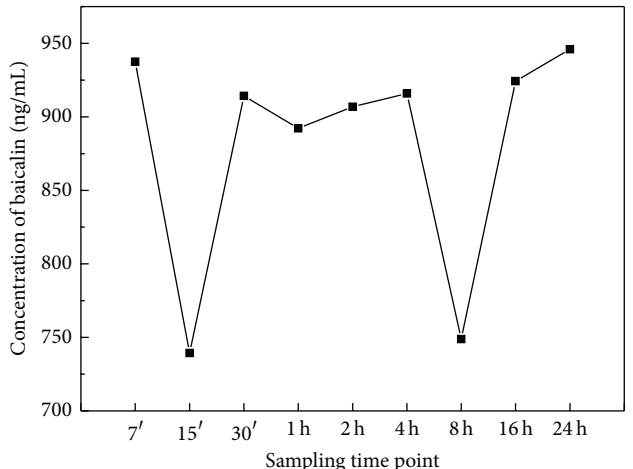


FIGURE 5: Baicalin blood concentrations versus time diagram.

samples. And the presence of baicalin intestinal absorption cycle that is absorbed into the blood baicalin reverted into scutellarein again into the intestine, to be absorbed by the next time, so there will be two absorption plateaus, as shown in Table 3 and Figure 5.

**3.6. Excretion Experiment.** Baicalin and baicalein absorption peak was not detected in urine samples. In faeces, the content of baicalin is higher than the content of baicalein, and

TABLE 4: Feces baicalin and baicalein content (ug/g feces).

	0-4 h	4-8 h	8-12 h	12-24 h
Baicalin	45.04	90.98	45.10	51.78
Scutellarein	18.59	39.49	22.01	55.59

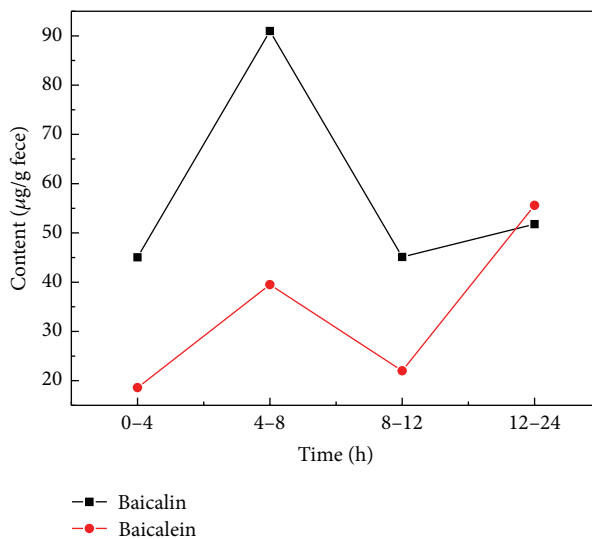


FIGURE 6: Baicalin and baicalein content at each time phase diagram in fecal content.

the content of baicalin and baicalein in feces are a double absorption peak. This is because baicalein is with a wide range of absorption in the gastrointestinal absorption system, and baicalin can only in the colonic bacteria secrete enzymes, into baicalein, without the enzyme action large number of baicalin out of body with feces [15]. So feces of mice have higher levels of baicalin. Double absorption peak is also due to the presence of intestinal loop sake. Data are shown in Table 4 and Figures 6 and 7.

**3.7. Metabolic Experiments.** Samples measured baicalin absorption peak area of  $56.12 \text{ mAU} \cdot \text{s}$  and scutellarein absorption peak area of  $2.99 \text{ mAU} \cdot \text{s}$  by HPLC. According to the standard curve formula, baicalin was  $2.37 \times 10^{-1} \text{ mg/mL}$  and scutellarein content was  $1.31 \times 10^{-2} \text{ mg/mL}$ . HPLC chromatographic result is shown in Figure 8.

**3.8. Tissue Distribution Experiments.** Just as blood samples, tissue samples can only detect baicalin absorption peak (1) but could not detect scutellarein absorption peaks as shown in Figures 3-10. After baicalin and baicalein medicine gavage 4 h, the content of baicalin in each tissue is heart > lung > cancer > kidney > liver. Since gavage 4 h, baicalin plasma concentration reached a plateau for the first time, so the drug concentration is the highest in the organization. Baicalin combined with biological heart and lung tissue easily, so the tissue drug concentrations are high. In tumor tissue, baicalin content is higher than that in kidneys and liver, indicating a high using degree of baicalin and baicalein medicine. Baicalin accumulated more in tumor tissue and took its role; excess

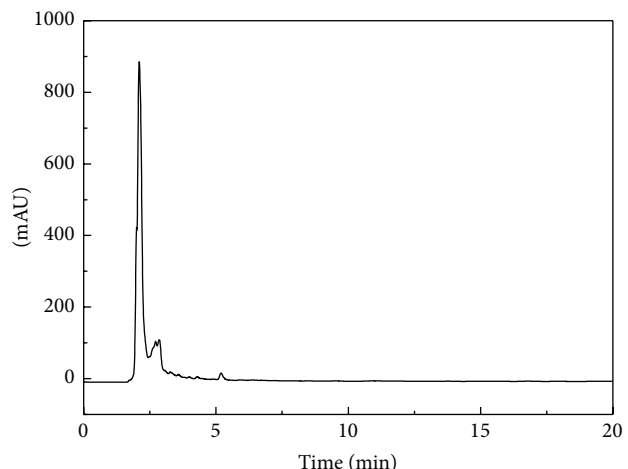


FIGURE 7: Test group and control group comparison chart fecal homogenates chromatography.

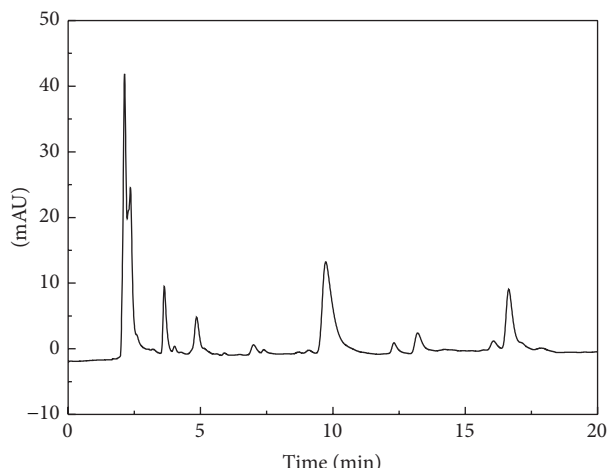


FIGURE 8: HPLC chromatogram of bile.

baicalin through the liver and kidneys and other metabolites organs were excreted out of body; the results were shown in Table 5 and Figures 9 and 10.

#### 4. Discussions

Baicalin and baicalein belong to polyphenolic compounds with weak acid; therefore, baicalin and baicalein which is the state of the molecule in the stomach may be easier to be absorbed through the mucosa. Rat gastric absorption test results showed that baicalin and baicalein are absorbed in the stomach, in which baicalein showed good absorption characteristics. The extent of absorption is far superior baicalin [14], which may be due to the removal of glycosylated aglycone baicalein having more fat-soluble and hydrophobic. Thus it is easier to pass through the gastric mucosa.

The liver is the major site of most drug metabolisms. Most flavonoids metabolism occurs in the digestive tract and liver. Baicalin metabolites in rat liver were baicalein

TABLE 5: U14 cervical cancer organizations mice baicalin.

Organization	Heart	Liver	Spleen	Lung	Kidney	Brain	Tumor
Content	3.708	1.104	0	3.029	1.334	0	1.690

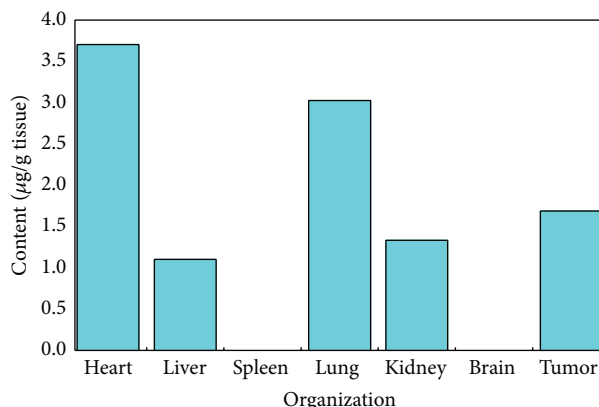


FIGURE 9: Baicalin content in each group.

## 5. Conclusions

Through the study of baicalin and baicalein absorption kinetics experiment, tissue distribution, excretion, and metabolism test, we can draw the following conclusions. The active pharmaceutical ingredient mainly exists in the form of baicalin in blood, which reached the highest concentration in 0.5~4 h and 12~24 h. This indicated that the baicalin is absorbed through the gastrointestinal circulation. Four hours later after gavage, the content of baicalin in tumor, heart, liver, and kidney reached a higher concentration. Baicalin and baicalein are mainly excreted through the fecal excretion and bile excretion. In this experiment, baicalin and baicalein, as an anticancer drug, and the two effects on U14 cervical cancer and the pharmacokinetic process in mice were discussed. It provided a data support for the development and improvement of *Scutellaria baicalensis*.

## Conflict of Interests

The authors declare that they have no any direct financial relation with the commercial identities mentioned in this paper that might lead to a conflict of interests for any of the authors.

## References

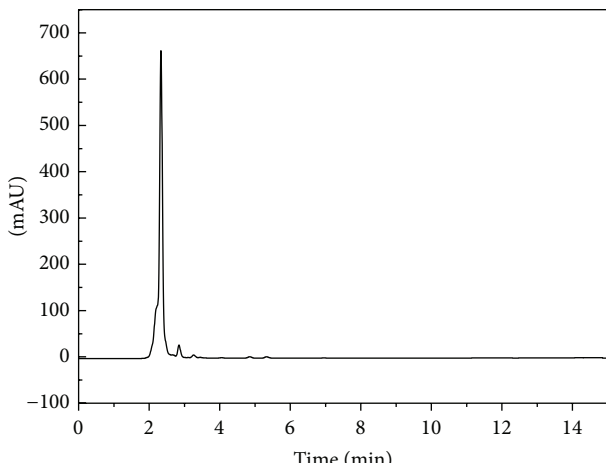


FIGURE 10: HPLC of lung homogenate.

6-O- $\beta$ -glucuronide (M1), 6-O-methyl-baicalein 7-O- $\beta$ -glucuronide (M2), baicalein 7-O- $\beta$ -glucuronide (M3), 6-O- $\beta$ -glucuronidase-baicalein-7-O-sulfate (M4), and baicalein 6,7-di-O- $\beta$ -glucuronide (MS), in which five metabolites, including M4 and M5, of polar metabolites are relatively high; a relatively large molecular weight is the major. Some traditional Chinese herbal formula changes will lead directly baicalin metabolites in the liver changes. Baicalin or baicalein metabolites way in urine mainly combines methylation and glucuronide. Baicalin exhibits enterohepatic circulation, after intravenous administration of baicalin solution, with its prototype and metabolites meter; enterohepatic circulation percentages were 4.8% and 13.3%. After oral administration of baicalin solution, with its prototype and metabolites meter, enterohepatic circulation percentage was 18.7% and 19.3%.

- [1] L. D. Yuan, H. Xu, and Z. Du, "Influence of Baicalin on Ehrlich ascites carcinoma cell: a preliminary study," *Journal of Nanjing Railway Medical College*, vol. 16, no. 4, pp. 231–233, 1997.
- [2] R. Liang, C. Chen, X. Yi et al., "Structural origins of the differential antioxidative activities between baicalein and Baicalin," *OALib Journal*, vol. 27, no. 1, pp. 132–140, 2010.
- [3] L. X. Yang, D. Liu, X. F. Feng et al., "Determination of flavone for *Scutellaria baicalensis* from different areas by HPLC," *Zhongguo Zhong Yao Za Zhi*, vol. 27, no. 3, pp. 166–170, 2002.
- [4] H. Shi, B. Zhao, and W. Xin, "Scavenging effects of Baicalin on free radicals and its protection on erythrocyte membrane from free radical injury," *Biochemistry and Molecular Biology International*, vol. 35, no. 5, pp. 981–994, 1995.
- [5] R. Su, X. Lin, and X. Zhuang, "Scutellarein study protective effects of hydrogen peroxide-induced injury in PC12 cells," *Pharmaceutical Journal*, vol. 35, no. 3, pp. 161–165, 2005.
- [6] N. Su, R. Luo, H. Su et al., "Effect of Baicalin on renal function in diabetic nephropathy rats and its anti-oxidative action," *Traditional Chinese Drug Research & Clinical Pharmacology*, vol. 18, no. 5, p. 341, 2007.
- [7] Y. Fang, D. Hu, and X. Li, "Baicalin and copper (II), scavenging zinc (II) complexes of superoxide radicals," *Xian Medical University*, vol. 18, no. 1, p. 41, 1997.
- [8] F. Yin, Y. Yang, and P. Yu, "Changes of glutamate and gamma-aminobutyric acid contents in brain tissue of brain edema and effects of Baicalin on them in rats," *Zhongguo Zhong Xi Yi Jie He Za Zhi*, vol. 20, no. 7, pp. 524–526, 2000.

- [9] Y. Hou, X. Zhu, and G. Cheng, "Study on the anti-inflammatory mechanism of Baicalin," *Yaoxue Xuebao*, vol. 35, no. 3, pp. 161–164, 2000.
- [10] A. S. Pannala, T. S. Chan, P. J. O'Brien, and C. A. Rice-Evans, "Flavonoid B-ring chemistry and antioxidant activity: fast reaction kinetics," *Biochemical and Biophysical Research Communications*, vol. 282, no. 5, pp. 1161–1168, 2001.
- [11] C. Cheng, N. Feng, Q. Tang et al., "Baicalin on common eye original in vitro antibacterial effect," *Chinese Journal of Hospital Pharmacy*, vol. 21, no. 6, p. 384, 2001.
- [12] M. Gong, L. Yu, Q. Chen et al., "Gavage Baicalin its aglycone baicalein pharmacokinetic study," *Herbal*, vol. 40, no. 3, 2009.
- [13] X.-B. Guan, L. Ye, B.-J. Xia, and Z.-Q. Liu, "Effects of various microsomal drug-metabolizing enzymes on specific glucuronidation of baicalein in rats' liver and intestine," *Chinese Journal of Cerebrovascular Diseases*, vol. 19, no. 36, pp. 2811–2813, 2008.
- [14] M.-Y. Lai, S.-L. Hsiu, C.-C. Chen, Y.-C. Hou, and P.-D. L. Chao, "Urinary pharmacokinetics of baicalein, wogonin and their glycosides after oral administration of scutellariae radix in humans," *Biological and Pharmaceutical Bulletin*, vol. 26, no. 1, pp. 79–83, 2003.
- [15] J. Xing, X. Chen, and D. Zhong, "Absorption and enterohepatic circulation of Baicalin in rats," *Life Sciences*, vol. 78, no. 2, pp. 140–146, 2005.
- [16] Q. Lan, K. Chu, S. Qiu, and X. Shen, "Experimental 23 study on stability of compound scutellaria solution," *China Pharmaceutical University*, vol. 20, no. 2, pp. 106–108, 1989.
- [17] Q. Wang, "HPLC method for the determination of Baicalin skullcap of," *Herbal*, vol. 20, no. 8, pp. 15-16, 1989.
- [18] Y. Zhou and J. Ni, "Determination of baicalin content in Children's lung cleaning oral liquid by HPLC," *Medicine*, vol. 15, no. 1, p. 16, 1993.

## Research Article

# Infrared Spectroscopic Characterization of Photoluminescent Polymer Nanocomposites

Kyle Gipson,<sup>1</sup> Kathryn Stevens,<sup>2</sup> Phil Brown,<sup>2</sup> and John Ballato<sup>2</sup>

<sup>1</sup> Department of Engineering and the Center for Materials Science, James Madison University, Harrisonburg, VA 22807, USA

<sup>2</sup> Center for Optical Materials Science and Engineering Technologies (COMSET) and the Department of Materials Science and Engineering, Clemson University, Clemson, SC 29634, USA

Correspondence should be addressed to Kyle Gipson; gipsonkg@jmu.edu

Received 22 August 2014; Accepted 20 October 2014

Academic Editor: Qingrui Zhang

Copyright © 2015 Kyle Gipson et al. This is an open access article distributed under the Creative Commons Attribution License, which permits unrestricted use, distribution, and reproduction in any medium, provided the original work is properly cited.

Organicallycoated inorganic nanoparticles were synthesized to produce photoluminescent nanocomposites based on a polymethyl methacrylate (PMMA) matrix. The nanoparticles comprised organic ligands (acetylsalicylic acid, ASA, and 2-picolinic acid, PA) attached to the lanthanum trifluoride ( $\text{LaF}_3$ ) host crystals that were doped with optically active terbium III ( $\text{Tb}^{3+}$ ) and synthesized using solution-based methods. The ligands were employed to functionalize the surface of  $\text{Tb}^{3+}:\text{LaF}_3$  nanocrystals to aid in dispersing the nanoparticles. In order to confirm the presence of the constituents within the inorganic-organic system, the nanoparticles were characterized by infrared spectroscopy and energy-dispersive X-ray spectroscopy. Absorption peaks observed from infrared spectroscopy for all the polymer nanocomposites loaded with organic surface treated nanocrystals exhibited peaks that were not present in undoped PMMA but were characteristic of the dopant and the ligand.

## 1. Introduction

Polymer optical materials (POMs) in devices (e.g., splitters, couplers, multiplexers, demultiplexers, and amplifiers) have been used in integrated lightwave circuits wherein polymer optical fibers and planar waveguides are combined for specific functionalities [1]. POM applications range from planar integrated optics (optical circuits on planar substrates) [2] to local area networks (LANs) [3] and sensing components for devices used for medical [4], manufacturing [5], and security applications [6]. Light-emitting polymer nanocomposites (a subset of POMs) are generally utilized in planar lightwave circuits and in telecommunication applications [1] as well as incoherent light-emitting devices, optical sensors, and photodetectors [7].

In order to create light-emitting polymer nanocomposites, various additives have been employed to change the optical properties of polymers, in particular polymethyl methacrylate (PMMA). PMMA has been shown to be a suitable matrix for optically active additives (dopants) [8]. Luminescent species that have the capability of fluorescing

and being dopants to overcome attenuation are organic dyes, quantum dots, and rare-earth (RE) ions doped in inorganic nanocrystals [9–12]. In this research, the dopants studied were RE ions doped into inorganic nanocrystals. The dopant is excited upon interaction with light to a higher electronic energy level. As a result, the dopant produces radiative (photon) and nonradiative emissions (phonon) upon relaxation to a lower lying state or the ground state.

Nanoscale inorganic materials (e.g., lanthanum trifluoride,  $\text{LaF}_3$ ) doped with RE (e.g., terbium,  $\text{Tb}^{3+}$ ) ions typically are incompatible with organic polymers. Inorganic material dispersed in organic polymers generally favors agglomeration. Nanoscale materials tend to form agglomerates as an attempt to reduce the surface area to minimize interfacial energy [13]. Therefore, surface treating of the inorganic material with an organic species, that is, ligands, is an option for aiding inorganic-organic compatibility.

Ligands are organic molecules that have the ability to create ion complexes or attach to the surface of nanocrystals in order to aid in dispersion within the polymer matrix. Aromatic acids, bipyridines, or donor groups containing

negatively charged atoms (e.g., carboxylate or phosphate groups) are examples of ligands utilized to attach to the surface of nanocrystals via ionic attraction [14, 15]. Such organic conjugated ligands typically absorb energy in the near ultraviolet (UV) spectral region ranging from 200 nm to about 400 nm [16]. The surface treatment or “capping” of nanocrystals [1, 14] with aromatic acids [17] (acetylsalicylic acid, ASA) [18] and bipyridines (2-picolinic acid, PA) have indicated that the ligands also serve the purpose of UV light harvesting ligands that enhance fluorescence of RE emissions by absorbing and transferring energy to the dopant RE ions [19–21]. The polymer optical nanocomposite studied in this work consists of ligand capped RE-doped nanocrystals.

Infrared spectroscopy, which is considered a useful tool for classification and identification, was used to investigate the relatively small changes in the chemical structures of various molecules [22]. The focus of this research is the IR characterization of ASA and PA plus the determination of the inorganic material within the polymer nanocomposite.

## 2. Materials and Methods

**2.1. Materials.** Solvents used were anhydrous tetrahydrofuran, THF (99%—Acros), methanol (99.8%—BDH), and ultrapure water (18.2 MΩ·cm). The following items were used as received: polymethyl methacrylate, PMMA, at an approximate weight average molecular weight of 130 k from Plaskolite West, Inc., lanthanum (III) nitrate hexahydrate ( $\text{La}(\text{NO}_3)_3 \cdot 6\text{H}_2\text{O}$ , 99.99%—Sigma-Aldrich), terbium (III) nitrate hydrate ( $\text{Tb}(\text{NO}_3)_3 \cdot 6\text{H}_2\text{O}$ , 99.9%—Sigma-Aldrich), acetylsalicylic acid, ASA (MP Biomedicals, LLC), 2-picolinic acid, PA (99%—Alfa Aesar), ammonium fluoride,  $\text{NH}_4\text{F}$  (99.3%—Fisher Scientific), ammonium hydroxide,  $\text{NH}_4\text{OH}$  (28–30% ACS—BDH Aristar-VWR), ethanol, EtOH (99.5%—Acros), and acetone (99.9%—BDH).

**2.2. Nanoparticle Synthesis.**  $\text{Tb}^{3+}\text{:LaF}_3$  nanocrystals were prepared in solutions with either water or methanol as the solvent and the nanoparticle syntheses are as described previously [18]. The rare-earth solution of  $\text{La}(\text{NO}_3)_3 \cdot 6\text{H}_2\text{O}$  (9 mmol) and  $\text{Tb}(\text{NO}_3)_3 \cdot 6\text{H}_2\text{O}$  (2 mmol) in 16 mL of solvent was prepared at room temperature.  $\text{NH}_4\text{OH}$  was added to the rare-earth solution to adjust the pH to a value of 8 for the aqueous synthesis. The pH of the methanol solution was not adjusted.

**2.3. Synthetic Route 1—Water Solvent Synthesis.** The rare-earth solution was added drop-wise into a stirring solution of  $\text{NH}_4\text{F}$  (11 mmol) and 20 mmol of the ligand (ASA or PA) in water at 70°C. The volume ratio of water/ligand was 40:1.  $\text{NH}_4\text{OH}$  was added to readjust the suspension to a pH value of 8; it was then stirred for 2 hours at 70°C. A centrifuge was used to separate the precipitate at 3000 rpm for 10 minutes. The nanoparticles (precipitate) were washed with 50 vol% of ethanol (EtOH) in water followed by an acetone wash and then dried over night in a vacuum oven at 30°C. The particles were then added to 5 wt% of PMMA in tetrahydrofuran, THF (PMMA/THF), to form a polymer nanoparticle suspension

of ligand:  $\text{Tb}^{3+}\text{:LaF}_3\text{:PMMA/THF}$ , that was added drop-wise to excess (v/v of suspension to MeOH; 1:400) stirred in methanol (MeOH) at ~3°C. The precipitated nanocomposite polymer powder was vacuum-filtered, washed in MeOH, and then dried over night in a vacuum oven.

**2.4. Synthetic Route 2—Methanol Solvent Synthesis.** The rare-earth solution (prepared in manner stated in Section 2.2) was added drop-wise to a stirring solution of  $\text{NH}_4\text{F}$  (12 mmol) and 23 mmol of the desired ligand (ASA or PA) in methanol at room temperature ~25°C and was stirred for 1 hour. The volume ratio of methanol/ligand was 40:1. pH was monitored and in the case where ≤5% water was present in the suspension; the relative pH is stated for the solution values. A centrifuge was used to separate the precipitate at a setting of 3000 rpm for 10 minutes. The particles were washed twice with methanol. Neat MeOH (v/v of PMMA/THF to MeOH; 1:400) was added to resuspend the particles and the temperature of the nanoparticle suspension in excess MeOH was decreased to approximately 3°C. After 30 minutes, a solution of 5 wt% of PMMA/THF was added drop-wise to the ligand:  $\text{Tb}^{3+}\text{:LaF}_3\text{:MeOH}$  suspension. The product was precipitate nanocomposite polymer powder. The precipitate nanocomposite polymer powder was vacuum-filtered, washed in MeOH, and then dried under vacuum over night.

**2.5. Attenuated Total Reflection (ATR) Infrared Spectroscopy.** Samples of the ligands as well as dried nanoparticles, precipitated polymer, and precipitated polymer nanocomposite were analyzed by ATR. A Thermo-Fisher Nicolet Magna 550 FTIR spectrometer equipped with a Thermo-SpectraTech Foundation Series Diamond ATR accessory, Nic-Plan microscope, and Omnic software acquired the spectra. Sixteen scans were conducted at room temperature and the spectral resolution was set at 8  $\text{cm}^{-1}$ .

**2.6. Energy-Dispersive X-ray Spectroscopy.** The compositions of the nanoparticles were characterized utilizing a scanning transmission electron microscope (STEM, Hitachi HD2000, Pleasanton, CA) equipped with an Oxford INCA Energy 200 Energy Dispersive Spectrometer (EDX). Samples were prepared by drop casting nanoparticle suspensions followed by subsequent solvent evaporation onto 200 mesh carbon coated copper TEM grids.

## 3. Results and Discussion

Inorganic nanoparticles doped with optically active rare-earth ions were synthesized in the presence of organic aromatic ligands. Two nanocomposite synthetic routes were evaluated as outlined in Sections 2.3 and 2.4 where the first synthesis method (Route 1) utilized water as the solvent and the second synthesis method (Route 2) utilized methanol as the solvent. After synthesis via Route 1, the nanoparticles were dried, ball milled, and dispersed in polymer/solvent solutions, which were subsequently phase inverted in methanol to form polymer nanocomposites. The work of Widiyandari et al. supported the potential use of mechanical milling

as a way to reduce agglomerates formed in nanoparticle suspensions of electrohydrodynamic atomization [23]. In this research, the dried particles and dried polymer nanocomposites were ball milled with Teflon spheres in a container that was vortex stirred.

In Route 2, nanoparticles were synthesized in methanol and were not dried. The resulting polymer/solvent solutions were phase inverted into nanoparticle suspensions in methanol to form polymer nanocomposites. Route 2 was devised to simplify the synthesis technique.

Two different aromatic ligands (acetylsalicylic acid, ASA, and 2-picolinic acid, PA) were utilized to functionalize the surface of  $\text{Tb}^{3+}:\text{LaF}_3$  nanocrystals (NC). The ligand to nanocrystal (L: NC) molar ratio was varied for each ligand system for two reasons. Firstly, the emission intensities of terbium have been observed to be dependent on the ratio of ligand to inorganic component [24]. Secondly, the amount of ligand attached to the surface of the nanocrystal may affect nanoparticle agglomeration [25–27]. The selected aromatic ligand systems were characterized using infrared spectroscopy and optical spectroscopy.

**3.1. Organic Ligand IR Characterization.** Powder samples of the ligands, nanoparticles, and polymer nanocomposites were used to conduct qualitative characterizations of ATR absorption peaks. The qualitative characterizations were based on data found in literature provided by the following researchers: Binev et al. [28] and Boczar et al. [29] investigated the infrared spectra of acetylsalicylic acid, both Silverstein et al. [30] and Dean [31] work offered spectrometric identification of organic compounds, Soman and Kelkar [32] research studied infrared spectra of doped PMMA, and Świderski et al. [33] and Koczóń et al. [34] research investigated the infrared spectra of picolinic acid. The vibration modes are classified using the following symbols:  $\nu$ —stretching,  $\delta$ —deformation, and  $\tau$ —torsion/wagging. Wavenumbers and IR band assignments for the spectra of PA (Figure 1) and ASA (Figure 2) are found in Tables 1 and 2, respectively.

Listed in Table 1 are absorption bands associated with picolinic acid and the IR spectrum is illustrated in Figure 1. The sharp peak located at  $3112\text{ cm}^{-1}$  denotes the C-H stretching mode from the aromatic ring. The broad peak with mid-center location of  $2591\text{ cm}^{-1}$  was attributed to the O-H stretching from the carboxylic acid. The peak located at  $1706\text{ cm}^{-1}$  is attributed to the C=O stretching of carboxylic acid. C-H stretching from the aromatic ring is assigned to the  $1658\text{ cm}^{-1}$  peak. Six bands represent the C-C stretching of the conjugated ring system of pyridine. Świderski et al. conducted experimental FT-IR, FT-Raman, and  $^1\text{H}$  NMR and theoretical studies of metals chelated by picolinic acid where the six bands were observed at  $1606$ ,  $1593$ ,  $1572$ ,  $1527$ ,  $1438$ , and  $1339\text{ cm}^{-1}$  without a contribution from the C-N [33]. The bands that are at  $1293$  and  $1083\text{ cm}^{-1}$  correspond to in plane deformation of C-H bonds in the pyridine ring. The absorption peak observed at  $750\text{ cm}^{-1}$  indicates deformation of the carbons within the ring.

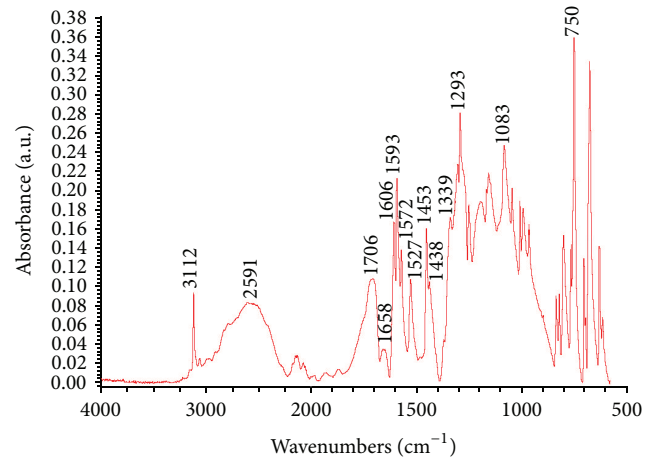


FIGURE 1: Infrared spectrum ( $4000\text{--}500\text{ cm}^{-1}$ ) of picolinic acid.

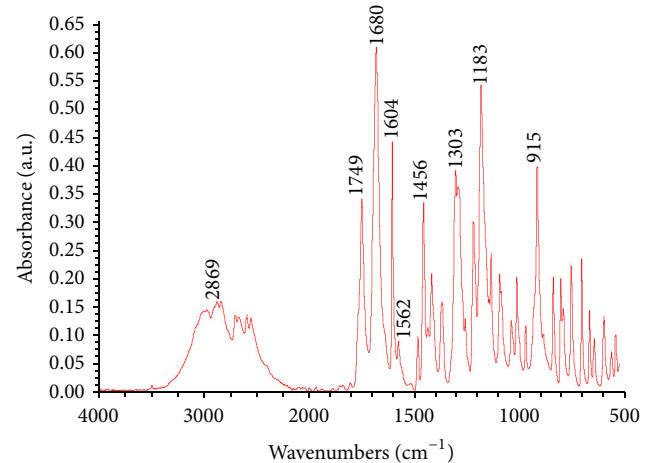


FIGURE 2: Infrared spectrum ( $4000\text{--}500\text{ cm}^{-1}$ ) of acetylsalicylic acid.

The broad absorption peak of ASA that spans from approximately  $3250$  to  $2500\text{ cm}^{-1}$  (Figure 2) contains stretching modes of the O-H group from the acid,  $\text{CH}_3$  group attached to the ketone, and C-H bonds located on the benzene ring. C=O stretching was assigned to the peaks observed at  $1749\text{ cm}^{-1}$  for the ester and  $1680\text{ cm}^{-1}$  for the carboxy group. The strong peak at  $1604\text{ cm}^{-1}$  is attributed to C-C stretching in the benzene ring, ring deformation, and C-C-C deformation [28]. The peaks located at  $1562\text{ cm}^{-1}$  and  $1456\text{ cm}^{-1}$  are also associated with benzene ring stretching of C=C and C-C bonds, respectively. The band at  $1303\text{ cm}^{-1}$  is related to O-H deformation and C-C stretching of the ring. The peak observed at  $915\text{ cm}^{-1}$  contains C-C, O-C, C-O, and C-CH<sub>3</sub> deformations. Deformation of the CH<sub>3</sub> and stretching of C-O-C and C-C bonds were assigned to the peak observed at  $1183\text{ cm}^{-1}$ .

**3.2. Nanoparticle IR Characterization.** The nanoparticle constitutes the doped nanocrystal, NC (NC =  $\text{Tb}^{3+}:\text{LaF}_3$ ), with attached ligand (PA or ASA). PA:NC refers to PA ligand

TABLE 1: Observed vibrational modes for picolinic acid [28–34].

Wavenumber ( $\text{cm}^{-1}$ )	Modes of vibration
3112	$\nu\text{CH}$ (ring)
3054	$\nu\text{CH}$ (ring)
2591	$\nu\text{OH}$ ( $\text{CO}_2\text{H}$ )
1706	$\nu\text{C=O}$ ( $\text{CO}_2\text{H}$ )
1658	$\nu\text{CH}$ (ring)
1606	$\nu\text{CC}$ (ring)
1593	$\nu\text{CC}$ (ring)
1572	$\nu\text{CC}$ (ring)
1527	$\nu\text{CC}$ (ring)
1453	$\nu\text{CH}$ (ring) $\nu\text{COO}$
1438	$\nu\text{CC}$ (ring)
1339	$\nu\text{CC}$ (ring)
1293	$\delta\text{CH}$
1250	$\delta\text{CH}$
1157	$\delta\text{CH}$
1083	$\delta\text{CH}$
1045	$\delta\text{CH}$
1008	$\nu\text{CH}$ (ring)
995	$\delta\text{CH}$
965	$\delta\text{CH}$
836	$\delta\text{CH}$
821	$\delta\text{CH}$
800	$\delta\text{CH}$
764	$\delta\text{CH}$
750	$\delta\text{CCC}$ (ring)
703	$\delta\text{CCC}$ (ring)

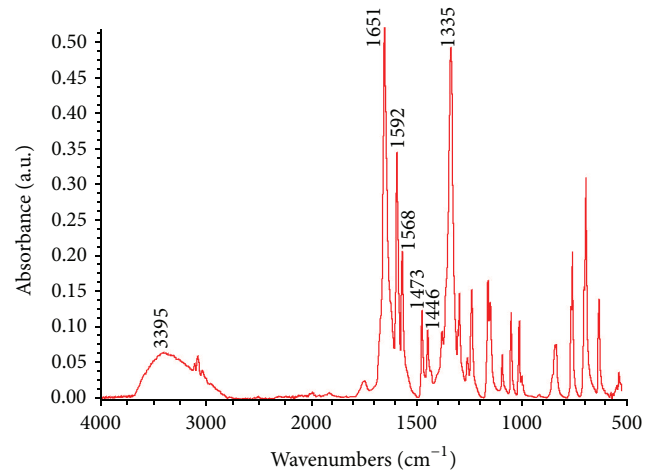
TABLE 2: Observed vibrational modes for acetylsalicylic acid [28–34].

Wavenumber ( $\text{cm}^{-1}$ )	Modes of vibration
3000–2500	$\nu\text{OH}$
3000–3100	$\nu\text{CH}$ (ring)
2975–2950	$\nu\text{CH}_3$
1749	$\nu\text{C=O}$ (ester)
1680	$\nu\text{C=O}$ (carboxy)
1604	$\nu\text{C=O}$ (ring) $\delta\text{OH}$
1562	$\nu\text{CC}$ (ring)
1456	$\nu\text{C=C}$ $\delta\text{CH}$ (ring) $\delta\text{CH}_3$
1418	$\delta\text{OH}$ $\delta\text{CH}_3$ $\delta\text{COH}$
1368	$\delta\text{CH}_3$ $\nu\text{CC}$ (ring) $\delta\text{CH}$ (ring)
1303	$\delta\text{COH}$
1292	$\delta\text{COH}$
1256	$\delta\text{CH}$ (ring)
1218	$\nu\text{-O-CO-CH}_3$ $\delta\text{CH}$ (ring)
1183	$\nu\text{-O-CO-CH}_3$ $\delta\text{CH}$ (ring)
1134	$\delta\text{CH}$ (ring)
1093	$\delta\text{CH}$ (ring) $\nu\text{CC}$ (ring)
1012	$\delta\text{-O-CO-CH}_3$ $\delta\text{CH}_3$
915	$\delta\text{-O-CO-CH}_3$ $\nu\text{CC}$ (ring)
839	$\delta\text{CH}$ (ring)
803	$\delta\text{-O-CO-CH}_3$ $\delta\text{CC}$ (ring) $\delta\text{CH}$ (ring)
791	$\delta\text{CH}$ (ring) $\nu\text{COOH}$
753	$\delta\text{CH}$ (ring)
704	$\delta\text{CH}$ (ring) $\delta\text{CC}$ (ring)
666	$\delta\text{CH}$ (ring) $\delta\text{COOH}$ $\delta\text{O-C=O}$

capped nanocrystals and ASA:NC corresponds with ASA ligand capped nanocrystals. Provided in Figures 3 and 4 are the IR spectra of PA:NC via synthesis Routes 1 and 2, respectively. Changes to the wavenumber of the observed peaks in the spectra of the nanoparticles could indicate perturbations to the ligand systems [33]. These perturbations (deformations of the uniform distribution of  $\pi$ -electron density within the ring) of aromatic systems may result in band elimination, band shifting to lower wavenumbers as a result of bond weakening, or band intensity reduction [33].

A representative IR spectrum for PA:NC via synthetic Route 1 is displayed in Figure 3 and via Route 2 in Figure 4. The spectra are similar and will be discussed as such. The broad peak with the mid-center point located at  $3395\text{ cm}^{-1}$  corresponds to O–H stretching of the residual solvent.

The observed  $1706\text{ cm}^{-1}$  peak of PA found in Figure 1 corresponds to the stretching of C=O bonds from the carboxylic acid. This peak was not observed in the study of metal picolinates (picolinic acid coordination of magnesium, calcium, strontium, and barium) [33]. However, Koczoń et al. observed the peak in picolinic acid. This work focused on experimental and theoretical IR and Raman spectra analyses of picolinic, nicotinic, and isonicotinic acids and their complexes with different metals [34]. This research indicated that stretching of the C=O from the carboxylic

FIGURE 3: Infrared spectrum ( $4000$ – $500\text{ cm}^{-1}$ ) of PA:NC via synthetic Route 1 (water synthesis).

acid occurred at  $1717\text{ cm}^{-1}$ . However they did not observe the  $1706\text{ cm}^{-1}$  band in the spectra of the PA:NC shown in Figures 3 and 4. The absence of this peak may indicate ligand attachment to the nanocrystal.

A peak at  $1651\text{ cm}^{-1}$  was observed in the spectra of PA:NC via Routes 1 and 2 in Figures 3 and 4, respectively.

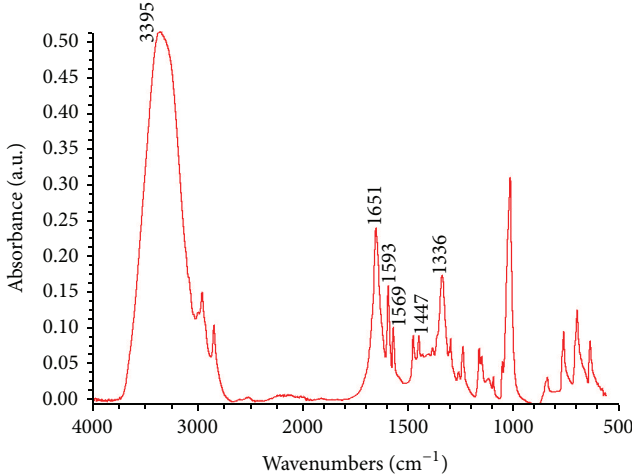


FIGURE 4: Infrared spectrum ( $4000\text{--}500\text{ cm}^{-1}$ ) of PA:NC via synthetic Route 2 (methanol synthesis).

The  $1651\text{ cm}^{-1}$  reflects the C–O stretching of the formed anion which is not related to the peak of  $1658\text{ cm}^{-1}$  associated with C–H stretching from the aromatic ring list in Table 1. The anion of the acid is formed as the result of ionization of the hydroxyl group.

The  $1606$ ,  $1527$ , and  $1339\text{ cm}^{-1}$  observed peaks of picolinic acid in Figure 1 are similar to the picolinic acid peaks at  $1607$ ,  $1528$ , and  $1343\text{ cm}^{-1}$  viewed by Świderski et al. These peaks are associated with stretching of the C–C bonds from the aromatic ring and were not observed in the metal picolinate spectra [33]. The lack of the  $1606$ ,  $1527$ , and  $1339\text{ cm}^{-1}$  peaks in this research as depicted in Figures 3 and 4 is an indication that the addition of the nanocrystals has an influence on the ligand structure.

The peaks associated with C–C stretching from the aromatic ring that are present in picolinic acid and remain in nanoparticles via Routes 1 and 2 are located at  $1593$  and  $1572\text{ cm}^{-1}$  (Figure 1) for the acid and  $\sim 1593$  and  $\sim 1568\text{ cm}^{-1}$  for the PA:NCs (Figures 3 and 4). There exists relatively little change to the peak values, which may indicate stronger vibrations as the result of perturbations in other areas of the ligand.

The IR spectra obtained for ASA:NC produced by water synthesis are shown in Figure 5 and via methanol synthesis are illustrated in Figure 6. The broad peaks located at  $3438\text{ cm}^{-1}$  for ASA:NC via Route 1 and  $3389\text{ cm}^{-1}$  via Route 2 are indicative of O–H stretching from the residual solvent. The  $1720\text{ cm}^{-1}$  peak is associated with C=O stretching of the carboxy group which is observed in ASA:NC via Route 2 but not in the IR spectra for Route 1. The peaks  $1625\text{ cm}^{-1}$  (synthetic Route 1 in Figure 5) and  $1624\text{ cm}^{-1}$  (synthetic Route 2 in Figure 6) which were not observed in the IR spectra for ASA were indications of C=C bond stretching of the ring. Observed peaks at  $1596\text{ cm}^{-1}$  for Route 1 and  $1593\text{ cm}^{-1}$  for Route 2 correlate to C=O stretching with the corresponding peak in acid at  $1604\text{ cm}^{-1}$ . O–H deformation was assigned to the peaks located at  $1399\text{ cm}^{-1}$

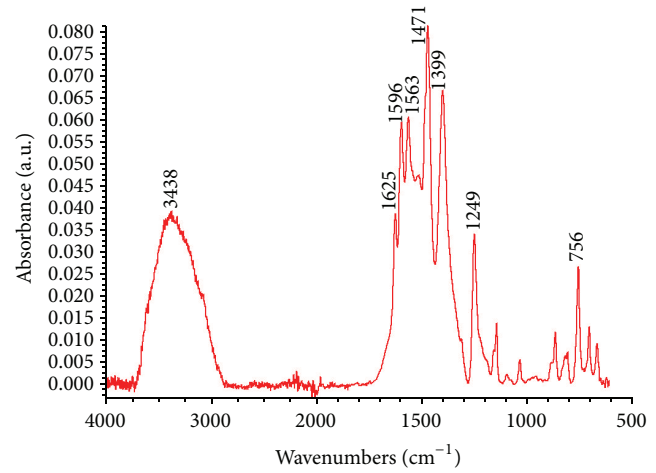


FIGURE 5: Infrared spectrum ( $4000\text{--}500\text{ cm}^{-1}$ ) of ASA:NC via synthetic Route 1 (water synthesis).

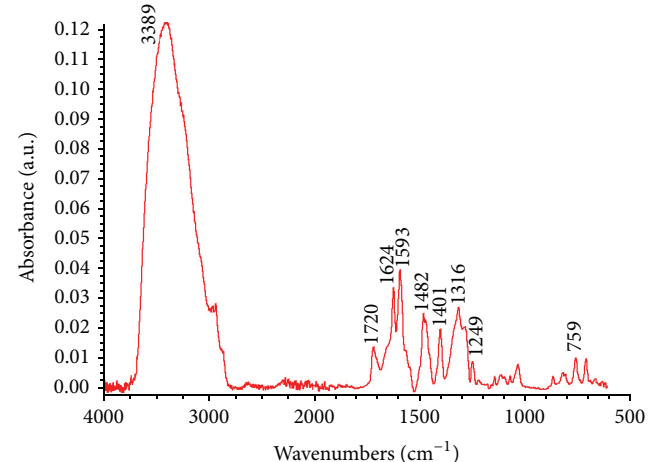


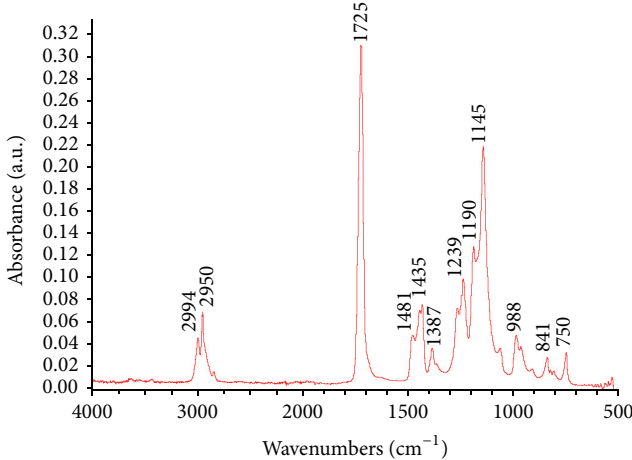
FIGURE 6: Infrared spectrum ( $4000\text{--}500\text{ cm}^{-1}$ ) of ASA system via Route 2 (methanol synthesis).

for water synthesis and  $1401\text{ cm}^{-1}$  for the methanol synthesis and both peaks were lower than the  $1418\text{ cm}^{-1}$  peak of the acid. C–H deformation at the ring linked to the peak located at  $1256\text{ cm}^{-1}$  of the acid was observed to occur at lower wavenumbers for the nanoparticles,  $1249\text{ cm}^{-1}$  for both synthesis procedures. These perturbations of ligand clearly indicate an influence of the nanocrystals on the ligand.

**3.3. PMMA IR Characterization.** The observed vibrational modes associated with PMMA are listed in Table 3 and the IR spectrum is illustrated in Figure 7. Shown in Figure 7 is a cluster of peaks found at  $2994$  and  $2950\text{ cm}^{-1}$  within the undoped precipitated PMMA spectra which typically represent CH<sub>3</sub>, CH<sub>2</sub>, and CH stretching. The stretching of the saturated aldehyde is generally characterized with a strong peak located around  $1725\text{ cm}^{-1}$ . The two peaks located at  $\sim 1480\text{ cm}^{-1}$  and  $1380\text{ cm}^{-1}$  may illustrate the two bands that designate C–CH<sub>3</sub> deformation. The CH<sub>3</sub> stretching may result in a peak

TABLE 3: Observed vibrational modes for PMMA.

Wavenumber ( $\text{cm}^{-1}$ )	Modes of vibration
2994	$\nu\text{CH}_3$
2950	$\nu\text{CH}_3$
1725	$\nu\text{COH}$
1481	$\delta\text{C}-\text{CH}_3$
1435	$\nu\text{CH}_3$
1387	$\delta\text{C}-\text{CH}_3$
1266	$\nu\text{OC}$
1239	$\nu\text{OC}$
1190	$\nu\text{C-C-O}$
1145	$\nu\text{CO}$
988	$\tau\text{CH}$
841	$\tau\text{CH}$
750	$\tau\text{CH}_2$
	$\nu\text{C-C-O}$

FIGURE 7: Infrared spectrum ( $4000\text{--}500\text{ cm}^{-1}$ ) of undoped precipitated PMMA.

located approximately at  $1435\text{ cm}^{-1}$  whereas the peaks located between  $1210$  and  $1320\text{ cm}^{-1}$  and at  $1145\text{ cm}^{-1}$  may indicate O-C and C-O stretching, respectively. The peaks located between  $750$  and  $988\text{ cm}^{-1}$  may correspond to torsional deformation of CH bonds.

**3.4. Polymer Nanocomposite IR Characterization.** The FT-IR spectra shown in Figure 8 compare undoped precipitated PMMA (red) with ASA ligand capped nanocrystals and PA ligand capped nanocrystals dispersed in PMMA. The ASA system was synthesized to 2:1, 3:1, 4:1, and 5:1 molar ligand to nanocrystal ratio via synthetic Routes 1 and 2. PA system was also synthesized to 2:1, 3:1, 4:1, and 5:1 L:NC through water synthesis and methanol synthesis.

The green spectra represent PMMA nanocomposites composed of the PA system (PMMA:PA system) via water synthesis (dark green) and methanol synthesis (light green). The blue spectra correspond to the PMMA nanocomposites

made from the ASA system (PMMA:ASA system) where the nanoparticles were synthesized in water (dark blue) and in methanol (light blue).

All the anticipated peaks for the undoped PMMA were present in the spectra of the nanoparticle loaded PMMA (PMMA nanocomposite). The IR spectra of PMMA overlapped many of the absorption bands of the ligand systems except in area of  $1700\text{--}1500\text{ cm}^{-1}$ , inset of Figure 8. The peaks located in this area were found to correlate to peaks observed in the IR spectra of the ligands and nanoparticles.

The spectra in Figure 8 for the PMMA nanocomposite composed of the PA system (PMMA:PA:NC) via water (dark green) and methanol (light green) nanoparticle synthesis exhibited absorption peaks at  $1653\text{ cm}^{-1}$ ,  $1593\text{ cm}^{-1}$ , and  $1568\text{ cm}^{-1}$  that are not present in undoped PMMA. The  $1653\text{ cm}^{-1}$  reflects the C-O stretching of the formed anion. The  $1593$  and  $1568\text{ cm}^{-1}$  peaks are associated with C-C stretching in the pyridine ring. Świderski et al. observed a peak located at  $1606\text{ cm}^{-1}$  in picolinic acid that did not appear for any of the studied metal complexes which is similar to this work where the this peak did not appear in the IR spectra of the ligand capped nanocrystals.

The C-C stretching associated with the  $1568\text{ cm}^{-1}$  band was observed at lower wavenumber compared to the observed band ( $1572\text{ cm}^{-1}$ ) in picolinic acid. The wavenumber shift was comparable with the ligand coordination of weak cations in a study conducted by Świderski et al. [33]. The wavenumber reduction may be an indication of nanocrystal influence on the perturbation on the ligand system. There was no observed change in the  $1593\text{ cm}^{-1}$  peak.

The synthetic Route 2 of the PMMA:PA:NC produced broad peaks observed at center mid-points of  $3394\text{ cm}^{-1}$  and  $1616\text{ cm}^{-1}$ . The band with the center point of  $3394\text{ cm}^{-1}$  is related to the O-H stretching associated with methanol.

The synthetic Route 2 of the PMMA:ASA:NC produced broad peaks at center mid-points of  $3549\text{ cm}^{-1}$  representing O-H stretching that corresponds to residual solvent.

Two peaks at  $1601\text{ cm}^{-1}$  and  $1559\text{ cm}^{-1}$  were observed for the PMMA:ASA:NC that were not present in undoped PMMA. These bands suggest C-C stretching within the aromatic ring. The peaks were located at lower wavenumbers compared to the corresponding bands of  $1604\text{ cm}^{-1}$  and  $1562\text{ cm}^{-1}$  observed in ASA. In ASA:NC these peaks were located at  $\sim 1596\text{ cm}^{-1}$  with a shoulder at  $1562\text{ cm}^{-1}$ . Again, these changes in vibrational signatures are an indication of nanocrystal and ligand interaction.

The work presented by Wang et al. on a one-step synthesis of  $\text{LaF}_3:\text{Yb}^{3+}$  and  $\text{LaF}_3:\text{Er}^{3+}$  nanocrystals in methanol without ligands reported a broad absorption band around  $3412\text{ cm}^{-1}$  which was attributed to O-H stretching vibrations, that is, hydrogen bonding of alcohols [35, 36]. The absorption peak at  $3200\text{--}3400\text{ cm}^{-1}$  observed in Figure 4 is similar to the work of Wang et al. These peaks do not occur in synthetic Route 1 as a result of two drying steps which eliminate the water and hence the associated OH groups. The nanoparticles are dried before incorporation into the polymer/solvent solution and the nanocomposite is dried after phase inversion.

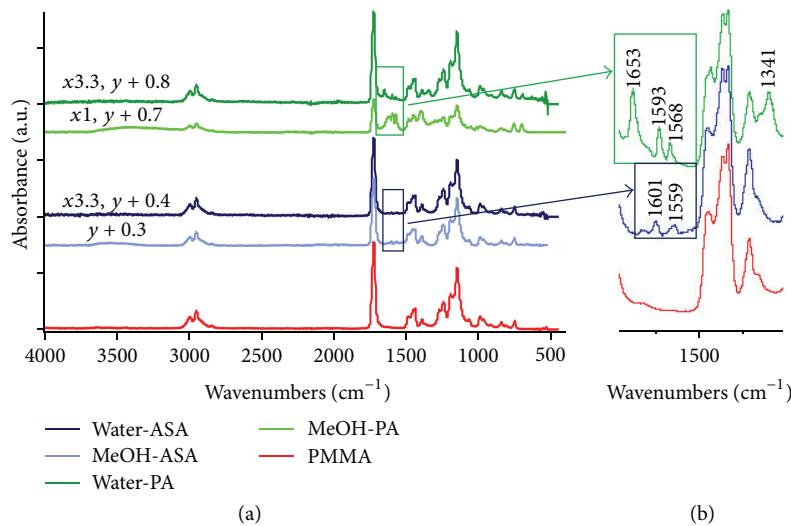


FIGURE 8: ATR infrared spectra (a) at 4000–500 cm<sup>-1</sup> of undoped precipitated PMMA (red), ASA systems via water (dark blue) and via methanol (light blue), and PA systems via water (dark green) and via methanol (light green). (b) Inset: representation of peaks located at 1700–1500 cm<sup>-1</sup>.

TABLE 4: Inorganic elemental composition and corresponding atomic percentage of nanoparticles synthesized in water and methanol at different molar ligand to nanocrystal ratios.

Synthetic route (solvent)	Molar ligand to nanocrystal ratio	PA : NC			ASA : NC		
		Elemental composition			Elemental composition		
		F atomic %	La atomic %	Tb atomic %	F atomic %	La atomic %	Tb atomic %
1 (water)	2:1	59	36	5	48	43	9
	3:1	46	46	8	61	31	8
	4:1	43	49	8	60	32	8
	5:1	64	31	5	62	31	7
2 (MeOH)	2:1	65	26	9	66	24	10
	3:1	54	36	10	67	24	9
	4:1	62	28	10	70	23	7
	5:1	64	22	14	61	31	8

**3.5. Elemental Analysis of Inorganic Component of Ligand Capped Nanocrystal.** The results of the elemental composition of the nanoparticles determined by energy dispersive X-ray (EDX) spectroscopy are summarized in Table 4. The ligand to nanocrystal ratios were calculated based on the molar concentrations of the ligand to those of the sum of La<sup>3+</sup> and Tb<sup>3+</sup>. The calculated atomic percentages were as follows: F, 75%, La, 20%, and Tb, 5%.

Data analysis through EDX confirmed the existence of Tb, La, and F in the doped nanocrystals. The desired lanthanum to terbium (La : Tb) molar ratio was 4:1 (80 : 20) since concentration quenching has been shown to occur when Tb<sup>3+</sup> levels exceeded 20% of the total RE ion component of the inorganic host nanocrystal [37].

In order to maintain an 80/20 ratio of La:Tb so as to minimize the possibility of concentration quench, the calculated fluoride to lanthanum ratio was 4:1 and fluoride to terbium was 14:1. The importance of the fluoride content

is related to its ability to act as a lattice stabilizer within the crystal allowing interspatial distance between the active ions [38]. All the experimental ratios were less than the calculated ratios. In the case of fluorine, this reduction could be attributed to the exchange of the fluoride anions with hydroxyl groups. The exchange between F and OH bonds throughout the nanoparticles is undesirable as a result of producing efficient deactivation pathways of the RE ion emissions [39].

#### 4. Conclusions

PMMA nanocomposites were produced via solution/precipitation chemistry using ligand capped nanocrystals doped with Tb<sup>3+</sup> ions. Two nanocomposite synthesis routes were evaluated with water being the solvent in Route 1 and methanol was used as the solvent in Route 2. The organic ligand (ASA and PA) and the inorganic nanocrystal (Tb<sup>3+</sup>:LaF<sub>3</sub>)

in the PMMA matrix were verified by ATR-FTIR spectroscopy and EDX analyses. PMMA nanocomposites produced with PA capped nanoparticles via synthesis Routes 1 and 2 exhibited absorption peaks that were not present in undoped PMMA. These peaks represented C–O stretching of the formed anion and the stretching vibrations of C–C bonds in the pyridine ring. For all the polymer nanocomposites loaded with ASA surface treated nanocrystals, C–H bond stretching of the aromatic ring structure produced absorption peaks that were not present in undoped PMMA. The EDX analysis confirmed the presence of  $Tb^{3+}$ ,  $La^{3+}$ , and F in the doped nanocrystals of all of the polymer nanocomposites.

## Conflict of Interests

The authors declare that there is no conflict of interests regarding the publication of the paper.

## Acknowledgments

The authors acknowledge the support and funding provided by the National Science Foundation Award HRD-0450279, Center of Optical Materials Science and Engineering Technologies (COMSET), Department of Materials Science and Engineering at Clemson University, Center for Materials Science, and Department of Engineering at James Madison University. A note of gratitude is given to Courtney Kucera and Kim Ivey for their help with this work.

## References

- [1] L. H. Slooff, A. van Blaaderen, A. Polman et al., “Rare-earth doped polymers for planar optical amplifiers,” *Journal of Applied Physics*, vol. 91, no. 7, pp. 3955–3980, 2002.
- [2] H. Ma, A. K. Jen, and L. R. Dalton, “Polymer-based optical waveguides: materials, processing, and devices,” *Advanced Materials*, vol. 14, pp. 1339–1365, 2002.
- [3] J. Zubia and J. Arrue, “Plastic optical fibers: an introduction to their technological processes and applications,” *Optical Fiber Technology*, vol. 7, no. 2, pp. 101–140, 2001.
- [4] K. Peters, “Polymer optical fiber sensors—a review,” *Smart Materials and Structures*, vol. 20, Article ID 013002, 2011.
- [5] A. M. Glass, D. J. DiGiovanni, T. A. Strasser et al., “Advances in fiber optics,” *Bell Labs Technical Journal*, vol. 5, no. 1, pp. 168–187, 2000.
- [6] L. G. Jacobsohn, C. J. Kucera, T. L. James et al., “Preparation and characterization of rare earth doped fluoride nanoparticles,” *Materials*, vol. 3, no. 3, pp. 2053–2068, 2010.
- [7] P. Wang, Y. Wang, and L. Tong, “Functionalized polymer nanofibers: a versatile platform for manipulating light at the nanoscale,” *Light: Science and Applications*, vol. 2, article e102, 2013.
- [8] H. Jiu, L. Zhang, G. Liu, and T. Fan, “Fluorescence enhancement of samarium complex co-doped with terbium complex in a poly(methyl methacrylate) matrix,” *Journal of Luminescence*, vol. 129, no. 3, pp. 317–319, 2009.
- [9] U. Resch-Genger, M. Grabolle, S. Cavaliere-Jaricot, R. Nitschke, and T. Nann, “Quantum dots versus organic dyes as fluorescent labels,” *Nature Methods*, vol. 5, no. 9, pp. 763–775, 2008.
- [10] J. Wang, S. Bo, L. Song, J. Hu, X. Liu, and Z. Zhen, “One-step synthesis of highly water-soluble  $LaF_3:Ln^{3+}$  nanocrystals in methanol without using any ligands,” *Nanotechnology*, vol. 18, no. 46, Article ID 465606, 2007.
- [11] D. Y. Kong, Z. L. Wang, C. K. Lin et al., “Biofunctionalization of  $CeF_3:Tb^{3+}$  nanoparticles,” *Nanotechnology*, vol. 18, no. 7, Article ID 075601, 2007.
- [12] M.-C. Daniel and D. Astruc, “Gold nanoparticles: assembly, supramolecular chemistry, quantum-size-related properties, and applications toward biology, catalysis, and nanotechnology,” *Chemical Reviews*, vol. 104, no. 1, pp. 293–346, 2004.
- [13] Y. Hiram and A. Nir, “A simulation of surface tension driven coalescence,” *Journal of Colloid And Interface Science*, vol. 95, no. 2, pp. 462–470, 1983.
- [14] F. C. J. M. Van Veggel, J. W. Stoudam, G. A. Hebbink, and J. Huskens, “In Lanthanide(III)-doped nanoparticles that emit in the near infrared,” in *Nanomaterials and Their Optical Applications*, vol. 5224 of *Proceedings of SPIE*, pp. 164–175, San Diego, Calif, USA, August 2003.
- [15] F. S. Richardson, “Terbium(III) and europium(III) ions as luminescent probes and stains for biomolecular systems,” *Chemical Reviews*, vol. 82, no. 5, pp. 541–552, 1982.
- [16] Y. Luo, X. Yu, W. Su et al., “Energy transfer in a ternary system composed of  $Tb(DBM)_3Phen$ ,  $Eu(DBM)_3Phen$ , and poly(N-vinylcarbazole),” *Journal of Materials Research*, vol. 24, no. 10, pp. 3023–3031, 2009.
- [17] S. Maji and K. S. Viswanathan, “Ligand-sensitized fluorescence of  $Eu^{3+}$  using naphthalene carboxylic acids as ligands,” *Journal of Luminescence*, vol. 128, no. 8, pp. 1255–1261, 2008.
- [18] K. Gipson, C. Kucera, D. Stadther, K. Stevens, J. Ballato, and P. Brown, “The influence of synthesis parameters on particle size and photoluminescence characteristics of ligand capped  $Tb^{3+}:LaF_3$ ,” *Polymers*, vol. 3, no. 4, pp. 2039–2052, 2011.
- [19] A. J. Kenyon, “Recent developments in rare-earth doped materials for optoelectronics,” *Progress in Quantum Electronics*, vol. 26, no. 4–5, pp. 225–284, 2002.
- [20] L. G. Jacobsohn, K. B. Sprinkle, C. J. Kucera et al., “Synthesis, luminescence and scintillation of rare earth doped lanthanum fluoride nanoparticles,” *Optical Materials*, vol. 33, no. 2, pp. 136–140, 2010.
- [21] B. Kokuzo, J. R. DiMaio, C. J. Kucera, D. D. Evanoff Jr., and J. Ballato, “Color kinetic nanoparticles,” *Journal of the American Chemical Society*, vol. 130, no. 37, pp. 12222–12223, 2008.
- [22] A. Alvarez-Ordóñez, D. J. M. Mouwen, M. López, and M. Prieto, “Fourier transform infrared spectroscopy as a tool to characterize molecular composition and stress response in foodborne pathogenic bacteria,” *Journal of Microbiological Methods*, vol. 84, no. 3, pp. 369–378, 2011.
- [23] H. Widiyandari, C. J. Hogan Jr., K. M. Yun, F. Iskandar, P. Biswas, and K. Okuyama, “Production of narrow-size-distribution polymer-pigment-nanoparticle composites via electrohydrodynamic atomization,” *Macromolecular Materials and Engineering*, vol. 292, no. 4, pp. 495–502, 2007.
- [24] H. G. Brittain, “Emission intensity of terbium(III) bound to benzene-carboxylic acid derivatives,” *Journal of Luminescence*, vol. 17, no. 4, pp. 411–417, 1978.
- [25] Y. Zhang, C. Gu, A. M. Schwartzberg, S. Chen, and J. Z. Zhang, “Optical trapping and light-induced agglomeration of gold nanoparticle aggregates,” *Physical Review B: Condensed Matter and Materials Physics*, vol. 73, no. 16, Article ID 165405, 2006.

- [26] J. Liu and Y. Li, "General synthesis of colloidal rare earth orthovanadate nanocrystals," *Journal of Materials Chemistry*, vol. 17, no. 18, pp. 1797–1803, 2007.
- [27] J.-Y. Shim and V. K. Gupta, "Reversible aggregation of gold nanoparticles induced by pH dependent conformational transitions of a self-assembled polypeptide," *Journal of Colloid and Interface Science*, vol. 316, no. 2, pp. 977–983, 2007.
- [28] I. G. Binev, B. A. Stamboliyska, and Y. I. Binev, "The infrared spectra and structure of acetylsalicylic acid (aspirin) and its oxyanion: an ab initio force field treatment," *Journal of Molecular Structure*, vol. 378, no. 3, pp. 189–197, 1996.
- [29] M. Boczar, M. J. Wójcik, K. Szczeponek, D. Jamróz, A. Zięba, and B. Kawalek, "Theoretical modeling of infrared spectra of aspirin and its deuterated derivative," *Chemical Physics*, vol. 286, no. 1, pp. 63–79, 2003.
- [30] R. Silverstein, G. Bassler, and T. Morrill, *Spectrometric Identification of Organic Compounds*, John Wiley & Sons, New York, NY, USA, 1991.
- [31] J. A. Dean, in *Analytical Chemistry Handbook*, G. F. Nalven and V. L. Miller, Eds., McGraw-Hill, New York, NY, USA, 1995.
- [32] V. V. Soman and D. S. Kelkar, "FTIR studies of doped PMMA—PVC blend system," *Macromolecular Symposia*, vol. 277, no. 1, pp. 152–161, 2009.
- [33] G. Świderski, M. Kalinowska, S. Wojtulewski, and W. Lewandowski, "Experimental (FT-IR, FT-Raman,  $^1\text{H}$  NMR) and theoretical study of magnesium, calcium, strontium, and barium picolinates," *Spectrochimica Acta Part A: Molecular and Biomolecular Spectroscopy*, vol. 64, no. 1, pp. 24–33, 2006.
- [34] P. Koczoń, J. C. Dobrowski, W. Lewandowski, and A. P. Mazurek, "Experimental and theoretical IR and Raman spectra of picolinic, nicotinic and isonicotinic acids," *Journal of Molecular Structure*, vol. 655, no. 1, pp. 89–95, 2003.
- [35] J. Wang, S. Bo, L. Song, J. Hu, X. Liu, and Z. Zhen, "One-step synthesis of highly water-soluble  $\text{LaF}_3:\text{Ln}^{3+}$  nanocrystals in methanol without using any ligands," *Nanotechnology*, vol. 18, no. 46, Article ID 465606, p. 6, 2007.
- [36] J. D. Roberts and M. C. Caserio, "Separation and purification. Identification of organic compounds by spectroscopic techniques," in *Basic Principles of Organic Chemistry*, pp. 257–349, W. A. Benjamin, Menlo Park, Calif, USA, 1977.
- [37] Z. L. Wang, Z. W. Quan, P. Y. Jia et al., "A facile synthesis and photoluminescent properties of redispersible  $\text{CeF}_3$ ,  $\text{CeF}_3:\text{Tb}^{3+}$ , and  $\text{CeF}_3:\text{Tb}^{3+}/\text{LaF}_3$  (core/shell) nanoparticles," *Chemistry of Materials*, vol. 18, no. 8, pp. 2030–2037, 2006.
- [38] W. Viehmann, "Influence of charge compensation on uv excitation of rare-earth fluorescence," *The Journal of Chemical Physics*, vol. 47, no. 3, pp. 875–883, 1967.
- [39] P. K. Sharma, R. Nass, and H. Schmidt, "Effect of solvent, host precursor, dopant concentration and crystallite size on the fluorescence properties of Eu(III) doped yttria," *Optical Materials*, vol. 10, no. 2, pp. 161–169, 1998.

## Research Article

# Characterization of Polysaccharide by HPLC: Extraction and Anticancer Effects

**Liming Gao,<sup>1</sup> Ya Di,<sup>1</sup> Jiandong Wu,<sup>1</sup> Ming Shi,<sup>2</sup> and Fulu Zheng<sup>1</sup>**

<sup>1</sup> The First Hospital of Qinhuangdao, No. 258 Wenhua Road, Qinhuangdao 066004, China

<sup>2</sup> Department of Biological Engineering, College of Environment & Chemical Engineering, Yanshan University, No. 438 Hebei Street, Qinhuangdao 066004, China

Correspondence should be addressed to Liming Gao; gaolimingerhao@163.com

Received 5 July 2014; Accepted 19 July 2014; Published 3 September 2014

Academic Editor: Tifeng Jiao

Copyright © 2014 Liming Gao et al. This is an open access article distributed under the Creative Commons Attribution License, which permits unrestricted use, distribution, and reproduction in any medium, provided the original work is properly cited.

Cervical cancer is a serious health hazard for women's reproductive system cancer; the method of treatment for cervical cancer is still in surgery, chemotherapy, and radiotherapy as the basic means, but with many complications. The effects of natural medicines for cervical cancer are increasingly becoming the focus of people's attentions. By studying the polysaccharide of cervical cancer in mice, we found that shark cartilage polysaccharide can increase the serum levels of T-SOD and GSH and decrease MDA level significantly in the tumor mice. The distribution of the drug in the tissue was determined by HPLC method; the drug can be drawn in the liver and kidney the highest, followed by the spleen, lung, and brain levels being the lowest. Polysaccharide can inhibit tumor growth in the mice which may be connected with the enhanced immunity and the antioxidant capacity.

## 1. Introduction

Cervical cancer is a common cancer of the female reproductive system, which ranks second in the incidence of cancer in women worldwide, second only to breast cancer; it is a serious threat to women's health. According to the statistics worldwide, the number of new cases of cervical cancer each year reached 500,000, particularly common in developing countries; China's new cases are about 100,000, according for about 1/5 of the world total new case, and more than 30,000 women die of cervical cancer every year [1]. In recent years, the number of young patients with cervical cancer processes upward trend clearly, which deserves people's attention. The method of treatment for cervical cancer is still in surgery at present, chemotherapy, and radiotherapy as the basic means; the disadvantage is more complications. The treatment model has changed and the local control rate and survival have been improved. Now western medicine had been widely used, but it still has some shortcomings, such as severe toxicities, increased drug-induced disorders, the efficacy being not ideal, and the high drug prices, so that people look forward to natural medicine more. Because the toxicity of natural plant and animal is little, they are easily accepted by patients,

playing an important role in the anticancer drugs. Looking for anti-tumor drugs from natural plants and animals in order to improve the therapeutic effect is increasingly becoming the focus of attention [2, 3].

Polysaccharides are a class of natural macromolecular polymers *in vivo* generally. It is made of aloes or ketoses which connected together by glycoside bonding. Since the 1970s, with the development of polysaccharides special physiological function (transportation intercellular substance, regulation of immune function, cell-cell recognition, etc.), Polysaccharides, whose antitumor and immunomodulatory effects of polysaccharides draw more attention, caught more attention of drug workers.; it has become one of the hot spots of cancer treatment [4–7].

At present, gained more and more novel structure and the unique role of bioactive polysaccharide from marine organisms has been expected to become a new drug resource of cancer treatment [8]. With further research, we have noted the so-called "sea scavenger" sharks which almost never suffer from cancer. After years of research, scientists found that shark cartilage polysaccharide, as an animal polysaccharide, has a variety of physiological effects: lowering blood pressure, antiradiation, anticoagulation of the blood,

antiviral, and antitumor [9–12]. For the study of the polysaccharide, predecessors mostly stay in the extraction process studied. In recent years there are only a few more reports in terms of functional studies. Currently, the country has listed health food products, shark cartilage capsules, made of shark cartilage. In other countries, the glycosaminoglycan chondroitin sulfate of shark's raw material products has been used in patients clinically [13, 14]. Research on shark cartilage mucopolysaccharide has caused widespread interest by scholars inside and outside.

The topic for the functional role of the polysaccharide to do further research and for the treatment of cervical cancer provides effective and less toxic side effects of natural medicine; the development of these drugs has a certain significance.

## 2. Experiments

**2.1. Materials.** In this experiment, we use the catshark cartilage as a raw material provided by Yanshan University Laboratory; the 8-week-old female Kunming mice were purchased from Beijing Military Medical Sciences weighing 20–24 g. U14 mouse cancer cell line was purchased from China Medical College Beijing tumor cell library.

**2.2. The Extraction of Shark Cartilage Polysaccharides.** In this study, shark cartilage was removed from sharks and taken into boiling water for 2.5 h to remove most of the bone marrow and adipose tissue, and then low-temperature drying, splintered and weight. Powder cartilage into 1000 mL 0.3 mol/L sodium hydroxide dilute alkali solution, followed by stirring at 65°C 3 hours, centrifuge, adjust the pH of the supernatant to 3, and centrifuge. We Sodium chloride solution was added slowly to the supernatant slowly until the precipitate to the most, the supernatant was centrifuged and the supernatant was concentrated by evaporation. The resultant product was washed by 60% and 80% ethanol solution.

**2.3. The Determination of the Polysaccharide.** We use phenol-sulfuric acid method to determine polysaccharide extract. Principle of this method is the polysaccharide in concentrated sulfuric acid; dehydration or furfural and HMF can condense orange-red phenol compounds, within a certain range proportional to the depth of its color and sugar content, and in the 490 nm wavelength of maximum absorption peak, the UV spectrophotometry available in this wavelength. Phenol method can be used for determination of methylated sugar, pentose sugars, and polysaccharides. The method is simple and sensitive. The experiment is unaffected by the presence of proteins substantially, and the resulting color stability is over 160 min.

**2.4. Preparation of U14 Cervical Tumor-Bearing Mouse Model.** Take three normal mice by intraperitoneal injection method U14 tumor cell inoculation 0.2 mL cell suspension. The first eight days, put the mice to death, collect the ascites,

centrifuged, dilute the supernatant into density of  $1.60 \times 10^6$  cells/mL, and inject 0.2 mL into mouse forelimb left armpit.

**2.5. Experimental Groups and Drug Program.** The inoculated mice were randomly divided into four groups of 8. The polysaccharide dissolved in distilled water to prepare a high-dose group (1000 mg/kg) and low-dose group (500 mg/kg); each group was fed 0.2 mL, negative control group was fed the same amount of distilled water, and positive control group was injected 0.2 mL CTX intraperitoneally (25 mg/kg), once a day. Administration continued for 14 days; first on day 15, all the mice were sacrificed.

**2.6. Determination of Tumor Inhibition Rate.** First on day 15 all the mice were sacrificed, and tumor of each group mice was taken and then weighed; the tumor inhibition rate is calculated according to the following formula:

$$\begin{aligned} &\text{Tumor inhibition rate (\%)} \\ &= \left[ \frac{\text{(the average tumor weight of negative control group}}{\text{– the average tumor weight of medication group}} \right. \\ &\quad \times \text{(the average tumor weight}} \\ &\quad \left. \text{of negative control group}} \right]^{-1} \times 100\%. \end{aligned} \quad (1)$$

**2.7. Determination of Thymus and Spleen Weight Index.** The mice were taken off the neck to death; we remove the thymus and spleen and observe them by naked eye. In accordance with the “immune organ weights law” in “immunized animals screening procedures” on the tumor-bearing mouse thymus, the spleen and thymus index [15] was calculated according to formula 2:

$$\begin{aligned} &\text{Thymus (spleen) Index (mg/10 g)} \\ &= \left[ \frac{\text{thymus (spleen) weight}}{\text{weight to tumor-bearing mice}} \right] \times 10. \end{aligned} \quad (2)$$

**2.8. Serum and Tissue Antioxidant Parameters Were Measured.** We prepare serum for the determination of serum SOD (superoxide dismutase), GSH (glutathione reductase), and MDA (malondialdehyde) level; we took liver tissue at the same time, plus saline formulated into 10% of the tissue homogenates, for the determination of their GSH, SOD, and MDA levels.

**Determination of SOD.** Serum total SOD activity is calculated as follows:

$$\begin{aligned} &\text{The total SOD activity} \\ &= \frac{\text{Control tube absorbance}}{\text{–Absorbance measurement tube}} \\ &\quad \times \left( \frac{\text{Control tube absorbance}}{\text{Control tube absorbance}} \right)^{-1} \\ &\quad \div 50\% \times \text{Dilution of the sample before the test.} \end{aligned} \quad (3)$$

The total tissue SOD activity is calculated using the following formula:

$$\begin{aligned}
 & \text{The total SOD activity} \\
 & = (\text{Control tube absorbance} \\
 & - \text{Absorbance measurement tube}) \\
 & \times (\text{Control tube absorbance})^{-1} \\
 & \div 50\% \times \left( \frac{\text{Total reaction volume}}{\text{Sample volume}} \right) \\
 & \div \text{Tissue protein content (mgprot/mL).}
 \end{aligned} \tag{4}$$

*Determination of Glutathione.* Consider

GSH content in serum

$$\begin{aligned}
 & = (\text{OD value measured} - \text{blank OD value}) \\
 & \times \text{standard concentration} \\
 & \times (20 \times 10^{-3} \text{ mmol/L}) \\
 & \times \text{GSH molecular weight (307)} \\
 & \times \text{prior to the test sample dilution factor} \\
 & \div (\text{OD value of the standard} - \text{blank OD value}),
 \end{aligned}$$

Liver GSH content

$$\begin{aligned}
 & = (\text{OD value measured} - \text{blank OD value}) \\
 & \times \text{standard concentration} (20 \times 10^{-3} \text{ mmol/L}) \\
 & \times \text{GSH molecular weight (307)} \\
 & \times \text{dilution of the test sample} \\
 & \div (\text{OD value of the standard} - \text{blank OD}) \\
 & \div \text{protein concentration.}
 \end{aligned} \tag{5}$$

*Determination of Malondialdehyde.* Consider

$$\begin{aligned}
 & \text{Serum (plasma) MDA content (nmol/mL)} \\
 & = (\text{measured OD values} - \text{control OD value})
 \end{aligned}$$

$$\begin{aligned}
 & \times \text{standard concentration} \\
 & \times \text{dilution of the sample prior to testing} \\
 & \div (\text{standard OD value} - \text{blank OD value}),
 \end{aligned} \tag{6}$$

$$\begin{aligned}
 & \text{Liver tissue MDA content (nmol/mgprot)} \\
 & = (\text{measured OD values} - \text{control OD value}) \\
 & \times \text{concentration of the sample standard} \\
 & \div \text{protein concentration (mgprot/mL)} \\
 & \div (\text{standard OD value} - \text{blank OD value}).
 \end{aligned} \tag{6}$$



FIGURE 1: Each concentration of the standard solution.

*Determination of Protein Content.* The formula is as follows:

$$\begin{aligned}
 & \text{Protein concentration (g/L)} \\
 & = (\text{measured OD value} - \text{blank OD value}) \\
 & \times \text{standard concentration (g/L)} \\
 & \div (\text{standard OD value} - \text{blank OD value}).
 \end{aligned} \tag{7}$$

**2.9. HPLC Determination of the Distribution of the Drug in Tissues.** Two hours after the last administration, the heart, liver, spleen, lung, kidney, and other tissues of the mice are completely removed, weighed, and ground, mixed with 10% saline, centrifuged for 10 min, adding methanol into supernatant and ultrasonic shock for 20 min. Mix well, centrifuge for 10 min, and filter the supernatant with 0.45  $\mu\text{m}$  membrane.

The column was Edipse XDB-C18 (4.6  $\times$  250 mm, 5  $\mu\text{m}$ ). A mobile phase of acetonitrile and mobile phase B were 0.1% phosphate buffered saline (pH = 3). Ratio of the two mobile phases is A : B = 15 : 85, with a gradient elution procedure to adjust the ratio of the two-phase flow; column temperature was room temperature; flow rate was 0.5 mL/min; injection volume was 20.0  $\mu\text{L}$ ; detection wavelength was 200 nm; and each run time was 5 min.

### 3. Result

**3.1. Shark Cartilage Extract Polysaccharides.** After pretreatment for shark cartilage, we say its weight: 62.7 g. After digestion of dilute alkali solution, a salt solution to dislodge the protein, ethanol precipitation, and a series of operations, we eventually dry the precipitate to obtain 1.98 g of the polysaccharide crude extract.

**3.2. Determination of Shark Polysaccharide.** Prepared according to the method of the standard, the concentration of glucose standard solution was obtained the color shown in Figure 1.

In the 490 nm wavelength measured absorbance standard concentrations are shown in Table 1.

Standard curve using Excel software, standard glucose levels ( $\mu\text{g}/\text{mL}$ ) for the  $x$ -axis and  $y$ -axis plotted as absorbance are obtained using the standard curve regression equation:  $Y = 0.0151X + 0.0364$ , and the correlation coefficient  $r^2 = 0.9933$ . The linear range is 10–60  $\mu\text{g}/\text{mL}$ . The resulting standard curve is as shown in Figure 2. In accordance with

TABLE 1: Glucose standard solution absorbance.

Glucose concentration absorbance ( $\mu\text{g/mL}$ )	10	20	30	40	50	60
First	0.221	0.347	0.515	0.608	0.782	0.945
Second	0.221	0.346	0.516	0.608	0.781	0.945
Third	0.222	0.347	0.516	0.608	0.782	0.944

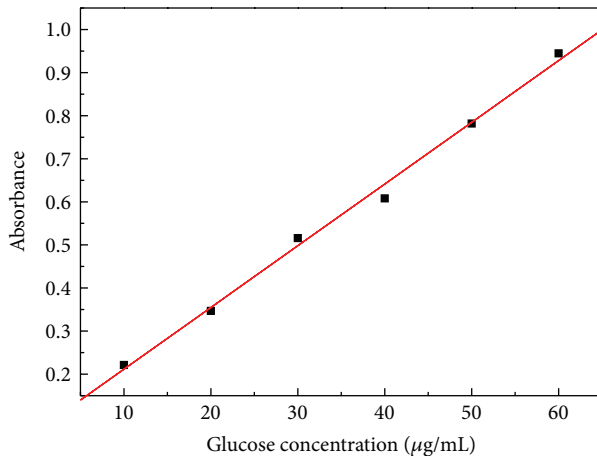


FIGURE 2: Glucose standard curve.

the standard curve regression equation, the sugar content can be drawn from the test corresponding absorbance. Calculated by the test solution to be tested for the average absorbance of 0.407, as the Y values into the regression equation, derived X value 24.54  $\mu\text{g/mL}$ , the final content of polysaccharide extract obtained was 81.8%, the total extraction rate of 2.58%.

**3.3. Animals Generally Observed.** After administration of the first four days, all mice grew visually observable mass, and mice are in good spirit and move freely, and no deaths occurred. After 14 days of continuous administration of each treatment group mice were having sparse dull hair, were lying curled with back arched, and were action-insensitive, apathetic, unresponsive, and so on, and because of the increasing of tumor weight, tumor-bearing mice significantly increased body weight. Negative control group and treated group were compared with the above symptoms of weight. Mental state of positive control group of mice is better, the action is more flexible, and weight gain is not obvious (shown in Table 2 and Figure 3).

**3.4. The Polysaccharide Solid Tumor Inhibition Rate.** The polysaccharide in mice results in tumor inhibition rates are shown in Table 3. High and low dose polysaccharides have anti-tumor effect; tumor inhibition rates were 34.73% and 65.81%, respectively, and the positive control group CTX tumor inhibition rate is 63.71%. Regarding weight compared with the negative control group tumors, average tumor weight difference between the polysaccharide low-dose group and positive control group was significant ( $P < 0.01$ ), and

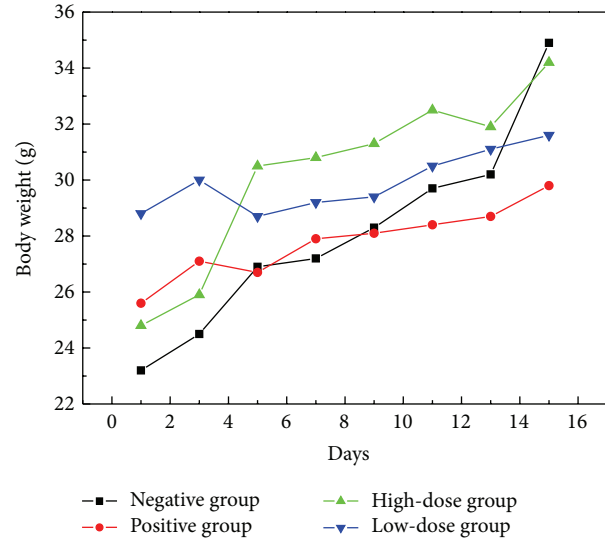


FIGURE 3: The average weight of the mice in each group situation.

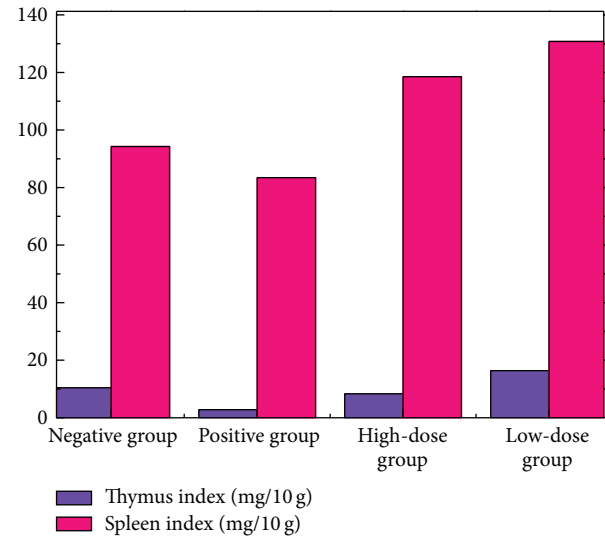


FIGURE 4: Thymus and spleen index of mice.

the average tumor weight difference between the high-dose group was significant ( $P < 0.05$ ). The average tumor weight of the low-dose group was compared with the CTX-positive control group, and the difference was not significant ( $P > 0.05$ ); the high-dose group was compared with the control group, CTX-positive, and the difference was significant ( $P < 0.05$ ); results suggest that low doses of shark cartilage have significant inhibition of solid tumor polysaccharide with mice.

**3.5. Determination of Mouse Thymus (Spleen) Index.** Each group of mice thymus (spleen) index as shown in Table 4 and Figure 4, the body of thymus and spleen was reduced in positive group mice was with significantly reduced volume of thymus and spleen, thymus color was gray, leaf was unclear, and spleen is pale red. The thymus index and spleen index of

TABLE 2: The average weight of each group of mice (g).

Days/group	1	3	5	7	9	11	13	15
Negative group	23.2	24.5	26.9	27.2	28.3	29.7	30.2	34.9
Positive group	25.6	27.1	26.7	27.9	28.1	28.4	28.7	29.8
High-dose group	24.8	25.9	30.5	30.8	31.3	32.5	31.9	34.2
Low-dose group	28.8	30.0	28.7	29.2	29.4	30.5	31.1	31.6

TABLE 3: Inhibition rate of each group of mice ( $\pm S$ ).

Group	Dose (mg/kg)	Starting weight (g)	Final weight (g)	Tumor weight (g)	Inhibition rate (%)
Negative group	—	23.24 $\pm$ 0.81	34.94 $\pm$ 1.21	3.896 $\pm$ 0.46	0
Positive group	25	25.66 $\pm$ 1.12	29.82 $\pm$ 1.43	1.474 $\pm$ 0.10**	63.71
High-dose group	1000	24.82 $\pm$ 1.58	34.23 $\pm$ 0.84	2.543 $\pm$ 0.52**#	34.73
Low-dose group	500	28.84 $\pm$ 1.26	31.64 $\pm$ 1.12	1.332 $\pm$ 0.23**	65.81

TABLE 4: Mice in each group thymus (spleen) index ( $\pm S$ ).

Group	Dose (mg/kg)	The final number of animals	Thymus index (mg/10 g body weight)	Spleen index (mg/10 g body weight)
Negative group	—	4	10.43 $\pm$ 1.36	94.26 $\pm$ 3.84
Positive group	25	6	2.81 $\pm$ 0.74#	83.45 $\pm$ 2.76
High-dose group	1000	4	8.32 $\pm$ 0.58*	118.54 $\pm$ 10.85**#
Low-dose group	500	5	16.38 $\pm$ 1.64***	130.78 $\pm$ 13.24***

TABLE 5: The polysaccharide impact ( $\bar{X} \pm S$ ) for mouse serum antioxidant capacity.

Group	Dose (mg/kg)	SOD (U/mL)	GSH (mg/L)	MDA (nmol/mL)
Negative group	NS	89.84 $\pm$ 8.87	3.43 $\pm$ 0.68	4.26 $\pm$ 0.78
Positive group	25	124.36 $\pm$ 9.96	2.91 $\pm$ 0.49	8.45 $\pm$ 0.69
High-dose group	1000	136.42 $\pm$ 10.52**#	4.32 $\pm$ 0.98*	7.54 $\pm$ 1.05*
Low-dose group	500	168.43 $\pm$ 9.48**#	6.78 $\pm$ 0.63***	3.78 $\pm$ 0.86*#

Note: compared with the positive control group, \*  $P < 0.05$ , \*\*  $P < 0.01$ ; compared with negative control group, #  $P < 0.05$ , ##  $P < 0.01$ .

the polysaccharide of both high- and low-dose groups were higher than the positive control group, and the thymus was observed to have more complete appearance and white color, the color of the normal spleen. The polysaccharide low-dose group and spleen index and thymus index have increased compared to CTX-positive and CTX-negative groups; the statistical analysis showed that the polysaccharide low-dose group and the positive control group showed significant difference ( $P < 0.01$ ); shark cartilage polysaccharide of high-dose group compared with the positive control group showed significant differences ( $P < 0.05$ ); high- and low-dose group and negative control group showed low doses of the negative control group, and the difference was significant ( $P < 0.05$ ) compared with high-dose group and negative control groups, but the difference did not reach a significant level ( $P > 0.05$ ), and negative control groups and the positive control group were significantly difference ( $P < 0.05$ ). This indicates that CTX will not be able to promote the growth of immune organs but will be destroyed, inhibiting the development of the thymus and spleen tissue, and high- and low-dose groups can promote the growth of the thymus and spleen, and thymus tissue of the high-dose group developed a certain promoting effect, but the effect is not obvious, to promote the development of the role of spleen tissue, and the

effect of low-dose group was significant, suggesting that the polysaccharide has better effect than CTX.

**3.6. Effects of Shark Cartilage Polysaccharides on Serum Antioxidant Capacity in Mice.** As shown in Table 5, the high- and low-dose group could significantly improve tumor-bearing mouse serum SOD activity, compared with the negative control group, and the difference was significant ( $P < 0.01$ ); and CTX-positive group was significantly higher ( $P < 0.05$ ), whereas serum CTX levels of SOD-positive group compared with the control group, although a certain degree rises, but the difference between the two has not yet reached a significant level ( $P > 0.05$ ), indicating that the polysaccharide can increase SOD activity in tumor-bearing mice, better than CTX. Meanwhile, the low-dose group had significantly higher serum GSH content compared with the negative group ( $P < 0.05$ ), while the high-dose group showed a rising trend, though, but has not yet reached a significant level ( $P > 0.05$ ); with CTX group phase ratio, serum GSH content of low-dose group increased significantly ( $P < 0.01$ ), but with no significant difference ( $P$  between the high-dose group and CTX-positive group  $> 0.05$ ). Those high doses of the polysaccharide treatment can significantly increase serum GSH levels in tumor-bearing mice, and CTX has similar

TABLE 6: The polysaccharide impact for mouse liver tissue antioxidant capacity.

Group	Dose (mg/kg)	SOD (mg/prot)	GSH (mg/prot)	MDA (nmol/mgprot)
Negative group	NS	189.21 ± 4.28	10.43 ± 0.36	17.26 ± 1.54
Positive group	25	223.23 ± 10.47 <sup>#</sup>	2.81 ± 0.74	10.43 ± 1.62
High-dose group	1000	242.54 ± 14.68 <sup>#</sup>	8.32 ± 0.58 <sup>**#</sup>	8.54 ± 0.85 <sup>**#</sup>
Low-dose group	500	284.68 ± 17.32 <sup>*#</sup>	15.32 ± 0.84 <sup>***#</sup>	4.76 ± 0.74 <sup>***#</sup>

Note: compared with the positive control group, \*P < 0.05, \*\*P < 0.01; compared with negative control group, <sup>#</sup>P < 0.05, <sup>##</sup>P < 0.01.

effect, but the effect of low-dose treatment is superior to the polysaccharide CTX-positive group. MDA activity was measured in serum tumor-bearing mice results which show that, compared with the negative control group, low-dose group had significantly lower serum MDA activity in mice ( $P < 0.05$ ), while the CTX group of tumor-bearing mice did not reduce the activity of serum MDA effect ( $P > 0.05$ ). Meanwhile, in low- and high-dose groups compared with the CTX group, serum MDA was significantly lower ( $P < 0.05$ ). Therefore, polysaccharide can reduce the content of serum MDA.

**3.7. Effects of the Polysaccharide on Liver Tissue Antioxidant Capacity.** Each group of mice administered continuously for 14 days was killed, the liver tissues were measured for SOD, GSH, and MDA activity, and the results are shown in Table 6. From the table, compared to the negative control group, high- and low-doses of SOD activity group and CTX group were significantly increased ( $P < 0.05$ ); differences were compared with the positive control group; the high-dose group and the positive group are not significant ( $P > 0.05$ ), low-dose group and CTX-positive group were significantly increased compared to the drop ( $P < 0.05$ ). For the determination of GSH, compared with the negative control group, low-dose group GSH levels were significantly higher ( $P < 0.05$ ); compared with CTX, high- and low-dose groups were significantly different in the level of activity ( $P < 0.01$ ). Compared with negative group, the content of MDA in high and low dose group mice liver were lower, the differences were highly significant ( $P < 0.01$ ); compared with the CTX group, the high- and low-dose groups were significantly lower than CTX treatment group ( $P < 0.05$ ). Hypoxia is one of the physiological abnormalities characteristic of solid tumors, and these results suggest that the polysaccharide, maybe by improving the organization's ability to achieve the antioxidant defenses, improves the hypoxic state.

### 3.8. HPLC Determination of the Distribution of the Drug in Tissues

**3.8.1. Chondroitin Sulfate Standard Curve and Regression Equation.** According to the standard method of preparation, the concentration of the prepared solution of the test sample to the standard chromatograms obtained from the map read out the corresponding peak area (Table 7) to obtain a standard curve (Figure 6 peak area under the concentration) and the linear regression equation. Figure 5 is chromatogram of standard 0.4 mg/mL

TABLE 7: Absorption peak area of each concentration of standard.

Standard concentration μg/mL	0.1	0.2	0.4	0.6	0.8
Peak area mAU * S	50.1421	63.0977	92.743	115.428	139.675

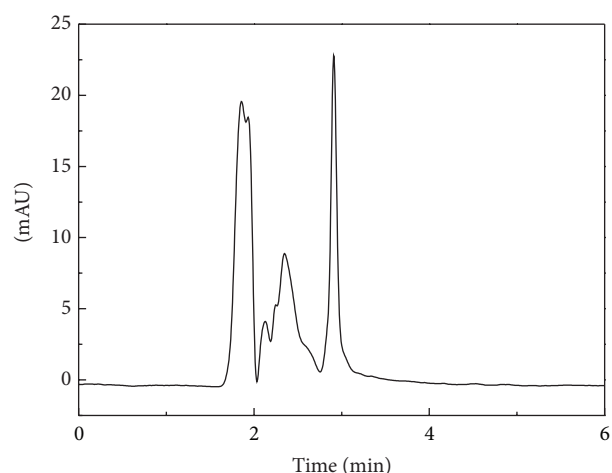


FIGURE 5: Chromatogram of standard 0.4 mg/mL.

Retention time is 3.594; DAD1 A; Sig is 200, 4; Ref = 360, 100. Residual standard error is 1.93706. Regression equation is  $y = 125.39383x + 40.14115$ , where  $x$  is the content of chondroitin sulfate and  $y$  is the peak area; dependency is 0.99891. Chondroitin sulfate at 0.1–0.9 μg/mL is in good linear relationship.

**3.8.2. The Concentration of Drug in the Tissue Sample.** Take the heart, liver, spleen, lung, and kidney of high- and low-dose group; after treating each tissue sample, we can obtain drug content shown in Table 8. From Figure 8 in each group it is observed that in liver and kidney tissue drug content is generally higher than in other tissues, followed by the content of the heart, spleen, and lung relatively little content. The result shows that drug distribution in mice was wide range. Figure 7 is samples of liver tissue of a low-dose of the chromatogram.

## 4. Discussions

In this study, shark cartilage polysaccharides was extracted with dilute and alcohol precipitation method, purified by phenol-sulfuric acid method, but the total withdrawal rate

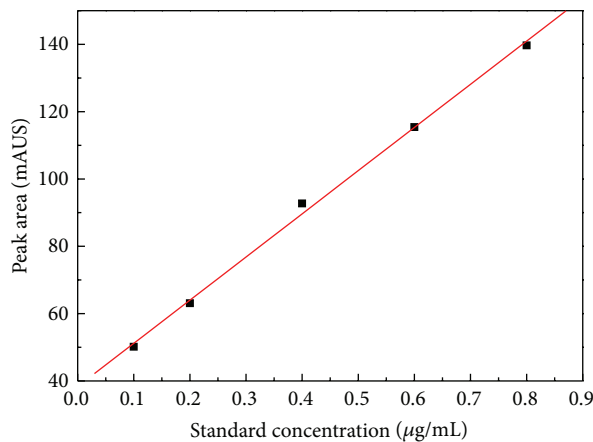


FIGURE 6: Chondroitin sulfate standard curves.

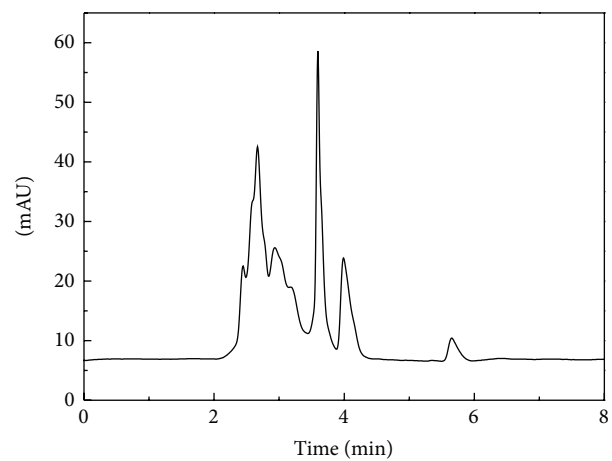


FIGURE 7: Samples of liver tissue of a low dose of the chromatogram.

TABLE 8: Distribution of drugs in different tissues.

Classes	Drug content of the low-dose group ( $\mu\text{g/mL}$ )	Drug content of the high-dose group ( $\mu\text{g/mL}$ )
Heart	0.33	0.62
Liver	0.88	0.73
Spleen	0.26	0.16
Lungs	0.19	0.10
Kidney	0.84	0.90

is low, and extraction conditions remain to be further optimized; overall for shark cartilage polysaccharide extraction method and content of appraisal provide research basis.

The body ability of antioxidant defense system strength and weakness are closely related to health, and the antioxidant effect of the defense system is mainly to eliminate free radicals and reactive oxygen species in order to prevent the occurrence of lipid peroxide, decomposition of peroxide, and peroxide blocking chain. The body produced oxygen free radicals by enzymes and nonenzyme system and formed lipid peroxides. Due to the excess of oxygen free radicals and lipid peroxides, DNA is damaged and mutations occur, leading to cell damage, which are closely associated with tumor formation. Such MDA is formed in the process of lipid peroxides, MDA is a kind of mutagen and genetic agent, and the development of human tumor probably has to do with it. Our study found that treatment group compared with negative control group and CTX-positive control group can significantly reduce the MDA in the serum in mice and that shark cartilage polysaccharide could inhibit the generation of MDA in the serum and inhibit portability tumor development. The body's antioxidant system mainly consists of antioxidant enzymes and antioxidants. SOD can clear the super oxide anion radicals in the body protecting cells from injury. It plays a key role at body's anti-oxidant. Thus, SOD activity is closely related to tumor and inflammation diseases. Positive compared with negative control group, CTX group, mice thymus index, spleen index, SOD content in serum and tissue, and GSH levels were significantly lower; this is

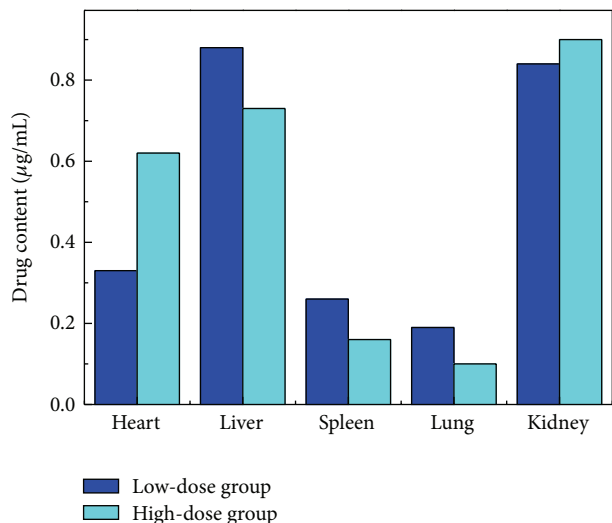


FIGURE 8: High- and low-dose group of organizations in the distribution of drug content.

mainly because of CTX being a kind of immunosuppressant and it caused, by inducing cell apoptosis, thymus and spleen shrinks, thus leading to the decrease of antioxidant defense system of organization. While, the thymus and spleen index SOD, MDA level of high and low does group have been increased, and tip shark cartilage polysaccharide probably inhibits lymphocyte apoptosis of immune organ and enhances the antioxidant capacity of organizations to inhibit tumor development. Shark cartilage polysaccharide probably inhibits lymphocyte apoptosis of immune organ and enhances the antioxidant capacity of organizations to inhibit tumor development.

## 5. Conclusions

Shark cartilage polysaccharide in mice tissues distribution is broad, most abundant in the liver and kidney, which may be related to the metabolism of the liver and kidney as the main

metabolic organs. Visibly, shark cartilage polysaccharide could inhibit tumor growth in mice solid tumor and improve the index of thymus and spleen in mice, showing that it can promote the growth of immune organs and increase the body's immune function and the antioxidant defense system ability, thus suppressing tumor growth.

## Conflict of Interests

The authors declare that they do not have any direct financial relation with the commercial identities mentioned in this paper that might lead to a conflict of interests for any of the authors.

## References

- [1] Y. Xu, Z. Ouyang, P. Liu, and C. Chen, "Magnetic resonance imaging in uterine fibroid embolization," *Chinese Journal of Gynecology and Obstetrics*, vol. 10, no. 4, pp. 23–25, 2011.
- [2] X. Zhuan and X. Gu, "Epidemiological investigation of cervical cancer risk factors," *Chinese Maternal and Child Health*, vol. 23, pp. 4053–4056, 2008.
- [3] L. Li and C. Li, "Prevention and screening of cervical cancer," *Chinese Journal of Practical Gynecology*, vol. 19, p. 151, 2003.
- [4] Z. Xiong and D. Chen, "Advances in tumor mechanism," *Chinese Medicine*, vol. 7, no. 12, pp. 112–114, 2001.
- [5] M. Yang, "Research on polysaccharide antitumor mechanism of action," *Zhejiang Journal of Medicine*, vol. 12, no. 6, pp. 65–68, 2002.
- [6] S. Sipka, G. Ábel, J. Csorong, G. Chihara, and J. Fachet, "Effect of lentinan on the chemiluminescence produced by human neutrophils and the murine macrophage cell line C4Mφ," *International Journal of Immunopharmacology*, vol. 7, no. 5, pp. 747–751, 1985.
- [7] R. Goldman, "Characteristics of the  $\beta$ -glucan receptor of murine macrophages," *Experimental Cell Research*, vol. 174, no. 2, pp. 481–490, 1988.
- [8] L. Zhao, "Li Ming Chun study mechanisms of tumor progression marine organisms Polysaccharide," *Practical Journal of Medicine*, vol. 9, no. 27, pp. 845–846, 2010.
- [9] X. Hao, S. Ye, and Z. Wu, "The polysaccharide anticoagulant effect," *China Marine Drugs*, vol. 44, no. 4, pp. 17–22, 1992.
- [10] D. Fu, Z. He, and L. Li, "Antithrombotic effect of shark cartilage glycosaminoglycan study," *China Marine Drugs*, vol. 43, no. 3, 1992.
- [11] F. Jia, Z. He, and L. Wang, "Cartilage angiogenesis anticancer mechanism of inhibition of the active ingredient," *Chinese Journal of Biochemical Pharmaceutics*, vol. 18, no. 2, pp. 68–71, 1997.
- [12] M. Zhang, L. Chen, and X. Mai, "Anticancer effect of shark cartilage progress," *Tianjin Pharmacy*, vol. 15, no. 1, pp. 44–46, 2003.
- [13] D. Gingras, A. Renaud, N. Mousseau et al., "Sharkearila-geextractsasantiangiogenieangents: smartofbitter1115," *Cancer metastasis*, vol. 19, no. 1, 2000.
- [14] H. Wu, B. Yuan, and B. Jiao, "Pharmacological and clinical research progress shark cartilage preparations," *China Marine Drugs*, vol. 4, no. 8, pp. 51–55, 2001.
- [15] Y. Chang, "Schisandra polysaccharide of H22, S180 experimental study inhibition of tumor-bearing mice," *TCM information*, vol. 4, no. 5, pp. 18–20, 2002.

## Research Article

# Experimental Study of the Composition and Structure of Granular Media in the Shear Bands Based on the HHC-Granular Model

Guang-jin Wang,<sup>1</sup> Xiang-yun Kong,<sup>1</sup> and Chun-he Yang<sup>2,3</sup>

<sup>1</sup> Kunming University of Science and Technology, Kunming 650093, China

<sup>2</sup> Institute of Rock and Soil Mechanics, Chinese Academy of Sciences, Wuhan 430071, China

<sup>3</sup> State Key Laboratory of Coal Mine Disaster Dynamics and Control, Chongqing University, Chongqing 400030, China

Correspondence should be addressed to Guang-jin Wang; wangguangjin2005@163.com

Received 9 June 2014; Accepted 25 July 2014; Published 31 August 2014

Academic Editor: Tifeng Jiao

Copyright © 2014 Guang-jin Wang et al. This is an open access article distributed under the Creative Commons Attribution License, which permits unrestricted use, distribution, and reproduction in any medium, provided the original work is properly cited.

The researchers cannot control the composition and structure of coarse grained soil in the indoor experiment because the granular particles of different size have the characteristics of random distribution and no sorting. Therefore, on the basis of the laboratory tests with the coarse grained soil, the HHC-Granular model, which could simulate the no sorting and random distribution of different size particles in the coarse-grained soil, was developed by use of cellular automata method. Meanwhile, the triaxial numerical simulation experiments of coarse grained soil were finished with the different composition and structure soil, and the variation of shear strength was discussed. The results showed that the internal friction angle was likely to reduce with the increasing of gravel contents in the coarse-grained soil, but the mean internal friction angle significantly increased with the increment of gravel contents. It indicated that the gravel contents of shear bands were the major factor affecting the shear strength.

## 1. Introduction

The strength parameters of granular media are the main factor to affect the stability of dumping site. However, the reasonable strength parameters of granular media are hard to get. Jiang Jingshan's studies showed that the composition and fabric granular particle were the fundamental reasons that induced the macromechanical properties to be complex and led the macroscopic mechanical properties to show strong dispersion characteristics [1, 2]. The influencing factors can be broadly divided into two kinds [3]. The first factor is the test site, load-applying manner, sample size, confining pressures, strain rate, drainage condition, the factors related with the material properties, and so forth. The second factor is human uncontrol. With the help of the traditional indoor tests method, the influence of artificial control factors on the strength of granular media had been thoroughly studied in order to obtain relatively reasonable values. Jiang et al. [4] discussed the effect of density and confining pressure on the

mechanical properties of granular media and the influence on the stress-strain curves caused by confining pressure. Liu et al. [5] researched on the shear properties of rockfill under different stress paths conditions through large scale triaxial tests. Jiang and Zhao [6] and Dang et al. [7] studied the influence of shear rate on the shear strength of soil in triaxial tests. Li et al. [8] and Bagherzadeh-Khalkhali et al. [9] investigated the effect of the maximum particle size in coarse grained soil on the shear strength. Mao-tian et al. [10] accomplished the triaxial experiments of two series of loading on the sand by use of conventional triaxial compression test apparatus and studied the stress history and lithology, over consolidation ratio.

"Granular particle materials of different particle size is distributed randomly in space" is an obvious feature of granular media samples. The thesis [11, 12] indicated that the arrangement of mutual position and interparticle force of granular particle had important effect on the mechanical properties. Actually, many problems were related to the fabric



FIGURE 1: The triaxial test of granular media.

of granular media. The granular media fabric of sample was uncontrolled in the indoor tests and the experiments would cost lots of time and labor. So it was, by far, that very few people studied this field. In fact, by reason of the random distribution of the different granular particle during the tests, the fabric of granular samples might be quite different. Even if the tests personnel, experimental method and material, experimental grading and density, and experimental apparatus are identical, the indoor tests results also are different. Therefore, using a few indoor tests results to stand for the strength parameters was unreasonable and such mechanical parameters had no representativeness. So it is necessary to introduce into the numerical simulation triaxial tests for coarse-grained soil.

## 2. HHC-Granular Model

**2.1. Laboratory Triaxial Experiment.** At first, a group of indoor triaxial tests of granular media was carried out, and the experimental image was shown in Figure 1. According to the classification and naming of granular media [13], the granular media of laboratory experiment was described as the gravel ( $0.005\sim 0.06$  m), sand ( $0.0001\sim 0.005$  m), and soil ( $<0.0001$  m). The particle size range was given in Table 1. The tests apparatus is the stress-control triaxial compression which was developed by Sichuan University. The maximum particle selected  $0.06$  m and its shear rate was  $5\cdot 10^{-7}$  m·s $^{-1}$ . The tests confining pressure selected 200 kPa, 400 kPa, 800 kPa, and 1600 kPa and the experiment was shut down in axial strain 15%.

In keeping with the laboratory experimental conditions as soon as possible, the granular media sample of numerical simulation test was considered to consist of three kinds of similar particle materials that were the coarse gravel,

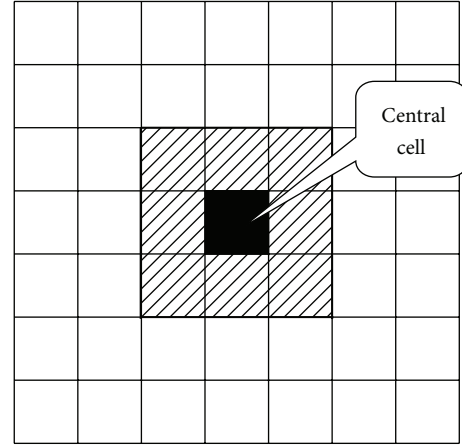


FIGURE 2: Schematic diagram of cellular, cellular space, and neighbor.

medium-grained sand, and fine-grained soil. Therefore, the cellular automata was employed to generate randomly the homogeneous hybrid composite in order to prepare the samples with different initial fabric of grain.

**2.2. HHC-Granular Model.** By use of the horizontal and vertical lines of equal intervals, two-dimensional space was divided into the cellular space consisted of square, and each square was cellular. The cellular spatial grid was  $50\times 100$ . The eight neighbors' Moore model was shown in Figure 2; when the black cellular was the central, the eight cellars with the diagonal line are its neighbor.

There are three kinds of cellular states representing three different materials, 2: gravel; 1: sand; 0: Soil. In the procedure, we used different colors to indicate the cellular of different states and took the periodic boundary conditions as the boundary condition.

Cellular automata has discrete features on the time and space and can make synchronized calculation, and its cellular state changed with the change in time and space. In the cellular space, at first, several nucleation-points appeared randomly; then the cellular gradually developed according to probability around the nucleation-point. The more the cellars around the nucleation-point, the greater the growing probability, and when there were no cellars around the nucleation-point, the growth probability was zero. As the ambient cellars were the same kind of cellular, the growth probability was 100%. The evolution would be continued until the material met the required content percentage.

The cellular was not the simultaneous evolution but the ergodic evolution in the cellular space. It was distinct from previous cellular automaton that cellular evolution depended on not only back state of neighbor cellular, but also current state of neighbor cellular evolved,

**2.3. Simulating Results.** Figure 3 was the interface of HHC-Granular model with three granular medias (gravel, sand, and soil). The granular media samples which were generated by HHC-Granular model could characterize the granular

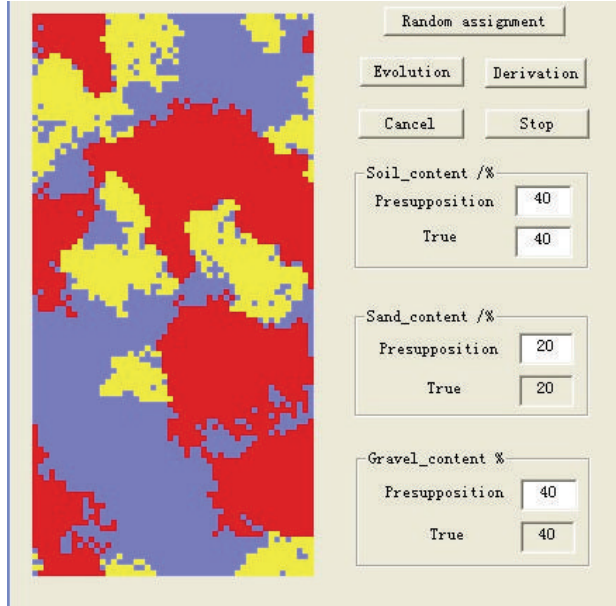


FIGURE 3: HHC-Granular model interface and generated granular sample.

inhomogeneous and random distribution from the graph. This model could define the different contents of soil, sand, and gravel and randomly generate samples with the different fabric in the same particle size grading so as to prepare the requiring granular media samples. The HHC-Granular model was maneuverable. Introducing the granular media sample which was simulated by the HHC-Granular model into the FLAC<sup>3D</sup>, we could realize that the distribution of each particle size was identical.

### 3. Triaxial Numerical Simulation Tests

**3.1. Numerical Calculating Model.** In the riaxial numerical calculating model of granular media, the specimen dimensions was  $0.5\text{ m} \times 0.01\text{ m} \times 1\text{ m}$ , the normal constraint was applied on the  $X = 0\text{ m}$  and  $X = 0.5\text{ m}$  planes and the normal stress was applied on the  $Y = 0\text{ m}$  and  $Y = 0.01\text{ m}$  planes; the  $Z = 0\text{ m}$  plane was applied on the normal constraint and the  $Z = 1\text{ m}$  plane was applied on the loading rate.

**3.2. Material Parameters and Experimental Schemes for Numerical Simulation Tests of Granular Media.** In keeping with indoor tests conditions, this simulation tests took the indoor triaxial tests of granular media as a reference. The loading rate is  $5 \times 10^{-7}\text{ m} \cdot \text{s}^{-1}$  and the normal stress adopted 200 kPa, 400 kPa, 800 kPa, and 1600 kPa. The material parameters of gravel, sand, and soil were acquired based on the parameters of indoor tests and the simulating test using the Mohr-Coulomb model; the simulating tests' material parameters were shown in Table 1.

According to the project names and classifications with the granular media [13], the granular media was divided into five categories to follow the contents of greater than 5 mm:

that was sand of soil, sandy soil of gravel, gravelly soil of sand, sandy gravel of soil, and sandy gravel of rubble. The classification is in Table 2.

To study the reasonable strength parameters with different granular media, the paper selected the HHC-Granular model to prepare the five different granular media samples and the simulating five samples of granular media were shown in Figure 4. Meanwhile, each granular media prepared 40 groups of samples with different fabric to do the triaxial simulation tests. The strength parameter  $\varphi$  of different initial fabric of grain was acquired.

### 4. Test Results

**4.1. Numerical Simulation.** Figure 5 contrasted the stress-strain curve of laboratory experiment with that of triaxial numerical simulation test in the experimental schemes II. The simulation curves were wave type from the chart, while the indoor tests were not so obvious, because the shear bands avoided the coarse particle and always had some coarse particles in the simulation test until the failure surface was formed. In the numerical simulation tests process, the simulation curve could form a wave rising trend line, while the indoor triaxial tests were completed to express mainly particle displacement and its curves performed for the smooth curve. Overall, the stress-strain curves between the simulation tests and the indoor triaxial tests were uniform largely, which indicated that the triaxial numerical simulation tests, which combined the FLAC<sup>3D</sup> with the HHC-Granular model, were feasible.

Figure 6 was the different fabric charts of FS.G, and Figure 7 was the corresponding contours of shear-strain rate. Combining Figure 6 with Figure 7, we could see that the gravel of Figure 6(a) appeared primarily near the shear bands and its internal friction angle was  $29.69^\circ$ . The sand accounted for a larger proportion near shear bands in Figure 6(b) and its internal friction angle was lower than that of Figure 6(a). The internal friction angle of Figure 6(c) was  $26.84^\circ$ , and the contents of soil in the shear bands was relatively higher. The results showed that when there was more gravel in the nearby shear bands, the internal friction angle values were higher, and the shear strength was relatively lower as a lot of soil lied in the nearby shear bands. Thus the shear strength of samples had to do with the particle distribution in the vicinity of shear bands.

Figure 7 showed that, as the influence of coarse particles on the tests, the shear failure plane was not regular shear plane, but some curved surface. However, the tendency of curve surface showed that the curves of shear bands appeared as a single shear bands or "X" shear bands. Therefore, in order to quantify the impact of coarse particles in the shear bands on the shear strength, this adopted the "X" shear bands to analyze the effect of gravel contents within the shear bands on the shear strength of sample.

**4.2. Shear Bands and Inclination Angle of Shear Bands.** The paper generated the total cell  $N$  (the HHC-Granular model unit numbers) and displayed the grid ID numbers of FLAC<sup>3D</sup>

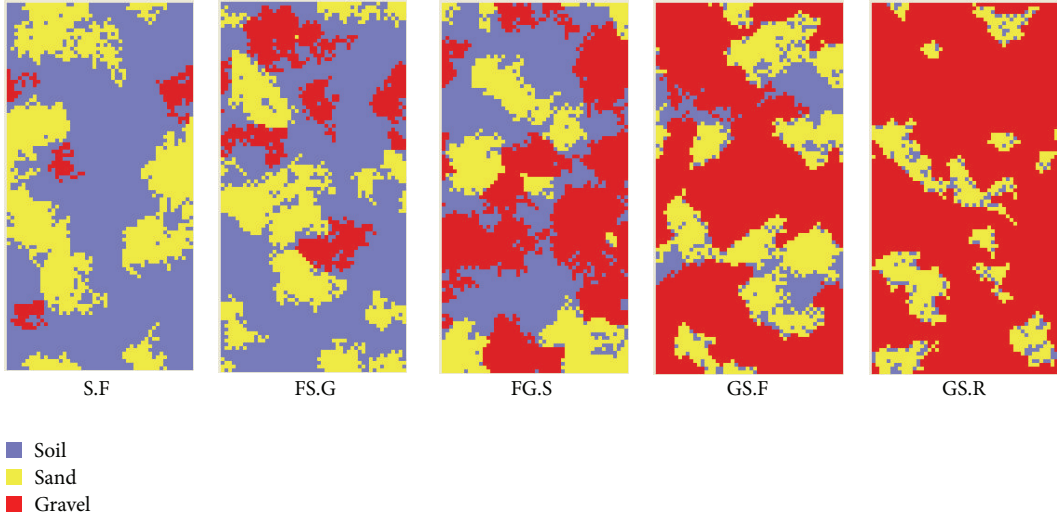


FIGURE 4: HHC-Granular model generated granular media samples.

TABLE 1: Material parameters for numerical simulation tests of granular media.

Names	Range of particle size (m)	Density (kg·m <sup>-3</sup> )	Cohesion ×10 <sup>3</sup> (Pa)	Internal frictional angle (°)	Dilation angle (°)	Bulk modulus ×10 <sup>9</sup> (Pa)	Shear modulus ×10 <sup>9</sup> (Pa)	Tensile strength ×10 <sup>6</sup> (Pa)
Soil (F)	<0.0001	2150	61	27	8	0.07	0.03	0.05
Sand (S)	0.0001~0.005	2300	75	32	10	2.5	1	0.35
Gravel (G)	0.005~0.06	2600	132	46	13	23	10	1.0

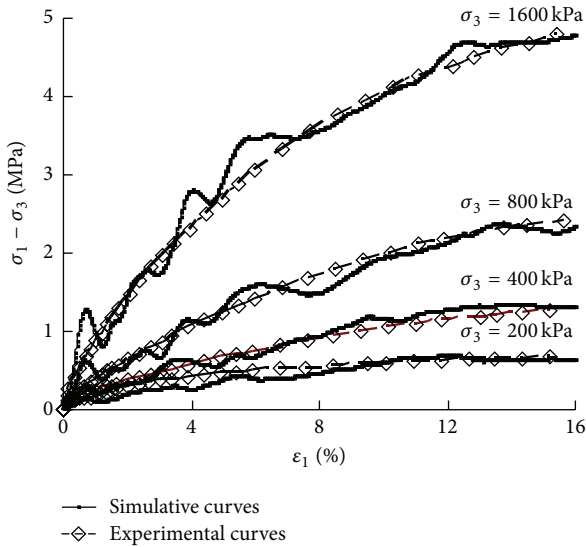


FIGURE 5: Stress-strain curves of between simulation tests and indoor tests.

in the triaxial simulation tests to obtain the gravel contents of shear bands. And then the producing grid image was induced into AutoCAD and shear bands were set. The schematic diagram was shown in Figure 8. The units  $n$  of gravel in the shear bands were acquired by comparing with the unit

number generated by the HHC-Granular model. Finally, we could calculate the gravel contents of shear bands:

$$P_5 = \left( \frac{n}{N} \right) \times 100\%, \quad (1)$$

where  $P_5$  is gravel contents of shear bands,  $n$  is total units of gravel in the shear bands, and  $N$  is total units  $n$  of sample.

According to Finno et al. [14], the inclination angle and thickness of shear bands with Sandy soil of gravel were taken as  $\psi = 65^\circ$  and  $D = 0.045$  m, with which we obtained the gravel contents of FS.G with 60 groups different fabric in the shear bands. The relationship between gravel contents in shear bands and internal friction angle of FS.G was shown in Figure 9.

Figure 9 showed that the internal friction angle is increasing with the increasing of the gravel contents with the shear bands, and there was a linear relation between the gravel contents of shear bands and the internal friction angle. It indicated that the gravel contents of shear bands were the major factor affecting the shear strength.

The range value of internal friction angles ( $\varphi$ ) with the five categories granular media, which were acquired through the triaxial simulation tests, was shown in Figure 10. The internal friction angle ( $\varphi$ ) was not always increment with the increase of the sample gravel contents from the chart. The higher  $\varphi$  of gravel contents 4% is greater than the lower  $\varphi$  as the gravel contents are 15%. When the gravel contents are 40%, the lower  $\varphi$  is less than the higher  $\varphi$  of gravel contents 15%. Similarly,

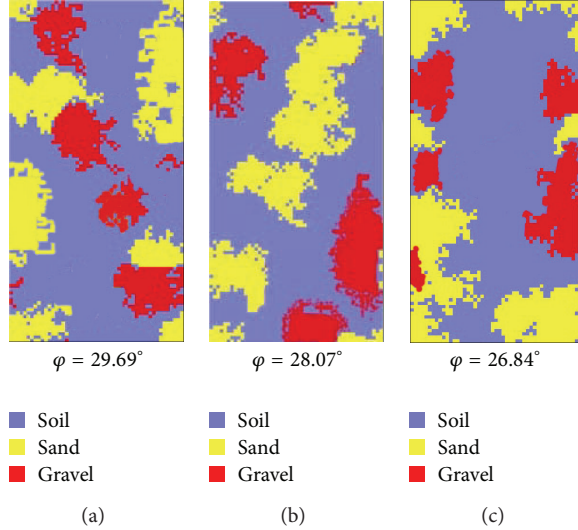


FIGURE 6: HHC-Granular model generated different initial fabric of grain of FS.G.

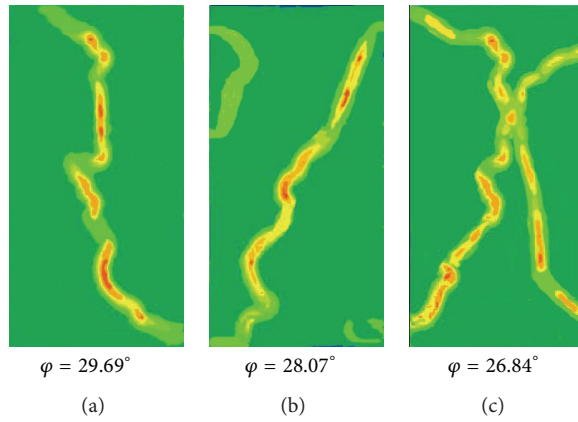


FIGURE 7: Contours of shear-strain rate indicating shear bands at different fabric.

the higher  $\varphi$ , as the gravel content is 40%, was greater than the lower  $\varphi$  when the gravel content is equal to 60%. Actually, the phenomenon, which the internal friction angle of higher gravel contents sample is less than that of lower sample gravel contents, can also appear in the indoor tests. It is caused by the different fabric of sample. Although the sample gravel contents were higher, due to the lower sample gravel contents in the shear bands, the internal friction angle may decrease. The analysis showed that the influence factors to the strength parameters of granular media were not always the sample gravel contents, but the gravel contents of shear bands in some situations.

Figure 11 expressed the relationship between the average internal friction angle that was got through the triaxial simulation test and the samples gravel contents with sand of soil, sandy soil of gravel, gravelly soil of sand, sandy gravel of soil, and sandy gravel of rubble. Figure 11 showed that although the  $\varphi$  of higher gravel contents was less than that of lower gravel contents, the average internal friction angle of different gravel contents obviously increased with

the increment of sample gravel contents and the relationship between  $\bar{q}$  and sample gravel contents could be expressed by exponential relation which could provide reference for the selection of mechanical parameters.

## 5. Conclusions

Generally, acquiring the mechanical properties of similar particle size with the granular media is relatively easy in the indoor tests. However, the granular media has characteristics of obvious heterogeneity and randomness, which caused the reasonable mechanical parameters to be obtained difficultly through a few indoor tests. The paper, combining HHC-Granular model with FLAC<sup>3D</sup>, tentatively discussed the influence of gravel contents on the shear strength of granular media. The results showed that the stress-strain curves of numerical simulation tests were consistent with that of indoor tests with granular media. With the increase of gravel contents within the shear bands, the internal friction angle was increasent and the relationship expressed linear relation,

TABLE 2: Classification and gradation schemes of simulation tests of granular media.

Test schemes	Project names	Symbols of classification	Contents of different grain size groups of classification		Simulated true values of different grain sizes		
			Gravel (%)	Soil (%)	Gravel (%)	Sand (%)	Soil (%)
I	Sand of soil	S.F	<5	≥10%	4.0%	30.0%	66.0%
II	Sandy soil of gravel	FS.G	<30	>10%	15.0%	25.0%	60.0%
III	Gravelly soil of sand	FG.S	30–50	>10%	40.0%	20.0%	40.0%
IV	Sandy gravel of soil	GS.F	50–70	>10%	60.0%	25.0%	15.0%
V	Sandy gravel of rubble	GS.R	>70	<5%	80.0%	16.0%	4.0%

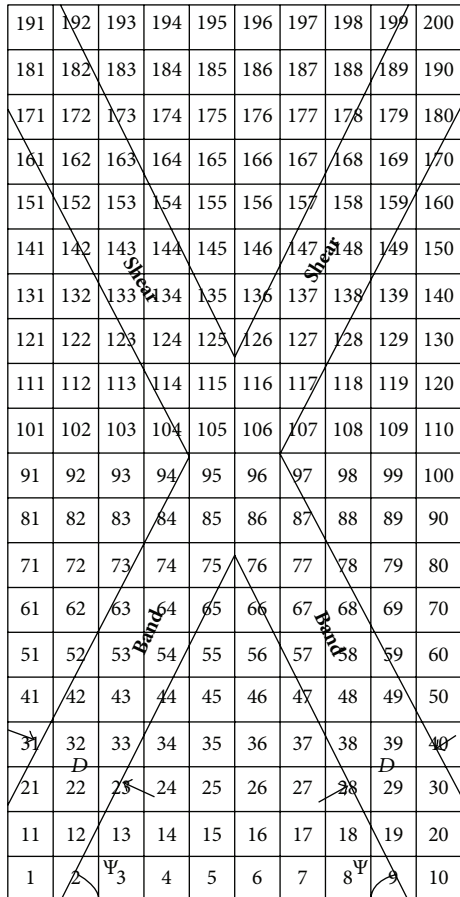


FIGURE 8: Schematic diagram of shear bands.

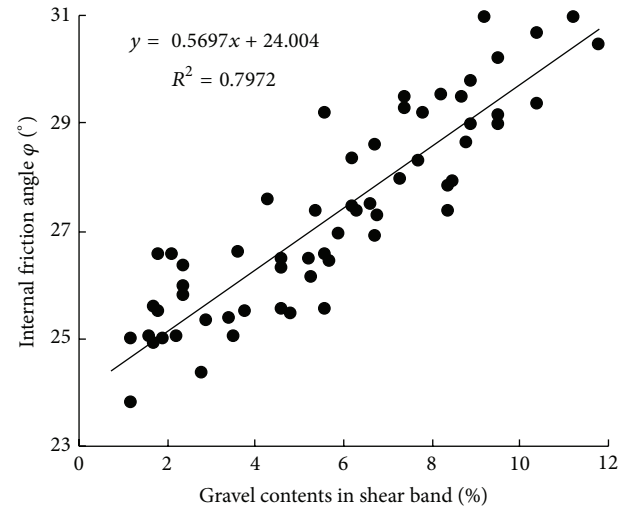


FIGURE 9: Relationship between gravel contents in shear bands and internal friction angle.

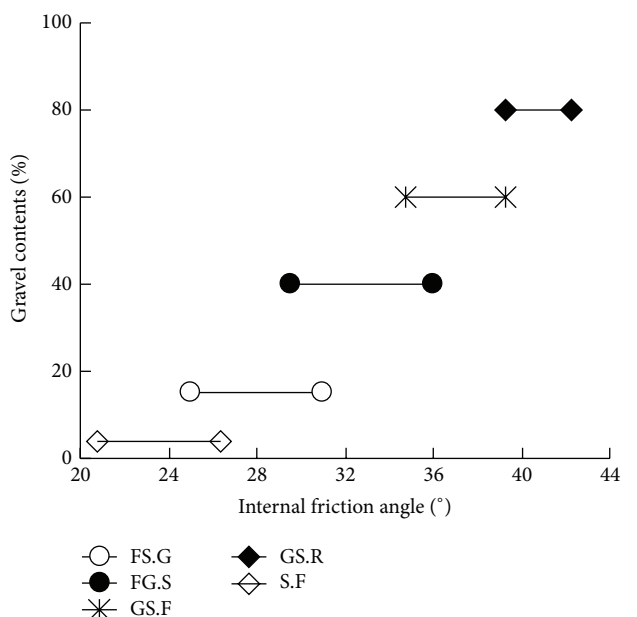


FIGURE 10: Range of internal friction angle at different granular media.

and the internal friction angle might decrease when the gravel contents increased. However, the average internal friction angle of different gravel contents is increasing obviously with the increase of sample gravel contents.

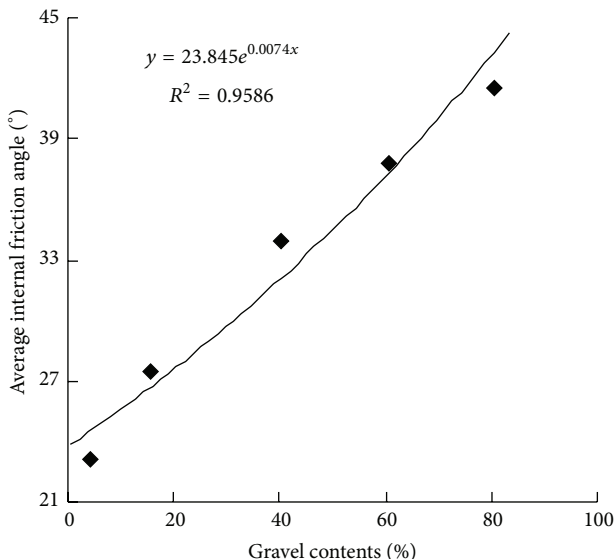


FIGURE 11: Relationship between  $\bar{\phi}$  and gravel contents of samples.

## Conflict of Interests

The authors declare that there is no conflict of interests regarding the publication of this paper.

## Acknowledgments

This research is supported by the project supported by the National Natural Science Foundation of China (no.51234004), the Open Projects with the State Key Laboratory of Coal Mine Disaster Dynamics and Control (Chongqing University) (no. 2011DA105287-KF201307), the School-Enterprise Funds with the Jinchuan Group co., Ltd.(no. KKZ4201221008), the Yunnan Provincial Fund project (no. KKSY201221070), and the Discipline Direction Team (no. KKZ4201414078312).

## References

- [1] J. Jiang, Z. Cheng, H. Liu, and H. Ding, "Fabric analysis of two-dimensional tests for coarse-grained soils," *Chinese Journal of Geotechnical Engineering*, vol. 31, no. 5, pp. 811–816, 2009.
- [2] C. Zhanlin, D. Hongshun, and W. Liangping, "Experimental study on mechanical behaviour of granular material," *Chinese Journal of Geotechnical Engineering*, vol. 29, no. 8, pp. 1152–1158, 2007.
- [3] L. I. Nenghui, *Recent Technolohy for High Concrete Face Rockfill Dams*, China Water Power Press, Beijing, China, 2007.
- [4] J.-S. Jiang, H.-L. Liu, and Z.-L. Cheng, "Influences of density and confining pressure on mechanical properties for coarse-grained soils," *Journal of Yangtze River Scientific Research Institute*, vol. 26, no. 8, pp. 46–50, 2009.
- [5] M. Liu, Y. Gao, and H. Liu, "Study on shear behaviors of rockfill in large-scale triaxial tests under different stress paths," *Chinese Journal of Rock Mechanics and Engineering*, vol. 27, no. 1, pp. 176–186, 2008.
- [6] H.-W. Jiang and X.-H. Zhao, "Analysis of the shearing rate effecton anisotropic undrained strength of clays," *Journal of Tong Ji University*, vol. 25, no. 4, pp. 390–395, 1997.
- [7] J. Dang, C. Jiang, and Z. Ji, "Effects of shear rate on mechanical behavior of structured loess," *Chinese Journal of Underground Space and Engineering*, vol. 5, no. 3, pp. 459–463, 2009.
- [8] C. Li, C.-R. He, C. Wang et al., "Study of scale effect of large-scale triaxial test of coarse-grained meterials," *Rock and Soil Mechanics*, vol. 29, supplement, pp. 563–566, 2008.
- [9] A. Bagherzadeh-Khalkhali and A. A. Mirghasemi, "Numerical and experimental direct shear tests for coarse-grained soils," *Particuology*, vol. 7, no. 1, pp. 83–91, 2009.
- [10] L. Mao-tian, L. Gao, and Y. Qing, "Review of geotechnical earthquake engineering and some latest progress in the soil dynamics," in *Proceedings of the 5th National Soil Dynamics Conference Proceedings*, Dalian University of Science and Technology Press, Dalian, China, 1998.
- [11] J.-S. Jiang, Z.-L. Chen, and X.-L. Jiang, "Two dimensional model test for coarsegrained soil," *Journal of Yangtze River Scientific Research Institute*, vol. 25, no. 2, pp. 38–41, 2008.
- [12] W. Xu, R. Hu, Z. Q. Yue, R. Zhang, and G. Wang, "Research on relationship between rock block proportion and shear strength of soil-rock mixtures based on digital image analysis and large direct shear test," *Chinese Journal of Rock Mechanics and Engineering*, vol. 27, no. 5, pp. 996–1007, 2008.
- [13] Q. Guo, *Engineering Properties and Application of Coarse-grained Soil*, Yellow River Water Conservancy Press, Zhengzho, China, 1999.
- [14] R. J. Finno, W. W. Harris, M. A. Mooney, and G. Viggiani, "Shear bands in plane strain compression of loose sand," *Geotechnique*, vol. 47, no. 1, pp. 149–165, 1997.

## Research Article

# Insights into the Synergistic Effect of Fungi and Bacteria for Reactive Red Decolorization

Dandan Zhou, Xueying Zhang, Yilin Du, Shuangshi Dong, Zhengxue Xu, and Lei Yan

Key Lab of Groundwater Resources and Environment, Jilin University, Ministry of Education, Changchun 130021, China

Correspondence should be addressed to Shuangshi Dong; sdong@jlu.edu.cn

Received 29 May 2014; Accepted 3 July 2014; Published 10 August 2014

Academic Editor: Qingrui Zhang

Copyright © 2014 Dandan Zhou et al. This is an open access article distributed under the Creative Commons Attribution License, which permits unrestricted use, distribution, and reproduction in any medium, provided the original work is properly cited.

Bacterial contamination is a prevalent problem in fungal dye wastewater decolorization that prevents the development of this technology in practical engineering. New insight into the relationship between fungi and bacteria is given in terms of settleability, bioadsorption, and biodegradation, which all confirm their synergistic effect. Sterilization is implied to be not the only mechanism for fungi decolorization. When the fungi and bacteria isolated from the activated sludge were cocultured, fungi removed more than 70% of the reactive red through sole bioadsorption in 5 min and enhanced the settleability of the bacteria group from 7.7 to 18.4 in the aggregation index. Subsequently, the bacteria played a more significant role in dye biodegradation according to the ultraviolet-visible spectrum analysis. They further enhanced the decolorization efficiency to over 80% when cocultured with fungi. Therefore, the advanced bioadsorption and settleability of fungi, combined with the good dye biodegradation ability of bacteria, results in the synergistic effect of the coculture microorganisms.

## 1. Introduction

Effluents from textile industries that contain dyes are highly colored and visually identifiable [1]. The complex aromatic structure of dyes is resistant to light, biological activity, ozone, and other degrading environmental conditions [2]. Fungi have attracted much attention because of their ability to decolorize dyes compared to simple single cell organisms as their increased cell-to-surface ratio provides a greater physical and enzymatic contact condition [3]. They produce lignin-modifying enzymes, such as laccase, manganese peroxidase, and lignin peroxidase, to tolerate the toxicity of dyes and mineralize them [4].

Bacterial contamination is a prevalent problem in fungal dye wastewater decolorization. Critical operational and environmental conditions, including temperature, pH, hydraulic residence time, and sludge residence time [5], are usually controlled to maintain the dominance of fungal biomass [6]. Fulfilling the above control conditions is extremely expensive and unrealistic for practical wastewater treatment.

The present work gives new insight into the synergistic relationship between fungi and bacteria. Fungi and bacteria were cultured together in flasks containing typical reactive dye, and no extra operational and environmental conditions

that favor the dominance of fungi were set during the whole experiment. The roles of fungi and bacteria in bioadsorption, biodegradation, total biomass concentration, and settleability were evaluated, and they were significant to the decolorization efficiency of industrial wastewater plant operation. The synergistic effect of fungi and bacteria enhanced their decolorization and settleability, and it gives a novel view on using fungi for textile wastewater treatment. Preventing bacterial contamination or controlling fungi dominance is not the best way to treat textile wastewater.

## 2. Materials and Methods

**2.1. Medium.** Basal salts medium (BSM) with additional 120 mg/L of reactive red X-3B (BSM-dye medium) was used. The composition of the BSM media was as described by Juhasz et al. [7]. The reactive red X-3B was purchased from the Dye Synthesis Laboratory of China. The pH of the medium was adjusted to 7.0, and the temperature was set to 25°C during cultivation.

**2.2. Enrichment, Isolation, and Identification.** A 100 mL portion of activated sludge sampled from a bioreactor in Jilin

University was shaken overnight in 100 mL of Ringer's solution (Dingguo, China) at 30°C and 110 rpm in an incubation shaker. BSM (95 mL) containing 120 mg/L red reactive X-3B was inoculated with 5 mL of the supernatant. When the growth of the microorganisms was observed, enrichment was continued by serially subculturing the sample several times in the same medium using a 10% inoculum from the previous culture.

Initial attempts to separate the resulting fungal-bacterial consortium involved subculturing it into the fresh BSM medium containing 0.1 g/L cycloheximide. The absence of fungi was confirmed by plating the subculture onto PDA after each transfer. The resulting bacterial consortium is referred to as the bacteria group hereinafter. To isolate the fungi, the enriched culture was diluted 10-fold, and 0.1 mL of the samples was spread onto PDA plates supplemented with 0.06 g/L penicillin G and 0.1 g/L streptomycin sulfate. Fungal colonies were selected and replated on the same medium until pure colonies were obtained. The pure colonies were subcultured on PDA and were identified. A 500  $\mu$ L portion of each colony spore suspension (with 0.2 OD<sub>600</sub>) was inoculated into the BSM-dye medium for the subsequent subculturing. This fungal consortium is referred to as the fungi group hereinafter.

The bacterial and fungal samples were obtained through centrifugation (8000 rpm) and washed twice with PBS buffer. Then, DNA extraction, polymerase chain reaction amplification, and denaturing gradient gel electrophoresis (DGGE) analysis of the bacteria/fungi group were consigned to a professional biological engineering company (Sangon Company, Shanghai, China).

**2.3. Analysis.** Absorbance measurements of the original dye and the decolorized dye by spectrophotometer were performed at 538 nm to estimate biodegradation occurrence using an ultraviolet-visible (UV-vis) spectrophotometer. Bioadsorption was evaluated using the decolorization efficiencies of the biomass after inactivation by supplementing 0.7 mg/L HgSO<sub>4</sub> in the BSM-dye medium. The decolorization efficiency of the X-3B was calculated by  $(1 - C/C_0) \times 100\%$ , where  $C_0$  and  $C$  represent the initial and the residual concentrations of X-3B, respectively.

The biomass suspension was collected, and the aggregation index was measured by monitoring the changes in absorbance at 600 nm using a UV-vis spectrophotometer. The aggregation index ( $I\%$ ) was calculated using [8]  $I\% = ((OD_0 - OD_{30})/OD_0) \times 100\%$ , where OD<sub>0</sub> and OD<sub>30</sub> represent the initial absorbance and the absorbance after 30 min of deposition, respectively.

All experiments were performed in duplicate, and the average values were used in the calculations.

### 3. Results

**3.1. Isolation and Identification.** Fungi and bacteria groups were obtained after separation. Two fungi were isolated from the fungi group. The 18S rRNA sequences revealed that the sequences were 99% homologous to those of *Geotrichum*

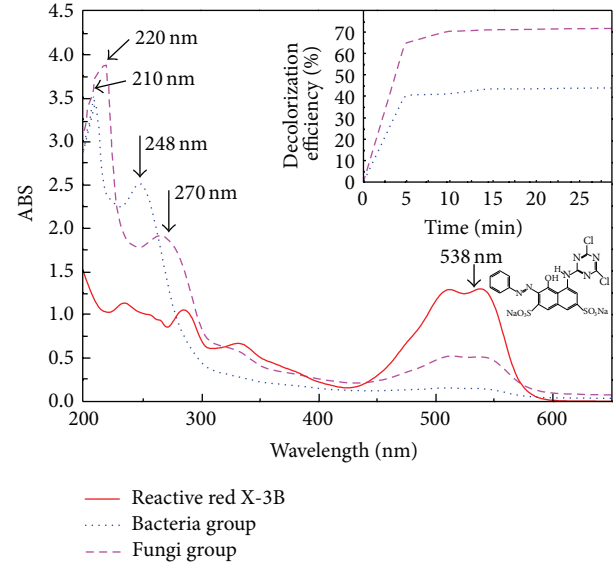


FIGURE 1: UV-vis spectra of the original reactive red X-3B and the residuals after culturing the bacteria and fungi groups in the BSM-dye medium for 3 days, respectively; X-3B adsorption efficiencies of bacteria and fungi groups, respectively (inset).

*candidum* (Genbank accession number: KJ543497) and *Candida pseudolambica* (Genbank accession number: KJ543498), respectively. *Geotrichum candidum* was filamentous under the microscope (Olympus, BX40, Japan) with a Pro-Micro Scan system and the size of the granules was determined using the Scopephoto software. For bacteria identification, the sequences of the 15 dominant bands that appeared in the DGGE profiles were identified and compared with those available in the GenBank library. The majority of the bacterial 16S rDNA sequences were grouped with the members of *proteobacteria* (9 in total), six of which were in the  $\beta$  subdivision. The other bacterial species in the bacteria group were *Sphingobacteriia*, *Flavobacteriia*, *Bacteroidia*, *Nitrospirales*, and *Phycisphaeraeae*.

**3.2. Decolorization Mechanisms of the Two Groups.** The reactive red X-3B decolorization mechanisms of the fungi group and bacteria group were attributed to both bioadsorption and biodegradation functions, as shown in Figure 1. However, the contributions of bioadsorption and biodegradation in the X-3B decolorization for the microbial groups were quite different. Bioadsorption, instead of biodegradation, plays a more significant role in fungi group decolorization as it achieved more than 70% decolorization in 5 min. Such great adsorption capability of fungi is due to their wide range of binding sites for azo dyes [9], that is, amino, carboxyl, phosphate, and hydroxyl functional groups located on the surface of fungi [10]. Using fungi as adsorbing agents has received much attention [11]. However, the removal efficiency of X-3B reached only 44% when absorption achieved equilibrium at 15 min.

The bacteria group seemed to have complementary advantages over fungi group in terms of bioadsorption and biodegradation. The living bacteria group had stronger

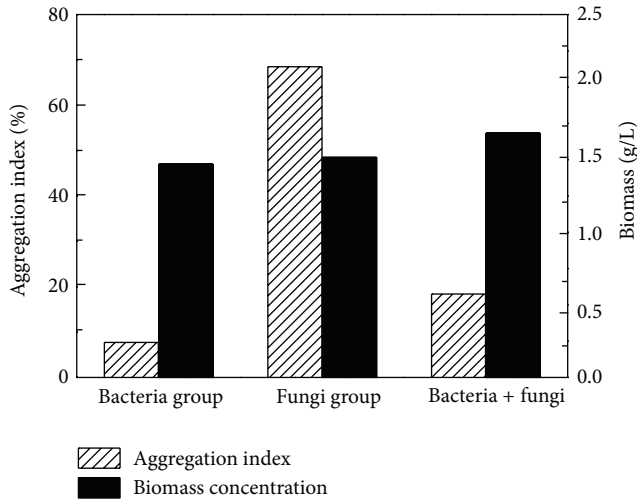


FIGURE 2: Aggregation indexes and biomass concentrations of the bacteria group, fungi group, and bacteria-fungi coculture at the stationary phase.

biodegradation ability than that of the fungi group (Figure 1). Reactive red X-3B has a maximum absorption peak at 538 nm, and this peak almost disappeared after the bacteria group biodegradation. The new products are found at wavelengths of 210 nm and 248 nm. The chromogenic group of X-3B was broken, and it generated other chromogenic groups. The biodegradation ability of fungus was not as strong as that of bacteria because the peak at the wavelength of 538 nm was still apparent. The products of the fungus group were different from those of the bacteria group, as confirmed by the shifting of the maximum absorption wavelength from 538 nm to 220 nm and 270 nm.

In brief, both bioadsorption and biodegradation decolorized reactive red X-3B for both the bacteria group and the fungi group. Fungi showed a much better bioadsorption capability and reached equilibrium in 5 min, whereas the bacteria group had a more radical biodegradation for decolorization.

**3.3. Settleability Enhancement of the Fungus Group.** The aggregation index was used to evaluate the aggregation capability of the microorganisms. At the stationary phase of the microbial groups (the 6th day of culture), the bacteria group had the poorest self-aggregation ability, with an aggregation index of 7.7. The aggregation index of the fungi group was 68.5, with a very clear boundary between the settled biomass and the supernatant (see Figure 2). Thus, the settleability of the mixed group reached an acceptable degree, with an aggregation index of 18.4. The biomass concentrations of these microbial groups were close. This finding indicates that the aggregation indexes of the groups are comparable and that the competition between bacteria and fungus in the cocultured group does not affect the total biomass. As expected, the fungus enhanced the settleability in the synergistic fungi-bacteria cocultured group and had no significant influence on the total biomass production.

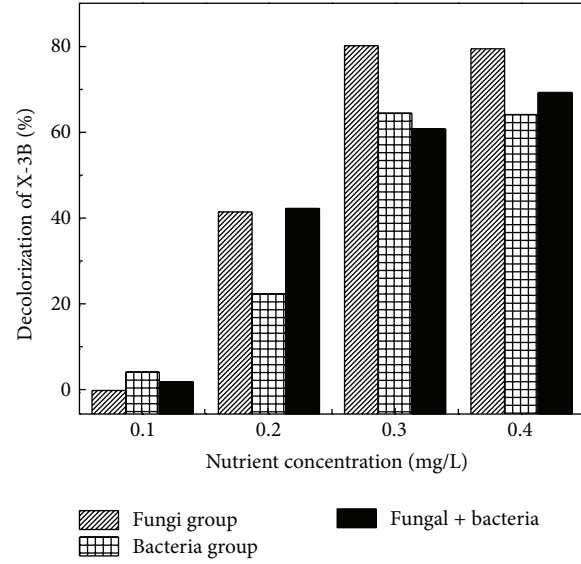


FIGURE 3: Reactive red X-3B decolorization efficiencies at different nutrient levels (each concentration of  $(\text{NH}_4)_2\text{SO}_4$ ,  $\text{KH}_2\text{PO}_4$ , and  $\text{K}_2\text{HPO}_4$  is 0.1, 0.2, 0.3, and 0.4 mg/L) for the bacteria group, fungi group, and bacteria-fungi coculture at the stationary phase.

**3.4. Decolorization Enhancement of the Bacteria Group.** The reactive red X-3B decolorization efficiencies with different kinds of nutrient (i.e.,  $(\text{NH}_4)_2\text{SO}_4$ ,  $\text{KH}_2\text{PO}_4$ , and  $\text{K}_2\text{HPO}_4$ ) at different levels were determined to identify the decolorization abilities of the individuals and the cocultured bacteria and fungi group (see Figure 3). The influence of nutrient feed levels on decolorization seemed to be generally consistent for the three groups, and the decolorization efficiencies tended to be higher when the nutrient supplications were more abundant. The efficiencies of the three groups with different kinds of nutrient at the same level were very close, and the bacteria group seemed to have a positive effect on the decolorization ability of the cocultured group because of its advanced biodegradation performance (see the UV-vis spectra results in Figure 1).

## 4. Discussion

Traditionally, bacterial proliferation is a problem in nonaseptic fungal decolorization. Bacteria compete with fungi for substrates, and they also deteriorate the dewatering ability [6]. An insight into the synergistic relationship between the fungi group and the bacteria group for azo dye wastewater treatment was given without artificial modification of any operational, environmental, and physiological conditions. These synergistic effects were expressed as both the enhanced settleability of the fungi group and the enhanced biodegradation ability of the bacteria group when the two groups were cocultured. The former is the main contributor to the separation of biomass and effluent, and the latter plays a more important role in the improvement of the quality of the effluent (Figure 4). The fungus in the cocultured group adsorbed the azo dye in several minutes. This adsorption is attributed to the many binding functional groups in their

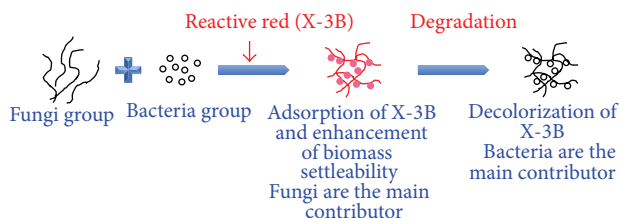


FIGURE 4: Insight into the synergistic effect of fungi and bacteria for reactive red X-3B decolorization.

cell walls, such as amino, carboxyl, thiol, and phosphate [2]. Then, the azo molecule dye closed around the fungal and bacterial cells that were wrapped together. The dye was easier to transfer into their cells for further biodegradation. The enzyme-mediated activity of fungi enabled the treatment of wastewater containing hazardous or xenobiotic organic pollutants [12]. Thus, the toxicity of the dye dramatically decreased when the bacteria, which presented a much greater growth speed, were added [13].

As discussed above, the synergistic effect of the fungi group and the bacteria group shows that they promoted their own bioaccumulation, bioadsorption, and biodegradation. The relationship between the fungi group and the bacteria group is implied to be not limited to completion, but it could also be a synergistic effect. Therefore, sterilization is not the only way to use fungi for wastewater treatment. The bacteria and fungi groups used in this work were isolated from the same source. The synergistic effect between them was stronger than that from different sources. This process may be an effective way to strengthen the synergistic effect rather than the competition between the two groups.

## 5. Conclusions

Two fungi and 15 bacteria were isolated from activated sludge and were identified and classified into the fungi group and the bacteria group, respectively. Fungi played a more significant role in bioadsorption and settleability, and bacteria were more efficient in reactive red X-3B decolorization when cocultured. The synergistic relationship was implied between the fungi group and the bacteria group for the azo dye wastewater treatment. Therefore, the expensive artificial modification of operational, environmental, and physiological conditions to prevent bacterial contamination is not necessary. The bacteria group and the fungi group used in this work were isolated from the same source. Using cocultured microorganisms from the same source is an effective way to strengthen the synergistic effect.

## Conflict of Interests

The authors declare that there is no conflict of interests regarding the publication of this paper.

## Acknowledgments

The authors are grateful to the financial support from the Natural Sciences Foundation of China (50908096 and 50908097)

and the Development Plan Project of Science and Technology of Jilin Province (20140101159JC and 20140101006JC).

## References

- [1] N. K. Kılıç, J. L. Nielsen, M. Yüce, and G. Dönmez, "Characterization of a simple bacterial consortium for effective treatment of wastewaters with reactive dyes and Cr(VI)," *Chemosphere*, vol. 67, no. 4, pp. 826–831, 2007.
- [2] P. Kaushik and A. Malik, "Fungal dye decolourization: Recent advances and future potential," *Environment International*, vol. 35, no. 1, pp. 127–141, 2009.
- [3] Z. Aksu and G. Karabayir, "Comparison of biosorption properties of different kinds of fungi for the removal of Gryfalan Black RL metal-complex dye," *Bioresource Technology*, vol. 99, no. 16, pp. 7730–7741, 2008.
- [4] A. Hatakka, "Lignin-modifying enzymes from selected white-rot fungi: production and role in lignin degradation," *FEMS Microbiology Reviews*, vol. 13, no. 2-3, pp. 125–135, 1994.
- [5] R. C. Leitão, A. C. van Haandel, G. Zeeman, and G. Lettinga, "The effects of operational and environmental variations on anaerobic wastewater treatment systems: a review," *Bioresource Technology*, vol. 97, no. 9, pp. 1105–1118, 2006.
- [6] S. Sankaran, S. K. Khanal, N. Jasti, B. Jin, A. L. Pometto, and J. H. Van Leeuwen, "Use of filamentous fungi for wastewater treatment and production of high value fungal byproducts: a review," *Critical Reviews in Environmental Science and Technology*, vol. 40, no. 5, pp. 400–449, 2010.
- [7] A. L. Juhasz, M. L. Britz, and G. A. Stanley, "Degradation of fluoranthene, pyrene, benz[a]anthracene and dibenz[a,h]anthracene by Burkholderia cepacia," *Journal of Applied Microbiology*, vol. 83, no. 2, pp. 189–198, 1997.
- [8] S. S. Adav and D. Lee, "Single-culture aerobic granules with *Acinetobacter calcoaceticus*," *Applied Microbiology and Biotechnology*, vol. 78, no. 3, pp. 551–557, 2008.
- [9] Y. Fu and T. Viraraghavan, "Removal of Congo Red from an aqueous solution by fungus *Aspergillus niger*," *Advances in Environmental Research*, vol. 7, no. 1, pp. 239–247, 2002.
- [10] G. Bayramoğlu, G. Çelik, and M. Y. Arica, "Biosorption of Reactive Blue 4 dye by native and treated fungus *Phanerocheate chrysosporium*: batch and continuous flow system studies," *Journal of Hazardous Materials*, vol. 137, no. 3, pp. 1689–1697, 2006.
- [11] N. S. Maurya, A. K. Mittal, P. Cornel, and E. Rother, "Biosorption of dyes using dead macro fungi: effect of dye structure, ionic strength and pH," *Bioresource Technology*, vol. 97, no. 3, pp. 512–521, 2006.
- [12] D. R. Ryan, W. D. Leukes, and S. G. Burton, "Fungal bioremediation of phenolic wastewaters in an airlift reactor," *Biotechnology Progress*, vol. 21, no. 4, pp. 1068–1074, 2005.
- [13] Y. Liu and Q. Liu, "Causes and control of filamentous growth in aerobic granular sludge sequencing batch reactors," *Biotechnology Advances*, vol. 24, no. 1, pp. 115–127, 2006.

## Research Article

# Characterization of Binary Organogels Based on Some Azobenzene Compounds and Alkyloxybenzoic Acids with Different Chain Lengths

**Yongmei Hu,<sup>1</sup> Qingshan Li,<sup>1</sup> Wei Hong,<sup>2</sup> Tifeng Jiao,<sup>3</sup>  
Guangzhong Xing,<sup>1</sup> and Qilong Jiang<sup>1</sup>**

<sup>1</sup> National Key Laboratory of Metastable Materials Science and Technology, Yanshan University, Qinhuangdao 066004, China

<sup>2</sup> Qinhuangdao Entry-Exit Inspection & Quarantine Bureau Coal Inspection Technique Center, Qinhuangdao 066000, China

<sup>3</sup> Hebei Key Laboratory of Applied Chemistry, School of Environmental and Chemical Engineering, Yanshan University, Qinhuangdao 066004, China

Correspondence should be addressed to Qingshan Li; [qsli@ysu.edu.cn](mailto:qsli@ysu.edu.cn) and Tifeng Jiao; [tfjiao@ysu.edu.cn](mailto:tfjiao@ysu.edu.cn)

Received 12 May 2014; Accepted 4 June 2014; Published 10 August 2014

Academic Editor: Xinqing Chen

Copyright © 2014 Yongmei Hu et al. This is an open access article distributed under the Creative Commons Attribution License, which permits unrestricted use, distribution, and reproduction in any medium, provided the original work is properly cited.

In this work the gelation behaviors of binary organogels composed of azobenzene amino derivatives and alkyloxybenzoic acids with different lengths of alkyl chains in various organic solvents were investigated and characterized. The corresponding gelation behaviors in 20 solvents were characterized and shown as new binary organic systems. It showed that the lengths of substituent alkyl chains in compounds have played an important role in the gelation formation of gelator mixtures in present tested organic solvents. Longer methylene chains in molecular skeletons in these gelators seem more suitable for the gelation of present solvents. Morphological characterization showed that these gelator molecules have the tendency to self-assemble into various aggregates from lamella, wrinkle, and belt to dot with change of solvents and gelator mixtures. Spectral characterization demonstrated different H-bond formation and hydrophobic force existing in gels, depending on different substituent chains in molecular skeletons. Meanwhile, these organogels can self-assemble to form monomolecular or multilayer nanostructures owing to the different lengths of due to alkyl substituent chains. Possible assembly modes for present xerogels were proposed. The present investigation is perspective to provide new clues for the design of new nanomaterials and functional textile materials with special microstructures.

## 1. Introduction

In recent years, organogels have been attracting more attention as one kind of special functional materials, in which various organic solvents are immobilized by different gelators [1–4]. Previously gels are widely found in polymer systems; however, there has recently been more increasing attention in low-molecular-mass organic gelators (LMOGs) [5–9]. In recent years, organized gelation of organic solvents by LMOGs has been reported as one of the hot areas in the soft matter and organized materials fields due to their scientific values and many potential applications in the biomedical field, including drug delivery, tissue engineering, and medical implants [10–14]. The gels based on LMOGs are commonly regarded as supramolecular gels, in which the

gelator molecules can self-assemble in an orderly manner and form three-dimensional nanostructures in which the solvent is captured via various noncovalent interactions, such as  $\pi$ - $\pi$  stacking, hydrogen bonding, van der Waals interaction, coordination, solvophobic interaction, dipole-dipole interaction, and host-guest interaction [15–17]. LMOGs have some advantages over polymer gels: the molecular structure of the gelator is defined and the gel process is usually reversible. Such properties make it possible and reasonable to design various functionalized assembly systems and produce more complicated and/or controllable nanocomposites and nanostructures [18–20].

In our previous reported research work, the gelation properties of some cholesterol imide compounds with cholesteryl units and azobenzene substituent headgroups

have been characterized and investigated [21]. We found that the change in azobenzene headgroup can produce an obvious change in the gelation formation and assembly modes of these compounds. Furthermore, another gels system based on some bolaform and trigonal cholestryl compounds with different molecular skeletons have been characterized [22]. In this paper, we have characterized the spacer effect on the gel formation and nanostructures of such organogels and found that different kinds of hydrogen bond interactions among the molecules play a crucial role in the self-assembly process.

As a subsequent research work, now, we have prepared new binary organogels composed of aminoazobenzene derivatives and alkyloxybenzoic acids with different lengths of alkyl chains. We have found that some of present mixtures could form various organogels in different organic solvents. Morphological investigation of present organogels indicated the formation of different nanostructures of the aggregates in the gels. In addition, we have characterized the effect of substituent methylene chains in gelators on the nanostructures of present organogel systems and found various kinds of self-assembly modes. This report may afford a specific approach to understanding the soft matter and design of new nanomaterials and functional textile materials.

## 2. Experiments

**2.1. Materials and Reagents.** 4-Aminoazobenzene and 2-aminoazotoluene were purchased from Alfa Aesar Tianjin Chemicals and TCI Shanghai Chemicals, respectively. Other used reagents with analysis purity were obtained from Beijing Chemicals and distilled before use. Deionized water was used in all process. 4-n-Alkyloxybenzoic acids with different substituent chain lengths (carbon numbers 18, 16, 14, and 12) were prepared in similar method according to previous paper [23] and confirmed by  $^1\text{H}$  NMR.

**2.2. Gelation Test.** All mixed organogels were prepared according to a simple procedure. Firstly, these alkyloxybenzoic Acids and amine compounds were mixed with 1:1 molar ratio according to the number matching of intermolecular carboxylic acid and amine group, respectively. Then, a fixed amount of binary mixtures and a volume of organic solvent were taken into a sealed glass bottle and ultrasonically dispersed evenly. Then the solution was heated in a water bath at 70°C for 20 min. After that, the solution was cooled to room temperature in air and the test bottle was inverted to see if a gel was formed. If the binary mixture formed a gel by immobilizing the solvent at this stage, it was designated as a gel system “G.” For the systems in which only solution obtained until the end of the tests, they were denoted by solution (S). When the binary mixtures formed into a few precipitates in some solvent, it was denoted as a “PS.” Critical gelation concentration (CGC) refers to the minimum concentration of the gelator for gel formation.

**2.3. Characterization Techniques.** Firstly, these xerogels were obtained by a vacuum pump for 12–24 h from the as-formed gels under the critical gelation concentration. Then the dried samples were attached to different substrates, such as copper

plates, glass slices, and  $\text{CaF}_2$  slice for morphological and spectral investigation, respectively. Before SEM measurement, the xerogels were coated on copper plates fixed by conductive adhesive tape and shielded by gold. SEM images of the xerogels were obtained from a Hitachi S-4800 field emission scanning electron microscopy with the accelerating voltage of 5–15 kV. Transmission FT-IR spectra of the xerogels were measured by Nicolet is/10 FT-IR spectrophotometer from Thermo Fisher Scientific Inc. by average 32 scans with a resolution of  $4\text{ cm}^{-1}$ . The XRD patterns were measured by a Rigaku D/max 2550PC diffractometer (Rigaku Inc., Tokyo, Japan). The curves were obtained by  $\text{CuK}\alpha$  radiation with an incident wavelength of 0.1542 nm under a voltage of 40 kV and a current of 200 mA with scan rate of  $0.5^\circ/\text{min}$ .

## 3. Results and Discussions

**3.1. Gelation Behaviors.** Firstly, the gelation properties of all binary mixtures in 20 solvents are investigated. The experimental data showed that the binary mixtures of alkyloxybenzoic acids with different alkyl chains and 4-aminoazobenzene/2-aminoazotoluene could form organogels in special organic solvents, as listed in Table 1. The binary mixtures of alkyloxybenzoic acids with different carbon numbers (18, 16, 14, and 12) and 4-aminoazobenzene are denoted as C18-Azo, C16-Azo, C14-Azo, and C12-Azo, respectively. Similarly, the binary mixtures of these acids and 2-aminoazotoluene are denoted as C18-Azo-Me, C16-Azo-Me, C14-Azo-Me, and C12-Azo-Me, respectively. Firstly, for the mixtures containing longer alkyl chains with carbon numbers of 18 and 16, 4 and 6 kinds of organogels can be formed in different solvents, respectively. For example, C18-Azo can form gels in toluene, nitrobenzene, ethanolamine, and benzene, respectively. In addition, for the cases with shorter alkyl chains, only two and one kinds of organogels can form organogels in present solvents for mixtures with carbon numbers of 14 and 12, respectively. The organogels have been only prepared in ethanolamine for C12-Azo and C12-Azo-Me systems, respectively. Their photographs of all as-made organogels in various solvents were shown in Figure 1. The present research results indicated that length change of alkyl substituent chains can have an obvious effect upon the gel formation of present studied mixtures. This phenomenon indicated that longer methylene chains in molecular skeletons in present gelators systems are more suitable for the present mixtures, which was similar to the recent reports [23, 24]. Furthermore, it should be noted that the difference of methyl groups in azobenzene segment seemed to have no obvious effect on the regulation of gelator behaviors in present cases, which is different from previous report [21].

**3.2. Morphological Investigation.** It has been reported that various gelator molecules can construct nanoscale superstructures such as fibers, ribbons, and sheets in a supramolecular gel [25–27]. In order to obtain more insight into the gel nanostructures, the organized structures of these organogels were characterized by SEM technique, as shown in

TABLE 1: Gelation behaviors of these binary organogels at room temperature.

Solvents	C18-Azo	C18-Azo-Me	C16-Azo	C16-Azo-Me	C14-Azo	C14-Azo-Me	C12-Azo	C12-Azo-Me
Acetone	PS	PS	PS	PS	PS	PS	PS	PS
Aniline	PS	PS	PS	PS	PS	PS	PS	PS
n-Hexane	S	S	S	S	S	S	S	S
Toluene	G (3.0)	G (3.0)	G (2.8)	G (2.8)	S	S	S	S
Pyridine	S	S	S	S	S	S	S	S
Isopropanol	S	S	S	S	S	S	S	S
Cyclopentanone	PS	PS	PS	PS	PS	PS	PS	PS
Cyclohexanone	PS	PS	PS	PS	PS	PS	PS	PS
Nitrobenzene	G (3.0)	G (3.0)	G (2.5)	G (2.5)	G (2.5)	G (2.5)	S	S
n-Butanol	S	S	S	S	S	S	S	S
Ethanolamine	G (3.0)	G (3.0)	G (2.8)	G (2.8)	G (2.5)	G (2.5)	G (2.5)	G (2.5)
n-Butyl acrylate	PS	PS	G (2.8)	G (2.8)	PS	PS	PS	PS
1,4-Dioxane	S	S	S	S	S	S	S	S
Petroleum ether	PS	PS	PS	PS	PS	PS	PS	PS
Ethyl acetate	PS	PS	PS	PS	PS	PS	PS	PS
Chloroform	PS	PS	G (2.5)	G (2.5)	PS	PS	PS	PS
THF	S	S	S	S	S	S	S	S
DMF	S	S	S	S	S	S	S	S
DMSO	S	S	S	S	S	S	S	S
Benzene	G (3.0)	G (3.0)	G (2.8)	G (2.8)	PS	PS	S	S

DMF, dimethylformamide; THF, tetrahydrofuran; DMSO, dimethyl sulfoxide; S: solution; PS: partially soluble; and G: gel; for gels, the critical gelation concentrations at room temperature are shown in parentheses (% w/v).

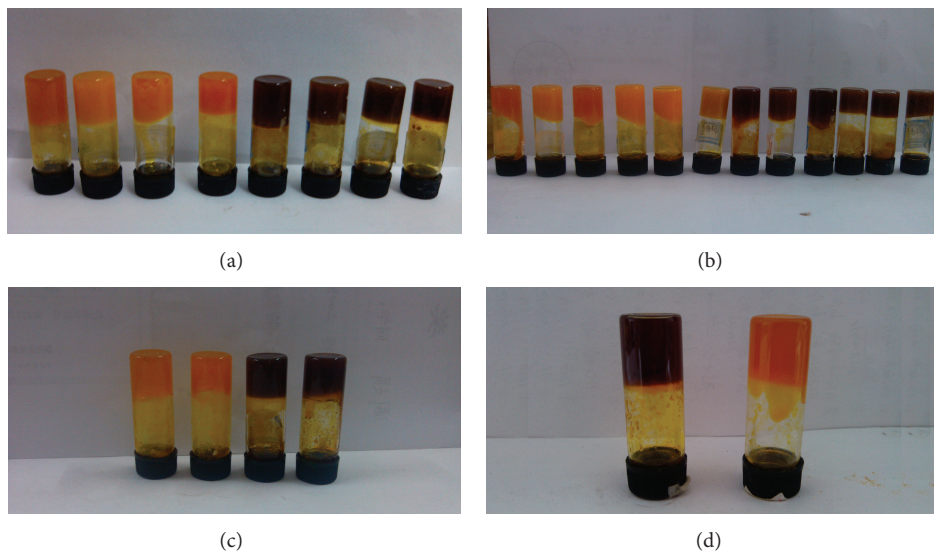


FIGURE 1: Photographs of as-made organogels: (a), C18-Azo and C18-Azo-Me; (b), C16-Azo and C16-Azo-Me; (c), C14-Azo and C14-Azo-Me; and (d), C12-Azo and C12-Azo-Me, respectively.

Figures 2, 3, and 4. From the present diverse images, it can be obviously observed that the nanostructures of all xerogels from various solvents are obviously different from each other, and the nanostructures of the aggregates change from lamella, wrinkle, and belt to dot with change of solvents and mixtures. Furthermore, more nanorod or nanobelt aggregates with different sizes were obtained in gels with longer alkyl substituent

chains. In addition, it should be noted that these belt-like aggregates showed a tendency to aggregate together due to highly directional intermolecular interactions and/or solvent evaporation. The difference of morphologies can be mainly attributed to the different strengths of the intermolecular forces, such as hydrophobic force between alkyl methylene chains and  $\pi$ - $\pi$  stacking of azobenzene segments, which

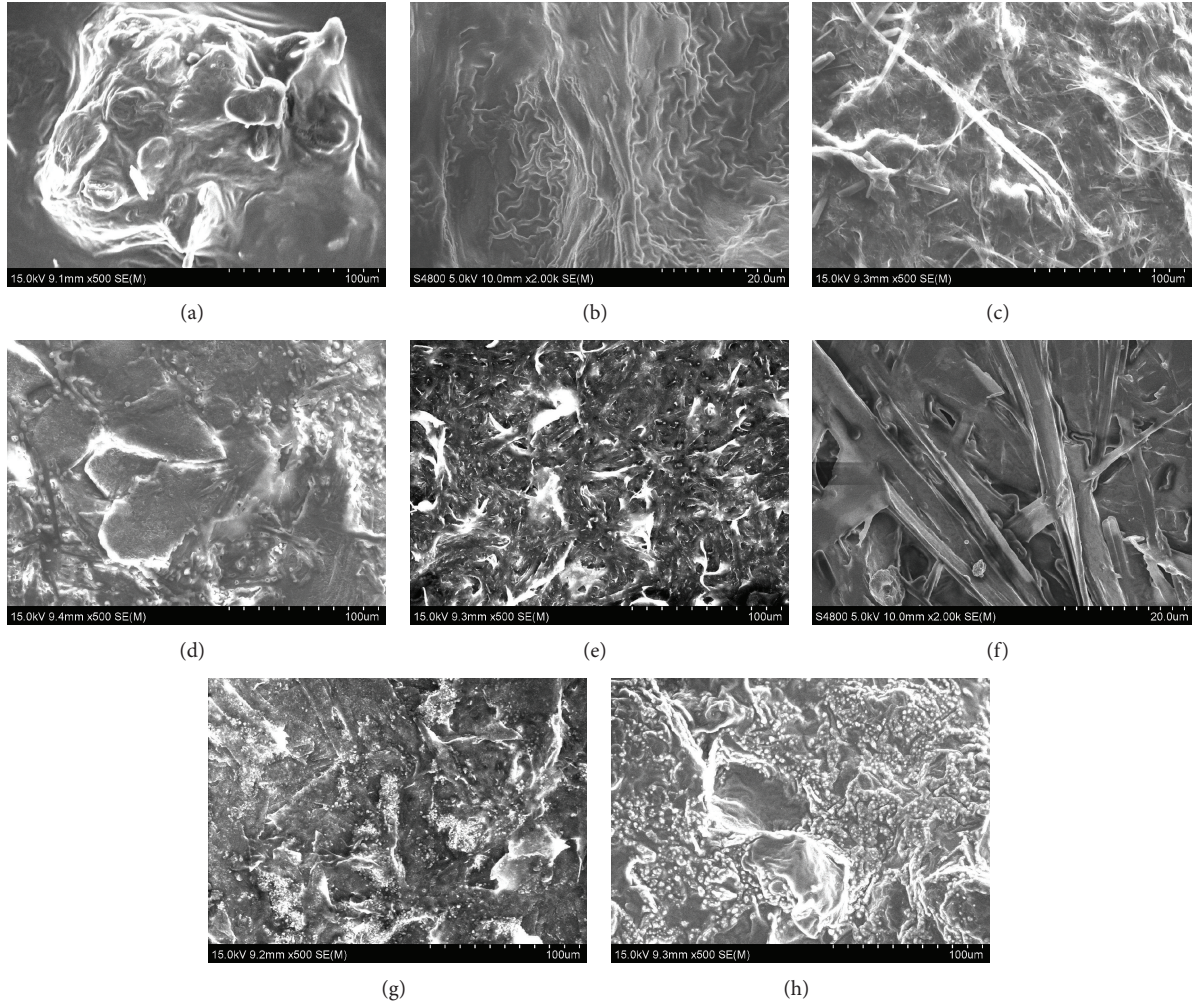


FIGURE 2: SEM images of xerogels. C18-Azo (a, b, c, and d) and C18-Azo-Me (e, f, g, and h) in toluene, nitrobenzene, ethanolamine, and benzene, respectively.

can regulate the orderly stacking and formation of organized aggregates in gel formation.

**3.3. Spectral Investigation.** In addition, in order to further characterize the organized stacking unit of xerogels nanostructures, XRD patterns of all xerogels were measured, as shown in Figure 5. Firstly, the curves of C18-Azo and C18-Azo-Me xerogels from various solvents show similar strong peaks in the angle region ( $2\theta$  values, 5.44, 6.02, 9.02, 16.78, and 19.38°) corresponding to  $d$  values of 1.63, 1.47, 0.98, 0.53, and 0.46 nm, respectively. In addition, for the curves of C16-Azo and C16-Azo-Me xerogels, the minimum peaks appeared at  $2\theta$  value of 5.92°, corresponding to  $d$  value of 1.49 nm. However, as for the curves of C14-Azo and C14-Azo-Me from nitrobenzene and ethanolamine, the small  $2\theta$  values are 2.18 and 3.44°, corresponding to  $d$  values of 4.06 and 2.57 nm, respectively. Meanwhile, as for the curves of C12-Azo and C12-Azo-Me from ethanolamine, the small  $2\theta$  values are 2.50 and 3.76°, corresponding to  $d$  values of 3.54 and 2.35 nm, respectively. The difference of values between C18-Azo and C16-Azo with longer alkyl methylene chains can be mainly

attributed to the change of length in substituent groups linked to azobenzene segment in the molecular skeleton, which affected the assembly modes in the 3D stacking of organogels [28]. At the same time, for these xerogels from gelators with shorter alkyl chains, the changed  $d$  values indicated organized multilayer formation in the self-assembly of organogels. The XRD results mentioned above demonstrated that the length of substituent alkyl chain in molecular skeletons had obvious effect on the assembly modes of these gelator mixtures.

It is reported that hydrogen bonding can be used to monitor the self-assembly process of organogels [29]. In present case, in order to investigate the effect of many factors on assembly, the FT-IR spectra of all xerogels were measured, as shown in Figure 6. Firstly, C18-Azo xerogel was taken as an example, as shown in Figure 6(a). Some main characteristic peaks were observed at 3374, 2917, 2848, 1705, 1602, and 1471  $\text{cm}^{-1}$ , respectively, which could be assigned to the N-H and O-H stretching, methylene stretching, carbonyl group band, amide I band, and methylene scissoring, respectively [30, 31]. These bands indicated that the formation of hydrogen bonding interactions between intermolecular amino and

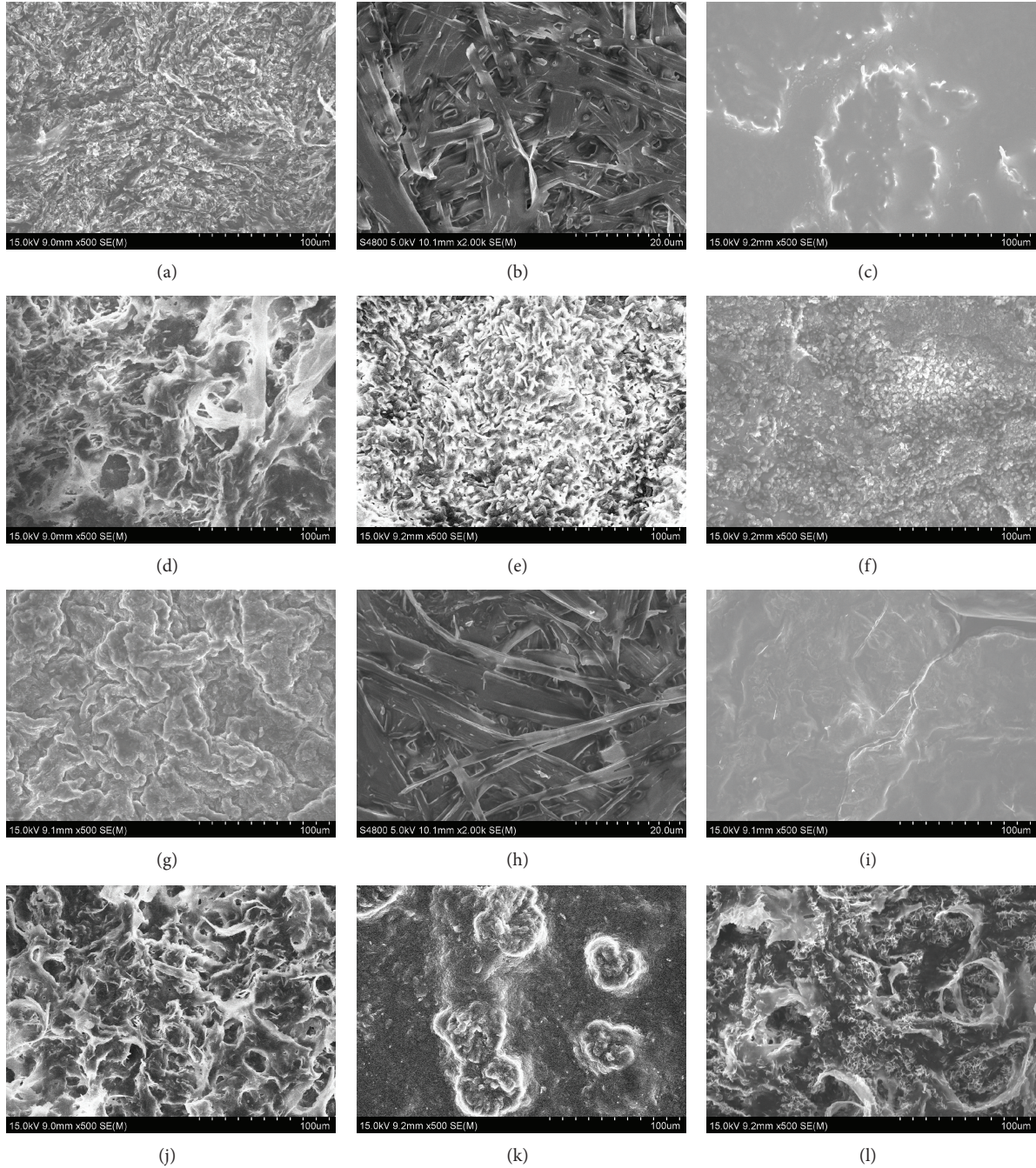


FIGURE 3: SEM images of xerogels. C16-Azo (a, b, c, d, e, and f) and C16-Azo-Me (g, h, i, j, k, and l) in toluene, nitrobenzene, ethanolamine, n-butyl acrylate, chloroform, and benzene, respectively.

carboxylic acid groups in the gel state can regulate the self-assembly modes of the gelator molecules to stack in ordered nanostructures. Similar spectra were observed for other xerogels.

**3.4. Discussion of Assembly Modes.** Considering the XRD results described above and the hydrogen bonding nature of these binary mixtures as confirmed by FT-IR measurements, the possible assembly modes for present xerogels were proposed and schematically shown in Figure 7. As for xerogel of C18-Azo and C16-Azo containing longer alkyl

chains, due to the strong intermolecular hydrophobic force between substituent alkyl chains and hydrogen bonding interaction between amino and carboxylic acid groups, these gelators can self-assemble to form orderly nanostructures. The calculated repeating unit with length of about 1.6~1.7 nm was obtained. The obtained experimental values were 1.63 and 1.49 nm for gels of C18-Azo and C16-Azo, respectively, which was in well accordance with the calculation result. In addition, for the xerogels of C14-Azo and C12-Azo with shorter alkyl chains, with the decrement of alkyl substituent chains, the weaker intermolecular hydrophobic

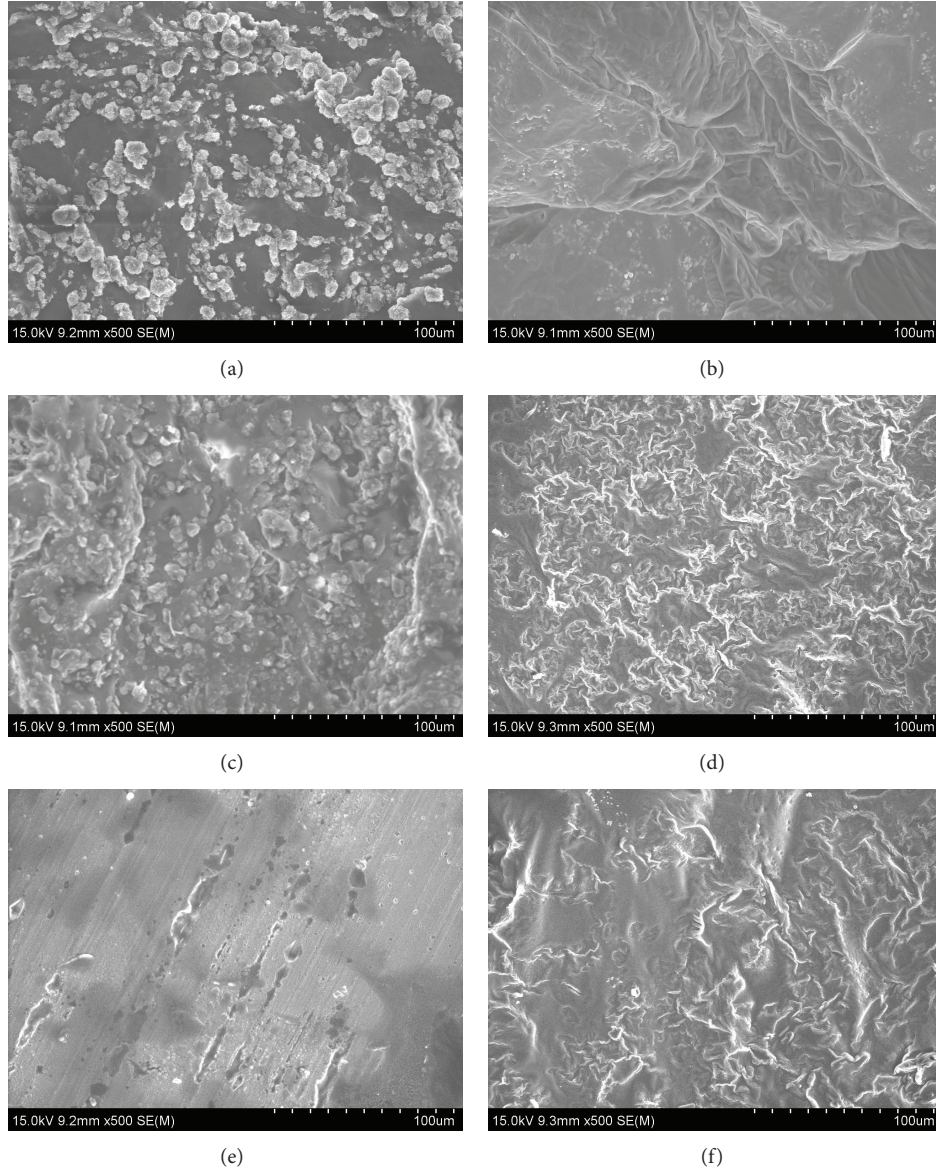


FIGURE 4: SEM images of xerogels. C14-Azo (a and b) and C14-Azo-Me (c and d) in nitrobenzene and ethanolamine, respectively; C12-Azo (e) and C12-Azo-Me (f) in ethanolamine, respectively.

force between the alkyl chains of the neighboring molecules will not enable present gelators to orderly assemble as those cases with longer chains and show a tendency to self-assemble to form multilayer structures and more disorderly stacking unit. Thus, the obtained experimental values were double or multilayer values compared to monomolecular lengths of C14-Azo and C12-Azo. Meanwhile, it should be noted that this phenomena is similar to the results of recent reports [21, 24, 30]. Therein, the substituent groups in azobenzene residue, luminol segment, or benzimidazole/benzothiazole imide compounds can have an obvious effect upon the gel formation, self-assembly, and the as-formed nanostructures of the studied compounds. For the present system, the experimental results also demonstrated that the substituent methylene chains had played a very crucial role in changing the assembly modes and nanostructures in these organogels.

#### 4. Conclusion

The gelation behaviors of binary organogels composed of azobenzene amino derivatives and alkyloxybenzoic acids with different lengths of alkyl chains in various organic solvents were investigated. The experimental results indicated that their gelation behaviors could be changed by varying the lengths of substituent methylene chains. Longer alkyl methylene chains in molecular skeletons in present gelation systems are suitable for the gel formation and self-assembly of organic solvents. For the mixtures containing longer alkyl chains with carbon numbers of 18 and 16, 4 and 6 kinds of organogels can be formed in different solvents, respectively. In addition, for the cases with shorter alkyl chains, only two and one kinds of organogels can form organogels in present solvents for mixtures with carbon numbers of 14 and 12,

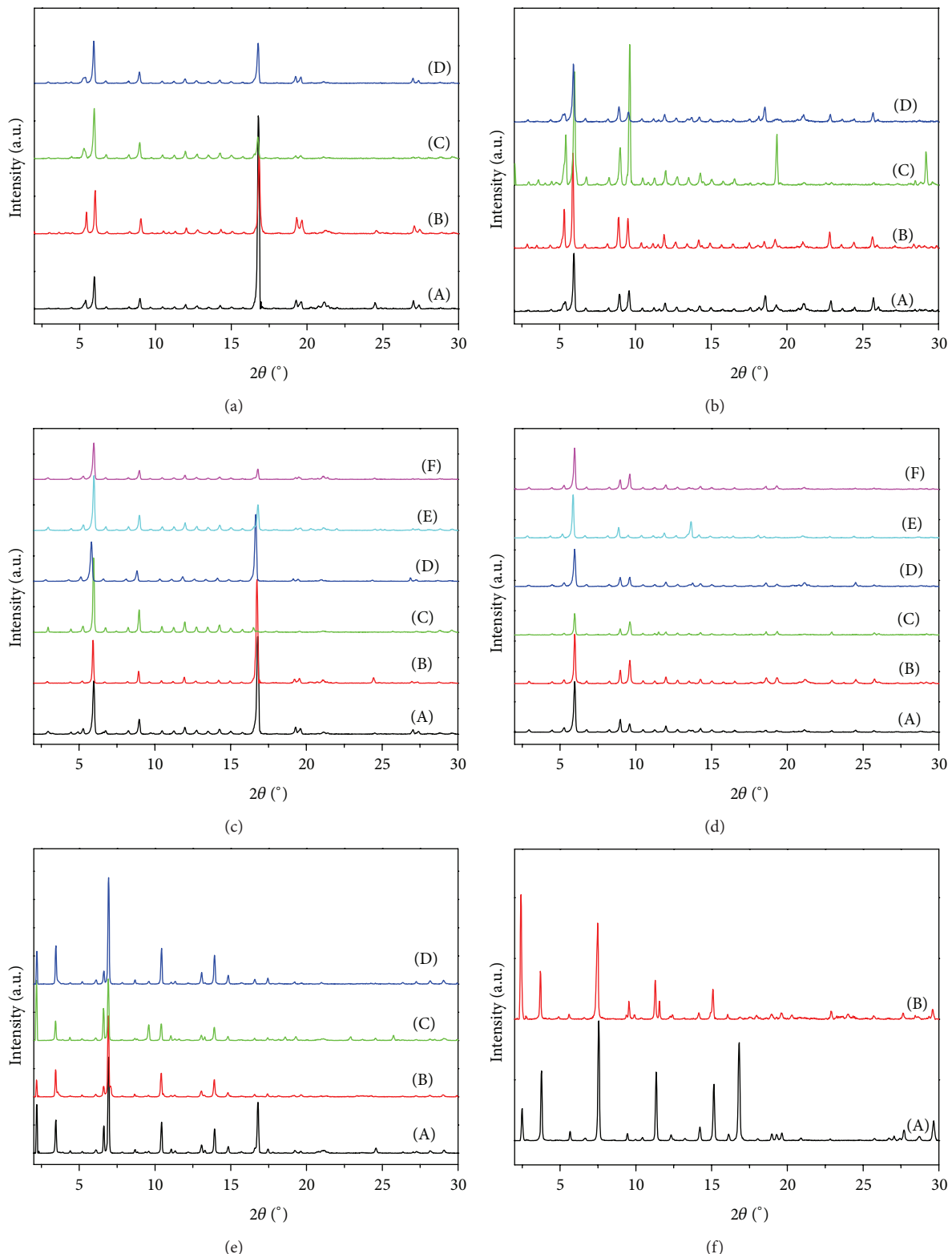


FIGURE 5: X-ray diffraction patterns of xerogels. C18-Azo (A) and C18-Azo-Me (B) in toluene (a), nitrobenzene (b), ethanolamine (c), and benzene (d), respectively; C16-Azo (C) and C16-Azo-Me (D) in toluene (a), nitrobenzene (b), ethanolamine (c), n-butyl acrylate (d), chloroform (e), and benzene (f), respectively; C14-Azo and C14-Azo-Me (E) in nitrobenzene (a and c) and ethanolamine (b and d), respectively; C12-Azo and C12-Azo-Me (F) in ethanolamine (a and b), respectively.

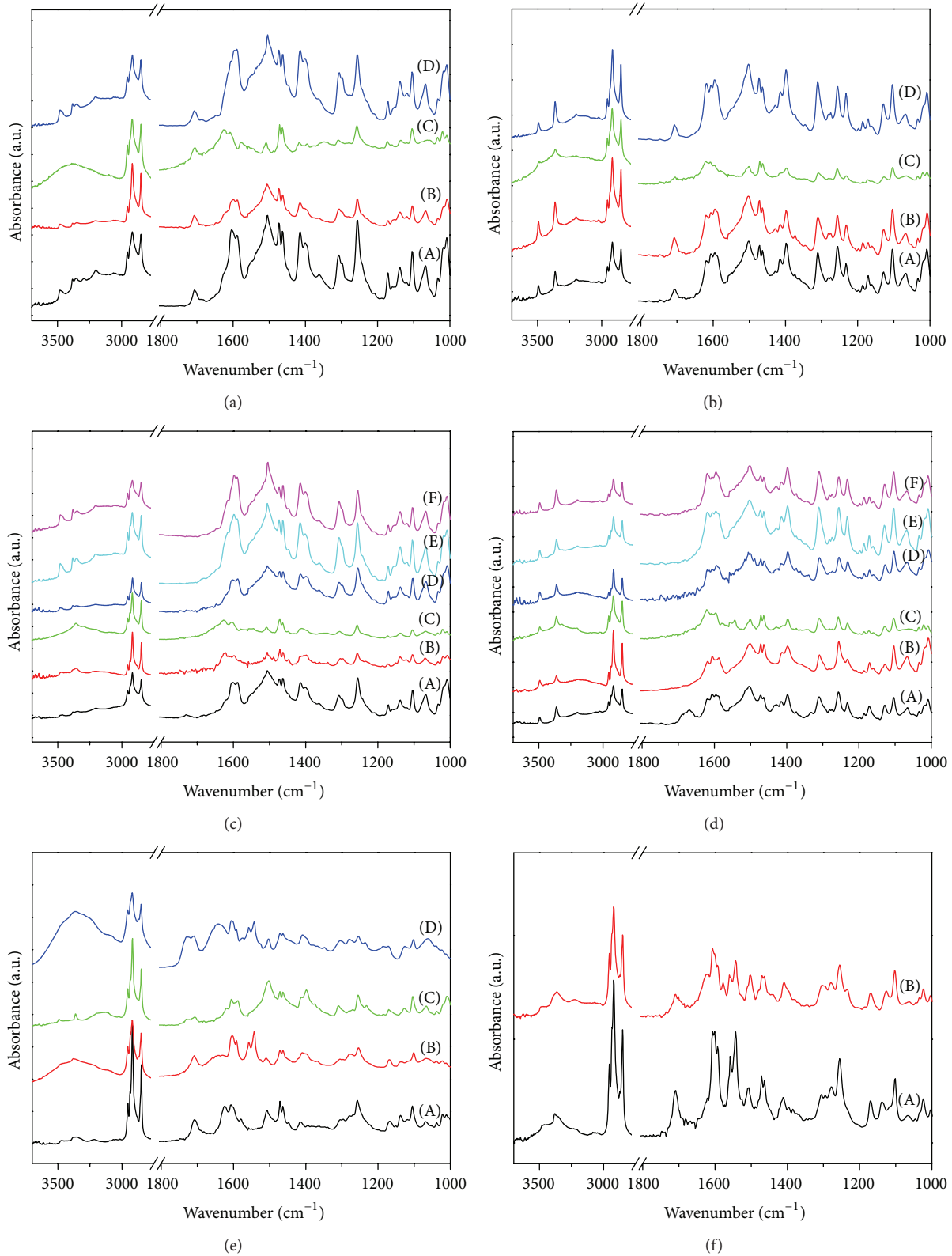


FIGURE 6: FT-IR spectra of xerogels. C18-Azo (A) and C18-Azo-Me (B) in toluene (a), nitrobenzene (b), ethanolamine (c), and benzene (d), respectively; C16-Azo (C) and C16-Azo-Me (D) in toluene (a), nitrobenzene (b), ethanolamine (c), n-butyl acrylate (d), chloroform (e), and benzene (f), respectively; C14-Azo and C14-Azo-Me (E) in nitrobenzene (a and c) and ethanolamine (b and d), respectively; C12-Azo and C12-Azo-Me (F) in ethanolamine (a and b), respectively.

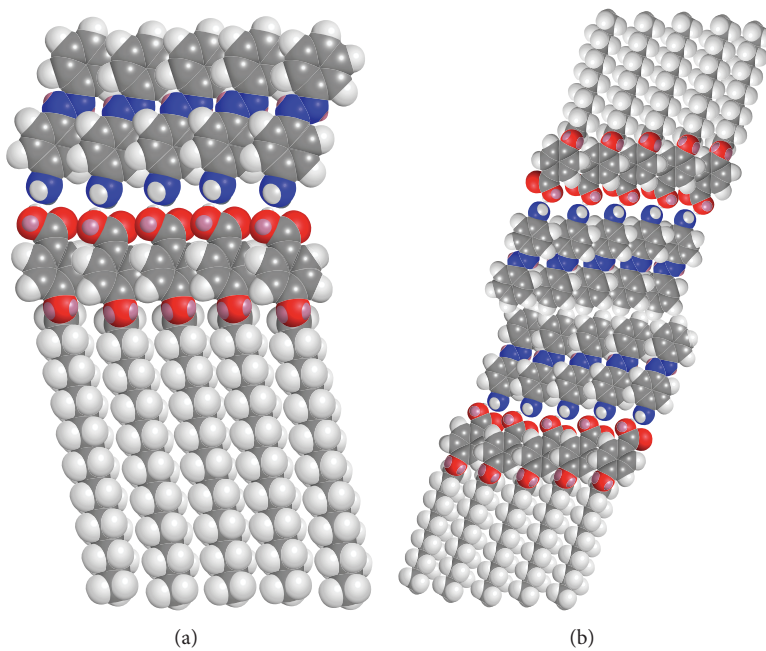


FIGURE 7: Schematic assembly modes for organogels of C18-Azo (a) and C12-Azo (b).

respectively. Morphological characterization indicated that the gelator molecules could organize in orderly stacking and self-assemble into different nanostructures from lamella, wrinkle, and belt to dot with change of solvents and gelator mixtures. Spectral characterization indicated that different H-bond formation and hydrophobic force could be obtained depending on different substituent chains in molecular skeletons. Meanwhile, these organogels can self-assemble to form monomolecular or multilayer nanostructures owing to the different lengths of due to alkyl substituent chains. Possible assembly modes for present xerogels were proposed. The prepared nanostructured materials have wide perspectives and many potential applications in nanoscience and material fields due to their scientific values. The present investigation is perspective to provide new clues for the design of new nanomaterials and functional textile materials with special microstructures.

### Conflict of Interests

The authors declare that they have no direct financial relations with the commercial identities mentioned in this paper that might lead to a conflict of interests for any of the authors.

### Acknowledgments

This work was financially supported by the Natural Science Foundation of Hebei Province (no. B2013203108), the Science Foundation for the Excellent Youth Scholars from Universities and Colleges of Hebei Province (no. YQ2013026), and the Support Program for the Top Young Talents of Hebei Province.

### References

- [1] H. Yu and Q. Huang, "Improving the oral bioavailability of curcumin using novel organogel-based nanoemulsions," *Journal of Agricultural and Food Chemistry*, vol. 60, no. 21, pp. 5373–5379, 2012.
- [2] G. M. Newbloom, K. M. Weigandt, and D. C. Pozzo, "Electrical, mechanical, and structural characterization of self-assembly in poly(3-hexylthiophene) organogel networks," *Macromolecules*, vol. 45, no. 8, pp. 3452–3462, 2012.
- [3] D. Liu, D. Wang, M. Wang et al., "Supramolecular organogel based on crown ether and secondary ammonium functionlized glycidyl triazole polymers," *Macromolecules*, vol. 46, no. 11, pp. 4617–4625, 2013.
- [4] H. Sawalha, R. den Adel, P. Venema, A. Bot, E. Flöter, and E. van der Linden, "Organogel-emulsions with mixtures of  $\beta$ -sitosterol and  $\gamma$ -oryzanol: influence of water activity and type of oil phase on gelling capability," *Journal of Agricultural and Food Chemistry*, vol. 60, no. 13, pp. 3462–3470, 2012.
- [5] P. Rajamalli and E. Prasad, "Low molecular weight fluorescent organogel for fluoride ion detection," *Organic Letters*, vol. 13, no. 14, pp. 3714–3717, 2011.
- [6] S. Bouquet-Bonnet, M. Yemloul, and D. Canet, "New application of proton nuclear spin relaxation unravelling the intermolecular structural features of low-molecular-weight organogel fibers," *Journal of the American Chemical Society*, vol. 134, no. 25, pp. 10621–10627, 2012.
- [7] S. O'Sullivan and D. W. M. Arrigan, "Impact of a surfactant on the electroactivity of proteins at an aqueous-organogel microinterface array," *Analytical Chemistry*, vol. 85, no. 3, pp. 1389–1394, 2013.
- [8] H. Takeno, A. Maehara, D. Yamaguchi, and S. Koizumi, "A structural study of an organogel investigated by small-angle neutron scattering and synchrotron small-angle X-ray scattering," *Journal of Physical Chemistry B*, vol. 116, no. 26, pp. 7739–7745, 2012.

- [9] J. Lu, J. Hu, Y. Song, and Y. Ju, "A new dual-responsive organogel based on uracil-appended glycyrrhetic acid," *Organic Letters*, vol. 13, no. 13, pp. 3372–3375, 2011.
- [10] M. Yemloul, E. Steiner, A. Robert et al., "Solvent dynamical behavior in an organogel phase as studied by NMR relaxation and diffusion experiments," *The Journal of Physical Chemistry B*, vol. 115, no. 11, pp. 2511–2517, 2011.
- [11] F. Xin, H. Zhang, B. Hao et al., "Controllable transformation from sensitive and reversible heat-set organogel to stable gel induced by sodium acetate," *Colloids and Surfaces A: Physicochemical and Engineering Aspects*, vol. 410, pp. 18–22, 2012.
- [12] F. S. Schoonbeek, J. H. van Esch, R. Hulst, R. M. Kellogg, and B. L. Feringa, "Geminal Bis-ureas as gelators for organic solvents: gelation properties and structural studies in solution and in the gel state," *Chemistry—A European Journal*, vol. 6, no. 14, pp. 2633–2643, 2000.
- [13] P. Anilkumar and M. Jayakannan, "A novel supramolecular organogel nanotubular template approach for conducting nano-materials," *The Journal of Physical Chemistry B*, vol. 114, no. 2, pp. 728–736, 2010.
- [14] P. D. Wadhavane, R. E. Galian, M. A. Izquierdo et al., "Photoluminescence enhancement of CdSe quantum dots: a case of organogel-nanoparticle symbiosis," *Journal of the American Chemical Society*, vol. 134, no. 50, pp. 20554–20563, 2012.
- [15] W. Liu, P. Xing, F. Xin et al., "Novel double phase transforming organogel based on  $\beta$ -cyclodextrin in 1,2-propylene glycol," *The Journal of Physical Chemistry B*, vol. 116, no. 43, pp. 13106–13113, 2012.
- [16] M. Bielejewski and J. Tritt-Goc, "Evidence of solvent-gelator interaction in sugar-based organogel studied by field-cycling NMR relaxometry," *Langmuir*, vol. 26, no. 22, pp. 17459–17464, 2010.
- [17] Y. Li, J. Liu, G. Du et al., "Reversible heat-set organogel based on supramolecular interactions of  $\beta$ -Cyclodextrin in N, N - dimethylformamide," *The Journal of Physical Chemistry B*, vol. 114, no. 32, pp. 10321–10326, 2010.
- [18] Y. Marui, A. Kikuzawa, T. Kida, and M. Akashi, "Unique organogel formation with macroporous materials constructed by the freeze-drying of aqueous cyclodextrin solutions," *Langmuir*, vol. 26, no. 13, pp. 11441–11445, 2010.
- [19] A. R. Hirst, D. K. Smith, and J. P. Harrington, "Unique nanoscale morphologies underpinning organic gel-phase materials," *Chemistry—A European Journal*, vol. 11, no. 22, pp. 6552–6559, 2005.
- [20] M. Moniruzzaman and P. R. Sundararajan, "Low molecular weight organogels based on long-chain carbamates," *Langmuir*, vol. 21, no. 9, pp. 3802–3807, 2005.
- [21] T. Jiao, Y. Wang, F. Gao, and J. Zhou, "Photoresponsive organogel and organized nanostructures of cholesterol imide derivatives with azobenzene substituent groups," *Progress in Natural Science: Materials International*, vol. 22, no. 1, pp. 64–70, 2012.
- [22] T. Jiao, F. Gao, Y. Wang, J. Zhou, F. Gao, and X. Luo, "Supramolecular gel and nanostructures of bolaform and trigonal cholesteryl derivatives with different aromatic spacers," *Current Nanoscience*, vol. 8, no. 1, pp. 111–116, 2012.
- [23] P. Mukhopadhyay, Y. Iwashita, M. Shirakawa, S. Kawano, N. Fujita, and S. Shinkai, "Spontaneous colorimetric sensing of the positional isomers of dihydroxynaphthalene in a 1D organogel matrix," *Angewandte Chemie: International Edition*, vol. 45, no. 10, pp. 1592–1595, 2006.
- [24] T. Jiao, Y. Wang, Q. Zhang, J. Zhou, and F. Gao, "Regulation of substituent groups on morphologies and self-assembly of organogels based on some azobenzene imide derivatives," *Nanoscale Research Letters*, vol. 8, no. 1, article 160, 8 pages, 2013.
- [25] J. L. Gurav, I. Jung, H. Park, E. S. Kang, and D. Y. Nadargi, "Silica aerogel: synthesis and applications," *Journal of Nanomaterials*, vol. 2010, Article ID 409310, 11 pages, 2010.
- [26] A. S. Al Dwayyan, M. N. Khan, and M. S. Al Salhi, "Optical characterization of chemically etched nanoporous silicon embedded in sol-gel matrix," *Journal of Nanomaterials*, vol. 2012, Article ID 713203, 7 pages, 2012.
- [27] H. Guo, T. Jiao, X. Shen et al., "Binary organogels based on glutamic acid derivatives and different acids: solvent effect and molecular skeletons on self-assembly and nanostructures," *Colloids and Surfaces A: Physicochemical and Engineering Aspects*, vol. 447, pp. 88–96, 2014.
- [28] M. Žinić, F. Vögtle, and F. Fages, "Cholesterol-based gelators," *Topics in Current Chemistry*, vol. 256, pp. 39–76, 2005.
- [29] T. Wang, Y. Li, and M. Liu, "Gelation and self-assembly of glutamate bolaamphiphiles with hybrid linkers: effect of the aromatic ring and alkyl spacers," *Soft Matter*, vol. 5, no. 5, pp. 1066–1073, 2009.
- [30] T. Jiao, Q. Huang, Q. Zhang, D. Xiao, J. Zhou, and F. Gao, "Self-assembly of organogels via new luminol imide derivatives: diverse nanostructures and substituent chain effect," *Nanoscale Research Letters*, vol. 8, no. 1, pp. 1–8, 2013.
- [31] Y. G. Li, T. Y. Wang, and M. H. Liu, "Ultrasound induced formation of organogel from a glutamic dendron," *Tetrahedron*, vol. 63, no. 31, pp. 7468–7473, 2007.

## Research Article

# Use of Novel Polyurethane Microspheres in a Curcumin Delivery System

**Yongmei Hu,<sup>1</sup> Qingshan Li,<sup>1</sup> Wei Hong,<sup>2</sup> Guangzhong Xing,<sup>1</sup> Qilong Jiang,<sup>1</sup> and Wenfeng Lv<sup>1</sup>**

<sup>1</sup> National Key Laboratory of Metastable Materials Science and Technology, Yanshan University, Qinhuangdao, Hebei, China

<sup>2</sup> Qinhuangdao Entry-Exit Inspection & Quarantine Bureau Coal Inspection Technique Center, Qinhuangdao, Hebei, China

Correspondence should be addressed to Qingshan Li; [qsli@ysu.edu.cn](mailto:qsli@ysu.edu.cn) and Qilong Jiang; [ohx31@163.com](mailto:ohx31@163.com)

Received 13 May 2014; Accepted 31 May 2014; Published 4 August 2014

Academic Editor: Xinqing Chen

Copyright © 2014 Yongmei Hu et al. This is an open access article distributed under the Creative Commons Attribution License, which permits unrestricted use, distribution, and reproduction in any medium, provided the original work is properly cited.

Despite having a wide range of beneficial pharmacological effects, curcumin is characterized by poor water solubility and absorption. In this study, novel polyurethane microspheres containing curcumin (Cur-PUMs) were prepared using carboxymethyl cellulose sodium to improve the bioavailability and prolong the retention time of curcumin. The prepared Cur-PUMs were characterized by Fourier transform infrared spectroscopy, scanning electron microscope, and ultraviolet spectrophotometer. The sustained-release effects of Cur-PUMs were demonstrated using stability tests *in vitro* and *in vivo* pharmacokinetic studies following oral administration. We found that the stability of Cur-PUMs was strongly affected by pH variation. Further, compared with free curcumin, Cur-PUMs showed significantly improved maximum concentration and half-life.

## 1. Introduction

Curcumin (diferuloylmethane, MW = 368.37), the main component of turmeric, possesses a wide range of pharmacological activities including anti-inflammatory, anticancer, antioxidant, wound healing, and antimicrobial effects and has been widely used for centuries in indigenous medicine for the treatment of inflammatory conditions and other diseases (Figure 1) [1]. Further, epidemiological studies suggest that curcumin consumption may reduce the risk of cancer as well as having other protective biological effects in humans [2].

Raw curcumin products contain a mixture of curcumin, demethoxycurcumin, and bisdemethoxycurcumin [3]. Currently, there are few methods to determine the amount of curcumin in food. Although alkaline extraction regimes have been used previously to determine levels of annatto in food, these methods are unsuitable for the extraction of curcumin as it is unstable in alkaline conditions [4–6]. Owing to this instability, it is unsurprising that the relative alkalinity of the intestines promotes the decomposition of curcumin, preventing its absorption. This effect has been demonstrated in rats via oral administration of different

doses of 3H-curcumin [7]. Following oral administration, only trace amounts of curcumin were found in urine. Rather, approximately 75% of curcumin was excreted in the feces because of its rapid metabolism and low aqueous solubility [8].

Several strategies have been developed to circumvent the limitations of curcumin, including encapsulation in liposomes, biodegradable microspheres, cyclodextrin, hydrogels, polymeric nanoparticles, and lipid-based nanoparticles [9]. Recently, Sun et al. showed that the anti-inflammatory activity of curcumin is enhanced when curcumin is encapsulated in exosomes [10]. Their work indicated that exosomes, but not lipids alone, are required for the enhanced effect. Further, Akhtar et al. [11] found that curcumin bound to chitosan nanoparticles did not degrade as rapidly as free curcumin when the particles were incubated in mouse plasma *in vitro* at room temperature. These results suggested that the binding of curcumin to chitosan nanoparticles increased its chemical stability and enhanced its bioavailability when fed to mice. Souguir et al. made a nanoencapsulation of curcumin in polyurethane and polyurea shells using an emulsion-diffusion method and investigated parameters affecting



FIGURE 1: The structure of curcumin.

the mean diameter and size distribution of the particles [12]. Finally, Cassano et al. successfully prepared a novel curcumin-based microsphere for the oral delivery of azathio-prine [13].

Understanding the effects of pH on curcumin may help achieve drug delivery in a manner that promotes a more concentrated release of curcumin and/or the protection of curcumin from rapid degradation. The progress of pH targeting nanotechnology has been reviewed previously [15]. In addition, the theory behind pH targeting has also been discussed by Filippov et al. [16]. A number of groups have published work reporting pH responsive drug delivery. Wang et al. recently prepared temperature- and pH responsive nanoparticles of biocompatible polyurethanes for the delivery of doxorubicin [17]. In addition, Hong et al. published PLGA-PEG-PLGA thermo- and pH responsive copolymer micelles [18]. Finally, Zhang et al. have developed pH responsive microspheres and evaluated them in different pH conditions [19].

In this paper, carboxymethylcellulose sodium (Na-CMC) polyurethane microspheres (PUMs) containing curcumin were prepared using isophorone diisocyanate (IPDI), polyethylene glycol (PEG), and Na-CMC. The primary metabolite of IPDI is an ester ring diamine, which is considered nontoxic to humans and is not known to cause inflammation. Moreover, pure CMC has undergone stringent biological research and toxicological testing and has been approved by the World Health Organization (WHO) for food applications. PEG is a nonimmunogenic, biodegradable molecule with many beneficial physical and biochemical properties. For example, PEG is nontoxic and miscible in many solvents. Moreover, PEG itself is not adsorbed by platelets or proteins.

The objective of this study was to prepare Cur-PUMs and optimize an encapsulation process based on the emulsion-diffusion method. Further, the drug release profile and pharmacokinetic parameters of Cur-PUMs were investigated *in vitro* and *in vivo* following oral administration to evaluate its sustained-release and pH responsive properties.

## 2. Experimental

**2.1. Materials.** PEG (MW = 1000.800 Da), IPDI (99%), Na-CMC (99%), N-(2,3-dimercaptopropyl)phthalimidic acid (DMPA, 99%), 1,4-butanediol (BDO, 99%), dibutyltin dilaurate (DBTDL, 99%), ethyl acetate (EA, 99%), triethylamine (TEA, 99%), and ethylenediamine (EDA, 99%) were purchased from Xi Reagent Co., Ltd. (Sichuan, China). Curcumin (Cur) was purchased from Aladdin Reagent Co., Ltd. (Shanghai, China). PEG, DMPA, and Na-CMC were

dehydrated in a vacuum oven at 110°C for 3 h. Curcumin must be dehydrated before placement in a nitrogen atmosphere.

**2.2. Preparation of Cur-PUMs.** Polyurethane was synthesized by a condensation reaction, via coupling reactions between the terminal hydroxyl groups (-OH) of PEG and Na-CMC and the isocyanate groups (-NCO) of IPDI and DMPA. BDO was used as a chain extender, DBTDL was used as a catalyst, and TEA and EDA were used as neutralization agents in this reaction.

First, IPDI, EA (as solvent), the requisite percent of Na-CMC, and 10 g PEG were added into three-neck round-bottom flask with a stirrer, reflux condenser, and thermometer. DBTDL was added dropwise (4-5 drops) as a catalyst. The flask was then heated to 70–90°C and stirred for 1–3 h. The flask was cooled to 50–70°C and DMPA was added. The reaction was incubated for 3 h. BDO was added and the reaction mixture was incubated for an additional 0.5 h. Next, the mixture was cooled to 40°C and 5 g of curcumin was added. TEA was added dropwise to the reaction for 30 min. This was followed by addition of EDA and incubation for 30 min. Finally, the flask was cooled to 30°C, and deionized water was added with stirring for 1–3 h until emulsified. The mixture was distilled at 65°C by reducing pressure.

**2.3. Characterizations.** Synthesized PUMs, curcumin, and Cur-PUMs were analyzed by Fourier transform infrared spectroscopy (FTIR) using a Jasco 4200 instrument. The test samples were prepared as described previously [12].

A standard curve was plotted to determine the concentration of curcumin versus ultraviolet spectrophotometer (UV) absorbance. To develop this curve, the absorbance of known concentration of curcumin dissolved in methanol (0.612 ng/mL, 1.244 ng/mL, 1.836 ng/mL, 2.448 ng/mL, 3.060 ng/mL, and 15.30 ng/mL) was determined via Nanodrop 1000 spectrophotometer.

Encapsulation efficiency (EE) is defined as the curcumin contained within the Cur-PUMs ( $m_E$ ) divided by the initial amount of curcumin used ( $m_I$ ).  $m_F$  is the curcumin left in solution during the loading study, as given by the following equation:

$$\text{EE (\%)} = \frac{m_E}{m_I}, \quad (m_E = m_I - m_F). \quad (1)$$

Drug loading efficiency (DL) is defined as the contained curcumin amount ( $m_E$ ) divided by the amount of microspheres ( $m_M$ ). The  $m_M$  could be obtained via filtration and distillation after the PU shells were dissolved and cleaned with DMF:

$$\text{DL (\%)} = \frac{m_E}{m_M}. \quad (2)$$

All the samples were deposited with gold before scanning with a scanning electron microscope (SEM) using JEOL JSMT 300A instrument, just as previously described [11].

**2.4. Influences of Process Parameters on EE and DL during Synthesis.** Several parameters were taken into account and should be defined first briefly as follows:

$$R = \frac{n(-\text{NCO})}{n(-\text{OH})} \quad (3)$$

$$M_{\text{Na-CMC}} = \frac{m(\text{Na-CMC})}{m_1} \times 100 \quad (4)$$

$$C_{\text{Cur}} = \frac{m(\text{curcumin})}{v(\text{solvent})}. \quad (5)$$

$n(-\text{NCO})$  and  $n(-\text{OH})$  are the molar contents of the -NCO group and -OH group of all the components.  $m(\text{Na-CMC})$  and  $m(\text{curcumin})$  are the mass content of Na-CMC and curcumin.  $m_1$  is the mass of all components except Na-CMC and curcumin. The influence of  $C_{\text{Cur}}$  on EE and DL was studied when  $R$  was 3.0 and  $M_{\text{Na-CMC}}$  was 2.0. The influences of  $M_{\text{Na-CMC}}$  were assessed when  $R$  was 3.0 and  $C_{\text{Cur}}$  was 0.3. The influences of  $R$  were assessed when  $M_{\text{Na-CMC}}$  was 0.3 and  $C_{\text{Cur}}$  was 2.0. Finally, the influences of  $R$  were assessed again in the optimized process, as were the effects of both  $M_{\text{Na-CMC}}$  and  $C_{\text{Cur}}$  on EE and DL.

**2.5. Analysis of Curcumin Concentration In Vitro and In Vivo.** A standard curve was established for use in both *in vitro* and *in vivo* studies. For the *in vitro* study, 0.5 mg/mL curcumin in acetonitrile was diluted to 5–50  $\mu\text{mol/L}$  with PBS (pH 7.4). Absorbance was measured with a spectrophotometer at 420 nm. For the *in vitro* assay, the standard curve was developed by diluting 0.5 mg/mL curcumin with plasma collected from Sprague Dawley rats. The samples were mixed with emodin and centrifuged to remove protein in the plasma. The samples were then detected by UV-HPLC with a C<sub>18</sub> column and at a wavelength of 420 nm, as previously reported by Sun et al. [10]. PBS solutions were prepared as previously reported [19].

Cur-PUMs were placed in an Eppendorf tube with 0.5 mg curcumin, and 5 mL of releasing medium was added. All samples were incubated at 37°C under gentle agitation in the dark. The absorbance of the samples was detected at various time points (0, 0.5, 1.0, 2.0, 3.0, and 20 h). The extractions were centrifuged at 10000 rpm for 15 min and the supernatant was discarded. The solution was then diluted and detected, as mentioned above.

To study the releasing properties of Cur-PUMs *in vivo*, Sprague Dawley rats were divided into two groups. Group A received an oral administration of curcumin (200 mg/kg), whereas Group B received Cur-PUMs (200 mg/kg). Blood (0.5 mL) was extracted at various time points (0.5, 1.0, 2.0, 3.0, 4.0, 5.0, 6.0, 8.0, 10, and 12 h) after feeding and frozen at -80°C. All measurements were made as described above, using plasma at room temperature.

### 3. Results and Discussion

**3.1. Characterization of Synthetic Cur-PUMs Chemical Structure.** The assignments of adsorption peaks for Na-CMC

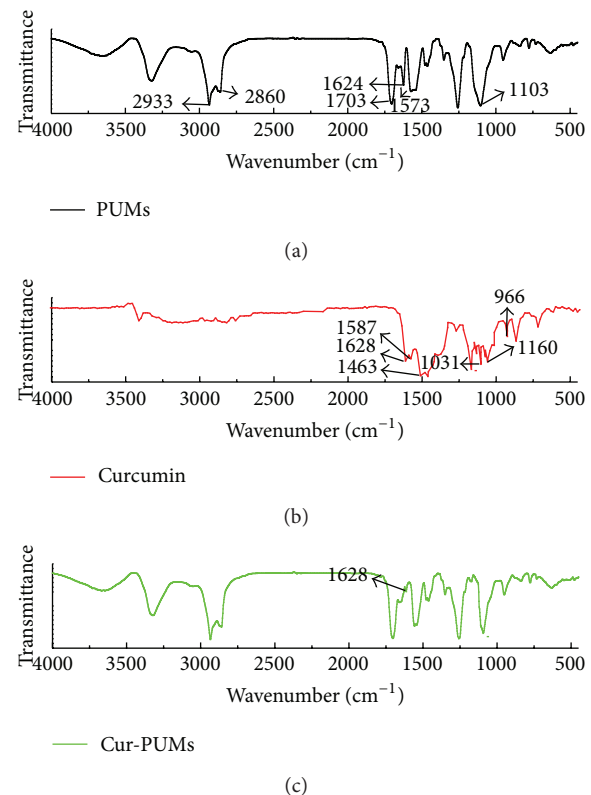


FIGURE 2: FTIR spectroscopy of PUMs (a), Cur (b), and Cur-PUMs (c).

polyurethane are presented in Figure 2(a). The peaks at 1703  $\text{cm}^{-1}$ , 1573  $\text{cm}^{-1}$ , and 3400  $\text{cm}^{-1}$  correspond to the C=O band, N–H deformation vibration band, and N–H stretching vibration band of urethane, respectively. The absence of a peak at 2250  $\text{cm}^{-1}$  indicates that no isocyanate groups remain in the obtained polymer. These records confirm the formation of polyurethane. The sharp peak at 1624  $\text{cm}^{-1}$  corresponds to C=O of  $-\text{CH}_2\text{COONa}$ , indicating the Na-CMC incorporated into the polyurethane successfully. However, few changes were observed in the encapsulated curcumin particles (Figure 2(c)). Nevertheless, two thin shoulders can be observed at 1630  $\text{cm}^{-1}$  and 1680  $\text{cm}^{-1}$ . The peak at 1680  $\text{cm}^{-1}$  is attributed to the enol groups in curcumin (Figure 2(b)). Thus, we can confirm that curcumin was incorporated into the PUMs. Our data indicates that Cur-PUMs were prepared successfully without new chemical bonds emerging, suggesting that there are no chemical interactions between polyurethane and curcumin.

**3.2. Influences of the Investigated Processing Parameters on EE and DL.** As shown in Figure 3, the optimal wavelength for measuring the concentration of curcumin in methanol is 415 nm. The absorbance measurements for the curcumin standard curve are shown in Table 1.

The standard curve was drawn with the peak absorbance as the vertical axis ( $A$ ) and the concentration of curcumin (ng/mL) as the horizontal axis ( $C$ ), as shown in Figure 4.

TABLE 1: Absorbance measurements for the curcumin standard curve.

C (ng/mL)	6.12	12.24	18.36	24.48	30.6
A	0.003761	0.006890	0.009953	0.013397	0.017074

TABLE 2: EE and DL values obtained with optimized parameters.

Sample	EE (%)	DL (%)
1	86.91	26.43
2	84.95	25.68
3	85.65	25.85
Average	<b>85.84</b>	<b>25.99</b>

EE: encapsulation efficiency; DL: drug loading efficiency ( $M_{\text{Na-CMC}} = 2.0$ ,  $C_{\text{Cur}} = 0.3$ ).

The regression equation for curcumin was determined as follows:

$$A = 5.4145C + 2.754, \quad R = 0.9979. \quad (6)$$

The optimized encapsulation parameters were determined ( $M_{\text{Na-CMC}} = 2.0$  and  $C_{\text{Cur}} = 0.3$ ), as shown in Figure 5. Using these parameters, the microspheres were prepared and characterized with variations in  $R$ . The effect of this variation on EE and DL is shown in Table 2. Morphology was then determined by SEM, as shown in Figure 6.

As shown in Table 2, the values of EE and of DL are stable and feasible using the optimized processes (Table 2). Further, Cur-PUMs are morphologically spherical and heterogeneous in size (Figure 6). The diameters of Cur-PUMs prepared with an  $R$  value of 1 ranged from 7.74 to 67.62  $\mu\text{m}$  (mean diameter  $28.26 \pm 18.46 \mu\text{m}$ ). The diameters of Cur-PUMs with an  $R$  value of 3 ranged from 8.35 to 47.5  $\mu\text{m}$  (mean diameter  $19.61 \pm 2.50 \mu\text{m}$ ). Based on these results, the optimized parameters with a maximum EE and DL ( $M_{\text{Na-CMC}} = 2.0$ ,  $C_{\text{Cur}} = 0.3$ ,  $R = 3$ ) were selected to prepare Cur-PUMs for the following experiments.

**3.3. The Study of Stability In Vitro and Pharmacokinetics In Vivo.** The optimal wavelength for measuring the absorbance of curcumin in PBS (pH 7.4) was 420 nm (Figure 7). This value was used to determine the concentration of curcumin in the following experiments.

We determined the time points at which 50% residual curcumin from the Cur-PUMs remained, using PBS with varying pH values. At pH 1.0, 4.0, 6.8, and 7.4, 50% of the residue among negatively charged groups. Swelling of the shell thereby promotes drug release. In contrast, the lower media pH will prevent the dissolution of the shell via a shielding effect, as the nonionized carboxylic acid group becomes more hydrophobic. This leads to the formation of a more compact surface structure. This mechanism will be beneficial to release curcumin in a more concentrated manner with a lower dosage. 50% of residual curcumin remained at 3.25, 1.24, 0.51, and 0.35 h, with pH 7.4, 6.8, 4.0, and 1.0, respectively (Figure 8). These results are consistent with the mechanism proposed (Figure 9) by Huang et al. [14]. Because carboxylic acid groups will obtain a negative charge

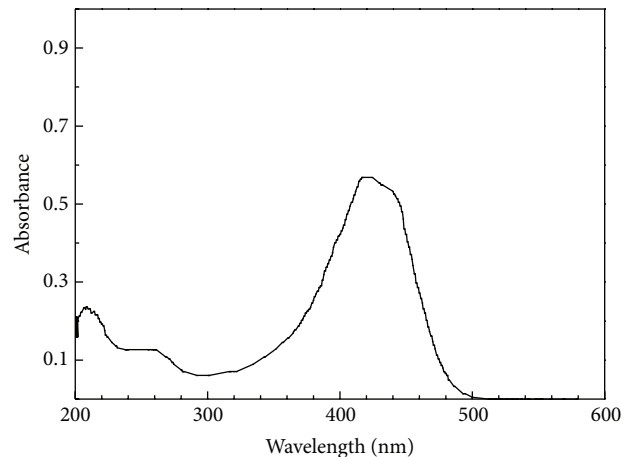


FIGURE 3: Scanning spectrogram for Cur in methanol.

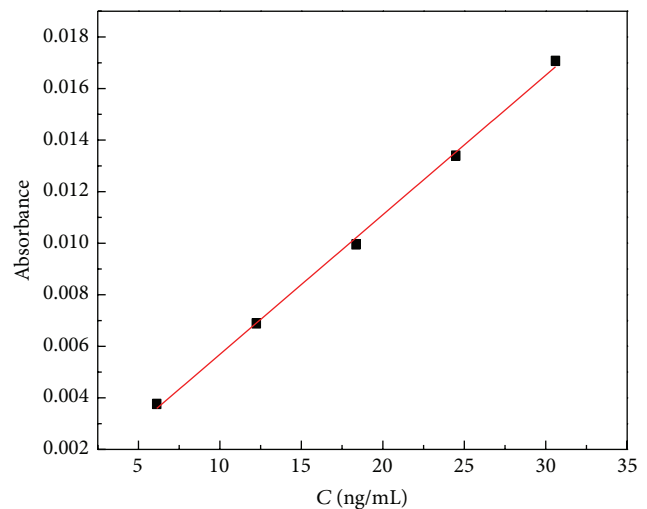


FIGURE 4: The standard curve obtained for use in the curcumin releasing profile.

as the pH increases, the shell will easily swell or decompose due to the electrostatic interaction.

The concentrations of curcumin in the plasma of rats demonstrated the sustained-release properties of Cur-PUMs (Figure 10). The  $T_{\text{max}}$  for Cur-PUMs treated rats (3 h) was six times higher than that of rats that received curcumin alone (0.5 h). Further, the  $C_{\text{max}}$  ( $803.27 \pm 50.81 \text{ ng/mL}$ ) for Cur-PUMs treated rats was 4 times higher than those that received curcumin ( $194.02 \pm 14.75 \text{ ng/mL}$ ) (Table 3). The pharmacokinetic parameters obtained reveal that Cur-PUMs enhanced the maximum curcumin concentration and prolonged the half-life of curcumin, resulting in a sustained-release effect.

#### 4. Conclusion

A series of Na-CMC incorporated PUMs containing curcumin were synthesized and confirmed by FTIR. Optimized processing parameters were obtained through the assessment

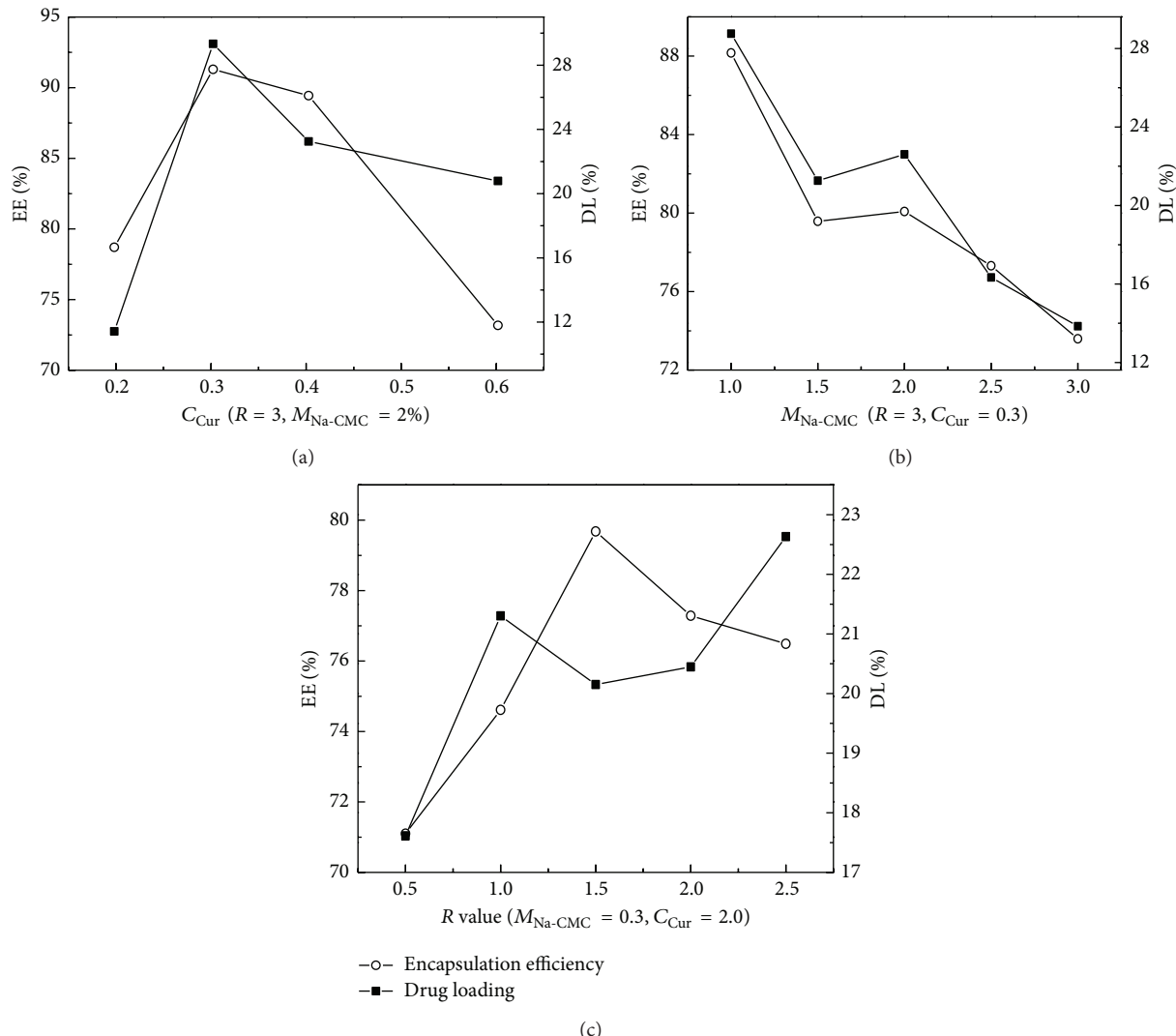


FIGURE 5: Influence on EE and DL at various concentrations of curcumin (a); at various concentrations of Na-CMC (b); and at various values of R (c).

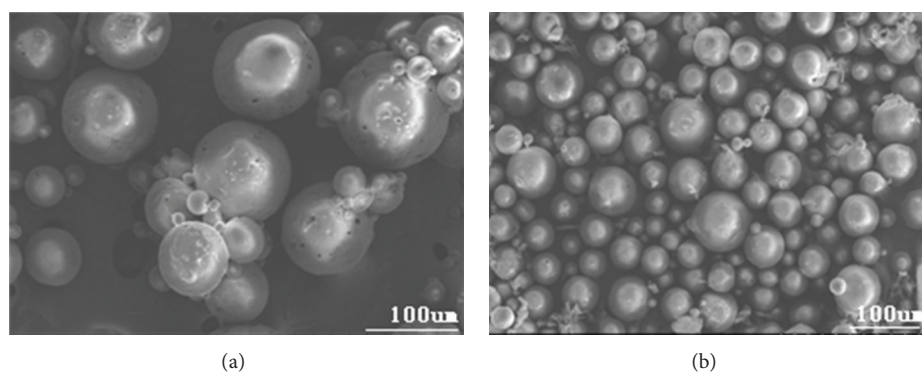


FIGURE 6: SEM photographs of (a) R = 1; (b) R = 3.

TABLE 3: Pharmacokinetic parameters of different curcumin formulations.

Formulation	$C_{\max}$ (ng/mL)	$T_{\max}$ (h)	$AUC_{0 \rightarrow \infty}$ (ng/mL h)	$T_{1/2}$ (h)
Curcumin	$194.02 \pm 14.75$	$0.5 \pm 0.12$	$348.77 \pm 44.83$	$0.91 \pm 0.28$
Cur-PUMs	$803.27 \pm 50.81$	$3.0 \pm 0.23$	$3873.95 \pm 265.22$	$5.61 \pm 0.53$

Values are reported as mean  $\pm$  S.E.M. ( $n = 5$ ).  $C_{\max}$ : maximum concentration;  $T_{\max}$ : time to reach peak concentration; AUC: area under the plasma concentration-time curve from 0 h to  $\infty$ ;  $T_{1/2}$ : half-life.

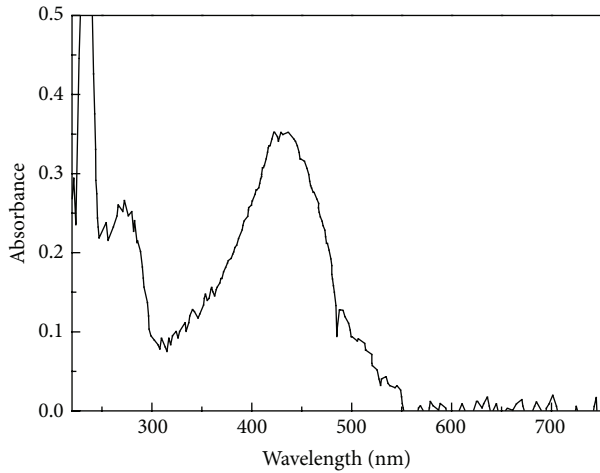
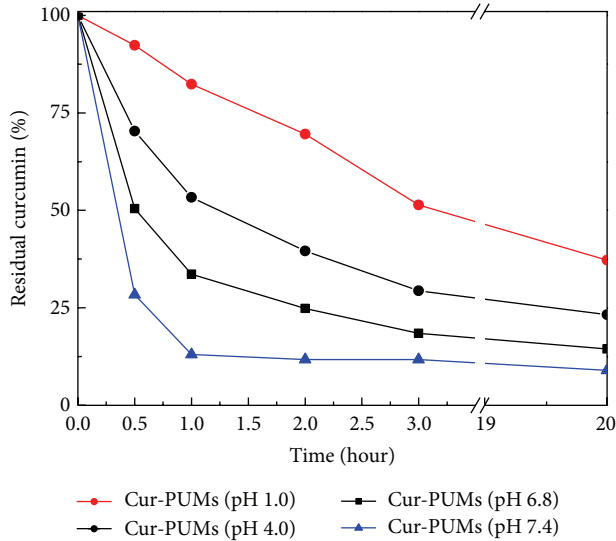


FIGURE 7: Scanning spectrogram of curcumin in PBS (pH 7.4).

FIGURE 8: *In vitro* stability of curcumin from Cur-PUMs in different pH conditions ( $n = 3$ ).

of drug loading and encapsulation efficiency. The optimized concentrations of Na-CMC and curcumin were 2 and 0.3, respectively, and  $R$  was defined as 3. The obtained Cur-PUMs had a spherical morphology. The pH responsive effects of Cur-PUMs were confirmed using *in vitro* stability tests. This analysis indicated that acidic conditions had a shielding

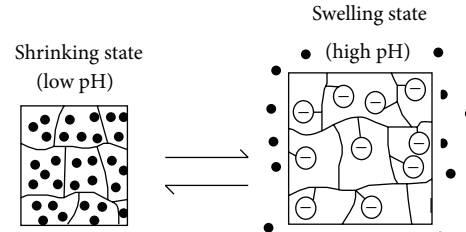


FIGURE 9: The mechanism of drug release in pH-sensitive hydrogels [14].

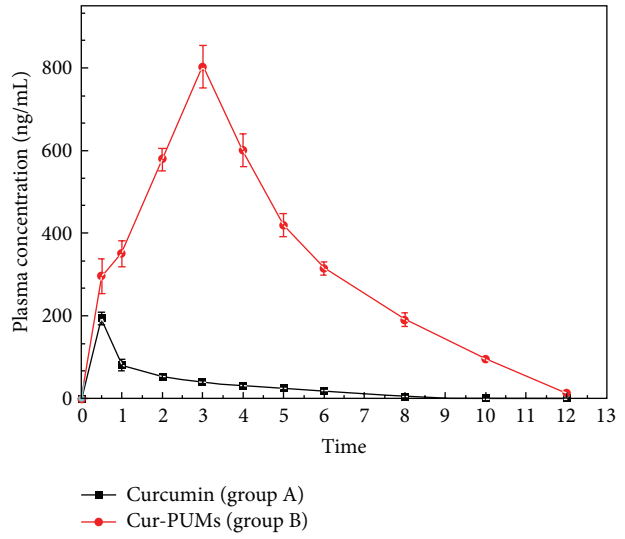


FIGURE 10: The concentration of curcumin in plasma versus time.

effect, which prevented curcumin diffusion, whereas alkaline conditions disrupted the shield allowing for curcumin release. The sustained-release effects of Cur-PUMs were demonstrated directly *in vivo*. Cur-PUMs displayed a prolonged retention time and higher maximum concentration in plasma as compared to curcumin alone. Together, our data suggest that Cur-PUMs may provide an opportunity to utilize curcumin more efficiently with lower doses and improved efficacies.

## Conflict of Interests

The authors declare that there is no conflict of interests regarding the publication of this paper.

## References

- [1] L. Shen and H. Ji, "The pharmacology of curcumin: is it the degradation products?" *Trends in Molecular Medicine*, vol. 18, no. 3, pp. 138–144, 2012.
- [2] R. K. Maheshwari, A. K. Singh, J. Gaddipati, and R. C. Srimal, "Multiple biological activities of curcumin: a short review," *Life Sciences*, vol. 78, no. 18, pp. 2081–2087, 2006.
- [3] G. K. Jayaprakasha, L. J. M. Rao, and K. K. Sakariah, "Improved HPLC method for the determination of curcumin, demethoxycurcumin, and bisdemethoxycurcumin," *Journal of Agricultural and Food Chemistry*, vol. 50, no. 13, pp. 3668–3672, 2002.
- [4] F. E. Lancaster and J. F. Lawrence, "Determination of annatto in high-fat dairy products, margarine and hard candy by solvent extraction followed by high-performance liquid chromatography," *Food Additives and Contaminants*, vol. 12, no. 1, pp. 9–19, 1995.
- [5] M. J. Scotter, L. Castle, C. A. Honeybone, and C. Nelson, "Method development and analysis of retail foods for annatto food colouring material," *Food Additives & Contaminants*, vol. 19, no. 3, pp. 205–222, 2002.
- [6] M. J. Scotter, "Synthesis and chemical characterisation of curcuminoid colouring principles for their potential use as HPLC standards for the determination of curcumin colour in foods," *LWT—Food Science and Technology*, vol. 42, no. 8, pp. 1345–1351, 2009.
- [7] V. Ravindranath and N. Chandrasekhara, "In vitro studies on the intestinal absorption of curcumin in rats," *Toxicology*, vol. 20, no. 2-3, pp. 251–257, 1981.
- [8] G. M. Holder, J. L. Plummer, A. J. Ryan et al., "The metabolism and excretion of curcumin (1,7-bis-(4-hydroxy-3-methoxyphenyl)-1,6-heptadiene-3,5-dione) in the rat," *Xenobiotica*, vol. 8, no. 12, pp. 761–768, 1978.
- [9] B. B. Aggarwal and B. Sung, "Pharmacological basis for the role of curcumin in chronic diseases: an age-old spice with modern targets," *Trends in Pharmacological Sciences*, vol. 30, no. 2, pp. 85–94, 2009.
- [10] D. M. Sun, X. Y. Zhuang, X. Y. Xiang et al., "A novel nanoparticle drug delivery system: the anti-inflammatory activity of curcumin is enhanced when encapsulated in exosomes," *Molecular Therapy*, vol. 18, no. 9, pp. 1606–1614, 2010.
- [11] F. Akhtar, M. M. A. Rizvi, and S. K. Kar, "Oral delivery of curcumin bound to chitosan nanoparticles cured *Plasmodium yoelii* infected mice," *Biotechnology Advances*, vol. 30, no. 1, pp. 310–320, 2012.
- [12] H. Souguir, F. Salaün, P. Douillet, I. Vroman, and S. Chatterjee, "Nanoencapsulation of curcumin in polyurethane and polyurea shells by an emulsion diffusion method," *Chemical Engineering Journal*, vol. 221, pp. 133–145, 2013.
- [13] R. Cassano, S. Trombino, T. Ferrarelli et al., "Preparation, characterization and in vitro activities evaluation of curcumin based microspheres for azathioprine oral delivery," *Reactive and Functional Polymers*, vol. 72, no. 7, pp. 446–450, 2012.
- [14] Y. W. Huang, X. G. Luo, and R. X. Zhuo, "Studies on the controlled release of aspirin in the temperature and pH-sensitive hydrogels," *Polymer Materials Science and Engineering*, vol. 14, no. 6, pp. 141–143, 1998.
- [15] E. S. Lee, Z. Gao, and Y. H. Bae, "Recent progress in tumor pH targeting nanotechnology," *Journal of Controlled Release*, vol. 132, no. 3, pp. 164–170, 2008.
- [16] S. Filippov, M. Hrubý, C. Koňák et al., "Novel pH-Responsive Nanoparticles," *Langmuir*, vol. 24, no. 17, pp. 9295–9301, 2008.
- [17] A. Wang, H. Gao, Y. Sun et al., "Temperature- and pH-responsive nanoparticles of biocompatible polyurethanes for doxorubicin delivery," *International Journal of Pharmaceutics*, vol. 441, no. 1-2, pp. 30–39, 2013.
- [18] W. Hong, D. Chen, J. Li et al., "Thermo- and pH-responsive copolymers based on PLGA-PEG-PLGA and poly(L-histidine): synthesis and in vitro characterization of copolymer micelles," *Acta Biomaterialia*, vol. 10, no. 3, pp. 1259–1271, 2014.
- [19] J. F. Zhang, Q. Tang, X. Y. Xu, and N. Li, "Development and evaluation of a novel phytosome-loaded chitosan microsphere system for curcumin delivery," *International Journal of Pharmaceutics*, vol. 448, no. 1, pp. 168–174, 2013.

## Research Article

# Heat-Activated Persulfate Oxidation of Chlorinated Solvents in Sandy Soil

Jialu Liu,<sup>1</sup> Xijun Gong,<sup>1</sup> Shijun Song,<sup>2</sup> Fengjun Zhang,<sup>1</sup> and Cong Lu<sup>1</sup>

<sup>1</sup> Key Laboratory of Groundwater Resources and Environment, Ministry of Education, Jilin University, Changchun 130021, China

<sup>2</sup> School of Nursing, Jilin University, Changchun 130021, China

Correspondence should be addressed to Cong Lu; lvcong@jlu.edu.cn

Received 1 July 2014; Accepted 15 July 2014; Published 3 August 2014

Academic Editor: Tifeng Jiao

Copyright © 2014 Jialu Liu et al. This is an open access article distributed under the Creative Commons Attribution License, which permits unrestricted use, distribution, and reproduction in any medium, provided the original work is properly cited.

Heat-activated persulfate oxidative treatment of chlorinated organic solvents containing chlorinated ethenes and ethanes in soil was investigated with different persulfate dosages (20 g/L, 40 g/L, and 60 g/L) and different temperatures (30°C, 40°C, and 50°C). Chlorinated organic solvents removal was increased as persulfate concentration increase. The persulfate dosage of 20 g/L with the highest OE (oxidant efficiency) value was economically suitable for chlorinated organic solvents removal. The increasing temperature contributed to the increasing depletion of chlorinated organic solvents. Chlorinated ethenes were more easily removed than chlorinated ethanes. Moreover, the persulfate depletion followed the pseudo-first-order reaction kinetics ( $k_{ps} = 0.0292 [PS]_0 + 0.0008$ ,  $R^2 = 0.9771$ ). Heat-activated persulfate appeared to be an effective oxidant for treatment of chlorinated hydrocarbons.

## 1. Introduction

The chlorinated organic solvents such as trichloroethene (TCE), cis-1,2-dichloroethene (cis-1,2-DCE), 1,1,1-trichloroethane (TCA), and 1,2-dichloroethane (1,2-DCA) have been widely used for decades as a degreasing agent, a cleaning agent, and organic synthesis intermediates in chemical, pharmaceutical, electronic, tanning, printing, and other industries [1–3]. The chlorinated organic solvents were considered as priority toxic pollutants and associated risks to humans representing a public health threat. Historically, the improper disposal of these chlorinated organic solvents has resulted in extensive contamination of soils and groundwater. Due to the high density and low water solubility, the chlorinated organic solvents sink beneath the water table, do not pool, and rather continue to migrate downward in the aquifer, displacing the water until reaching a formation of sufficient impermeability to prevent further migration. That is, it will last a long time, once subsurface medium was contaminated. Therefore, it is urgent to find a fast and efficient method to remediate chlorinated solvents in soils.

In situ chemical oxidation (ISCO) is a remediation technology used to clean up contaminated soils and groundwater

in-place. It has been greatly recognized and widely applied in many contaminated field sites. The typical oxidants used for ISCO are potassium permanganate, hydrogen peroxide (Fenton's reagent), and ozone [4]. Each oxidant has its limitations (e.g., persistence, reactivity, etc.) within a soil matrix [5]. Recently, persulfate ( $\text{Na}_2\text{S}_2\text{O}_8$ , PS) emerged as an efficient oxidant for ISCO applications with the properties of high water solubility, no odor, effectiveness of oxidation over a wide range of pH, and lower affinity for soil organics [6]. The use of persulfate for soil and groundwater treatment holds a lot of promise as persulfate can combine the strength of hydrogen peroxide with the stability of permanganate [4]. Persulfate can be thermally [2, 7–9], chemically [10–12], or photochemically [13] activated to generate the powerful oxidant known as the sulfate free radical ( $\text{SO}_4^{\cdot-}$ ), with a redox potential of 2.6 V [14], which can be instrumental in the destruction of most organic contaminants commonly present in soil and groundwater including trichloroethylene [5, 6, 15], naphthalene [11], and phenol [8, 13, 16]. Compared with other activations, heat activation is the most effective activation technology. Thermally activated persulfate oxidation of chlorinated organic solvents such as TCE has been quite successful in remediating groundwater contaminant.

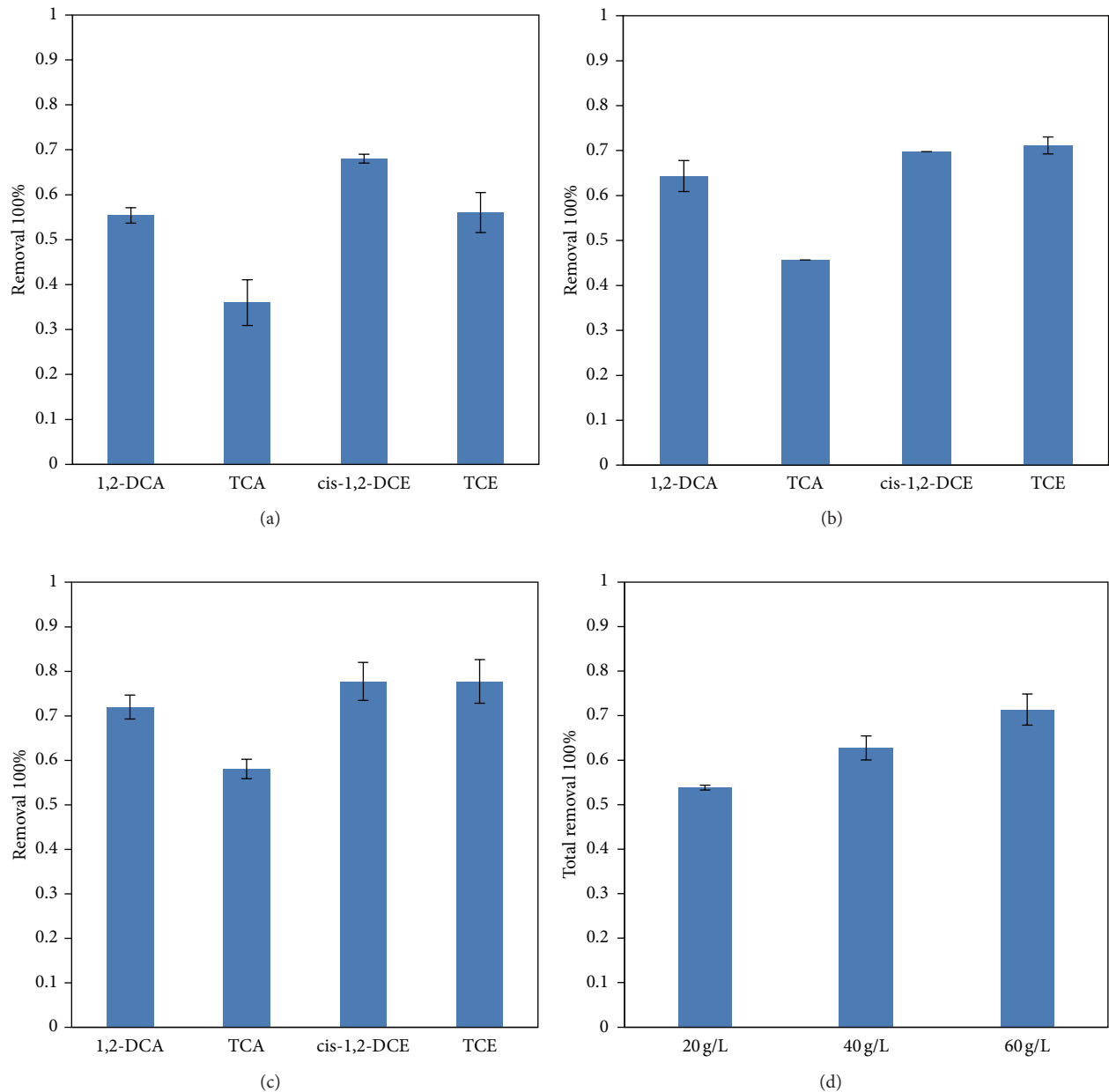


FIGURE 1: The depletion of chlorinated organic solvents by activated persulfate at 30°C with different persulfate dosages: (a) 20 g/L, (b) 40 g/L, and (c) 60 g/L, and (d) the total removal of chlorinated organic solvents.

However, most studies focus on the treatment of single contaminants, such as TCE or TCA, and focus on the treatment of groundwater rather than soils.

In this study, research focuses on the heat-activated persulfate oxidative treatment of organic compounds containing chlorinated ethenes and ethanes in the subsurface medium. The most suitable persulfate dosage for chlorinated organic compounds depletion was determined and the influence of activated persulfate oxidative chlorinated organic compounds under different temperature was investigated.

## 2. Materials and Methods

**2.1. Materials.** All chemicals were of analytical grade except for methanol ( $\text{CH}_3\text{OH}$ , >99.5%, Sinopharm Chemical Reagent Co., Ltd.) which was of HPLC grade. Persulfate ( $\text{Na}_2\text{S}_2\text{O}_8$ , >98.0%) was purchased from Sinopharm Chemical Reagent Co., Ltd, and used as oxidizer. The pure trichloroethene (TCE, >99.0%), cis-1,2-dichloroethene (cis-1,2-DCE, >99.0%), 1,1,1-trichloroethane (TCA, >94.0%), and 1,2-dichloroethane (1,2-DCA, >99.0%) were purchased from

Sinopharm Chemical Reagent Co., Ltd, and diluted to the certain concentration for each experiment. Methanol was used to extract the organic contaminants from soil slurry samples and to quench the oxidation reaction. Sodium bicarbonate ( $\text{NaHCO}_3$ , >99.0%) and potassium iodide (KI, >99.0%) were purchased from Sinopharm Chemical Reagent Co., Ltd, and used for persulfate analysis. Mixed standard solutions (10  $\mu\text{g/mL}$ ) of trichloroethene (TCE), cis-1,2-dichloroethene (cis-1,2-DCE), 1,1,1-trichloroethane (TCA), and 1,2-dichloroethane (1,2-DCA) in purge and trap grade methanol were purchased from Sinopharm Chemical Reagent Co., Ltd, and used as an internal standard for gas chromatography analysis. Ultrapure water from a Millipore system was used in the experiments.

Coarse sandy soil (0.5–2 mm) was prepared.

**2.2. Laboratory Experiments.** The mixed solution of TCE, cis-1,2-DCE, TCA, and 1,2-DCA was prepared as stock solution and diluted to the certain concentration (81.8, 71.2, 75.0, and 70.6 mg/L of TCE, cis-1,2-DCE, TCA, and 1,2-DCA, resp.) for each experiment. And a series of 30 mL brown reaction bottles equipped with Agilent caps and TFE liners were used for all tests. For each test, 25 mL water and 25 g soil were sequentially added to the reaction bottle with the solid-water ratio of 1:1 and mixed followed by injection of 7  $\mu\text{L}$  mixed contaminated solution and a predetermined amount of persulfate solution. Finally, a predetermined amount of water was added via a syringe to make sure the reaction bottle filled with no air bubbles. All the reaction bottles were shaken continuously on a ZWY-240 thermostatic reciprocating shaker at 100 r/min. At each time interval, 50  $\mu\text{L}$  sample was collected via a syringe from each reaction bottle for persulfate analysis and 50  $\mu\text{L}$  sample was collected with methanol addition for organic compounds analysis. All experiments were conducted in duplicate. Control tests in the absence of persulfate were also carried out.

**2.3. Analysis.** Persulfate anion concentration was determined using a spectrophotometric method with potassium iodide [17]. The organic compounds (TCE, DCE, TCA, and DCA) were quantified using HP7890A gas chromatography equipped with a column HP-5MS (30 m  $\times$  0.25 mm  $\times$  0.25  $\mu\text{m}$ ) capillary column.

### 3. Results and Discussion

**3.1. Influence of Persulfate Dosage.** The depletion of chlorinated organic solvents by activated persulfate at 30°C was illustrated in Figure 1. The low TCA removal was obtained at the persulfate concentration of 20, 40, or 60 g/L. The high removal was up to 79.5%, 74.0%, 69.7%, and 54.8% of TCE, cis-1,2-DCE, 1,2-DCA, and TCA, respectively, while the persulfate concentration of 60 g/L was carried out. The phenomenon showed that chlorinated ethenes (TCE and cis-1,2-DCE) were more easily removed than chlorinated ethanes (TCA and 1,2-DCA). Chlorinated organic solvents removal was increased as persulfate concentration increased (shown in Figure 1(d)), but meanwhile, more persulfate could

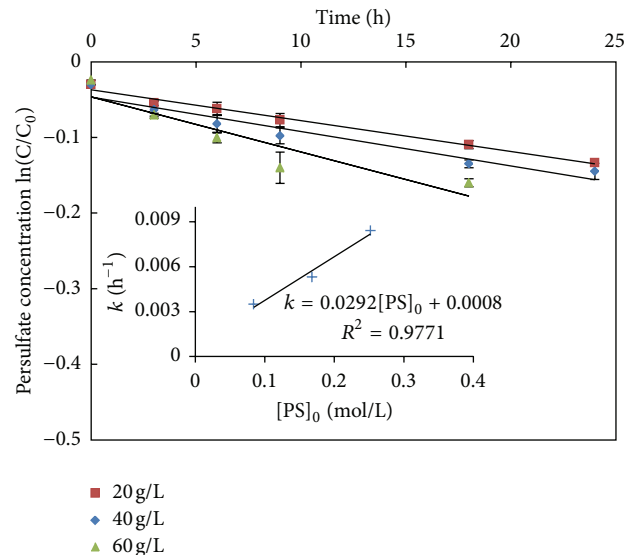


FIGURE 2: The decomposition of persulfate in the reactive system.

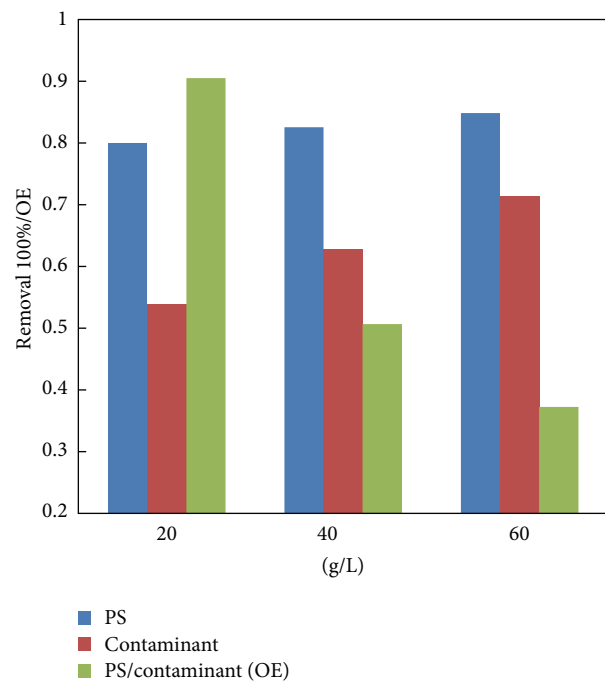


FIGURE 3: The decomposition of persulfate and contaminants after 72 h reaction time and the oxidant efficiency in the reactive system.

be decomposed (shown in Figure 2). The semilogarithmic graphs of  $[\text{PS}]/[\text{PS}]_0$  under different initial persulfate concentration as a function of reaction time were shown in Figure 2. Results demonstrated that the depletion rate was pseudo-first-order with respect to the initial persulfate concentration, and a similar result was described by Deng et al. [9]. For a given  $[\text{PS}]_0$ , the depletion rate constant  $k_{ps}$  decreased from 0.0035 to 0.0084  $\text{h}^{-1}$  with increasing initial persulfate concentration ( $[\text{PS}]_0$ ) from 20 to 60 g/L. As shown in the

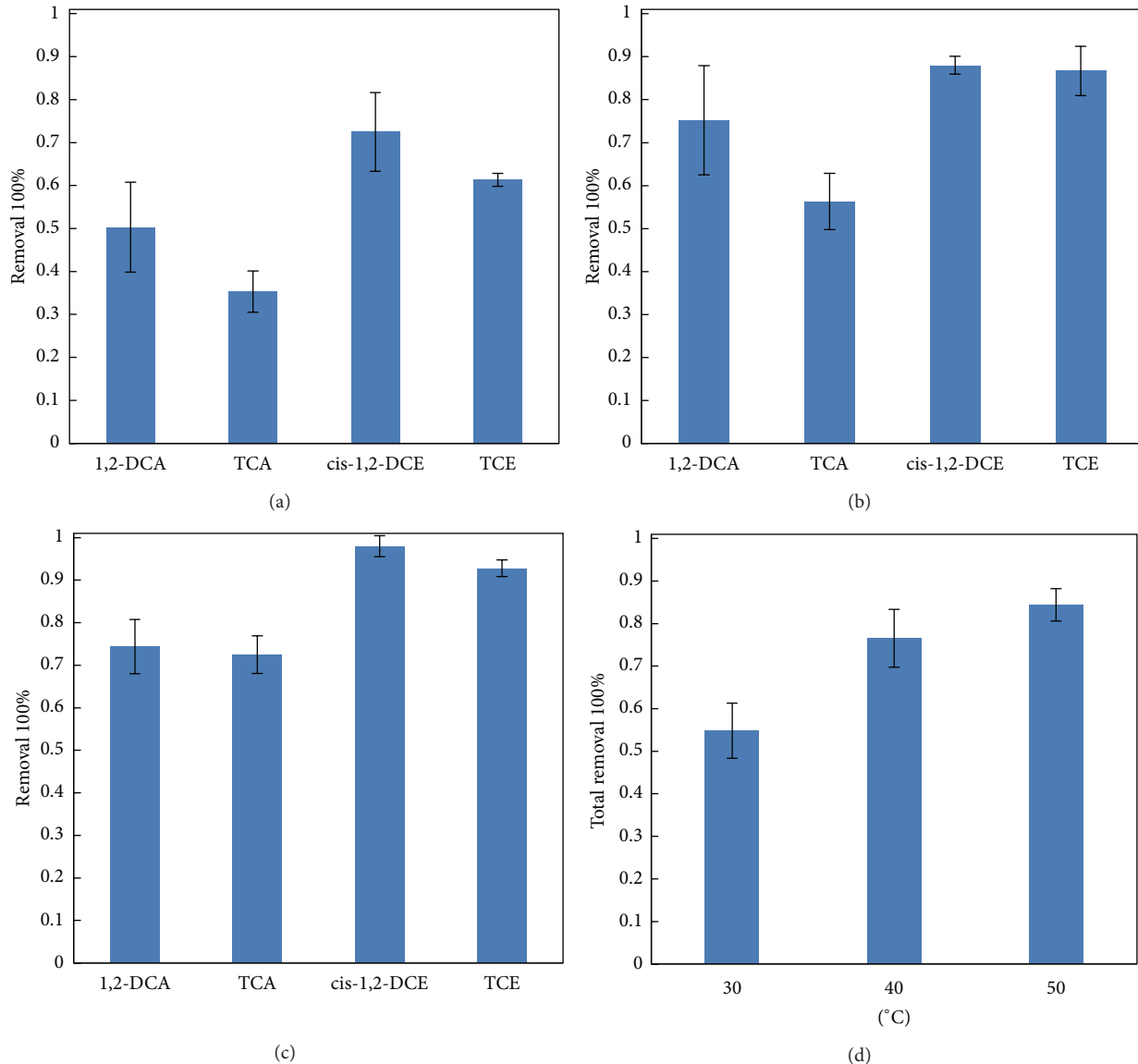


FIGURE 4: The depletion of chlorinated organic solvents by activated persulfate at different temperatures: (a) 30°C, (b) 40°C, and (c) 50°C after 72 h reaction time.

insert image of Figure 2, the depletion rate constant exhibits a linear trend ( $k_{ps} = 0.0292 [PS]_0 + 0.0008$ ,  $R^2 = 0.9771$ ). Therefore, the test with increasing persulfate dosage resulted in more decomposed persulfate. Moreover, the test with 20 g/L persulfate concentration resulted in the highest OE value (the oxidant efficiency (mmol of contaminant depletion per g of persulfate decomposition)) [18], shown in Figure 3. Thus, the persulfate dosage of 20 g/L was economically suitable for chlorinated organic solvents removal.

**3.2. Influence of Temperature.** The depletion of chlorinated solvents by thermal activated persulfate at different temperatures was illustrated in Figure 4. Results showed that cis-1,2-DCE obtained the highest removal by activated persulfate, followed by TCE, 1,2-DCA, and TCA at 30°C, 40°C, or 50°C.

The test with 30°C resulted in the low 1,2-DCA, TCA, cis-1,2-DCE, and TCE removal of 50.3%, 35.3%, 72.5%, and 61.3%, respectively. Compared with TCA and TCE, 1,2-DCA and cis-1,2-DCE obtained higher removal which related to the active molecular structure. The highest TCE, cis-1,2-DCE, 1,2-DCA, and TCA removal was up to 79.5%, 74.0%, 69.7%, and 54.8%, respectively, while the test with temperature 50°C was carried out. In general, the depletion of chlorinated solvents was increased with increasing temperature. First, the increasing temperature resulted in higher activation energy, which is in favor of generating the significant oxidant ( $\text{SO}_4^{2-}\bullet$ ). Second, the high temperature can accelerate the reaction of chlorinated organic solvents with persulfate. Moreover, heat can also accelerate desorption from soil phase to aqueous phase, which contributes to the further destruction of chlorinated organic solvents.

## 4. Conclusion

In this study, heat-activated persulfate appeared to be the most effective oxidant for treatment of chlorinated organic solvents. Chlorinated organic solvents removal was increased as persulfate concentration increased. The persulfate dosage of 20 g/L with the highest OE (oxidant efficiency) value was economically suitable for chlorinated organic solvents removal. The increasing temperature contributed to the increasing depletion of chlorinated organic solvents. Chlorinated ethenes (TCE and cis-1,2-DCE) were more easily removed than chlorinated ethanes (TCA and 1,2-DCA). Moreover, the persulfate depletion followed the pseudo-first-order reaction kinetics ( $k_{ps} = 0.0292 [PS]_0 + 0.0008$ ,  $R^2 = 0.9771$ ).

## Conflict of Interests

The authors declare that there is no conflict of interests regarding the publication of this paper.

## Acknowledgment

The present work was funded by National Natural Science Foundation of China (Grant no. 41302182).

## References

- [1] K. R. Weeks, C. J. Bruell, and N. R. Mohanty, "Use of Fenton's reagent for the degradation of TCE in aqueous systems and soil slurries," *Soil and Sediment Contamination*, vol. 9, no. 4, pp. 331–345, 2000.
- [2] X. G. Gu, S. G. Lu, L. Li et al., "Oxidation of 1,1,1-trichloroethane stimulated by thermally activated persulfate," *Industrial and Engineering Chemistry Research*, vol. 50, no. 19, pp. 11029–11036, 2011.
- [3] X. Gu, S. Lu, Z. Qiu et al., "Comparison of photodegradation performance of 1,1,1-trichloroethane in aqueous solution with the addition of  $H_2O_2$  or  $S_2O_8^{2-}$  oxidants," *Industrial and Engineering Chemistry Research*, vol. 51, no. 21, pp. 7196–7204, 2012.
- [4] A. Tsitonaki, B. Petri, M. Crimi, H. Mosbk, R. L. Siegrist, and P. L. Bjerg, "In situ chemical oxidation of contaminated soil and groundwater using persulfate: a review," *Critical Reviews in Environmental Science and Technology*, vol. 40, no. 1, pp. 55–91, 2010.
- [5] C. Liang, Z.-S. Wang, and C. J. Bruell, "Influence of pH on persulfate oxidation of TCE at ambient temperatures," *Chemosphere*, vol. 66, no. 1, pp. 106–113, 2007.
- [6] C. Liang, Z.-S. Wang, and N. Mohanty, "Influences of carbonate and chloride ions on persulfate oxidation of trichloroethylene at 20°C," *Science of the Total Environment*, vol. 370, no. 2–3, pp. 271–277, 2006.
- [7] S. Bougie and J.-S. Dubé, "Oxidation of the isomers of dichlorobenzene with the aid of thermally activated sodium persulfate," *Journal of Environmental Engineering and Science*, vol. 6, no. 4, pp. 397–407, 2007.
- [8] V. C. Mora, J. A. Rosso, D. O. Martíre, and M. C. Gonzalez, "Phenol depletion by thermally activated peroxydisulfate at 70°C," *Chemosphere*, vol. 84, no. 9, pp. 1270–1275, 2011.
- [9] J. Deng, Y. Shao, N. Gao, Y. Deng, S. Zhou, and X. Hu, "Thermally activated persulfate (TAP) oxidation of antiepileptic drug carbamazepine in water," *Chemical Engineering Journal*, vol. 228, pp. 765–771, 2013.
- [10] G. P. Anipsitakis and D. D. Dionysiou, "Radical generation by the interaction of transition metals with common oxidants," *Environmental Science and Technology*, vol. 38, no. 13, pp. 3705–3712, 2004.
- [11] D. Y. S. Yan and I. M. C. Lo, "Removal effectiveness and mechanisms of naphthalene and heavy metals from artificially contaminated soil by iron chelate-activated persulfate," *Environmental Pollution*, vol. 178, pp. 15–22, 2013.
- [12] Y. Leng, W. Guo, X. Shi et al., "Degradation of Rhodamine B by persulfate activated with  $Fe_3O_4$ : effect of polyhydroquinone serving as an electron shuttle," *Chemical Engineering Journal*, vol. 240, pp. 338–343, 2014.
- [13] Y.-T. Lin, C. Liang, and J.-H. Chen, "Feasibility study of ultraviolet activated persulfate oxidation of phenol," *Chemosphere*, vol. 82, no. 8, pp. 1168–1172, 2011.
- [14] R. E. Huie, C. L. Clifton, and P. Neta, "Electron transfer reaction rates and equilibria of the carbonate and sulfate radical anions," *International Journal of Radiation Applications and Instrumentation C: Radiation Physics and Chemistry*, vol. 38, no. 5, pp. 477–481, 1991.
- [15] K. Li, M. I. Stefan, and J. C. Crittenden, "Trichloroethene degradation by UV/ $H_2O_2$  advanced oxidation process: product study and kinetic modeling," *Environmental Science & Technology*, vol. 41, no. 5, pp. 1696–1703, 2007.
- [16] C. Liang and H.-W. Su, "Identification of sulfate and hydroxyl radicals in thermally activated persulfate," *Industrial & Engineering Chemistry Research*, vol. 48, no. 11, pp. 5558–5562, 2009.
- [17] C. Liang, C.-F. Huang, N. Mohanty, and R. M. Kurakalva, "A rapid spectrophotometric determination of persulfate anion in ISCO," *Chemosphere*, vol. 73, no. 9, pp. 1540–1543, 2008.
- [18] L. R. Bennedsen, J. Muff, and E. G. Søgaard, "Influence of chloride and carbonates on the reactivity of activated persulfate," *Chemosphere*, vol. 86, no. 11, pp. 1092–1097, 2012.

## Research Article

# Microstructural and Mössbauer Spectroscopy Studies of $\text{Mg}_{1-x}\text{Zn}_x\text{Fe}_2\text{O}_4$ ( $x = 0.5, 0.7$ ) Nanoparticles

Jinpei Lin,<sup>1</sup> Yun He,<sup>1</sup> Qing Lin,<sup>1,2</sup> Ruijun Wang,<sup>2</sup> and Henian Chen<sup>2</sup>

<sup>1</sup> College of Physics and Technology, Guangxi Normal University, Guilin 541004, China

<sup>2</sup> Department of Information Technology, Hainan Medical College, Haikou 571101, China

Correspondence should be addressed to Qing Lin; [hy@gxnu.edu.cn](mailto:hy@gxnu.edu.cn)

Received 9 June 2014; Accepted 11 July 2014; Published 24 July 2014

Academic Editor: Tifeng Jiao

Copyright © 2014 Jinpei Lin et al. This is an open access article distributed under the Creative Commons Attribution License, which permits unrestricted use, distribution, and reproduction in any medium, provided the original work is properly cited.

Zinc substituted magnesium ferrite  $\text{Mg}_{1-x}\text{Zn}_x\text{Fe}_2\text{O}_4$  ( $x = 0.5, 0.7$ ) powders have been prepared by a sol-gel autocombustion method. XRD patterns show that the specimens with  $x = 0.5$  and  $0.7$  exhibit single-phase spinel structure, and more content of Zn in specimens is favorable for the synthesis of pure Mg-Zn ferrites. Room temperature Mössbauer spectra of  $\text{Mg}_{1-x}\text{Zn}_x\text{Fe}_2\text{O}_4$  annealed at  $800^\circ\text{C}$  display transition from ferrimagnetic behavior to super paramagnetic behavior with increase in zinc concentration. The Mössbauer spectra of  $\text{Mg}_{0.5}\text{Zn}_{0.5}\text{Fe}_2\text{O}_4$  annealed at different temperatures display the magnetic phase change of the ferrite particles.

## 1. Introduction

$\text{MgFe}_2\text{O}_4$  is regarded as an important candidate of the spinel ferrite family. Nanocrystalline Mg ferrite shows more enhanced magnetization than its crystalline counterpart and has been found to exhibit some unusual magnetic properties, such as super paramagnetism and a noncollinear ordering of the magnetic moments of  $\text{Fe}^{3+}$  ions, known as spin canting [1]. If the  $\text{MgFe}_2\text{O}_4$  structure was completely inverted, its magnet moment would be zero because the magnetic moment of  $\text{Mg}^{2+}$  ion is zero. Manjurul Haque et al. [2] studied saturation of  $\text{Zn}^{2+}$  substitution on the magnetic properties of  $\text{Mg}_{1-x}\text{Zn}_x\text{Fe}_2\text{O}_4$  ferrites. Saturation magnetization and magnetic moment are observed to increase up to  $x = 0.4$  and thereafter decrease due to the spin canting in B-sites. Similar results of saturation magnetization's variation should be reported in the other literature [3, 4]. In this paper, ferrite  $\text{Mg}_{1-x}\text{Zn}_x\text{Fe}_2\text{O}_4$  ( $x = 0.5, 0.7$ ) powders were prepared by a sol-gel autocombustion method. The aim of this study is to investigate variation structural and magnetic properties of magnesium ferrite powders by partial replacement of nonmagnetic zinc cations.

## 2. Experimental

2.1. Sample Preparation. Zinc substituted magnesium ferrite  $\text{Mg}_{1-x}\text{Zn}_x\text{Fe}_2\text{O}_4$  ( $x = 0.5, 0.7$ ) powders were prepared

by a sol-gel autocombustion method. The analytical grade  $\text{Mg}(\text{NO}_3)_2 \cdot 6\text{H}_2\text{O}$ ,  $\text{Zn}(\text{NO}_3)_2 \cdot 6\text{H}_2\text{O}$ ,  $\text{Fe}(\text{NO}_3)_3 \cdot 9\text{H}_2\text{O}$ , citric acid ( $\text{C}_6\text{H}_8\text{O}_7 \cdot \text{H}_2\text{O}$ ), and ammonia ( $\text{NH}_3 \cdot \text{H}_2\text{O}$ ) were used as raw materials. The molar ratio of metal nitrates to citric acid was taken as 1:1. The metal nitrates and citric acid were dissolved into deionized water to form solution, respectively. The pH value of metal nitrates solution was changed from 7 to 9 by adding ammonia. And then, the mixed solution was maintained at  $80^\circ\text{C}$  in a thermostat water bath under constant stirring to transform into a dried gel. Citric acid was dropped continually in the process of heating. The gel were dried at  $120^\circ\text{C}$  in a dry-oven for 2 h, being ignited in air at room temperature, the dried gel burnt in a self-propagating combustion way to form loose powder. The powder was grounded and annealed.

2.2. Characterization. The crystalline structure was investigated by X-ray diffraction (D/max-2500 V/PC, Rigaku) with  $\text{Cu K}_\alpha$  radiation ( $\lambda = 0.15405 \text{ nm}$ ). The micrographs were obtained by scanning electron microscopy (NoVa Nano SEM 430). The Mössbauer spectrum was performed at room temperature, using a conventional Mössbauer spectrometer (American Fast Com Tec PC-mossII), in constant acceleration mode. The  $\gamma$ -rays were provided by a  $^{57}\text{Co}$  source in a rhodium matrix.

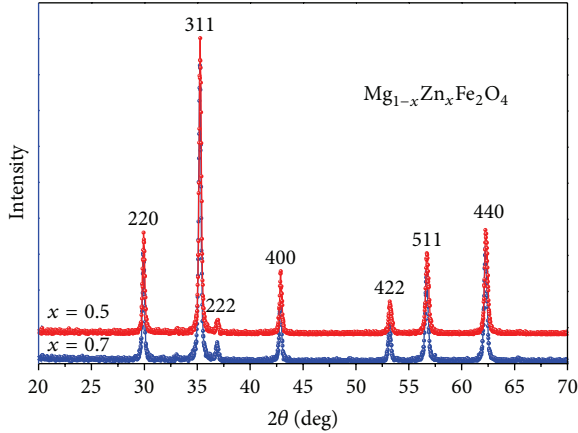


FIGURE 1: Room temperature X-ray diffraction patterns of  $\text{Mg}_{1-x}\text{Zn}_x\text{Fe}_2\text{O}_4$  annealed at  $800^\circ\text{C}$ .

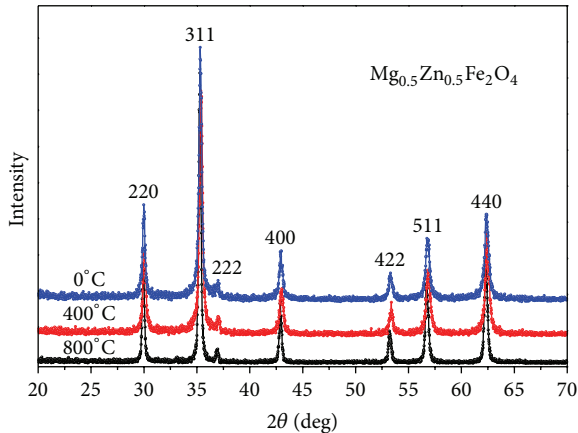


FIGURE 2: X-ray diffraction patterns of  $\text{Mg}_{0.5}\text{Zn}_{0.5}\text{Fe}_2\text{O}_4$  annealed at different temperatures.

### 3. Results and Discussion

**3.1. XRD Patterns Analysis.** Figure 1 shows the XRD patterns of  $\text{Mg}_{1-x}\text{Zn}_x\text{Fe}_2\text{O}_4$  ( $x = 0.5, 0.7$ ) ferrites calcined at  $800^\circ\text{C}$  for 3 h. It is clear that the specimens with  $x = 0.5$  and  $0.7$  exhibit single-phase spinel structure. Obviously, increasing the content of Zn is favorable for the synthesis of pure Mg-Zn ferrites. Similar results also are reported in the other literature [4]. Table 1 indicates that the X-ray density increases with  $\text{Zn}^{2+}$  concentration for all samples. The increase in lattice parameter is probably due to replacement of smaller  $\text{Mg}^{2+}$  ions by larger  $\text{Zn}^{2+}$  ions [5, 6].

The X-ray patterns of  $\text{Mg}_{0.5}\text{Zn}_{0.5}\text{Fe}_2\text{O}_4$  annealed at different temperatures are shown in Figure 2. All the samples are the single-phase cubic spinel structure. No additional phase was detected. The lattice parameter showed changes for all the samples from Table 2. Average crystallite size of  $\text{Mg}_{0.5}\text{Zn}_{0.5}\text{Fe}_2\text{O}_4$  tends to increase with the increase of the calcining temperature, due to the coalescence of small grains through grain boundary diffusion [7]. In other people's work [8], the diffraction peaks of  $\text{Cu}_{0.7}\text{Mg}_{0.3}\text{Fe}_2\text{O}_4$  annealed at low temperature are not very sharp, but in our result the diffraction peaks of  $\text{Mg}_{0.5}\text{Zn}_{0.5}\text{Fe}_2\text{O}_4$  without burning are very

sharp. The result suggests that magnesium substituted cobalt ferrite powders prepared by a sol-gel autocombustion method still have a good crystallinity without calcining.

**3.2. Structures and Grain Sizes.** The SEM micrographs of  $\text{Mg}_{1-x}\text{Zn}_x\text{Fe}_2\text{O}_4$  ( $x = 0.5$ ) annealed  $800^\circ\text{C}$  for 3 h are shown in Figure 3. It can be observed the distribution of grains with almost uniform size, well crystallized for  $\text{Mg}_{0.5}\text{Zn}_{0.5}\text{Fe}_2\text{O}_4$ . Some particles are agglomerated due to the presence of magnetic interactions among particles [9].

Figure 4 shows the histogram of grain size distribution of  $\text{Mg}_{1-x}\text{Zn}_x\text{Fe}_2\text{O}_4$  ( $x = 0.5$ ) ferrites. The average grain size of  $\text{Mg}_{0.5}\text{Zn}_{0.5}\text{Fe}_2\text{O}_4$  estimated by a statistical method is approximately 90.74 nm, respectively. It shows that the ferrite powers are nanoparticles, and the average grain size decreases with the increase of Zn content. The average grain size is slightly larger than the average crystallite size determined by XRD. This shows that every particle is formed by a number of crystallites [10, 11].

**3.3. Mössbauer Spectroscopy.** Mössbauer absorption spectra measured at room temperature for  $\text{Mg}_{0.5}\text{Zn}_{0.5}\text{Fe}_2\text{O}_4$  powders

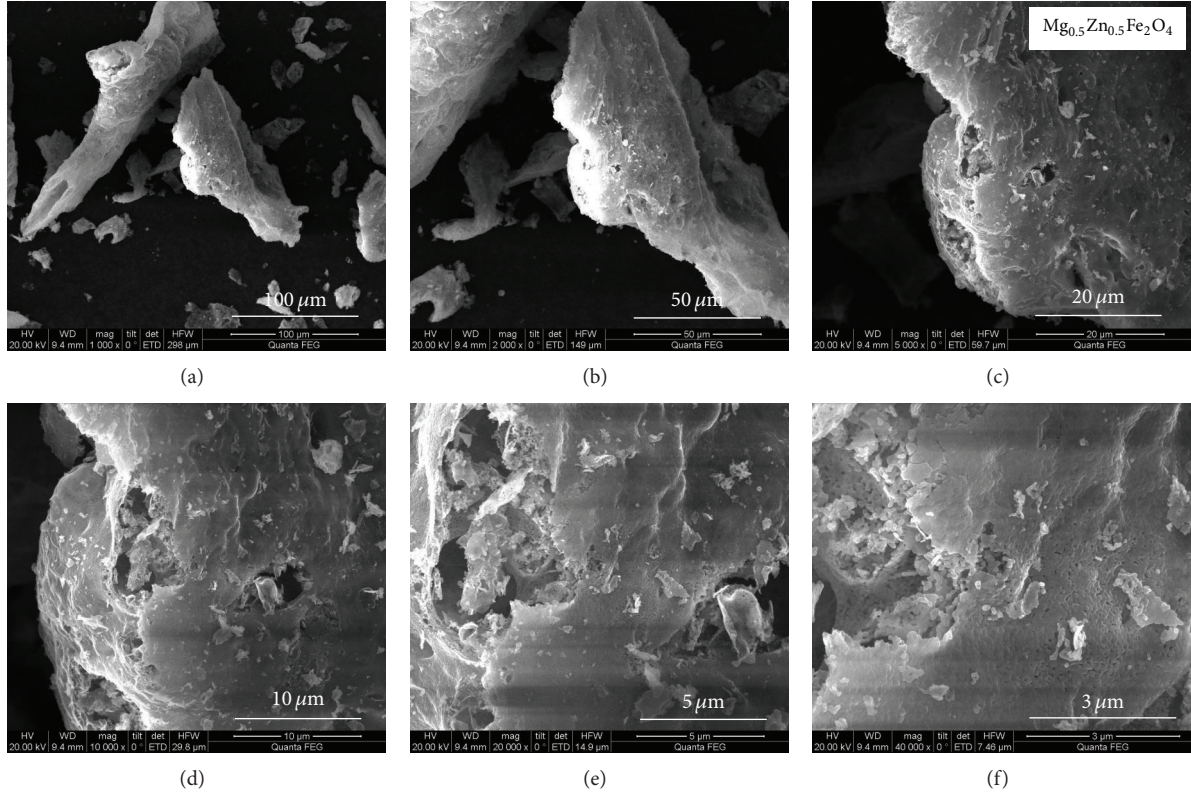


FIGURE 3: SEM micrographs depict  $\text{Mg}_{0.5}\text{Zn}_{0.5}\text{Fe}_2\text{O}_4$  ( $x = 0.5$ ) ferrites with diameters of  $100 \mu\text{m}$  (a),  $50 \mu\text{m}$  (b),  $20 \mu\text{m}$  (c),  $10 \mu\text{m}$  (d),  $5 \mu\text{m}$  (e), and  $3 \mu\text{m}$  (f).

annealed at different temperatures are shown in Figure 5. All samples have been analyzed using Mösswin 3.0 program.

Spectra of the samples without calcining and annealed at  $400^\circ\text{C}$  are fitted into a single sextet and a central paramagnetic doublet, and the sample annealed at  $800^\circ\text{C}$  was analyzed to only a single sextet. The Mössbauer spectra of  $\text{Mg}_{0.5}\text{Zn}_{0.5}\text{Fe}_2\text{O}_4$  sample show a paramagnetic doublet, which is due to the super paramagnetic relaxation, in other words, some particles are a single domain. Table 3 shows that the Mössbauer absorption area of paramagnetic doublet decreases with the increase of the annealed temperature; it is attributed to the change in particle size as a function of heat treatment [12]. Therefore the Mössbauer spectra of  $\text{Mg}_{0.5}\text{Zn}_{0.5}\text{Fe}_2\text{O}_4$  annealed at different temperatures display the magnetic phase change of the ferrite particles.

#### 4. Conclusion

The analysis of XRD patterns for  $\text{Mg}_{1-x}\text{Zn}_x\text{Fe}_2\text{O}_4$  annealed at  $800^\circ\text{C}$  shows that the specimens with  $x = 0.5$  and  $0.7$  exhibit single-phase spinel structure, and more content of Zn in specimens is favorable for the synthesis of pure Mg-Zn ferrites. The XRD patterns of  $\text{Mg}_{0.5}\text{Zn}_{0.5}\text{Fe}_2\text{O}_4$  annealed at different temperatures indicate that all  $\text{Mg}_{1-x}\text{Zn}_x\text{Fe}_2\text{O}_4$  ferrite powders prepared by a sol-gel autocombustion method have good crystallinity. SEM results indicate the distribution of grains and morphology of the samples. Room temperature

TABLE 1: Lattice parameters, average crystallite size, and X-ray densities date of  $\text{Mg}_{1-x}\text{Zn}_x\text{Fe}_2\text{O}_4$  annealed at  $800^\circ\text{C}$ .

Sample (X)	Lattice parameter (Å)	Average crystallite size (Å)	Density (g·cm <sup>-3</sup> )
0.5	8.43133	377	4.8879
0.7	8.43576	385	5.0620

TABLE 2: Lattice parameters, average crystallite size, and X-ray densities date of  $\text{Mg}_{0.5}\text{Zn}_{0.5}\text{Fe}_2\text{O}_4$  annealed at different temperatures.

$\text{Mg}_{0.5}\text{Zn}_{0.5}\text{Fe}_2\text{O}_4$	Lattice parameter (Å)	Average crystallite size (Å)	Density (g·cm <sup>-3</sup> )
$0^\circ\text{C}$	8.42130	298	4.9054
$400^\circ\text{C}$	8.41157	274	4.9224
$800^\circ\text{C}$	8.43133	377	4.8879

Mössbauer spectra of  $\text{Mg}_{1-x}\text{Zn}_x\text{Fe}_2\text{O}_4$  annealed at  $800^\circ\text{C}$  display transition from ferrimagnetic behavior to super paramagnetic behavior with increase in zinc concentration. Furthermore, the Mössbauer spectra of  $\text{Mg}_{0.5}\text{Zn}_{0.5}\text{Fe}_2\text{O}_4$  annealed at different temperatures display the magnetic phase change of the ferrite particles.

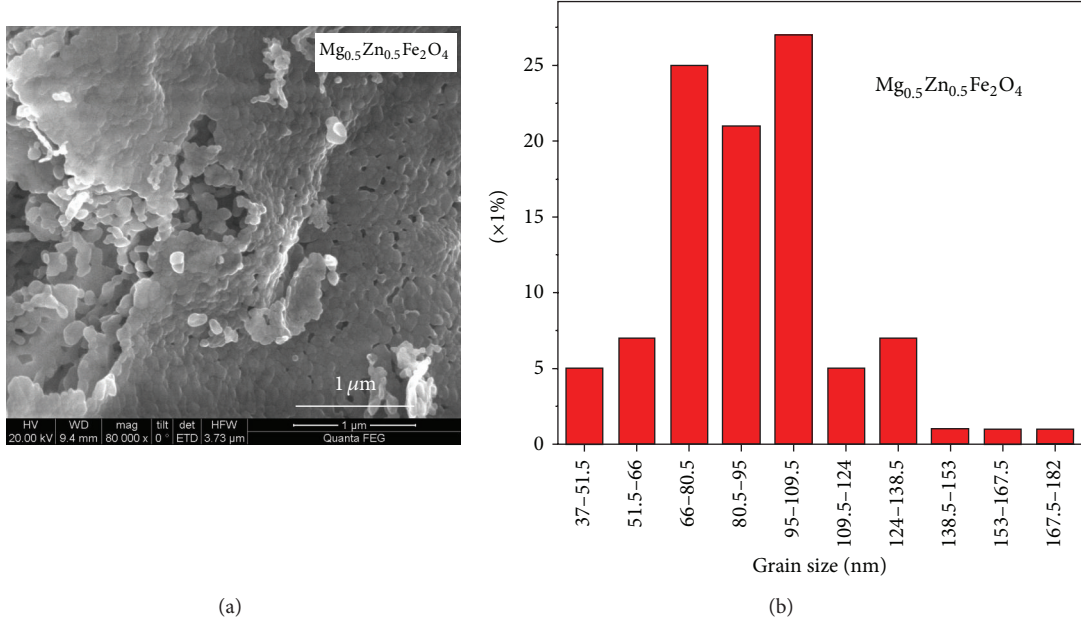


FIGURE 4: Histogram of grain size distribution of  $\text{Mg}_{0.5}\text{Zn}_{0.5}\text{Fe}_2\text{O}_4$  annealed at 800°C.

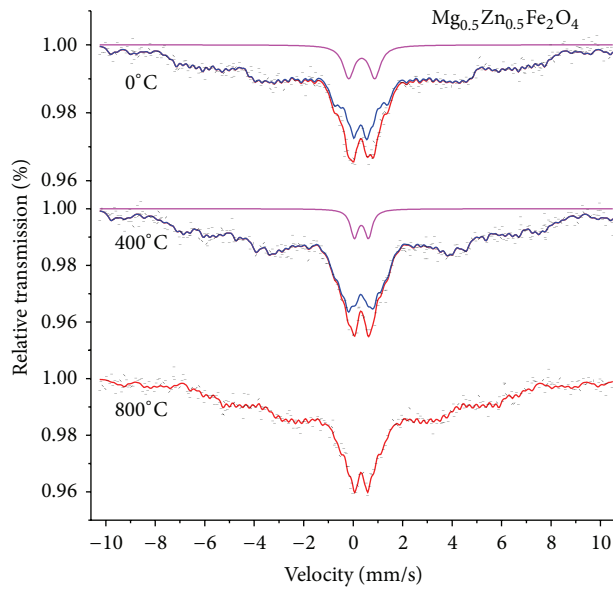


FIGURE 5: Room temperature Mössbauer spectra of  $\text{Mg}_{0.5}\text{Zn}_{0.5}\text{Fe}_2\text{O}_4$  annealed at different temperatures.

TABLE 3: Mössbauer parameters of isomer shift (IS), quadrupole splitting (QS), magnetic hyperfine field ( $H$ ), line width ( $\Gamma$ ), and absorption area ( $A_0$ ) for  $\text{Mg}_{0.5}\text{Zn}_{0.5}\text{Fe}_2\text{O}_4$  annealed at different temperatures.

$\text{Mg}_{0.5}\text{Zn}_{0.5}\text{Fe}_2\text{O}_4$	Component	IS (mm/s)	QS (mm/s)	$H$ (T)	$\Gamma$ (mm/s)	$A_0$ (mm/s)
$0^\circ\text{C}$	Sextet (B)	0.313	-0.027	28.556	0.288	91.8
	Double	0.348	1.05	—	0.547	8.2
$400^\circ\text{C}$	Sextet (B)	0.306	0.032	28.503	0.322	95.6
	Double	0.333	0.570	—	0.376	4.4
$800^\circ\text{C}$	Sextet (B)	0.318	0.005	24.234	0.268	100

## Conflict of Interests

The authors declare that there is no conflict of interests regarding the publication of this paper.

## Acknowledgments

This work was financially supported by the National Natural Science Foundation of China (nos. 11364004, 11164002); Innovation Project of Guangxi Graduate Education under Grant (no. 2010106020702 M47).

## References

- [1] M. Sinha, H. Dutta, and S. K. Pradhan, "Phase stability of nanocrystalline Mg-Zn ferrite at elevated temperatures," *Japanese Journal of Applied Physics*, vol. 47, no. 11, pp. 8667–8672, 2008.
- [2] M. Manjurul Haque, M. Huq, and M. A. Hakim, "Effect of Zn<sup>2+</sup> substitution on the magnetic properties of Mg<sub>1-x</sub>Zn<sub>x</sub>Fe<sub>2</sub>O<sub>4</sub> ferrites," *Physica B*, vol. 404, no. 21, pp. 3915–3921, 2009.
- [3] C. Choodamani, G. P. Nagabhushana, S. Ashoka, B. Daruka Prasad, B. Rudraswamy, and G. T. Chandrappa, "Structural and magnetic studies of Mg<sub>(1-x)</sub>Zn<sub>x</sub>Fe<sub>2</sub>O<sub>4</sub> nanoparticles prepared by a solution combustion method," *Journal of Alloys and Compounds*, vol. 578, pp. 103–109, 2013.
- [4] A. Xia, S. Liu, C. Jin, L. Chen, and Y. Lv, "Hydrothermal Mg<sub>1-x</sub>Zn<sub>x</sub>Fe<sub>2</sub>O<sub>4</sub> spinel ferrites: phase formation and mechanism of saturation magnetization," *Materials Letters*, vol. 105, pp. 199–201, 2013.
- [5] K. Verma, A. Kumar, and D. Varshney, "Dielectric relaxation behavior of A<sub>x</sub>Co<sub>1-x</sub>Fe<sub>2</sub>O<sub>4</sub> (A = Zn, Mg) mixed ferrites," *Journal of Alloys and Compounds*, vol. 526, pp. 91–97, 2012.
- [6] H. Mohseni, H. Shokrollahi, I. Sharifi, and K. Gheisari, "Magnetic and structural studies of the Mn-doped Mg-Zn ferrite nanoparticles synthesized by the glycine nitrate process," *Journal of Magnetism and Magnetic Materials*, vol. 324, no. 22, pp. 3741–3747, 2012.
- [7] C. Choodamani, G. P. Nagabhushana, B. Rudraswamy, and G. T. Chandrappa, "Thermal effect on magnetic properties of Mg-Zn ferrite nanoparticles," *Materials Letters*, vol. 116, pp. 227–230, 2014.
- [8] M. A. Ahmed, H. H. Afify, I. K. El Zawawia, and A. A. Azab, "Novel structural and magnetic properties of Mg doped copper nanoferrites prepared by conventional and wet methods," *Journal of Magnetism and Magnetic Materials*, vol. 324, no. 14, pp. 2199–2204, 2012.
- [9] S. Rahman, K. Nadeem, M. Anis-Ur-Rehman, M. Mumtaz, S. Naeem, and I. Letofsky-Papst, "Structural and magnetic properties of ZnMg-ferrite nanoparticles prepared using the co-precipitation method," *Ceramics International*, vol. 39, no. 5, pp. 5235–5239, 2013.
- [10] S. Hajarpour, K. Gheisari, and A. Honarbakhsh Raouf, "Characterization of nanocrystalline Mg<sub>0.6</sub>Zn<sub>0.4</sub>Fe<sub>2</sub>O<sub>4</sub> soft ferrites synthesized by glycine-nitrate combustion process," *Journal of Magnetism and Magnetic Materials*, vol. 329, pp. 165–169, 2013.
- [11] L. Bih, M. Azrour, B. Manoun, M. P. F. Graça, and M. A. Valente, "Raman spectroscopy, X-Ray, SEM, and DTA analysis of alkali-phosphate glasses containing WO<sub>3</sub> and Nb<sub>2</sub>O<sub>5</sub>," *Journal of Spectroscopy*, vol. 1, no. 1, Article ID 123519, 2013.
- [12] T. K. Pathak, N. H. Vasoya, V. K. Lakhani, and K. B. Modi, "Structural and magnetic phase evolution study on needle-shaped nanoparticles of magnesium ferrite," *Ceramics International*, vol. 36, no. 1, pp. 275–281, 2010.

## Research Article

# Performance of a Novel Hydrophobic Mesoporous Material for High Temperature Catalytic Oxidation of Naphthalene

Guotao Zhao,<sup>1</sup> Zhenxiao Zhao,<sup>2</sup> Junliang Wu,<sup>1</sup> and Daiqi Ye<sup>1</sup>

<sup>1</sup> College of Environment and Energy, South China University of Technology, Guangzhou 510006, China

<sup>2</sup> School of Chemistry and Chemical Engineering, Guangxi University, Nanning 530004, China

Correspondence should be addressed to Daiqi Ye; cedqye@scut.edu.cn

Received 20 May 2014; Accepted 18 June 2014; Published 3 July 2014

Academic Editor: Qingrui Zhang

Copyright © 2014 Guotao Zhao et al. This is an open access article distributed under the Creative Commons Attribution License, which permits unrestricted use, distribution, and reproduction in any medium, provided the original work is properly cited.

A high surface area, hydrophobic mesoporous material, MFS, has been successfully synthesized by a hydrothermal synthesis method using a perfluorinated surfactant, SURFLON S-386, as the single template. N<sub>2</sub> adsorption and TEM were employed to characterize the pore structure and morphology of MFS. Static water adsorption test indicates that the hydrophobicity of MFS is significantly higher than that of MCM-41. XPS and Py-GC/MS analysis confirmed the existence of perfluoroalkyl groups in MFS which led to its high hydrophobicity. MFS was used as a support for CuO in experiments of catalytic combustion of naphthalene, where it showed a significant advantage over MCM-41 and ZSM-5. SEM was helpful in understanding why CuO-MFS performed so well in the catalytic combustion of naphthalene. Experimental results indicated that MFS was a suitable support for catalytic combustion of large molecular organic compounds, especially for some high temperature catalytic reactions when water vapor was present.

## 1. Introduction

In recent years, more and more efforts have been focused on the catalytic removal of VOC or PAHs in ambient air and industrial emissions [1, 2]. However, traditional catalyst carriers have pore sizes that are too small to be used effectively in the catalytic combustion of large molecular organic pollutants [3]. Recently, many researchers have studied the catalytic removal process of VOC and PAHs on various mesoporous materials (refers to the kind of aperture between 2 and 50 nm porous materials) [4–7]. However, the presence of H<sub>2</sub>O molecules still has significant negative impacts on the decomposition of VOCs under these conditions [8]. Therefore, a popular, near-term research goal has been to develop hydrophobic carrier materials that will reduce the negative impacts of H<sub>2</sub>O on catalytic combustion.

Currently, there are many methods for synthesizing hydrophobic mesoporous materials [9–12]. One of the most promising methods involves the use of fluorine-containing materials [13, 14]. If the method is optimized, the fluorine-containing groups are introduced onto the surface, even on the inner surfaces of the framework of the mesoporous materials, which enhances the hydrophobicity of the

material [15–17] because of strong electronegativity of the fluorine-containing groups.

This paper presents a new method for synthesizing mesoporous materials using the perfluorinated surfactant SURFLON S-386 (a polymeric perfluorocarboxylic acid) as the single template. The resulting mesoporous material (MFS) has a large surface area, high hydrophobicity, and excellent hydrothermal stability for use in the catalytic combustion of naphthalene.

## 2. Experimental

**2.1. Materials and Catalyst Preparation.** SURFLON S-386 (99%) was received from Asahi Glass Company, Japan. TEOS (98%) was received from J&K Scientific Company, China. The chemicals were used without additional purification.

The catalyst was prepared by mixing deionized water (120 mL) and SURFLON S-386 (0.8 g) in a 250 mL beaker. After stirring for 1 h at 40°C, a mixture of TEOS (10 g) and HCl (5 mL) was added drop by drop in a period of 30 min while stirring with a magnetic stirrer. After the mixture was added, the stirring was continuous for about 24 h. The mixture was then transferred into an autoclave and was

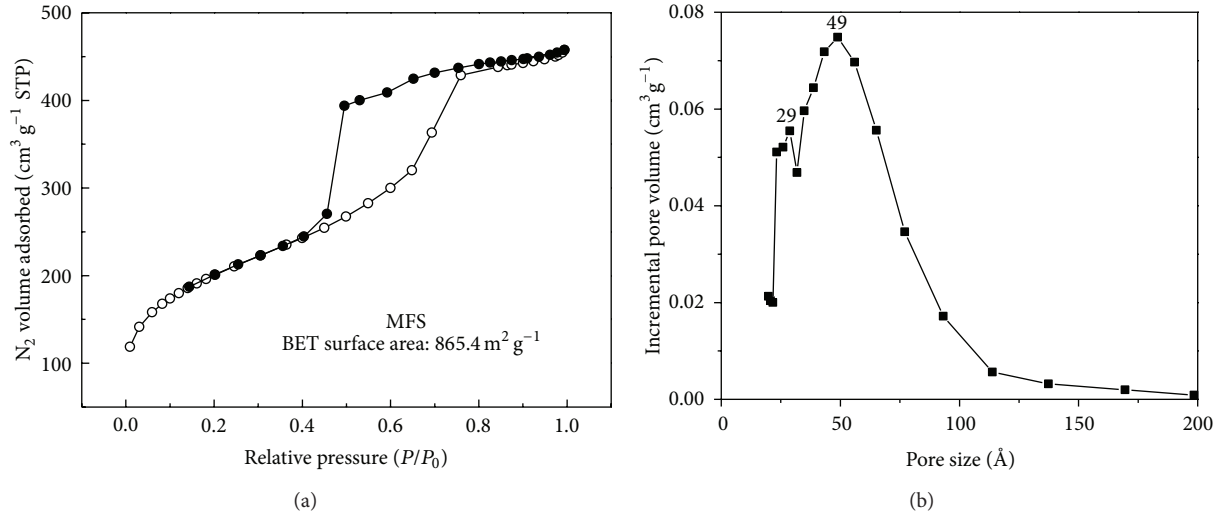


FIGURE 1: (a)  $N_2$  sorption isotherms of MFS 77 K and (b) pore size distribution in MFS as determined from the BJH model.  $P/P_0$  is the ratio of gas pressure ( $P$ ) to saturation pressure ( $P_0 = 101.3 \text{ kPa}$ ).

heated for 48 h at  $100^\circ\text{C}$ . The resulting solid was centrifuged, washed (with water and alcohol), and dried in an oven at  $100^\circ\text{C}$  for 12 h. The final mesoporous material was calcined at  $550^\circ\text{C}$  for 6 h with the average heating rate of  $1^\circ\text{C}/\text{min}$ . The resulting product was marked as MFS.

$\text{CuO}$  was loaded on the MFS via the impregnation method by using  $\text{Cu}(\text{NO}_3)_2 \cdot 3\text{H}_2\text{O}$  [18]. After evaporation and drying, the resulting solid material was calcined at  $500^\circ\text{C}$  for 4 h. After tabletting and screening through with 40~60 mesh different concentrations of the catalyst were prepared by using different amounts of  $\text{Cu}(\text{NO}_3)_2 \cdot 3\text{H}_2\text{O}$ . These catalysts were noted as  $\text{CuO-MFS}$ . The percentage of  $\text{CuO}$  ranged from 2 to 25%, expressed as the weight ratio of  $W_{\text{CuO}}/W_{\text{support}}$ .

**2.2. Hydrophobicity Test.** The hydrophobicities of the MFS samples were measured by the GBT6287-86 method (National Standards, China). The results obtained from the various materials were characterized by static adsorption rate.

**2.3. Catalyst Activity Test.** The catalytic activity test was performed with a continuous flow fixed-bed reactor with 8 mm ID, similar to that reported in the literature [19]. In each test run, 100 mg of catalyst was diluted with an appropriate amount of inert quartz beads (40~60 mesh) placed at the center of the reactor, above which a thermocouple was located to monitor the reaction temperatures. To create the stream containing naphthalene, a stream of pure dry air was passed through a U-shaped tube (contain naphthalene) at constant temperature ( $30^\circ\text{C}$ ) to produce a mixed gas containing a high concentration of naphthalene. The total flow rate was set at  $180 \text{ mL min}^{-1}$  with a concentration of 300 ppm naphthalene by adjusting the flow rate. The gas hourly space velocity (GHSV) in the tests was kept at  $120000 \text{ h}^{-1}$ .

An on-line gas chromatograph equipped with a FID detector was used to analyze the concentration of naphthalene in the inlet and outlet gas. Before each measurement,

the temperature of the catalytic bed was raised to  $200^\circ\text{C}$  and stabilized at that temperature until the concentration of naphthalene became constant. No conversion of naphthalene was observed at this temperature. Then the temperature of catalyst bed was raised at  $20^\circ\text{C}/\text{min}$  until the experimental temperature was reached. Then the export concentration of naphthalene could be analyzed.

**2.4. Materials Characterization.** The specific surface areas (SSAs) of the catalysts (0.1~0.3 g) were determined with the BET method using an ASAP 2020 Micropore System (Micromeritics, USA). A vacuum pretreatment with vacuum at  $300^\circ\text{C}$  for 2 h was followed by nitrogen adsorption at  $-196^\circ\text{C}$ . TEM (transmission electron microscopy) images were obtained using JEM-2010HR transmission electron microscope (Japan).

The elements and their valances were measured by XPS (XML Paper Specification) using VG Multilab 2000 spectrometer (Germany) equipped with a hemispherical electron analyzer and Mg Ka radiation source ( $h\nu = 1253.6 \text{ eV}$ ). All binding energies were referenced to the  $\text{C}_{1s}$  line at  $284.6 \text{ eV}$ , which provided an accuracy of  $\pm 0.48 \text{ eV}$  within full scanning of 0~1000 eV.

Py-GC/MS (pyrolysis-gas chromatography/mass spectrometry) analysis was carried out using a GC/MS-QP2010 PLUS pyrolysis gas chromatograph (Shimadzu, Japan) with a CDS (USA) cracker. SEM (scanning electron microscopy) images were obtained on a Philips FEI XL-30, operated with a 10 kV accelerating voltage after gold deposition.

### 3. Results and Discussion

#### 3.1. Samples Characterization

**3.1.1. Nitrogen Adsorption.** MFS sample was subjected to  $N_2$  adsorption studies [20]. The specific surface area was calculated according to the Brunauer-Emmett-Teller (BET)

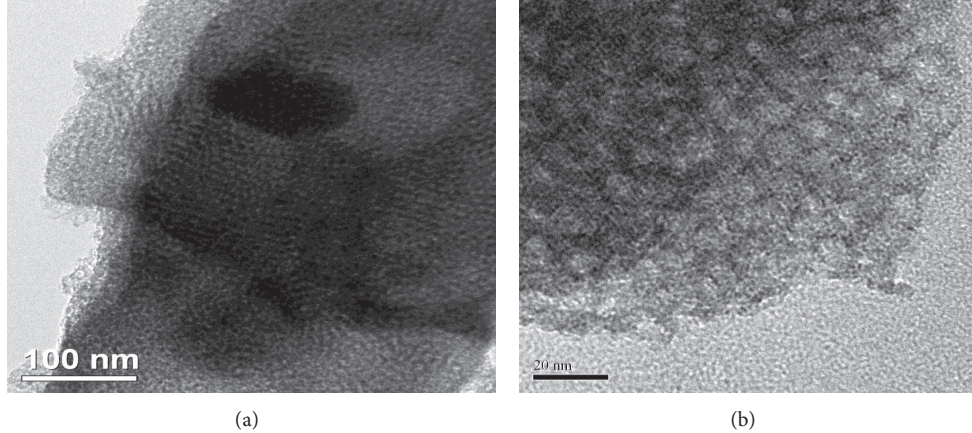
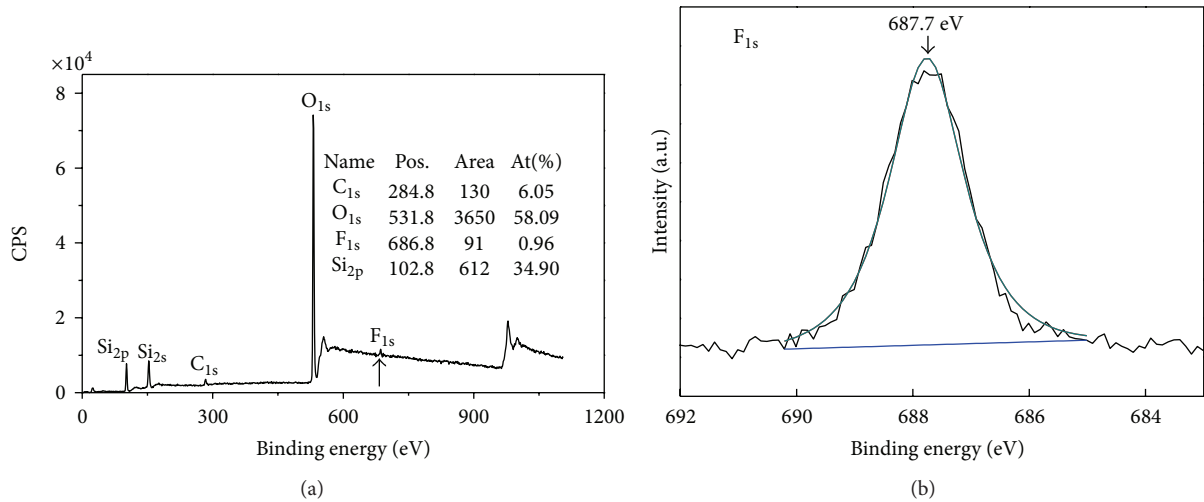


FIGURE 2: TEM ((a) and (b)) images of the synthesized MFS.

FIGURE 3: (a) XPS full spectra of MFS and (b) XPS spectra of F<sub>1s</sub> in MFS.

method and the average pore diameter was obtained according to the Barrett-Soyner-Halenda (BJH) method. A typical nitrogen adsorption isotherm is shown in Figure 1(a). Its BET surface area, Langmuir surface area, and pore volume were calculated to be  $865.4 \text{ m}^2 \text{ g}^{-1}$ ,  $1205.1 \text{ m}^2 \text{ g}^{-1}$ , and  $0.74 \text{ cm}^3 \text{ g}^{-1}$ , respectively. Its mesopore area and mesopore volume were  $928.0 \text{ m}^2 \text{ g}^{-1}$  and  $0.7 \text{ cm}^3 \text{ g}^{-1}$ . In BJH differential pore volume plot, two sharp peaks are observed at about 2.9 nm and 4.9 nm for the MFS (Figure 1(b)), indicating a very narrow pore size for this mesoporous material.

**3.1.2. Transmission Electron Microscopy (TEM).** Figures 2(a) and 2(b) show the TEM images of the MFS sample [20]. Some clear amorphous channel can be seen on the surface of the material. The light and dark stripes that are typical of mesoporous structures can also be observed in the MFS [16].

**3.1.3. XML Paper Specification (XPS).** Figure 3(a) shows the XPS full spectrum of MFS, which shows the electron energy states of five elements: Si<sub>2s</sub>, Si<sub>2p</sub>, C<sub>1s</sub>, O<sub>1s</sub>, and F<sub>1s</sub>, and content of fluoride element accounts for about 1% (At%).

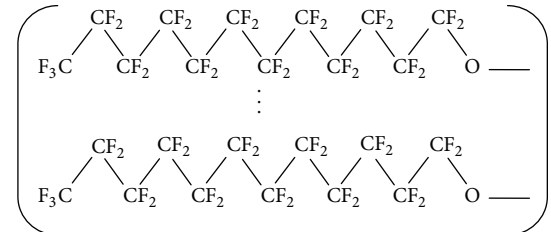


FIGURE 4: Molecular structure of SURFLON S-386.

Figure 3(b) shows the XPS spectrum of F<sub>1s</sub>. F species were detected centered around 687.7 eV and are attributed to the  $-\text{CF}_x$  bonds [21] which are related to the molecular structure of SURFLON S-386 (Figure 4). Therefore, it implies that a portion of the SURFLON S-386 fragments remain on the surface of MFS after calcination.

**3.1.4. Pyrolysis-Gas Chromatography/Mass Chromatogram (PY-GC/MS).** Pyrolysis-gas chromatography/mass spectrometry (Py-GC/MS) was employed to obtain structural

TABLE 1: Main pyrolytic products of MFS according to Py-GC/MS.

Number	R. time (min)	Compound (matching)	Molecular weight	Peak
1	1.575	Carbon dioxide	44	a
2	1.742	Propanone	58	b
3	1.950	1-Decene,3,3,4,4,5,5,6,6,7,7,8,8,9,9,10,10, 10-heptadecafluoro-	77	c
4	2.100	alpha-Methylfuran	82	—
5	2.308	2-Propanone	74	—
6	2.967	Propylene glycol	76	—
7	3.208	Succinaldehyde	86	—
8	3.892	Heptane	112	—
9	4.050	2-Cyclopenten-1-one	82	—
10	4.383	1-Decanol,3,3,4,4,5,5,6,6,7,7,8,8,9,9,10,10, 10-heptadecafluoro-	464	d

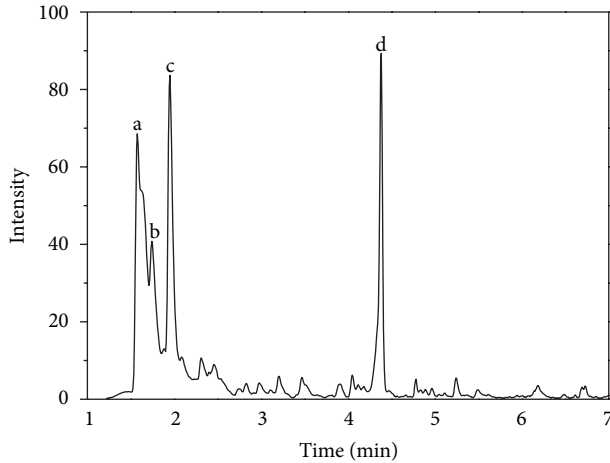


FIGURE 5: PY-GC/MS chromatogram of MFS.

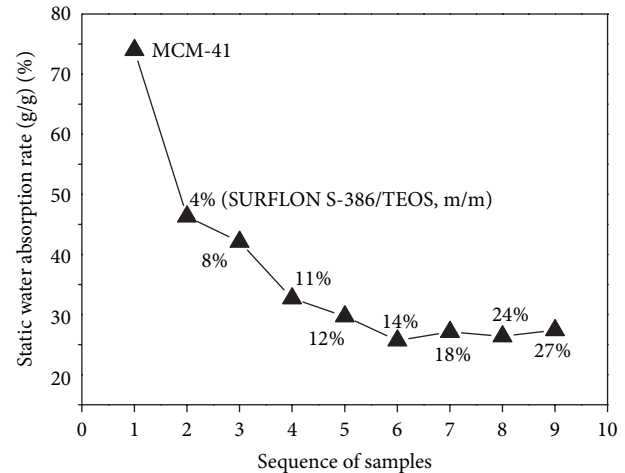


FIGURE 6: Adsorption of static water on MFSs and MCM-41 (100% humidity).

information about MFS. The analytical procedure used in this study is similar to that reported previously [22]. The pyrolysis temperature was set at 800°C and held for 10 s from room temperature, with an average heating rate of 20°C/ms. The main pyrolytic products identified are listed in Table 1, and main peaks of the chromatogram are shown in Figure 5. The peak at 1.575 min is attributed to CO<sub>2</sub>, a combustion product of organic matter at high temperatures. Peak c at 1.950 min is attributed to the fluorine-containing decene according to the MS database, which is likely the residue of the template SURFLON S-386. Peak b at 1.742 min and other peaks from 2.10–4.05 min are also ascribed to the fragments of the template or intermediate species generated under high temperature. Peak d at 4.383 min is attributed to the fluorine-containing decanol according to MS database, which can be regarded as a new combination of SURFLON S-386 fragments with silicon-hydroxyl on the MFS surface. These findings indicate that fluorine-containing species exist

on the MFS surface, which are a result of SURFLON S-386 fragments remaining on the surface of MFS after calcinations.

**3.2. Results of Hydrophobicity Test.** A series adsorption of static water tests was conducted to investigate the hydrophobic properties of MFSs and MCM-41. Various MFS samples were synthesized with different amounts of SURFLON S-386 (g<sub>SURFLON S-386</sub>/g<sub>TEOS</sub>, m/m) used during the process of synthesis. Different materials gave different static water adsorption rates as shown in Figure 6. Static water adsorption rate of MCM-41 is 74% (g<sub>water</sub>/g<sub>adsorbent</sub>, m/m), while the adsorption rate of MFS with 4% SURFLON S-386 is 46.3%. Then adsorption rate starts to decrease with the increase of the dosage. Adsorption rate dropped to 25.7%, when the dosage of SURFLON S-386 increased to 27%. Adsorption rate did not change significantly with increase of SURFLON S-386 dosage. Compared with MCM-41, the largest decrease of adsorption rate for SURFLON S-386 was greater than

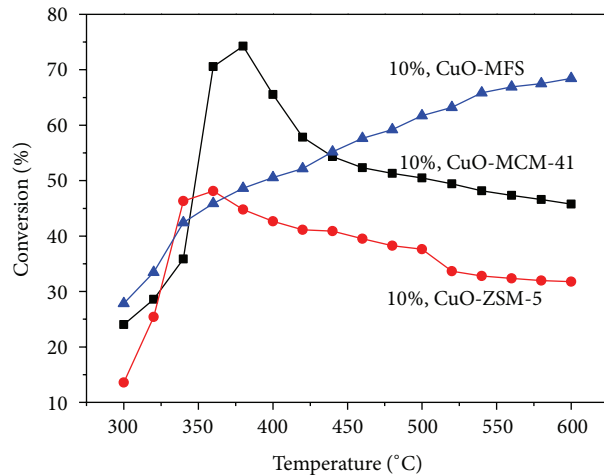


FIGURE 7: Conversion curves of naphthalene combustion over various materials.

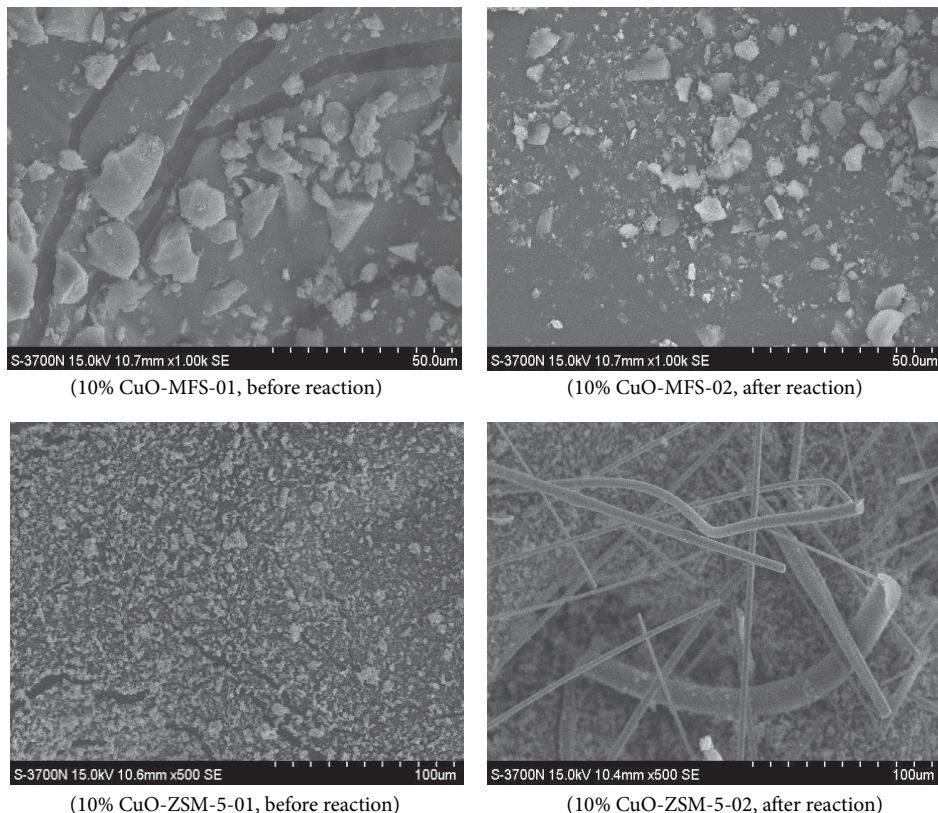


FIGURE 8: SEM of CuO-MFS and CuO-ZSM-5 before reaction and after reaction.

50%. This means the hydrophobicity of MFS is significantly stronger than that of MCM-41. This behavior may be due to the existence of perfluoroalkyl groups remaining from SURFLON S-386 which reduces the surface tension and reduces the adsorption chances with water.

**3.3. Results of Catalytic Performance Experiments.** Catalytic combustion of naphthalene has been investigated, and the results are shown in Figures 7–9. Figure 7 shows the results of catalytic combustion of naphthalene with three catalysts:

10% CuO-ZSM-5, 10% CuO-MCM-41, and 10% CuO-MFS at temperatures from 300°C to 600°C.

With 10% CuO-MCM-41, the conversion of naphthalene at first increases sharply, reaching a maximum conversion of 74.3% at 380°C and then decreasing at higher temperatures. A possible reason is that the hydrothermal stability of MCM-41 decreases at high temperature [23], which leads to the decrease in the conversion of naphthalene. Generally, MCM-41 is mainly used as a carrier for catalysts of combustion of small hydrocarbon molecules [24, 25]. If the temperature

is higher than 400°C, the structure of MCM-41 may be disrupted due to the presence of water vapor.

As for CuO-ZSM-5, its conversion also initially increases sharply, reaching a maximum conversion of 48% at 386°C and then decreasing at higher temperatures. One possible explanation for this behavior is that intermediate products generated in the reaction process block the channels of ZSM-5, which reduce the adsorption capacity for organic compounds, limiting the opportunities for naphthalene to enter the pores of ZSM-5. Hence, ZSM-5 is probably not appropriate for use as a catalyst carrier for catalytic combustion of large molecular organic compounds.

Figure 8 shows the SEM images of 10% CuO-ZSM-5 and 10% CuO-MFS before and after reaction. Comparing the paired images for 10% CuO-ZSM5-01A and for 10% CuO-ZSM5-02A, it can be seen that many stacked rod-like structures have formed on the surface of catalyst after reaction. The rod-like structure is probably the deposition of coke generated by the decomposition of naphthalene during the conversion process. When the catalytic reaction is going on, the larger incomplete oxidation products of naphthalene have difficulty entering the pores of ZSM-5. After continual accumulation and recombination, the rod-like structures start to form and grow at higher temperature.

In contrast, Figure 8 shows there is no significant change observed on the surface of MFS before and after reaction from the two images of MFS. However, for 10% CuO-MFS, the conversion of naphthalene increases slowly without maximum within the whole operation temperature range. The maximum conversion of 10% CuO-MFS is lower than 10% CuO-MCM-41, which may be due to the strong electronegativity of F, leading to the reduced activity of active species.

The light-off curve of CuO-MFS for catalytic combustion of naphthalene is shown in Figure 9. When the loading reaches 10%, the conversion reaches a maximum at all temperatures. Increasing the CuO loading further to 20%, results in a decline of the naphthalene conversion, which can be attributed to the agglomeration of the catalyst particles.

## 4. Conclusion

A novel fluorine-containing, high surface area, hydrophobic mesoporous material, MFS, has been successfully synthesized by a hydrothermal synthesis method using a perfluorinated surfactant SURFLON S-386 as the single template. Some perfluoroalkyl groups from the SURFLON S-386 remain on the surface of MFS which leads to a high hydrophobicity of the material. MFS has significant advantages for use in the catalytic combustion of large molecular organic pollutants, especially those found in high temperature flue gases that contain water vapor. These advantages stem from MFS's high hydrophobicity and larger pore diameter. Further work is needed to reduce the negative impacts of fluorine on the catalytic combustion reaction and to improve the naphthalene conversion at lower temperatures.

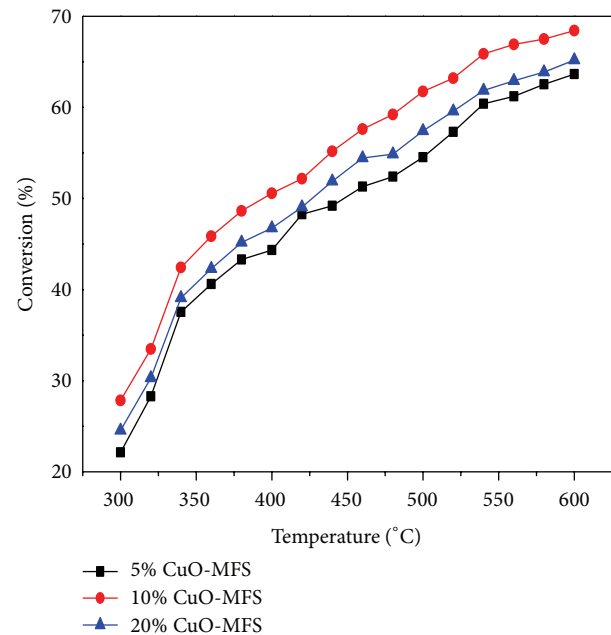


FIGURE 9: Conversion curves of naphthalene combustion over CuO-FS-01.

## Conflict of Interests

The authors declare that there is no conflict of interests regarding the publishing of this paper.

## Acknowledgments

The authors gratefully acknowledge the project supported by the National High Technology Research and Development Program of China (grant no. 2013AA065005) and the National Natural Science Foundation of China (no. 21376090). The project was sponsored by the Scientific Research Foundation of GuangXi University (Grant No. XGZ130963).

## References

- [1] X. Y. Wang, Q. Kang, and D. Li, "Catalytic combustion of chlorobenzene over MnO<sub>x</sub>-CeO<sub>2</sub> mixed oxide catalysts," *Applied Catalysis B*, vol. 86, no. 3-4, pp. 166–175, 2009.
- [2] W. B. Li, J. X. Wang, and H. Gong, "Catalytic combustion of VOCs on non-noble metal catalysts," *Catalysis Today*, vol. 148, no. 1-2, pp. 81–87, 2009.
- [3] H. S. Kim, T. W. Kim, H. L. Koh, S. H. Lee, and B. R. Min, "Complete benzene oxidation over Pt-Pd bimetal catalyst supported on  $\gamma$ -alumina: influence of Pt-Pd ratio on the catalytic activity," *Applied Catalysis A: General*, vol. 280, no. 2, pp. 125–131, 2005.
- [4] Z. Mu, J. J. Li, H. Tian, Z. P. Hao, and S. Z. Qiao, "Synthesis of mesoporous Co/Ce-SBA-15 materials and their catalytic performance in the catalytic oxidation of benzene," *Materials Research Bulletin*, vol. 43, no. 10, pp. 2599–2606, 2008.
- [5] G. Laugel, J. Arichi, M. Mollière, A. Kienemann, F. Garin, and B. Louis, "Metal oxides nanoparticles on SBA-15: efficient

- catalyst for methane combustion," *Catalysis Today*, vol. 138, no. 1-2, pp. 38–42, 2008.
- [6] Y. S. Xia, H. X. Dai, L. Zhang, J. Deng, H. Hea, and C. T. Au, "Ultrasound-assisted nanocasting fabrication and excellent catalytic performance of three-dimensionally ordered mesoporous chromia for the combustion of formaldehyde, acetone, and methanol," *Applied Catalysis B: Environmental*, vol. 100, no. 1-2, pp. 229–237, 2010.
- [7] Z.-J. Wang, Y. Liu, P. Shi, C.-J. Liu, and Y. Liu, "Al-MCM-41 supported palladium catalyst for methane combustion: effect of the preparation methodologies," *Applied Catalysis B: Environmental*, vol. 90, no. 3-4, pp. 570–577, 2009.
- [8] Q.-H. Xia, K. Hidajat, and S. Kawi, "Adsorption and catalytic combustion of aromatics on platinum-supported MCM-41 materials," *Catalysis Today*, vol. 68, no. 1-3, pp. 255–262, 2001.
- [9] M. Park, S. S. Park, M. Selvaraj, D. Zhao, and C. Ha, "Hydrophobic mesoporous materials for immobilization of enzymes," *Microporous and Mesoporous Materials*, vol. 124, no. 1-3, pp. 76–83, 2009.
- [10] E. Serra, E. Díez, I. Díez, and R. M. Blanco, "A comparative study of periodic mesoporous organosilica and different hydrophobic mesoporous silicas for lipase immobilization," *Microporous and Mesoporous Materials*, vol. 132, pp. 487–493, 2010.
- [11] H. Yamashita, Y. Horiuchi, S. Imaoka, S. Nishio, N. Nishiyama, and K. Mori, "Surface hydrophilic–hydrophobic property on transparent mesoporous silica thin films containing chromium oxide single-site photocatalyst," *Catalysis Today*, vol. 132, no. 1–4, pp. 146–152, 2008.
- [12] B. Dou, J. Li, Q. Hu et al., "Hydrophobic micro/mesoporous silica spheres assembled from zeolite precursors in acidic media for aromatics adsorption," *Microporous and Mesoporous Materials*, vol. 133, no. 1-3, pp. 115–123, 2010.
- [13] Y. Di, X. J. Meng, S. G. Li, and F. S. Xiao, "Ordering improvement of mesoporous silica materials templated from semi-fluorinated nonionic surfactants by introduction of organic additives," *Microporous and Mesoporous Materials*, vol. 82, no. 1-2, pp. 121–127, 2005.
- [14] L. G. Hortiguela, F. Cora, and J. P. Pariente, "Supramolecular assemblies of fluoro-aromatic organic molecules as structure directing agents of microporous materials: different effects of fluorine," *Microporous and Mesoporous Materials*, vol. 109, pp. 494–504, 2008.
- [15] R. García, M. Arranz, T. Blasco, and J. P. Pariente, "Fluorine-containing organic molecules as structure directing agents in the synthesis of crystalline microporous materials. Part III: Synthesis of all-silica zeolites from fluorine-containing derivatives of 1-benzyl-1-methylpyrrolidinium," *Microporous and Mesoporous Materials*, vol. 114, no. 1-3, pp. 312–321, 2008.
- [16] S. C. Sharma, H. Kunieda, J. Esquena, and C. Rodríguez Abreu, "Phase behavior and preparation of mesoporous silica in aqueous mixtures of fluorinated surfactant and hydrophobic fluorinated polymer," *Journal of Colloid and Interface Science*, vol. 299, no. 1, pp. 297–304, 2006.
- [17] J. L. Blin, N. Henzel, and M. J. Stébé, "Mixed fluorinated-hydrogenated surfactant-based system: preparation of ordered mesoporous materials," *Journal of Colloid and Interface Science*, vol. 302, no. 2, pp. 643–650, 2006.
- [18] T. García, B. Solsona, and S. H. Taylor, "Naphthalene total oxidation over metal oxide catalysts," *Applied Catalysis B: Environmental*, vol. 66, no. 1-2, pp. 92–99, 2006.
- [19] Z. Mu, J. J. Li, Z. P. Hao, and S. Z. Qiao, "Direct synthesis of lanthanide-containing SBA-15 under weak acidic conditions and its catalytic study," *Microporous and Mesoporous Materials*, vol. 113, no. 1-3, pp. 72–80, 2008.
- [20] G. Zhao, Z. Zhao, J. Wu, and D. Ye, "Synthesis of hydrophobic mesoporous material MFS and its adsorption properties of water vapor," *Journal of Spectroscopy*, vol. 2014, Article ID 965037, 7 pages, 2014.
- [21] X. Y. Wu, P. Cong, H. Nanao, K. Kobayashi, and S. Mori, "Chemisorption and tribochemical reaction mechanisms of HFC-134a on nascent ceramic surfaces," *Langmuir*, vol. 18, no. 26, pp. 10122–10127, 2002.
- [22] Q. Lu, X. F. Zhu, W. Z. Li, Y. Zhang, and D. Yu. Chen, "On-line catalytic upgrading of biomass fast pyrolysis products," *Chinese Science Bulletin*, vol. 54, no. 11, pp. 1941–1948, 2009.
- [23] P. A. Jalil, "Investigations on MCM-41 as a fume catalytic incinerator: a heptane case study," *Fuel Processing Technology*, vol. 85, no. 11, pp. 1317–1332, 2004.
- [24] W. B. Li, M. Zhuang, and J. X. Wang, "Catalytic combustion of toluene on Cu-Mn/MCM-41 catalysts: influence of calcination temperature and operating conditions on the catalytic activity," *Catalysis Today*, vol. 137, no. 2–4, pp. 340–344, 2008.
- [25] E. V. Makshina, N. S. Nesterenko, S. Siffert, E. A. Zhilinskaya, A. Aboukais, and B. V. Romanovsky, "Methanol oxidation on LaCo mixed oxide supported onto MCM-41 molecular sieve," *Catalysis Today*, vol. 131, no. 1–4, pp. 427–430, 2008.

## Research Article

# Study on the Gelation of Foamed Gel for Preventing the Spontaneous Combustion of Coal

Leilin Zhang<sup>1</sup> and Botao Qin<sup>2</sup>

<sup>1</sup> School of Mining and Safety Engineering, Anhui University of Science & Technology, Huainan 232001, China

<sup>2</sup> School of Safety Engineering, China University of Mining & Technology, Xuzhou 221116, China

Correspondence should be addressed to Leilin Zhang; leilinzhang@126.com

Received 28 May 2014; Revised 15 June 2014; Accepted 16 June 2014; Published 26 June 2014

Academic Editor: Tifeng Jiao

Copyright © 2014 L. Zhang and B. Qin. This is an open access article distributed under the Creative Commons Attribution License, which permits unrestricted use, distribution, and reproduction in any medium, provided the original work is properly cited.

According to the existing deficiencies in fire prevention technology, a new technique named foamed gel is developed to prevent coal mine fire efficiently. Foamed gel, formed by adding the type F3 foam agent, polymer H, and AL into water, introducing nitrogen and stirring physically and mechanically, is a complex multicomponent foam system. The effects of the mass fraction and mixed ratios of polymer H and polymer AL blends on gelation were comprehensively studied. The results show that the optimum performance can be got when the mass fraction of blends was 0.6% and the mixed ratio was 5 : 5. In addition, the interaction between molecules of these polymer blends was also investigated with the help of atomic force microscope. It can be found that the polymers H and AL, through having crosslinking reaction with each other, formed three-dimensional network structures, which can not only increase the nodes of the foamed gel system but also enhance the structures.

## 1. Introduction

Spontaneous combustion of coal in goaf is one of the main natural disasters in coal mine production [1, 2]. In recent years, in China, technology of fully mechanized sublevel caving mining is extensively used; besides, gas extraction technique has been widely promoted in the gas treatment. The significant improvement of production efficiency and the dramatical reduction of gas emission have caused leakage serious in goaf, making the coal spontaneous combustion occur frequently [3–5]. For the past few years, the number of the working face of China key state-owned coal mines closed has been over one hundred because of spontaneous fire and the freezing coals caused by the work of closing were more than ten million tons. Closing working face often makes tens of millions of equipment of fully mechanized face and fully mechanized sublevel caving face closed in spontaneous fire area, a great deal of coal frozen and reasonable sequence of deployment disposed and mining preparation broken, which bring a large economic loss and major hidden danger to mine. In order to prevent the spontaneous combustion of coal, the techniques of grouting, nitrogen, inhibitor, gel, foam, and

so on are adopted to prevent coal spontaneous combustion since 1950s [6–8]. Although those techniques have supplied an important guarantee for the mine safety production, due to the extremely complex condition of coal mine, all of them can not completely meet the need of fire prevention and extinguishing. When grouting, slurry can only flow to the low-lying areas and can not cover the coal in higher places in goaf. While injecting nitrogen, it is easy for gas to spread with air but it is difficult to stay in the infuse area and thereby the effect of fire extinguishing and cooling is not ideal. If injecting inhibitor, which is hard to evenly disperse on the coal and has corrosive action, threatening both equipment and the health of workers. When injecting polymer gelatin, the small flow is difficult to be applied to put out the fire in large areas of goaf. If injecting foam, which can not realize curing and whose normally stability is 8~12 h. Therefore, the work of fire prevention and extinguishing in coal mine is still an arduous task for scholars at home and abroad [9].

In order to overcome the deficiencies in conventional fire prevention and extinguishing technology, foamed gel, for the first time, is developed to prevent the spontaneous combustion of coal. Foamed gel, a complex mixed system, is

formed by adding polymers and foaming agent into water and stirring physically and mechanically under the function of nitrogen. After a while, different polymers take crosslinking reaction in foam films and form three-dimensional network structures, which constitute the rigid backbone of foamed gel. The foamed gel not only has the properties of gel but also has the characteristics of foam; at the same time, it can also overcome the shortages of both and thus significantly improve the effect of fire prevention and extinguishing. At present, foamed gel, preliminarily investigated in petroleum exploitation and related industries, is mostly used as plugging agent and profile control so as to increase the mining rate of petroleum. Researchers at home and abroad have made many great contributions in this field. Fogler research team of Michigan College carried out a deep experiment on foamed gel's infiltration, flow direction, mechanical strength, and so on in the 1990s [10–14]. Zhiguo et al. studied the selective water plugging agent of foamed gel [15]. Qibin et al. explored the stability of foamed gel [16]. Although the foamed gel has a lot of advantages and good application result, the study on the effect of fluidity and formation mechanism is far from satisfactory, limiting its application. Furthermore, foaming multiple of foamed gel adopted in petroleum exploitation is small and gelation time is long, while those of foamed gel used in coal mine for fire prevention and extinguishing are high and controllable (generally 10~20 min), more difficult to investigate, and with more complex influencing factors.

This paper takes type F3 foaming agent, polymer H, and AL as the basic material, pays more attention to the effect of mass concentration and mixed ratio of polymer blends on gelation property, and analyzes the mechanism of crosslinking action between two polymers with the help of atomic force microscope, which provide a foundation for this system as a new type of material for preventing spontaneous combustion of coal.

## 2. Experimental Preparation

**2.1. Experimental Material.** Polymers H and AL are produced by Henan Kuangyuan Chemical Product Co., Ltd. The polymer H is an anionic polysaccharide produced by fermentation from *Xanthomonas campestris*. The polymer AL is a kind of galactomannan polysaccharide obtained from *Cyamopsis tetragonoloba* seeds. Both of them dissolve readily in water at room temperature. They are polysaccharides, which are particularly used for the food industry. The main role of these is to serve as a thickening agent and texture modifiers for food products. The unique characteristic of them is that not only do they owe significant viscosity values at lower concentrations in aqueous solutions but also they can exhibit excellent crosslinking when they are mixed.

Type F3 foaming agent was made by us; the concentration of active matter was 30~32%.

**2.2. Experimental Equipment.** Philips type HR2006 agitator, atomic force microscope, and type NDJ-5s digital viscometer

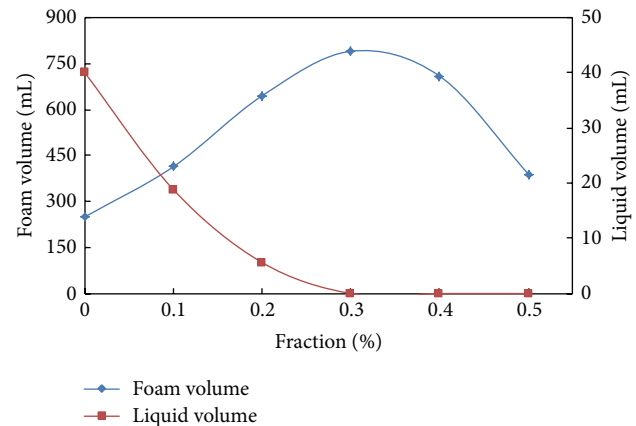


FIGURE 1: Gelation against the mass fraction of polymer blends.

are used. The viscometer is divided into four crosspieces: 4.2, 8.5, 22.2, and 42.4/s, respectively.

### 2.3. Experimental Methods

- (1) Put polymers H and AL blends into a suitable amount of water, then add certain type F3 foaming agent, and finally form the base fluid of foamed gel.
- (2) Take 100 mL of the base fluid into agitator, foam by means of stirring physically and mechanically (for 5 min), measure the foam volume and liquid dropout volume through its own measuring device, and use viscosimeter to test the viscosity of foamed gel.

## 3. Results and Analysis

**3.1. Effect of Mass Fraction of Polymer Blends on Gelation of Foamed Gel.** At room temperature, mass fraction of type F3 foaming agent is fixed at 0.4%, and mixed ratio of polymers H and AL is 1:1, investigating the effects of mass fraction of the polymer blends on the foam volume and liquid dropout volume, which is shown in Figure 1.

As shown in Figure 1, with the increase of the mass fraction of polymer blends, the foam volume first increased and then decreased, but the liquid dropout volume rapidly decreased to zero. This is because the optimal polymer H has the high surface activity, which can increase the intersolubility between components and control cell size and uniformity, increasing the foam volume. However, the viscosity of the solution was low when the mass fraction of polymer was small, and crosslinking points in the polymers were less and three-dimensional network structures can not be formed; thus a small amount of liquid can be seen in the foam bottom after standing for some time. With the increasing of mass fraction of polymer blends, polymers H and AL firstly fully diffuse in foam films and then have crosslinking reaction with each other to form three-dimensional network structures, constituting the rigid backbone of foam and greatly enhancing the stability of foam [17]. Furthermore, the molecular chains of the polymers contain a lot of  $-OH$ ,

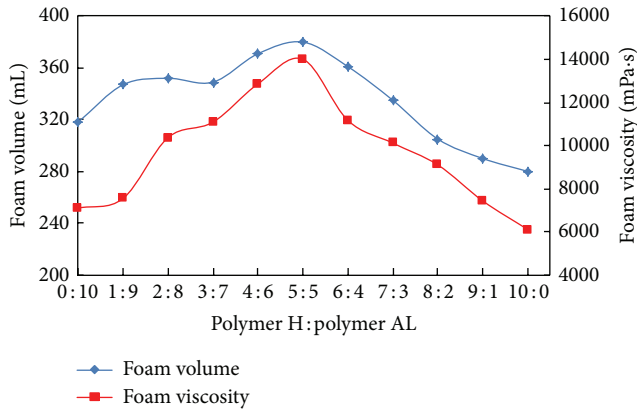


FIGURE 2: The influence of mixed ratio on gelation of foamed gel.

which can interact with the water molecules by hydrogen bonds. Consequently, water is absorbed in three-dimensional network structures, which can maintain the stability of foam. If the mass fraction of polymer blends exceeds 0.6%, the viscosity of the system rapidly increases, the penetration of gas is poor, and foam volume decreases gradually [18]. Therefore, when the mass fraction of polymer blends is 0.6%, the best foaming effect of polymer solution can be got and the gelation properties of foamed gel produced are the best.

**3.2. Effect of Mixed Ratio of Polymer Blends on Gelation of Foamed Gel.** The mass fraction of type F3 foaming agent is fixed at 0.4%, the total mass fraction of polymer blends is 0.6%, and the polymers H and AL are mixed at different compound proportions so as to form foamed gel, respectively. The effects of mixed ratios on foam volume and foam viscosity are shown in Figure 2.

From Figure 2, it can be seen that, with the increase of compound ratio, both foaming multiple and foam viscosity first rise and then decline. When the compound proportion of polymers H and AL is 5:5, foaming multiple and foam viscosity are the maximum. If the ratio continues to change, foaming multiple and foam viscosity begin to fall, which means that there exists a best compound ratio of the blends, and by this time, their crosslinking reaction with each other is maximum.

The reason for this phenomenon is that when polymers H and AL mixed in the solution, they can fully react with each other and form three-dimensional network structures, making the viscosity of foamed gel increase. Whereas if the mass fraction of polymer H is less, the polymer AL will be excessive, unexpectedly its dense galactose will hinder the interaction with polymer H, causing the viscosity of the system to descend and not to form foamed gel with satisfactory stability and good appearance. With the rise of polymer H, foaming property and stability of the solution increase gradually. However, when mass fraction of polymer H is more than 50%, the polymer AL relatively reduces and the crosslinking points decrease, unhelpful to form gel [19–21]. Foam property becomes worse and stratification

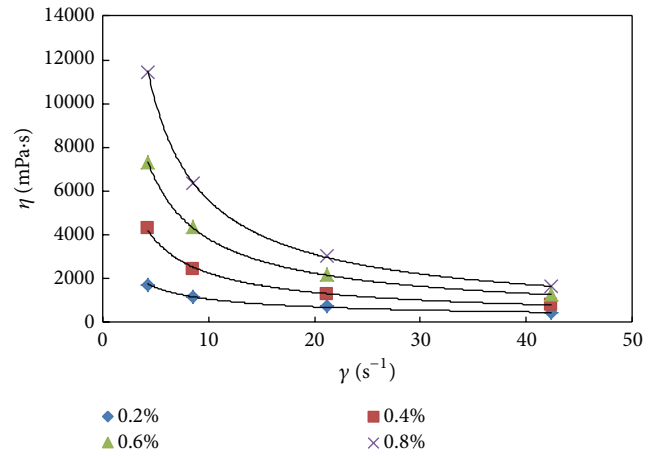


FIGURE 3: Relationship between apparent viscosity and shear rate of foamed gel.

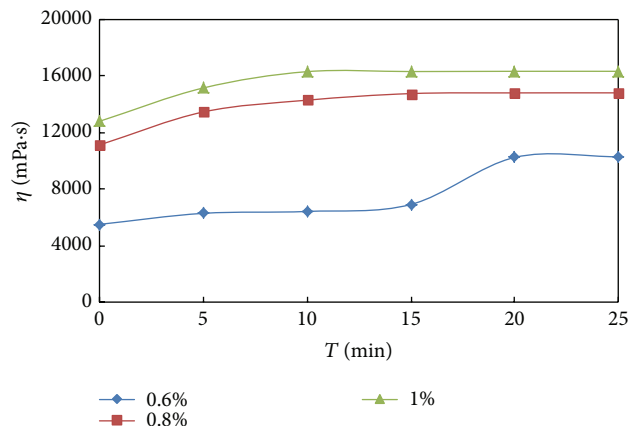


FIGURE 4: Relationship between mass fraction of blends and gelation time of foamed gel.

phenomenon can be seen after standing for a while. Consequently, when the mixed ratio of the blend is 5:5, foam property and gelation effect are the best.

**3.3. Characteristics of Gelation of Foamed Gel.** According to the research conducted above, the foamed gel is formed when the mass fraction of type F3 foaming agent is fixed at 0.4% and the mass fractions of polymers H and AL are both 0.3%. Viscometer is adopted to measure the apparent viscosity so as to discuss the relationship between gelation property and shear rate, as shown in Figure 3.

According to the research conducted above, the concentration of type F3 foaming agent is fixed at 0.4%, and the mass ratio of polymers H and AL is 1:1. Then change the concentration of mixture so as to form the foamed gel samples at different concentrations and use viscometer to measure the apparent viscosity at different shear rate, as shown in Figure 3.

It can be seen from Figure 3 that the apparent viscosity of foamed gel at various concentrations of the mixture formed

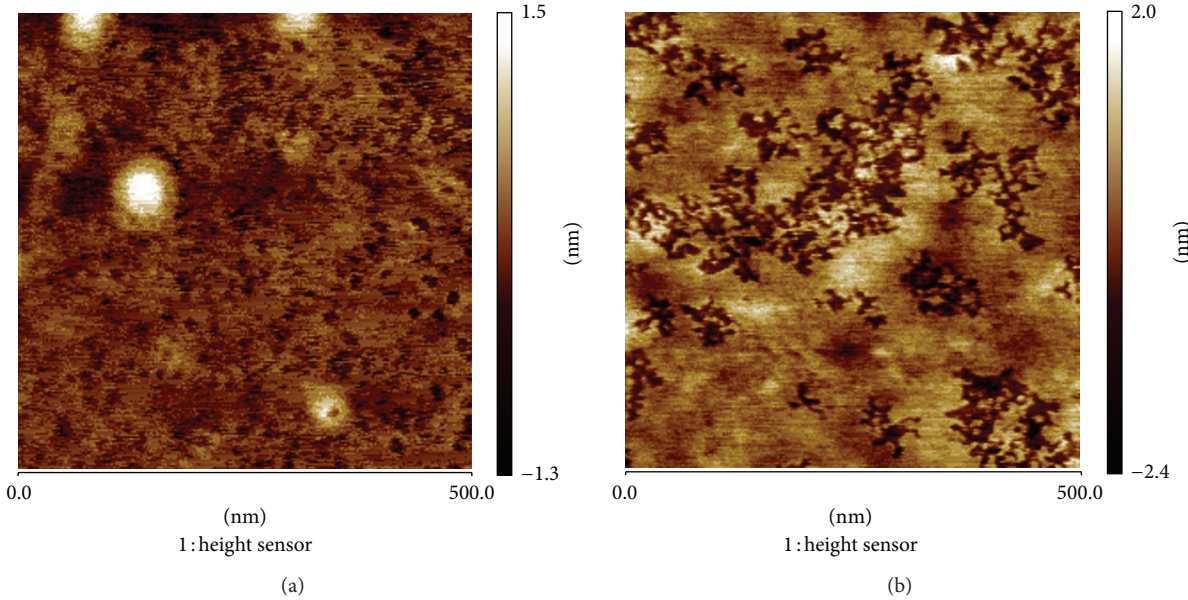


FIGURE 5: AFM images of foamed gel samples in the scanning range of 500 nm. (a) Polymer H; (b) polymers H and AL blends.

by polymers H and AL drops rapidly with the shear rate increasing, and the higher the concentration is, the more obviously apparent the viscosity decrease is. This law fits the fluid character of shear thinning. In static foamed gel, the arrangement of molecular chains in polymers is ruleless. And those molecular chains entangle with each other to form three-dimensional network structures, producing viscous resistance to flow [22]. Therefore, when the shear rate is low, the apparent viscosity of foamed gel is high. With the increase of shear rate, the shear effect subjected to three-dimensional network structures rises, and the molecules curved and entangled was open. Molecules nodes reduce, thus apparent viscosity decreases. When the shear rate reaches a certain value, the apparent viscosity is stable [23, 24]. Hence, under the function of shear rate, polymers H and AL can not have crosslinking reaction with each other in foam films, which can meet the property of large range flow and diffusion of foamed gel in goaf.

**3.4. Gelation Time.** The formation process of foamed gel is that, after the system foams, polymers H and AL contained in foam films react with each other and form foamed gel. If the time of crosslinking reaction between polymers is too early, the viscosity of solution will be too high and hard to form foam. Even if foamed gel is formed, the large viscosity makes it difficult to flow; the limited coverage can not meet the need of fire prevention and extinguishing. Foam belongs to unstable system of thermodynamics; if the time of crosslinking reaction between polymers is too late and even exceeds its stable time, it will break and dehydrate. At this time, even if crosslinking reaction has been taken place, the foamed gel can not be formed. Therefore, the best gelation time is after the solution foaming and before its breaking. Considering that the pipe transport is used in coal mines, the time is controlled between 10~20 min. After the blends

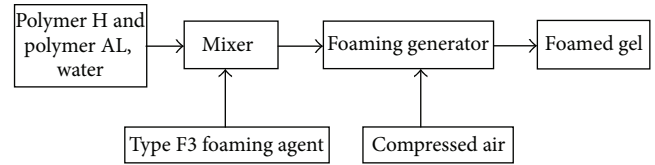


FIGURE 6: The flowchart for preparation of foamed gel.

mixed, the viscosity begins to increase. After some time, the viscosity is essentially constant and forms stable foamed gel. Polymers H and AL are chosen to investigate how the gelation time changes at different mass concentrations of the polymer blends.

The mass fraction of type F3 foaming agent is fixed at 0.4%. The compound proportion of polymers H and AL is 1:1; then prepare the polymer blends with the mass fraction of 0.6%, 0.8%, and 1%, respectively. To study on the effect of various mass fractions on gelation time, the results are shown as follows.

From Figure 4, it can be found that, when the mass fraction of blends was 0.6%, the gelation time was 20 min. When the mass concentration of the blends increased to 1%, the gelation time decreased to 10 min. This is because the rise of mass fraction leads to shortening of the distance and increasing of the collision between molecules. The crosslinking reaction between polymers H and AL becomes stronger, which makes great contributions to forming three-dimensional network structures with strong continuity [25]. Therefore, the gelling rate of foamed gel increased with the rise of the mass fraction of polymer blends. Moreover, the highest gelation viscosity of the system increased with the rising of the mass concentration. Nevertheless, if the mass concentration is too high, the reaction rate among polymers increases and gelling rate of the system speeds up, not easy to

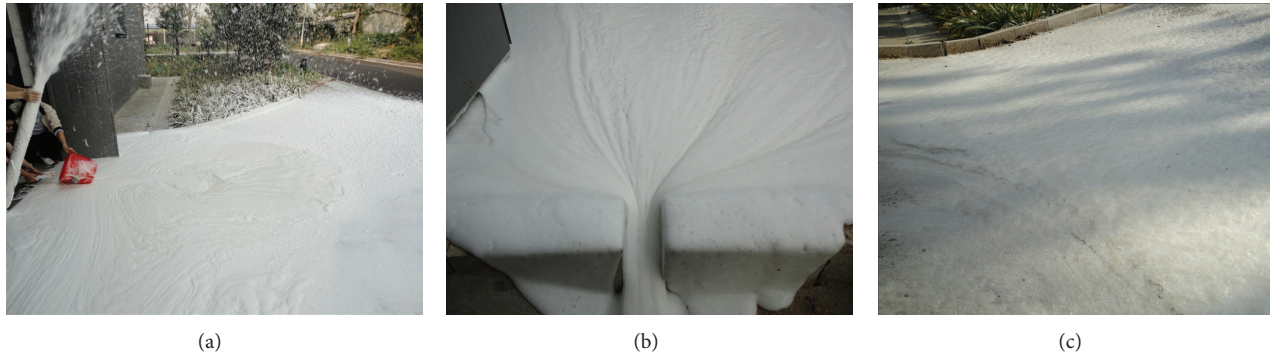


FIGURE 7: The foamed gel prepared in lab. (a) Foaming, (b) fluidity, and (c) film forming ability.

control the gelation time. Furthermore, the rise of the mass fraction of polymer increases the viscosity of the solution, reducing foaming ability.

**3.5. Microstructure Analysis.** Prepare the mass fraction of 0.3% of polymer H and the mass fraction of 0.3% of both polymers H and AL, respectively; take  $10\ \mu\text{L}$  of the two solution samples on mica sheet, and make it spread as possible as you can, heating slightly into membrane. Use AFM to observe the microstructure under the scanning range of 500 nm, as shown in Figure 5.

We can see from Figure 5 that the microstructure map of polymer H without polymer AL is chaotic, granularly distributed in the solution, and thus unable to form three-dimensional network structures, as shown in Figure 5(a). With the adding of polymer AL, filled in the molecules of polymer H, making the scattered polymer H form a uniform continuous phase and thereby form three-dimensional network structures, as shown in Figure 5(b). This is because when polymer H is dispersed into water, it first becomes pieces of random line structures. Then the random molecular chains will coalesce together to the double helix rigid structures similar to the rod by hydrogen bond between the side chain and main chain of polymer H. The rod-like structures, with the help of  $\text{Na}^+$ ,  $\text{K}^+$ , and  $\text{Ca}^{2+}$  ionized by polymer H itself, make the double helix structures decentralized in the solution connected together to the helical mesh polymer or double helix cluster by chains of  $-\text{COO}-\text{Na}-\text{H}_2\text{O}-\text{Na}-\text{COO}-$ ,  $-\text{COO}-\text{K}-\text{H}_2\text{O}-\text{K}-\text{COO}-$ , and  $-\text{COO}-\text{Ca}-\text{COO}-$  [17, 26]. If polymer AL is not added, polymer and cluster can only be uniformly dispersed into the solution and can not form three-dimensional network structures. After adding polymer AL,  $-\text{CH}_2\text{OH}$  in polymer or cluster and the  $-\text{CH}_2\text{OH}$  in main chain of polymer AL contact and fully collide, forming three-dimensional network structures in the form of  $-\text{CH}_2-\text{O}-\text{CH}_2-$  and making the scattered polymer and cluster form a uniform continuous phase [27–29]. Consequently, polymer AL and polymer H can react with each other in foam films to form foamed gel and keep the stability of foam.

#### 4. Preparation and Effect

In order to investigate the foaming effect of foamed gel, compressed air replacing nitrogen is used, and foaming device of foamed gel has been constructed to conduct a simulation test. Firstly, directly mix and stir polymer H, polymer AL, and water based on the fixed proportion to form the solution of blends. Then, put the blends solution into grouting pipes through consistency pump and take type F3 foaming agent into grouting pipes by fixed displacement pump. After fully mixed in the flow mixer, solution of polymers and foaming agent flow to the foaming generator. Then compressed air is introduced. Finally the air interacts with the blends solution with type F3 foaming agent and forms foamed gel. The process of preparing foamed gel is shown in Figure 6.

According to the experimental parameters above, the mass fraction of 0.4% of type F3 foaming agent and the mass fraction of 0.3% of both polymer H and polymer AL are used to form foamed gel, as shown in Figure 7(a). And the foamed gel prepared has good fluidity, as shown in Figure 7(b). After one day, polymer H and polymer AL have crosslinking interaction with each other in foam films and obtain compacted thin films, as shown in Figure 7(c).

#### 5. Conclusions

- (1) Experimental study on the properties of foamed gel shows it has the characteristics of high foaming multiple, strong stability, good fluidity, adjustable gelation time, and so forth. So using the foamed gel can significantly improve the efficiency of preventing spontaneous combustion of coal.
- (2) The mass fractions of polymers H and AL and the compound proportion of the blends greatly influence the performances of foamed gel. When the mass fraction of polymer H and polymer AL blends is 0.6% and the mixed ratio is 1:1, the properties of foamed gel formed for fire prevention and extinguishing are the best, and the foamed gel prepared has the maximum viscosity without affecting its fluidity.

(3) Through the analysis of AFM, polymers H and AL have crosslinking reaction with each other and form three-dimensional network structures, increasing the nodes of the system and enhancing the structures. Moreover, foaming device of foamed gel is constructed in lab and foamed gel for fire prevention and extinguishing with optimum performance is prepared.

## Conflict of Interests

The authors declare that there is no conflict of interests regarding the publication of this paper.

## Acknowledgment

The authors deeply appreciate the financial support of this work by the National Natural Science Foundation of China (no. U1361213).

## References

- [1] W. Jo, H. Choi, S. Kim et al., "A comparison of spontaneous combustion susceptibility of coal according to its rank," *Korean Journal of Chemical Engineering*, vol. 30, no. 5, pp. 1034–1038, 2013.
- [2] A. K. Singh, R. V. K. Singh, M. P. Singh, H. Chandra, and N. K. Shukla, "Mine fire gas indices and their application to Indian underground coal mine fires," *International Journal of Coal Geology*, vol. 69, no. 3, pp. 192–204, 2007.
- [3] W. Deming, D. Guolan, Z. Xiaoxing, X. Haihui, and Q. Botao, "An experimental approach to selecting chemical inhibitors to retard the spontaneous combustion of coal," *Fuel*, vol. 117, part A, pp. 218–223, 2014.
- [4] Z. Xie, Z. Yu, and J. Cai, "Prediction of coal spontaneous combustion in goaf based on the BP Neural network," *Procedia Engineering*, vol. 43, pp. 88–92, 2012.
- [5] J. Xie, S. Xue, W. Cheng, and G. Wang, "Early detection of spontaneous combustion of coal in underground coal mines with development of an ethylene enriching system," *International Journal of Coal Geology*, vol. 85, no. 1, pp. 123–127, 2011.
- [6] F. Zhou, W. Ren, D. Wang, T. Song, X. Li, and Y. Zhang, "Application of three-phase foam to fight an extraordinarily serious coal mine fire," *International Journal of Coal Geology*, vol. 67, no. 1-2, pp. 95–100, 2006.
- [7] Y. Xu, D. Wang, L. Wang, X. Zhong, and T. Chu, "Experimental research on inhibition performances of the sand-suspended colloid for coal spontaneous combustion," *Safety Science*, vol. 50, no. 4, pp. 822–827, 2012.
- [8] G. B. Stracher and T. P. Taylor, "Coal fires burning out of control around the world: thermodynamic recipe for environmental catastrophe," *International Journal of Coal Geology*, vol. 59, no. 1-2, pp. 7–17, 2004.
- [9] X. Xuefu, W. Hongtu, and J. Deyi, "The summarization of the investigation on coal mine fire prevention and fire extinguishing techniques in China," *Engineering Science*, vol. 3, no. 12, pp. 28–32, 2001.
- [10] J. M. Matthew, "Permeability of foamed gel barriers used for physical control of subterranean fluid movement," *Dissertation Abstract International*, vol. 56, no. 1, p. 382, 1995.
- [11] M. J. Miller, K. Khilar, and H. S. Fogler, "Aging of foamed gel used for subsurface permeability reduction," *Journal of Colloid and Interface Science*, vol. 175, no. 1, pp. 88–96, 1995.
- [12] M. J. Miller and H. S. Fogler, "A mechanistic investigation of waterflood diversion using foamed gels," *SPE Production & Facilities*, vol. 10, no. 1, pp. 62–69, 1995.
- [13] M. J. Miller and H. S. Fogler, "Foamed gel barriers in porous media: breakdown and permeability evolution," *AIChE Journal*, vol. 41, no. 11, pp. 2487–2398, 1995.
- [14] J. M. Matthew and H. S. Fogler, "A model to estimate the performance of foamed gel for conformance control," in *SPE/DOE Improved Oil Recovery Symposium*, vol. 9, pp. 461–473, 1994.
- [15] S. Zhiguo, Su. Guo, and D. Yujie, "Development and application of a selective foamed gel plugging agent," *Drilling & Production Technology*, vol. 23, no. 1, pp. 70–71, 2000.
- [16] C. Qibin, M. Baoqi, and N. Binghua, "Effects of several factors on the properties of a foamed gel," *Journal of East China University of Science and Technology (Natural Science Edition)*, vol. 33, no. 1, pp. 71–75, 2007.
- [17] C.-F. Mao, Y.-C. Zeng, and C.-H. Chen, "Enzyme-modified guar gum/xanthan gelation: an analysis based on cascade model," *Food Hydrocolloids*, vol. 27, no. 1, pp. 50–59, 2012.
- [18] S. N. Tan, A. Jiang, J. J. Liau, S. R. Grano, and R. G. Horn, "The surface dilational viscosity of polypropylene glycol solutions and its influence on water flow and foam behavior," *International Journal of Mineral Processing*, vol. 93, no. 2, pp. 194–203, 2009.
- [19] H. A. Khouryieh, T. J. Herald, F. Aramouni, and S. Alavi, "Intrinsic viscosity and viscoelastic properties of xanthan/guar mixtures in dilute solutions: effect of salt concentration on the polymer interactions," *Food Research International*, vol. 40, no. 7, pp. 883–893, 2007.
- [20] H. A. Khouryieh, T. J. Herald, F. Aramouni, and S. Alavi, "Influence of mixing temperature on xanthan conformation and interaction of xanthan-guar gum in dilute aqueous solutions," *Food Research International*, vol. 39, no. 9, pp. 964–973, 2006.
- [21] J. A. Casas and F. García-Ochoa, "Viscosity of solutions of xanthan/locust bean gum mixtures," *Journal of the Science of Food and Agriculture*, vol. 79, no. 1, pp. 25–31, 1999.
- [22] X. Zhou, F. Chen, and Zhang B., "Studies on the rheological properties of oxidized waxy maize starch paste," *Cereal and Feed Industry*, no. 9, pp. 27–30, 2010.
- [23] T. G. Matuda, S. Chevallier, P. de Alcântara Pessôa Filho, A. LeBail, and C. C. Tadini, "Impact of guar and xanthan gums on proofing and calorimetric parameters of frozen bread dough," *Journal of Cereal Science*, vol. 48, no. 3, pp. 741–746, 2008.
- [24] B. Heyman, W. H. de Vos, F. Depypere, P. van der Meer, and K. Dewettinck, "Gums tuning the rheological properties of modified maize starch pastes: differences between guar and xanthan," *Food Hydrocolloids*, vol. 39, pp. 85–94, 2014.
- [25] M. Tako and S. Nakamura, "Synergistic interaction between xanthan and guar gum," *Carbohydrate Research*, vol. 138, no. 2, pp. 207–213, 1985.
- [26] M. Chaisawang and M. Suphantharika, "Pasting and rheological properties of native and anionic tapioca starches as modified by guar gum and xanthan gum," *Food Hydrocolloids*, vol. 20, no. 5, pp. 641–649, 2006.
- [27] K. P. Shatwell, I. W. Sutherland, S. B. Ross-Murphy, and I. C. M. Dea, "Influence of the acetyl substituent on the interaction of xanthan with plant polysaccharides—II. Xanthan-guar gum systems," *Carbohydrate Polymers*, vol. 14, no. 2, pp. 115–130, 1990.

- [28] J. M. R. Patino, C. C. Sánchez, and Ma. R. R. Niño, "Implications of interfacial characteristics of food foaming agents in foam formulations," *Advances in Colloid and Interface Science*, vol. 140, no. 2, pp. 95–113, 2008.
- [29] D. He, Y. Shi, F. Feng, and D. Zhan, "Study on gelation of chitosan and xanthan gum," *Journal of Wuhan University*, vol. 47, no. 6, pp. 717–720, 2001.

## Research Article

# Analysis of the Oil Content of Rapeseed Using Artificial Neural Networks Based on Near Infrared Spectral Data

Dazuo Yang,<sup>1,2</sup> Hao Li,<sup>3</sup> Chenchen Cao,<sup>1</sup> Fudi Chen,<sup>1</sup> Yibing Zhou,<sup>1</sup> and Zhilong Xiu<sup>2</sup>

<sup>1</sup> Key Laboratory of Marine Bio-Resources Restoration and Habitat Reparation in Liaoning Province, Dalian Ocean University, Dalian 116023, China

<sup>2</sup> College of Life Science and Technology, Dalian University of Technology, Dalian 116021, China

<sup>3</sup> College of Chemistry, Sichuan University, Chengdu, Sichuan 610064, China

Correspondence should be addressed to Dazuo Yang; [dzyang1979@hotmail.com](mailto:dzyang1979@hotmail.com)

Received 9 May 2014; Accepted 2 June 2014; Published 23 June 2014

Academic Editor: Qingrui Zhang

Copyright © 2014 Dazuo Yang et al. This is an open access article distributed under the Creative Commons Attribution License, which permits unrestricted use, distribution, and reproduction in any medium, provided the original work is properly cited.

The oil content of rapeseed is a crucial property in practical applications. In this paper, instead of traditional analytical approaches, an artificial neural network (ANN) method was used to analyze the oil content of 29 rapeseed samples based on near infrared spectral data with different wavelengths. Results show that multilayer feed-forward neural networks with 8 nodes (MLFN-8) are the most suitable and reasonable mathematical model to use, with an RMS error of 0.59. This study indicates that using a nonlinear method is a quick and easy approach to analyze the rapeseed oil's content based on near infrared spectral data.

## 1. Introduction

Infrared absorption spectroscopy is a common approach for analyzing food composition [1–3]. For a certain characteristic absorption frequency, Lambert's law provides the following equation [4, 5]:

$$\log \frac{I_0}{I} = \varepsilon \ell c, \quad (1)$$

where  $I_0$  represents incident light intensity,  $I$  represents transmission light intensity,  $\varepsilon$  represents the attenuation coefficient,  $\ell$  represents the distance the light travels through the material, and  $c$  represents concentration.

Equation (1) is widely used for determining food composition. However, because the wavelengths in the infrared absorption spectrum are diverse and the force of penetration is tiny, infrared absorption spectroscopy can only be used for analyzing transparent liquids. It is of great difficulty to analyze the oil content of rapeseed using infrared absorption spectroscopy. Therefore, to solve this problem, this study instead uses a nonlinear approach to analyze near-spectral data to determine the oil content of rapeseed.

## 2. Artificial Neural Networks

**2.1. Fundamental of ANN Models.** Artificial neural networks (ANN) model is composed of an interconnected group of artificial neurons. In most circumstances, an artificial neural network is an adaptive system that is equipped to be adapting continuously to new data and learning from the accumulated experience and noisy data [6, 7]. Apart from that, the system structure can be changed based on external or internal information that flows through the network during the learning phase. Meanwhile, essential information can be abstracted from data or model complex relationships between inputs and outputs [8–10].

As can be seen from Figure 1, the main structure of the artificial neural network (ANN) is made up of the input layer and the output layer. The input variables are introduced to the network by the input layer [11]. Also, the response variables with predictions, which stand for the output of the nodes in this certain layer, are provided by the network. Additionally, the hidden layer is included. The type and the complexity of the process or experimentation usually iteratively determine the optimal number of the neurons in the hidden layers [12].

TABLE 1: Data of 29 rapeseed samples.

Sample	$c$ (%)	Wavelength ( $\mu\text{m}$ )				
		$\lambda = 1.68$	$\lambda = 1.73$	$\lambda = 1.94$	$\lambda = 2.10$	$\lambda = 2.18$
1	39.60	0.70059	0.76184	0.85572	0.86851	0.87385
2	40.33	0.70218	0.77053	0.89213	0.87777	0.88360
3	38.71	0.69428	0.75829	0.88461	0.86710	0.87264
4	38.53	0.70560	0.77184	0.89991	0.88426	0.88747
5	37.57	0.69840	0.76610	0.90143	0.88410	0.88841
6	37.76	0.69448	0.76032	0.89164	0.87292	0.87551
7	38.22	0.73863	0.81279	0.93508	0.92134	0.92534
8	37.57	0.69165	0.76566	0.90251	0.88688	0.88994
9	39.17	0.68090	0.74233	0.87103	0.85752	0.85983
10	39.98	0.68634	0.75908	0.88710	0.87267	0.87799
11	38.93	0.69500	0.76286	0.88532	0.87407	0.87893
12	36.61	0.69674	0.76537	0.89669	0.88421	0.89025
13	39.74	0.69335	0.76262	0.88754	0.87327	0.87888
14	38.12	0.69504	0.76614	0.89400	0.88275	0.88853
15	38.89	0.69658	0.76258	0.88753	0.87480	0.87960
16	39.85	0.68976	0.75463	0.85723	0.86513	0.86898
17	39.90	0.68955	0.75582	0.87775	0.86404	0.86850
18	38.84	0.69057	0.75927	0.88184	0.87312	0.87900
19	38.32	0.69654	0.76187	0.88378	0.87097	0.88071
20	38.21	0.69645	0.76287	0.89703	0.87551	0.87432
21	38.13	0.70596	0.77703	0.90508	0.88704	0.89242
22	38.51	0.69456	0.76413	0.89476	0.87563	0.88302
23	38.31	0.70629	0.77119	0.89479	0.88420	0.88730
24	39.21	0.68059	0.74624	0.87088	0.85682	0.86421
25	38.61	0.68567	0.75328	0.88502	0.86225	0.87175
26	39.03	0.68050	0.75124	0.87930	0.86176	0.87014
27	39.31	0.68053	0.74778	0.87492	0.85486	0.86043
28	36.50	0.68824	0.75139	0.88715	0.86963	0.87842
29	37.40	0.69583	0.76104	0.89541	0.88044	0.88611

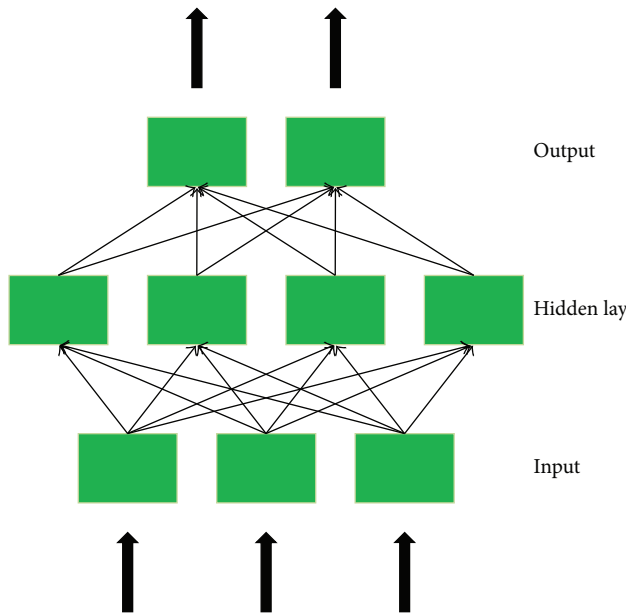


FIGURE 1: A schematic view of artificial neural network structure.

**2.2. Model Development.** Gu and Wang [12] have accomplished a series of researches from correlative precision instrument from which we could obtain data of rapeseeds' near infrared spectroscopy by analyzing absorbance under different wavelengths. We defined  $c$  (%) as the percentage composition of the oil in rapeseed. Data of 29 rapeseed samples are shown on Table 1.

In order to confirm the most suitable and robust ANN model in analyzing the oil content of rapeseed, 21 models were established including linear prediction model, general regression neural networks (GRNN) [14] and multilayer feed-forward neural networks (MLFN) [15, 16]. Into that matter, nodes of MLFN models were set to be from 2 to 20, so that the most robust MLFN model could be found. The independent variables are the absorbancies under the wavelength of  $1.68 \mu\text{m}$  (reference wavelength),  $1.73 \mu\text{m}$  (characteristic absorption wavelength of fat),  $1.94 \mu\text{m}$  (characteristic absorption wavelength of water),  $2.10 \mu\text{m}$  (characteristic absorption wavelength of starch), and  $2.18 \mu\text{m}$  (characteristic absorption wavelength of protein), respectively, while the dependent variable is the percentage composition of the oil in rapeseed. Training set is consist of 24 samples while the rest

TABLE 2: Results of different models in analyzing oil content of rapeseed.

Model	Trained samples	Tested samples	RMS error	Stopped reason
Linear prediction	24	5	0.60	Autostopped
GRNN	24	5	0.74	Autostopped
MLFN 2 nodes	24	5	1.04	Autostopped
MLFN 3 nodes	24	5	1.23	Autostopped
MLFN 4 nodes	24	5	0.88	Autostopped
MLFN 5 nodes	24	5	1.29	Autostopped
MLFN 6 nodes	24	5	1.31	Autostopped
MLFN 7 nodes	24	5	2.20	Autostopped
MLFN 8 nodes	24	5	0.59	Autostopped
MLFN 9 nodes	24	5	3.39	Autostopped
MLFN 10 nodes	24	5	1.93	Autostopped
MLFN 11 nodes	24	5	0.83	Autostopped
MLFN 12 nodes	24	5	1.54	Autostopped
MLFN 13 nodes	24	5	1.10	Autostopped
MLFN 14 nodes	24	5	1.57	Autostopped
MLFN 15 nodes	24	5	3.02	Autostopped
MLFN 16 nodes	24	5	1.67	Autostopped
MLFN 17 nodes	24	5	1.07	Autostopped
MLFN 18 nodes	24	5	1.72	Autostopped
MLFN 19 nodes	24	5	0.85	Autostopped
MLFN 20 nodes	24	5	2.79	Autostopped

of the samples are considered to be the testing set. To ensure the accuracy of the experiments, we did the training process repeatedly. The composing of trained samples and tested samples is different in each experiment. Results of the 21 models were obtained by correlative software, which are shown in Table 2.

Results presented by Table 2 imply that the lowest RMS error of testing exists in the MLFN model with 8 nodes (MLFN-8), which is 0.59, lower than those generated by linear prediction model and GRNN model. And the accuracy rate of the testing is 100% with the permission error. Therefore, the MLFN-8 model is proved to be an accurate and robust model.

### 3. Results and Discussion

**3.1. Training Results of MLFN-8.** Training and testing results of MLFN-8 model were extracted from the experiments. For more intuitionistic, six figures described by data are used to portray the training and testing results, which are shown in Figures 2 to 7.

In training process, the comparison result between predicted values and actual values is depicted by Figure 2. The regulation between predicted values and actual values implies that the training process is precise.

Figure 3 depicts the relationship between residual values and actual values during training process, showing that the residual values are relatively concentrated.

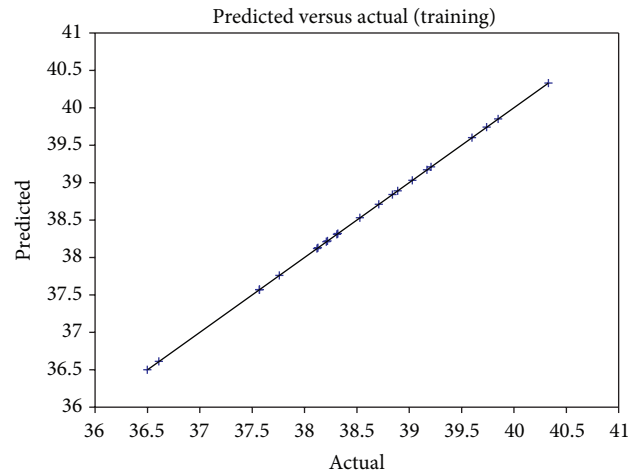


FIGURE 2: Comparison between predicted values and actual values during training process.

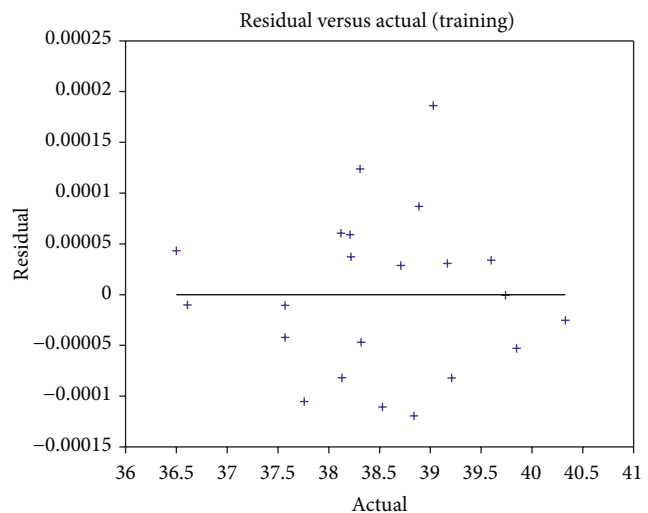


FIGURE 3: Comparison between residual values and actual values during training process.

Different from Figure 3, Figure 4 depicts the relationship between residual values and predicted values during training process. Similar to the result shown in Figure 3, the residual values present the same phenomenon as Figure 3, which indicates that the training process is precise.

In general, Figures 2, 3, and 4 depict the results of training process, showing that the values are concentrated and correspond with the normal training process of MLFN-8 model. It is worth mentioning that the residue values are generally tiny and close to zero, which implies that the training process is correct and precise.

**3.2. Testing Results of MLFN-8.** To analyze the testing process, three figures were used to present the average values of testing results, which are shown in Figures 5 to 7.

In testing process, as shown in Figure 5, the comparison between predicted values and actual values is also close to linear situation, which means that the MLFN-8 model is precise while predicting.

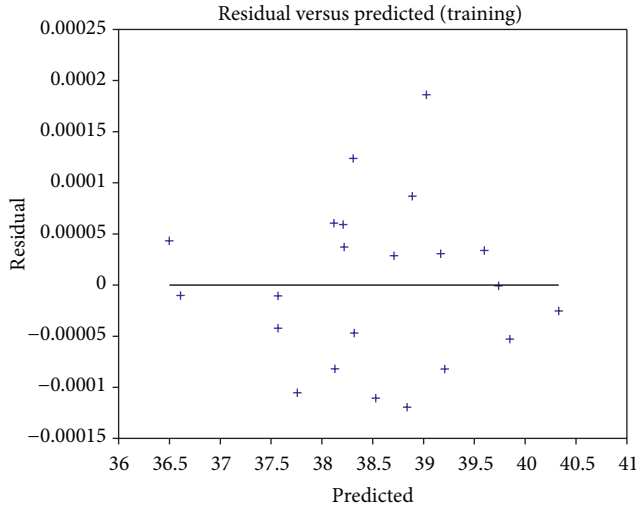


FIGURE 4: Comparison between residual values and predicted values during training process.

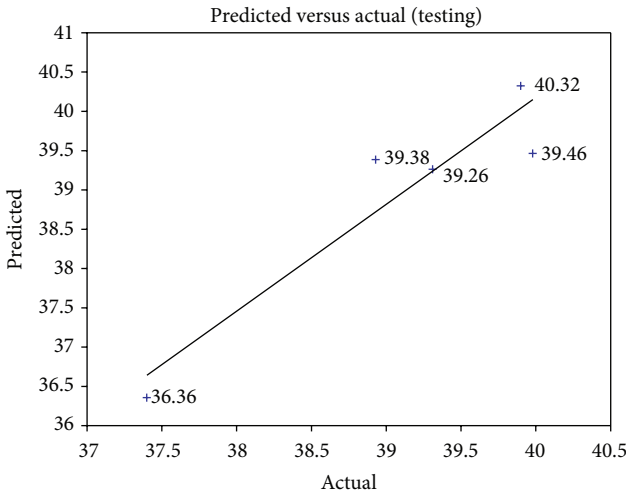


FIGURE 5: Comparison between predicted values and actual values during testing process.

In order to confirm the robustness of comparison between residual values and actual values as well as the comparison between residual values and predicted values, we plotted the comparison between residual values and these two kinds of values, which are shown in Figures 6 and 7.

Figures 5, 6, and 7 depict the average testing process of the MLFN-8 model. All the values shown in the three figures are the average values, from which we can draw a conclusion that the model is accurate and robust.

According to the results presented above, MLFN-8 model is proved to be a suitable and rational model in determining the oil content of rapeseed.

**3.3. Discussion.** There are several previous studies that are relative to the field we studied [12, 17–20]. Gu and Wang [12] analyzed the oil content of rapeseed by multiple linear regression based on near spectral data, which is the chief inspiration

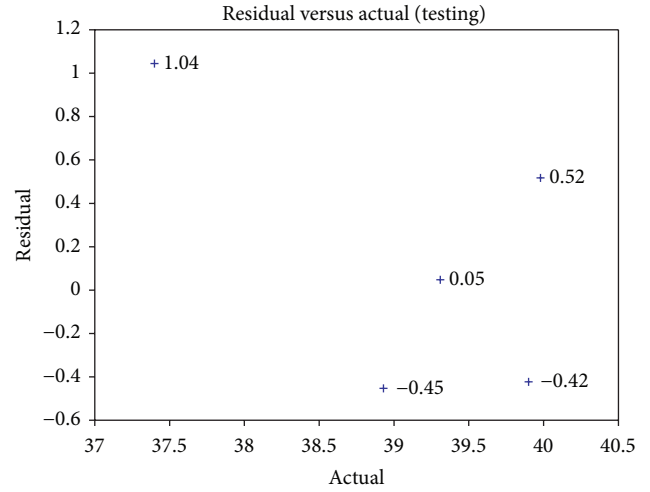


FIGURE 6: Comparison between residual values and actual values during testing process.

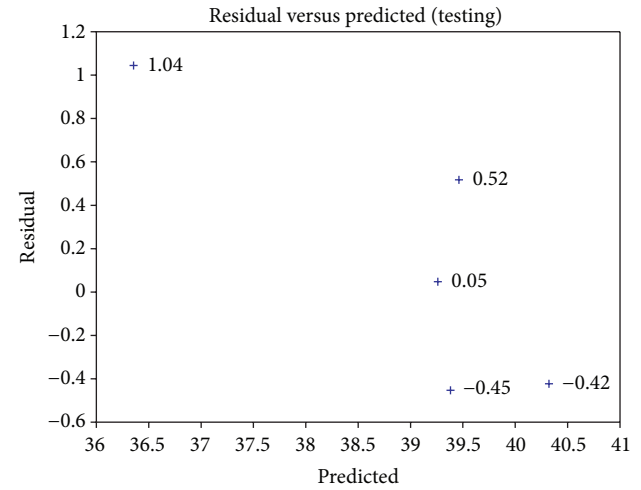


FIGURE 7: Comparison between residual values and predicted values during testing process.

of our work. In contrast, our work has a higher robustness and precision since the core we paid attention to is the well-fitted nonlinear function. Besides, Madsen [17] established a quick determination approach of oil content in rapeseed by a commercial nuclear magnetic resonance spectrometer. Tkachuk [18] utilized a near infrared reflectance technique to determine oil, protein, chlorophyll, and glucosinolate content in whole rapeseed kernels. In addition, Velasco and relative coworkers [19] used near-infrared reflectance spectroscopy to estimate the seed weight, oil content, and fatty acid composition in intact single seeds of rapeseed. Shafii and his coworkers [20] analyzed the interaction effects on the winter rapeseeds yield and oil content. These researches can analyze the oil content and other properties of rapeseeds effectively, which can be seen as the great references. However, these analytical approaches still need complex manual operation and the process is intricate to some extent. Our study has successfully proved that the oil content of rapeseed can

be analyzed by artificial neural networks, which is a quick and easy method that can be calculated automatically by computer.

In the field of food science and analytical chemistry, oil content of rapeseed reveals the yield of the relative products in practical applications. Taking one of the production steps as an example, people should estimate and evaluate the oil content of the rapeseed samples before mass run. Therefore, using artificial neural networks can achieve this step in a high effective way.

## 4. Conclusion

Oil content of rapeseed is a crucial aspect on practical applications of food science and chemistry. In this paper, instead of using traditional analytical methods, we successfully used artificial neural networks (ANNs) method to analyze the oil content of 29 rapeseed samples based on near spectral data with different wavelengths. Results show that the multilayer feed-forward neural networks with 8 nodes (MLFN-8) are the most suitable and reasonable mathematical model during experiments. In future research, we will aim at looking for the explicit nonlinear functions of near spectral data in the analysis of rapeseed's oil content.

## Conflict of Interests

The authors declare that there is no conflict of interests regarding the publication of this paper.

## Acknowledgments

This work was funded by the National Marine Public Welfare Research Project (nos. 201305002 and 201305043) and the Natural Science Foundation of Dalian (no. 2012003219).

## References

- [1] K. Motobayashi, K. Minami, N. Nishi et al., "Hysteresis of potential-dependent changes in ion density and structure of an ionic liquid on a gold electrode: in situ observation by surface-enhanced infrared absorption spectroscopy," *The Journal of Physical Chemistry Letters*, vol. 4, no. 18, pp. 3110–3114, 2013.
- [2] L. V. Brown, K. Zhao, N. King, H. Sobhani, P. Nordlander, and N. J. Halas, "Surface-enhanced infrared absorption using individual cross antennas tailored to chemical moieties," *Journal of the American Chemical Society*, vol. 135, no. 9, pp. 3688–3695, 2013.
- [3] Y.-T. Su, Y.-H. Huang, H. A. Witek, and Y.-P. Lee, "Infrared absorption spectrum of the simplest criegee intermediate  $\text{CH}_2\text{OO}$ ," *Science*, vol. 340, no. 6129, pp. 174–176, 2013.
- [4] J. M. Parnis and K. B. Oldham, "Beyond the Beer-Lambert law: the dependence of absorbance on time in photochemistry," *Journal of Photochemistry and Photobiology A: Chemistry*, vol. 267, pp. 6–10, 2013.
- [5] K. Fuwa and B. L. Vallee, "The physical basis of analytical atomic absorption spectrometry: the pertinence of the Beer-Lambert law," *Analytical Chemistry*, vol. 35, no. 8, pp. 942–946, 1963.
- [6] N. Gupta, "Artificial neural network," *Network and Complex Systems*, vol. 3, no. 1, pp. 24–28, 2013.
- [7] H. Li, X. F. Liu, S. J. Yang et al., "Prediction of polarizability and absolute permittivity values for hydrocarbon compounds using artificial neural networks," *International Journal of Electrochemical Science*, vol. 9, no. 7, pp. 3725–3735, 2014.
- [8] Y. Wang, H.-C. Han, J. Y. Yang, M. L. Lindsey, and Y. Jin, "A conceptual cellular interaction model of left ventricular remodelling post-MI: dynamic network with exit-entry competition strategy," *BMC Systems Biology*, vol. 4, no. 1, article S5, 2010.
- [9] Y. Wang, T. Yang, Y. Ma et al., "Mathematical modeling and stability analysis of macrophage activation in left ventricular remodeling post-myocardial infarction," *BMC Genomics*, vol. 13, supplement 6, article S21, 2012.
- [10] T. Yang, Y. A. Chiao, Y. Wang et al., "Mathematical modeling of left ventricular dimensional changes in mice during aging," *BMC Systems Biology*, vol. 6, supplement 3, article S10, 2012.
- [11] C. H. Aladag, A. Kayabasi, and C. Gokceoglu, "Estimation of pressuremeter modulus and limit pressure of clayey soils by various artificial neural network models," *Neural Computing and Applications*, vol. 23, no. 2, pp. 333–339, 2013.
- [12] W. Z. Gu and Y. X. Wang, "Analysis of rapeseed oil by linear regression using near spectral data," *Journal of the Chinese Cereals and Oils Association*, vol. 10, no. 2, pp. 57–64, 1995 (Chinese).
- [13] Ö. Polat and T. Yıldırım, "FPGA implementation of a General Regression Neural Network: an embedded pattern classification system," *Digital Signal Processing*, vol. 20, no. 3, pp. 881–886, 2010.
- [14] C. H. Chen, T. K. Yao, C. M. Kuo et al., "Evolutionary design of constructive multilayer feedforward neural network," *Journal of Vibration and Control*, vol. 19, no. 16, pp. 2413–2420, 2013.
- [15] S. Mirjalili, S. Z. Mohd Hashim, and H. Moradian Sardroud, "Training feedforward neural networks using hybrid particle swarm optimization and gravitational search algorithm," *Applied Mathematics and Computation*, vol. 218, no. 22, pp. 11125–11137, 2012.
- [16] R. Pahlavan, M. Omid, and A. Akram, "Energy input-output analysis and application of artificial neural networks for predicting greenhouse basil production," *Energy*, vol. 37, no. 1, pp. 171–176, 2012.
- [17] E. Madsen, "Nuclear magnetic resonance spectrometry as a quick method of determination of oil content in rapeseed," *Journal of the American Oil Chemists Society*, vol. 53, no. 7, pp. 467–469, 1976.
- [18] R. Tkachuk, "Oil and protein analysis of whole rapeseed kernels by near infrared reflectance spectroscopy," *Journal of the American Oil Chemists' Society*, vol. 58, no. 8, pp. 819–822, 1981.
- [19] L. Velasco, C. Möllers, and H. C. Becker, "Estimation of seed weight, oil content and fatty acid composition in intact single seeds of rapeseed (*Brassica napus* L.) by near-infrared reflectance spectroscopy," *Euphytica*, vol. 106, no. 1, pp. 79–85, 1999.
- [20] B. Shafii, K. A. Mahler, W. J. Price et al., "Genotype X environment interaction effects on winter rapeseed yield and oil content," *Crop Science*, vol. 32, no. 4, pp. 922–927, 1992.

## Research Article

# Infrared Spectroscopic Study on the Modified Mechanism of Aluminum-Impregnated Bone Charcoal

**Hao Li,<sup>1</sup> Yufan Yang,<sup>2</sup> Shuangjun Yang,<sup>3</sup> Anpu Chen,<sup>1</sup> and Dazuo Yang<sup>4</sup>**

<sup>1</sup> College of Chemistry, Sichuan University, Chengdu, Sichuan 610064, China

<sup>2</sup> West China School of Public Health, Sichuan University, Sichuan 610064, China

<sup>3</sup> College of Light Industry, Sichuan University, Chengdu, Sichuan 610064, China

<sup>4</sup> College of Life Science and Technology, Dalian University of Technology, Dalian 116021, China

Correspondence should be addressed to Hao Li; lihao\_chem\_92@hotmail.com

Received 16 May 2014; Accepted 2 June 2014; Published 22 June 2014

Academic Editor: Qingrui Zhang

Copyright © 2014 Hao Li et al. This is an open access article distributed under the Creative Commons Attribution License, which permits unrestricted use, distribution, and reproduction in any medium, provided the original work is properly cited.

Fluoride contamination in drinking water is a prominent and widespread problem in many parts of the world. Excessive ingestion of fluoride through water can lead to the high risk of fluorosis in human body. Bone charcoal, with the principal active component of hydroxyapatite, is a frequently used adsorbent for fluoride removal. Many laboratory experiments suggest that the aluminum-impregnated bone charcoal is an effective adsorbent in defluoridation. However, the mechanisms underlying this modification process are still not well understood, which in turn greatly impedes the further studies on other different modified adsorbents. To address this issue, we used the infrared spectroscopy to examine the bone charcoal and the aluminum-impregnated bone charcoal, respectively. The comparative results show that the -OH peak of infrared spectroscopy has been intensified after modification. This significant change helped speculate the modified mechanism of the aluminum-impregnated bone charcoal. In addition, it is found that the hydroxide ion dissociates from hydroxyapatite in the modification process. Such finding implies that the tetrahydroxoaluminate can be combined with the hydroxyapatite and the aluminum ion can be impregnated onto the bone charcoal surface.

## 1. Introduction

Fluoride is widely distributed in nature, which mainly exists in lithosphere, hydrosphere, biosphere, and atmosphere [1, 2]. Most fluorides are soluble, even the lowest solubility of calcium fluoride can reach 40 mg/L in normal condition [3]. The soluble fluorides in rocks can dissolve in water, which are the main sources of the fluorides in fresh water. Therefore, humans obtain fluorides largely from drinking water [4]. There exists about 2 to 3 g (commonly 2.6 g) fluorine in a healthy adult body, 90% of which distributes in bones and teeth [5, 6]. A trace of fluorine is useful to prevent sapromyces but excessive amount tends to be harmful [7, 8]. It is supposed to be poisonous if the intake of fluorine is higher than 4 mg/d; therefore, people are more likely to develop fluorosis of bone when the amount of fluorine in drinking water is more than 4 ppm [9].

As the fluorine-containing substances are increasingly applied in industry, the amount of the fluorine-containing

wasted water tends to become higher. Purification and defluoridation of high-fluorinated drinking water have drawn more and more attention. Conventional methods of defluoridation are precipitation and adsorption [10–13]. Adsorption method is mainly used in the deep disposal of low fluorine-containing waste water and natural water. Because the adsorption method of disposing fluorine-containing waste water has the advantages of lower cost and higher removal rate [14], the modification of traditional fluorine removal agent and the research of new fluorine removal materials are popular topic in relative area [15–17]. Traditional fluorine removal agents include alumina, natural zeolite, and rare earth while the new adsorbent with good adsorption effects is calcium aluminate slag, aluminum sulfate modified bamboo charcoal, and bone charcoal [18–23]. In the midst of these adsorbents, bone charcoal is now considered to be one of the most recommendatory adsorbents in defluoridation since World Health Organization regarded bone charcoal as

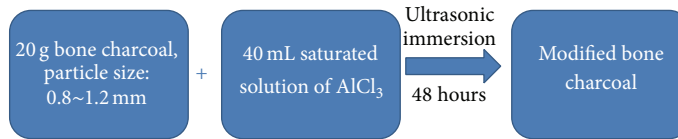
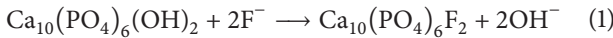


FIGURE 1: Manufacturing approach of aluminum-impregnated bone charcoal.

the high-performance absorbent of fluorion in undeveloped regions [24]. Based on this reason, we aimed at studying the defluoridation effect of bone charcoal and finding out the mechanism of the modification and adsorption.

Bone charcoal is a porous, black, granular material produced by charring animal bones [25]. It is made up of hydroxyapatite (57–80%), calcium carbonate (6–10%), and activated carbon (7–10%). In the development of purification, bone charcoal was primarily used for filtration and decolorisation, which can also adsorb a large quantity of pollutants like pigments as well as fluorine from water [26]. Based on the absorption theory, the hydroxylapatite in bone chars can be used to remove fluoride and metal ions from water, making it useful for the treatment of drinking supplies.

Adsorption is a separation method with the equilibrium principle. The main components of bone charcoal are hydroxyapatite. The mechanism of the removal of fluorine is mainly the adsorption and ion exchange reaction, which is shown as follows:



Previous research [27] reported that, being immersed in aluminum solution for certain temporal, bone charcoal can be modified. The aluminum can impregnate onto the surface of bone charcoal, improving the effect of the defluoridation, which is the main core of our work. However, although this novel modified approach to optimize the performance of aluminum-impregnated bone charcoal in defluoridation has been discovered, the mechanism of the modification is still undefined. It is undoubtedly a huge impediment for us to explore the further studies of modified adsorbent. Therefore, we paid our attention to construct a probable reaction during the modified process in order to resolve this crucial problem.

Infrared spectroscopy is one of the most common analytic techniques in material characterization [28]. It is the spectroscopy that deals with the infrared region of the electromagnetic spectrum, with longer wavelength and lower frequency compared to the visible light. It covers a range of techniques, mostly based on absorption spectroscopy. As with all spectroscopic techniques, it can be used to study chemicals and relative substances [29]. In recent years, there are more and more explorations of reaction mechanism detected by spectroscopic methods [30–37]. Green and his coworkers [30] obtained the information of dual catalytic sites during oxidation of CO on Au/TiO<sub>2</sub> catalyst by spectroscopic observation. Roithová [31] concluded the characterization approaches of reaction intermediates by ion spectroscopy. Acik and his coworkers [32] have detected the role of oxygen during thermal reduction of graphene oxide using infrared absorption spectroscopy. Black and his coworkers [33] used spectroscopic method to screen

for superoxide reactivity in Li–O<sub>2</sub> batteries. Chen and his coworkers [34] used FT-IR spectroscopy as a part of the instruments to determine mechanisms in water-gas-shift reaction on Au/CeO<sub>2</sub>. Huang and his coworkers [35] utilized surface-enhanced Raman spectroscopy to study p-aminothiophenol. Costa and his coworkers [36] used relative spectroscopic methods to determine the clues to the internal barrier layer capacitance mechanism. Xu and his coworkers [37] clarified the thermal deterioration mechanism of bio-oil pyrolyzed from rice husk using Fourier transform infrared spectroscopy. The common point of the studies listed above is that all of them utilized the relative spectroscopic approaches to determine or infer the mechanism of the chemical reaction and process, proving that the spectroscopy is an available approach to estimate the mechanism of chemical reactions. What is worth mentioning is that all of these listed researches were published in the recent three years, showing that using spectroscopic approaches to establish the conjecture of chemical reactions is becoming a popular method among relative academic fields. Since detecting the modified mechanism of aluminum-impregnated bone charcoal and calculating the main reaction process by the modeling approach are difficult, in our study, we innovatively used infrared spectroscopy to obtain the infrared spectrums of the modified bone charcoal and the unmodified one, so that the mechanism can be inferred during the change of the modification.

## 2. Materials and Methods

**2.1. Material Source and Treatment.** Raw materials of bone charcoal in our experiments were supplied by Langfang Huaya Water Treatment Ltd., Hebei Province, China. All the bone charcoals were sieved by screens, of which the granularity is approximately from 0.8 to 1.2 mm. Because of the adsorption mechanism shown in (1), alkaline environment of solution can provide a better effect of defluoridation; thus to ensure the good adsorbability materials were firstly immersed in saturated solution of sodium hydrate for 12 hours and then immersed in deionized water for 12 hours. After repetitive scrubbing, these raw bone charcoals were stoved by electric thermostatic drying oven under the temperature of 120°C. Afterwards, the bone charcoals were sealed in the desiccator.

The manufacturing approach of aluminum-impregnated bone charcoal in our study met the standards of modified approaches created by previous studies. 20 g bone charcoal was immersed in 40 mL saturated solution of AlCl<sub>3</sub>, and the modification system was immersed in the ultrasonic oscillator, so that aluminum ion can impregnate onto the bone charcoal better. The modification procedure is shown in Figure 1.

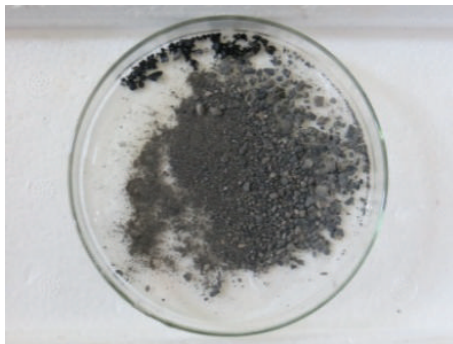


FIGURE 2: Aluminum-impregnated bone charcoal.

To guarantee the modification, we chose the saturated solution so the aluminum ion can impregnate onto the bone charcoal during the process of ultrasonic immersion. The dried aluminum-impregnated bone charcoal is shown as Figure 2.

The aluminum-impregnated bone charcoal takes on a color of silvery white and grey, while the unmodified bone charcoal is atrous. The change of macroscopic features can be observed obviously from this characteristic.

For comparison, we also designed a series of other modified bone charcoals. After the testing results, ferri-impregnated bone charcoal and magnesium-impregnated bone charcoal are also considered to be good modified adsorbents, with high removal rates of fluorinon. Therefore, we used these two modified bone charcoals together with the blank control group (those ultrasonic immersed in the saturated solution of sodium hydroxide) as the control groups in the analysis of adsorption isotherm (see Section 3.1: *Adsorption Isotherm*).

**2.2. Preparation of Fluoride Solution.** The sodium fluoride ( $\text{NaF}$ , AR) with deionized water configured to stock fluorinon solution of 1.0 g/L. Then it was diluted to be 5.0 mg/L, as to be used for the follow-up test. This actual initial mass concentration was determined by fluoride selective electrode.

**2.3. Adsorption Isotherms.** To test the rationality of choosing aluminum-impregnated bone char as the object of study, we chose ferri-impregnated bone charcoal, aluminum-impregnated bone charcoal, and magnesium-impregnated bone charcoal as the main objects of studying the adsorption isotherms. All the metal-modified bone charcoals were modified under the same conditions and procedures. In addition, those raw bone charcoals immersed in the saturated solution of sodium hydroxide ultrasonically were taken as the blank control group. In the midst of these four types of bone charcoal, each kind of bone charcoals was divided into 6 groups, respectively: 0.2, 0.4, 0.8, 1.2, 1.6, and 2.0 g. After three-hour defluoridation, adsorption isotherms were developed during sample analysis.

### 3. Results and Discussion

**3.1. Adsorption Isotherm.** Previous studies show that the adsorption process of bone charcoal is corresponded with

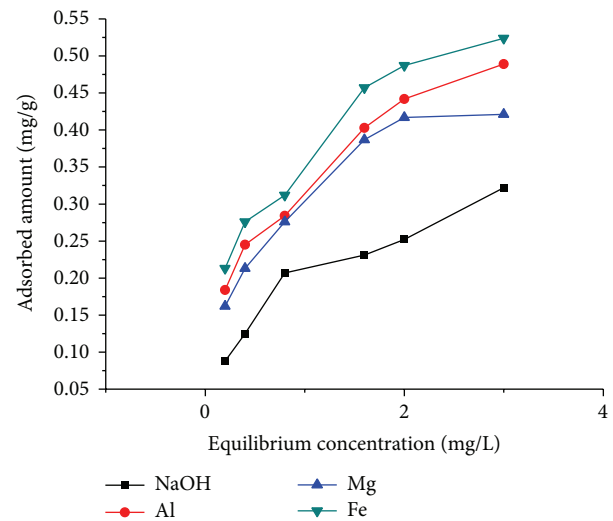


FIGURE 3: Adsorption isotherms of different modified bone charcoals in defluoridation.

Langmuir isotherm [38–41], which is an ordinary adsorption process of general adsorbents. For a better comparison, several modification experiments with different immersed ions were done and we obtained the adsorption isotherms for different ion-modified bone charcoal in defluoridation, which is shown in Figure 3 (blank control group: bone charcoal immersed in saturated solution of sodium hydrate).

Results shown in Figure 3 indicate the descending order of the corresponding defluoridation efficiency as follows: ferri-impregnated bone charcoal, aluminum-impregnated bone charcoal, magnesium-impregnated bone charcoal, and sodium hydrate immersed bone charcoal. Nevertheless, our experimental results are quite different from Shen's previous study [42]. In Shen's study, the defluoridation effect of aluminum bone charcoal is higher than those of ferri-impregnated bone charcoal. However, due to the different source of raw bone charcoals and the precise procedure of our modification experiments, we considered our results are accurate and reliable.

Although ferri-impregnated bone charcoal had the best defluoridation effect in our experiments, however, ferri ion is toxic and harmful to human body, which means that it cannot be applied to the practical applications [43]. Therefore, aluminum-impregnated bone charcoal is still the most rational option for defluoridation. Besides, results also prove that the aluminum-impregnated bone charcoal of our research is effective and can be used for further studies of the modified mechanism.

**3.2. Infrared Spectroscopic Study on Aluminum-Impregnated Bone Charcoal.** In order to study the modified mechanism of aluminum-impregnated bone charcoal, two samples from the same raw bone charcoal were determined by infrared spectrum. Figure 4 shows the infrared spectrum of raw bone charcoal without modification, while Figure 5 shows the infrared spectrum of aluminum-impregnated bone charcoal.

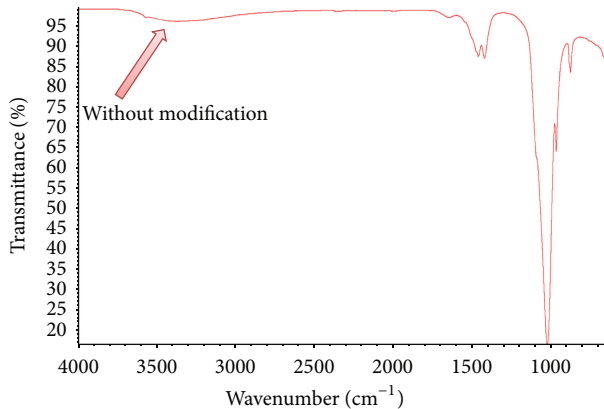


FIGURE 4: Infrared spectrum of bone charcoal without modification.

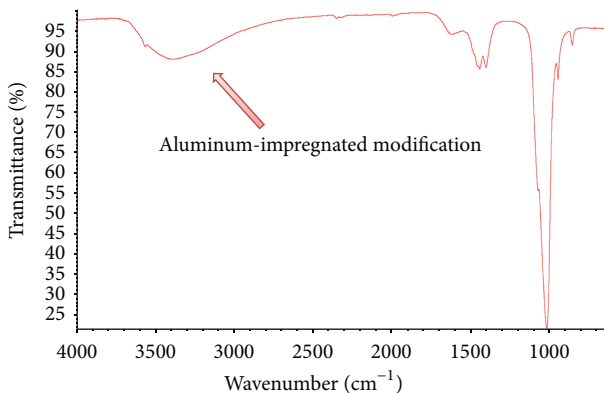


FIGURE 5: Infrared spectrum of aluminum-impregnated bone charcoal.

Figures 4 and 5 show the infrared spectrums of the two samples of bone charcoal, respectively. It is obvious that there are some differences of the peaks between the two infrared spectrums. The arrow heads in Figures 4 and 5 are the indexes of these main differences. In order to present these differences in a more evident way, Figures 4 and 5 were overlapped into the one picture, which is shown in Figure 6.

Figure 6 depicts an interesting phenomenon: after modification, in the stretching vibration area of hydrogen bond held together with -OH, intensity of the typical absorption band of hydroxyapatite ( $3400 \text{ cm}^{-1}$  nearby) [44, 45] has risen obviously. In contrast, other peaks have tiny significant change. This strange phenomenon attracted our attention: under the theoretically dry condition, how to explain this bizarre change of the peak?

To explain the interesting phenomenon presented in Figure 6, we should consider the possible reaction between aluminum ion and bone charcoal at first. One of the most striking explanations of this phenomenon is that anion exchange has happened during the modified process. Hydroxide ion is dissociated from Ca-OH during the anion exchange, elevating the PH value. Under this circumstance, aluminum ion can combine with hydroxyl ion, forming tetrahydroxoaluminate ion. Based on this conjecture, the

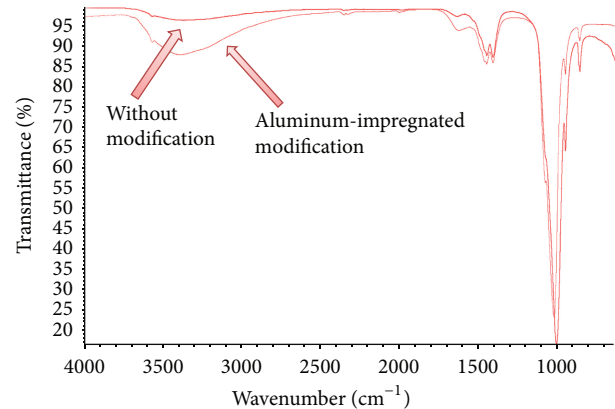
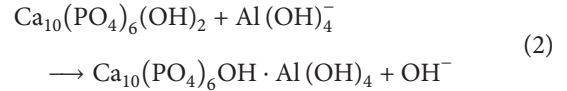
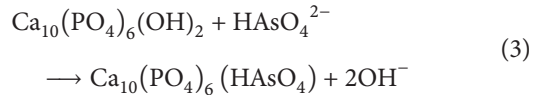


FIGURE 6: The overlapped infrared spectrum of Figures 4 and 5.

modified mechanism is constructed as the reaction shown as follows:

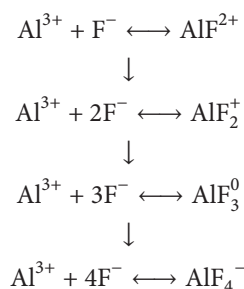


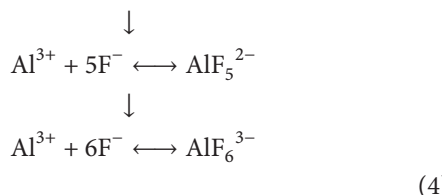
In previous study, Chen and her coworkers [46] offered an explanation for the mechanism of removal of arsenic (V) using bone charcoal as the adsorbent:



Compared to our conjecture of the modified mechanism, Chen's research indicates that bone charcoal can arise from the ion exchange reaction during the adsorption, from which we can infer that the mechanism of adsorption and modification is extremely similar. In other words, during the modification process, aluminum ion can be "adsorbed" onto the surface of bone charcoal, and we deduce that this combination is stable and thus the aluminum can impregnate firmly.

As for the adsorption mechanism of aluminum-impregnated bone charcoal, Dong [47] offered an explanation for the high performance of the modified bone charcoal. This explanation discusses that because the aluminum ion has the unoccupied orbital, there exists the complex reaction between aluminum ion and fluorion, and the maximum coordination number is considered to be six:





Dong's explanation of aluminum-impregnated bone charcoal seems reasonable. However, according to our study, some of the unoccupied orbitals of the aluminum impregnated onto the bone charcoal had actually been occupied during the modified process. Therefore, the average maximum coordination number of aluminum in the aluminum-impregnated bone charcoal may be less than six. Based on our opinion, the adsorption mechanism explained by Dong [47] is not totally perfect, which may overestimate the adsorption effects of aluminum-impregnated bone charcoal. Our research indicates that, in the process of defluoridation, aluminum-impregnated bone charcoal is undergoing two kinds of adsorption process. On the one hand, hydroxyapatite in bone charcoal is undergoing the adsorption process as (1) presents; on the other hand, aluminum which has been impregnated onto the bone charcoal's surface is undergoing the process of coordination reaction: aluminum combines with fluorine in a stable way.

According to previous studies [48–51], some similar researches on determining the mechanisms of different adsorbents were used to make comparison. Namasivayam and Kavitha [48] detected the adsorption interactions of dye, phenol, and chlorophenol onto coir pith carbon from aqueous solution using various detection techniques. Nadeem and his coworkers [49] detected the modified carbon adsorbents by SEM. In addition, Ahmad and Kumar [50] also utilize SEM to detect the adsorption information of amaranth dye onto alumina reinforced polystyrene. Gupta and his coworkers [51] detected the details about banana pseudostem fiber in the removal of harmful malachite green dye using Fourier transform infrared spectroscopy, scanning electron microscope, and X-ray diffractometer. These studies are advanced in detecting the properties of adsorbents which can seem as the excellent references. Nevertheless, these researches did not detect the adsorption processes of the modification mechanisms of the studied adsorbents by infrared spectroscopic methods. Hence, our research has successfully made up the blank of this area. According to the comparison, using infrared spectroscopy to detect and infer the modification mechanism of bone charcoal is proved to be effective and available.

#### 4. Conclusion

Fluoride contamination is a prominent and widespread problem in many parts of the world. Such contamination in drinking water is mostly natural and unpreventable that affects the health for human beings. There is a common agreement that drinking fluoridated water can lead to a high risk of fluorosis in human body. To reduce the risk, metal-impregnated bone charcoal has been frequently used as an ideal material for fluoride removal. In this

study, the defluoridation efficiency of the bone charcoals modified by different metal ions was investigated. Their adsorption isotherms help highlighting the descending order of the corresponding defluoridation efficiency as follows: ferri-impregnated bone charcoal, aluminum-impregnated bone charcoal, magnesium-impregnated bone charcoal, and sodium hydrate immersed bone charcoal. Considering the potential toxicity of ferri-impregnated bone charcoal, the aluminum-impregnated bone charcoal was adapted as the most rational adsorbent for defluoridation in our experiments. Its modified mechanism was further successfully explored using the infrared spectroscopy. The strengthening of the hydroxyl peak intensified in infrared spectrum was examined. The results imply that the probable modified reaction is ion exchange and tetrahydroxoaluminate can combine with hydroxyapatite, which in turn suggests that aluminum ion can be impregnated onto the surface of the bone charcoal. In future study, more attention deserves to be paid to the adsorption of lead and arsenic as some advanced researches provide great inspirations on the topic [46, 52–55].

#### Conflict of Interests

The authors declare that there is no conflict of interests regarding the publication of this paper.

#### Authors' Contribution

Hao Li and Yufan Yang contributed equally to this paper.

#### Acknowledgment

This work was supported by the Fund for Fostering Talents in Basic Science of the National Natural Science (Grant no. J1103315).

#### References

- [1] P. J. Riordan, "Fluoride supplements for young children: an analysis of the literature focusing on benefits and risks," *Community Dentistry and Oral Epidemiology*, vol. 27, no. 1, pp. 72–83, 1999.
- [2] R. C. Maheshwari, "Fluoride in drinking water and its removal," *Journal of Hazardous Materials*, vol. 137, no. 1, pp. 456–463, 2006.
- [3] G. Rolla and E. Saxegaard, "Critical evaluation of the composition and use of topical fluorides, with emphasis on the role of calcium fluoride in caries inhibition," *Journal of Dental Research*, vol. 69, pp. 780–785, 1990.
- [4] M. N. Anjum, M. T. Shah, F. Ali et al., "Geochemical studies of fluoride in drinking water of union council ganderi, district nowshera, Khyber Pakhtunkhwa, Pakistan," *World Applied Sciences Journal*, vol. 27, no. 5, pp. 632–636, 2013.
- [5] D. Taylor, J. G. Hazenberg, and T. C. Lee, "Living with cracks: damage and repair in human bone," *Nature Materials*, vol. 6, no. 4, pp. 263–268, 2007.
- [6] H. Yamamoto, Y. Iwami, T. Unezaki, Y. Tomii, and S. Ebisu, "Fluoride uptake in human teeth from fluoride-releasing restorative

- material in vivo and in vitro: two-dimensional mapping by EPMA-WDX," *Caries Research*, vol. 35, no. 2, pp. 111–115, 2001.
- [7] K. K. Cheng, I. Chalmers, and T. A. Sheldon, "Adding fluoride to water supplies," *British Medical Journal*, vol. 335, no. 7622, pp. 699–702, 2007.
- [8] X. Zhan, H. Xu, and G. Li, "The toxicity of sodium fluoride on pulmonary arterial smooth muscle cell proliferation," *Chinese Journal of Control of Endemic Disease*, vol. 6, p. 11, 2003.
- [9] Y. Kim and F. P. Gabbai, "Cationic boranes for the complexation of fluoride ions in water below the 4 ppm maximum contaminant level," *Journal of the American Chemical Society*, vol. 131, no. 9, pp. 3363–3369, 2009.
- [10] N. Parthasarathy, J. Buffle, and W. Haerdi, "Combined use of calcium salts and polymeric aluminium hydroxide for defluoridation of waste waters," *Water Research*, vol. 20, no. 4, pp. 443–448, 1986.
- [11] A. K. Yadav, C. P. Kaushik, A. K. Haritash, A. Kansal, and N. Rani, "Defluoridation of groundwater using brick powder as an adsorbent," *Journal of Hazardous Materials*, vol. 128, no. 2-3, pp. 289–293, 2006.
- [12] S. Jagtap, M. K. N. Yenkie, N. Labhsetwar, and S. Rayalu, "Defluoridation of drinking water using chitosan based mesoporous alumina," *Microporous and Mesoporous Materials*, vol. 142, no. 2-3, pp. 454–463, 2011.
- [13] P. Loganathan, S. Vigneswaran, J. Kandasamy, and R. Naidu, "Defluoridation of drinking water using adsorption processes," *Journal of Hazardous Materials*, vol. 248–249, no. 1, pp. 1–19, 2013.
- [14] A. Bhatnagar, E. Kumar, and M. Sillanpää, "Fluoride removal from water by adsorption—a review," *Chemical Engineering Journal*, vol. 171, no. 3, pp. 811–840, 2011.
- [15] Y. Sun, Q. Fang, J. Dong, X. Cheng, and J. Xu, "Removal of fluoride from drinking water by natural stilbite zeolite modified with Fe(III)," *Desalination*, vol. 277, no. 1-3, pp. 121–127, 2011.
- [16] Y. Nie, C. Hu, and C. Kong, "Enhanced fluoride adsorption using Al (III) modified calcium hydroxyapatite," *Journal of Hazardous Materials*, vol. 233–234, pp. 194–199, 2012.
- [17] Q. Zhang, Q. Du, T. Jiao et al., "Rationally designed porous polystyrene encapsulated zirconium phosphate nanocomposite for highly efficient fluoride uptake in waters," *Scientific Reports*, vol. 3, pp. 1–9, 2013.
- [18] E. Kumar, A. Bhatnagar, U. Kumar, and M. Sillanpää, "Defluoridation from aqueous solutions by nano-alumina: characterization and sorption studies," *Journal of Hazardous Materials*, vol. 186, no. 2-3, pp. 1042–1049, 2011.
- [19] L. Gómez-Hortigüela, A. B. Pinar, J. Pérez-Pariente et al., "Ion-exchange in natural zeolite stilbite and significance in defluoridation ability," *Microporous and Mesoporous Materials*, vol. 193, pp. 93–102, 2014.
- [20] A. M. Raichur and M. Jyoti Basu, "Adsorption of fluoride onto mixed rare earth oxides," *Separation and Purification Technology*, vol. 24, no. 1-2, pp. 121–127, 2001.
- [21] M.-J. Bai and Y.-Y. Chu, "Removal of fluorine ions from wastewater using calcium aluminate slag," *Environmental Science & Technology*, vol. 9, no. 34, pp. 117–120, 2008.
- [22] Q. Zhang and G. Wang, "Research on removing effects of the bamboo-carbon for fluoride from drink water," *Guangdong Weiliang Yuansu Kexue*, vol. 12, no. 3, p. 63, 2005.
- [23] C. K. Rojas-Mayorga, A. Bonilla-Petriciolet, I. A. Aguayo-Villarreal et al., "Optimization of pyrolysis conditions and adsorption properties of bone char for fluoride removal from water," *Journal of Analytical and Applied Pyrolysis*, vol. 104, pp. 10–18, 2013.
- [24] J. K. Fawell, *Fluoride in Drinking-Water*, World Health Organization, 2006.
- [25] M. E. Kaseva, "Optimization of regenerated bone char for fluoride removal in drinking water: a case study in Tanzania," *Journal of Water and Health*, vol. 4, no. 1, pp. 139–147, 2006.
- [26] F. Ospitali, D. C. Smith, and M. Lorblanchet, "Preliminary investigations by Raman microscopy of prehistoric pigments in the wall-painted cave at Roucadour, Quercy, France," *Journal of Raman Spectroscopy*, vol. 37, no. 10, pp. 1063–1071, 2006.
- [27] N. A. Medellin-Castillo, R. Leyva-Ramos, R. Ocampo-Perez et al., "Adsorption of fluoride from water solution on bone char," *Industrial and Engineering Chemistry Research*, vol. 46, no. 26, pp. 9205–9212, 2007.
- [28] B. C. Smith, *Fundamentals of Fourier Transform Infrared Spectroscopy*, CRC Press, Boca Raton, Fla, USA, 2011.
- [29] C. Krafft and V. Sergo, "Biomedical applications of Raman and infrared spectroscopy to diagnose tissues," *Spectroscopy*, vol. 20, no. 5-6, pp. 195–218, 2006.
- [30] I. X. Green, W. Tang, M. Neurock, and J. T. Yates Jr., "Spectroscopic observation of dual catalytic sites during oxidation of CO on a Au/TiO<sub>2</sub> catalyst," *Science*, vol. 333, no. 6043, pp. 736–739, 2011.
- [31] J. Roithová, "Characterization of reaction intermediates by ion spectroscopy," *Chemical Society Reviews*, vol. 41, no. 2, pp. 547–559, 2012.
- [32] M. Acik, G. Lee, C. Mattevi et al., "The role of oxygen during thermal reduction of graphene oxide studied by infrared absorption spectroscopy," *The Journal of Physical Chemistry C*, vol. 115, no. 40, pp. 19761–19781, 2011.
- [33] R. Black, S. H. Oh, J.-H. Lee, T. Yim, B. Adams, and L. F. Nazar, "Screening for superoxide reactivity in Li-O<sub>2</sub> batteries: effect on Li<sub>2</sub>O<sub>2</sub>/LiOH crystallization," *Journal of the American Chemical Society*, vol. 134, no. 6, pp. 2902–2905, 2012.
- [34] Y. Chen, H. Wang, R. Burch, C. Hardacre, and P. Hu, "New insight into mechanisms in water-gas-shift reaction on Au/CeO<sub>2</sub>(111): a density functional theory and kinetic study," *Faraday Discussions*, vol. 152, pp. 121–133, 2011.
- [35] Y.-F. Huang, D.-Y. Wu, H.-P. Zhu et al., "Surface-enhanced Raman spectroscopic study of p-aminothiophenol," *Physical Chemistry Chemical Physics*, vol. 14, no. 24, pp. 8485–8497, 2012.
- [36] S. I. R. Costa, M. Li, J. R. Frade, and D. C. Sinclair, "Modulus spectroscopy of CaCu<sub>3</sub>Ti<sub>4</sub>O<sub>12</sub> ceramics: clues to the internal barrier layer capacitance mechanism," *RSC Advances*, vol. 3, no. 19, pp. 7030–7036, 2013.
- [37] F. Xu, Y. Xu, R. Lu, G.-P. Sheng, and H.-Q. Yu, "Elucidation of the thermal deterioration mechanism of bio-oil pyrolyzed from rice husk using fourier transform infrared spectroscopy," *Journal of Agricultural and Food Chemistry*, vol. 59, no. 17, pp. 9243–9249, 2011.
- [38] G. Ghanizadeh and G. Asgari, "Adsorption kinetics and isotherm of methylene blue and its removal from aqueous solution using bone charcoal," *Reaction Kinetics, Mechanisms and Catalysis*, vol. 102, no. 1, pp. 127–142, 2011.
- [39] J. A. Wilson, I. D. Pulford, and S. Thomas, "Sorption of Cu and Zn by bone charcoal," *Environmental Geochemistry and Health*, vol. 25, no. 1, pp. 51–56, 2003.
- [40] M. T. Ghaneian, G. Ghanizadeh, M. T. H. Alizadeh et al., "Equilibrium and kinetics of phosphorous adsorption onto bone charcoal from aqueous solution," *Environmental Technology*, vol. 35, no. 7, pp. 882–890, 2014.

- [41] C. W. Cheung, C. K. Chan, J. F. Porter, and G. Mckay, "Combined diffusion model for the sorption of cadmium, copper, and zinc ions onto bone char," *Environmental Science & Technology*, vol. 35, no. 7, pp. 1511–1522, 2001.
- [42] X. W. Shen, *Research on the Defluoridation of Bone Charcoal in Low Concentration Wastewater*, Jiangxi University of Technology, 2011.
- [43] B. Halliwell, "Antioxidants in human health and disease," *Annual Review of Nutrition*, vol. 16, pp. 33–50, 1996.
- [44] J. G. Wu, *Modern FTIR Technology and Application*, vol. 35, Science and Technology Literature Press, Beijing, China, 1st edition, 1994.
- [45] Y. Mikhaylova, G. Adam, L. Häussler, K.-J. Eichhorn, and B. Voit, "Temperature-dependent FTIR spectroscopic and thermoanalytic studies of hydrogen bonding of hydroxyl (phenolic group) terminated hyperbranched aromatic polyesters," *Journal of Molecular Structure*, vol. 788, no. 1–3, pp. 80–88, 2006.
- [46] Y.-N. Chen, L.-Y. Chai, and Y.-D. Shu, "Arsenic(V) removal from drinking water by bone char," *Journal of Central South University (Science and Technology)*, vol. 39, no. 2, pp. 279–283, 2008 (Chinese).
- [47] S. M. Dong, *Research on Defluoridation in Water and Soil System the Removal Mechanism*, Changan University, 2004.
- [48] C. Namasivayam and D. Kavitha, "IR, XRD and SEM studies on the mechanism of adsorption of dyes and phenols by coir pith carbon from aqueous phase," *Microchemical Journal*, vol. 82, no. 1, pp. 43–48, 2006.
- [49] M. Nadeem, A. Mahmood, S. A. Shahid, S. S. Shah, A. M. Khalid, and G. McKay, "Sorption of lead from aqueous solution by chemically modified carbon adsorbents," *Journal of Hazardous Materials*, vol. 138, no. 3, pp. 604–613, 2006.
- [50] R. Ahmad and R. Kumar, "Adsorption of amaranth dye onto alumina reinforced polystyrene," *Clean—Soil, Air, Water*, vol. 39, no. 1, pp. 74–82, 2011.
- [51] N. Gupta, A. K. Kushwaha, and M. C. Chatopadhyaya, "Adsorption of brilliant green dye from aqueous solution by banana pseudo-stem fibers," *Journal of the Indian Chemical Society*, vol. 89, no. 7, pp. 891–902, 2012.
- [52] Q. Zhang, Q. Du, M. Hua, T. Jiao, F. Gao, and B. Pan, "Sorption enhancement of lead ions from water by surface charged polystyrene-supported nano-zirconium oxide composites," *Environmental Science & Technology*, vol. 47, no. 12, pp. 6536–6544, 2013.
- [53] Q. Peng, J. Guo, Q. Zhang et al., "Unique lead adsorption behavior of activated hydroxyl group in two-dimensional titanium carbide," *Journal of the American Chemical Society*, vol. 136, no. 11, pp. 4113–4116, 2014.
- [54] M. B. Baskan and A. Pala, "Batch and fixed-bed column studies of arsenic adsorption on the natural and modified clinoptilolite," *Water, Air, & Soil Pollution*, vol. 225, no. 1, pp. 1–10, 2014.
- [55] K. Kwok, L. F. Koong, G. Chen et al., "Mechanism of arsenic removal using chitosan and nanochitosan," *Journal of Colloid and Interface Science*, vol. 416, pp. 1–10, 2014.

## Research Article

# Spectral Separation for Multispectral Image Reproduction Based on Constrained Optimization Method

Bangyong Sun,<sup>1,2</sup> Han Liu,<sup>2</sup> and Shisheng Zhou<sup>1</sup>

<sup>1</sup> School of Printing and Packing Engineering, Xi'an University of Technology, Xi'an 710048, China

<sup>2</sup> School of Automation and Information Engineering, Xi'an University of Technology, Xi'an 710048, China

Correspondence should be addressed to Bangyong Sun; sunbangyong@xaut.edu.cn

Received 11 May 2014; Accepted 2 June 2014; Published 22 June 2014

Academic Editor: Qingrui Zhang

Copyright © 2014 Bangyong Sun et al. This is an open access article distributed under the Creative Commons Attribution License, which permits unrestricted use, distribution, and reproduction in any medium, provided the original work is properly cited.

The constrained optimization method is employed to calculate the colorant values of the multispectral images. Because the spectral separation from the 31-dimensional spectral reflectance to low dimensional colorant values is very complex, an inverse process based on spectral Neugebauer model and constrained optimization method is performed. Firstly, the spectral Neugebauer model is applied to predict the colorants' spectral reflectance values, and it is modified by using the Yule-Nielsen  $n$ -value and the effective area coverages. Then, the spectral reflectance root mean square (RRMS) error is established as the objective function for the optimization method, while the colorant values are constrained to 0~1. At last, when the nonlinear constraints and related parameters are set appropriately, the colorant values are accurately calculated for the multispectral images corresponding to the minimum RRMS errors. In the experiment, the colorant errors of the cyan, magenta and yellow inks are all below 2.5% and the average spectral error is below 5%, which indicate that the precision of the spectral separation method in this paper is acceptable.

## 1. Introduction

The objective of color reproduction is to obtain the same visual perception of the original images, and it is mainly implemented based on the metameric reproduction principle [1, 2]. However, when the illuminants or observers change, the color consistency between the original and the hard copy is hardly maintained. Thus, in many high-accuracy reproduction areas, the originals are represented as multispectral images, not the common RGB/CMYK images [3, 4]. If the image's spectral information is reproduced correctly, the hard copy will look the same as the original under different illuminants.

Within the multispectral image reproduction workflow, after the spectral reconstruction [5–7] and gamut mapping process [8–10], the image pixel's spectral values should be precisely converted into ink values for printing, while the conversion process is often defined as spectral separation [11, 12]. For most printers, the primary inks are cyan, magenta, yellow, and black; hence the input spectral images'

reflectances are transformed to CMYK values during spectral separation.

In fact, as most of the multispectral image pixels are 31-dimensional, it is difficult to calculate the colorant values from the spectral data straightly. Most of the spectral separation processes are based on the spectral predication models and iteration methods. The spectral predication models can be used to calculate different ink combinations' spectral values. And the iteration of the separation process will stop when the image pixel's spectral matches with the predicated spectral. Several spectral predication models can be used for spectral separation, such as multiinterpolation techniques [13], spectral Neugebauer model [14, 15], Yule-Nielsen model [16, 17], and Kubelka-Munk model [18, 19]. Because the spectral Neugebauer model uses less sample colors and often generates acceptable accuracy, it is widely applied to the spectral separation process. However, there are many factors which influence the separation accuracy. In this paper, the spectral Neugebauer model is modified and a non-linear optimization method is analyzed, in order to improve

the multispectral image's spectral separation accuracy for CMYK printers.

## 2. Modification of Spectral Neugebauer Model

*2.1. The Expression of Spectral Neugebauer Model.* The spectral Neugebauer model is a halftone color predication model, which calculates the spectral reflectance values within the visual wavelength from printers' colorant space. In fact it is developed from Murray-Davies model which is a monochromatic model [20]. When a primary ink is printed on the paper, if the spectral reflectance of the solid and substrate are represented as  $R_{\lambda,t}$  and  $R_{\lambda,s}$ , respectively, and the patch's dot area is given, then its reflectance values  $\hat{R}_{\lambda}$  can be predicted by using Murray-Davies model as follows:

$$\hat{R}_{\lambda} = a_t R_{\lambda,t} + (1 - a_t) R_{\lambda,s}, \quad (1)$$

where  $\lambda$  is the wavelength of light within 400 nm–700 nm and  $a_t$  is the fractional dot area of the printed patch.

When the monochrome Murray-Davies model is extended to predict color halftones, the spectral Neugebauer model is generated. Take the cyan, magenta, and yellow colorants printing, for example; eight possible colors exist in the halftone patch which are white (bare substrate), cyan, magenta, yellow, red (magenta + yellow), green (cyan + yellow), blue (cyan + magenta), and black (cyan + magenta + yellow), respectively. These eight halftone colors are usually defined as Neugebauer primaries. When the spectral reflectance values of the primaries are measured, the halftone patch's overall reflectance can be predicted by using the spectral Neugebauer model as follows [21]:

$$\hat{R}_{\lambda} = \sum_{i=1}^8 w_i R_{\lambda,i}, \quad (2)$$

where  $R_{\lambda,i}$  is the  $i$ th Neugebauer primary's reflectance value at full colorant coverage, and  $w_i$  is the corresponding weighting factor calculated by the dot areas of the cyan, magenta, and yellow inks. If  $c$ ,  $m$ , and  $y$  represent the cyan, magenta, and yellow inks' area coverage, respectively, the eight Neugebauer primaries' weighting factors can be deduced using Demichel equations, and the full expression of (2) is written as follows:

$$\begin{aligned} \hat{R}_{\lambda} = & (1 - c)(1 - m)(1 - y)R_{\lambda,W} + c(1 - m)(1 - y)R_{\lambda,C} \\ & + (1 - c)m(1 - y)R_{\lambda,M} + (1 - c)(1 - m)yR_{\lambda,Y} \\ & + (1 - c)myR_{\lambda,R} + c(1 - m)yR_{\lambda,G} \\ & + cm(1 - y)R_{\lambda,B} + cmyR_{\lambda,K}. \end{aligned} \quad (3)$$

When the CMY three-color spectral Neugebauer model is extended to CMYK four colors, there are 16 Neugebauer primaries, and the weighting factors are listed in Table 1 ( $c$ ,  $m$ ,  $y$ , and  $k$  represent the cyan, magenta, yellow, and black ink's area coverage).

TABLE 1: The respective fractional area coverages of the CMYK combinations.

Index	Weighting factor	Fractional area coverage
1	$w_w$	$(1 - c) * (1 - m) * (1 - y) * (1 - k)$
2	$w_c$	$c * (1 - m) * (1 - y) * (1 - k)$
3	$w_m$	$(1 - c) * m * (1 - y) * (1 - k)$
4	$w_y$	$(1 - c) * (1 - m) * y * (1 - k)$
5	$w_k$	$(1 - c) * (1 - m) * (1 - y) * k$
6	$w_{cm}$	$c * m * (1 - y) * (1 - k)$
7	$w_{cy}$	$c * (1 - m) * y * (1 - k)$
8	$w_{my}$	$(1 - c) * m * y * (1 - k)$
9	$w_{cmy}$	$C * m * y * (1 - k)$
10	$w_{ck}$	$c * (1 - m) * (1 - y) * k$
11	$w_{mk}$	$(1 - c) * m * (1 - y) * k$
12	$w_{yk}$	$(1 - c) * (1 - m) * y * k$
13	$w_{cmk}$	$c * m * y * (1 - k)$
14	$w_{cyk}$	$c * (1 - m) * y * k$
15	$w_{myk}$	$(1 - c) * m * y * k$
16	$w_{cmyk}$	$c * m * y * k$

In fact, the spectral Neugebauer model is also suitable for multi-ink color systems. If  $p$  colorants are included as follows:

$$c = [c_1, \dots, c_j, \dots, c_p]^T \quad c_j \in [0, 1] \text{ for } j \in \{1, \dots, p\}, \quad (4)$$

there will be  $2^p$  Neugebauer primaries, and their weighting factors can be determined by the following equation [11, 22]:

$$w_i = \prod_{j=1}^p \begin{cases} c_j; & \text{if colorant } j \text{ is part of} \\ & \text{the } i\text{th Neugebauer primary,} \\ (1 - c_j); & \text{else.} \end{cases} \quad (5)$$

It can be concluded that the primaries' area coverages are expressed as fractions of the total area, and they satisfy the constraint  $\sum_{i=1}^{2^p} w_i = 1$ .

Because there are only eight Neugebauer primaries within the spectral Neugebauer model for three-color printers, the predication accuracy is very limited. In order to employ more measured halftone patches as Neugebauer primaries, the cellular spectral Neugebauer model is frequently used in which the colorant space is divided into more cellular subdomains [23]. For example, when the individual ink's area coverages are partitioned into two parts with three points [0%, 50%, and 100%], the CMY colorant space will be divided into eight cellular subdomains.

*2.2. The Optimization of Spectral Neugebauer Model.* There are actually several reasons which decrease the predication accuracy of the spectral Neugebauer model, such as the dot gain, light scattering and penetration, and nonlinearity between the summed and the individual primaries' reflectances. For the purpose of reducing the influence of these factors, some optimization approaches should be performed.

**2.2.1. Calculating the Effective Area Coverage Values.** Within the spectral Neugebauer model, the colorants' area coverages are employed to calculate the primaries' weighting factors; thus the spectral predication accuracy is highly dependent on these area coverage values, and it is significant to obtain their optimal values. For halftone color reproduction images, the change in dot diameter is the critical factor for the print image transfer, and these changes usually lead to tonal and color shifts. For a monochrome halftone patch, its spectral reflectance is usually calculated from the remitted light reflectance of solid and halftone areas as follows:

$$a_t = \frac{R_{\lambda,m} - R_{\lambda,s}}{R_{\lambda,t} - R_{\lambda,s}}, \quad (6)$$

where  $a_t$  is the predicted area coverage and  $R_{\lambda,m}$  is the measured reflectance values of the halftone patch. Because the reflectance values change with the wavelength, the minimum reflectance value within 400 nm~700 nm is usually used. Actually in conventional printing techniques, a widely adopted form of area coverage is deduced from the optical density values and (6) is written as

$$a_t = \frac{1 - 10^{-D_r}}{1 - 10^{-D_t}}, \quad (7)$$

where  $D_t$  is the optical density of solid tone, and  $D_r$  is the halftone optical density.

When the halftone patch is measured with a densitometer, it is not the geometrical area coverage (the ratio between dots and white paper on the measuring patch), but the “optically effective area coverage.” The difference between geometric and optically effective area coverage is due to the fact of light penetration and trapping. For example, as shown in Figure 1, part of the arriving light penetrates into the paper between the dots at the unprinted areas and are trapped under the dots during reflection; thus this light seems to be absorbed (as shown in Figure 1) [24].

The above phenomenon is called “light gathering,” and it causes the dots to appear optically larger than they are in reality. For this reason, the optically effective area coverage consists of the geometric area coverage and the optical area gain. The optical area gain is usually defined as dot gain value increase, and it is calculated from the area coverage of the film as a master for platemaking and the tone value printed on the substrate via the printing form. The area coverage of the film (or the pixel values after color separation for Computer-to-Plate techniques) is called theoretical value  $a_t$ , and the printed halftone's area coverage is the effective value  $a_{\text{eff}}$ ; thus the dot gain  $Z$  is  $Z = a_{\text{eff}} - a_t$ . In fact, dot gain essentially depends on the paper's surface and its absorption/ink setting behavior, the ink rheology, the blanket, printing pressure, and so on.

In order to acquire the real area coverage for the spectral Neugebauer model, all the spectral reflectance values within the visual wavelength are considered during the effective area coverage calculation. By using the least squares analysis, (6) is described into a spectral form:

$$\begin{aligned} a_{\text{eff}} &= (R_{\lambda,m} - R_{\lambda,s})(R_{\lambda,t} - R_{\lambda,s})^T \\ &\times [(R_{\lambda,t} - R_{\lambda,s})(R_{\lambda,t} - R_{\lambda,s})^T]^{-1}. \end{aligned} \quad (8)$$

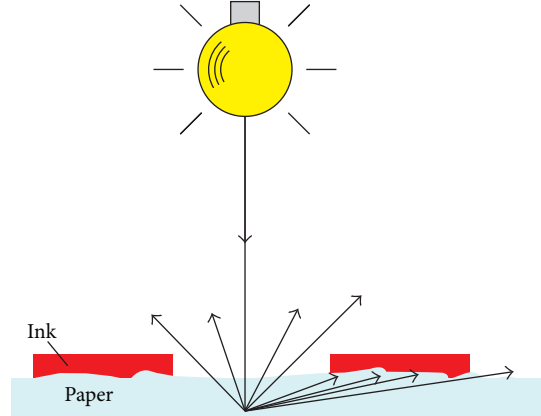


FIGURE 1: Light gathering in the area of the inked paper surface.

As we measure the reflectance from 400 nm to 700 nm with the interval of 10 nm, all the reflectance terms above are  $1 \times 31$  row vectors, while the superscripts  $T$  and  $-1$  indicate matrix transpose and inverse, respectively. Because most of the reflectances within 400nm~700nm are involved during effective area coverage calculation in (8), it is usually more precise than (6) and (7), and we use this equation for spectral predication in the experiment.

**2.2.2. Calculating the Optimal  $n$ -Values.** As a result of light penetration and scattering effect, the relationship between measured and predicted reflectance is nonlinear for the Murray-Davies and spectral Neugebauer models. An effective solution for this problem is to add an exponent  $1/n$  to the reflectance values, which is developed by Yule and Nielsen [25]. Taking the Murray-Davies model, for example, the modified form can be described as follows:

$$\hat{R}_\lambda = [a_{\text{eff}} R_{\lambda,t}^{1/n} + (1 - a_{\text{eff}}) R_{\lambda,s}^{1/n}]^n, \quad (9)$$

where  $a_{\text{eff}}$  is the effective area coverage value and  $n$  is a parameter accounting for light spreading in paper, and it is referred to as the Yule-Nielsen  $n$ -value. Generally, the modified Yule-Nielsen model is more accurate than the original Murray-Davies model. Likewise, the Yule-Nielsen model can be extended to the spectral Neugebauer model, which is called Yule-Nielsen spectral Neugebauer (YNSN) model as follows:

$$\hat{R}_\lambda = \left[ \sum_{i=1}^8 w_i R_{\lambda,i}^{1/n} \right]^n. \quad (10)$$

Because the  $n$ -value is not a constant, it is significant to acquire the optimal value for the specific halftone patches. Pearson [26] recommended using  $n = 1.7$  by testing a variety of substrates, halftone screens, and area coverages, and most of his experiment results showed that using  $n = 1.7$  always improved performance over using  $n = 1$ . However, Wyble and Berns have noted that values of  $n$  greater than 2 are often required for modern, high-resolution printers [27]. Arney et

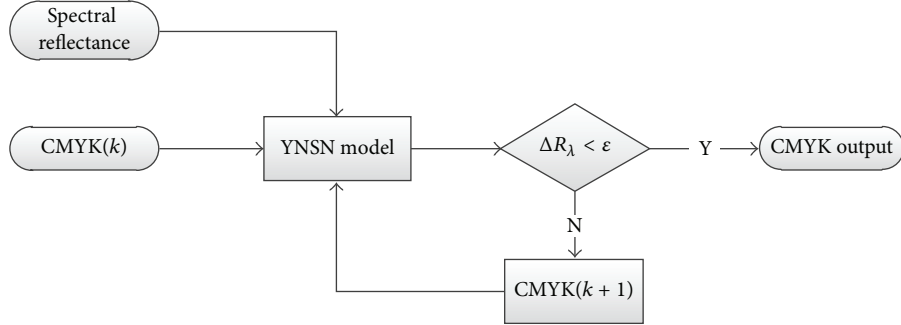


FIGURE 2: Diagram of spectral separation process based on optimization method.

al. [28] analyzed the process of light spreading in paper and approximated  $n$ -value as

$$n = 2 - e^{-Ak_p^v}, \quad (11)$$

where  $A$  is a constant relating to dot geometry,  $k_p$  is a constant relating to modulation transfer function, and  $v$  is the halftone dot frequency in dots per millimeter. In addition, Shiraiwa and Mizuno interpreted the  $n$ -value in another form [29], and (9) is modified as follows based on it:

$$\hat{R}_\lambda = \left[ a_{\text{eff}}(R_{\lambda,s}T_\lambda^n)^{1/n} + (1 - a_{\text{eff}}) R_{\lambda,s}^{1/n} \right]^n, \quad (12)$$

where the solid ink's reflectance  $R_{\lambda,s}$  is replaced by the term  $R_{\lambda,s}T_\lambda^n$  and  $T_\lambda$  is the ink transmittance. It should be noted that this model is valid only for integer values of  $n$ -value, and the overall effect of this is to make the predicted reflectance lower, which is consistent with the fact that the Murray-Davies model overpredicts reflectance values.

In this paper, we use a spectral-error-comparing method to find the optimal  $n$ -value. Firstly, the YNSN model is established with the  $n$ -value initialized from 1, and then a certain number of testing patches are selected to calculate the YNSN model's spectral error. We set  $n$ -value ranging from 1 to 5 with the increment  $\Delta n = 0.1$ ; thus when all the spectral errors of different  $n$ -values are obtained and compared, the optimal value is determined corresponding to the minimal spectral error.

### 3. Spectral Separation Based on Constrained Optimization Method

For CMYK printers, it is very difficult to convert the 31-dimensional spectral reflectances into the 4-dimensional CMYK colorant values. However, as the 31-D spectral reflectance can be precisely predicted from CMYK values by spectral Neugebauer model, it is more feasible to convert the spectral separation process into the constrained optimization process based on the spectral predication model. Actually, the spectral separation is an iteration process, where the optimal CMYK values are continually searched until the predicated spectral values match well with the given spectral reflectances. Generally, the spectral separation workflow based on constrained optimization method can be described as in Figure 2.

It can be seen from the separation workflow that the objective function and the nonlinear constraints should be accurately defined for the optimization problem. Because the major purpose for printing multispectral images is to reproduce the same spectral reflectance values, the objective function is defined as the spectral reflectance error:

$$\Delta R_\lambda = \|\hat{R}_{\lambda,\text{CMYK}} - R_{\lambda,\text{image}}\|, \quad (13)$$

where  $\hat{R}_{\lambda,\text{CMYK}}$  is predicated reflectance values using YNSN model and  $R_{\lambda,\text{image}}$  is the multispectral image's reflectance values. The iteration process in Figure 2 will stop when the difference of (13) is smaller than a threshold value  $\epsilon$  predefined.

In addition, as the colorant values have the specific scale range, the nonlinear constraints can be defined as follows:

$$0 \leq a_{\text{eff}} \leq 1, \quad \sum a_{\text{eff}} \leq a_{\text{limit}}, \quad (14)$$

where  $a = \{c, m, y, k\}$ , and  $a_{\text{limit}}$  represents the limit of the total ink amount. Thus, the nonlinear optimization process for spectral separation is described as

$$\begin{aligned} \min \quad & \|\hat{R}_{\lambda,\text{CMYK}} - R_{\lambda,\text{image}}\| \\ \text{s.t.} \quad & a_{\text{eff}} \in [0, 1], \\ & \sum a_{\text{eff}} \leq a_{\text{limit}}. \end{aligned} \quad (15)$$

It should be noted that the use of an optimization technique may lead to a nonoptimal solution (e.g., a local minimum will stop the iteration process) as Mahy and Delabastita presented [30]. Thus, Gerhardt and Hardeberg [11] analyzed the parameters which determined the right colorant combination obtained, including the limitations on the minimum difference between the desired value and its estimation, difference between colorant values in successive iterations, and initial guess values to start the iterative search.

### 4. Experiment and Analysis

In the experiment, the cyan, magenta, and yellow inks are used to print the multispectral images, and the three-color spectral Neugebauer model is employed for spectral predication. The halftone patches are printed with a HP digital

TABLE 2: The colorant and spectral reflectance error for 50 testing halftone samples.

	$\Delta C$	$\Delta M$	$\Delta Y$	$\Delta E_{cmy}$	RRMS
Avg. (error)	1.43	2.26	2.21	3.85	0.0047
Std. (error)	0.98	1.54	2.00	2.13	0.0030
Max. (error)	4.54	6.07	7.23	9.86	0.0128

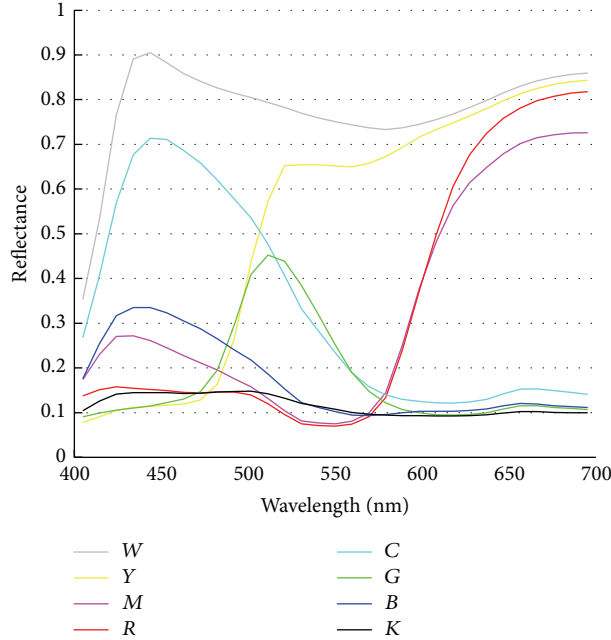


FIGURE 3: Spectral reflectance data of eight Neugebauer primaries.

printer, and the spectral reflectance values are measured with an *X-Rite* 530 spectrophotometer with geometry ( $d: 10^\circ$ ) under a D65 illuminant. Take the eight Neugebauer primaries of CMY space, for example, the spectral reflectances within 400 nm–700 nm are illustrated as in Figure 3.

Besides, 50 testing halftone patches are selected to test the spectral separation method in the paper. Firstly, the testing patches are printed with the defined ink values  $C_1M_1Y_1$ , and then the spectral reflectance values  $R_{\lambda,1}$  are measured. Secondly, by using the spectral separation method described in Sections 2 and 3, new ink values  $C_2M_2Y_2$  are calculated from the measured spectral reflectance  $R_{\lambda,1}$ . At last, when these  $C_2M_2Y_2$  values are printed and measured, new spectral reflectance values  $R_{\lambda,2}$  are obtained. The difference of CMY values between  $C_1M_1Y_1$  and  $C_2M_2Y_2$  and the spectral error between  $R_{\lambda,1}$  and  $R_{\lambda,2}$  are calculated to test the separation accuracy [23, 31]. The CMY ink difference and the reflectance error are expressed as follows:

$$\Delta E_{CMY} = \sqrt{\Delta C^2 + \Delta M^2 + \Delta Y^2}, \quad (16)$$

where  $\Delta C = |C_1 - C_2|$ ,  $\Delta M = |M_1 - M_2|$ , and  $\Delta Y = |Y_1 - Y_2|$ . While for the spectral errors, the reflectance root mean square (RRMS) difference is represented as

$$RRMS = \sqrt{\frac{\sum_{\lambda} [R_{\lambda,1} - R_{\lambda,2}]^2}{N}}, \quad (17)$$

where  $N$  is the dimensionality of spectral reflectance,  $R_{\lambda,1}$  is the input and given reflectance values, and  $R_{\lambda,2}$  is newly predicted CMY inks' reflectance values, and they are both scaled to 0~1. The RRMS error reveals the matching degree of two spectral reflectance values, so it may favorably evaluate the precision of spectral separation method.

In Table 2 the errors in the form of  $\Delta C$ ,  $\Delta M$ ,  $\Delta Y$ , and RRMS are listed, where the Avg(Error) represents the average of the errors, Std(Error) is the standard deviation of the errors, and Max(Error) is the maximum of the errors.

From Table 2, it can be seen that the differences of ink values are about 2%, and most of the spectral reflectance errors are below 5%, which indicates that the accuracy of the spectral separation method in this paper is acceptable. For all the 50 testing halftone patches, the colorant errors of cyan, magenta, and yellow inks are shown in Figure 4.

The spectral reflectance error is depicted in Figures 5 and 6. In Figure 5, the distribution of RRMS errors for 50 halftone patches is listed, while, in Figure 6, the original and newly separated spectral reflectance values are compared, and it can be seen that these two figures match very well.

## 5. Conclusions

The spectral separation algorithm is significant for the multi-spectral image printing devices, which can calculate the accurate colorant values. In the traditional printing process, the

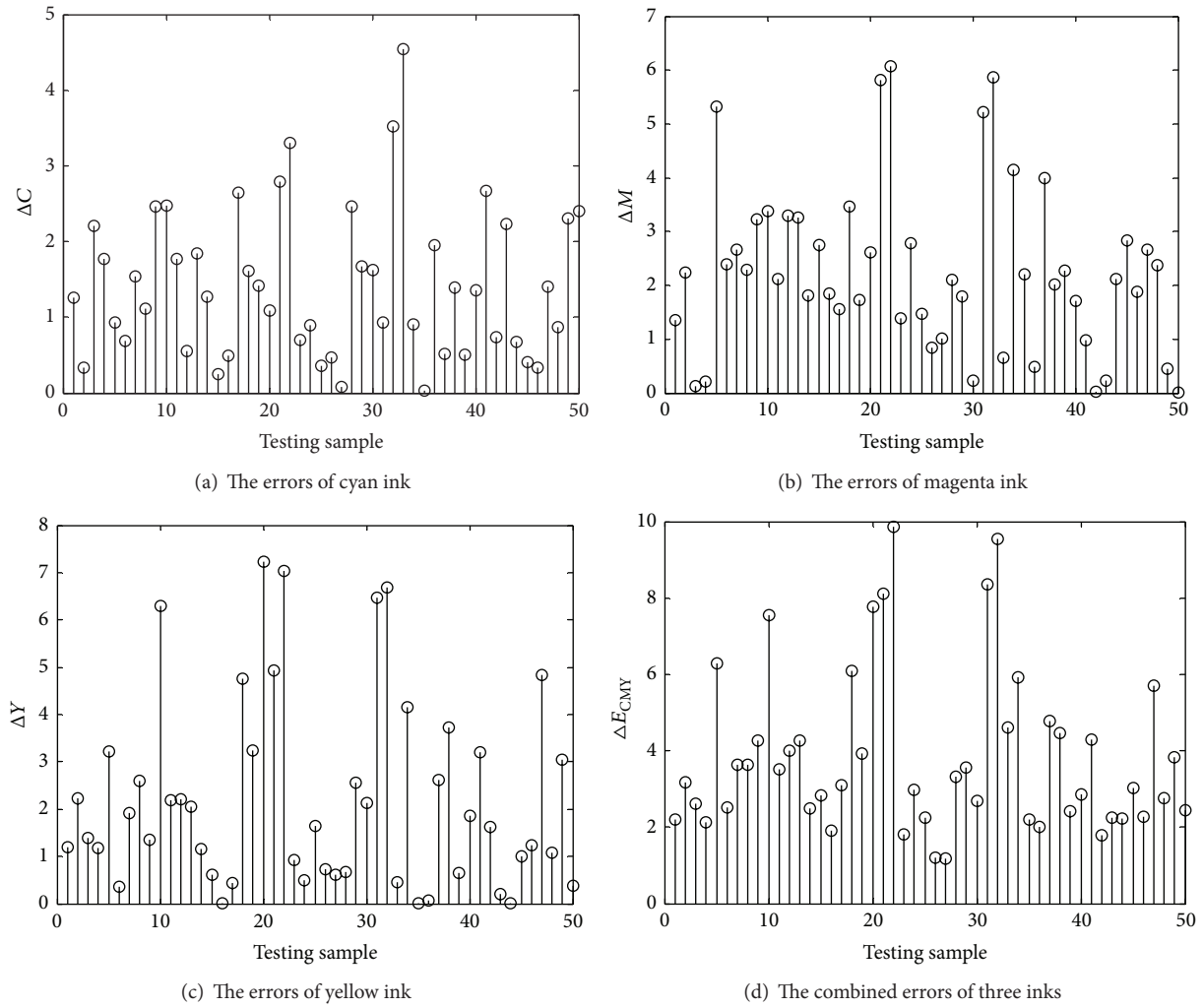


FIGURE 4: Colorant errors of cyan, magenta, and yellow inks.

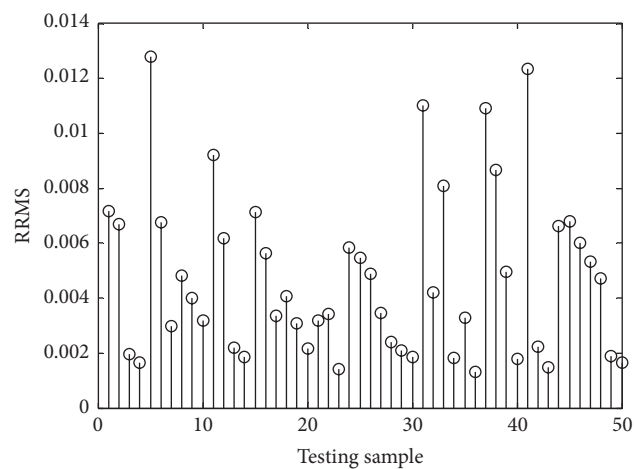


FIGURE 5: Spectral reflectance error of the 50 halftone patches.

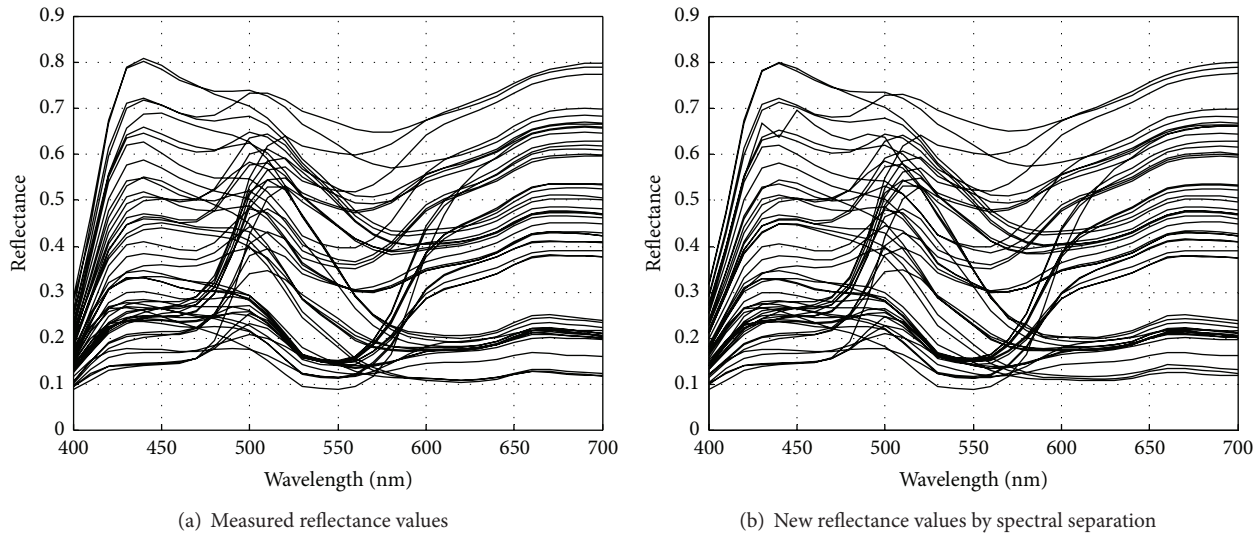


FIGURE 6: Comparison of the original and newly separated spectral values of the 50 testing samples.

multispectral images are firstly converted into the CIE color values under specific illuminant, and then the colorant values are calculated from the CIE colors. Because the connection space is the 3-dimentional CIEXYZ or CIELAB under one illuminant, the original and reproduced multispectral images cannot keep same color appearance under different observing circumstances. In this paper, the spectral separation method is employed to calculate the spectral reflectance's colorant values and the purpose of which is to generate the identical spectral values of the input multispectral images. Thus, the original and reproduced images reveal the same visual colors under different illuminants. The accuracy of the spectral separation method is evaluated in the experiment. The experiment results show that the colorants errors of three inks are about 2%, and the average spectral error is below 5%, which can guarantee the spectral consistence between the original and the printed multispectral images.

## Conflict of Interests

The authors declare that there is no conflict of interests regarding the publication of this paper.

## Acknowledgments

The authors gratefully acknowledge the financial support by research foundation of Department of Education of Shaanxi Province (no. 11JK0541), Doctor Foundation of Xi'an University of Technology (no. 104-211302), and "13115" Creative Foundation of Science and Technology (no. 2009ZDGC-06), Shaanxi Province of China.

## References

- [1] I. Zjakic, D. Parac-Osterman, and I. Bates, "New approach to metamerism measurement on halftone color images," *Measurement*, vol. 44, no. 8, pp. 1441–1447, 2011.
- [2] M. Rump and R. Klein, "Spectralization: reconstructing spectra from sparse data," *Computer Graphics Forum*, vol. 29, no. 4, pp. 1347–1354, 2010.
- [3] N. Hagen and W. Kudenov Michael, "Review of snapshot spectral imaging technologies," *Optical Engineering*, vol. 52, no. 9, Article ID 090901, 2013.
- [4] F. Wang, A. Behrooz, M. Morris, and A. Adibi, "High-contrast subcutaneous vein detection and localization using multispectral imaging," *Journal of Biomedical Optics*, vol. 18, no. 5, Article ID 050504, 2013.
- [5] P. Xia, Y. Shimozato, Y. Ito et al., "Improvement of color reproduction in color digital holography by using spectral estimation technique," *Applied Optics*, vol. 50, no. 34, pp. H177–H182, 2011.
- [6] P.-Y. Ren, N.-F. Liao, B.-H. Chai, W.-P. Yang, and S.-X. Li, "Spectral reflectance recovery based on multispectral imaging," *Optical Technique*, vol. 31, no. 3, pp. 427–433, 2005.
- [7] Z. Liu, X.-X. Wan, X.-G. Huang, Q. Liu, and C. Li, "The study on spectral reflectance reconstruction based on wideband multispectral acquisition system," *Spectroscopy and Spectral Analysis*, vol. 33, no. 4, pp. 1076–1081, 2013.
- [8] H. Li, J. Feng, W. Yang et al., "Spectral-based rendering method and Its application in multispectral color reproduction," *Laser and Optoelectronics Progress*, vol. 47, no. 12, Article ID 122301, 2010.
- [9] P. Urban and R. S. Berns, "Paramer mismatch-based spectral gamut mapping," *IEEE Transactions on Image Processing*, vol. 20, no. 6, pp. 1599–1610, 2011.
- [10] B. Sun, H. Liu, S. Zhou, and W. Li, "A color gamut description algorithm for liquid crystal displays in CIELAB space," *The Scientific World Journal*, vol. 2014, Article ID 671964, 9 pages, 2014.
- [11] J. Gerhardt and J. Y. Hardeberg, "Spectral color reproduction minimizing spectral and perceptual color differences," *Color Research and Application*, vol. 33, no. 6, pp. 494–504, 2008.
- [12] P. Urban and R.-R. Grigat, "Spectral-based color separation using linear regression iteration," *Color Research and Application*, vol. 31, no. 3, pp. 229–238, 2006.

- [13] D.-W. Kang, Y.-T. Kim, Y.-H. Cho, K.-H. Park, W.-H. Choe, and Y.-H. Ha, "Color decomposition method for multi-primary display using 3D-LUT in linearized LAB space," in *Color Imaging X: Processing, Hardcopy, and Applications*, vol. 5667 of *Proceedings of SPIE*, pp. 354–363, San Jose, Calif, USA, January 2005.
- [14] C. Lana, M. Rotea, and D. E. Viassolo, "Robust estimation algorithm for spectral Neugebauer models," *Journal of Electronic Imaging*, vol. 14, no. 1, pp. 1–10, 2005.
- [15] S. Xi and Y. Zhang, "Neugebauer reflectance model of frequency modulation halftone image," *Optik*, vol. 124, no. 15, pp. 2103–2105, 2013.
- [16] B. Wang, H. Xu, M. Ronnier Luo, and J. Guo, "Maintaining accuracy of cellular Yule-Nielsen spectral Neugebauer models for different ink cartridges using principal component analysis," *Journal of the Optical Society of America A: Optics and Image Science, and Vision*, vol. 28, no. 7, pp. 1429–1435, 2011.
- [17] M. Hébert and R. D. Hersch, "Yule-nielsen based recto-verso color halftone transmittance prediction model," *Applied Optics*, vol. 50, no. 4, pp. 519–525, 2011.
- [18] C. Sandoval and D. Kim Arnold, "Deriving Kubelka-Munk theory from radiative transport," *Journal of the Optical Society of America A: Optics and Image Science, and Vision*, vol. 31, no. 3, pp. 628–636, 2014.
- [19] L. M. Schabbach, F. Bondioli, and M. C. Fredel, "Color prediction with simplified Kubelka-Munk model in glazes containing  $\text{Fe}_2\text{O}_3$ - $\text{ZrSiO}_4$  coral pink pigments," *Dyes and Pigments*, vol. 99, no. 3, pp. 1029–1035, 2013.
- [20] J. Seymour and P. Noffke, "A universal model for halftone reflectance," in *Proceedings of the Technical Association of the Graphic Arts (TAGA '12)*, pp. 1–40, March 2012.
- [21] T. Bugnon and R. D. Hersch, "Calibrating ink spreading curves by optimal selection of tiles from printed color images," *Journal of Electronic Imaging*, vol. 21, no. 1, Article ID 013024, pp. 1–15, 2012.
- [22] B. Wang, H. Xu, and L. M. Ronnier, "Color separation criteria for spectral multi-ink printer characterization," *Chinese Optics Letters*, vol. 10, no. 1, Article ID 013301, 2012.
- [23] J. Guo, H. Xu, and L. M. Ronnier, "Novel spectral characterization method for color printer based on the cellular Neugebauer model," *Chinese Optics Letters*, vol. 8, no. 11, pp. 1106–1109, 2010.
- [24] H. Kipphan, *Handbook of Print Media*, Springer, Berlin, Germany, 2001.
- [25] J. A. C. Yule and W. J. Nielsen, "The penetration of light into paper and its effect on halftone reproductions," *TAGA Proc*, vol. 3, pp. 65–76, 1951.
- [26] M. Pearson, " $n$  value for general conditions," *TAGA Proc*, vol. 32, pp. 415–425, 1980.
- [27] D. R. Wyble and R. S. Berns, "A critical review of spectral models applied to binary color printing," *Color Research and Application*, vol. 25, no. 1, pp. 4–19, 2000.
- [28] J. S. Arney, C. D. Arney, M. Katsume, and P. G. Engeldrum, "The impact of paper optical properties on hard copy image quality," in *Proceeding of the International Conference on Digital Printing Technologies*, pp. 166–167, 1996.
- [29] Y. Shiraiwa and T. Mizuno, "Equation to predict colors of halftone prints considering the optical property of paper," *Journal of Imaging Science and Technology*, vol. 37, no. 4, pp. 385–391, 1993.
- [30] M. Mahy and P. Delabastita, "Inversion of the Neugebauer equations," *Color Research and Application*, vol. 21, no. 6, pp. 404–411, 1996.
- [31] S. Shen and R. S. Berns, "Color-difference formula performance for several datasets of small color differences based on visual uncertainty," *Color Research and Application*, vol. 36, no. 1, pp. 15–26, 2011.

## Research Article

# Liquid Chromatography-Tandem Mass Spectrometric Assay for Determination of Stavudine in Human Plasma

Fengdan Jin

Key Laboratory of Applied Chemistry, Yanshan University, Qinhuangdao, Hebei 066004, China

Correspondence should be addressed to Fengdan Jin; fengdanjin@ysu.edu.cn

Received 10 March 2014; Revised 9 May 2014; Accepted 21 May 2014; Published 17 June 2014

Academic Editor: Bing Wu

Copyright © 2014 Fengdan Jin. This is an open access article distributed under the Creative Commons Attribution License, which permits unrestricted use, distribution, and reproduction in any medium, provided the original work is properly cited.

A LC-MS/MS method for determination of stavudine in human plasma was established and validated, and it was applied to the pharmaceutical formulations bioequivalence study. 0.5 mL plasma sample was extracted by liquid-liquid extraction. Stavudine was detected by a LC-MS/MS system. The pharmacokinetic parameters of stavudine in different formulations were calculated by noncompartment model statistics. The method was linear over the concentration ranges 5.00–1000 ng/mL in plasma. The intra- and interassay relative standard deviation (RSD) was <10%. The average accuracies for the assay at three concentrations (5.00, 80.0, and 900 ng/mL) were from 100.2% to 102.5%. Pharmacokinetic parameters of stavudine reference formulation were obtained as follows:  $T_{\max}$  was  $0.6 \pm 0.2$  h,  $C_{\max}$  was  $480.7 \pm 150.9$  g/L,  $t_{1/2}$  was  $1.7 \pm 0.4$  h, and  $AUC_{0-t}$  was  $872.8 \pm 227.8$  g·h/L, and pharmacokinetic parameters of stavudine test formulation were obtained as follows:  $T_{\max}$  was  $0.5 \pm 0.2$  h,  $C_{\max}$  was  $537.5 \pm 178.5$  g/L,  $t_{1/2}$  was  $1.7 \pm 0.3$  h, and  $AUC_{0-t}$  was  $(914.1 \pm 284.5)$  g·h/L. Calculated with  $AUC_{0-t}$ , the bioavailability of two formulations was 105.0%.

## 1. Introduction

Stavudine is the first four approved for marketing the treatment of human immunodeficiency virus (HIV) infections following zidovudine, hydroxy glycosides, and go after zalcitabine by the U.S. Food and Drug Administration (FDA). It contains nucleoside reverse transcriptase inhibitors which can inhibit the replication of HIV-1 and HIV-2 in different kinds of cells. Stavudine triphosphate formed by cell kinase phosphorylation can prevent the HIV virus replication in human cells. Stavudine has been used in the adult HIV-infected people and AIDS patients who do not tolerate zidovudine and who can no longer be zidovudine-treated, and it also has been used in HIV-infected children from 3 months to 12 years old [1].

Determination of stavudine in plasma by high performance liquid chromatography method has been described [2, 3]; analysis time was more than 12 minutes. The liquid chromatography-tandem mass spectrometry (LC-MS/MS) method [4] was established for the simultaneous monitoring of multiple anti-HIV drugs *in vivo* plasma concentrations after long-term combination therapy of AIDS. The LC-MS/MS [5] method needs a larger workload because external

standard was used. Two sets of standard curves and quality control (QC) samples were made to each analytical batch, and the system performance correction fluid was injected to confirm whether the response of ionization mass spectrometry is stable. This paper intends to establish a rapid, sensitive LC-MS/MS method to determinate stavudine plasma concentrations for bioequivalence and pharmacokinetic study.

## 2. Materials and Methods

**2.1. Reagents and Chemicals.** Purity of stavudine and  $\beta$ -thymidine (internal standard) was more than 99.7% and 99.4%. They were purchased from the Institute of Northeast General Pharmaceutical Factory (Shenyang, China). Zerit capsules were kindly supplied from Bristol-Myers Squibb Company (Canada). All chemicals and reagents were of analytical grade, and water was bidistilled water which was prepared from demineralized water.

**2.2. Apparatus.** Analyses were performed on an LC-MS/MS system composed of a Shimadzu LC-10AD pump (Kyoto, Japan), a Thermo Finnigan TSQ Quantum Ultra tandem

mass spectrometer (San Jose, CA, USA), an LC-10ADVP pump, and a SIL-HTA autosampler.

**2.3. Chromatographic Conditions.** The analytical column was a Zorbax Extend C18 column (150 mm × 4.6 mm, inner diameter, 5 µm; Agilent, Wilmington, DE, USA) and a SecurityGuard C18 guard column (4 mm × 3.0 mm inner diameter; Phenomenex, Torrance, CA, USA). The mobile phase was methanol-water 1% ammonia (50 : 50 : 0.5, v/v/v). The liquid flow rate was set at 0.5 mL/min. The sample injection volume was 20 µL. The column temperature was maintained at 20°C.

**2.4. Mass Spectrometric Conditions.** Stavudine and internal standard were monitored in the negative ion mode using a Turboion spray interface. The spray voltage was set at 3.8 kV and the source temperature at 350°C. Nitrogen was used as sheath gas (20 Arb) and auxiliary gas (2 Arb). The collision gas was argon at a pressure of 1.0 mTorr. Collision-induced dissociation voltage was 22 eV for both the analyte and internal standard. The selected reaction monitoring (SRM) was selected to monitor precursor-product ion transitions. These corresponded to  $m/z$  223 →  $m/z$  42 for stavudine and  $m/z$  241 →  $m/z$  42 for internal standard. The dwell time was 0.3 s per transition.

**2.5. Sample Preparation Procedure.** A volume of 0.5 mL thawed human plasma was transferred to a 10 mL tube and 100 µL of β-thymidine and 100 µL methanol-water (50 : 50, v/v) were spiked and briefly vortex-mixed. To each sample, 250 µL phosphate buffer (50 mmol/L, pH 6) and 3 mL acetic ether were added. The tubes were capped and shaken for 10 minutes and then centrifuged at 3,500 rpm for 5 minutes. The upper organic phase was divided to a test tube and evaporated to dryness at 50°C by a gentle flow of air. The residue was dissolved in 100 µL mobile phase, and a 20 µL aliquot was injected into the LC-MS/MS system.

**2.6. Bioequivalence and Pharmacokinetics Study.** Cross double cycle test was adopted to invest bioequivalence study of two stavudine capsules. 20 healthy male volunteers were divided into two (I and II) groups stochastically, each group of 10 people. At the first cycle, group I and group II received the oral dosing of reference and text formulation (stavudine 20 mg), respectively. At the second cycle, groups I and II received the text and reference formulation, oppositely. Each test interval was for a week. Forearm venous blood (3 mL) was collected in tubes containing sodium heparin before taking the medicine (0 h) and at 0.25, 0.50, 0.75, 1.0, 1.5, 2.0, 3.0, 4.0, 6.0, 8.0, and 10.0 h after a single oral dose. The blood samples were centrifuged at 2,000 g for 10 min immediately. The plasma samples were separated and stored at -20°C until analysis. Clinical trials were performed in Liaoning Province People's Hospital.

The plasma samples were prepared according to Section 2.5. One standard curve was established in each analytical batch, and double QC samples of three concentrations (high, medium and low) were analyzed, at the same

time. The concentration data of the unknown sample and the QC sample were calculated by the standard curve.

### 3. Results and Discussion

**3.1. Chromatographic and Mass Spectrometric Conditions.** The selection of internal standard for LC-MS/MS method was different for HPLC-UV method. The ideal internal standard is isotope marker of analyte, but it is expensive and difficult to get, generally. Because of the instrument, the pressure of collision gas changes within a day. This leads the ratio of mass spectrometry signal intensity for analyte and internal standard to change. As a result, the intra-assay deviation of QC samples was large. Therefore, the requirement of internal standard is as follows: when the collision gas pressure changed, the signal intensity change of analyte and internal standard should trend accordingly. Zidovudine and β-thymidine were structural analogues of stavudine and were tried to be used as internal standard. In selected mass spectrometry conditions and chromatographic conditions, zidovudine response was high, but the retention time is 1 min longer than stavudine. β-thymidine also has a good response, and retention time was similar to stavudine, with good reproducibility. Considering the analysis time, β-thymidine was selected as the internal standard substance. The analyte and the internal standard formed predominately protonated molecules  $[M-H]^-$ ,  $m/z$  223 and  $m/z$  241. Through collision-induced dissociation, and thire major fragment ions were both at  $m/z$  42 (Figure 1).

**3.2. Sample Preparation.** Biological sample pretreatment method was improved as liquid-liquid extraction (LLE) which is most commonly used. LLE can remove fats, proteins, and endogenous ions effectively, and the operation is simple. LLE method lies in choosing the right extraction solvent and acidification and alkalization reagent according to the analyte polarity and acid-base property. Stavudine and β-thymidine are polar compounds, and both have acid group. The ether-dichloromethane (3 : 2) and ethyl acetate were tried as the extraction solvent. The pH 4 and pH 6 phosphate buffer (50 mmol/L) were tried as acidifying agents. The ethyl acetate and pH 6 phosphate buffer (50 mmol/L) were determined as extraction solvent and acidifying agents, because the extraction rate of analyte and the internal standard was higher (about 50% of both) and stable.

**3.3. Selectivity.** Blank plasma samples of six volunteers were prepared according to Section 2.5 (no internal standard), and the chromatogram was shown in Figure 2(a). A certain concentration of stavudine reference solution and internal standard solution was joined in blank plasma, with the same operation, and the chromatogram was shown in Figure 2(b). The retention time was 2.98 min and 2.83 min, respectively. The chromatogram of plasma sample of a volunteer after oral dosing was shown in Figure 2(c). The results showed that the endogenous substances of blank plasma do not interfere with the determination of the analytes and internal standard.

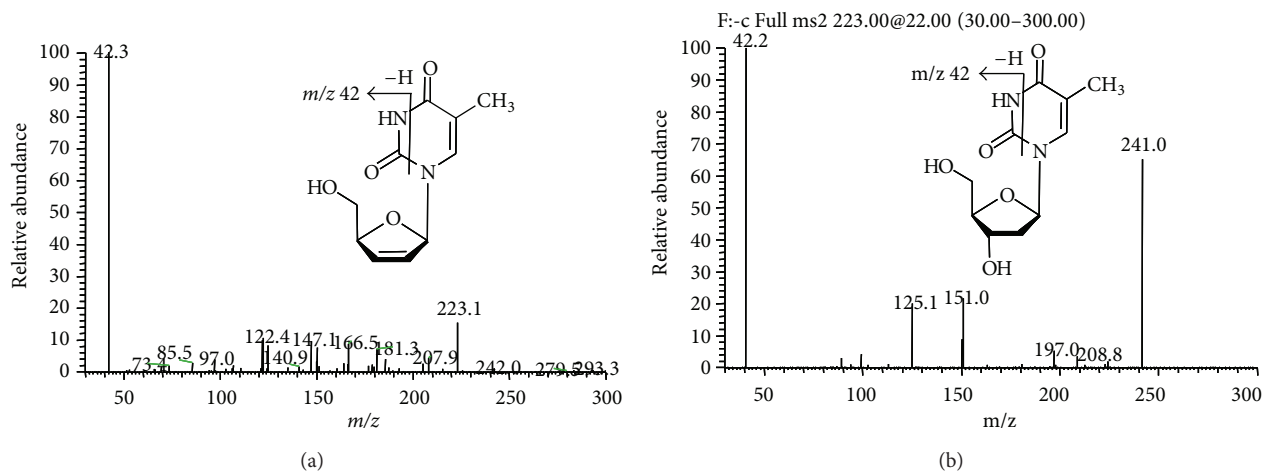


FIGURE 1: Full-scan product ion spectra of  $[M-H]^-$  of (a) stavudine and (b)  $\beta$ -thymidine (internal standard).

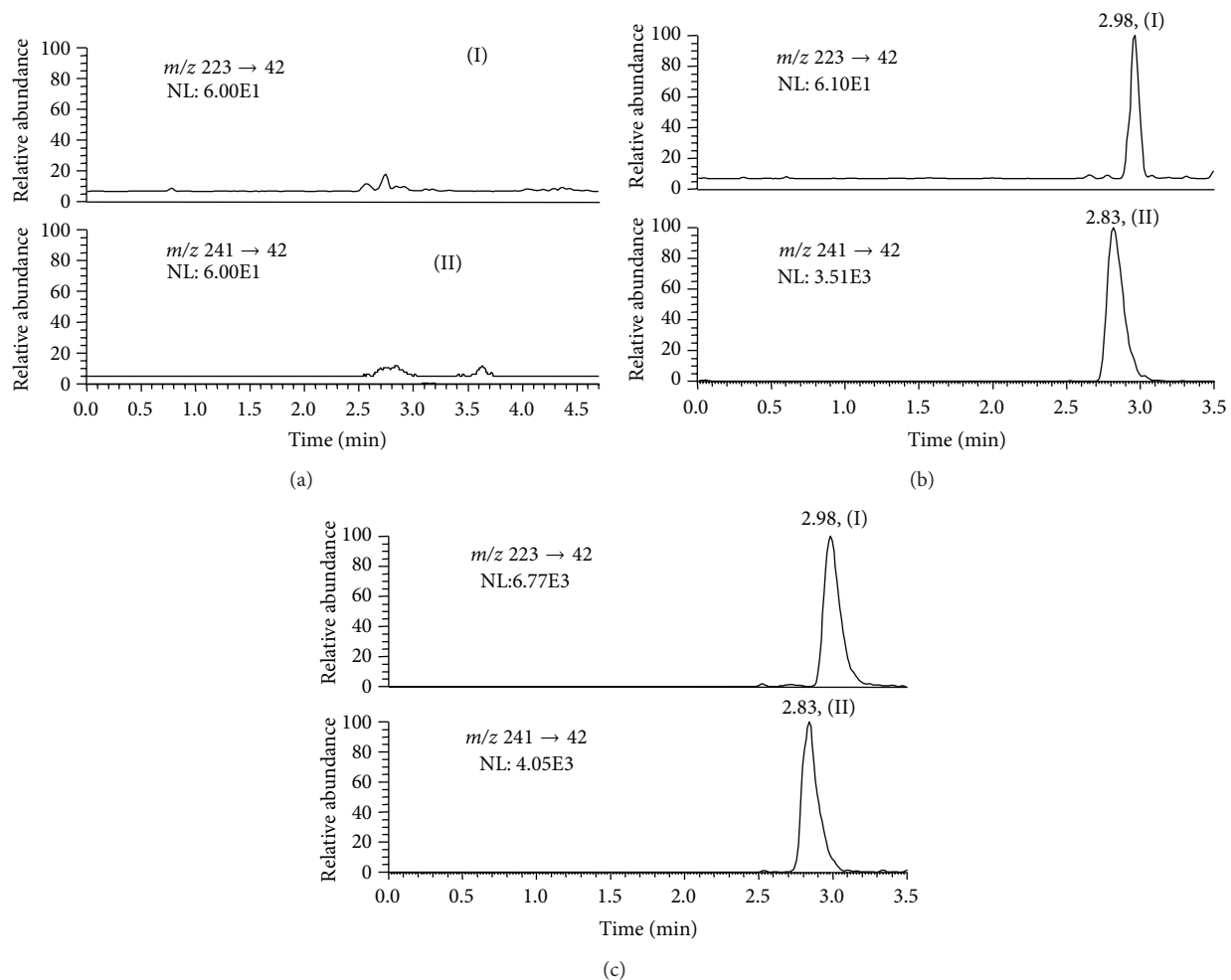


FIGURE 2: Representative selected reaction monitoring chromatograms of stavudine (I) and the internal standard (II). (a) Blank plasma sample; (b) plasma sample spiked with stavudine (LLOQ, 5.00 ng/mL) and internal standard (400 ng/mL); (c) plasma sample from a volunteer 0.75 h after an oral dose of 20 mg stavudine.

TABLE 1: Precision and accuracy data for the analysis of stavudine.

Conc. added (ng/mL)	Conc. found (ng/mL)	Intraday RSD (%)	Interday RSD (%)	Accuracy (%)	<i>n</i>
5.00	5.12	6.1	0.9	102.5	18
80.0	80.7	6.4	6.6	100.8	18
900	902.2	2.9	9.7	100.2	18

TABLE 2: Stability of stavudine.

	Conc. added (ng/mL)	Conc. found (ng/mL)	RSD (%)	Accuracy (%)	<i>n</i>
Short-term stability	5.00	4.63	0.3	92.6	3
	900	871	6.4	96.7	3
Postpreparative stability	5.00	4.61	0.3	92.2	3
	900	831	6.2	92.3	3

**3.4. Linearity and LLOQ.** According to stavudine plasma concentration levels of the preliminary experiment, the linear range was selected from 5.00 ng/mL to 1,000 ng/mL. The LLOQ was 5.00 ng/mL, which was more sensitive than the reported methods. The concentration of analyte was as the abscissa. The peak area ratio of analyte to the internal standard was as the ordinate. Using weighted least-squares method ( $w = 1/x^2$ ) [6], linear regression equation was calculated. A weighted least-squares ( $w = 1/x^2$ ) linear regression of response versus concentration was used for the calibration. A typical equation was as follows:  $y = 3.070 \times 10^{-3}x - 1.129 \times 10^{-4}$  ( $r = 0.9975$ ). The RSD at the LLOQ was 6.1%, and the accuracy was 102.5%.

**3.5. Precision and Accuracy.** The accuracy and precision of the method were determined by assaying QC samples. The intra- and interbatch precisions and the accuracy were summarized in Table 1. The results indicated that the values were within the acceptable range and the method was accurate and precise.

**3.6. Extraction Recovery and Stability Study.** The extraction recovery for stavudine was estimated at the three QC concentrations ( $n = 6$ ). The extraction recoveries were 55.8%, 54.3%, and 54.4%, respectively, and the recovery of the internal standard was 45.8%. These data showed that the recovery values were similar and stable, and therefore no significant degradation occurred during the extraction and sample storage processes for stavudine in plasma samples.

The stability experiments were aimed at testing the effects of possible conditions that the analytes might experience during collection, storage, and analysis. It was reported that the stavudine plasma samples were stable at room temperature for 12 h. Stavudine in plasma was stable at  $-20^{\circ}\text{C}$  for a period of 30 days and after three freeze ( $-20^{\circ}\text{C}$ ) thaw (room temperature) cycles [2, 5]. The short-term stability (at room temperature for 2 h) and the postpreparative stability (at  $20^{\circ}\text{C}$  for 12 h) were investigated. The data are demonstrated in Table 2.

**3.7. Bioequivalence and Pharmacokinetics Study.** The mean plasma concentration-time curves were shown in Figure 3.

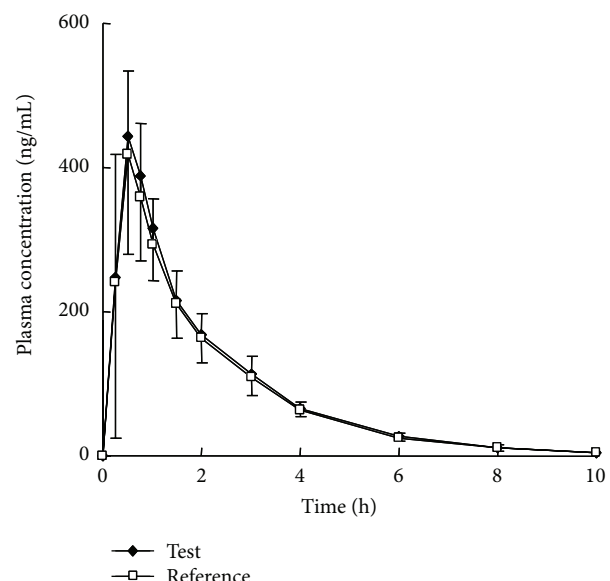


FIGURE 3: Mean plasma concentration versus time curve of stavudine after oral administration of 20 mg stavudine capsule test and reference formulations to 18 healthy volunteers ( $n = 20, \bar{x} \pm s$ ).

The main pharmacokinetic parameters are shown in Table 3. These data showed that  $\text{AUC}_{0-t}$  and  $C_{\max}$  of stavudine reject not bioequivalent hypothesis. The test results of  $T_{\max}$  nonparametric method showed that there was no significant difference between two formulations. Therefore, these two formulations were bioequivalent.

#### 4. Conclusions

A LC-MS/MS method was established for determination of stavudine in human plasma. The linear range of stavudine plasma concentration was 5.00–1,000 ng/mL. The LLOQ was 5.00 ng/mL. Calculated by QC samples, the intra- and interassay precision (RSD) was less than 10%. The accuracy was from 100.2% to 102.5%. The results show that this method was rapid and sensitive, with good precision and accuracy. The separation time of every sample was 3.5 min. Nearly 200

TABLE 3: The main pharmacokinetic parameters.

Parameter	Reference	Test	90% confidence interval (%)
AUC <sub>0-t</sub> (ng·h/mL)	872 ± 228	914 ± 284	98.6–109.8
AUC <sub>0-∞</sub> (ng·h/mL)	889 ± 228	931 ± 287	
C <sub>max</sub> (ng/mL)	480 ± 151	574 ± 178	97.8–125.1
T <sub>max</sub> (h)	0.55 ± 0.19	0.54 ± 0.20	
k <sub>e</sub> (h <sup>-1</sup> )	0.42 ± 0.09	0.42 ± 0.07	
t <sub>1/2</sub> (h)	1.72 ± 0.43	1.68 ± 0.29	
F (%)		105.0 ± 13.6	

plasma samples could be analyzed per day. This method was applied to human bioavailability and bioequivalence study of stavudine capsules.

## Conflict of Interests

The author declares that there is no conflict of interests regarding the publication of this paper.

## Acknowledgments

Financial support from the National Natural Science Foundation of China (Grant 51202213), Excellent Young Scientist Funding of Hebei Province (Grant Y2012005), and Qinhuangdao City Science & Technology Research & Development Program (no. 201001A120) is acknowledged.

## References

- [1] S. M. Cheer and K. L. Goa, "Stavudine once daily," *Drugs*, vol. 62, no. 18, pp. 2667–2674, 2002.
- [2] M. Sarasa, N. Riba, L. Zamora, and X. Carne, "Determination of stavudine in human plasma and urine by high-performance liquid chromatography using a reduced sample volume," *Journal of Chromatography B*, vol. 746, no. 2, pp. 183–189, 2000.
- [3] E. Kano, C. dos Reis Serra, E. Koono, S. S. Andrade, and V. Porta, "Determination of lamivudine in human plasma by HPLC and its use in bioequivalence studies," *International Journal of Pharmaceutics*, vol. 297, no. 1–2, pp. 73–79, 2005.
- [4] Z. Li, C. Ding, Q. Ge, Z. Zhou, X. Zhi, and X. Liu, "Simultaneous determination of lamivudine, stavudine and nevirapine in human plasma by LC-MS/MS and its application to pharmacokinetic study in clinic," *Biomedical Chromatography*, vol. 24, no. 9, pp. 926–934, 2010.
- [5] J. L. Wiesner, F. C. W. Sutherland, M. J. Smit et al., "Sensitive and rapid liquid chromatography-tandem mass spectrometry method for the determination of stavudine in human plasma," *Journal of Chromatography B*, vol. 773, no. 2, pp. 129–134, 2002.
- [6] D. Zhong, "Some aspects in establishing standard curves in bioanalyses with the weighted least squares method," *Chinese Journal of Pharmaceutical Analysis*, vol. 16, no. 5, pp. 343–346, 1996.

## Research Article

# Thickness-Controllable Silica Coating of CdTe QDs by Reverse Microemulsion Method for the Application in the Growth of Rice

Aiwu Wang,<sup>1,2</sup> Yuhong Zheng,<sup>1</sup> and Feng Peng<sup>1</sup>

<sup>1</sup> Institute of Botany, Jiangsu Province and Chinese Academy of Sciences, Nanjing Botanical Garden, Memorial Sun Yat-Sen, Nanjing 210014, China

<sup>2</sup> Department of Physics and Materials Science and Centre for Functional Photonics (CFP), City University of Hong Kong, 88 Tat Chee Avenue, Kowloon, Hong Kong

Correspondence should be addressed to Yuhong Zheng; friend266@163.com

Received 3 May 2014; Accepted 28 May 2014; Published 15 June 2014

Academic Editor: Qingrui Zhang

Copyright © 2014 Aiwu Wang et al. This is an open access article distributed under the Creative Commons Attribution License, which permits unrestricted use, distribution, and reproduction in any medium, provided the original work is properly cited.

Herein, we report the synthesis and surface modification of CdTe quantum dots (QDs) and the application in the rice growth. Water-soluble thioglycolic acid (TGA) stabilized CdTe quantum dots were synthesized firstly and then the surface modification was conducted. II–VI semiconductor nanocrystals prefer to be coated with silica as inert materials to improve their chemical properties. The toxicity of QDs reduced after the modification. Silica coated QDs were used in the growth of rice seed and the effect was discussed. In our knowledge it is the first time we report that the silica coated QDs had nice effect on the growth of rice.

## 1. Introduction

Colloidal II–VI semiconductor nanocrystals (quantum dots) have shown nice size-dependent optical properties with narrow bandgap [1] like CdS [2], CdSe [3], CdTe [4], CdHgTe [5], HgTe [6], and ZnSe [7] which exhibit great potential as a labeling material due to their unique size-tunable photoluminescence. In the past 20 years, great progress has been made in the synthesis of the quantum dots, and the quantum dots have applications for fluorescent biological research [8–12].

However, QDs have disadvantages in their applications: toxicity due to the heavy metal ions [13], the chemical stabilities, and oxidation in the surface area. To solve these problems, coating QDs with inert materials like silica would be a good choice [14]. Silica coating of semiconductor nanocrystals has received specific effects [15–17]. The methods of silica coating can be divided into two groups, that is, the reverse microemulsion method and Stober method. For the aqueous QDs, the reverse microemulsion (water in oil) can be used in silica coating with better controlling of particle

size than the Stober method. As for the Stober method, the silica sphere is usually large as 200 nm and bigger. By the reverse microemulsion method, the particle size can be controlled in a range of 30–150 nm [18] so that the reverse microemulsion method is more suitable. In our reported work, not only 40 nm of silica coating can be synthesized but also 400 nm of silica coating can be synthesized by the reverse microemulsion method.

In the past ten years, nanotechnology and nanomaterials were widely applied as life science [19]. But the research about their applications in agriculture began relatively late. Some work reported that silver nanoparticles reduced bacterial contaminations during tissue culture of *Araucaria excelsa* var. *Glauca* [20]; multiwall carbon nanotubes (MWNTs) had the ability to enhance the proliferation of callus cells of tobacco (*Nicotiana tabacum*) and make tomato produce two times more flowers and fruits [21, 22]; TiO<sub>2</sub> and MWNTs significantly promoted the germination, seedlings growth of tomato (*Lycopersicon esculentum*), and spinach (*Spinacia oleracea*) [23, 24]. Khodakovskaya et al. even illustrated

MWNTs have the potential to act as plant growth regulators [22]. Some results proved several kinds of nanomaterials had the positive effects at every stage of plant life cycle and showed great capacity to regulate the plant growth and development. We investigated that silica coated CdTe QDs had good effects on the rice root growth.

## 2. Experimental Section

**2.1. Chemicals.** Cd ( $\text{CH}_3\text{COO}$ )<sub>2</sub>\*2H<sub>2</sub>O (Aldrich, 99%), tetraethyl orthosilicate (TEOS) (98%), thioglycolic acid (TGA) (98%), sodium hydroxide, polyoxyethylene octyl phenyl ether (TritonX-100), cyclohexane, n-hexanol, ethanol, and ammonium solution were purchased from Sigma-Aldrich.

**2.2. Synthesis of CdTe QDs Stabilized by Thioglycolic Acid.** CdTe QDs were synthesized according to the method reported previously [25]. First of all, 0.08 mmol of Na<sub>2</sub>TeO<sub>3</sub>, 0.4 mmol of Cd ( $\text{CH}_3\text{COO}$ )<sub>2</sub>\*2H<sub>2</sub>O, and 160 mg of NaBH<sub>4</sub> were prepared. Secondly, the Cd ( $\text{CH}_3\text{COO}$ )<sub>2</sub>\*2H<sub>2</sub>O was dissolved in 50 mL deionized water and then poured into a flask with a magnetic bar. The solution was kept stirring. After that 100 mL of deionized water was added followed by the 36  $\mu\text{L}$  of TGA into the flask. Then the pH of the solution was adjusted to 11.5 by 2 M NaOH (several drops); next the Na<sub>2</sub>TeO<sub>3</sub> was dissolved in 50 mL deionized water. After 5 minutes, Na<sub>2</sub>TeO<sub>3</sub> with NaBH<sub>4</sub> was added to the solution; other five minutes later, the flask was connected to a reflux condenser and through the opening at 100°C—up to 1 to 7 hours under air conditions. Finally, after cooling the filtered solution was poured into the bottle and stored in 4°C without washing.

**2.3. Synthesis of Silica Coated CdTe QDs.** Silica coated QDs were prepared according to previous reports by the reverse microemulsion method [16]. In detail, 4 mL of the solution prepared CdTe QDs was washed one time by 4 mL of isopropanol. The microemulsion solution was combined by 15 mL of cyclohexane, 2.25 mL of Triton X-100, and 1.5 mL of n-hexanol under the N<sub>2</sub> atmosphere for half an hour (solution 1). Then 40  $\mu\text{L}$  of ammonia solution (25% by weight) was introduced and several drops of 1 M NaOH were added to make the pH to 12 (solution 2). The washed CdTe QDs dissolved in 1 mL of solution 2 (solution 3). Then the solution 3 was introduced into the prepared solution 1 (microemulsion liquid system). After 10 minutes of stirring, fixed amount of PDDA was introduced. 200  $\mu\text{L}$  TEOS was introduced under vigorous magnetic stirring. The reaction system was then sealed and kept in the dark; mixture was stirred at room temperature for 3 days. Isopropanol, ethanol, and water were used for washing the CdTe @ silica composite particles. In each washing process, a sonicator was needed. Firstly the ratio 1:1 with isopropanol was centrifuged; after that the precipitate was dissolved in the ethanol and deionized water. Finally CdTe @ silica composite particles were dissolved in the deionized water stored in 4°C.

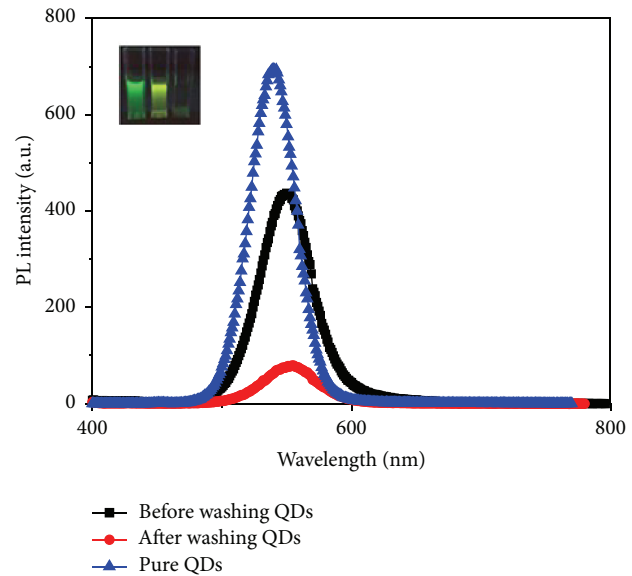


FIGURE 1: Fluorescence spectra of pure uncoated QDs, silica coated before washing QDs, and silica coated after washing QDs.

**2.4. Rice Seed Germination and Root Development.** Rice (*Oryza sativa* cv. 'Nanjing 45') seeds were immersed in a 0.1% potassium permanganate (KMnO<sub>4</sub>) solution for 24 h for sterilization. After rinsing three times with deionized water, the seeds were soaked in 100 mL 1/2 MS solution with silica coated QDs suspensions at various concentrations (0.13  $\mu\text{M}$ , 0.26  $\mu\text{M}$ , and 0.52  $\mu\text{M}$ ) in thermostat incubator (25  $\pm$  1°C, 60% rH, and 16/8 light/day) for germination, which 1/2 MS with no silica coated QDs was used as a control. The root length was measured at 8, 11, and 15 days after treatment. Each treatment was conducted with thirty seeds, and the results were presented as increasing percent of ten seedlings root length average from 8 to 11 and 11 to 15 days.

**2.5. Characterizations.** Steady-state photoluminescence (PL) spectra were measured on an Edinburgh Instrument FLS920P fluorescence spectrometer. TEM machine model used for the images of CdTe@SiO<sub>2</sub> is Philips-CM20 with the operation voltage 200 kV.

## 3. Results and Discussion

**3.1. Silica Coating of CdTe QDs and Thickness Controlling.** The fluorescence spectra and particles before and after silica coating were shown below in Figure 1.

After the reverse microemulsion method, the silica coated QDs are oil-soluble. After being washed in the ethanol and water, water-soluble silica coated QDs were available. After the washing, the amounts of QDs reduced so that the PL intensity decreased.

Transmission electron microscopy (TEM) images of silica coated QDs sample were presented in Figure 2.

As Figure 2 showed the nice effect with the coating is spherical and uniform. The chemical properties of QDs may

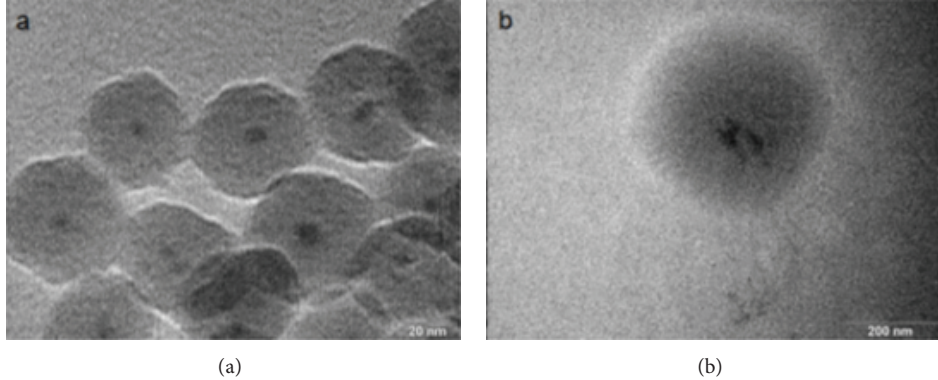


FIGURE 2: TEM images of samples of good silica coating of QDs under the suitable adjustment of conditions. (a) The size of silica is 40 nm; (b) the size of silica is 400 nm.

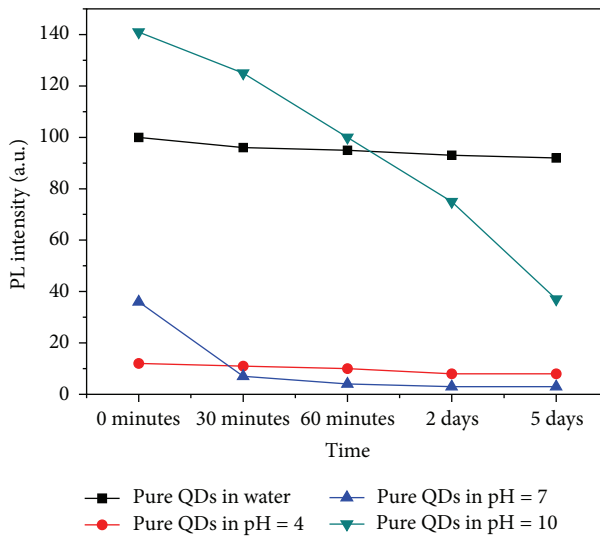


FIGURE 3: PL spectra of pure QDs in the different buffers tested for different times.

be better and also the stability. What is more, we can adjust the thickness of silica coating by controlling the amount of TEOS; the thickness of the silica coating is as large as 400 nm in comparison to the previous 40 nm.

**3.2. Stability Test between the Pure Uncoated QDs and Silica Coated QDs.** The pure CdTe and silica coated after washing CdTe QDs were tested for stability in water and the buffers with different pH (4, 7, and 10 corresponding) for 4 days. Results are presented in Figure 3 for uncoated samples and in Figure 5 for silica coated.

From Figure 3 we can realize that the pure QDs in the water are stable, in the buffer with pH = 10 had an increase of PL than that of in the water, in the buffers with pH = 7 and pH = 4 are of low PL compared to that of in the water. What is more, the buffer with pH = 4 can quench the QDs in a short time, which implied that the QDs are sensitive to the pH of solution.

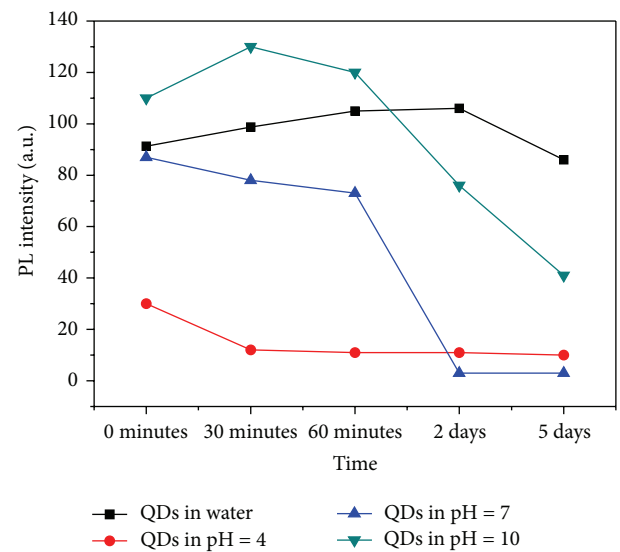


FIGURE 4: PL spectra of silica coating of QDs in the different buffers tested for different times.

From Figure 4 we can observe that the PL of silica coated QDs in the buffer with pH = 10 had a slight increase at first compared to the pure uncoated QDs in the pH = 10. And the PL of silica coated QDs in the buffer with pH = 7 had a higher increase than the pure QDs in the pH = 7. And the PL of silica coated QDs in the buffer with pH = 4 was slightly higher than the pure uncoated QDs. With the good effect we can infer that the stability of silica coated QDs is better than the pure uncoated QDs.

**3.3. Rice Seed Germination and Root Development.** Each treatment was conducted with thirty seeds, and the results are presented as increasing percent of ten seedlings root length average from 8 to 11 and 11 to 15 days.

As we can observe from Figure 5 that the rice roots with silica coated QDs were longer than the rice roots without silica coated QDs inside. The pure QDs significantly inhibited the growth of root due to its toxicity. The different increment

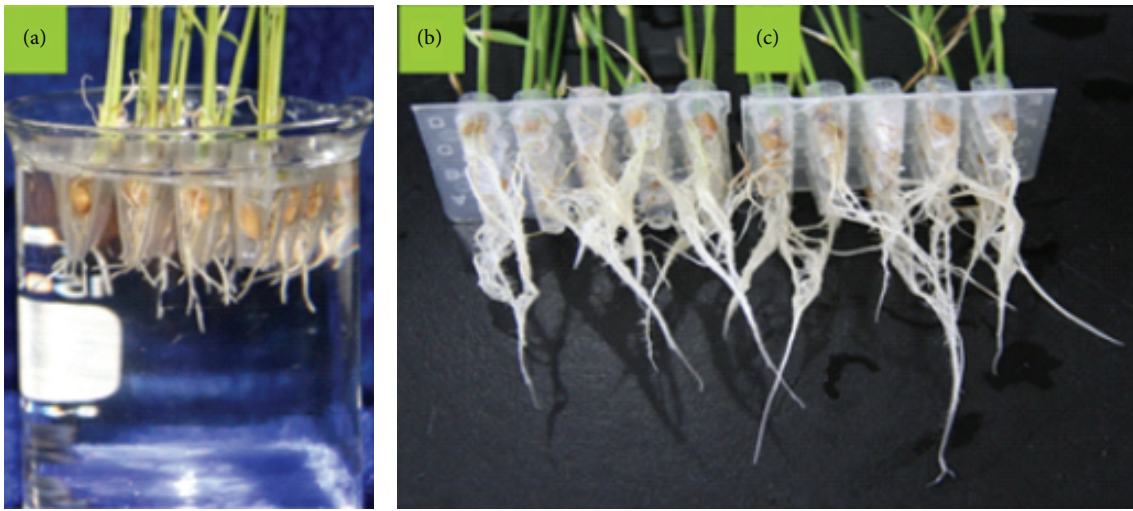


FIGURE 5: Image of rice roots (a) with pure QDs; (b) without QDs; and (c) with silica coated QDs.

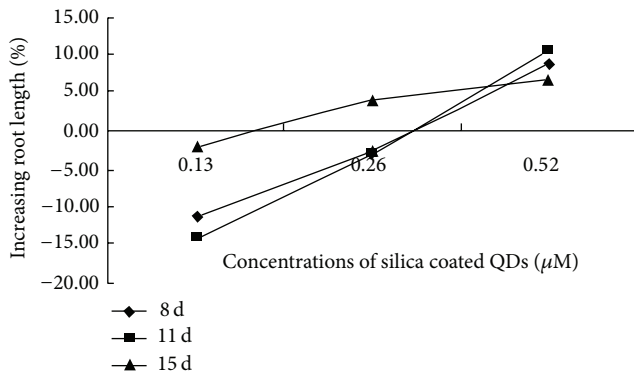


FIGURE 6: Effects of silica coated QDs at different concentrations on rice root length.

of different concentrations of silica coated QDs was shown below as Figure 6.

To test the action of the synthesized silica coated QDs, we placed the seeds in 1/2 Murashige and Skoog solution supplemented with different concentrations of silica coated QDs ( $0.13 \mu\text{M}$ ,  $0.26 \mu\text{M}$ , and  $0.52 \mu\text{M}$ ). As shown in Figures 5 and 6, all the treatments led to the growth of the increasing percent of root length. Silica coated CdTe QDs did not have toxic effect but promoted root elongation of rice seedlings. The roots grew faster in shorter time under low concentrations. The results were different from many other researches about the nanomaterials affecting the plant growth [26–29]. Many investigations in the past were negative mainly due to the toxicity of nanoparticles. For example,  $\text{TiO}_2$  nanoparticles significantly inhibited the germination rates, root lengths, and biomasses of tobacco seedlings [30]. Iron ions/NPs did not affect the physiological parameters with respect to water control. Conversely, Cu ions/NPs reduced water content, root length, and dry biomass of the lettuce plants [31]. Toxicity of  $\text{CuO}$  NPs was mainly due to NPs solubilization in the media [32]. However, there are some nanoparticles that can

promote the growth of plant. Iron nanoparticles can enhance root elongation of *arabidopsis thaliana* by triggering cell wall loosening [33]. Silica coated QDs are minority nanomaterials that are helpful in the growth of plants. And the mechanism needs to be further studied.

#### 4. Conclusion

Silica coating of CdTe QDs particles has successfully been prepared by a reverse microemulsion method and the thickness of silica sphere can be varied from 40 nm to 440 nm. The amount of TEOS is critical for the experiments. The stability test was made which approved the better stability of silica coated QDs than pure uncoated QDs. At last the 40 nm size of silica coated CdTe QDs had good effect on the rice roots growth for the first time reported.

#### Conflict of Interests

The authors declared that there is no conflict of interests regarding the publication of this paper.

#### Acknowledgments

The authors thank the support from Institute of Botany, Jiangsu Province, and Chinese Academy of Sciences, Nanjing Botanical Garden.

#### References

- [1] M. Bruchez Jr., M. Moronne, P. Gin, S. Weiss, and A. P. Alivisatos, "Semiconductor nanocrystals as fluorescent biological labels," *Science*, vol. 281, no. 5385, pp. 2013–2016, 1998.
- [2] T. Vossmeyer, L. Katsikas, M. Giersig et al., "CdS nanoclusters: synthesis, characterization, size dependent oscillator strength, temperature shift of the excitonic transition energy, and reversible absorbance shift," *Journal of Physical Chemistry*, vol. 98, no. 31, pp. 7665–7673, 1994.

- [3] A. L. Rogach, A. Kornowski, M. Gao, A. Eychmüller, and H. Weller, "Synthesis and characterization of a size series of extremely small thiol-stabilized CdSe nanocrystals," *Journal of Physical Chemistry B*, vol. 103, no. 16, pp. 3065–3069, 1999.
- [4] A. L. Rogach, L. Katsikas, A. Kornowski et al., "Synthesis and characterization of thiol-stabilized CdTe nanocrystals," *Berichte der Bunsengesellschaft für Physikalische Chemie*, vol. 100, no. 11, pp. 1772–1778, 1996.
- [5] M. T. Harrison, S. V. Kershaw, M. G. Burt, A. Eychmüller, H. Weller, and A. L. Rogach, "Colloidal nanocrystals for telecommunications complete coverage of the low-loss fiber windows by mercury telluride quantum dots," *Materials Science and Engineering B*, vol. 335, pp. 69–70, 2000.
- [6] A. Rogach, S. Kershaw, M. Burt et al., "Optical properties of semiconductor nanostructures," *Advanced Materials*, vol. 11, pp. 552–555, 1999.
- [7] A. Shavel, N. Gaponik, and A. Eychmüller, "Efficient UV-blue photoluminescing thiol-stabilized water-soluble alloyed ZnSe (S) nanocrystals," *Journal of Physical Chemistry B*, vol. 108, no. 19, pp. 5905–5908, 2004.
- [8] M. Green, "Semiconductor quantum dots as biological imaging agents," *Angewandte Chemie International Edition*, vol. 43, no. 32, pp. 4129–4131, 2004.
- [9] X. Gao, Y. Cui, R. M. Levenson, L. W. K. Chung, and S. Nie, "In vivo cancer targeting and imaging with semiconductor quantum dots," *Nature Biotechnology*, vol. 22, no. 8, pp. 969–976, 2004.
- [10] K. J. Jaiswal and M. S. Sanford, "Potentials and pitfalls of fluorescent quantum dots for biological imaging," *Trends in Cell Biology*, vol. 14, no. 9, pp. 497–504, 2004.
- [11] D. Gerion, F. Pinaud, S. C. Williams et al., "Synthesis and properties of biocompatible water-soluble silica-coated CdSe/ZnS semiconductor quantum dots," *Journal of Physical Chemistry B*, vol. 105, no. 37, pp. 8861–8871, 2001.
- [12] W. C. W. Chan and S. Nie, "Quantum dot bioconjugates for ultrasensitive nonisotopic detection," *Science*, vol. 281, no. 5385, pp. 2016–2018, 1998.
- [13] A. M. Derfus, W. C. W. Chan, and S. N. Bhatia, "Probing the cytotoxicity of semiconductor quantum dots," *Nano Letters*, vol. 4, no. 1, pp. 11–18, 2004.
- [14] S. T. Selvan, T. T. Tan, and J. Y. Ying, "Robust, non-cytotoxic, silica-coated CdSe quantum dots with efficient photoluminescence," *Advanced Materials*, vol. 17, no. 13, pp. 1620–1625, 2005.
- [15] A. L. Rogach, D. Nagesha, J. W. Ostrander, M. Giersig, and N. A. Kotov, "'Raisin bun'-type composite spheres of silica and semiconductor nanocrystals," *Chemistry of Materials*, vol. 12, no. 9, pp. 2676–2685, 2000.
- [16] Y. H. Yang and M. Y. Gao, "Preparation of fluorescent SiO<sub>2</sub> particles with single CdTe nanocrystal cores by the reverse microemulsion method," *Advanced Materials*, vol. 17, no. 19, pp. 2354–2357, 2005.
- [17] T. Nann and P. Mulvaney, "Single quantum dots in spherical silica particles," *Angewandte Chemie International Edition*, vol. 43, no. 40, pp. 5393–5396, 2004.
- [18] S. Chang, L. Liu, and S. A. Asher, "Preparation and properties of tailored morphology, monodisperse colloidal silica-cadmium sulfide nanocomposites," *Journal of the American Chemical Society*, vol. 116, no. 15, pp. 6739–6744, 1994.
- [19] C. Bai, "Ascent of nanoscience in China," *Science*, vol. 309, no. 5731, pp. 61–63, 2005.
- [20] M. Sarmast, H. Salehi, and M. Khosh-Khui, "Nano silver treatment is effective in reducing bacterial contaminations of Araucaria excelsa R. Br. var. glauca explants," *Acta Biologica Hungarica*, vol. 62, no. 4, pp. 477–484, 2011.
- [21] M. V. Khodakovskaya, K. de Silva, A. S. Biris, E. Dervishi, and H. Villagarcia, "Carbon nanotubes induce growth enhancement of tobacco cells," *ACS Nano*, vol. 6, no. 3, pp. 2128–2135, 2012.
- [22] M. V. Khodakovskaya, B. S. Kim, J. N. Kim et al., "Carbon nanotubes as plant growth regulators: effects on tomato growth, reproductive system, and soil microbial community," *Small*, vol. 9, no. 1, pp. 115–123, 2013.
- [23] L. Zheng, F. S. Hong, S. P. Lu, and C. Liu, "Effect of nano-TiO<sub>2</sub> on strength of naturally aged seeds and growth of spinach," *Biological Trace Element Research*, vol. 104, no. 1, pp. 83–91, 2005.
- [24] M. V. Khodakovskaya, E. Dervishi, M. Mahmood et al., "Carbon nanotubes are able to penetrate plant seed coat and dramatically affect seed germination and plant growth," *ACS Nano*, vol. 3, no. 10, pp. 3221–3227, 2009.
- [25] S. Wu, J. Dou, J. Zhang, and S. Zhang, "A simple and economical one-pot method to synthesize high-quality water soluble CdTe QDs," *Journal of Materials Chemistry*, vol. 22, no. 29, pp. 14573–14578, 2012.
- [26] A. Menard, D. Drobne, and A. Jemec, "Ecotoxicity of nanosized TiO<sub>2</sub>. Review of in vivo data," *Environmental Pollution*, vol. 159, no. 3, pp. 677–684, 2011.
- [27] Q. M. Peng, J. X. Guo, Q. R. Zhang, A. G. Zhou, and Y. J. Tian, "Unique lead adsorption behavior of activated hydroxyl group in two-dimensional titanium carbide," *Journal of the American Chemical Society*, vol. 136, no. 11, pp. 4113–4116, 2014.
- [28] Q. Zhang, Q. Du, M. Hua, T. Jiao, F. Gao, and B. Pan, "Sorption enhancement of lead ions from water by surface charged polystyrene-supported nano-zirconium oxide composites," *Environmental Science and Technology*, vol. 47, no. 12, pp. 6536–6544, 2013.
- [29] Q. Zhang, Q. Du, T. Jiao et al., "Rationally designed porous polystyrene encapsulated zirconium phosphate nanocomposite for highly efficient fluoride uptake in waters," *Scientific Reports*, vol. 3, article 2551, 2013.
- [30] T. P. Frazier, C. E. Burkew, and B. Zhang, "Titanium dioxide nanoparticles affect the growth and microRNA expression of tobacco (*Nicotiana tabacum*)," *Functional & Integrative Genomics*, vol. 14, no. 1, pp. 75–83, 2014.
- [31] J. Trujillo-Reyes, S. Majumdar, C. E. Botez, J. R. Peralta-Videa, and J. L. Gardea-Torresdey, "Exposure studies of core-shell Fe/Fe<sub>3</sub>O<sub>4</sub> and Cu/CuO NPs to lettuce (*Lactuca sativa*) plants: are they a potential physiological and nutritional hazard?" *Journal of Hazardous Materials*, vol. 267, pp. 255–263, 2014.
- [32] F. Perreault, R. Popovic, and D. Dewez, "Different toxicity mechanisms between bare and polymer-coated copper oxide nanoparticles in *Lemna gibba*," *Environmental Pollution*, vol. 185, pp. 219–227, 2014.
- [33] J.-H. Kim, Y. Lee, E.-J. Kim et al., "Exposure of iron nanoparticles to arabidopsis thaliana enhances root elongation by triggering cell wall loosening," *Environmental Science & Technology*, vol. 48, no. 6, pp. 3477–3485, 2014.

## Research Article

# Size Effects: The Relation to the Percentage of Atoms That Participate in the Deformation of ZrCu Metallic Glass

L. K. Gao, F. L. Zhao, N. Xu, L. Qi, and R. P. Liu

State Key Laboratory of Metastable Materials Science & Technology, Yanshan University,  
Hebei Street 438, Qinhuangdao 066004, China

Correspondence should be addressed to L. Qi; qili@ysu.edu.cn and R. P. Liu; riping@ysu.edu.cn

Received 29 April 2014; Accepted 28 May 2014; Published 15 June 2014

Academic Editor: Xinqing Chen

Copyright © 2014 L. K. Gao et al. This is an open access article distributed under the Creative Commons Attribution License, which permits unrestricted use, distribution, and reproduction in any medium, provided the original work is properly cited.

Molecular dynamics simulations indicate that with the model diameter gradually decreasing the deformation mode of ZrCu metallic glass evolves from highly localized shear band formation to homogeneous deformation with obvious transition in  $D = 7\text{--}9\text{ nm}$ . Through the statistic of atoms that sustain shear strain larger than 8% in the models with 8% strain along  $z$ -direction, we found that the main reason for the uniform deformation that occurs in the smallest size model is that there are 61% atoms involved in the deformation, which significantly decrease the strain assigned to individual atoms, avoiding large atomic rearrangement and making those atoms evenly distributed in the model matrix.

## 1. Introduction

Metallic glasses (MGs) are a relatively new materials that have many excellent properties, such as high strength, high elastic limit, and high corrosion resistance [1]. But they almost have no plasticity under low temperature loads; this is mainly due to the highly spontaneous localization within a narrow shear band during the plastic deformation process, which rapidly expands along the shear plane and disables the material instantaneously [2]; this defect seriously affects the MGs as the application of engineering material. So how to improve the plasticity of MGs under low temperature loads became the focus of study. Similar to the crystalline alloy, reducing the size of the amorphous alloy is a kind of possible way to improve the plasticity [3, 4], but there are many controversies about size effects on amorphous alloy. (i) The preparation of micron or nanometer MGs usually uses focused ion beam (FIB) in experiments, the high-energy ion beam would damage the surface [5–7] and the fabricated sample generally exists 1°–2° deviation and forms a cone, and the cone sample inevitably induces complex stress states and deformation localization on the end of the sample [8]. (ii) With the decrease of the sample size, the change of deformation behavior is gradual or abrupt due to the difficulty to preparation of nanoscale sample, making

the problem hard to get a system discussion and proof in experiment. So the size effects on the deformation behavior and deformation mechanism of MGs has always been a continuous explore problem.

In this paper, we systematically study the size effects on the deformation behavior of the nanoscale MGs using molecular dynamics simulation. Molecular dynamics simulation can prepare perfect nanoscale cylindrical model, and the preparation process would not damage the surface state, so we can cleverly avoid some experiment shortages and play a supplement and guiding role in experimental study.

## 2. Model and Method

In our MD simulation, we studied the deformation behavior and the deformation mechanism of ZrCu metallic glass (MG) with different size models. ZrCu amorphous alloy is a binary alloy [9], since the binary alloys easier to model and analyse than the multielement alloys, it makes ZrCu an attractive MG to study theoretically. The simulations are carried out using the embedded atom method (EAM) potential, supplied in LAMMPS [10]. A small box of 10000 random configuration atoms with 3D periodic boundary conditions (PBCs) is first equilibrated at 2600 K for 50 ps, and then we cool the system from 2600 K down to 50 K in

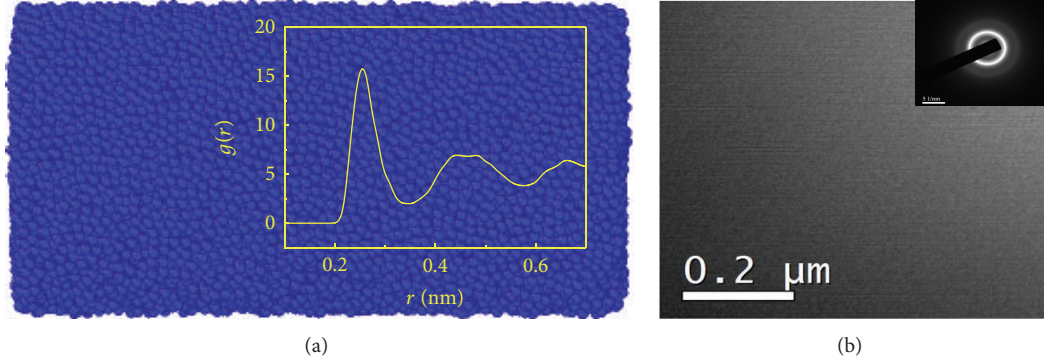


FIGURE 1: (a) The amorphous alloy model and (b) TEM photo of the ZrCu alloy.

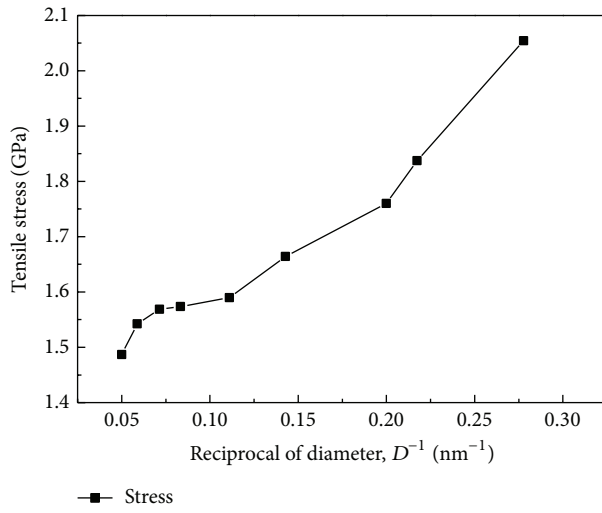


FIGURE 2: Tensile strength change curve with the decrease of the model size.

50 K decrements at a constant quenching rate of 2 K/ps to the glass state (50 K), at zero external pressure as shown in Figure 1. Figure 1(a) is the RDF of the simulation model which indicates the amorphous structure. Figure 1(b) shows a typical bright-field TEM image of ZrCu alloy and its corresponding selected-area electron diffraction (SAED) pattern. It can be seen that a uniform image without any contrast and sharp electron diffraction rings were observed, indicating a typical amorphous structure. To get large samples, we replicate the 10000 atom configuration, which then annealed for 500 ps at 800 K to remove the increased surface energy and then relaxation under 50 K for 500 ps. By deleting the redundant atoms from cube configuration we get a series of diameters ( $D$ ) from 3.6 nm to 20 nm amorphous cylindrical model with aspect ratio of 2:1. A constant strain rate of  $1 \times 10^8$  s<sup>-1</sup> along  $z$ -direction is used at low temperature of 50 K by moving the rigid atoms at one end along the  $z$  axis, while keeping the rigid atoms at the other end unchanged.

### 3. Results and Discussion

Figure 2 shows the relationship of the tensile strength and the reciprocal of diameter for different size models. We find that

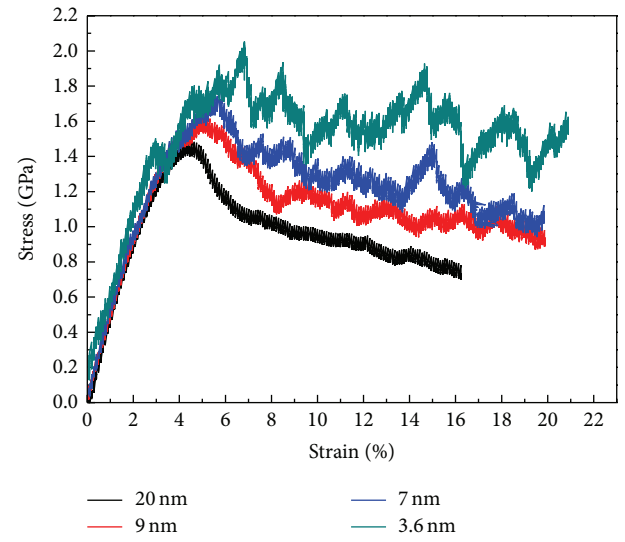


FIGURE 3: The typical stress-strain curves for different size models during the tensile process.

with the decrease of the model size the corresponding tensile strength increased significantly, and the smaller the model size the more significant increase of the tensile strength, suggesting the stronger ability to resist deformation of the model. It is worth noting that along the decreasing of model size the tensile strength is increased gradually.

Figure 3 shows the typical stress-strain curves, from which we observe that in the smallest size model the stress-strain curve shows an obvious “rise and fall” phenomenon due to the stress is sensitive to the formation and propagation of individual plastic events in the small size model. In the  $D = 7\text{--}9$  nm model the wave amplitude and the number of fluctuation decreased greatly; this is mainly because with the increase of the model size, more local strain starts at the same time during the deformation process which weakens the mutation of stress and the wave amplitude of fluctuation. In the 20 nm cylindrical model the fluctuation phenomenon disappears completely and presents a smooth stress strain curve; however when the stress reaches its maximum then accompanied by shear softening occurs a sharply decline,

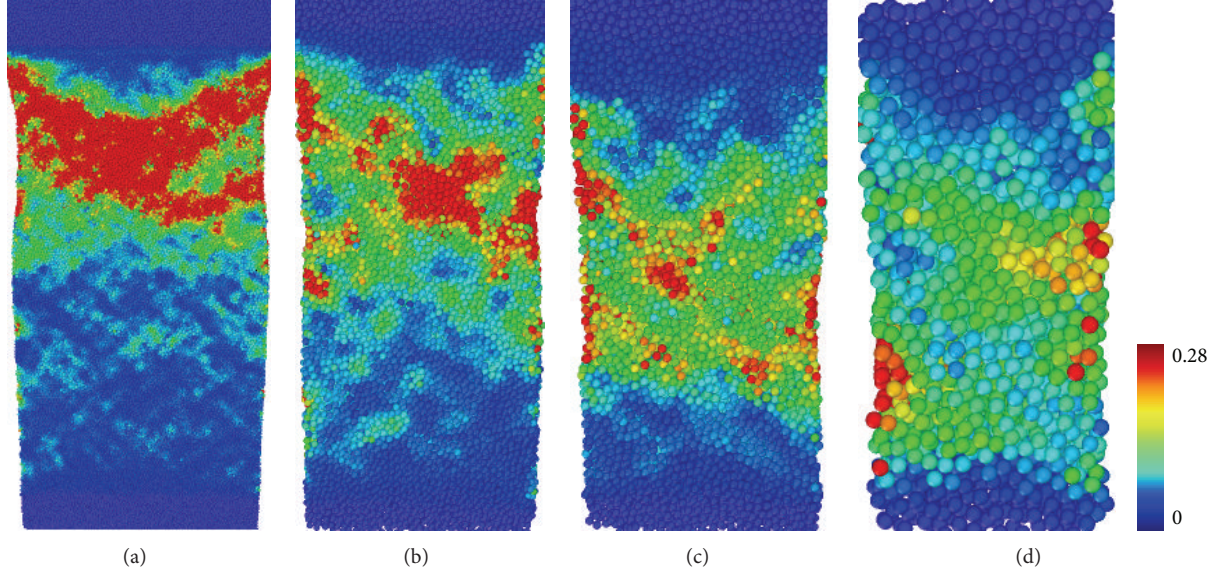


FIGURE 4: The distribution of local strain along the diameter: (a)  $D = 20 \text{ nm}$ , (b)  $D = 9 \text{ nm}$ , (c)  $D = 7 \text{ nm}$ , and (d)  $D = 3.6 \text{ nm}$ .

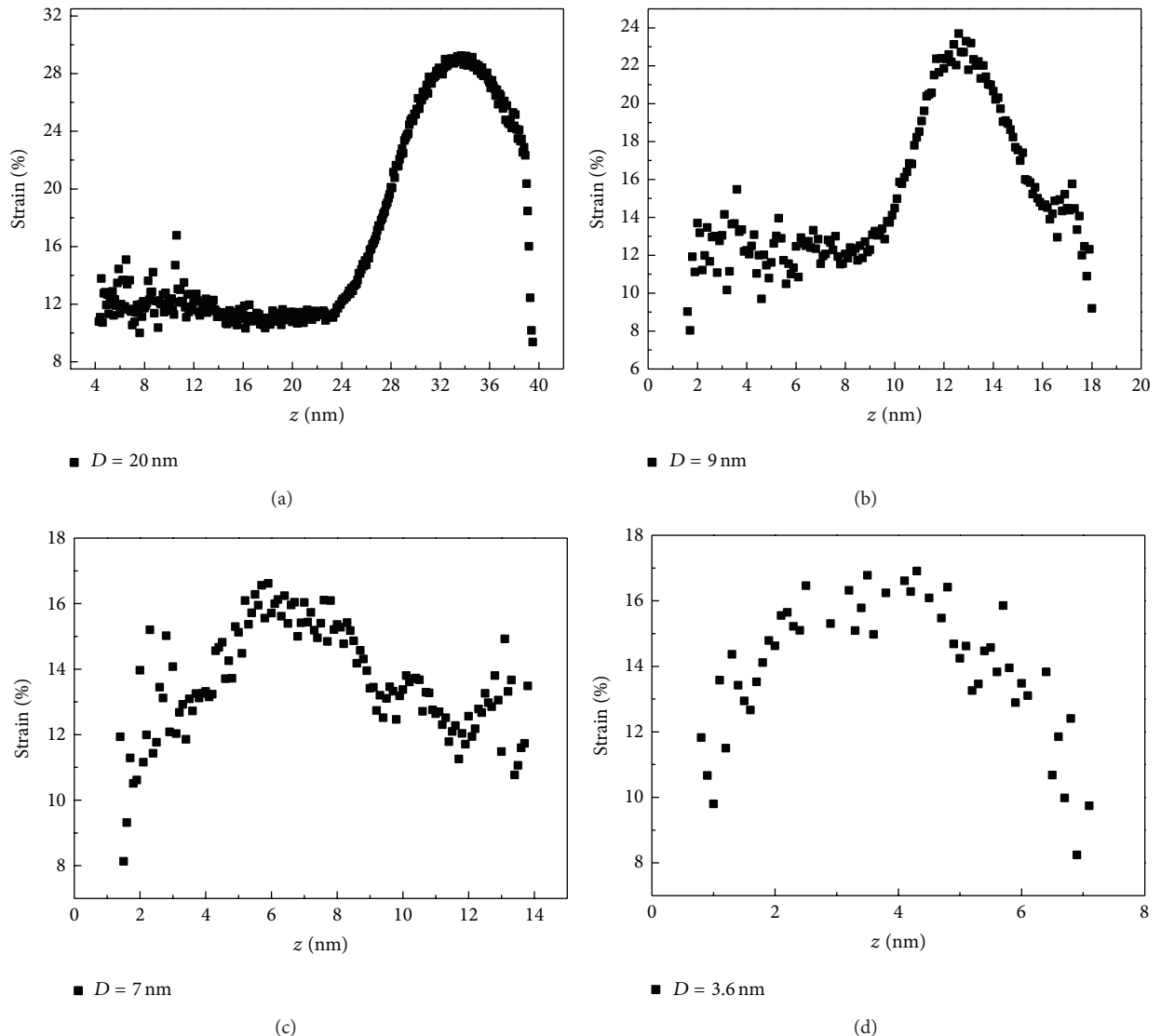


FIGURE 5: Statistical distribution of individual atom with shear strain  $> 8\%$  ((a), (b), (c), and (d) are  $D = 20 \text{ nm}, 9 \text{ nm}, 7 \text{ nm}$ , and  $3.6 \text{ nm}$  model, resp.).

heralding the formation of highly localized shear band along the shear plane [11].

In order to further understand the distribution of shear bands and the local strain along the decrease of model size during the deformation process, we use the local strain  $\eta_i^{\text{Mises}}$  to monitor the difference of the deformation [12].  $\eta_i^{\text{Mises}}$  is measured by referenced to the relaxed glass prior to employing uniaxial tensile deformation along  $z$ -direction. The atoms in the Figure 4 are colored by the  $\eta_i^{\text{Mises}}$  which tend to blue representing the smaller local strain value and tend to red representing larger local strain value.

From Figure 4(a) we can clearly see the shear band apparent on the direction of 45° and 135° and throughout the entire model, which can lead to shear instability with the increase of following strain. While Figures 4(b) and 4(c) present obvious transition process; 9 nm model appeared stress localization on the 45° and 135° direction, but without the formation of shear band, is a kind of transition to shear transformation process. The stress localization in  $D = 7$  nm model is distributed scatteredly on the surface and inside with blurred direction and Figure 4(d) model only with several obvious localization on the surface, with the internal strain values almost uniformly distributed. This shows that the size has a very large effect on the deformation behavior of ZrCu MGs, with the decrease of the size, ZrCu MGs have experienced from the highly localized shear band formation to the homogeneous deformation, and the deformation process exists with obvious transition in  $D = 7\text{--}9$  nm which demonstrate that the size decreased deformation mode is a gradual process instead of abrupt.

Statistic has been further performed on the individual atom along the  $z$ -direction strained 8% of the model and found that the number of atoms that is under the same shear strain accounts for different percentages of the total atoms in different models; the atoms that sustain shear strain larger than 8% in 3.6 nm model account for about 61% of the total atoms, while in 20 nm are only 37% and in 7 nm and 9 nm are about 55% and 49%, respectively. To some extent, this illustrates that in the large size model, only a small fraction of the atoms are involved in deformation, while in small size model there are more atoms participating in deformation. We define those atoms as participating deformation atoms. How those atoms are distributed in the model is of great concern. So we divided each model into 0.1 nm along the loading axis and plot the average von Mises shear strain in Figure 5 as a function of position.

From Figure 5 we can find that the maximum shear strain of schematic atoms decreases along the decrease of model size. And in the model in Figures 5(a) and 5(b) there are about 57% and 35% atoms, respectively, gathered in tensile end and sustained larger shear strain, which is a kind of unstable distribution state. While in the model in Figures 5(c) and 5(d) those atoms are basically evenly distributed in the matrix model, sharing the strain caused by the plastic deformation, making the model a high tensile strength and plastic deformation ability.

Rearrangement would take place when local atomic strain beyond a certain critical threshold [13–15], which exhibits a

strong autocatalytic behavior, is responsible for a considerable flow softening [16, 17]. That is larger local atomic strain more propensity of strain localization and the formation of shear band. In our study we find that in the smallest model there are 61% atoms that participate in deformation; thus the strain assigned to individual atom will significantly decrease, which avoids large atomic rearrangement during the deformation process, so these atoms basically diffuse in the model matrix. While there are only 37% atoms involved in the deformation of the  $D = 20$  nm model, the strain assigned to a single atom is greatly increased, so these atoms are more prone to restructuring. As a consequence, plastic deformation suffers a severe instability and forms the highly localized shear band. With the decrease of the model size, the fraction of atoms participating in deformation gradually increase, and this is the reason why the transition of the deformation mode is gradual instead of abrupt.

## 4. Conclusion

In summary, our MD simulations indicate that with the decrease of the model size the tensile strength of ZrCu metallic glass increases significantly and its deformation mode evolves from highly localized shear band formation to homogeneous deformation with obvious transition in  $D = 7\text{--}9$  nm. We further find that when the models strained 8% along the  $z$ -direction there are 61% atoms involved in the deformation in the smallest model and due to avoiding large atomic rearrangement those atoms evenly distributed in the matrix. While only 37% atoms participate in deformation in the  $D = 20$  nm model and because of an inevitable atomic rearrangement, the model exhibits a severe instability and forms the highly localized shear band.

## Conflict of Interests

The authors declare that there is no conflict of interests regarding the publication of this paper.

## Acknowledgments

This work was supported by the National Basic Research Program of China (2010CB731600) and the National Natural Science Foundation of China (51271161 and 51271162).

## References

- [1] E. Pekarskaya, C. P. Kim, and W. L. Johnson, “In situ transmission electron microscopy studies of shear bands in a bulk metallic glass based composite,” *Journal of Materials Research*, vol. 16, no. 9, pp. 2513–2518, 2001.
- [2] C. A. Schuh, T. C. Hufnagel, and U. Ramamurty, “Mechanical behavior of amorphous alloys,” *Acta Materialia*, vol. 55, no. 12, pp. 4067–4109, 2007.
- [3] D. Jang and J. R. Greer, “Transition from a strong-yet-brittle to stronger-and-ductile state by size reduction of metallic glasses,” *Nature Materials*, vol. 9, no. 3, pp. 215–219, 2010.

- [4] C. A. Volkert, A. Donohue, and F. Spaepen, "Effect of sample size on deformation in amorphous metals," *Journal of Applied Physics*, vol. 103, no. 8, Article ID 083539, 6 pages, 2008.
- [5] M. T. Myers, S. Charnvanichborikarn, C. C. Wei et al., "Phase transition, segregation and nanopore formation in high-energy heavy-ion-irradiated metallic glass," *Scripta Materialia*, vol. 67, no. 11, pp. 887–890, 2012.
- [6] E. G. Fu, J. Carter, M. Martin et al., "Ion irradiation induced nanocrystal formation in amorphous Zr<sub>55</sub>Cu<sub>30</sub>Al<sub>10</sub>Ni<sub>5</sub> alloy," *Nuclear Instruments and Methods in Physics Research B: Beam Interactions with Materials and Atoms*, vol. 267, no. 17, pp. 2827–2831, 2009.
- [7] J. Carter, E. G. Fu, M. Martin et al., "Effects of Cu ion irradiation in Cu<sub>50</sub>Zr<sub>45</sub>Ti<sub>5</sub> metallic glass," *Scripta Materialia*, vol. 61, no. 3, pp. 265–268, 2009.
- [8] C. Q. Chen, Y. T. Pei, O. Kuzmin, Z. F. Zhang, E. Ma, and D. Hossen, "Intrinsic size effects in the mechanical response of taper-free nanopillars of metallic glass," *Physical Review B—Condensed Matter and Materials Physics*, vol. 83, no. 18, Article ID 180201, 4 pages, 2011.
- [9] D. Wang, Y. Li, B. B. Sun, M. L. Sui, K. Lu, and E. Ma, "Bulk metallic glass formation in the binary Cu-Zr system," *Applied Physics Letters*, vol. 84, no. 20, pp. 4029–4031, 2004.
- [10] S. Plimpton, "Fast parallel algorithms for short-range molecular dynamics," *Journal of Computational Physics*, vol. 117, no. 1, pp. 1–19, 1995.
- [11] A. J. Cao, Y. Q. Cheng, and E. Ma, "Structural processes that initiate shear localization in metallic glass," *Acta Materialia*, vol. 57, no. 17, pp. 5146–5155, 2009.
- [12] F. Shimizu, S. Ogata, and J. Li, "Theory of shear banding in metallic glasses and molecular dynamics calculations," *Materials Transactions*, vol. 48, no. 11, pp. 2923–2927, 2007.
- [13] A. S. Argon and H. Y. Kuo, "Plastic flow in a disordered bubble raft (an analog of a metallic glass)," *Materials Science and Engineering*, vol. 39, no. 1, pp. 101–109, 1979.
- [14] A. S. Argon, "Mechanisms of inelastic deformation in metallic glasses," *Journal of Physics and Chemistry of Solids*, vol. 43, no. 10, pp. 945–961, 1982.
- [15] V. V. Bulatov and A. S. Argon, "A stochastic model for continuum elasto-plastic behavior. I. Numerical approach and strain localization," *Modelling and Simulation in Materials Science and Engineering*, vol. 2, no. 2, pp. 167–184, 1994.
- [16] M. L. Falk and J. S. Langer, "Dynamics of viscoplastic deformation in amorphous solids," *Physical Review E—Statistical Physics, Plasmas, Fluids, and Related Interdisciplinary Topics*, vol. 57, no. 6, pp. 7192–7205, 1998.
- [17] H. Bei, S. Xie, and E. P. George, "Softening caused by profuse shear banding in a bulk metallic glass," *Physical Review Letters*, vol. 96, no. 10, Article ID 105503, 4 pages, 2006.

## Research Article

# Preparation and Characterization of Binary Organogels via Some Azobenzene Amino Derivatives and Different Fatty Acids: Self-Assembly and Nanostructures

Haiying Guo,<sup>1</sup> Tifeng Jiao,<sup>1</sup> Xihai Shen,<sup>2</sup> Qingrui Zhang,<sup>1</sup> Adan Li,<sup>1</sup> and Faming Gao<sup>1</sup>

<sup>1</sup> Hebei Key Laboratory of Applied Chemistry, School of Environmental and Chemical Engineering, Yanshan University, Qinhuangdao 066004, China

<sup>2</sup> Department of Chemistry, Hebei Normal University of Science and Technology, Qinhuangdao 066004, China

Correspondence should be addressed to Tifeng Jiao; [tfjiao@ysu.edu.cn](mailto:tfjiao@ysu.edu.cn) and Qingrui Zhang; [zhangqr@ysu.edu.cn](mailto:zhangqr@ysu.edu.cn)

Received 9 March 2014; Accepted 7 April 2014; Published 11 June 2014

Academic Editor: Xinqing Chen

Copyright © 2014 Haiying Guo et al. This is an open access article distributed under the Creative Commons Attribution License, which permits unrestricted use, distribution, and reproduction in any medium, provided the original work is properly cited.

In present work the gelation behaviors of binary organogels composed of azobenzene amino derivatives and fatty acids with different alkyl chains in various organic solvents were designed and investigated. Their gelation behaviors in 20 solvents were tested as new binary organic gelators. It showed that the length of alkyl substituent chains and azobenzene segment have played a crucial role in the gelation behavior of all gelator mixtures in various organic solvents. Longer alkyl chains in molecular skeletons in present gelators are favorable for the gelation of organic solvents. Morphological studies revealed that the gelator molecules self-assemble into different aggregates from lamella, wrinkle, to belt with change of solvents. Spectral studies indicated that there existed different H-bond formation and hydrophobic force, depending on different substituent chains in molecular skeletons. The present work may also give new perspectives for designing new binary organogelators and soft materials.

## 1. Introduction

In recent years, organogels have been attracting more attention as one class of important soft materials, in which organic solvents are immobilized by gelators [1–4]. Although gels are widely found in polymer systems, there has recently been an increasing interest in low-molecular-mass organic gelators (LMOGs) [5–8]. In recent years, physical gelation of organic solvents by LMOGs has become one of the hot areas in the soft matter research due to their scientific values and many potential applications in the biomedical field, including tissue engineering, controlled drug release, and medical implants [9–12]. The gels based on LMOGs are usually considered as supramolecular gels, in which the gelator molecules self-assemble into three-dimensional networks in which the solvent is trapped via various noncovalent interactions, such as hydrogen bonding,  $\pi$ - $\pi$  stacking, van der Waals interaction, dipole-dipole interaction, coordination, solvophobic interaction, and host-guest interaction [13–16]. Such organogels

have some advantages over polymer gels: the molecular structure of the gelator is defined and the gel process is usually reversible. Such properties make it possible to design various functional gel systems and produce more complicated and defined, as well as controllable, nanostructures [17–20].

In our reported work, the gelation properties of some cholesterol imide derivatives consisting of cholesteryl units and photoresponsive azobenzene substituent groups have been investigated [21]. We found that a subtle change in the headgroup of azobenzene segment can produce a dramatic change in the gelation behavior of both compounds. In addition, the gelation properties of bolaform and trigonal cholesteryl derivatives with different aromatic spacers have been characterized [22]. Therein, we have investigated the spacer effect on the microstructures of such organogels and found that various kinds of hydrogen bond interactions among the molecules play an important role in the formation of gels. Furthermore, in another relative research work, the gelation behaviors of some new azobenzene imide derivatives

with different alkyl substituent chains and headgroups of azobenzene residues were investigated [23]. The experimental results indicated that more alkyl chains in molecular skeletons in synthesized imide gelators were favorable for the gelation of organic solvents.

As a continuous research work, herein, we have designed and prepared new binary organogels composed of aminoazobenzene derivatives and fatty acids with different alkyl chains. We have found that some of present mixtures of acid/amine compounds could form different organogels in various organic solvents. Morphological characterization of the organogels revealed different structures of the aggregates in the gels. We have investigated the effect of alkyl substituent chains in gelators on the microstructures of such organogels in detail and found different kinds of hydrogen bond interactions.

## 2. Experiments

**2.1. Materials.** The starting materials, 4-aminoazobenzene, 2-aminoazotoluene, stearic acid, palmitic acid, tetradecanoic acid, and dodecanoic acid, were purchased from Alfa Aesar Tianjin Chemicals, Aldrich Chemicals, and TCI Shanghai Chemicals, respectively. Other used reagents were all for analysis purity from Beijing Chemicals and were distilled before use.

**2.2. Gelation Test.** All mixed organogels were prepared according to a simple procedure. Firstly, these fatty acid and amine derivatives were mixed with 1:1 molar ratio according to the number matching of intermolecular carboxylic acid and amine group, respectively. Then, a weighted amount of binary mixtures and a measured volume of selected pure organic solvent were placed into a sealed glass bottle and the solution was heated in a water bath until the solid was dissolved. Then, the solution was cooled to room temperature in air and the test bottle was inverted to see if a gel was formed. When the binary mixtures formed a gel by immobilizing the solvent at this stage, it was denoted as "G." For the systems in which only solution remained until the end of the tests, they were referred to as solution (S). When the binary mixtures formed into a few precipitate in some solvent, it was denoted as a "PS." Critical gelation concentration refers to the minimum concentration of the gelator for gel formation.

**2.3. Measurements.** Firstly, the xerogel was prepared by a vacuum pump for 12–24 h. The dried sample thus obtained was attached to copper foil, glass, and  $\text{CaF}_2$  slice for morphological and spectral investigation, respectively. Before SEM measurement, the samples were coated on copper foil fixed by conductive adhesive tape and shielded by gold. SEM pictures of the xerogel were taken on a Hitachi S-4800 field emission scanning electron microscopy with the accelerating voltage of 5–15 kV. Transmission FT-IR spectra of the xerogel were obtained by Nicolet is/10 FT-IR spectrophotometer from Thermo Fisher Scientific Inc. by average 32 scans and at a resolution of  $4 \text{ cm}^{-1}$ . The XRD measurement was conducted

using a Rigaku D/max 2550PC diffractometer (Rigaku Inc., Tokyo, Japan). The XRD pattern was obtained using  $\text{CuK}\alpha$  radiation with an incident wavelength of 0.1542 nm under a voltage of 40 kV and a current of 200 mA. The scan rate was  $0.5^\circ/\text{min}$ .

## 3. Results and Discussions

**3.1. Gelation Behaviors of These Binary Mixtures.** The gelation performances of all binary mixtures in 20 solvents are tested. The experimental data showed that the binary mixtures of fatty acids with different alkyl chains and 4-aminoazobenzene/2-aminoazotoluene could form organogels in special organic solvents, as listed in Table 1. The binary mixtures of fatty acids with different carbon numbers (18, 16, 14, and 12) and 4-aminoazobenzene are denoted as C18-Azo, C16-Azo, C14-Azo, and C12-Azo, respectively. Similarly, the binary mixtures of these acids and 2-aminoazotoluene are denoted as C18-Azo-Me, C16-Azo-Me, C14-Azo-Me, and C12-Azo-Me, respectively. Firstly, for the mixtures containing 4-aminoazobenzene, C18-Azo, C16-Azo, and C14-Azo can form organogel in ethanolamine, while C12-Azo do no form any organogel in present solvents. In addition, it is interesting to note that C16-Azo can form another organogel in nitrobenzene. However, for the mixtures containing 2-aminoazotoluene, only C18-Azo-Me and C16-Azo-Me can form gel in ethanolamine, respectively. Their photographs of all as-made organogels in different solvents were shown in Figure 1. The present research results indicated that length change of alkyl chains can have a profound effect upon the gelation abilities of these studied mixtures. It seemed that longer alkyl chains in molecular skeletons in present mixture gelators are more favorable for the present mixtures, which was similar to the recent reports [21, 22].

**3.2. Morphological Investigation of Organogels.** Many researchers have reported that a gelator molecule constructs nanoscale superstructures such as fibers, ribbons, and sheets in a supramolecular gel [23, 24]. To obtain a visual insight into the gel nanostructures, the typical organized structures of these organogels were studied by SEM technique, as shown in Figure 2. From the present diverse images, it can be obviously observed that the nanostructures of all xerogels from ethanolamine and nitrobenzene are significantly different from each other, and the morphologies of the aggregates change from lamella, wrinkle, to belt with change of solvents and mixtures. In addition, more rod-like or belt-like aggregates with different sizes were prepared in gels of C16-Azo in nitrobenzene. In addition, it is interesting to note that these belt aggregates showed a tendency to aggregate together due to highly directional intermolecular interactions and/or solvent evaporation. The difference of morphologies can be mainly due to the different strengths of the intermolecular hydrophobic force between alkyl chains of fatty acids, which have played an important role in regulating the intermolecular orderly staking and formation of special aggregates.

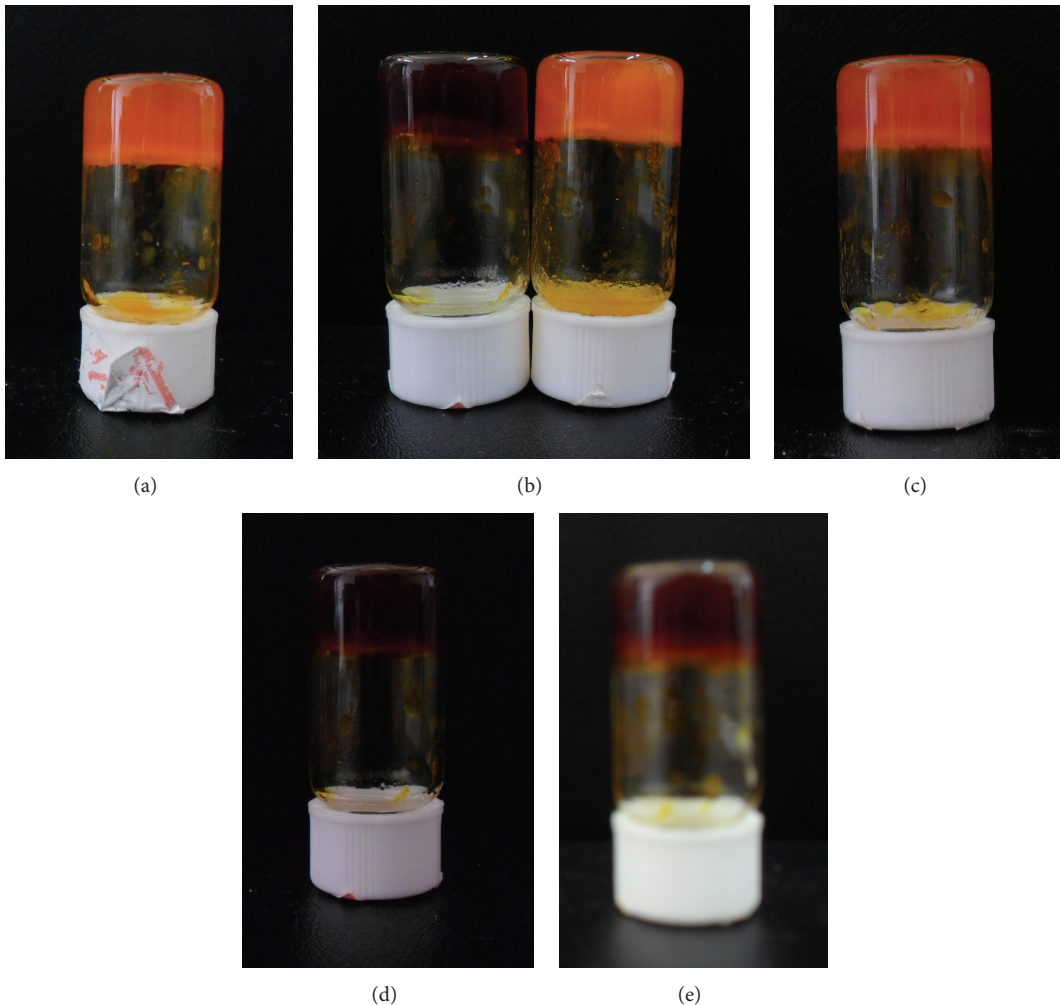


FIGURE 1: Photographs of as-made organogels: (a) C18-Azo; (b) C16-Azo; (c) C14-Azo; (d) C18-Azo-Me; (e) C16-Azo-Me, respectively.

**3.3. Spectral Investigation of Organogels.** In addition, in order to further investigate the orderly stacking of xerogels nanostructures, XRD of all xerogels from gels were measured, as shown in Figure 3. Firstly, the curves of C16-Azo xerogels from ethanolamine and nitrobenzene show similar strong peaks in the angle region ( $2\theta$  values, 3.56, 7.18, 10.90, 18.28, and 21.94°) corresponding to  $d$  values of 2.48, 1.23, 0.81, 0.49, and 0.41 nm, respectively. In addition, for the curves of C14-Azo and C18-Azo xerogels from ethanolamine, weaker peaks appeared, suggesting more disordered structures in the gels. However, as for the curves of C18-Azo-Me and C16-Azo-Me from ethanolamine, the minimum  $2\theta$  values are 3.20 and 3.32°, corresponding to  $d$  values of 2.76 and 2.66 nm, respectively. The difference of values between C16-Azo and C16-Azo-Me can be mainly assigned to the change of substituent groups linked to azobenzene segment in the molecular skeleton, which affected the assembly modes in the 3D stacking of organogels [22]. The XRD results described above demonstrated again that the many factors, such as chain length and substituent group, had great effect on the assembly modes of these gelator mixtures.

It is well-known that hydrogen bonding plays an important role in the self-assembly process of organogels [25–27]. At present, in order to further clarify this and investigate the effect of many factors on assembly, we have measured the FT-IR spectra of all xerogels, as shown in Figure 4. Firstly, C18-Azo xerogel was taken as examples, as shown in Figure 4(a). Some main peaks were observed at 3354, 3224, 2918, 2850, 1724, 1633, and 1470  $\text{cm}^{-1}$ , respectively, which can be assigned to the N-H and O-H stretching, methylene stretching, carbonyl group band, amide I band, and methylene scissoring, respectively [28–31]. These bands indicated the formation of hydrogen bonding interactions between intermolecular amino and carboxylic acid groups in the gel state, which can regulate the stacking of the gelator molecules to self-assemble into ordered structures. Similar spectra were observed for other xerogels.

Considering the XRD results described above and the hydrogen bonding nature of these binary mixtures as confirmed by FT-IR measurements, a possible assembly mode for present xerogels was proposed and schematically shown in Figure 5. As for C18-Azo containing longer alkyl

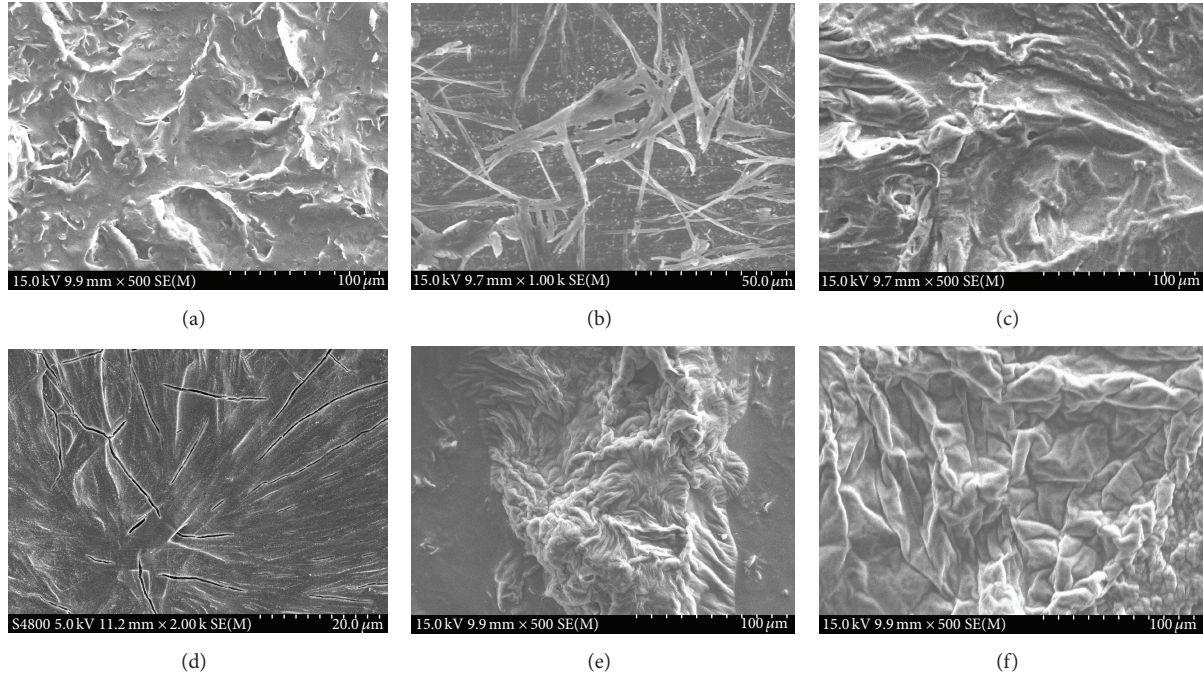


FIGURE 2: SEM images of xerogels: (a) and ((c)–(f)): C18-Azo, C16-Azo, C14-Azo, C18-Azo-Me, and C16-Azo-Me in ethanolamine, respectively; (b) C16-Azo in nitrobenzene.

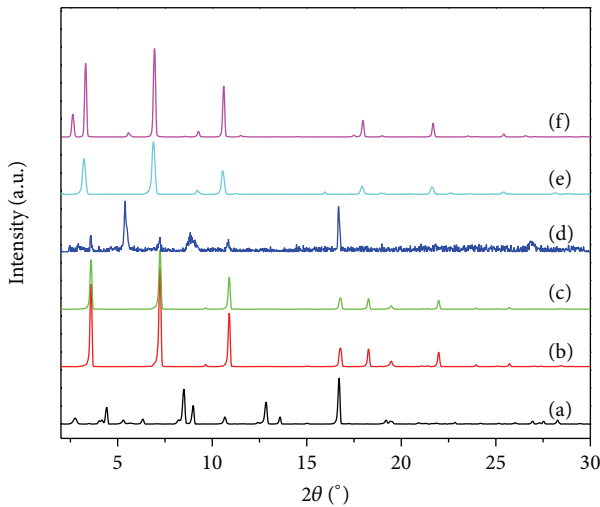


FIGURE 3: X-ray diffraction patterns of xerogels: (a) and ((c)–(f)): C18-Azo, C16-Azo, C14-Azo, C18-Azo-Me, and C16-Azo-Me in ethanolamine, respectively; (b) C16-Azo in nitrobenzene.

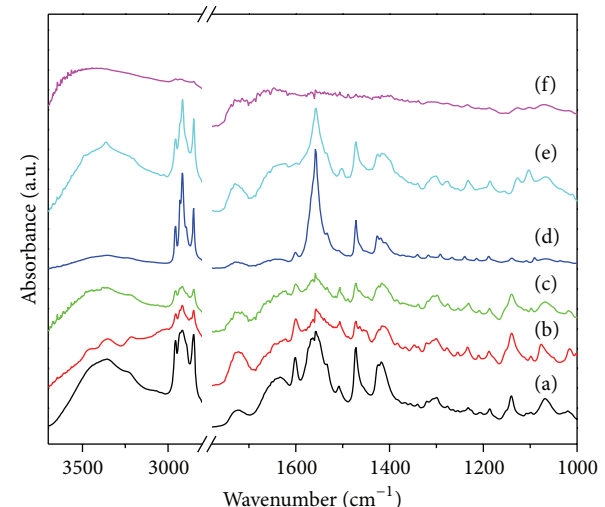


FIGURE 4: FT-IR spectra of xerogels: (a) and ((c)–(f)): C18-Azo, C16-Azo, C14-Azo, C18-Azo-Me, and C16-Azo-Me in ethanolamine, respectively; (b) C16-Azo in nitrobenzene.

chain, due to the hydrophobic force of methylene chains, after the intermolecular hydrogen bonding and orderly stacking, the nanostructures of supramolecular assembly were obtained. For the binary mixture C12-Azo with shorter alkyl chain, the intermolecular interaction is not enough to connect the repeating units with each other, so no gels were formed.

#### 4. Conclusion

In summary, the gelation behaviors of binary organogels composed of azobenzene amino derivatives and fatty acids with different alkyl chains in various organic solvents were investigated. The experimental results indicated that their gelation behaviors solvents can be regulated by changing length of alkyl substituent chains and azobenzene segment.

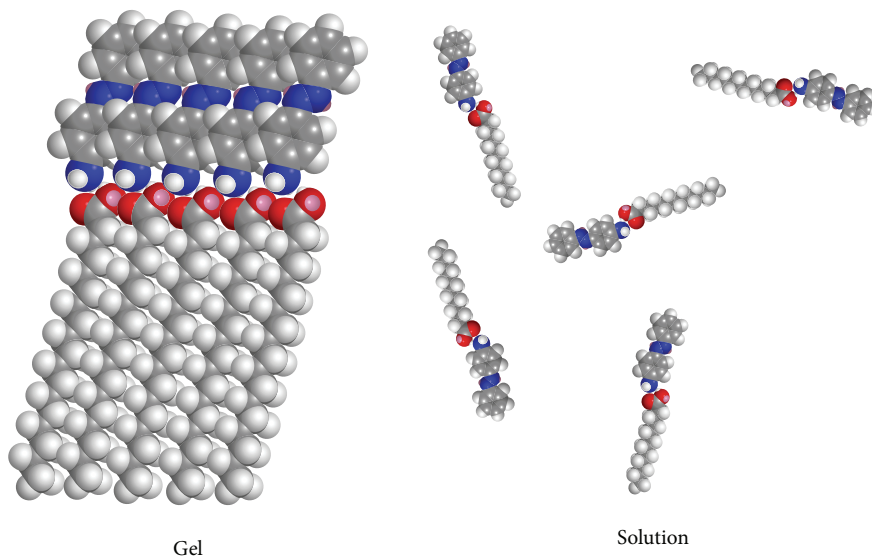


FIGURE 5: Assembly modes for C18-Azo in organogel and C12-Azo in solution.

TABLE 1: Gelation behaviors of these binary organogels.

Solvents	C18-Azo	C16-Azo	C14-Azo	C12-Azo	C18-Azo-Me	C16-Azo-Me	C14-Azo-Me	C12-Azo-Me
Acetone	S	S	S	S	S	S	S	S
Aniline	PS	PS	S	PS	PS	S	PS	S
n-Hexane	S	PS	PS	PS	S	PS	PS	S
Toluene	PS	S	S	S	PS	S	S	S
Pyridine	S	S	S	S	S	S	S	S
Isopropanol	S	S	S	S	S	S	S	S
Cyclopentanone	PS	S	S	PS	S	S	S	S
Cyclohexanone	S	S	S	S	S	S	S	S
Nitrobenzene	PS	<b>G (2.0)</b>	PS	PS	PS	S	S	S
n-Butanol	S	S	S	S	S	S	S	S
Ethanolamine	<b>G (2.5)</b>	<b>G (2.0)</b>	<b>G (2.0)</b>	S	<b>G (2.5)</b>	<b>G (2.0)</b>	S	S
n-Butyl acrylate	PS	S	S	PS	PS	S	S	S
1,4-Dioxane	S	S	S	S	S	S	S	S
Petroleum ether	S	PS	PS	S	S	PS	PS	PS
Ethyl acetate	S	S	S	PS	S	S	S	S
Dichloromethane	PS	PS	S	PS	S	S	S	S
THF	S	S	S	S	S	S	S	S
DMF	PS	S	S	PS	PS	S	S	S
DMSO	S	S	S	S	S	PS	S	S
Benzene	S	S	S	PS	S	PS	S	S

DMF: dimethylformamide; THF: tetrahydrofuran; DMSO: dimethyl sulfoxide; S: solution; PS: partially soluble; G: gel; I: insoluble; for gels, the critical gelation concentrations at room temperature are shown in parentheses (% w/v).

Longer alkyl chains in molecular skeletons in present gelators are favorable for the gelation of organic solvents. For the mixtures containing 4-aminoazobenzene, only C12-Azo cannot form any organogel in present solvents. While for the mixtures containing 2-aminoazotoluene, only C18-Azo-Me and C16-Azo-Me can form gel in ethanolamine, respectively. Morphological studies revealed that the gelator molecules self-assemble into different aggregates from lamella, wrinkle,

to belt with change of solvents. Spectral studies indicated that there existed different H-bond formation and hydrophobic force, depending on different substituent chains in molecular skeletons. The prepared nanostructured materials have wide perspectives and many potential applications in nanoscience and material fields due to their scientific values. The present work may also give some insight to design and character new organogelators and soft materials.

## Conflict of Interests

The authors declare that they have no direct financial relation with the commercial identities mentioned in this paper that might lead to a conflict of interests for any of the authors.

## Acknowledgments

This work was financially supported by the National Natural Science Foundation of China (no. 21207112), the Natural Science Foundation of Hebei Province (nos. B2012203060 and B2013203108), the Science Foundation for the Excellent Youth Scholars from Universities and Colleges of Hebei Province (nos. Y2011113 and YQ2013026), and the Support Program for the Top Young Talents of Hebei Province.

## References

- [1] H. Sawalha, R. den Adel, P. Venema, A. Bot, E. Flöter, and E. van der Linden, "Organogel-emulsions with mixtures of  $\beta$ -sitosterol and  $\gamma$ -oryzanol: influence of water activity and type of oil phase on gelling capability," *Journal of Agricultural and Food Chemistry*, vol. 60, no. 13, pp. 3462–3470, 2012.
- [2] P. Rajamalli and E. Prasad, "Low molecular weight fluorescent organogel for fluoride ion detection," *Organic Letters*, vol. 13, no. 14, pp. 3714–3717, 2011.
- [3] S. Bouquet-Bonnet, M. Yemloul, and D. Canet, "New application of proton nuclear spin relaxation unravelling the intermolecular structural features of low-molecular-weight organogel fibers," *Journal of the American Chemical Society*, vol. 134, no. 25, pp. 10621–10627, 2012.
- [4] H. Yu and Q. Huang, "Improving the oral bioavailability of curcumin using novel organogel-based nanoemulsions," *Journal of Agricultural and Food Chemistry*, vol. 60, no. 21, pp. 5373–5379, 2012.
- [5] G. M. Newbloom, K. M. Weigandt, and D. C. Pozzo, "Electrical, mechanical, and structural characterization of self-assembly in poly(3-hexylthiophene) organogel networks," *Macromolecules*, vol. 45, no. 8, pp. 3452–3462, 2012.
- [6] D. Liu, D. Wang, M. Wang et al., "Supramolecular organogel based on crown ether and secondary ammonium functionalized glycidyl triazole polymers," *Macromolecules*, vol. 46, no. 11, pp. 4617–4625, 2013.
- [7] S. O'Sullivan and D. W. M. Arrigan, "Impact of a surfactant on the electroactivity of proteins at an aqueous-organogel microinterface array," *Analytical Chemistry*, vol. 85, no. 3, pp. 1389–1394, 2013.
- [8] H. Takeno, A. Maehara, D. Yamaguchi, and S. Koizumi, "A structural study of an organogel investigated by small-angle neutron scattering and synchrotron small-angle X-ray scattering," *The Journal of Physical Chemistry B*, vol. 116, no. 26, pp. 7739–7745, 2012.
- [9] J. Lu, J. Hu, Y. Song, and Y. Ju, "A new dual-responsive organogel based on uracil-appended glycyrrhetic acid," *Organic Letters*, vol. 13, no. 13, pp. 3372–3375, 2011.
- [10] M. Yemloul, E. Steiner, A. Robert et al., "Solvent dynamical behavior in an organogel phase as studied by NMR relaxation and diffusion experiments," *The Journal of Physical Chemistry B*, vol. 115, no. 11, pp. 2511–2517, 2011.
- [11] P. D. Wadhavane, R. E. Galian, M. A. Izquierdo et al., "Photoluminescence enhancement of CdSe quantum dots: a case of organogel-nanoparticle symbiosis," *Journal of the American Chemical Society*, vol. 134, no. 50, pp. 20554–20563, 2012.
- [12] W. Liu, P. Xing, F. Xin et al., "Novel double phase transforming organogel based on  $\beta$ -cyclodextrin in 1,2-propylene glycol," *The Journal of Physical Chemistry B*, vol. 116, no. 43, pp. 13106–13113, 2012.
- [13] M. Bielejewski and J. Tritt-Goc, "Evidence of solvent-gelator interaction in sugar-based organogel studied by field-cycling NMR relaxometry," *Langmuir*, vol. 26, no. 22, pp. 17459–17464, 2010.
- [14] Y. Li, J. Liu, G. Du et al., "Reversible heat-set organogel based on supramolecular interactions of  $\beta$ -Cyclodextrin in *N*, *N*-dimethylformamide," *The Journal of Physical Chemistry B*, vol. 114, no. 32, pp. 10321–10326, 2010.
- [15] F. Xin, H. Zhang, B. Hao et al., "Controllable transformation from sensitive and reversible heat-set organogel to stable gel induced by sodium acetate," *Colloids and Surfaces A: Physicochemical and Engineering Aspects*, vol. 410, pp. 18–22, 2012.
- [16] F. S. Schoonbeek, J. H. van Esch, R. Hulst, R. M. Kellogg, and B. L. Feringa, "Geminal bis-ureas as gelators for organic solvents: gelation properties and structural studies in solution and in the gel state," *Chemistry*, vol. 6, no. 14, pp. 2633–2643, 2000.
- [17] P. Anilkumar and M. Jayakannan, "A novel supramolecular organogel nanotubular template approach for conducting nano-materials," *The Journal of Physical Chemistry B*, vol. 114, no. 2, pp. 728–736, 2010.
- [18] Y. Marui, A. Kikuzawa, T. Kida, and M. Akashi, "Unique organogel formation with macroporous materials constructed by the freeze-drying of aqueous cyclodextrin solutions," *Langmuir*, vol. 26, no. 13, pp. 11441–11445, 2010.
- [19] A. R. Hirst, D. K. Smith, and J. P. Harrington, "Unique nano-scale morphologies underpinning organic gel-phase materials," *Chemistry*, vol. 11, no. 22, pp. 6552–6559, 2005.
- [20] M. Moniruzzaman and P. R. Sundararajan, "Low molecular weight organogels based on long-chain carbamates," *Langmuir*, vol. 21, no. 9, pp. 3802–3807, 2005.
- [21] T. Jiao, Y. Wang, F. Gao, J. Zhou, and F. Gao, "Photoresponsive organogel and organized nanostructures of cholesterol imide derivatives with azobenzene substituent groups," *Progress in Natural Science: Materials International*, vol. 22, no. 1, pp. 64–70, 2012.
- [22] T. Jiao, F. Gao, Y. Wang, J. Zhou, F. Gao, and X. Luo, "Supramolecular gel and nanostructures of bolaform and trigonal cholesteryl derivatives with different aromatic spacers," *Current Nanoscience*, vol. 8, no. 1, pp. 111–116, 2012.
- [23] T. Jiao, Y. Wang, Q. Zhang, J. Zhou, and F. Gao, "Regulation of substituent groups on morphologies and self-assembly of organogels based on some azobenzene imide derivatives," *Nanoscale Research Letters*, vol. 8, no. 1, article 160, pp. 1–8, 2013.
- [24] P. Mukhopadhyay, Y. Iwashita, M. Shirakawa, S. Kawano, N. Fujita, and S. Shinkai, "Spontaneous colorimetric sensing of the positional isomers of dihydroxynaphthalene in a 1D organogel matrix," *Angewandte Chemie*, vol. 45, no. 10, pp. 1592–1595, 2006.
- [25] J. L. Gurav, I.-K. Jung, H.-H. Park, E. S. Kang, and D. Y. Nadargi, "Silica aerogel: synthesis and applications," *Journal of Nanomaterials*, vol. 2010, Article ID 409310, 11 pages, 2010.
- [26] A. S. Al Dwayyan, M. N. Khan, and M. S. Al Salhi, "Optical characterization of chemically etched nanoporous silicon embedded in sol-gel matrix," *Journal of Nanomaterials*, vol. 2012, Article ID 713203, 7 pages, 2012.

- [27] H. Guo, T. Jiao, X. Shen et al., "Binary organogels based on glutamic acid derivatives and different acids: solvent effect and molecular skeletons on self-assembly and nanostructures," *Colloids and Surfaces A: Physicochemical and Engineering Aspects*, vol. 447, pp. 88–96, 2014.
- [28] M. Zinic, F. Vögtle, and F. Fages, "Cholesterol-based gelators," *Topics in Current Chemistry*, vol. 256, pp. 39–76, 2005.
- [29] T. Y. Wang, Y. G. Li, and M. H. Liu, "Gelation and self-assembly of glutamate bolaamphiphiles with hybrid linkers: effect of the aromatic ring and alkyl spacers," *Soft Matter*, vol. 5, no. 5, pp. 1066–1073, 2009.
- [30] T. F. Jiao, Q. Q. Huang, Q. R. Zhang, D. B. Xiao, J. X. Zhou, and F. M. Gao, "Self-assembly of organogels via new luminol imide derivatives: diverse nanostructures and substituent chain effect," *Nanoscale Research Letters*, vol. 8, no. 1, article 278, pp. 1–8, 2013.
- [31] Y. G. Li, T. Y. Wang, and M. H. Liu, "Ultrasound induced formation of organogel from a glutamic dendron," *Tetrahedron*, vol. 63, no. 31, pp. 7468–7473, 2007.

## Research Article

# Preparation and Characterization of P(AN-VAc-PMMT) Nanocomposites and Nanofibers

Jun Liu,<sup>1,2</sup> Yuguo Zhuo,<sup>1,2</sup> Qingshan Li,<sup>1</sup> Wei Hong,<sup>3</sup> and Guangzhong Xing<sup>1</sup>

<sup>1</sup> National Key Laboratory of Metastable Materials Preparation Technology and Science, Yanshan University, Qinhuangdao 066004, China

<sup>2</sup> Environmental Management College of China, Qinhuangdao 066004, China

<sup>3</sup> People's Republic of China Qinghuangdao Entry-Exit Inspection & Quarantine Bureau Coal Inspection Technique Center, Qinhuangdao 066003, China

Correspondence should be addressed to Qingshan Li; [qsli@ysu.edu.cn](mailto:qsli@ysu.edu.cn)

Received 25 March 2014; Revised 26 May 2014; Accepted 27 May 2014; Published 9 June 2014

Academic Editor: Bing Wu

Copyright © 2014 Jun Liu et al. This is an open access article distributed under the Creative Commons Attribution License, which permits unrestricted use, distribution, and reproduction in any medium, provided the original work is properly cited.

P(AN-VAc-PMMT) nanocomposites were prepared using *in situ* emulsion polymerization and further confirmed by FTIR. A polymerizable quaternary ammonium ion monomer was used to modify montmorillonite. XRD testing showed that the quaternary ammonium ion was successfully intercalated into the montmorillonite clay layer. This is the first paper to discuss an investigation of P(AN-VAc-PMMT) nanofiber morphology using SEM. The fibers were prepared through electrospinning.

## 1. Introduction

In recent years, a significant amount of work has been carried out on polymer-clay nanocomposites because they show more favorable mechanical properties than pure polymers and conventional inorganic-polymer composites [1–3]. The most common approaches [4] to achieving exfoliated nanocomposite structures are modification of the chemistry of the clay surface from hydrophilic to organophilic, which improves compatibility with the host polymer [5, 6] matrix, and special processing techniques, such as *in situ* polymerization, high shear solution blending, and melt blending [7, 8].

Electrospinning is an effective method for the production of polymeric fibers [9] with diameters ranging from tens of nanometers to microns. The feasibility of incorporating nanometer-sized particulates into fibers has made this process even more attractive in the production of composite fibers.

The purpose of this project was to improve the thermal properties of PAN-based fibers via electrospinning. Specifically, this paper describes the formation of electrospun

fibers from solutions of poly (AN-co-VAc) copolymers and dispersions of their layered-silicate nanocomposites. Fibers have also been formed under the same conditions. The nanocomposites were prepared using *in situ* emulsion polymerization to enhance the dispersion and exfoliation of clay in the polymer matrix. The polymerized nanocomposites were then dispersed into solutions of dimethylformamide (DMF), from which fibers were electrospun. The morphology and thermal properties of the electrospun fibers from the copolymer and nanocomposite solutions were characterized.

## 2. Experiments

**2.1. MSDQA (Methyl Styrene Dodecyl Quaternary Ammonium) Preparation.** A certain amount of acetone, chloromethyl styrene, and dodecyl dimethyl amine was added to a 250 mL three-neck bottle equipped with a stirrer, reflux condenser, and thermometer. It was heated until the acetone was refluxed. A yellow emulsion was produced after 2 hours. The product was precipitated by n-heptane and then washed with

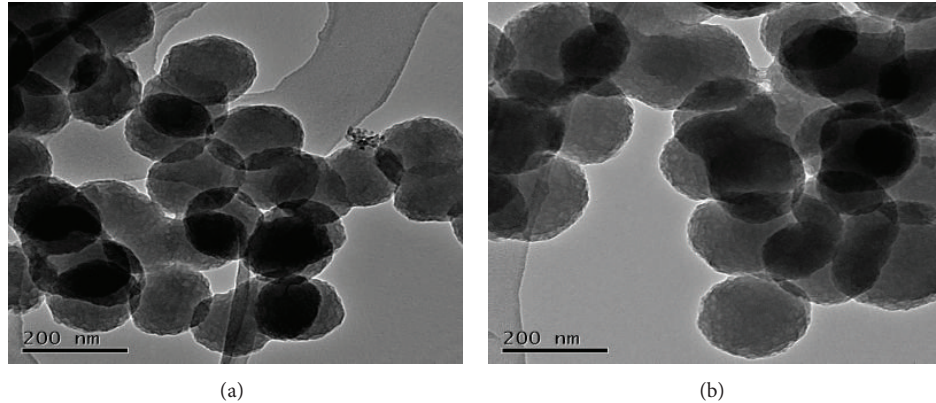


FIGURE 1: TEM of P(AN-VAc-PMMT) ((a) 2%, (b) 5%).

acetone three times. After centrifugation, the sediment was washed with deionized water, dried in vacuum at 60°C for 24 hours, and ground into fine powder.

One gram of Na-MMT was dispersed in 30 mL of distilled water with vigorous stirring for 0.5 hours at room temperature. Three-tenths of a gram of methyl styrene dodecyl quaternary ammonium was dissolved in 20 mL of distilled water. The two solutions were mixed under nitrogen and kept at 80°C with stirring at 800 rpm for 3 hours. After centrifugation, the sediment was washed with deionized water, dried in a vacuum at 80°C for 24 hours, and ground to a fine powder.

**2.2. *P(AN-VAc-PMMT) Nanocomposite Preparation.*** The P(AN-co-VAc) copolymers containing 10 wt% VAc and layered-silicate nanocomposites with the same nominal compositions were prepared individually via emulsion polymerization.

Details follow: a given weight of PMMT was dispersed in admixture of 9 g acrylonitrile (AN) and 1 g vinyl acetate (VAc). The solution was surged ultrasonically for 30 minutes when the ultrasonic frequency was 400 KHz and ultrasonic power was 250 W. 90 mL deionized water and 0.2 g sodium dodecyl benzene sulfonate (SDBS) were placed in a three-neck bottle with a battle stirrer, a reflux condenser, and a thermometer. The solution was mixed thoroughly and then added to a PMMT and polymerizable quaternary ammonium ion monomer mixture while being continuously mixed by ultrasonic. When the temperature reached 70°C, the solution of  $K_2S_2O_8$  was added to the three-neck bottle and allowed to react for about 2 hours. Then it was swilled into beakers and various 13 wt% NaCl solutions were added to the beakers to precipitate the product. After centrifugation, the sediment was washed with deionized water, dried in a vacuum at 70°C for 24 hours, and ground to a fine powder.

### 3. Results and Discussion

**3.1. Characterization of Materials.** P(AN-VAc-PMMT) composites prepared by *in situ* emulsion polymerization presented as nanometer microspheres of about 150 nm in

size (Figure 1). When montmorillonite content was below 5%, the surface morphology of the composite microspheres appeared clear because long chains of polymers curl naturally.

The spectrum contained characteristic absorbance bands of all components. The spectrum of pure MSDQA (Figure 2(a)) shows the peak whose wave numbers are in the region of  $1470\text{ cm}^{-1}$  due to the substance's quaternary ammonium ions. The peaks at  $2920\text{ cm}^{-1}$  and  $2850\text{ cm}^{-1}$  were characteristic of  $\text{CH}_3$  and  $\text{CH}_2$  absorption peaks, respectively. The peak at  $3450\text{ cm}^{-1}$  was attributed to the band of water in MSDQA. MSDQA also showed peaks at  $1630\text{ cm}^{-1}$  and  $1514\text{ cm}^{-1}$  due to its phenyl group. Absorbance peaks from C–N stretching at  $1221\text{ cm}^{-1}$  confirmed the successful synthesis of MSDQA. Figure 2(b) shows the FTIR spectra of P(AN-VAc-PMMT). The spectrum of P(AN-VAc-PMMT) contained characteristic absorbance bands for all components. C–H stretching at  $2930\text{ cm}^{-1}$ , C≡N stretching at  $2240\text{ cm}^{-1}$ , and C–H bending at  $1454\text{ cm}^{-1}$  are characteristic of P(AN-VAC). Absorbance peaks from phenyl groups at  $1630\text{ cm}^{-1}$  and  $1514\text{ cm}^{-1}$  confirmed the presence of MSDQA in the nanocomposite. Absorbance peaks from O–H stretching at about  $3464\text{ cm}^{-1}$ , Si–O stretching at about  $1027\text{ cm}^{-1}$ , and Si–O bending at about  $520\text{ cm}^{-1}$  confirmed the presence of PMMT in the nanocomposite. C=O stretching at  $1740\text{ cm}^{-1}$  was detected.

As shown in Figure 3, the quaternary ammonium salt was intercalated into the montmorillonite layers on chip by cation exchange, thereby forming composites with the required nanometer-sized spaces. PMMT reflection in the nanocomposite was not observed when PMMT content was below 5 wt%. At the PMMT content of 8 wt%, the PMMT reflection appeared at  $2\theta = 1.94^\circ$ , corresponding to a basal spacing of 4.54 nm. This indicated that the polymer chains were intercalated into the PMMT.

**3.2. Analysis of Fiber Morphology.** Fiber morphology was characterized using SEM. Figure 4 shows that, as the montmorillonite content increased, the diameters of the P(AN-VAc-PMMT) fibers did not change significantly and line

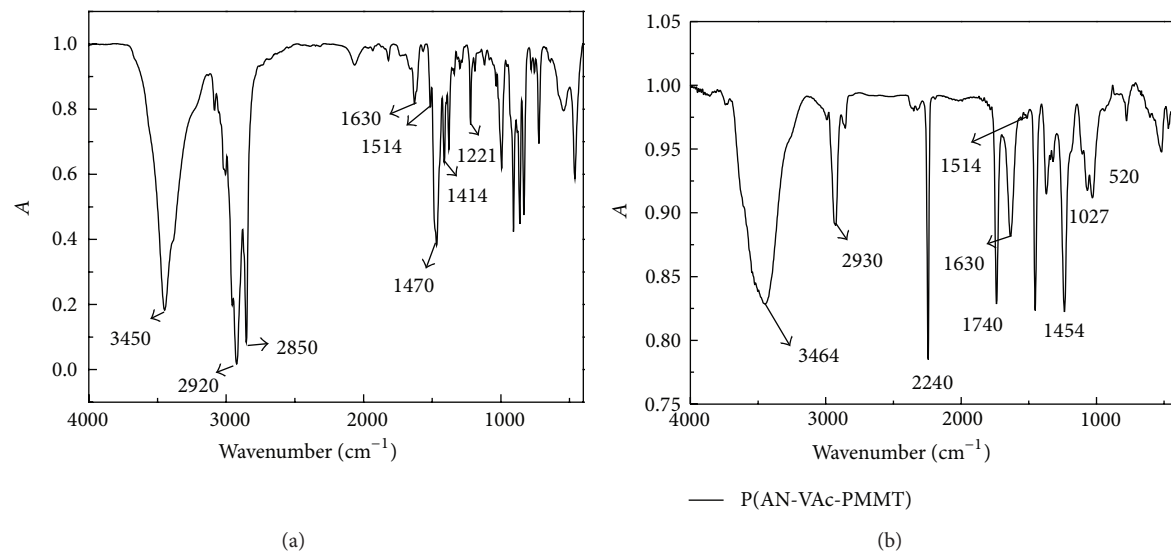


FIGURE 2: FTIR spectra of (a) MSDQA and (b) P(AN-VAc-PMMT).

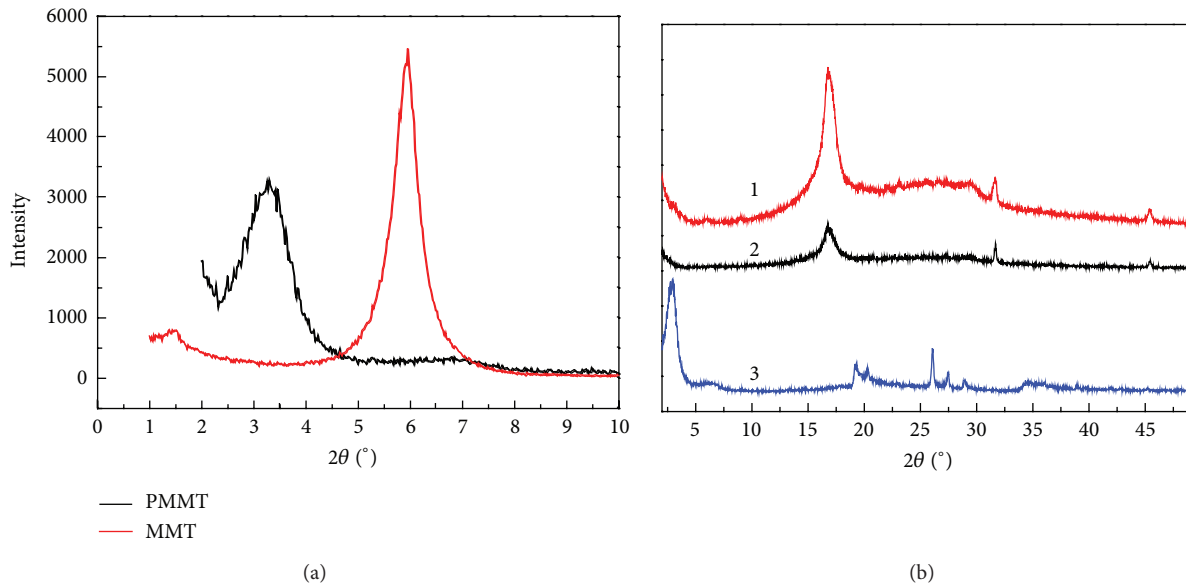


FIGURE 3: XRD: (a) Na-MMT and PMMT; (b) 1: the PMMT content 5 wt%, 2: the PMMT content 8 wt%, and 3: PMMT.

densities were the same. This may have been due to the effect of the molecular weight of composite materials. When montmorillonite was added, the molecular weight of the polymers increased, leading to thickening of the P(AN-VAc-PMMT) fibers. As MMT content increased, the adsorption capacity of MMT to free radicals gradually became preponderant. This caused the molecular weight to decrease slightly. However, this trend was not very obvious. The average diameters of the fibers that were prepared with MMT may have been affected in an inconspicuous way.

Figure 4(a) shows that the electrospun P(AN-VAc) fibers contained a certain number of small beads. After montmorillonite was added, the surfaces of the fibers became smooth because the negative charge of the montmorillonite

surfaces increased the conductivity of the solution during electrospinning. The polymer chain can be arranged parallel to the surface of the montmorillonite lamellae when the montmorillonite is introduced. In this way, the electrospinnability of P(AN-VAc-PMMT) composite fibers is better than that of P(AN-VAC) fibers.

#### 4. Conclusions

- (1) P(AN-VAc-PMMT) nanocomposites were prepared by the method of emulsion intercalation polymerization. It is a result that P(AN-VAc-PMMT) nanocomposite was synthesized token by FTIR spectra and

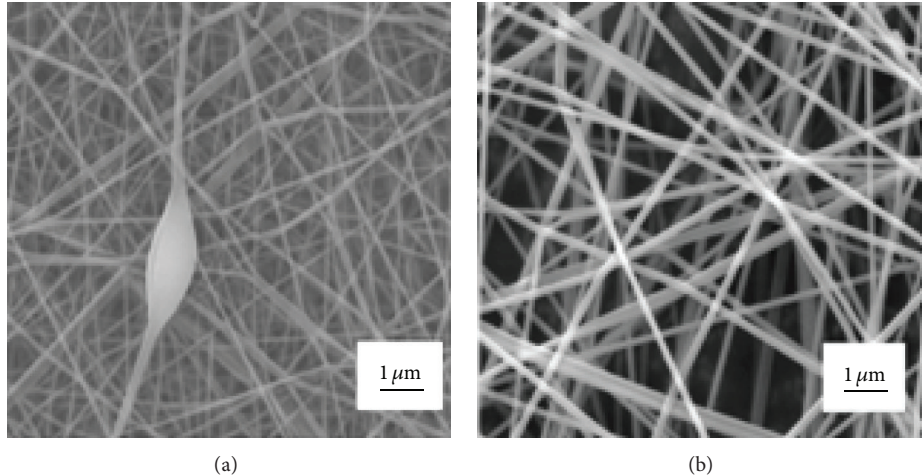


FIGURE 4: SEM images of P(AN-VAc-PMMT) ((a) 0%, (b) 2%) electrospinning fibers processed in a capillary tube with an inner diameter of 0.7 mm at a voltage of 30 KV, a spinning distance of 25 cm, and a speed of 0.5 mL/h.

the copolymer P(AN-VAc) is intercalated into montmorillonite layer by XRD.

- (2) P(AN-VAc) and P(AN-VAc-PMMT) composites can be made into nanofibers by electrospinning. The electrospinnability of P(AN-VAc) fiber composites was found to be better than that of P(AN-VAC).

## Conflict of Interests

The authors declare that they have no direct financial relation with the commercial identities mentioned in this paper that might lead to a conflict of interests for any of them regarding the publication of this paper.

## Acknowledgments

This work was supported by the National “Eleventh Five-Year” Technology Support Program Foundation (2006BAD10B08) and the Natural Science Foundation of Hebei Province (E2009000448).

## References

- [1] R. S. Sinha and M. Okamoto, “Polymer/layered silicate nanocomposites: a review from preparation to processing,” *Progress in Polymer Science*, vol. 28, no. 11, pp. 1539–1641, 2003.
- [2] G. Beyer, “Nanocomposites: a new class of flame retardants for polymers,” *Plastics, Additives and Compounding*, vol. 4, no. 10, pp. 22–28, 2002.
- [3] P. Meneghetti and S. Qutubuddin, “Synthesis, thermal properties and applications of polymer-clay nanocomposites,” *Thermochimica Acta*, vol. 442, no. 1-2, pp. 74–77, 2006.
- [4] K. Chang, M. Lai, C. Peng et al., “Comparative studies on the corrosion protection effect of DBSA-doped polyaniline prepared from in situ emulsion polymerization in the presence of hydrophilic Na<sup>+</sup>-MMT and organophilic organo-MMT clay platelets,” *Electrochimica Acta*, vol. 51, no. 26, pp. 5645–5653, 2006.
- [5] X. Zhao, K. Urano, and S. Ogasawara, “Adsorption of polyethylene glycol from aqueous solution on montmorillonite clays,” *Colloid & Polymer Science*, vol. 267, no. 10, pp. 899–906, 1989.
- [6] X. H. Liu and Q. J. Wu, “PP/clay nanocomposites prepared by grafting-melt intercalation,” *Polymer*, vol. 42, no. 25, pp. 10013–10019, 2001.
- [7] P. Heikkilä and A. Harlin, “Parameter study of electrospinning of polyamide-6,” *European Polymer Journal*, vol. 44, no. 10, pp. 3067–3079, 2008.
- [8] Y. T. Jia, J. Gong X, and H. Gu, “Fabrication and characterization of poly (vinyl alcohol)/chitosan blend nanofibers produced by electrospinning method,” *Carbohydrate Polymers*, vol. 67, no. 3, pp. 403–409, 2007.
- [9] J. Bai, Y. X. Li, S. T. Yang et al., “A simple and effective route for the preparation of poly(vinylalcohol) (PVA) nanofibers containing gold nanoparticles by electrospinning method,” *Solid State Communications*, vol. 141, no. 5, pp. 292–295, 2007.

## Research Article

# Synthesis of Hydrophobic Mesoporous Material MFS and Its Adsorption Properties of Water Vapor

Guotao Zhao,<sup>1</sup> Zhenxiao Zhao,<sup>2</sup> Junliang Wu,<sup>1</sup> and Daiqi Ye<sup>1</sup>

<sup>1</sup> College of Environment and Energy, South China University of Technology, Guangzhou 510006, China

<sup>2</sup> School of Chemistry and Chemical Engineering, Guangxi University, Nanning 530004, China

Correspondence should be addressed to Daiqi Ye; cedqye@scut.edu.cn

Received 25 April 2014; Accepted 18 May 2014; Published 5 June 2014

Academic Editor: Qingrui Zhang

Copyright © 2014 Guotao Zhao et al. This is an open access article distributed under the Creative Commons Attribution License, which permits unrestricted use, distribution, and reproduction in any medium, provided the original work is properly cited.

Fluorine-containing hydrophobic mesoporous material (MFS) with high surface area is successfully synthesized with hydrothermal synthesis method by using a perfluorinated surfactant SURFLON S-386 template. The adsorption properties of water vapor on the synthesized MFS are also investigated by using gravimetric method. Results show that SEM image of the MFS depicted roundish morphology with the average crystal size of 1–2  $\mu\text{m}$ . The BET surface area and total pore volume of the MFS are  $865.4 \text{ m}^2 \text{ g}^{-1}$  and  $0.74 \text{ cm}^3 \text{ g}^{-1}$  with a narrow pore size distribution at 4.9 nm. The amount of water vapor on the MFS is about  $0.41 \text{ mmol g}^{-1}$  at 303 K, which is only 52.6% and 55.4% of MCM-41 and SBA-15 under the similar conditions, separately. The isosteric adsorption heat of water on the MFS is gradually about  $27.0\text{--}19.8 \text{ kJ mol}^{-1}$ , which decreases as the absorbed water vapor amount increases. The value is much smaller than that on MCM-41 and SBA-15. Therefore, the MFS shows more hydrophobic surface properties than the MCM-41 and SBA-15. It may be a kind of good candidate for adsorption of large molecule and catalyst carrier with high moisture resistance.

## 1. Introduction

With the development of industry, air pollution and its adverse impact on the environment and human health has been an ongoing issue for decades, especially in developing countries. The growing world population and the emergence of recently industrialized countries make this issue even more pronounced. Volatile organic compounds (VOCs) are the main pollutants in the ambient air released by chemical, petrochemical, and related industries and have drawn more and more attention in recent years. Release of VOCs into the atmosphere may significantly reduce air quality and do harm to our health and welfare directly [1]. In addition, VOCs are key reactants involved in photochemical reactions occurring in the atmosphere, which lead to serious environmental hazards when they reach a certain concentration [2]. So, the VOCs concentration in air needs to be strictly regulated to an extremely low level and an efficient method to reduce the concentration in atmosphere is now strongly demanded.

There are many techniques available to abate the emission of VOCs, such as adsorption [3], catalytic oxidation [4],

condensation [5], membrane separation [6], and biological treatments. Catalysis method has been considered as one of the most cost-effective and environmentally friendly technologies for the removal of VOCs, especially at high concentrations.

Mesoporous materials, with a pore size range of 2–50 nm, offer unique opportunities to catalysis thanks to the large surface area. The wide range of acid/base or redox catalysts will be developed after loading some active elements inside the pore walls of such materials [7, 8]. Mesoporous inorganic materials possess high specific surface area, nanometer-sized channels [9] with an ordered interconnected internal structure, and high thermal stability [10], which has made feasible potential applications as the carrier of many kinds of catalysts [11]. Recently, the ordered mesoporous silica MCM-41 [12], MCM-48 [13], SBA-15 [14], SBA-16 [15], and SBA-12 [16] have been investigated to introduce active elements to prepare the catalysts.

However, water vapor is often present in polluted air under the real situations and may affect the catalytic characteristics of catalysts. Sometimes, water will become a poison

for the catalytic combustion of VOCs [17]. Zelenak et al. [15] investigated the effect of water vapor on the activity of copper loaded catalysts with different supports such as CuO/ $\gamma$ -Al<sub>2</sub>O<sub>3</sub>, CuO/SiO<sub>2</sub>, and CuO/TiO<sub>2</sub> for styrene oxidation and found that the presence of water vapor had a significant negative effect on the activity of the copper based catalysts for styrene oxidation. Li et al. [18] reported the catalytic activity of copper and manganese based catalysts prepared with different supports for toluene oxidation. Results showed that the conversion of toluene decreased by about 90% on the CuMn(1)O<sub>x</sub>/ $\gamma$ -Al<sub>2</sub>O<sub>3</sub> and 50% on the CuMn(1)O<sub>x</sub>/TiO<sub>2</sub> in the presence of water vapor (3.78, vol%) at 180°C. Jacobs et al. [19] studied the effects of water on the deactivation of Pt-promoted Co/Al<sub>2</sub>O<sub>3</sub> catalyst by XAFS and found that the catalyst activity depicted a sudden irreversible loss when the humidity reached 25%. Therefore, the improvement of the water resistance of catalyst supports by different methods of surface treatment is the key issue in practice applications. Xia et al. [20] prepared a Pt supported on MCM-41 catalyst synthesized in the presence of fluoride anions for combustion of toluene and discovered that the presence of the additional H<sub>2</sub>O had almost no effect on the oxidation activity of this catalyst. The synthesized MCM-41 support showed the more hydrophobic properties than the common MCM-41 without adding fluoride anions. Thus, it can be seen that adding fluoride element may be a promising way to strengthen the hydrophobicity of materials.

In this work we proposed to use a novel template (perfluorinated-surfactant SURFLON S-386, polymeric perfluorocarboxylic acid) to synthesize a more hydrophobic mesoporous MFS with higher surface area. The element of fluorine was successfully introduced into the structure of the mesoporous MFS and formed a more hydrophobic surface on it. The adsorption performance of water vapor at different temperatures on the MFS was investigated and compared with traditional mesoporous materials MCM-41 and SBA-15. Meanwhile, the water isosteric heat of adsorption on the synthesized MFS was estimated and the interaction between water molecules and the MFS was studied.

## 2. Experimental

**2.1. Synthesis of the MFS Material.** The MFS samples were synthesized using SURFLON S-386 ( $\geq 99\%$ , ASAHI glass) and tetraethylorthosilicate ( $>98\%$ , J&K Scientific, TEOS) under acidic conditions from a hydrothermal reaction. First, SURFLON S-386 (0.4, 1.0, and 1.6 g) was dissolved into 120 mL deionized water at 313 K in a 250 mL beaker. After strong stirring for 60 min, TEOS (10.0 g) and aqueous HCl (5 mL, 1 mol L<sup>-1</sup>, Donghong) were added to the solution and stirred for 30 min. The derived homogenous solution was then transferred into an autoclave and aged for 24 h in air to produce a rigid gel. The gel was covered and heated at 373 K for 48 h. The obtained samples were centrifuged and then washed with water and alcohol. After that these samples were dried in an oven at 373 K for 12 h. Finally, the samples were calcined at 823 K for 6 h with a heating rate of 1 K min<sup>-1</sup>. The obtained samples were named as MFS-01 (0.4 g SURFLON

S-386), MFS-02 (1.0 g SURFLON S-386), and MFS-03 (1.6 g SURFLON S-386), separately.

**2.2. Materials Characterization.** Scanning electron microscope (SEM) images were obtained on a Philips FEI XL-30 operated by using a 10 kV accelerating voltage after gold deposition. Transmission electron microscope (TEM) images were taken with a JEM-2010HR electron microscope operating at 200 kV. In TEM measurements, the samples were prepared by dispersing the powdered product as slurry in ethanol, after which they were dispersed and dried on a holey carbon film on a copper grid. Small-angle X-ray diffraction (XRD) pattern was obtained with a D-MAX 2200 VPC using CuK $\alpha$  radiation. Langmuir and Brunauer-Emmett-Teller (BET) surface areas and pore volume of the synthesis MFS-02 were measured with a Micromeritics ASAP 2020 sorptometer using N<sub>2</sub> adsorption at 77 K. Fourier Transform-infrared spectroscopy (FT-IR) measurements were recorded on a Nicolet 6700 spectrophotometer.

**2.3. Measurements of Adsorption Isotherms of Water Vapor.** Water vapor adsorption on the synthesized MFS-02, MCM-41 (from Novel chemical Technology Co.), and SBA-15 (from Novel chemical Technology Co.) at 283–313 K was performed gravimetrically in a water sorption analyzer (Aquadyne DVS, USA). Prior to each sorption experiment, approximately 20–30 mg of preactivated sample (heated at 408–413 K under vacuum overnight) was charged into the sample pan with an accuracy of  $\pm 0.1 \mu\text{g}$  to acquire data. Microbalance system can provide a direct measurement of adsorption. The temperature and humidity of the sorption chamber can be controlled by thermal couple and a dehumidifier and a humidifier with an accuracy of  $\pm 0.1 \text{ K}$  and  $\pm 0.1 \text{ RH\%}$ , respectively.

**2.4. Measurements of the Isosteric Heat of Adsorption.** The isosteric heat of adsorption can be used to evaluate the interaction between the adsorbate molecules and the adsorbent surfaces. The isosteric heats of adsorption as a function of the surface coverage can be calculated from isotherms at different temperatures by using Clausius-Clapeyron equation (1) [21, 22]:

$$\ln(P) = -\frac{\Delta H_s}{RT} + C, \quad (1)$$

where  $\Delta H_s$  is isosteric heat of water vapor adsorption, kJ mol<sup>-1</sup>,  $R$  is the ideal gas constant, kJ mol<sup>-1</sup> K,  $P$  is the water vapor feed pressure, Pa, and  $C$  is an integration constant.

The isotherms of water vapor on the MFS-02 at different temperatures can be used to estimate the heat of adsorption [23]. Firstly, the water vapor isotherms were converted to water vapor adsorption isosteres. After that,  $\ln P$  is plotted to  $1/T$ , and thus it yields a straight line with a slope  $-\Delta H_s/R$ . Finally, the isosteric heat ( $\Delta H_s$ ) of water vapor adsorption can be calculated directly from the slope  $-\Delta H_s/R$  of the plotted straight line. It is similar to calculating isosteric heat of water vapor adsorption for MCM-41 and SBA-15.

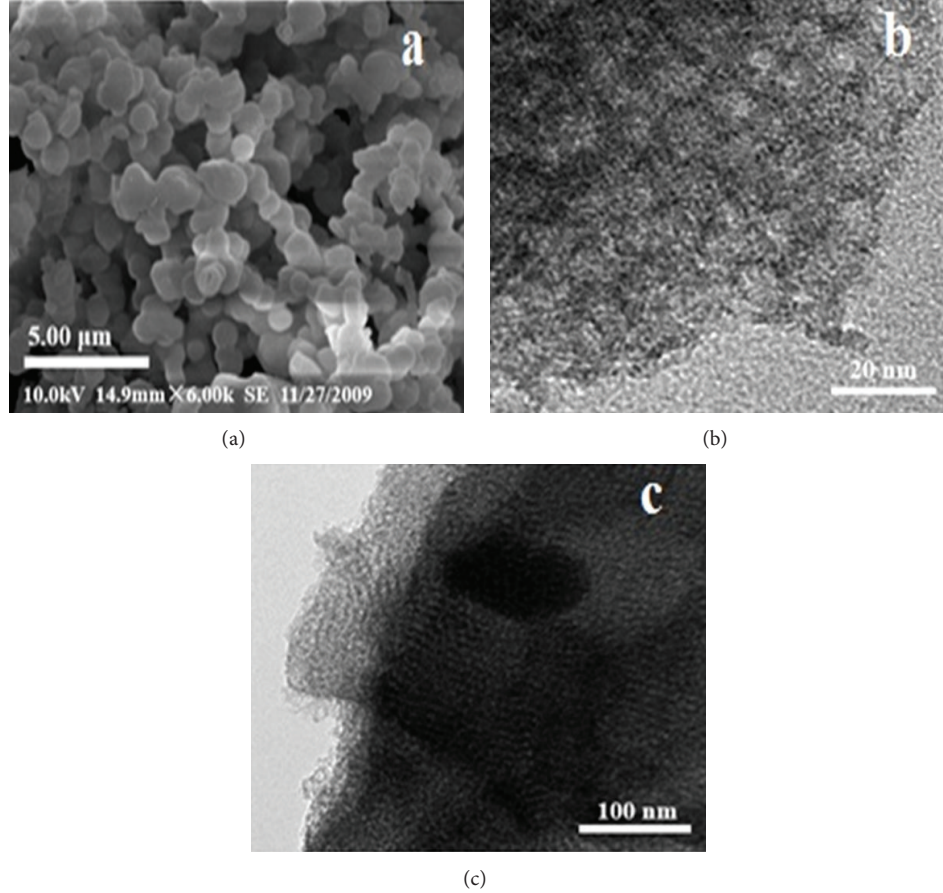


FIGURE 1: SEM (a) and TEM (b and c) images of the synthesis MFS-02.

### 3. Results and Discussion

#### 3.1. Samples Characterization

(1) *SEM and TEM*. Figure 1(a) shows the SEM image of the MFS-02 sample. It can be seen that the MFS-02 shows a spherical-like morphological characteristic with a uniform diameter around 1-2  $\mu\text{m}$ .

Figures 1(b) and 1(c) show the TEM images of the MFS-02 sample. Some clear amorphous channel displays on the surface of the material. The light and dark stripes of typical mesoporous structure can also be observed, revealing the presence of mesopores in the MFS [24].

(2) *XRD*. Figure 2 shows the small-angle X-ray diffraction (XRD) patterns of the MFS-01, MFS-02, and MFS-03 samples. It can be seen that only one diffraction peak was detected at  $2\theta = 0.7^\circ$ . The characteristic peak at low angle indicates a short-range order in the structure [24], which is consistent with the TEM images shown in Figures 1(b) and 1(c). Moreover, the intensity of the peak was very weak in XRD pattern of the MFS-01, indicating a weak crystallinity in the structure. With the increase of SURFLON S-386 content in the mother solution, the intensity of this peak was gradually increased firstly and then decreased. It was indicated that the appropriate amount of the template will favor to form a relative order structure and high crystallinity.

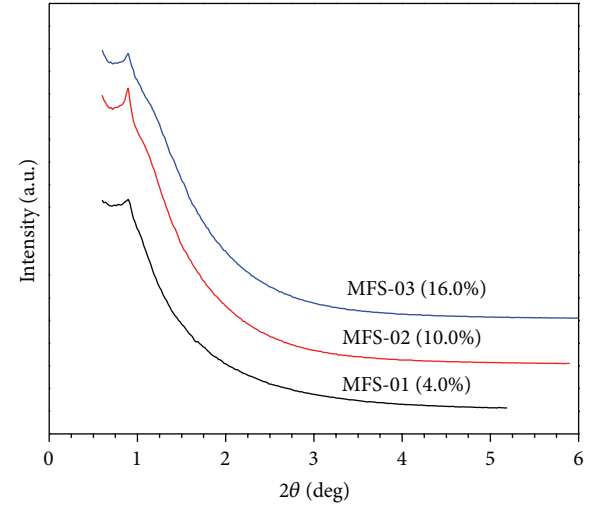


FIGURE 2: PXRD pattern of the synthesized MFS crystals.

(3) *ASAP*. The specific surface area was calculated according to the Brunauer-Emmett-Teller (BET) model and the average pore diameter was obtained according to the Barrett-Joyner-Halenda (BJH) model. Figure 3(a) shows  $\text{N}_2$  adsorption/desorption isotherms of the MFS-02 at 77 K and its pore size distribution of the MFS-02 crystals from BJH model.

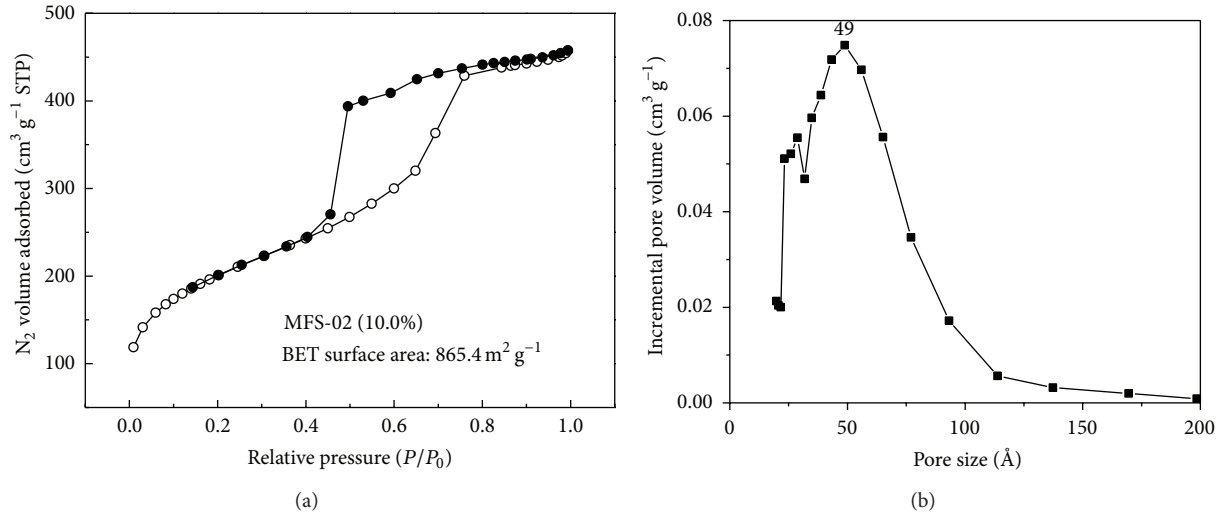


FIGURE 3: (a)  $N_2$  sorption isotherms of the MFS-02 crystals at 77 K; (b) pore size distribution the MFS-02 crystals from the BJH model.  $P/P_0$  is the ratio of gas pressure ( $P$ ) to saturation pressure ( $P_0 = 101.3 \text{ kPa}$ ).

TABLE 1: The parameters of the porous texture of the synthesized MFSs.

Sample (According to SURFLON S-386 contents, %)	BET Surface Area ( $\text{m}^2 \text{ g}^{-1}$ )	Langmuir Surface Area ( $\text{m}^2 \text{ g}^{-1}$ )	Pore volume ( $\text{cm}^3 \text{ g}^{-1}$ )
4	563.9	785.7	0.74
8	766.6	1062.7	0.64
10	865.4	1205.3	0.75
14	718.1	989.5	0.70
24	544.2	760.2	0.78

The  $N_2$  adsorption isotherm exhibits a reversible type IV isotherm with a clear hysteresis at  $P > 0.4 \text{ atm}$ , which is a characteristic of mesoporous material. Its BET surface area, Langmuir surface area, and pore volume were calculated to be  $865.4\text{--}1205.1 \text{ m}^2 \text{ g}^{-1}$  and  $0.74 \text{ cm}^3 \text{ g}^{-1}$ , respectively. Its mesopore area and mesopore volume were  $928.0 \text{ m}^2 \text{ g}^{-1}$  and  $0.7 \text{ cm}^3 \text{ g}^{-1}$ . In BJH differential pore volume plot, only one sharp peak is observed at about 4.9 nm for the MFS-02 crystals (Figure 3(b)), indicating a very narrow mesoporous material.

Table 1 shows the parameters of the porous texture of the series MFSs synthesized by using different amounts of the SURFLON S-386 template. It can be seen that the BET surface areas and Langmuir surface areas were increased gradually with the increase of the addition of SURFLON S-386 content. The surface areas reached the maximum when the SURFLON S-386 contents was up to 10% and then declined gradually. It indicates that concentration of template may create greater impact on the formation of micelles and crystalline phases. It is favourable for the formation of liquid crystalline phases as increase of the template under low concentration. However, agglomeration of surfactant molecules will appear at high

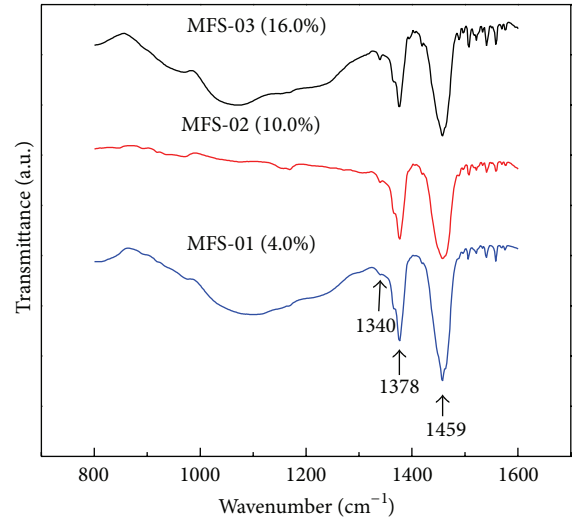


FIGURE 4: FT-IR spectra of MFSs with various dosage of SURFLON S-386 (a: MFS-01; b: MFS-02; c: MFS-03).

template concentration, which may affect the formation of liquid crystalline phases and mesoscopic structures self-assemble and then lead to the lower specific surface area of MFS ultimately.

(4) FTIR. Figure 4 shows the FTIR spectra of the MFS samples synthesized with different SURFLON S-386 contents. For each sample, the spectra show two strong distinct peaks at  $1378$  and  $1459 \text{ cm}^{-1}$  as well as and a weak peak at  $1340 \text{ cm}^{-1}$ , respectively.

The peak at  $1378 \text{ cm}^{-1}$  is assigned to the symmetric deformation vibration of methyl groups [25, 26], which came from the residual of TEOS. The peak at  $1459 \text{ cm}^{-1}$  is associated with  $-\text{CF}_2$  asymmetric stretch vibration [27], and the peak at  $1340 \text{ cm}^{-1}$  represents  $-\text{CF}_3$  stretch vibration of

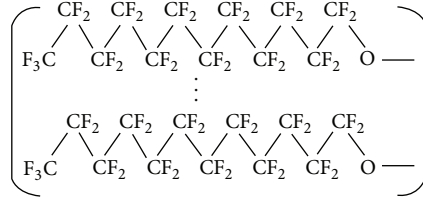


FIGURE 5: Molecular structure of SURFLON S-386.

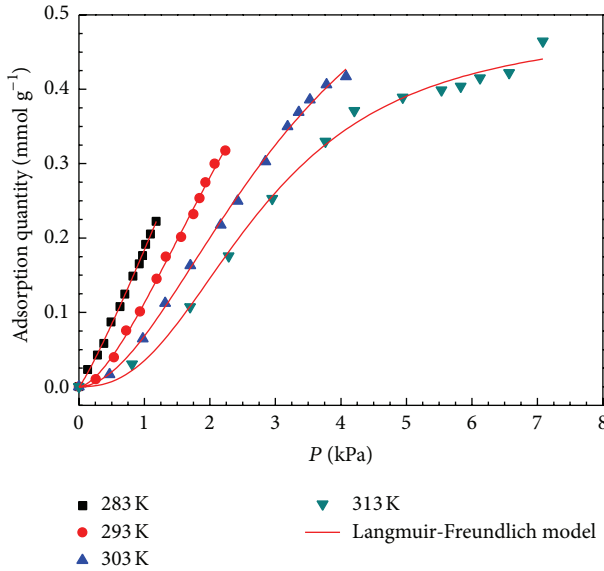


FIGURE 6: Langmuir-Freundlich isotherms of water vapor on the synthesized MFS-02 at different temperatures.

carbon-fluorine bond [28]. These two peaks are all attributed to the residual of the SURFLON S-386 after calcination. The SURFLON S-386 was composed of  $-CF_2$  groups (Figure 5). The carbon-fluorine bond is the strongest single bond in organic chemistry due to its partial ionic character [29]. It was hard to break the bond during the calcinations step of the synthesis process. Therefore, a portion of the SURFLON S-386 fragments might remain in the MFSs. The presence of carbon-fluorine groups on the surface of the MFSs may lead to more hydrophobicity [24, 30].

**3.2. Adsorption of Water Vapor on the MFS-02.** Figure 6 shows the adsorption isotherms of water vapor on the MFS-02 at 283–313 K measured experimentally by gravimetric method and fitted by Langmuir-Freundlich (L-F) model (2):

$$Q_e = Q_m \frac{b_{L-F} P^{1/n_{L-F}}}{1 + b_{L-F} P^{1/n_{L-F}}}, \quad (2)$$

where  $Q_e$  ( $\text{mmol g}^{-1}$ ) is the adsorbed amount at equilibrium pressure  $P$  (mbar),  $Q_m$  ( $\text{mmol g}^{-1}$ ) is the saturated adsorbed amount,  $b_{L-F}$  is the affinity coefficients ( $\text{mbar}^{-1/n}$ ), and  $1/n_{L-F}$  represents the deviations from an ideal homogeneous surface (heterogeneity factor) [31]. All the adsorption isotherms of water vapor on the MFS-02 show a typical type-V profile with an initial unfavorable adsorption isotherms at the at

TABLE 2: Langmuir-Freundlich equation fitting of water vapor adsorption on the MFS-02 at 283–313 K.

Temperature (K)	$Q_e = Q_m \frac{b_{L-F} P^{1/n_{L-F}}}{1 + b_{L-F} P^{1/n_{L-F}}}$		
	$Q_m$ ( $\text{mmol g}^{-1}$ )	$b_{L-F}$ ( $\times 10^{-6}$ )	$1/n_{L-F}$
283	0.43	2.54	3.65
293	0.39	9.11	3.18
303	0.39	9.18	3.13
313	0.38	3.98	3.07

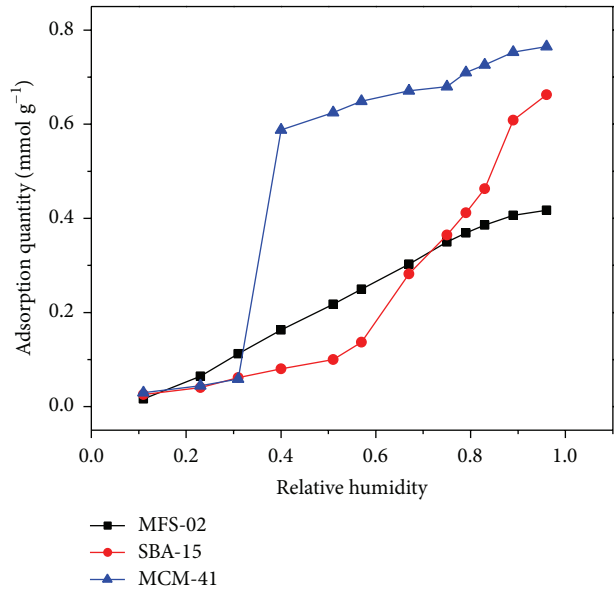


FIGURE 7: Comparison of the adsorption isotherms of water vapor on the MFS-02, SBA-15, and MCM-41 at 303 K.

low absolute pressure and pore condensation at low absolute pressure. This type of isotherm of water vapour indicated a very weak adsorption interaction of water with the pores in the MFS-02. Thus, it can be seen that the surface of the MFS-02 became more hydrophobic through grafting fluorine element on the surface of the mesoporous MFS-02. Meanwhile, it can also be seen that the adsorption capacity of water vapour on the MFS-02 was decreased with the increase of temperature, indicating a physisorption-type interaction. Table 2 lists the fitted parameters,  $Q_m$ ,  $b_{L-F}$ , of the L-F model as well as the regression coefficients for linear regression of data of water vapor adsorption on the MFS-02. As shown, the experimental adsorption isotherms were well fitted by the L-F isotherm model with high regression coefficient ( $R^2 > 0.97$ ). Table 2 shows a slight decrease in the value of  $Q_m$  as well as  $1/n_{L-F}$  as the temperature increases, suggesting a decrease in the adsorption interaction and less heterogeneous surface of the MFS-02 as the temperature increases [32].

Figure 7 shows the comparison of the adsorption isotherms of water vapor on the MFS-02, SBA-15, and MCM-41 at 303 K. As shown, the amounts of adsorbed water of these three materials were similar when the relative humidity was lower than 30%, while the amount of adsorbed water on

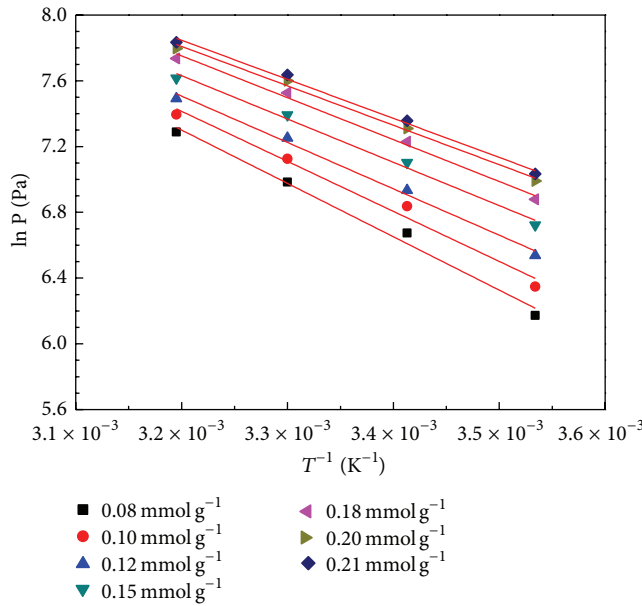


FIGURE 8: Temperature dependence of  $\ln P$  for water vapor adsorption on the MFS-02.

the MFS-02 was much lower than those on the MCM-41 and SBA-15 when the relative humidity was higher than 80%. It indicated that the presence of fluorine-containing group in MFS-02 might effectively increase the hydrophobic property of the porous surface, as mentioned in Figure 4.

**3.3. The Isosteric Heat of Water Vapor Adsorption on the MFS.** According to the method described in Section 2.4, Figure 8 can be obtained, which exhibits a series of plots of  $\ln P$  versus  $1/T$  at different amounts of water vapor on the MFS-02. From the slope of the plotted straight lines, the isosteric adsorption heats ( $\Delta H_s$ ) of water vapor adsorbed on the MFS-02 under various water vapor loadings were available. Figure 9 shows the dependence of the isosteric adsorption heats on the amounts of adsorbed water vapor on the MFS-02. It indicates that the isosteric adsorption heats are in the range of  $27.0\text{--}19.8 \text{ kJ mol}^{-1}$ , gradually decreasing with the amount of adsorbed water vapor increasing from  $0.08$  to  $0.22 \text{ mmol g}^{-1}$ . This means that an energetically heterogeneous surface for water vapor adsorption leads to the discrepant sorbate-sorbent interaction potential under different surface loadings [33]. The isosteric heat of water adsorption on the MFS-02 was much lower than that of water adsorption on the MCM-41 ( $57 \text{ kJ mol}^{-1}$ ) and SBA-15 ( $45 \text{ kJ mol}^{-1}$ ) at  $Q_m = 0.08 \text{ mmol g}^{-1}$ , indicating the more hydrophobic surface property of the MFS-02 compared to MCM-41 and SBA-15. Therefore, the MFS-02 can be used as the adsorbent for large VOCs capture or as the catalyst carrier under the condition of higher relative humidity.

#### 4. Conclusions

Fluorine-containing hydrophobic mesoporous material (MFS) with high surface area was successfully synthesized

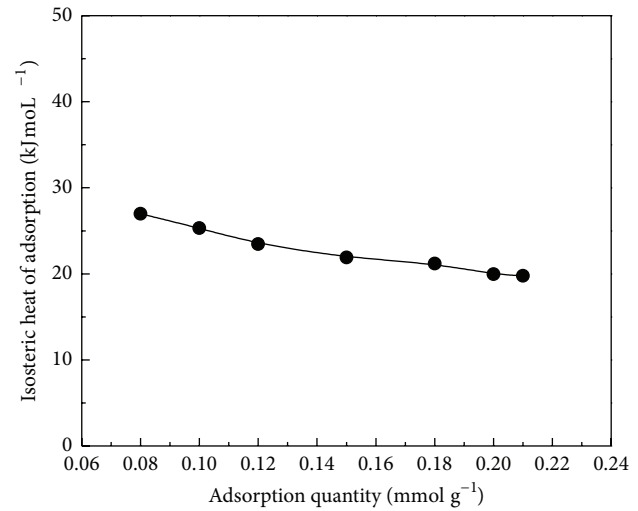


FIGURE 9: Isosteric heat of the amounts of adsorbed water vapor on the MFS-02.

with hydrothermal synthesis method by using a perfluorinated-surfactant SURFLON S-386 template. The adsorbed amount of water on the MFS-02 was much lower than that on the MCM-41 and SBA-15 at high relative humidity. The adsorption isotherms and the isosteric heat of water adsorption on the MFS-02 suggested the weak interaction between the water vapor and the MFS surface. Material characterization results showed that MFS has stronger hydrophobicity than SBA-15 and MCM-41 due to the presence of fluorine-containing group. It may be a kind of good candidate for MFS to be a good material for adsorption of large molecule and catalyst carrier under high moisture environments.

#### Conflict of Interests

The authors declare that there is no conflict of interests regarding the publishing of this paper.

#### Acknowledgments

The authors gratefully acknowledge the project supported by the National High Technology Research and Development Program of China (Grant no. 2013AA065005), the National Natural Science Foundation of China (no. 21376090), and the Project Sponsored by the Scientific Research Foundation of GuangXi University (Grant no. XGZ130963).

#### References

- [1] A. Saral, S. Demira, and S. Yildiz, "Assessment of odorous VOCs released from a main MSW landfill site in Istanbul-Turkey via a modelling approach," *Journal of Hazardous Materials*, vol. 168, no. 1, pp. 338–345, 2009.
- [2] N. Abbas, M. Hussaina, N. Russo, and G. Saracco, "Studies on the activity and deactivation of novel optimized  $\text{TiO}_2$  nanoparticles for the abatement of VOCs," *Chemical Engineering Journal*, vol. 175, pp. 330–340, 2011.

- [3] Y. S. Chen, Y. C. Hsu, C. C. Lin, C. Y. D. Tai, and H. S. Liu, "Volatile organic compounds absorption in a cross-flow rotating packed bed," *Environmental Science & Technology*, vol. 42, no. 7, pp. 2631–2636, 2008.
- [4] J. C. Fang, X. Chen, Q. B. Xia, H. X. Xi, and Z. Li, "Effect of relative humidity on catalytic combustion of toluene over copper based catalysts with different supports," *Chinese Journal of Chemical Engineering*, vol. 17, no. 5, pp. 767–772, 2009.
- [5] H. Zaitan, D. Bianchi, O. Achak, and T. Chafik, "A comparative study of the adsorption and desorption of o-xylene onto bentonite clay and alumina," *Journal of Hazardous Materials*, vol. 153, no. 1-2, pp. 852–859, 2008.
- [6] S. Modelska, A. Koltuniewicz, and A. Witek-Krowiak, "Kinetics of VOC absorption using capillary membrane contactor," *Chemical Engineering Journal*, vol. 168, no. 3, pp. 1016–1023, 2011.
- [7] D. E. De Vos, M. Dams, B. F. Sels, and P. A. Jacobs, "Ordered mesoporous and microporous molecular sieves functionalized with transition metal complexes as catalysts for selective organic transformations," *Chemical Reviews*, vol. 102, no. 10, pp. 3615–3640, 2002.
- [8] M. Guillemot, J. Mijoin, S. Mignard, and P. Magnoux, "Volatile organic compounds (VOCs) removal over dual functional adsorbent/catalyst system," *Applied Catalysis B: Environmental*, vol. 75, no. 3-4, pp. 249–255, 2007.
- [9] G. L. Athens, Y. Ein-Eli, and B. F. Chmelka, "Acid-functionalized mesostructured aluminosilica for hydrophilic proton conduction membranes," *Advanced Materials*, vol. 19, no. 18, pp. 2580–2587, 2007.
- [10] M. T. Colomer, "Nanoporous anatase thin films as fast proton-conducting materials," *Advanced Materials*, vol. 18, no. 3, pp. 371–374, 2006.
- [11] G. A. Eimer, S. G. Casuscelli, C. M. Chanquia, V. Elías, M. E. Crivello, and E. R. Herrero, "The influence of Ti-loading on the acid behavior and on the catalytic efficiency of mesoporous Ti-MCM-41 molecular sieves," *Catalysis Today*, vol. 133–135, pp. 639–646, 2008.
- [12] P. J. E. Harlick and A. Sayari, "Applications of pore-expanded mesoporous silica. 5. Triamine grafted material with exceptional CO<sub>2</sub> dynamic and equilibrium adsorption performance," *Industrial & Engineering Chemistry Research*, vol. 46, no. 2, pp. 446–458, 2007.
- [13] W.-J. Son, J.-S. Choi, and W.-S. Ahn, "Adsorptive removal of carbon dioxide using polyethyleneimine-loaded mesoporous silica materials," *Microporous and Mesoporous Materials*, vol. 113, no. 1–3, pp. 31–40, 2008.
- [14] R. Sanz, G. Calleja, A. Arencibia, and E. S. Sanz-Pérez, "CO<sub>2</sub> adsorption on branched polyethyleneimine-impregnated mesoporous silica SBA-15," *Applied Surface Science*, vol. 256, no. 17, pp. 5323–5328, 2010.
- [15] V. Zelenak, D. Halamova, L. Gaberova, E. Bloch, and P. Llewellyn, "Amine-modified SBA-12 mesoporous silica for carbon dioxide capture: effect of amine basicity on sorption properties," *Microporous and Mesoporous Materials*, vol. 116, no. 1–3, pp. 358–364, 2008.
- [16] A. Kumar and D. Srinivas, "Selective oxidation of cyclic olefins over framework Ti-substituted, three-dimensional, mesoporous Ti-SBA-12 and Ti-SBA-16 molecular sieves," *Catalysis Today*, vol. 198, no. 1, pp. 59–68, 2012.
- [17] D. Z. Zhao, C. Shi, X. S. Li, A. M. Zhu, and B. W.-L. Jang, "Enhanced effect of water vapor on complete oxidation of formaldehyde in air with ozone over MnO<sub>x</sub> catalysts at room temperature," *Journal of Hazardous Materials*, vol. 239–240, pp. 362–369, 2012.
- [18] X. Li, L. J. Wang, Q. B. Xia, Z. M. Li, and Z. Li, "Catalytic oxidation of toluene over copper and manganese based catalysts: effect of water vapor," *Catalysis Communications*, vol. 14, no. 1, pp. 15–19, 2011.
- [19] G. Jacobs, T. K. Das, P. M. Patterson, J. Li, L. Sanchez, and B. H. Davis, "Fischer-Tropsch synthesis XAFS: XAFS studies of the effect of water on a Pt-promoted Co/Al<sub>2</sub>O<sub>3</sub> catalyst," *Applied Catalysis A: General*, vol. 247, no. 2, pp. 335–343, 2003.
- [20] Q.-H. Xia, K. Hidajat, and S. Kawi, "Improvement of the hydrothermal stability of fluorinated MCM-41 material," *Materials Letters*, vol. 42, no. 1, pp. 102–107, 2000.
- [21] D. Shen, M. Bülow, F. Siperstein, M. Engelhard, and A. L. Myers, "Comparison of experimental techniques for measuring isosteric heat of adsorption," *Adsorption*, vol. 6, no. 4, pp. 275–286, 2000.
- [22] A. Ansón, M. A. Callejas, A. M. Benito et al., "Hydrogen adsorption studies on single wall carbon nanotubes," *Carbon*, vol. 42, no. 7, pp. 1237–1241, 2004.
- [23] Z. X. Zhao, X. M. Li, and Z. Li, "Adsorption equilibrium and kinetics of p-xylene on chromium-based metal organic framework MIL-101," *Chemical Engineering Journal*, vol. 173, no. 1, pp. 150–157, 2011.
- [24] S. C. Sharma, H. Kunieda, J. Esquena, and C. Rodríguez Abreu, "Phase behavior and preparation of mesoporous silica in aqueous mixtures of fluorinated surfactant and hydrophobic fluorinated polymer," *Journal of Colloid and Interface Science*, vol. 299, no. 1, pp. 297–304, 2006.
- [25] Y.-L. Su, J. Wang, and H.-Z. Liu, "FTIR spectroscopic study on effects of temperature and polymer composition on the structural properties of PEO-PPO-PEO block copolymer micelles," *Langmuir*, vol. 18, no. 14, pp. 5370–5374, 2002.
- [26] Z. Sarbak, "FT-IR studies on coke formation over low loaded Mo catalyst supported on Al<sub>2</sub>O<sub>3</sub>," *Reaction Kinetics and Catalysis Letters*, vol. 84, no. 2, pp. 263–270, 2005.
- [27] J. W. Yi, Y. H. Lee, and B. Farouk, "Low dielectric fluorinated amorphous carbon thin films grown from C<sub>6</sub>F<sub>6</sub> and Ar plasma," *Thin Solid Films*, vol. 374, no. 1, pp. 103–108, 2000.
- [28] J. F. Kang, A. Ulman, R. Jordan, and D. G. Kurth, "Optically induced band shifts in infrared spectra of mixed self-assembled monolayers of biphenyl thiols," *Langmuir*, vol. 15, no. 17, pp. 5555–5559, 1999.
- [29] D. O'Hagan, "Understanding organofluorine chemistry. An introduction to the C-F bond," *Chemical Society Reviews*, vol. 37, pp. 308–319, 2008.
- [30] J. L. Blin and M. J. Stébé, "Effect of fluorocarbon addition on the structure and pore diameter of mesoporous materials prepared with a fluorinated surfactant," *Microporous and Mesoporous Materials*, vol. 87, no. 1, pp. 67–76, 2005.
- [31] A. Anson, Y. Wang, C. C. H. Lin, T. M. Kuznicki, and S. M. Kuznicki, "Adsorption of ethane and ethylene on modified ETS-10," *Chemical Engineering Science*, vol. 63, no. 16, pp. 4171–4175, 2008.
- [32] A. R. Zimmerman, K. W. Goyne, J. Chorover, S. Komarneni, and S. L. Brantley, "Mineral mesopore effects on nitrogenous organic matter adsorption," *Organic Geochemistry*, vol. 35, no. 3, pp. 355–375, 2004.
- [33] R. T. Yang, *Adsorbents: Fundamentals and Applications*, Wiley-Interscience, 1st edition, 2003.

## Research Article

# The Application of Resonance-Enhanced Multiphoton Ionization Technique in Gas Chromatography Mass Spectrometry

**Adan Li, Jianzheng Song, Yang Sun, and Tifeng Jiao**

*Hebei Key Laboratory of Applied Chemistry, School of Environmental and Chemical Engineering, Yanshan University, Qinhuangdao 066004, China*

Correspondence should be addressed to Adan Li; [adanli@ysu.edu.cn](mailto:adanli@ysu.edu.cn)

Received 23 March 2014; Accepted 27 April 2014; Published 12 May 2014

Academic Editor: Xinqing Chen

Copyright © 2014 Adan Li et al. This is an open access article distributed under the Creative Commons Attribution License, which permits unrestricted use, distribution, and reproduction in any medium, provided the original work is properly cited.

Gas chromatography resonance-enhanced multiphoton ionization time-of-flight mass spectrometry (GC/REMPI-TOFMS) using a nanosecond laser has been applied to analyze the 16 polycyclic aromatic hydrocarbons (PAHs). The excited-state lifetime, absorption characters, and energy of electronic states of the 16 PAHs were investigated to optimize the ionization yield. A river water sample pretreated by means of solid phase extraction was analyzed to evaluate the performance of the analytical instrument. The results suggested that REMPI is superior to electron impact ionization method for soft ionization and suppresses the background signal due to aliphatic hydrocarbons. Thus, GC/REMPI-TOFMS is a more reliable method for the determination of PAHs present in the environment.

## 1. Introduction

The ionization technique for the analyte molecules is of particular importance to mass spectrometry (MS); the application of varied ion sources of the MS introduces selectivity features of the analysis result, that is, species, isomers, or state-selective ionization and control of fragment intense [1–3]. Electron impact (EI) represents one of the most useful ionization methods used in the current studies of gas chromatography/mass spectrometry (GC/MS) analysis. The method, however, suffers from the mass information caused by the hard ionization, which results in the difficulty of identifying the complicated matrix of samples. The typical soft ionization including chemical ionization (CI), field ionization (FI), and photoionization (PI) has been developed to overcome the weakness of the hard ionization method. PI is superior to CI and FI on the mass spectrometric analysis because there is no limitation caused by the chemical reaction in CI and oxidation of the emitter in FI. Laser based PI methods, such as resonance-enhanced multiphoton ionization (REMPI) and single-photon ionization (SPI), have been very successfully applied to research and practical applications [4–7]. REMPI is more elective and sensitive than

SPI for the ionization of aromatic hydrocarbons using UV wavelengths that are readily accessible with standard pulsed lasers. Most applications of REMPI-MS involve direct-inlet MS, but successful couplings of REMPI-MS to GC and LC as well as laser desorption have also been reported [5, 7]. The coupling of such techniques with mass-spectrometry has expanded considerably the realm of analytical capabilities of MS. A laser with different pulse durations has been employed for ionization [8–10]. For example, a femtosecond laser has been successfully used for efficient ionization before relaxation process of internal conversion and intersystem crossing of some chlorinated, brominated compounds [11, 12]. Unfortunately, a high cost, a large dimension, and difficulties in the maintenance prevent practical use of this method in environmental analysis. In addition, if the laser pulse width is much shorter than the time scale of relaxation, the use of such high intensive laser leads to unfavorable dissociation of both neutrals and ions, thus making sensitive and reliable analysis more difficult [13]. To date, a number of studies have been reported to investigate the importance of laser parameters on the ionization yield for various chemical species [9, 10, 14–16].

In this study, a combination of gas chromatography (GC) and REMPI/MS (GC-REMPI/MS) using a nanosecond laser

was utilized for trace analysis of 16 polycyclic aromatic hydrocarbons (PAHs) in the priority list of US Environmental Protection Agency (EPA) to investigate the best performance of this technique. With REMPI, the molecule absorbs the first photon for excitation and the second photon for subsequent ionization. Since only a molecule absorbing the first photon can be ionized, interference arising from aliphatic hydrocarbons can be reduced. Thus, this technique provides superior selectivity since each congener can be selectively ionized via resonance excitation. A river water sample was also analyzed after pretreatment by solid phase extraction (SPE) method using this system to demonstrate the advantage especially in selectivity in environmental analysis.

## 2. Materials and Methods

**2.1. Apparatus.** Figure 1 shows the experimental setup in this study. The fourth harmonic emission of a Nd:YAG laser (Crylas, 266 nm, 1 ns, 1 kHz) was employed as an ionization source. One  $\mu\text{L}$  of the analyte was injected into a GC system (Agilent Technologies, 6890N) using an autosampler (Agilent Technologies, 7683B) followed by a DB-5 (30 m  $\times$  0.32 mm I.D.) capillary column. Helium was used as a carrier gas at a constant flow rate of 1 mL/min. The temperature program for analysis of PAHs was set at a rate of 20°C/min from 40 to 120°C. It was further increased at a rate of 5°C/min from 120°C to 250°C and held for 3 min and was then increased at a rate of 5°C/min to 280°C and held for 10 min. The temperatures of the injection port and the transfer line were maintained at 300°C. The sample eluting from GC was introduced into a linear-type TOF-MS as an effusive molecular beam. A microchannel plate (Hamamatsu, F4655-11) was utilized for the detection of the ions induced by multiphoton ionization. The signal of the mass spectrum was optimized using a digital oscilloscope (Tektronix DPO7104, 1 GHz, 20 GS/s). The two-dimensioned data of GC/REMPI-TOFMS was recorded by a digitizer (Agilent Technologies, 8 bit PCI High-speed Signal Analyzers, Acqiris AP240, 1 GHz, 1-2 GS/s). The final results of the data were analyzed and displayed using Labview software.

**2.2. Reagents.** A standard mixture of PAHs in the priority list of US EPA (acenaphthene (ACE), acenaphthylene (ACY), anthracene (ANT), benzo(a)anthracene (BaA), benzo(b)fluoranthene (BbF), benzo(k)fluoranthene (BkF), benzo(ghi)perylene (BPY), benzo(a)pyrene (BaP), chrysene (CHR), dibenzo(a,h)anthracene (DBA), fluoranthene (FLT), fluorene (FLU), indeno(1,2,3-cd)pyrene (IND), naphthalene (NAP), phenanthrene (PHE), and pyrene (PYR)) prepared at a concentration of 2000  $\mu\text{g}/\text{mL}$  in methylene chloride-benzene (1:1 v/v) and a mixture of deuterated internal standards (I.S.) (acenaphthene-d<sub>10</sub>, phenanthrene-d<sub>10</sub>, and chrysene-d<sub>12</sub>) prepared at a concentration of 500  $\mu\text{g}/\text{mL}$  in acetone were purchased from Supelco (Bellefonte, PA, USA). All the solutions were stored in containers made of amber glass at 4°C. Analytical-reagent grade of acetonitrile, acetone, methanol, and dichloromethane was purchased from Kanto

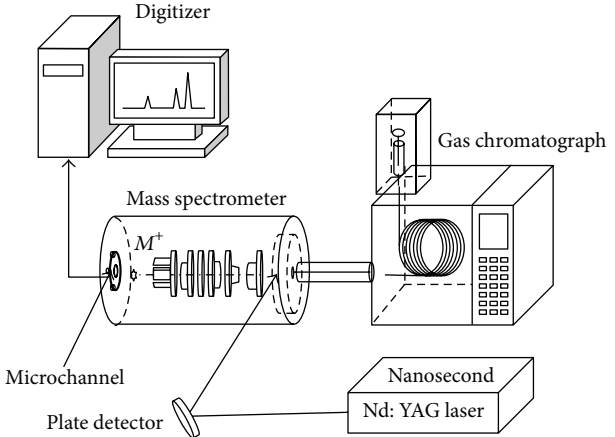


FIGURE 1: Experimental setup of the GC/REMPI-TOFMS based on the forth harmonic emission of a nanosecond Nd:YAG laser.

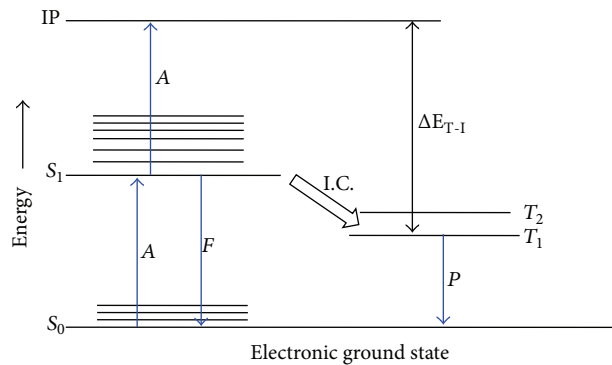


FIGURE 2: Schematic diagram of one-color two-photon ionization process and the relaxation process. A: photon absorption; F: fluorescence; S: singlet state; P: phosphorescence; I.C.: intersystem crossing.

Kagaku (Tokyo). Deionized water was obtained from a Milli-Q water purification system (Millipore, Molsheim, France).

**2.3. SPE.** A surface water sample was collected from a river located in the northern part of Kyushu area in Japan. A river water sample was spiked with 0.5 mL (200  $\mu\text{g}/\mu\text{L}$ ) of I.S. to investigate the recovery of PAHs in the SPE process. The 500 mL of water sample was passed through an SPE cartridge (Sep-Pak Plus C18 with 10 mL of dichloromethane, 10 mL of methanol, and 10 mL of Milli-Q water) at a flow rate of 10 mL/min. The PAHs and dioxin were eluted with 5 mL of dichloromethane from the Sep-Pak Plus C18 cartridge connected with the Sep-Pak Dry cartridge. The solvent of the extract was evaporated under a nitrogen flow and filled with 0.5 mL of acetonitrile for analysis by GC/REMPI-TOFMS.

## 3. Results and Discussion

**3.1. Excited-State Lifetime.** Figure 2 shows a total ion chromatogram (TIC) of the standard mixture sample that contained 16 PAHs (200  $\mu\text{g}/\mu\text{L}$ ). Generally, the excited-state lifetimes ( $\tau_s$ ) have an important influence on the ionization

TABLE 1: Quality parameter obtained using REMPI-GC/MS and determination of PAHs in a spiked water sample obtained from the artificial lake.

Retention order	Compound	Structure	MW (relative intensity)	Peak area (relative intensity)	LOD (pg)	PAHs in the river	$r_s$ in jet (ns) <sup>a</sup>	$r_s$ in sol (ns) <sup>b</sup>	Absorption in sol (log) <sup>c</sup>	REMPI (mV/( $\mu$ J·pmol)) <sup>a</sup>
1	NAP		128	16	0.18	D	nf	96	3.4 <sup>c</sup>	30
2	ACY		152	0.1	18	ND	nf	nf	3.4 <sup>c</sup>	2
3	ACE		154	31	0.20	ND	nf	46	3.5 <sup>d</sup>	15
4	FLU		166	56	0.42	ND	nf	10	4.2 <sup>c</sup>	80
5	PHE		178	87	0.29	D	76	60	4.0 <sup>c</sup>	100
6	ANT		178	7.7	2.2	ND	8	5.3	3 <sup>e</sup>	1
7	FLT		202	10	1.9	D	38	53	nf	5

TABLE I: C,Continued.

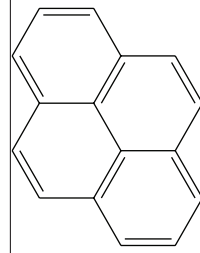
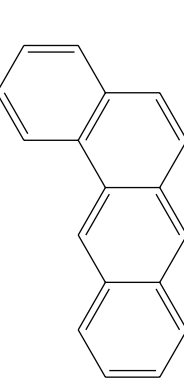
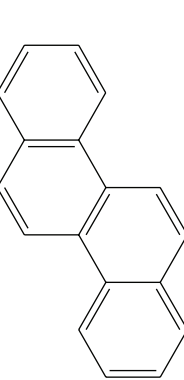
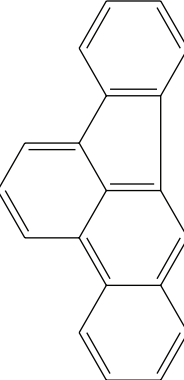
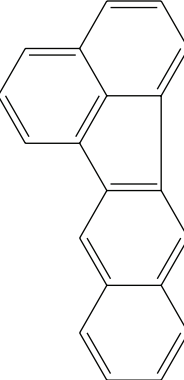
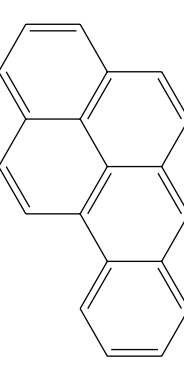
Retention order	Compound	Structure	MW	Peak area (relative intensity)	LOD (pg)	PAHs in the river	$\tau_s$ in jet (ns) <sup>a</sup>	$\tau_s$ in sol (ns) <sup>b</sup>	Absorption in sol (log) <sup>c</sup>	REMPI (mV/(μJ·pmol)) <sup>a</sup>
8	PYR		202	110	0.24	D	1400	650	nf	150
9	BaA		228	200	0.19	D	nf	45	nf	200
10	CHR		228	110	0.24	D	nf	44.7	4.8 <sup>c</sup>	120
11	BbF		252	71	0.32	D	nf	44.3	4.1 <sup>c</sup>	40
12	BlkF		252	140	0.23	D	nf	11.3	nf	nf
13	BaP		252	190	0.19	D	270	49	nf	100

TABLE I: Continued.

Retention order	Compound	Structure	MW (relative intensity)	Peak area (relative intensity)	LOD (pg)	PAHs in the river	$\tau_s$ in jet (ns) <sup>a</sup>	$\tau_s$ in sol (ns) <sup>b</sup>	Absorption in sol (log $\epsilon$ ) <sup>c</sup>	REMPI (mV/( $\mu$ J·pmol)) <sup>d</sup>
14	IND		276	29	1.3	D	nf	9.1	nf	nf
15	DBA		278	180	0.38	D	nf	37	4.2 <sup>c</sup>	90
16	BPY		276	99	0.6	D	nf	203	4.3 <sup>c</sup>	50

<sup>a</sup> Reference [17], nf: not found. <sup>b</sup> Reference [18]. <sup>c</sup> Data compiled from NIST Standard Reference Database, Database, March 1998 Release; NIST Chemistry Web Book. <sup>d</sup> calculated from [19] and <sup>e</sup> calculated from [20]. D: detected, ND: not detected.

TABLE 2: Electronic states energy of the 16 PAHs in U.S. EPA list.

Compound	NAP	ACY	ACE	FLU	PHE	ANT	FLT	PYR	BaA	CHR	BbF	BkF	BaP	IND	DBA	BPY
IP (eV)	8.12 <sup>a</sup>	8.22 <sup>a</sup>	7.68 <sup>a</sup>	7.88 <sup>a</sup>	7.90 <sup>a</sup>	7.44 <sup>a</sup>	7.9 <sup>a</sup>	7.43 <sup>a</sup>	7.53 <sup>a</sup>	7.6 <sup>a</sup>	7.70 <sup>b</sup>	7.48 <sup>b</sup>	7.10 <sup>a</sup>	nf	7.38 <sup>a</sup>	7.16 <sup>a</sup>
$S_1$ (eV) <sup>c</sup>	4.03 <sup>d</sup>	nf	nf	4.12 <sup>c</sup>	3.61 <sup>d</sup>	3.31 <sup>c</sup>	3.06 <sup>c</sup>	3.34 <sup>c</sup>	3.22 <sup>c</sup>	3.44 <sup>c</sup>	3.38 <sup>c</sup>	3.10 <sup>c</sup>	3.08 <sup>c</sup>	nf	3.14 <sup>c</sup>	3.05
$T_1$ (eV) <sup>c</sup>	2.88 <sup>d</sup>	nf	nf	2.95 <sup>c</sup>	2.7 <sup>d</sup>	1.85 <sup>c</sup>	2.92 <sup>c</sup>	2.11 <sup>c</sup>	2.07 <sup>c</sup>	2.48 <sup>c</sup>	2.49 <sup>c</sup>	2.19 <sup>c</sup>	1.84 <sup>c</sup>	nf	2.26 <sup>c</sup>	2.00
$E_{T-I}$ (eV)	5.24	nf	nf	4.93	5.2	5.59	4.98	5.32	5.46	5.12	5.21	5.29	5.26	nf	5.12	5.16

<sup>a</sup>Data compiled from NIST Standard Reference Database. Database, March 1998 Release: NIST Chemistry Web Book; nf: not found. <sup>b</sup>Reference [21]. <sup>c</sup>calculated from [22] and <sup>d</sup>calculated from [23].

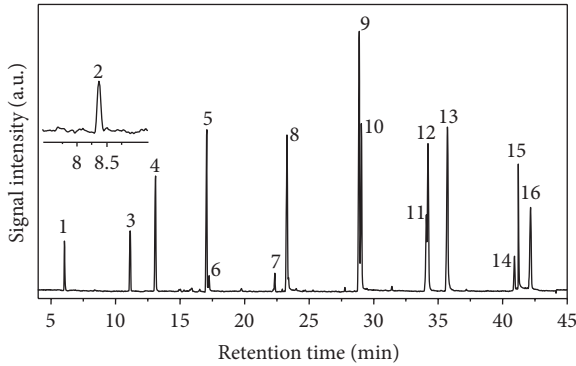


FIGURE 3: The total ion chromatogram (TIC) of GC/REMPI-TOFMS obtained for a standard solution of PAHs at 200 pg/ $\mu$ L. Peak numbers are 1, NAP; 2, ACY; 3, ACE; 4, FLU; 5, PHE; 6, ANT; 7, FLT; 8, PYR; 9, BaA; 10, CHR; 11, BbF; 12, BkF; 13, BaP; 14, IND; 15, DBA; and 16, BPY.

efficiency of PAHs, because an important feature of the PAHs molecules considered is the close-to-unity sum of the quantum yields of fluorescence  $\Phi_F$  and of triplet formation  $\Phi_T$  due to the intersystem crossing transition  $S_1 \rightarrow T_1$ . The photophysical properties of the PAHs and the experimental results are shown in Table 1. There are only a few reports on the lifetime of isolated PAHs in the gas phase, although the lifetimes of PAHs in the condensed phase are well known [17]. The lifetimes of PAHs in solution are similar to, or slightly shorter than, those in the gas phase due to an additional relaxation pathway from collisions between the analyte and solvent molecules [18]. Therefore, the lifetimes of the 16 PAHs (8–1400 ns in the gas phase and 6–650 ns in the condensed phase, except for ACY and IND) were much longer than the pulse width of the laser used in the present study (1 ns). Thus, no obvious loss of ionization efficiency could be observed for most of the 16 PAHs except of ACY. In ACY molecule, the major deactivation pathway from the  $S_1$  state was an efficient  $S_1 \rightarrow S_0$  internal conversion. The lifetime of the  $S_1$  state of ACY had been determined to be 345 ps and 0.2 ns, which were shorter than the pulse width of the laser in the present study [24, 25]. In the other cases, the  $\tau_s$  was not the determination factor to the ionization efficiency. For example, the  $\tau_s$  of PYR is the longest in all the analytes in this research, but the ionization efficiency of it is even lower than that of BaP. Thus, only when the  $\tau_s$  of the PAHs is shorter than the pulse width of the laser, the ionization efficiency can be increased using a more intensive laser.

**3.2. Energy of Electronic States.** The schematic diagram of the photochemical conversion in the one-color two-photon ionization process is shown in Figure 3. When the gas molecules absorb photons, the electrons can be elevated to higher energy state to form the excited state. The PAHs molecules having absorbed the first photon in the excited state could absorb another photon to the ionization potential (IP) to accomplish the 1 + 1 REMPI process. Simultaneously, it could lose energy through the intersystem crossing or the internal conversation to the triplet state or the ground state because the crossing and conversation from the upper to the lower excited state are normally fast and very efficient; the states mentioned here are the lowest singlet-state  $S_1$  and lowest triplet-state  $T_1$ . The photochemistry properties of the 16 PAHs are shown in Table 2. The energy from triplet state to IP was shown as  $E_{T-I}$  in Table 2. It should be noticed that, in the case of ANT,  $S_1$  may cross to  $T_2$ , which is nearly isoenergetic with  $S_1$  [26]. Thus, in ANT, a small energy gap and consequently a favorable Frank-Condon factor exist for intersystem crossing, thus leading to a higher limit of detection (LOD) ( $S/N = 3$ ) of it. From Table 2, it was obvious that the two-photon energy applied in this study (266 nm + 266 nm = 9.32 eV) was qualified for a 1 + 1 REMPI for all the 16 PAHs in this research, but one-photon energy could not provide the subsequent exciting from the triplet-state.

**3.3. Absorption Character.** During 1 + 1 REMPI absorption process, the ionization efficiency of a molecule depended primarily on two factors:  $\sigma_1$ , the cross section for absorption of the first photon which excites the molecule from the ground electronic state into an electronically excited intermediate state;  $\sigma_2$ , the cross section for absorption of the second photon which pumps the excited molecule into the ionization continuum. In the theory when the first photon absorption event is the rate-limiting step of the ionization process (i.e.,  $\sigma_1 \ll \sigma_2$ ), then similarities are expected between the absorption or fluorescence excitation spectra and the 1 + 1 REMPI spectra. If, on the other hand, the second photon absorption event is the rate-determining step (i.e.,  $\sigma_1 \gg \sigma_2$ ), then the spectroscopy of the molecules in the excited state is expected to dominate the spectrum. As to  $\sigma_1$ , it can be derived from the distinction coefficient ( $\epsilon$ ) as follows:

$$\sigma_1 = 2.303 \frac{\epsilon}{N_A} = 3.82 \times 10^{-21} \epsilon \quad (1)$$

$(N_A : \text{Avogadro constant}).$

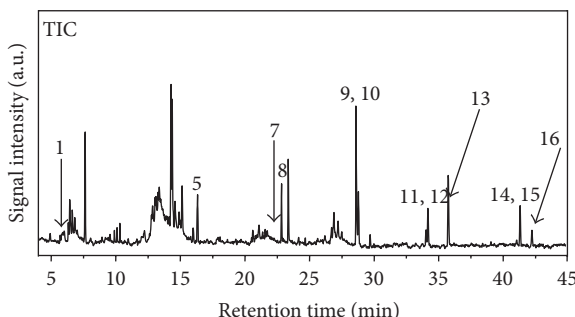


FIGURE 4: The TIC obtained by GC/REMPI-TOFMS from a river sample spiked with an I.S. standard mixture of PAHs. Peak numbers are 1, NAP; 5, PHE; 7, FLT; 8, PYR; 9, BaA; 10, CHR; 11, BbF; 12, BkF; 13, BaP; 14, IND; 15, DBA; and 16, BPY.

There were few reports about the gas phase UV absorption spectra of PAHs because in most cases the UV absorption spectra were given in solution phase. But the shape and width of these two phases were the same and they shift generally between 6 and 18 nm [27]. Thus the extinction coefficients absorption discussed here was the data obtained from the solution phase.

From the peak area of PHE and ANT, shown in Table 1, it was clear that the ionization efficiency of PHE was about 11 times that of ANT. The dominant ionization efficiency at 266 nm of PHE would change if a wavelength was more selective to ANT. For example, at 310 nm, ANT was preferentially ionized in the presence of PHE due to the different  $\sigma_1$  absorption character [28]. On the other hand, the  $\sigma_2$  could determine the intensity of the REMPI spectra as well. As shown in Table 1, the  $\epsilon$  of NAP and ACY was the same, but the REMPI intensity of NAP was 15 times that of ACY, which resulted in the lower ionization efficiency of ACY compared to NAP.

**3.4. Measurement of a Water Sample.** A sample derived from surface water was spiked with three deuterated compounds, which served as internal standards, and was analyzed by GC/REMPI-TOFMS. The TIC was displayed by extracting the data between  $m/z = 100$  and 400 in Figure 4, in which 12 PAHs on the U.S. EPA list and the internal standards were evident. We noticed that several of the chromatograph peaks had  $m/z$  values that were identical to those of the PAHs on the U.S. EPA list. These peaks might have been due to isomers of the PAHs. Therefore, the signal peaks should be carefully identified, even though the REMPI technique had superior selectivity. For example, several NAP isomers with the chemical formula  $C_{10}H_8$  were detected, which might be either 1H-indene-1-methylene, azulene, or 2-methylene-2H-indene. A more serious case was observed for FLT; there were several peaks with larger signal intensities than that of FLT. These isomers could be either acephenanthrylene, aceanthrylene, or their analogues. However, for all the compounds detected in this research, the mass chromatogram was much simplified and generally no fragments except the parent ion could be detected. Compared to the conventional ionization technique

of GC/EI-MS, the background of the mass spectra was much reduced and the selectivity was improved greatly.

## 4. Conclusions

The forth harmonic emission of a nanosecond Nd:YAG laser emitting at 266 nm was employed to detect 16 PAHs of US EPA both in standard samples and in a water sample. The detection limits of the 16 PAHs were determined to be 0.18~18 pg. The absorption characters at 266 nm can influence the ionization efficiency obviously, owing to the longer lifetime of the 16 PAHs compared to the pulse width of the laser. As to ionization potential, the photon energy of the laser applied in this study is enough to induce the REMPI process but not an ionization process from triplet state. In the analysis of the river sample, few compounds except PAHs can be detected in the mass chromatogram due to selective ionization of REMPI. The GC/REMPI-TOFMS based on nanosecond laser ionization is suitable for the trace detection of PAHs in environmental sample due to the high selectivity and sensitivity.

## Conflict of Interests

The authors declare that there is no conflict of interests regarding the publication of this paper.

## Acknowledgments

This research was supported by the Science and Technology Research of Higher Education Institute of Hebei province of China (QN20131038) and the Independent Research Project for Yong Teachers of Yanshan University (13LGA014).

## References

- [1] T. Uchimura, Y. Sakoda, and T. Imasaka, "On-line concentration by analyte adsorption and subsequent laser desorption in supersonic jet spectrometry," *Analytical Chemistry*, vol. 80, no. 10, pp. 3798–3802, 2008.
- [2] D. M. Lubman, "Optically selective molecular mass spectrometry," *Analytical Chemistry*, vol. 59, no. 1, pp. 31A–40A, 1987.
- [3] F. Mühlberger, J. Wieser, A. Ulrich, and R. Zimmermann, "Single photon ionization (SPI) via incoherent VUV-excimer light: robust and compact time-of-flight mass spectrometer for on-line, real-time process gas analysis," *Analytical Chemistry*, vol. 74, no. 15, pp. 3790–3801, 2002.
- [4] U. Boesl, H. J. Neusser, and E. W. Schlag, "Multi-photon ionization in the mass spectrometry of polyatomic molecules: cross sections," *Chemical Physics*, vol. 55, no. 2, pp. 193–204, 1981.
- [5] A. Li, T. Uchimura, Y. Watanabe-Ezoe, and T. Imasaka, "Analysis of dioxins by gas chromatography/resonance-enhanced multi-photon ionization/mass spectrometry using nanosecond and picosecond lasers," *Analytical Chemistry*, vol. 83, no. 1, pp. 60–66, 2011.
- [6] T. Streibel, J. Weh, S. Mitschke, and R. Zimmermann, "Thermal desorption/pyrolysis coupled with photoionization time-of-flight mass spectrometry for the analysis of molecular organic

- compounds and oligomeric and polymeric fractions in urban particulate matter," *Analytical Chemistry*, vol. 78, no. 15, pp. 5354–5361, 2008.
- [7] R. Zimmermann, F. Mühlberger, K. Fuhrer, M. Gonin, and W. Welthagen, "An ultracompact photo-ionization time-of-flight mass spectrometer with a novel vacuum ultraviolet light source for on-line detection of organic trace compounds and as a detector for gas chromatography," *Journal of Material Cycles and Waste Management*, vol. 10, no. 1, pp. 24–31, 2008.
- [8] Q. Wang, Y. A. Dyakov, D. Wu et al., "Ionization/dissociation processes of methyl-substituted derivates of cyclopentanone in intense femtosecond laser field," *Chemical Physics Letters*, vol. 586, pp. 21–28, 2013.
- [9] A. Li, T. Uchimura, H. Tsukatani, and T. Imasaka, "Trace analysis of polycyclic aromatic hydrocarbons using gas chromatography-mass spectrometry based on nanosecond multiphoton ionization," *Analytical Sciences*, vol. 26, no. 8, pp. 841–846, 2010.
- [10] S. Yamaguchi, F. Kira, Y. Miyoshi et al., "Near-ultraviolet femtosecond laser ionization of dioxins in gas chromatography/time-of-flight mass spectrometry," *Analytica Chimica Acta*, vol. 632, no. 2, pp. 229–233, 2009.
- [11] O. Shitamichi, T. Matsui, Y. Hui, W. Chen, and T. Imasaka, "Determination of persistent organic pollutants by gas chromatography/laser multiphoton ionization/time-of-flight mass spectrometry," *Frontiers of Environmental Science and Engineering in China*, vol. 6, no. 1, pp. 26–31, 2012.
- [12] A. Li, T. Imasaka, T. Uchimura, and T. Imasaka, "Analysis of pesticides by gas chromatography/multiphoton ionization/mass spectrometry using a femtosecond laser," *Analytica Chimica Acta*, vol. 701, no. 1, pp. 52–59, 2011.
- [13] E. Sekreta, K. G. Owens, and J. P. Reilly, "Intensity-dependent laser ionization experiments involving the  ${}^1\text{b}_{1u}$  state of benzene," *Chemical Physics Letters*, vol. 132, no. 4–5, pp. 450–455, 1986.
- [14] N. Kirihara, H. Yoshida, M. Tanaka et al., "Development of a rimmpa-tofms: isomer selective soft ionization of PCDDs/DFs," *Organohalogen Compound*, vol. 66, pp. 731–738, 2004.
- [15] T. Itoh, T. Uchimura, T. Uchida, M. Kawano, and T. Imasaka, "GC-MPI-MS of pentachlorodibenzofurans in flue gas using a UV picosecond laser," *Chromatographia*, vol. 68, no. 1–2, pp. 89–94, 2008.
- [16] M. van den Berg, L. S. Birnbaum, M. Denison et al., "The 2005 World Health Organization reevaluation of human and mammalian toxic equivalency factors for dioxins and dioxin-like compounds," *Toxicological Sciences*, vol. 93, no. 2, pp. 223–241, 2006.
- [17] O. P. Haefliger and R. Zenobi, "Laser mass spectrometric analysis of polycyclic aromatic hydrocarbons with wide wavelength range laser multiphoton ionization spectroscopy," *Analytical Chemistry*, vol. 70, no. 13, pp. 2660–2665, 1998.
- [18] S. L. Murov, I. Carmichael, and G. L. Hug, *Handbook of Photochemistry*, Marcel Dekker, New York, NY, USA, 1993.
- [19] I. B. Berliner, *Handbook of Fluorescence Spectra of Aromatic Molecules*, Academic Press, New York, NY, USA, 1971.
- [20] A. Gutierrez-Llorente, R. Perez-Casero, B. Pajot et al., "Growth of anthracene thin films by matrix-assisted pulsed-laser evaporation," *Applied Physics A: Materials Science and Processing*, vol. 77, no. 6, pp. 785–788, 2003.
- [21] A. Majcherczyk, C. Johannes, and A. Hüttermann, "Oxidation of polycyclic aromatic hydrocarbons (PAH) by laccase of *Trametes versicolor*," *Enzyme and Microbial Technology*, vol. 22, no. 5, pp. 335–341, 1998.
- [22] J. L. Newsted and J. P. Giesy, "Predictive models for photoinduced acute toxicity of polycyclic aromatic hydrocarbons to *Daphnia magna*, strauss (cladocera, crustacea)," *Environmental Toxicology and Chemistry*, vol. 6, no. 6, pp. 445–461, 1987.
- [23] J. B. Birks, *Photophysics of Aromatic Molecules*, Wiley, New York, NY, USA, 1963.
- [24] A. Samanta, C. Devadoss, and R. W. Fessenden, "Picosecond time-resolved absorption and emission studies of the singlet excited states of acenaphthylene," *Journal of Physical Chemistry*, vol. 94, no. 18, pp. 7106–7110, 1990.
- [25] B. F. Plummer, M. J. Hopkinson, and J. H. Zoeller, "Dual wavelength fluorescence from acenaphthylene and derivatives in fluid media," *Journal of the American Chemical Society*, vol. 101, no. 22, pp. 6779–6781, 1979.
- [26] Z. Wang, S. J. Weininger, and W. G. McGimpsey, "Photochemistry of the  $\text{T}_2$  state of anthracene," *Journal of Physical Chemistry*, vol. 97, no. 2, pp. 374–378, 1993.
- [27] C. W. Wilkerson Jr., S. M. Colby, and J. P. Reilly, "Determination of polycyclic aromatic hydrocarbons using gas chromatography/laser ionization mass spectrometry with picosecond and nanosecond light pulses," *Analytical Chemistry*, vol. 61, no. 23, pp. 2669–2673, 1989.
- [28] D. Helmig and W. P. Harger, "OH radical-initiated gas-phase reaction products of phenanthrene," *Science of the Total Environment*, vol. 148, no. 1, pp. 11–21, 1994.

## Review Article

# Remote Sensing of CO<sub>2</sub> Absorption by Saline-Alkali Soils: Potentials and Constraints

Wenfeng Wang,<sup>1,2</sup> Xi Chen,<sup>1</sup> and Zhi Pu<sup>3</sup>

<sup>1</sup> State Key Laboratory of Desert and Oasis Ecology, Xinjiang Institute of Ecology and Geography, Chinese Academy of Sciences, Urumqi 830011, China

<sup>2</sup> University of Chinese Academy of Sciences, Beijing 100093, China

<sup>3</sup> College of Computer and Information Engineering, Xinjiang Agricultural University, Urumqi 830052, China

Correspondence should be addressed to Xi Chen; chenxi@ms.xjb.ac.cn

Received 6 March 2014; Accepted 29 March 2014; Published 17 April 2014

Academic Editor: Qingrui Zhang

Copyright © 2014 Wenfeng Wang et al. This is an open access article distributed under the Creative Commons Attribution License, which permits unrestricted use, distribution, and reproduction in any medium, provided the original work is properly cited.

CO<sub>2</sub> absorption by saline-alkali soils was recently demonstrated in the measurements of soil respiration fluxes in arid and semiarid ecosystems and hypothetically contributed to the long-thought “missing carbon sink.” This paper is aimed to develop the preliminary theory and methodology for the quantitative analysis of CO<sub>2</sub> absorption by saline-alkali soils on regional and global scales. Both the technological progress of multispectral remote sensing over the past decades and the conjectures of mechanisms and controls of CO<sub>2</sub> absorption by saline-alkali soils are advantageous for remote sensing of such absorption. At the end of this paper, the scheme for remote sensing is presented and some unresolved issues related to the scheme are also proposed for further investigations.

## 1. Introduction

Energy shortage and environment security are hot issues on economy and social development in the world today [1–3]. Global trends of soil desertification and degradation pose a direct threat to the food safety and human survival and become the hottest part of the issues. Soil salinization is one of the main types of soil desertification and degradation. It is caused by soil water and salt movement, usually occurring in arid and semiarid areas of strong evaporation and high-table groundwater with dissolvable salt [4]. Because of the alternating affection of rainfall, irrigation, and evaporation, soil salt further accumulates in unsaturated zone and leads to the secondary salinization, which induces a great loss of the resources of arable land and the agricultural production and meanwhile poses a serious threat to biosphere and ecological environment [5]. In order to manage saline-alkali soils and prevent further soil degradation, people must be timely informed about the nature and geographic distribution of saline-alkali soils and the degrees of salinity/alkalinity. Therefore, accurately acquiring the information on saline-alkali soils is significant to protect soil quality and agricultural

yield. Remote sensing data allows us to dynamically monitor saline-alkali soils on large scales [6]. Such information reflects the soil nature, geographical distribution, and its dynamic changes in the degrees of salinity/alkalinity, which is essentially significant for the reasonable planning of agricultural production and the steady development of social economy in arid and semiarid regions [4–6].

Exactly, such information not only can be used to monitor soil salinization, but also can be used to quantify the effects of other environmental processes, especially the geochemical processes related to the long-thought “missing carbon sink” [7]. It has been demonstrated that saline-alkali soils are absorbing CO<sub>2</sub> and may significantly contribute to the “missing carbon sink” [8–10]. A global quantification of CO<sub>2</sub> absorption by saline-alkali soils is important to readdress the “missing carbon sink” [7–9]. However, there is still no theory and methodology developed for quantifying the CO<sub>2</sub> absorption by saline-alkali soils on large scales. Some empirical models are presented to approximately quantify the absorption on site scales, but the model was parameterized using the collected data from the Gubantonggut desert and the environmental controls on model parameters were poorly

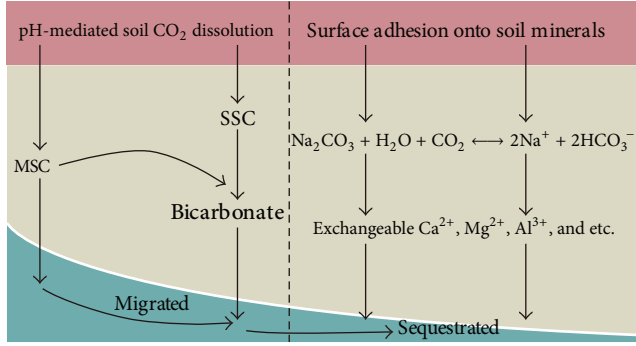


FIGURE 1: Conjectured mechanisms for  $\text{CO}_2$  absorption by saline-alkali soils. Note: MSC (the molecular solubility of  $\text{CO}_2$ ); SSC (the soil storage of  $\text{CO}_2$ ).

understood [11–14]. It is emergent to take further readings in other arid and semiarid regions and develop theory and methodology for remote sensing of  $\text{CO}_2$  absorption by saline-alkali soils on regional and global scales [13].

This paper is aimed to develop some preliminary theory and methodology for remote sensing of  $\text{CO}_2$  absorption by saline-alkali soils on large scales. As a first attempt, the theory potentials of and constraints on applying the methodology are also discussed. Strategies against the constraints are presented. Theoretical feasibility for remote sensing of  $\text{CO}_2$  absorption by saline-alkali soils on large scales is discussed. At the end of this paper, the strategies against the constraints and some unresolved issues about the theory and methodology are proposed.

## 2. Theory and Methodology

Although there are a series of studies speculated the mechanisms of  $\text{CO}_2$  absorption by saline-alkali soils, none of those speculations has been widely accepted. Conjectured mechanisms in the previous publications [7, 9, 10, 13] include (1) the soil storage of  $\text{CO}_2$ ; (2) the molecular dissolution of  $\text{CO}_2$  in soil water films; (3) the surface adhesion of  $\text{CO}_2$  onto soil minerals; (4) pH-mediated  $\text{CO}_2$  dissolution; and (4) migration and sequestration of  $\text{CO}_2$  into groundwater. The molecular solubility of  $\text{CO}_2$  (MSC) and the pH-mediated  $\text{CO}_2$  dissolution are two determining physiochemical parameters [10].

Spectral data from laboratory and field observations suggested that spectral reflectance of saline-alkali soil was affected by soil salt, organic matter content, structure, and soil color [16]. In addition, the solar altitude and soil salt composition also affect the spectral response mode of saline-alkali soils. Spectral reflectance increases/decreases when soil salt content increases for the difference in soil salt composition [6]. Although spectral reflectance of saline-alkali soils is the integrated effect of a series of environmental factors, soil salts and soil minerals content, soil surface morphology and soil water content are more determining factors. These are right the materials that contribute to  $\text{CO}_2$  absorption by saline-alkali soils (Figure 1).

Soil water not only directly affects the spectral characteristics of soils, but also controls the vertical movement of soil salt [16]. Saline-alkali soil usually contains  $\text{Na}^+$ ,  $\text{K}^+$ ,  $\text{Mg}^{2+}$ ,  $\text{Ca}^{2+}$ ,  $\text{Cl}^-$ ,  $\text{SO}_4^{2-}$ ,  $\text{CO}_3^{2-}$ , and so forth. Special salts (aqueous sodium chloride, sodium sulfate, potassium sulfate, calcium sulfate, and magnesium sulfate) absorb solar radiation and present additional spectral information [17–20]. These chemical materials, driven by soil water movements, are accumulated in the soil surface as salt crystals. Saline-alkali soils containing the heavier mass of sodium also have higher spectral reflectance than common saline-alkali soils [6]. Soil salinization and alkalinization were caused by the increases of soluble salts (sodium carbonate, sodium sulfate, and sodium chloride) in soils. The higher sodium content in the soils implies more  $\text{CO}_2$  can be dissolved [10]. The spectral characteristics also reflect the different stages of soil salinization and alkalinization [21, 22], while the alkalinity degree is a determining factor of  $\text{CO}_2$  absorption intensity [13].

Both the technological progress of multispectral remote sensing over the past decades and the conjectures of mechanisms and controls of  $\text{CO}_2$  absorption by saline-alkali soils are advantageous for remote sensing of such absorption on large scales. As a preliminary attempt, we need only to know well about how much soil dew can be accumulated in these soils and how much  $\text{CO}_2$  can be dissolved in the dew. These will help us to finally calculate the rate of  $\text{CO}_2$  absorption by saline-alkali soils. Estimation of the soil  $\text{CO}_2$  flux (i.e., soil respiration flux:  $F_c$ ) along a field gradient of air temperature 10 cm above the soil surface ( $T$ ) with  $F_c = 2.58 * 1.17^{(T-10)/10} - 2.86$  ( $R^2 = 0.86$ , RMSE = 0.23) and the contribution analysis of soil dew in the unexplained part of  $F_c$  by the  $Q_{10}$  model (denoted by  $F_x$ ) with  $F_x = 4.07 * e^{-10 * \text{dew}} - 6.38$  (dew > 1 mm;  $R^2 = 0.53$ , RMSE = 0.75) present further evidence (Figure 3). It recommends that remote sensing of  $\text{CO}_2$  absorption by saline-alkali soils should be based on the following equation. Let  $C_0$  be the initial amounts of  $\text{CO}_2$  in soil dew at  $t_0$  and the rate of  $\text{CO}_2$  increases in dew is  $r$ . Ignoring the restricting effect of history  $\text{CO}_2$  absorption, it is straight that

$$\frac{dC(t)}{dt} = rC(t), \quad C(t_0) = C_0, \quad (1)$$

where  $C(t)$  represents the  $\text{CO}_2$  dissolution dynamics on time scales.

It is easy to see that the analytic solution of (1) is  $C(t) = C_0 e^{r(t-t_0)}$ . Noting that  $C_0$  and  $r$  determine the dynamic changes of soil  $\text{CO}_2$  dissolution and the absorption rate, remote sensing of  $\text{CO}_2$  absorption by saline-alkali soils is equivalent to the retrieval of these two parameters. These two parameters are largely determined by soil pH (determines the amounts of soil  $\text{CO}_2$  dissolution), soil water content (reflects the dynamic changes of dew amounts in the soil), and air temperature (controls the dew deposition/evaporation). Exactly, it was found that  $\text{CO}_2$  absorption by saline-alkali soils correlates well with these three determining factors and an alternative form of (1) has been employed in large-scale applications [13].

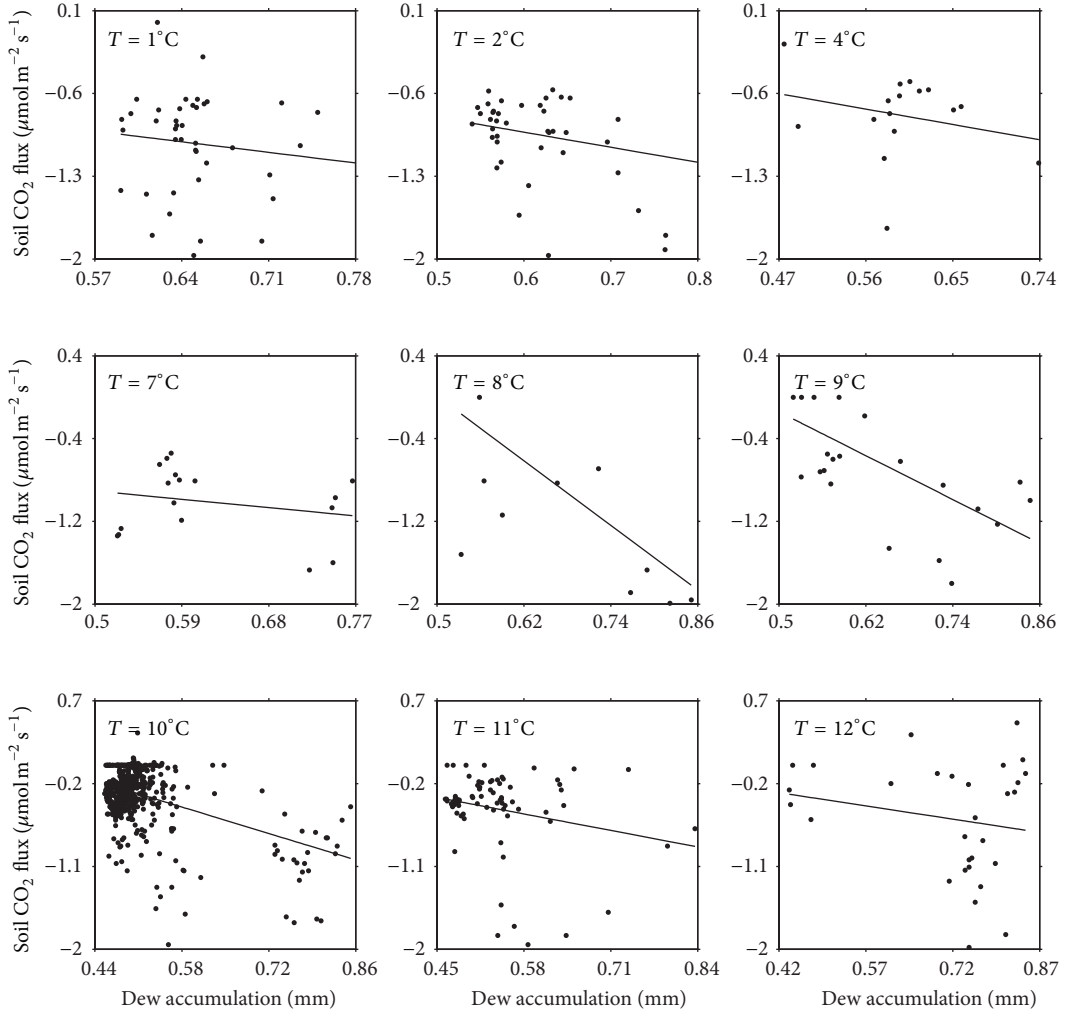


FIGURE 2: Variations of soil  $\text{CO}_2$  fluxes (soil respiration fluxes) with dew accumulation along a laboratory gradient of colder air temperatures [from [12]].

It is worthy to be noted that soil  $\text{CO}_3^{2-}$  content largely determines soil alkalinity degree, which in turn determines the intensity of  $\text{CO}_2$  absorption by saline-alkali soils. Soil  $\text{CO}_3^{2-}$  strongly absorbs infrared radiation and may present additional helpful spectral information [23]. When soils are sufficiently dry, salt crystal is accumulated onto the soil surface and hence the surface  $\text{CO}_2$  adhesion onto soil minerals is increasingly important since it makes chances for this  $\text{CO}_2$  on the soil surface to be further dissolved in soil water when soil dew amounts increase at lower temperatures (Figure 2). The significance of soil  $\text{CO}_3^{2-}$  content on  $\text{CO}_2$  absorption by saline-alkali soils is mainly determined by its close relation with soil pH, soil water content, and air temperature.

### 3. Potential and Constraints

The spectral characteristics of saline-alkali soils are vulnerable to the effects of the external environmental factors. If such an issue is not properly addressed, then it is easy to

generate cumulative errors, which increased the uncertainties in model parameters and in quantifying  $\text{CO}_2$  absorption by saline-alkali soils. These external environmental factors are also the main determinants of the model parameters. So it is an inevitable challenge to the traditional multispectral remote sensing. Fortunately, the development of modern spectroscopic techniques, especially the development of hyperspectral technology, allows researchers to detect specific substances in the soil using spectral diagnosis characteristics and further reduces uncertainties in remote sensing of  $\text{CO}_2$  absorption by saline-alkali soils.

Vegetation coverage can change spectral reflectance mode of saline-alkali soils and result in external interference [6, 24, 25]. Remote sensing of  $\text{CO}_2$  absorption by saline-alkali soils deserves the remote sensing images of high spatial resolution. Currently, the  $\text{CO}_2$  absorption phenomenon is mainly observed at saline-alkali sites of arid and semiarid regions. Remote sensing of the absorption on large scales should be naturally focused on arid and semiarid ecosystems. Some natural phenomena occurred at soil surface, such as the

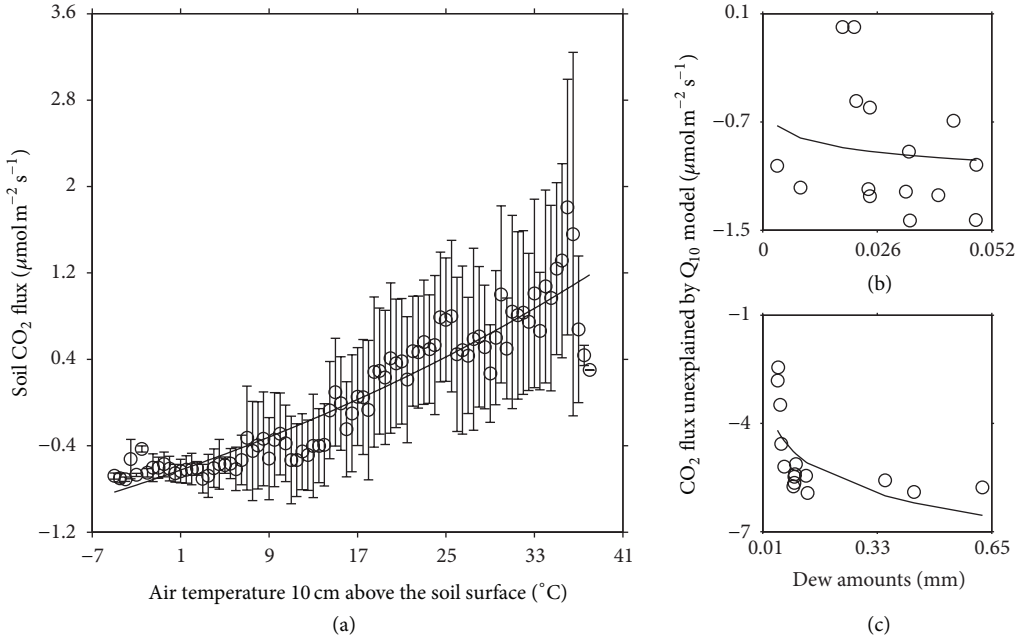


FIGURE 3: Estimation of soil CO<sub>2</sub> fluxes (soil respiration fluxes:  $F_c$ ) along a field gradient of the air temperature 10 cm above the soil surface ( $T$ ) with  $F_c = 2.58 * 1.17^{(T-10)/10} - 2.86$  (a;  $R^2 = 0.86$ , RMSE = 0.23) and analysis of the contributions of dew amounts in  $F_c$  with  $F_x = -0.82 * e^{10 * \text{dew}} + 0.18$  (b;  $R^2 = 0.1008$ , RMSE = 0.4219) and  $F_x = 4.07 * e^{-10 * \text{dew}} - 6.38$  (c;  $R^2 = 0.53$ , RMSE = 0.75), where  $F_x$  is defined as the unexplained part of  $F_c$  by the Q<sub>10</sub> model (from [12]).

dry river-bed, the erosion of soil surface, the muddy crust, and their dynamic changes may generate the spectral characteristics similar to saline-alkali soils and cause confusions of the spectrum. These bring technological difficulties in remote sensing of the dynamic changes of the soil salt content on time and spatial scales.

The spectral characteristics are also closely related to the surface morphology of saline-alkali soils, including the salt incrustation of different thickness and salt content, the loose soil structure with aggregated and crystalline salt, and the loose formation caused by wind erosion. Soil surface roughness of different surface morphology is different and the spectral reflectance characteristics become different [26]. These external interferences can affect the surface spectral information of soil surface texture and caused bigger errors in the retrieval of model parameters [27–29]. Other physical and chemical characteristics also affect the spectral characteristics of saline-alkali soils [30–32]. Human farming causes higher surface roughness because the soils are reconstructed and soil surface roughness is significantly increased. However, spatial and spectral resolution of the multispectral remote sensing are relatively low and it is difficult to differentiate the complex spectral characteristics of soil surface and to obtain the precise and quantitative results if we only use the soil spectral characteristics [33]. When the salt content is less than 10~15%, it is almost impossible to distinguish saline-alkali soils from other soils [34].

Hyperspectral images are feasible for the synchronization acquisition of spatial features, radiation information, and spectral characteristics. These images of higher spectral resolution can even reflect the subtle characteristics of landmark

spectrum. Quantitative analysis of the distribution of saline-alkali soils and their surface morphology becomes possible, reducing the interference from external environmental factors [35–38]. Hyperspectral remote sensing data improve the accuracy of classification of halophyte and the degrees of salinity/alkalinity [39, 40], which further cut down the subjective errors in remote sensing of the model parameters.

#### 4. Schemes for Remote Sensing

Quantitative mapping of the properties of global saline-alkali soils according to hyperspectral data (including soil salinity) is feasible. Exactly, some scientists have proved the feasibility on regional scales [41–43]. In addition, hyperspectral remote sensing can be provided for each pixel the information of high-quality (similar to the laboratory accuracy) and can accurately monitor the vegetation information (such as the growth and distribution of different types of vegetation). This allows a pretreatment of the vegetation-covered part in hyperspectral images, overcomes the interference of vegetation, and helps to indirectly infer the salinity and alkalinity of the soil according to the vegetation types [44–46], since the vegetation types reflect the ranges of soil salt content and soil pH. These preliminary illustrations present necessary theoretical basis for remote sensing of CO<sub>2</sub> absorption by saline-alkali soil on large scales.

Now we are going to design remote sensing schemes for CO<sub>2</sub> absorption by saline-alkali soil on the global scale. First, collect the representative soil samples for chemical, physical analysis, and the field and laboratory measurements

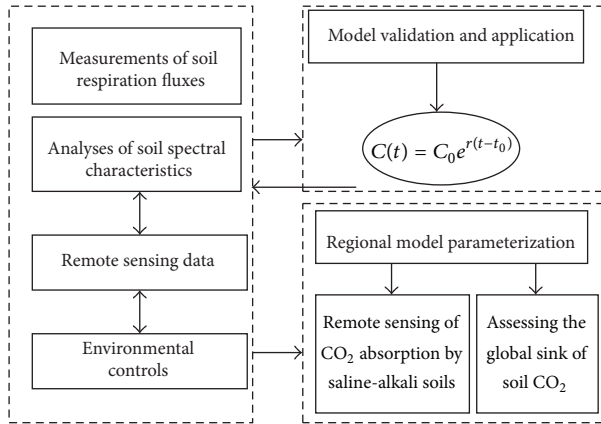


FIGURE 4: Remote sensing schemes for  $\text{CO}_2$  absorption by saline-alkali soil on large scales.

of the soil spectral characteristics. This helps to obtain the spectral information related to physical and chemical characteristics. The model parameters are determined by the sampling measurements of soil  $\text{CO}_2$  fluxes. Second, conduct the atmospheric correction of high reflectance spectrum image, the retrieval of soil surface reflectance, and the pretreatment of vegetation-covered areas. The retrieval of model parameters is implemented using multiple stepwise regression analyses. Finally, the model with the determined parameters is employed in remote sensing of  $\text{CO}_2$  absorption by saline-alkali soil on region scales and then integrated to the global scale. Sketch of the full scheme for quantitative remote sensing of  $\text{CO}_2$  absorption by saline-alkali soils on the global scales is presented in Figure 4.

Over the last three decades, the sources of remote sensing data became more abundant and the methods for retrieval became more sophisticated. Saline-alkali soils and other soils can be easily distinguished according to the spectral characteristics from the hyperspectral images when combined with the GIS assessment of the degrees of soil salinity and alkalinity. Soil salt content can also be accurately predicted by the standard reflectance spectrum, using the data-mining technologies (such as PLSR and ANN) [47]. Spectral reflectance of saline-alkali soils has been applied in studies on soil science, ecology, environmental science, biophysiology, ecology, and economics [48–51]. The scheme for retrieval of  $\text{CO}_2$  absorption by saline-alkali soil on the global scale seems feasible under the strong backgrounds. However, there are still some unresolved issues to be investigated for further reducing uncertainties in the retrieval as follows.

- (1) Visual interpretation remains as an important means of monitoring and analysis on saline-alkali soil and its dynamics [52]. But in fact, the imaging characteristics of saline-alkali soils can vary depending on the resolution and the image sensor at different times. Interpretation of saline-alkali soils should be done not only in accordance with their image features, but also in accordance with a comprehensive analysis of the geographical and landscape features of the saline-alkali soils [53–56].

(2) Remote sensing of  $\text{CO}_2$  absorption by saline-alkali soils deserves a better understanding of spectral reflectance of the different types of saline-alkali soils and the relationship between them and the degrees of soil salinity and alkalinity. This deserves the hyperspectral images of high spatial resolution, which is essentially significant to enhance the reliability of retrieval of model parameters. But the access of hyperspectral remote sensing data remains too expensive, especially, when the retrieval is considered on the global scale.

(3) Salts dissolution in the soil during the rainy seasons and salts migration due to the seasonal changes of land-cover changes will also cause interference in the extraction of information for saline-alkali soils. These will increase the difficulty of detecting dynamic changes in remote sensing data, which is partly because of the integrated effects of vegetation and soil types and other factors on spectral information of the pilot land farming. This can be resolved using the multitemporal image and by the adoption of different tillage.

Study on these issues will not only help us to distinguish different types of saline-alkali soils, but will also imply the comprehensive applications of multitemporal remote sensing data in zoning soil  $\text{CO}_2$  source or sink over arid and semiarid regions [15, 57–59]. In addition, the large-scale effort on measuring soil respiration fluxes in arid and semiarid ecosystems around the world must be organized for a reliable quantitative inversion of soil  $\text{CO}_2$  absorption. This is a laborious challenge and needs the common attention by the world scientific communities.

## 5. Conclusions

With the increases of the spectral resolution, the radiation resolution, the time resolution, and the spatial resolution of remote sensing data, retrieval of soil salt content becomes more active and researches on the mechanisms are prized. In particular, research on the applications of the hyperspectral remote sensing data on soil salinization and alkalinization has tremendous potential. Utilizing the hyperspectral remote sensing data, it becomes possible to accurately distinguish the special salt content in the soils (Figure 5). Remote sensing of  $\text{CO}_2$  absorption by saline-alkali soils is theoretical feasible. However, the spectroscopy studies on the saline-alkali soil are mainly restricted to monitor the salinity degree, the spatial scope, and the geographic distribution of saline-alkali soils, mainly using the multispectral remote sensing data (the hyperspectral remote sensing data were less employed because it is expensive). As a first attempt, this paper presented remote sensing scheme for  $\text{CO}_2$  absorption by saline-alkali soil on large scales. But the qualitative research of spectral reflectance properties of saline-alkali soils was less focused on  $\text{CO}_2$  absorption by saline-alkali soil, which is partly because of traditional ignoring of such absorption. There are still a series of unresolved issues to be further addressed before the remote sensing scheme is carried out.

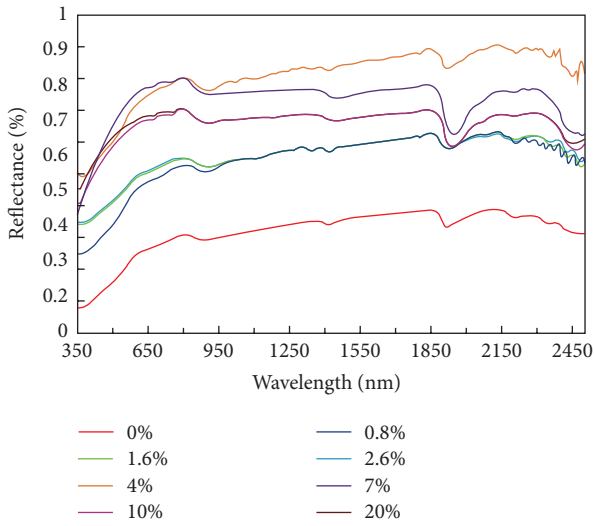


FIGURE 5: Reflectance of soils rich in  $\text{Na}_2\text{SO}_4$  with different salt content (adapted from [15]).

## Conflict of Interests

The authors declared that there is no conflict of interests regarding the publication of this paper.

## Acknowledgments

The author thanks the anonymous referees for their careful reading, very detailed comments, and many constructive suggestions which greatly improved the presentation. The research is supported by the CAS/SAFEA International Partnership Program for Creative Research Teams (Transects studies on the special ecological process in arid regions) and the NSFC-UNEP International-Cooperative Projects (no. 41361140361).

## References

- [1] Y. F. Yan, Z. E. Zhang, L. Zhang, and L. Zhang, "Influence of coal properties on the co-combustion characteristics of low-grade coal and city mud," *Global NEST Journal*, vol. 16, no. 2, pp. 330–339, 2014.
- [2] H. F. Tuo, "Energy and exergy-based working fluid selection for organic Rankine cycle recovering waste heat from high temperature solid oxide fuel cell and gas turbine hybrid systems," *International Journal of Energy Research*, vol. 37, no. 4, pp. 1831–1841, 2013.
- [3] H. F. Tuo and P. S. Hrnjak, "Periodical reverse flow and boiling fluctuations in a microchannel evaporator of an air-conditioning system," *International Journal of Refrigeration*, vol. 36, no. 4, pp. 1263–1275, 2013.
- [4] K. Sreenivas, L. Venkataraman, and P. V. N. Rao, "Dielectric properties of salt-affected soils," *International Journal of Remote Sensing*, vol. 16, no. 4, pp. 641–649, 1995.
- [5] G. R. Taylor, A. H. Mah, F. A. Kruse, K. S. Kierein-Young, R. D. Hewson, and B. A. Bennett, "Characterization of saline soils using airborne radar imagery," *Remote Sensing of Environment*, vol. 57, no. 3, pp. 127–142, 1996.
- [6] B. R. M. Rao, "Spectral behaviour of salt-affected soils," *International Journal of Remote Sensing*, vol. 16, no. 12, pp. 2125–2136, 1995.
- [7] R. Stone, "Ecosystems: have desert researchers discovered a hidden loop in the carbon cycle?" *Science*, vol. 320, no. 5882, pp. 1409–1410, 2008.
- [8] J. X. Xie, Y. Li, C. X. Zhai, C. H. Li, and Z. D. Lan, " $\text{CO}_2$  absorption by alkaline soils and its implication to the global carbon cycle," *Environmental Geology*, vol. 56, no. 5, pp. 953–961, 2009.
- [9] E. L. Yates, A. M. Detweiler, L. T. Iraci et al., "Assessing the role of alkaline soils on the carbon cycle at a playa site," *Environmental Earth Sciences*, vol. 70, no. 3, pp. 1047–1056, 2013.
- [10] J. Ma, Z. Y. Wang, B. A. Stevenson, X. J. Zhang, and Y. Li, "An inorganic  $\text{CO}_2$  diffusion and dissolution process explains negative  $\text{CO}_2$  fluxes in saline/alkaline soils," *Scientific Reports*, vol. 3, article 2025, 2013.
- [11] W. F. Wang, X. Chen, G. P. Luo, and L. H. Li, "Modeling the contribution of abiotic exchange to  $\text{CO}_2$  flux in alkaline soils of arid areas," *Journal of Arid Land*, vol. 6, no. 1, pp. 27–36, 2014.
- [12] X. Chen and W. F. Wang, "On the apparent  $\text{CO}_2$  absorption by alkaline soils," *Biogeosciences Discussions*, vol. 11, no. 2, pp. 2665–2683, 2014.
- [13] X. Chen, W. F. Wang, G. P. Luo, and H. Ye, "Can soil respiration estimate neglect the contribution of abiotic exchange?" *Journal of Arid Land*, vol. 6, no. 2, pp. 129–135, 2014.
- [14] X. Chen, W. F. Wang, G. P. Luo, L. H. Li, and Y. Li, "Time lag between carbon dioxide influx to and efflux from bare saline-alkali soil detected by the explicit partitioning and reconciling of soil  $\text{CO}_2$  flux," *Stochastic Environmental Research and Risk Assessment*, vol. 27, no. 3, pp. 737–745, 2013.
- [15] Z. Pu, *Quantitive retrieval of saline soil salt content in arid region using hyperspectral data -take the Sangong river watershed as a case [Ph.D. thesis]*, Xinjiang Institute of Ecology and Geography, Chinese Academy of Sciences, Xinjiang, China, 2010.
- [16] G. I. Metternicht and J. A. Zinck, "Remote sensing of soil salinity: potentials and constraints," *Remote Sensing of Environment*, vol. 85, no. 1, pp. 1–20, 2003.
- [17] R. L. Dehaan and G. R. Taylor, "Field-derived spectra of salinized soils and vegetation as indicators of irrigation-induced soil salinization," *Remote Sensing of Environment*, vol. 80, no. 3, pp. 406–417, 2002.
- [18] F. M. Howari, *Reflectance spectra of common salts in arid soils (320–2500 nm): application of remote sensing [Ph.D. thesis]*, University of Texas at El Paso, El Paso, Tex, USA, 2001.
- [19] F. M. Howari, P. C. Goodell, and S. Miyamoto, "Spectral properties of salt crusts formed on saline soils," *Journal of Environmental Quality*, vol. 31, no. 5, pp. 1453–1461, 2002.
- [20] F. M. Howari, "Chemical and environmental implications of visible and near-infrared spectral features of salt crusts formed from different brines," *Annali di Chimica*, vol. 94, no. 4, pp. 315–323, 2004.
- [21] F. Csillag, L. Pásztor, and L. L. Biehl, "Spectral band selection for the characterization of salinity status of soils," *Remote Sensing of Environment*, vol. 43, no. 3, pp. 231–242, 1993.
- [22] E. Ben-Dor, "Quantitative remote sensing of soil properties," *Advances in Agronomy*, vol. 75, pp. 173–243, 2002.
- [23] G. Metternicht and J. A. Zinck, "Spatial discrimination of salt-and sodium-affected soil surfaces," *International Journal of Remote Sensing*, vol. 18, no. 12, pp. 2571–2586, 1997.

- [24] G. I. Metternicht, "Analysing the relationship between ground-based reflectance and environmental indicators of salinity processes in the Cochabamba valleys (Bolivia)," *International Journal of Ecology and Environmental Sciences*, vol. 24, no. 4, pp. 359–370, 1998.
- [25] C. L. Wiegand, J. D. Rhoades, D. E. Escobar, and J. H. Everitt, "Photographic and videographic observations for determining and mapping the response of cotton to soil salinity," *Remote Sensing of Environment*, vol. 49, no. 3, pp. 212–223, 1994.
- [26] J. Farifteh, A. Farshad, and R. J. George, "Assessing salt-affected soils using remote sensing, solute modelling, and geophysics," *Geoderma*, vol. 130, no. 3-4, pp. 191–206, 2006.
- [27] S. M. de Jong, "The analysis of spectroscopic data to map soil types and soil crusts of Mediterranean eroded soils," *Soil Technology*, vol. 5, no. 3, pp. 199–211, 1992.
- [28] N. Goldshleger, E. Ben-Dor, Y. Benyamin, M. Agassi, and D. G. Blumberg, "Characterization of soil's structural crust by spectral reflectance in the SWIR region (1.2–2.5  $\mu\text{m}$ )," *Terra Nova*, vol. 13, no. 1, pp. 12–17, 2001.
- [29] G. I. Metternicht and J. A. Zinck, "Modelling salinity-alkalinity classes for mapping salt-affected topsoils in the semiarid valleys of Cochabamba (Bolivia)," *ITC Journal*, no. 2, pp. 125–135, 1996.
- [30] G. R. Hunt and J. W. Salisbury, "Visible and near infrared spectra of minerals and rocks. II. Carbonates," *Modern Geology*, no. 2, pp. 23–30, 1971.
- [31] E. Ben-Dor, J. R. Irons, and G. F. Epema, "Soil reflectance," in *Remote Sensing for the Earth Sciences: Manual of Remote Sensing*, N. Rencz, Ed., pp. 111–188, John Wiley & Sons, New York, NY, USA, 1999.
- [32] J. R. Irons, R. A. Weismiller, and G. W. Petersen, "Soil reflectance," in *Theory and Applications of Optical Remote Sensing*, G. Asrar, Ed., Wiley Series of Remote Sensing, pp. 66–106, John Wiley & Sons, New York, NY, USA, 1989.
- [33] R. Dehaan and G. R. Taylor, "Image-derived spectral end-members as indicators of salinisation," *International Journal of Remote Sensing*, vol. 24, no. 4, pp. 775–794, 2003.
- [34] B. Mougenot, M. Pouget, and G. F. Epema, "Remote sensing of salt affected soils," *Remote Sensing Reviews*, vol. 7, no. 3-4, pp. 241–259, 1993.
- [35] F. M. Howari, "Comparison of spectral matching algorithms for identifying natural salt crusts," *Journal of Applied Spectroscopy*, vol. 70, no. 5, pp. 782–787, 2003.
- [36] F. M. Howari, "The use of remote sensing data to extract information from agricultural land with emphasis on soil salinity," *Australian Journal of Soil Research*, vol. 41, no. 7, pp. 1243–1253, 2003.
- [37] F. M. Howari, "Chemical and environmental implications of visible and near-infrared spectral features of salt crusts formed from different brines," *Annali di Chimica*, vol. 94, no. 4, pp. 315–323, 2004.
- [38] A. F. Goetz, G. Vane, J. E. Solomon, and B. N. Rock, "Imaging spectrometry for earth remote sensing," *Science*, vol. 228, no. 4704, pp. 1147–1153, 1985.
- [39] G. R. Taylor, A. H. Mah, F. A. Kruse, K. S. Kierein-Young, R. D. Hewson, and B. A. Bennett, "Characterization of saline soils using airborne radar imagery," *Remote Sensing of Environment*, vol. 57, no. 3, pp. 127–142, 1996.
- [40] T. Schmid, M. Koch, J. Gumuzzio, and P. M. Mather, "A spectral library for a semi-arid wetland and its application to studies of wetland degradation using hyperspectral and multispectral data," *International Journal of Remote Sensing*, vol. 25, no. 13, pp. 2485–2496, 2004.
- [41] E. Ben-Dor, K. Patkin, A. Banin, and A. Karnieli, "Mapping of several soil properties using DAIS-7915 hyperspectral scanner data—a case study over soils in Israel," *International Journal of Remote Sensing*, vol. 23, no. 6, pp. 1043–1062, 2002.
- [42] Y. Weng, P. Gong, and Z. Zhu, "Soil sail content estimation in the yellow river delta with satellite hyperspectral data," *Canadian Journal of Remote Sensing*, vol. 34, no. 3, pp. 259–270, 2008.
- [43] Y. L. Weng, P. Gong, and Z. L. Zhu, "Reflectance spectroscopy for the assessment of soil salt content in soils of the yellow river delta of China," *International Journal of Remote Sensing*, vol. 29, no. 19, pp. 5511–5531, 2008.
- [44] E. N. Bui and B. L. Henderson, "Vegetation indicators of salinity in northern Queensland," *Austral Ecology*, vol. 28, no. 5, pp. 539–552, 2003.
- [45] F. Al-Khaier, *Soil salinity detection using satellite remote sensing—International institute for Geo-information science and earth observation [Ph.D. thesis]*, Enschede, The Netherlands, 2003.
- [46] D. Wang, C. Wilson, and M. C. Shannon, "Interpretation of salinity and irrigation effects on soybean canopy reflectance in visible and near-infrared spectrum domain," *International Journal of Remote Sensing*, vol. 23, no. 5, pp. 811–824, 2002.
- [47] J. Farifteh, F. van der Meer, C. Atzberger, and E. J. M. Carranza, "Quantitative analysis of salt-affected soil reflectance spectra: a comparison of two adaptive methods (PLSR and ANN)," *Remote Sensing of Environment*, vol. 110, no. 1, pp. 59–78, 2007.
- [48] G. R. Cramer, "Differential effects of salinity on leaf elongation kinetics of three grass species," *Plant and Soil*, vol. 253, no. 1, pp. 233–244, 2003.
- [49] L. K. Smedema and K. Shiati, "Irrigation and salinity: a perspective review of the salinity hazards of irrigation development in the arid zone," *Irrigation and Drainage Systems*, vol. 16, no. 2, pp. 161–174, 2002.
- [50] C. J. Clarke, R. W. Bell, R. J. Hobbs, and R. J. George, "Incorporating geological effects in modeling of revegetation strategies for salt-affected landscapes," *Environmental Management*, vol. 24, no. 1, pp. 99–109, 1999.
- [51] D. Wichelns, "An economic model of waterlogging and salinization in arid regions," *Ecological Economics*, vol. 30, no. 3, pp. 475–491, 1999.
- [52] T. G. Sommerfeldt, M. D. Thompson, and N. A. Prout, "Delineation and mapping of soil salinity in southern Alberta from Landsat data," *Canadian Journal of Remote Sensing*, vol. 10, no. 2, pp. 104–110, 1984.
- [53] R. C. Sharma and G. P. Bhargava, "Landsat imagery for mapping saline soils and wet lands in north-west India," *International Journal of Remote Sensing*, vol. 9, no. 1, pp. 39–44, 1988.
- [54] R. S. Dwivedi and B. R. M. Rao, "The selection of the best possible Landsat TM band combination for delineating salt-affected soils," *International Journal of Remote Sensing*, vol. 13, no. 11, pp. 2051–2058, 1992.
- [55] N. K. Kalra and D. C. Joshi, "Potentiality of Landsat, SPOT and IRS satellite imagery, for recognition of salt affected soils in Indian Arid Zone," *International Journal of Remote Sensing*, vol. 17, no. 15, pp. 3001–3014, 1996.
- [56] B. R. M. Rao, "Mapping the magnitude of sodicity in part of the Indo-Gangetic plains of Uttar Pradesh, northern India using Landsat-TM data," *International Journal of Remote Sensing*, vol. 12, no. 3, pp. 419–425, 1991.
- [57] B. R. M. Rao, R. S. Dwivedi, K. Sreenivas et al., "An inventory of salt-affected soils and waterlogged areas in the Nagarjunsagar Canal Command Area of southern India, using space-borne

- multippectral data," *Land Degradation & Development*, vol. 9, no. 4, pp. 357–367, 1998.
- [58] R. S. Dwivedi, K. Sreenivas, and K. V. Ramana, "Inventory of salt-affected soils and waterlogged areas: a remote sensing approach," *International Journal of Remote Sensing*, vol. 20, no. 8, pp. 1589–1599, 1999.
- [59] I. McGowen and S. Mallyon, "Detection of dryland salinity using single and multitemporal landsat imagery," in *Proceedings of the 8th Australasian Remote Sensing Conference*, pp. 26–34, Canberra, Australia, 1996.